Contents

Figures

Tables

9.0 Ground Motion Characterization

This chapter presents the models developed to characterize median ground motions, aleatory variability (sigma), and the epistemic uncertainty in each, both for shallow crustal and subduction earthquakes. The development of the models for the calculation of the seismic hazard at the baserock horizon is presented in Sections 9.2 through 9.5. Presented also are models for the Saddle Mountain basalt/interbed sequence to be used in site response analyses (Section 9.6) and proposed vertical-to-horizontal (V/H) ratios for response spectral ordinates (Section 9.7). The chapter begins with an overview of the overall approach adopted for the development of the GMC model for the Hanford Site, which draws on the databases presented and evaluated in Chapter 7.0.

9.1 GMC Model: Overview and Methodology

In this section, the boundary conditions defined for the definition of the GMC model are presented, together with an overview of the approaches adopted to develop the complete suite of deliverables needed for the subsequent calculation of surface motions at facility locations on the Hanford Site.

9.1.1 Reference Baserock Model and Site Response Interface

As previously explained in Chapters 1.0 and 7.0, the ultimate goal of the Hanford sitewide PSHA is to enable the characterization of the ground-shaking hazard at the location of several surface facilities on the Hanford Site. At the time of initiating the project the near-surface layers were only fully characterized in term of their dynamic properties at the WTP (Waste Treatment Plant) site (Rohay and Brouns 2007)—and to an extent also at the site of the Columbia Generating Station (formerly WPN-2) (Bechtel 2013)—so it was not possible to produce surface motions at all of the five sites selected for the hazard calculations (Figure 1.1). The approach adopted, therefore, was to limit the scope of the PSHA project to the characterization of the ground-shaking hazard at a specified baserock elevation, which would then provide the input into subsequent site response calculations at the facility locations. The characterization of the near-surface deposits and execution of the site response analyses are outside the scope of the PSHA project and responsibility for these tasks was left with the project sponsors. However, the GMC Technical Integration (TI) Team was charged to provide guidance about how the site response analyses should be conducted in terms of the characterization of variability and uncertainty to ensure both that uncertainties are correctly accounted for, and also that there is no double counting of any uncertainties.

For reasons that are explained in Section 7.2.5, the baserock elevation was selected as being the top of the Wanapum basalts (minus the ~4-m flowtop of the uppermost Lolo flow), which is encountered at depths of between 332 and 446 m at the hazard calculation Sites A−E. This decision means that the subsequent site response calculations are to be performed for much thicker columns than would have been the case had the top of the Saddle Mountains basalts (SMBs) been selected as the reference baserock: the suprabasalt sediments have thicknesses ranging from 59 to 156 m at the reference locations for the hazard calculations. As a consequence, the GMC TI Team assumed responsibility for providing the full characterization of the stacks above the baserock elevation to the top of the basalts (essentially the layers of SMBs together with the Ellensburg Formation sedimentary interbeds) required for the site response analyses. This includes layer thicknesses, densities, shear-wave velocities and low-strain damping, in addition to stiffness degradation and nonlinear damping curves for the sediment interbeds (Section 9.6.3).

These profiles are presented in Section 9.6. Together with the profiles for the stacks and the randomization of the dynamic properties, the GMC TI Team is providing guidance on how uncertainty in the suprabasalt sediments should be modeled and how the baserock hazard should be convolved with the site amplification functions calculated for the combined column of SMB stack plus overlying sediments. The GMC TI Team is recommending convolution following Approach 3 (McGuire et al. 2001) as explained in Chapter 10.0; a fully worked example of this convolution is presented in Appendix K.

There is a point regarding the treatment of aleatory variability with respect to the interface between the baserock hazard and the site response analyses that is worthy of special note in closing this section. Because uncertainty is modeled in both the V_S-kappa adjustments to the baserock conditions (Section 9.3) and in the randomizations of the profiles for the site response calculations (Section 9.6.5), the repeatable component of the site variability is removed from the models for aleatory variability in the ground motion prediction to avoid double counting, using the concept of single-station sigma (Section 9.5). However, at longer response periods, the GMC TI Team concluded that the single-station sigma could not be fully invoked for two reasons, namely the lack of variability in the site response calculations at long periods (Section 9.6.5) and the possible presence of basin effects at intermediate periods (Section 7.6.3). Because both of these factors are related to the behavior of layers above the baserock elevation, it was not considered appropriate to capture their effect by the use of ergodic sigma in the baserock for these period ranges. Rather, the effective variability due to the increase above single-station sigma is estimated at the relevant periods and then specified as a minimum level of variability to be associated with the site amplification factors (Section 9.6.6). As is explained in Section 9.6.6, it is not recommended that this be achieved through inflated variability in the dynamic properties of the site response models, but rather that if these do not produce sufficient variability in the resulting amplification factors, that the latter be increased to ensure sufficient variability is included to account for the effects noted above.

9.1.2 Seismic Sources for Which Ground Motion Predictions Are Required

In developing the GMC model, it is important to ensure that the ground motion prediction equations deployed on the logic-tree branches account for the range earthquake characteristics defined by the SSC model (Chapter 8.0). This means that the prediction equations should be well calibrated for the ranges of predictor variables or can be adjusted to match these ranges, or else that the additional uncertainty in the predictions is accounted for in the GMC logic tree.

The seismic sources in the SSC model can effectively be grouped into three categories:

- shallow crustal earthquakes (largest magnitude: **M** 7.85)
- subduction interface earthquakes (largest magnitude: **M** 9.4)
- subduction slab earthquakes (largest magnitude: **M** 7.5)

The largest values of maximum or characteristic magnitudes in the SSC model are indicated in the list above. The hazard calculations are performed using a M_{min} of **M** 5.0, so the models need to be applicable at this magnitude, although this holds true more for the crustal than the subduction earthquakes.

In terms of distances, the area sources (Figure 8.1) extend out to about 200 km from the hazard location points. The zone that hosts the Hanford Site (Yakima Fold and Thrust Belt [YFTB]) allows for the occurrence of earthquakes effectively below each of the five selected locations at which seismic hazard is calculated. Most of the shallow crustal fault sources (Figure 8.2) are located at distances of a

few to tens of kilometers from the hazard calculation sites. The Seattle fault source, which is the most distant shallow crustal source included in the SSC model, is located about 200 km to the northwest. For the subduction sources (Figure 8.8), the slab earthquakes are located at about 200 km from the Hanford Site and the interface earthquakes at about 300 km.

Fault ruptures within the area sources may be reverse, strike-slip, or normal, whereas the fault sources are modeled as generating reverse, reverse-oblique, and strike-slip ruptures. The maximum seismogenic depths for both area and fault sources range from 13−20 km. Moderate-to-large earthquakes on shallow dipping ruptures confined entirely within the upper Columbia River Basalts (CRBs) are not included in the SSC model as an explicit source, but the GMC TI Team does give consideration to the fact that ruptures that extend close to the surface will potentially include high stress drop regions—due to the presence of the thick, high-velocity, CRB layer—at rather shallow depths. This last feature is captured by setting a minimum value on the depth-to-top-of-rupture parameter, Z_{TOR}, in the selected ground motion prediction equation (GMPE), but only for the explicit term in this parameter rather than the calculation of rupture distances; in other words, this constraint on Z_{TOR} is applied in the third term of Equation (9.1) (in Section 9.2.1) but not in the final term.

9.1.3 Selection of "Scaled Backbone GMPE" Approach for Baserock Motions

In Section 7.4, currently available GMPEs were reviewed and evaluated in terms of selection criteria specific to the application in the Hanford PSHA. The outcome of this evaluation was a single GMPE for subduction earthquakes and a very small number of GMPEs for crustal earthquakes. The selection of a single GMPE for subduction earthquakes reflects the experience of the Senior Seismic Hazard Analysis Committee (SSHAC) Level 3 PSHA conducted for hydro-electric dams operated by BC Hydro in British Columbia (BC Hydro 2012), which concluded that a new GMPE needed to be developed because none of the existing subduction GMPEs were deemed suitable. A modified version of this same equation has been developed specifically for the Hanford PSHA (Section 9.2.3). For the shallow crustal seismic sources, the hazard is dominated by reverse and reverse-oblique faulting earthquakes occurring on faults with a wide range of dips. The GMC TI Team considered only four of the Next-Generation Attenuation (NGA)-West2 models to be suitable for assessing earthquake ground motions from these types of earthquakes. A small number of other crustal GMPEs were judged to be fit for use in comparisons to check the range of predicted median motions.

With so few equations available for both types of seismic source, it is clear that the center, body, and range of possible median ground motions from potential future earthquakes that may affect the Hanford Site could not be captured simply from the distribution of median predictions from these GMPEs. Therefore, the only way to develop a sufficiently broad distribution of median predictions is to generate additional equations through appropriate adjustments and scaling of these selected GMPEs. Such an approach is not an innovation of this project—although there are features of this specific application that are innovative—and there are numerous examples of such an approach from PSHA practice (Bommer 2012; Atkinson et al. 2014). Numerous examples of a scaled backbone approach can be encountered in the development of ground motion models for PSHA applications in the Central and Eastern United States (CEUS), including Toro et al. (1997) and Electric Power Research Institute (EPRI 2004, 2013a); it is noteworthy that the latter two models have been accepted by the NRC in license applications and in responses to the 50.54(f) letter (NRC 2012). In developing the GMC logic tree for seismic hazard mapping, Petersen et al. (2008) included additional branches that carried scaled versions of the three

NGA-West2 GMPEs selected for the PSHA in order to ensure adequate capture of epistemic uncertainty. Atkinson and Adams (2013) used GMC logic trees for crustal earthquakes in active and stable regions, and also for subduction earthquakes, in which the upper and lower branches carried models that are scaled versions of a central "backbone" model. In the SSHAC Level 3 PSHA for the Thyspunt nuclear site in South Africa (Bommer et al. 2014), the median GMC logic tree was developed by first transforming three selected GMPEs into nine new equations through the application of three sets of host-to-target V_S-kappa adjustment (capturing the uncertainty in both host and target values); these were then translated into 36 new equations through the application of four scaling factors representing uncertainty in host-to-target differences in stress drops.

The approach adopted for crustal GMPEs in the Hanford project is comparable to that used for Thyspunt except that instead of using three different GMPEs as separate backbones, the backbone itself was developed from a small number of equations, and additional branches were generated to capture the inherent epistemic uncertainty, including uncertainty in magnitude scaling (Section 9.4.2). Additional logic-tree branches were obtained by the application of multiple V_S-kappa adjustments (Section 9.3.3), and then these were transformed into a larger number of equations through the application of factors representing uncertainty in host- to target-region scaling.

For the subduction GMPE, the full range of models was obtained through branches for uncertainty in the large-magnitude scaling and for host- to target-region differences in both scaling and attenuation. Thereafter, the application of scaling factors for uncertainty in the host-to-target adjustments to the baserock condition at the Hanford Site created additional branches.

One of the advantages of this scaled backbone GMPE approach, as applied to both crustal and subduction earthquakes in the Hanford PSHA, is that the models on the branches of the GMC logic tree become mutually exclusive and, provided that they have been scaled sufficiently to capture the full range of epistemic uncertainty, collectively exhaustive. In this case, the treatment of the weights on the branches as probabilities becomes uncontroversial (Abrahamson and Bommer 2005; McGuire et al. 2005; Musson 2005).

9.1.4 Overview of GMC Models and Deliverables

The GMC model consists essentially of two logic trees, one for ground motions from crustal earthquakes and the other for motions caused by subduction earthquakes. In both cases, GMC models apply to the baserock elevation at the top of the Wanapum basalts (WBs), which have a shear-wave velocity, V_S, very close to 3,000 m/s. For both the crustal and subduction logic trees, there are branches for the median motions and also for the associated aleatory variability (sigma). The GMC model is defined by suites of equations with coefficients at 20 response frequencies, which were selected in agreement with the project sponsors (Table 9.1). All of the information in the GMC logic tree is presented in the HID, which is included as Appendix D of this report.

The other deliverable of the GMC model is the suite of models of the SMB stacks for use in subsequent site response analyses. These models, which satisfy the requirements of both sponsors determined through exchanges between the GMC TI Team and consultants Dr. Carl Costantino (on behalf of DOE) and Dr. Farhang Ostadan (on behalf of Energy Northwest) are summarized in Section 9.6. In addition, the GMC TI Team has formulated guidelines for the execution of the site response analyses and the convolution of the baserock hazard and the calculated site amplification factors. These instructions are listed in Section 10.5 and illustrated through a fully worked example in Appendix K.

The final element of the GMC deliverables is a recommendation for V/H response spectral ratios that may be used to transform the horizontal motions at the surface to the vertical component. These recommendations are presented in Section 9.7.

Table 9.1. Selected response periods for which the GMC model is developed. Values in bold are those specified in the NRC's 50.54(f) letter (NRC 2012).

Period (s)	Frequency (Hz)	Period (s)	Frequency (Hz)
0.01	**100**	**0.4**	**2.5**
0.02	50	0.5	2.0
0.03	33.3	0.75	1.33
0.04	**25**	**1.0**	**1.0**
0.05	20	1.5	0.67
0.075	13.3	**2.0**	**0.5**
0.1	**10**	3.0	0.33
0.15	6.67	5.0	0.2
0.2	**5.0**	7.5	0.13
0.3	3.3	10.0	0.1

9.2 Selection and Development of Backbone GMPEs

In light of the review and evaluation of currently available GMPEs that were presented in Section 7.4, the GMC TI Team began the construction of the GMC logic tree for median motions in the reference baserock by selecting appropriate GMPEs to be used as backbones. The selection of the backbone GMPEs for both crustal and subduction earthquakes is described in the following sections, together with parameter settings and adjustments to the models for this specific application.

9.2.1 GMPEs for Crustal Earthquakes

The TI Team adopted a set of backbone selection criteria for crustal GMPEs that represent a middle ground between the relatively lenient criteria of Cotton et al. (2006) and the somewhat stricter criteria of Bommer et al. (2010), supplemented by project-specific criteria that are necessitated by the characteristics of the seismic sources that contribute significantly to the hazard at the Hanford Site, and project needs regarding response frequencies of interest and the need for explicit inclusion of V_{S30} as a predictor variable to facilitate site-specific adjustments (see Sections 9.1.2 and 9.1.4 above). The development and application of these criteria are documented in Section 7.4.1.1. The result of this selection process is a set of eight GMPEs, namely AC10, ASB14, ASK14, BI14, BSSA14, CB14, CY14, and DE14 (see Table 7.26 for the names corresponding to these abbreviations). Models that use R_{jb} were later dropped because of concerns about the inability of these GMPEs to capture hanging-wall effects accurately, leaving only ASK14, CB14, and CY14 (i.e., three NGA-East GMPEs that use rupture distance).

To investigate the amplitude and spectral shapes of these selected GMPEs for the parameter range of interest, seven of them are plotted in Figure 9.1 through Figure 9.7 for the seven representative scenarios with parameters given in Table 9.2 (some of the quantities used in this table are defined following Equation 9.1). These scenarios were defined by the GMC TI Team in consultation with SSC TI Team Lead.

Table 9.2. Scenarios used for comparison of the selected GMPEs.

Scenario	M	R_{rup} (km)	R_{jb} (km)	Dip (deg)	Z_{TOR} (km)	Rupture Width (km)	Style of Faulting	HW/FW
Saddle Mountains Scenario 1	7.50	18.89	0.00	40	0	20	Reverse	HW
Saddle Mountains Scenario 2	7.50	27.61	14.83	70	0	20	Reverse	HW
Umtanum Ridge Scenario 1	7.25	4.43	0.00	40	0	20	Reverse	HW
Umtanum Ridge Scenario 2	7.25	6.79	0.00	80	0	20	Reverse	HW
Rattlesnake Mountain Scenario	7.00	11.80	11.80	50	0	20	Reverse	FW
Random Scenario 1	5.50	7.07	5.00	45	2	3	Reverse	HW
Random Scenario 2	5.50	5.00	5.00	45	2	3	Reverse	FW

HW = hanging wall; FW = footwall.

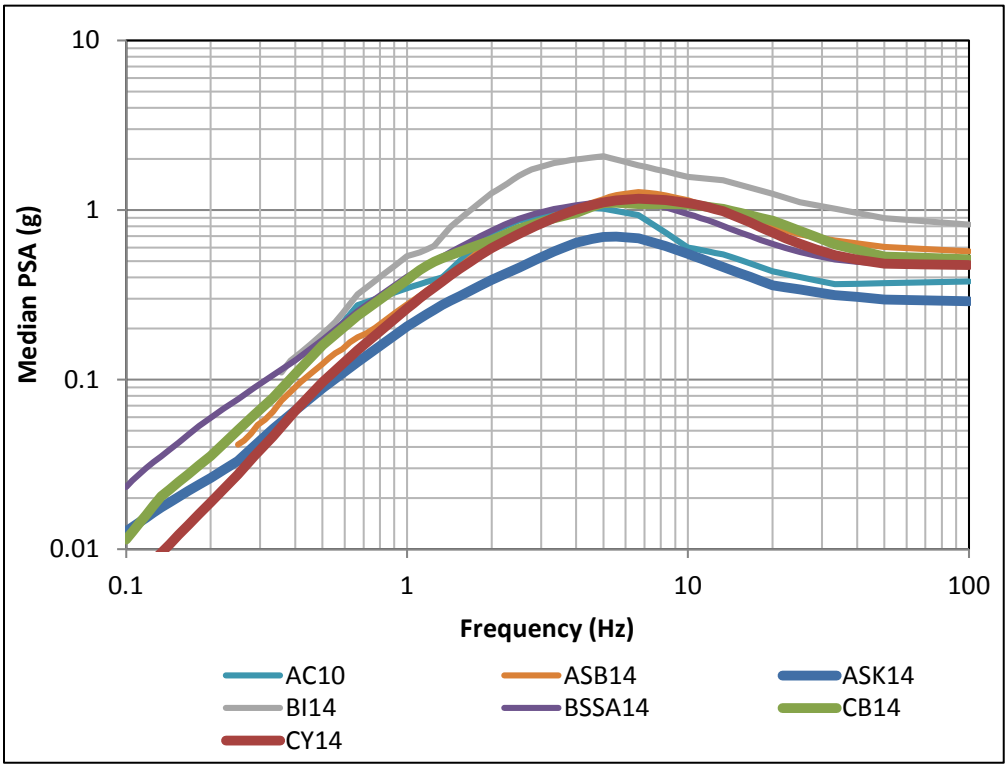

Figure 9.1. Comparison of the selected GMPEs for Saddle Mountains Scenario 1: $M_W = 7.5$, $R_{rup} = 18.89$ km, $R_{jb} = 0$, Dip = 40, $Z_{TOR} = 0$, Width = 20 km, Reverse, HW.

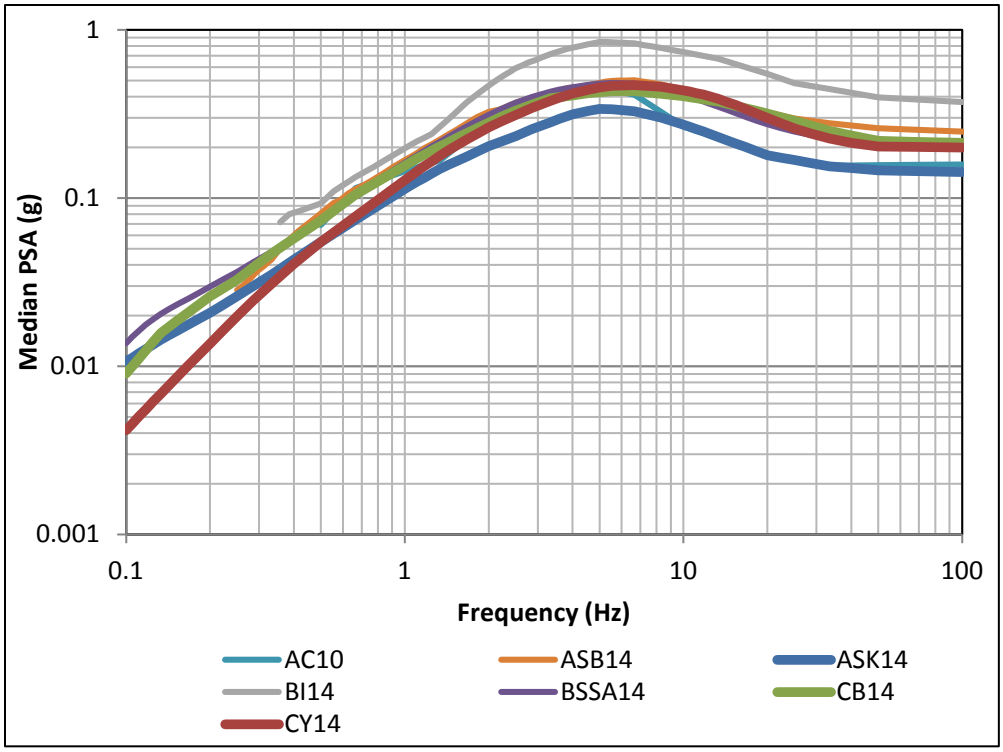

Figure 9.2. Comparison of the selected GMPEs for Saddle Mountains Scenario 2: $M_W = 7.5$, $R_{rup} = 27.61$ km, $R_{jb} = 14.83$ km, Dip = 70, $Z_{TOR} = 0$, Width = 20 km, Reverse, HW.

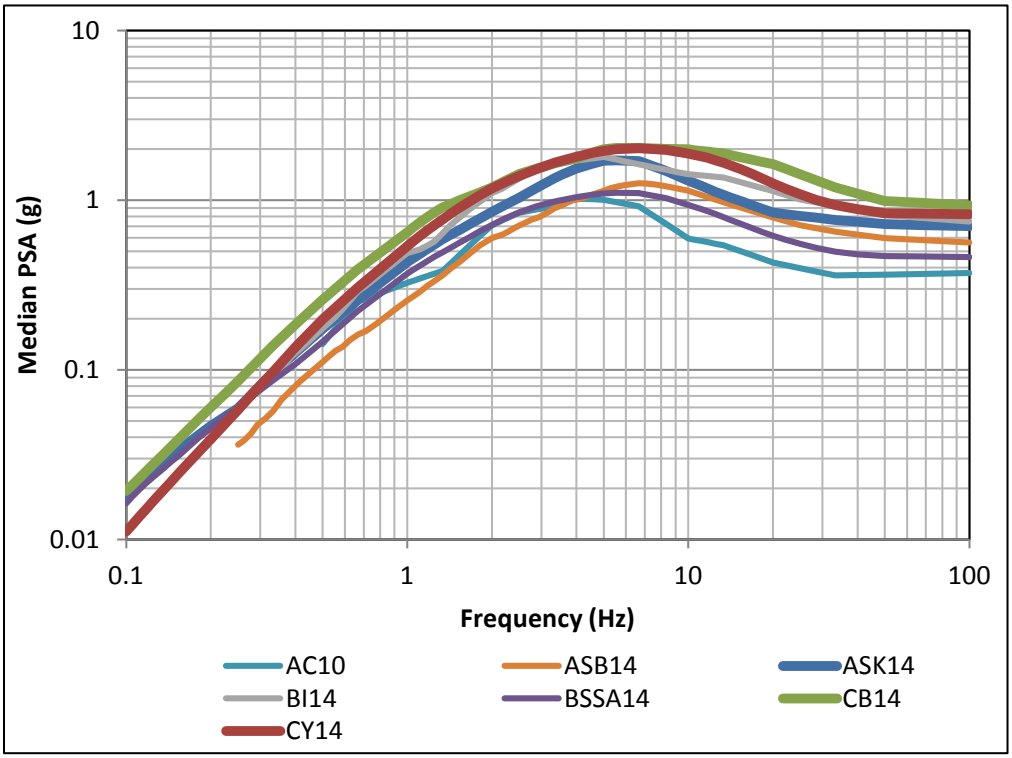

Figure 9.3. Comparison of the selected GMPEs for Umtanum Ridge Scenario 1: $M_W = 7.25$, $R_{rup} = 4.43$ km, $R_{jb} = 0$, Dip = 40, $Z_{TOR} = 0$, Width = 20 km, Reverse, HW.

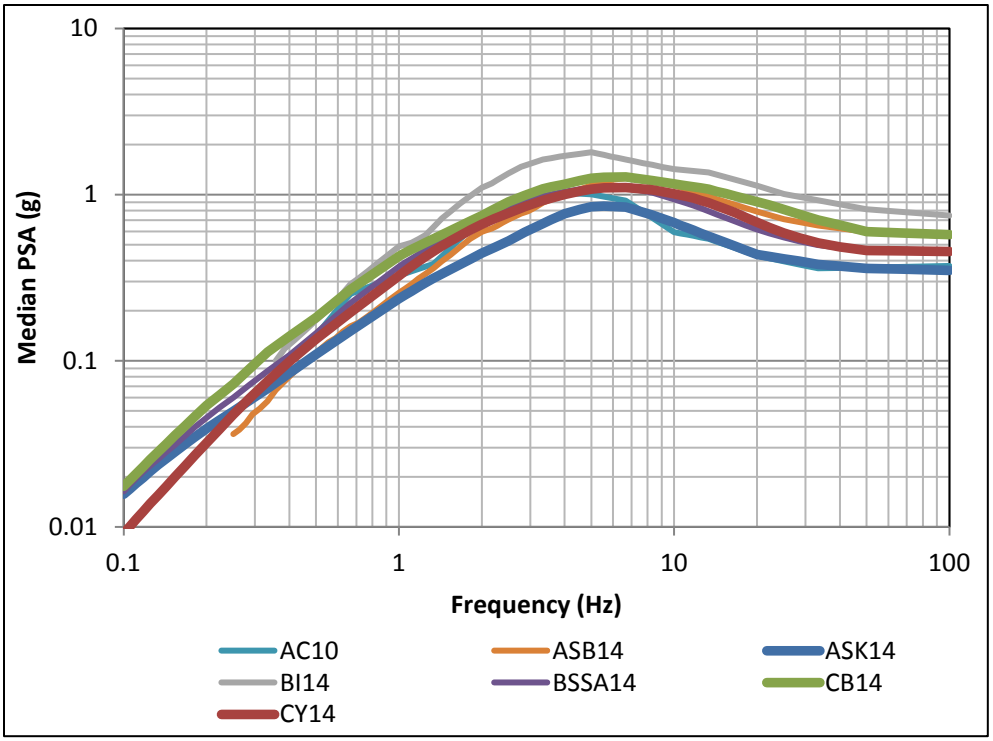

Figure 9.4. Comparison of the selected GMPEs for Umtanum Ridge Scenario 2: $M_W = 7.25$, $R_{rup} = 6.79$ km, $R_{jb} = 0$, Dip = 80, $Z_{TOR} = 0$, Width = 20 km, Reverse, HW.

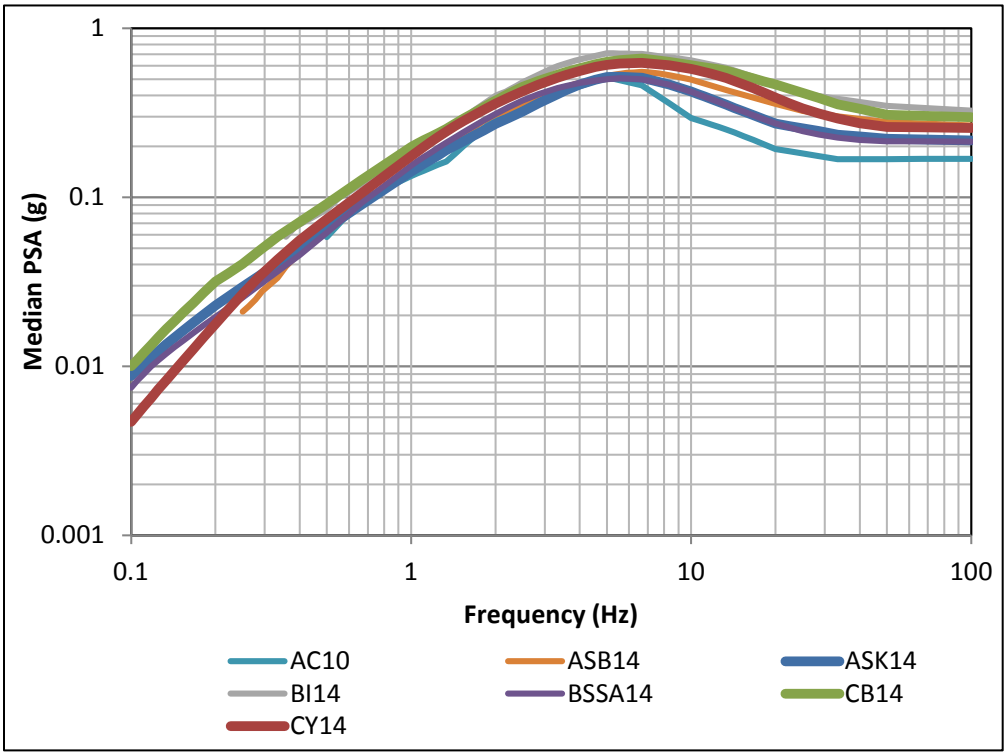

Figure 9.5. Comparison of the selected GMPEs for Rattlesnake Mountain Scenario: $M_W = 7$, $R_{rup} = 11.8$ km, $R_{jb} = 11.8$ km, Dip = 50, $Z_{TOR} = 0$, Width = 20 km, Reverse, FW.

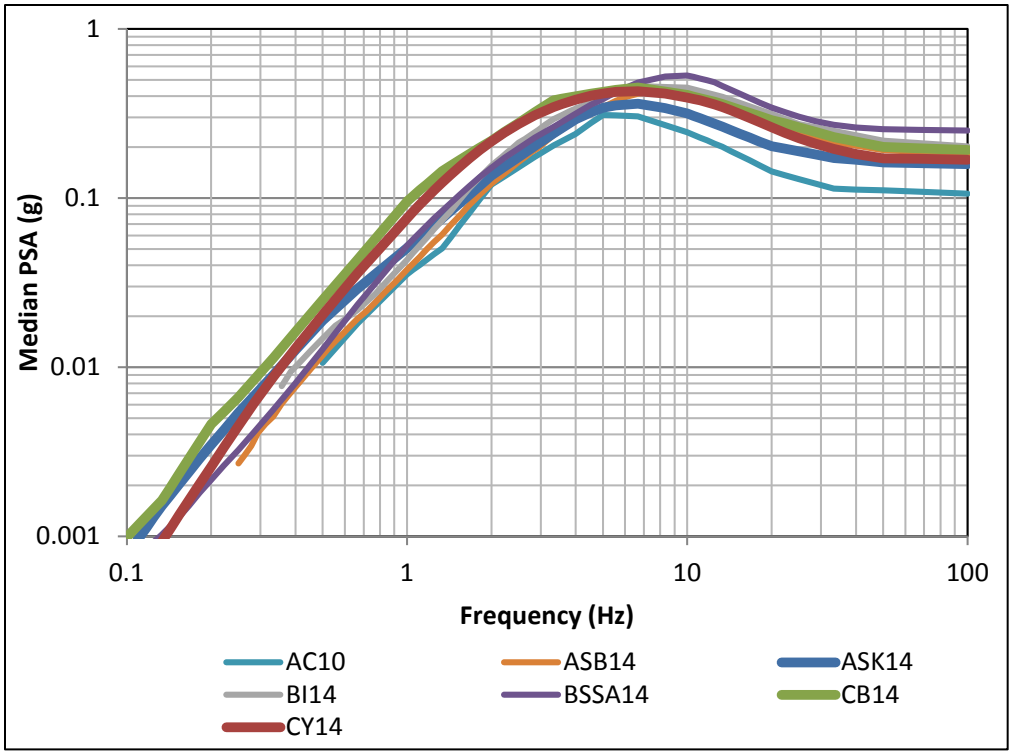

Figure 9.6. Comparison of the selected GMPEs for Random Scenario 1: $M_W = 5.5$, $R_{rup} = 7.07$ km, $R_{jb} = 5$ km, Dip = 45, $Z_{TOR} = 2$, Width = 3 km, Reverse, HW.

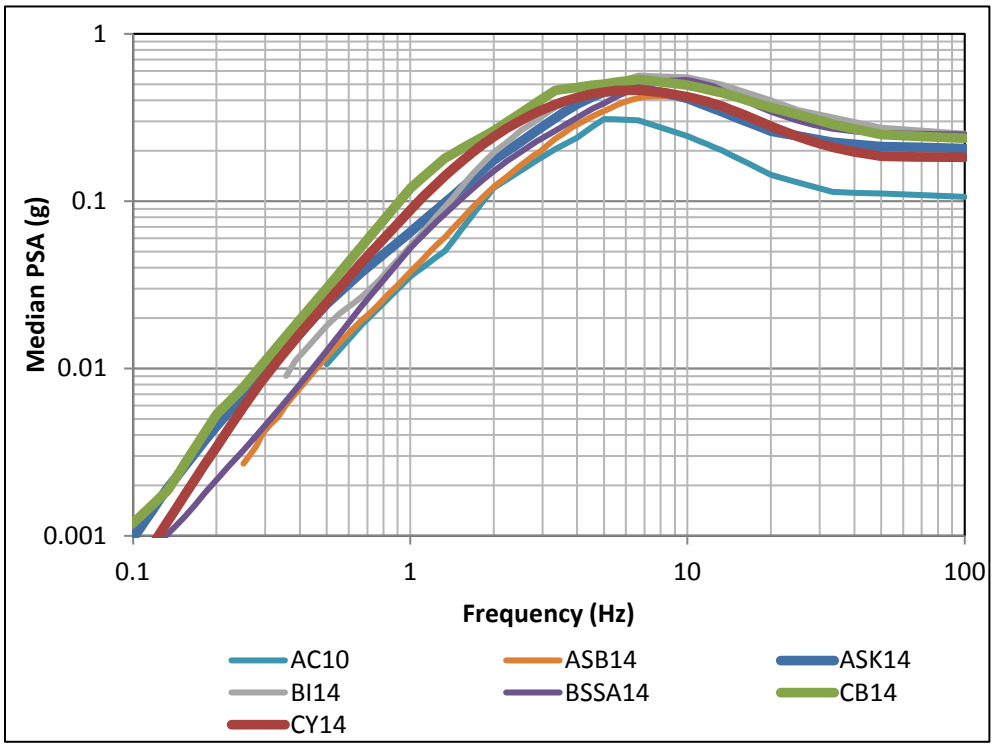

Figure 9.7. Comparison of the selected GMPEs for Random Scenario 2: $M_W = 5.5$, $R_{rup} = 5$ km, $R_{jb} = 5$ km, Dip = 45, $Z_{TOR} = 2$ km, Width = 3 km, Reverse, FW.

The exclusion of the R_{jb} GMPEs from the list of candidate backbone models, and the fact that the remaining GMPEs have similar behavior, implies that it is sufficient to use only one backbone.

From these three GMPEs, CY14 was selected as the backbone model. This selection does not mean that CY14 is superior to ASK14 or CB14, only that it is necessary to use only one model. Furthermore, differences among these three GMPEs are captured by the crustal scaling factors in Section 9.4.2.

The CY14 model for spectral accelerations is composed of two parts, the first predicting the spectral acceleration at a reference rock site, y_{ref}, which corresponds to a V_{S30} value of 1,130 m/s; this is then transformed to the target V_{S30} through application of a nonlinear site adjustment factor. The equation for predicting y_{ref} (in units of g) is as follows:

$$\ln(\boldsymbol{y_{ref}}) = \boldsymbol{c}_1 + \left\{\boldsymbol{c}_{1a} + \frac{\boldsymbol{c}_{1c}}{\cosh(2.\max(\boldsymbol{M}-4.5,0))}\right\}\boldsymbol{F_{RV}} + \left\{\boldsymbol{c}_{1b} + \frac{\boldsymbol{c}_{1d}}{\cosh(2.\max(\boldsymbol{M}-4.5,0))}\right\}\boldsymbol{F_{NM}}$$

$$+ \left\{\boldsymbol{c}_7 + \frac{\boldsymbol{c}_{7b}}{\cosh(2.\max(\boldsymbol{M}-4.5,0))}\right\}\Delta\boldsymbol{Z_{TOR}} + \left\{\boldsymbol{c}_{11} + \frac{\boldsymbol{c}_{11b}}{\cosh(2.\max(\boldsymbol{M}-4.5,0))}\right\}(\cos\boldsymbol{\delta})^2$$

$$+ \boldsymbol{c}_2(\boldsymbol{M}-6) + \frac{\boldsymbol{c}_2-\boldsymbol{c}_3}{\boldsymbol{c}_n}\ln(1+\boldsymbol{e}^{\boldsymbol{c}_n(\boldsymbol{c}_M-\boldsymbol{M})}) + \boldsymbol{c}_4\ln(\boldsymbol{R_{rup}} + \boldsymbol{c}_5\cosh(\boldsymbol{c}_6.\max(\boldsymbol{m}-\boldsymbol{c_{HM}},0)))$$

$$+ (\boldsymbol{c}_{4a}-\boldsymbol{c}_4)\ln(\sqrt{\boldsymbol{R}_{\boldsymbol{RUP}}^2 + \boldsymbol{c}_{\boldsymbol{RB}}^2}) + \left\{\boldsymbol{c}_{\gamma 1} + \frac{\boldsymbol{c}_{\gamma 2}}{\cosh(\max(\boldsymbol{M}-\boldsymbol{c}_{\gamma 3},0))}\right\}\boldsymbol{R_{RUP}}$$

$$+ \boldsymbol{c}_8\max\left(1-\frac{\max(\boldsymbol{R_{RUP}}-40,0)}{30},0\right)\min\left(\frac{\max(\boldsymbol{M}-5.5,0)}{0.8},1\right)\boldsymbol{e}^{-\boldsymbol{c}_{8a}(\boldsymbol{M}-\boldsymbol{c}_{8b})^2}.\Delta\boldsymbol{DPP}$$

$$+ \boldsymbol{c}_9\boldsymbol{F_{HW}}\cos(\boldsymbol{\delta})\left\{\boldsymbol{c}_{9a} + (1-\boldsymbol{c}_{9a})\tanh\left(\frac{\boldsymbol{R_x}}{\boldsymbol{c}_{9b}}\right)\right\}\left\{1-\frac{\sqrt{\boldsymbol{R}_{\boldsymbol{JB}}^2 + \boldsymbol{Z}_{\boldsymbol{TOR}}^2}}{\boldsymbol{R_{RUP}}+1}\right\} \quad (9.1)$$

The median (mean log) spectral acceleration for the target site condition is then obtained from the following expression:

$$\overline{\ln(y)} = \ln(y_{ref}) + \phi_1.\min\left[\ln\left(\frac{V_{s30}}{1130}\right),0\right] + \phi_5\left(1-e^{-\Delta Z_{1.0}/\phi_6}\right)$$

$$+ \phi_2\left(e^{\phi_3(\min(V_{s30},1130)-360)} - e^{\phi_3(1130-360)}\right)\ln\left(\frac{y_{ref}+\phi_4}{\phi_4}\right) \quad (9.2)$$

where $\boldsymbol{c}_1$, $\boldsymbol{c}_{1a}$, …, and ϕ_1, …, etc. represent numerical coefficients for the CY14 GMPE functional form. See Chiou and Youngs (2014) and Section 9.4.2 for more details on the role of these coefficients.

The predictor variables in these equations are as follows:

M	Moment magnitude
R_{RUP}	Closest distance to rupture plane (km)
R_{JB}	Joyner-Boore distance (km)
R_x	Perpendicular (to fault strike) distance to site from the fault line (surface projection of top of rupture), positive in the downdip direction (km)
F_{HW}	Hanging-wall factor: 1 for $R_X \geq 0$, 0 for $R_X < 0$.
δ	Fault dip angle
Z_{TOR}	Depth to top of rupture (km)
ΔZ_{TOR}	Z_{TOR} centered on M-dependent average Z_{TOR}; see Equation (9.3)
F_{RV}	Flag for reverse/reverse-oblique faulting: 1 for $30° \leq \lambda \leq 150°$, 0 otherwise
F_{NM}	Flag for normal faulting: 1 for $-120° \leq \lambda \leq -60°$, 0 otherwise; excludes normal-oblique faulting
V_{s30}	Time-averaged shear-wave velocity over top 30 m (m/s); this is set to 760 m/s for these calculations (assumed host value)
$Z_{1.0}$	Depth to shear-wave velocity of 1.0 km/s (m); set to 27.4 m, as explained below
$\Delta Z_{1.0}$	$Z_{1.0}$ centered on the V_{s30}-dependent average $Z_{1.0}$; set to zero, as explained below
ΔDPP	DPP (Direct Point Parameter) centered on site- and earthquake-specific average DPP; this parameter is set to zero for reasons explained below.

The parameter ΔZ_{TOR} is calculated as the value of Z_{TOR} for the earthquake under consideration minus the mean value for earthquakes of magnitude **M,** $\overline{Z_{TOR}(M)}$**.** At the Hanford Site, there is the unusual situation of a thick layer of hard basalts (the CRB formation) very close to the ground surface, which means that fault ruptures extending into these near-surface basalts may be associated with unusually high stress drops at very shallow depths. To account for the higher near-surface crustal strength of the basalts compared to typical active tectonic region crust, ΔZ_{TOR} is computed by the following equation:

$$\Delta Z_{TOR} = \max[Z_{TOR},3] - \overline{Z_{TOR}(M)} \tag{9.3}$$

The value of $\overline{Z_{TOR}(M)}$ is computed from Equation (9.4a) for reverse and reverse-oblique faulting or from Equation (9.4b) for strike-slip or normal faulting:

$$\overline{Z_{TOR}(M)} = \max[2.704 - 1.266.\max(M - 5.849,0),0]^2 \tag{9.4a}$$

$$\overline{Z_{TOR}(M)} = \max[2.673 - 1.136.\max(M - 4.970,0),0]^2 \tag{9.4b}$$

This constraint of the Z_{TOR} parameter, in effect never allowing it to take a value less than 3 km, only affects the value of ΔZ_{TOR} in the fourth term of Equation (9.1) and does not influence the calculation of distances (for example, in the final term of the equation). The effect of this constraint in parameter Z_{TOR} was explored as part of the Workshop 3 hazard sensitivities, and it was found that the sensitivity to this constraint is low.

For the host region (California) classification, for V_{S30} = 760 m/s (see Section 9.3.2.1), the estimated value of $Z_{1.0}$ for all locations is 27.4 m. Because this is an estimated rather than measured value (since it corresponds to an ideal host site profile), the term $\Delta Z_{1.0}$ is 0.0 for all sites.

For these hazard calculations, rupture directivity effects will not be included, hence the term ΔDPP is set to zero. At Workshop 1 (WS1) of the Hanford sitewide PSHA, Dr. Paul Spudich of the USGS was invited, as a resource expert, to present an overview of the five directivity models being developed as candidates for adoption by the NGA-West2 model developers (Spudich et al. 2013). Chiou and Youngs (2014) chose the DPP as the preferred model for predicting directivity effects in their model. However, for this application the GMC TI Team made the simplifying assumption that directivity effects could be neglected because they are small for reverse faults. This decision is supported by results obtained by the southwestern United States ground motion project (as documented in Watson-Lamprey 2014).

In addition to the ASK14, CB14, and CY14 candidate models selected to construct the equivalent backbone models that capture the inherent epistemic uncertainty in the host region predictions from these equations, the following additional GMPEs are considered in Section 9.4.2 for the development and evaluation of the scaling factors: BSSA14, Id14, and Zhea06.

9.2.2 GMPEs for Subduction Earthquakes

No formal backbone selection process was required for subduction GMPEs. As indicated earlier in Sections 7.4.2 and 9.1.3, it was clear to the TI Team since the early stages of the project that there was only one acceptable subduction GMPE in the literature and current practice (namely the BC Hydro GMPE; Abrahamson et al. 2014a), which this project adopted and revised. In the remainder of this section we refer to the Abrahamson et al. (2014a) model simply as the BC Hydro model.

Revisions of the BC Hydro model were necessary for various reasons. The model is robust at short distances, but there are very few data at distances of interest in this project (200 to 400 km), and as a result the predicted spectral shapes are not smooth. Moreover, the backarc and forearc scaling is poorly constrained at long periods, resulting in stronger attenuation for forearc motions for long periods. While this might be predicted by the sparse data at these distances and oscillator periods, it is considered to be an unphysical effect and thus should be removed from the predictive equation. An additional reason to revise the BC Hydro model is that additional data have become available since the introduction of the model. The data include data from Japan, Chile, and Central America (see Section 7.1.3).

The modifications of the BC Hydro model were made with particular consideration of the constraints of this project. In particular, the Hanford Site is located at distances of about 200 to 400 km from the subduction sources, and the site is always located at a backarc location. The magnitude range of interest is between 6 and 7.5 for intraslab earthquakes, and magnitudes greater than about 7.5 for interface earthquakes. To accommodate these constraints, the regressions performed to fit the modified BC Hydro model are done giving higher weights to motions recorded at larger distances than motions recorded close to the fault. The discussion below focuses first on data selection, then we present the functional form for the model, followed by a description of the regression analysis. We conclude with a discussion of the results and an analysis of residuals.

9.2.2.1 Data Selection

The BC Hydro data set consists of ground motion records that were used to fit earlier subduction GMPEs (e.g., Crouse et al. 1988; Crouse 1991; Youngs et al. 1997; Atkinson and Boore 2003, 2008; Zhao et al. 2006; Lin and Lee 2008) and some additional recent data. Overall, the BC Hydro data set

consists of data from Alaska, Central America, Chile, Cascadia, Japan, Mexico, Peru, Solomon Island, and Taiwan. There are a total of 9,946 earthquake recordings from 292 earthquakes. Out of these, 3,557 recordings were from 163 interface earthquakes, and 6,389 recordings were from 129 intraslab earthquakes. The BC Hydro data are augmented with data from Japan recorded by the KiK-net sensors (Dawood et al. 2014), data from Maule earthquake recorded in Chile (Nick Gregor, personal communication; see also Gregor et al. 2012), and data from Central America compiled by Arango et al. (2011). The compilation and processing of these data are discussed in Section 7.1.3.

To prepare the data for regression we use the following criteria to filter out some of the data:

- Only the usable periods within the low-pass and high-pass frequencies reported in the BC Hydro flatfile are used.
- The maximum usable period of the KiK-net data is set to 70% of the inverse of the corner frequency used for filtering (Akkar and Bommer 2006).
- The criteria used to filter out ground motions in the BC Hydro project are followed. These criteria filter out motions with bad data, earthquakes with a single recording, no site information, no rupture distance, very high residuals, interface earthquakes with magnitudes less than 6.0, intraslab earthquakes with magnitudes less than 5.0, and duplicate listings. The BC Hydro flatfile includes a "usable" flag that applies these criteria, which was respected for this project.
- A magnitude- and distance-based censoring criterion is used to avoid using motions that are not strong enough to trigger the recording instrument. This censoring is required to remove biased data at large distances. For interface earthquakes we censor all motions at distances greater than 400 km. For intraslab earthquakes, we censor motions at distances greater than 200 km for magnitudes less than 7 and at distance greater than 400 km for magnitudes greater than 7. These censoring criteria, which are discussed in more detail below, are different than the criteria used in the BC Hydro project.

In addition to the criteria listed above, the following data were excluded from the regression:

- Taiwan data that do not differentiate forearc and backarc. These data behaved poorly when compared both with forearc and backarc regression.
- The 2011 Tohoku data. This earthquake has a stronger attenuation rate than other earthquakes in the database; because there is a significant amount of data from this earthquake, these data have a strong effect on the predicted attenuation. This effect remains after accounting for differences in forearc and backarc attenuation. The GMC TI Team chose to exclude this earthquake from the regression because of the potential pitfall of having one earthquake control the long-distance attenuation. The ΔC_1 term (which will be discussed later) was calibrated by Abrahamson et al. (2014a) using the Tohoku data, hence this important data set is still considered in the magnitude scaling of the proposed model.
- One earthquake from the BC Hydro flatfile (Earthquake 10080, interface earthquake from Japan, **M** = 7.4) was removed from the data set. This earthquake had only five records, but some were repeated records. Due to questions regarding data quality, the final choice was to remove this earthquake.
- The Cape Mendocino earthquake was not included because of questions about whether it is an

interface or a shallow crustal earthquake (BC Hydro 2012). This earthquake is included in the BC Hydro flatfile but was excluded from the regressions for that model. In addition, four earthquakes that are flagged as "not usable" in the BC Hydro flatfile (Events ID 10283, 10284, 10287, 10288) were added to the database. These earthquakes had been flagged as not usable because they had no rupture distance. This distance was replaced with the hypocentral distance (which at the values of distance for the stations in these earthquakes should be a good approximation of rupture distance). The 13 January, 2001 El Salvador earthquake is included both in the BC Hydro flatfile and in the Arango et al. (2011) data. The GMC TI Team elected to use the metadata of Arango et al. (2011). Most noticeably, Arango et al. (2011) report a magnitude of 7.7, while the BC Hydro flatfile reports two different magnitudes for this earthquake (7.6 and 7.7).

The magnitude and distance range covered by the final data set selected for regression is shown in Figure 9.8 and Figure 9.9.

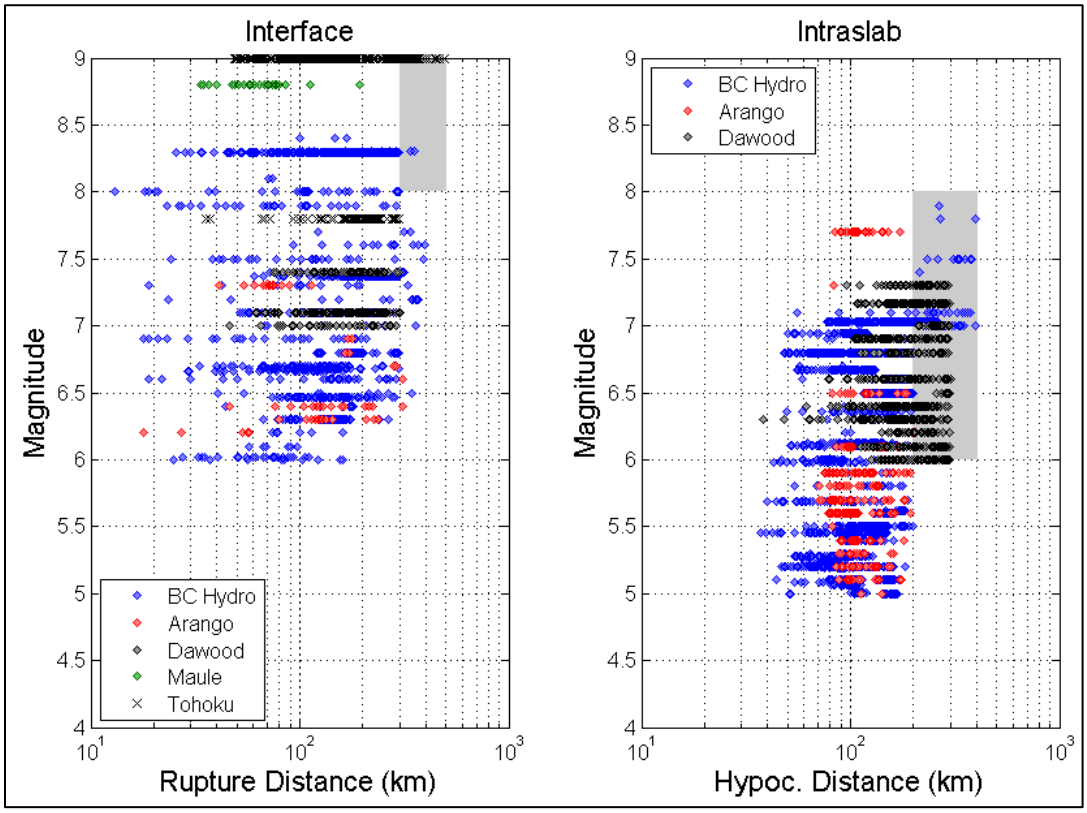

Figure 9.8. Magnitude and distance distribution of recordings used in the regression. The data are differentiated by database source. The gray boxes indicate magnitude-distance regions of interest to this project. The Tohoku earthquake records are included in the figure, but are not used in the regression analyses.

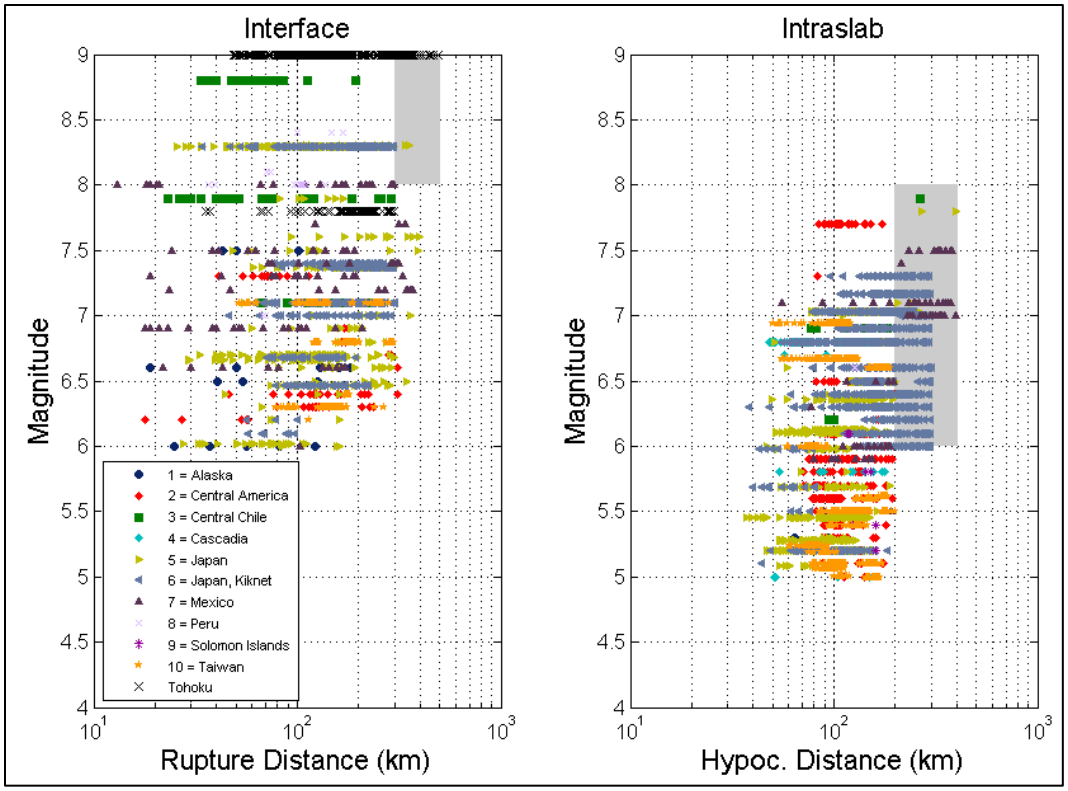

Figure 9.9. Magnitude and distance distribution of recordings used in the regression. The data are differentiated by geographical origin. The gray boxes indicate magnitude-distance regions of interest to this project. The Tohoku earthquake records are included in the figure, but are not used in the regression analyses.

9.2.2.1.1. Censoring Algorithm

At large distances the ground motion intensity may attenuate to a point where not all recording instruments are triggered. At these distances only the motions that are stronger than average will trigger the instrument and be recorded. Because the weak motions at large distances are not recorded, the data at these distances are biased high. The distance at which this bias is introduced depends on the earthquake magnitude. The motions from smaller magnitude earthquakes become biased at lower distances than those from larger magnitude earthquakes.

Because ground motion model residuals (log-space) are generally normally distributed (Abrahamson 1998; Jayaram and Baker 2008), not recording weaker motions will remove the lower tail of the distribution and introduce skewness. We divide the data into magnitude bins and compute the residuals with respect to the BC Hydro model. We use the LOESS method (Cleveland 1979; Cleveland and Devlin 1988) to compute a nonparametric estimate of the mean value of residuals as a function of distance. The mean is subtracted from all the data points in a magnitude bin and the resulting value is cubed. The mean of this cubed value gives us an estimate of the third central moment, which is related to the skewness of the distribution. We use the nonparametric LOESS fit to estimate the third central moment as a function of distance. The distance at which the third central moment deviates significantly from zero (we define a *significant* deviation from zero as the case when the 95% confidence interval does not contain zero) gives the distance after which the residuals become skewed. We use this information to censor the data. Figure 9.10 illustrates the method in detail.

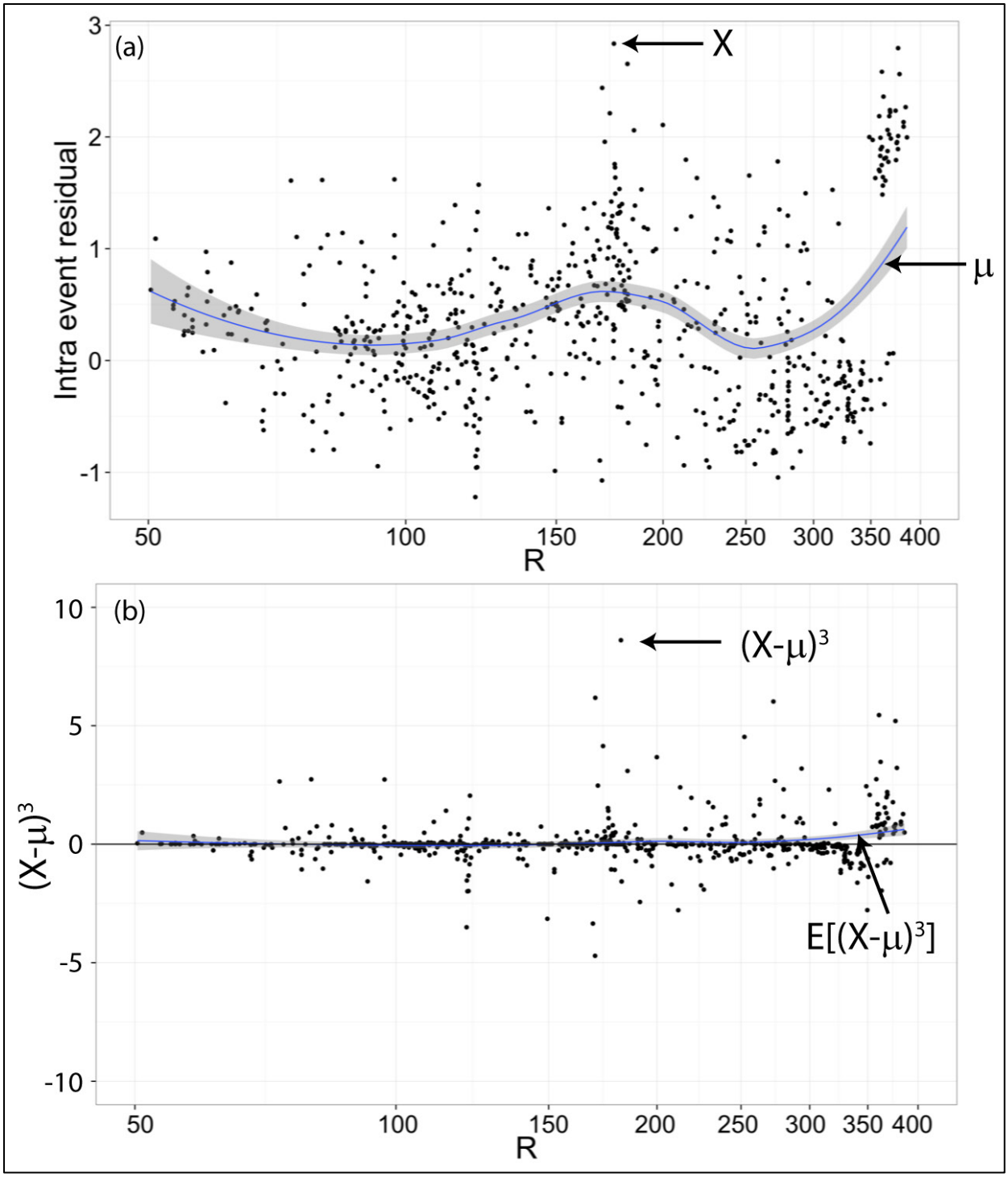

Figure 9.10. Computation of skewness as a function of distance. The distance where $\boldsymbol{E}[(\boldsymbol{X}-\boldsymbol{\mu})^{\boldsymbol{3}}]$ deviates significantly from 0 is used to censor the data.

The skewness plots for peak ground acceleration (PGA) for several magnitude bins (Figure 9.11) indicate that the interface data are not skewed for distances up to 400 km. For intraslab earthquakes, the data are skewed at a distance of around 200 km for magnitude bins of 6 to 6.5 and 6.5 to 7. For these reasons, we decided to use the following censoring criteria:

$R_{rup} > 400$ for interface earthquakes
$R_{hyp} > 200$ for $M < 7$ and intraslab earthquakes
$R_{hyp} > 400$ for $M \geq 7$ and intraslab earthquakes.

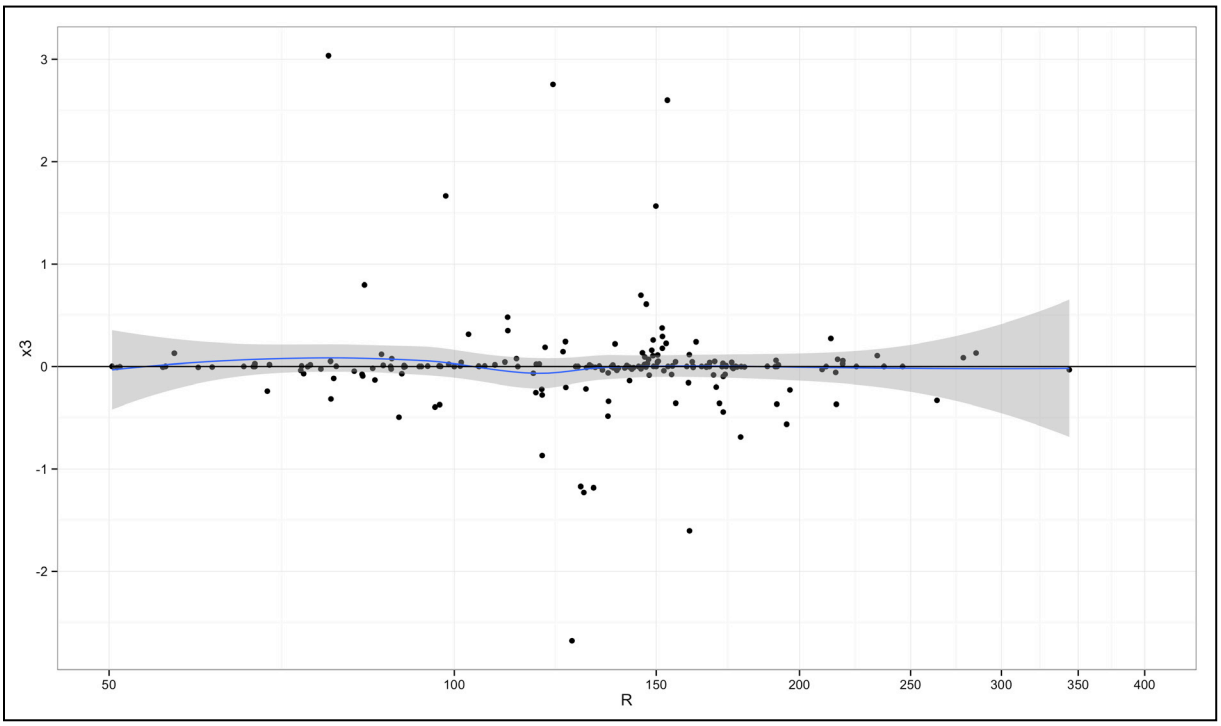

(a) $6.0 < M \leq 6.5$, interface earthquakes.

Figure 9.11. Plots of $(X-\mu)^3$, where X is PGA and μ is the median prediction of PGA, and its expected value as a function of distance to determine censoring distances for different magnitude bins and for interface and intraslab earthquakes. The shaded region indicates the 95% confidence interval of the expected value.

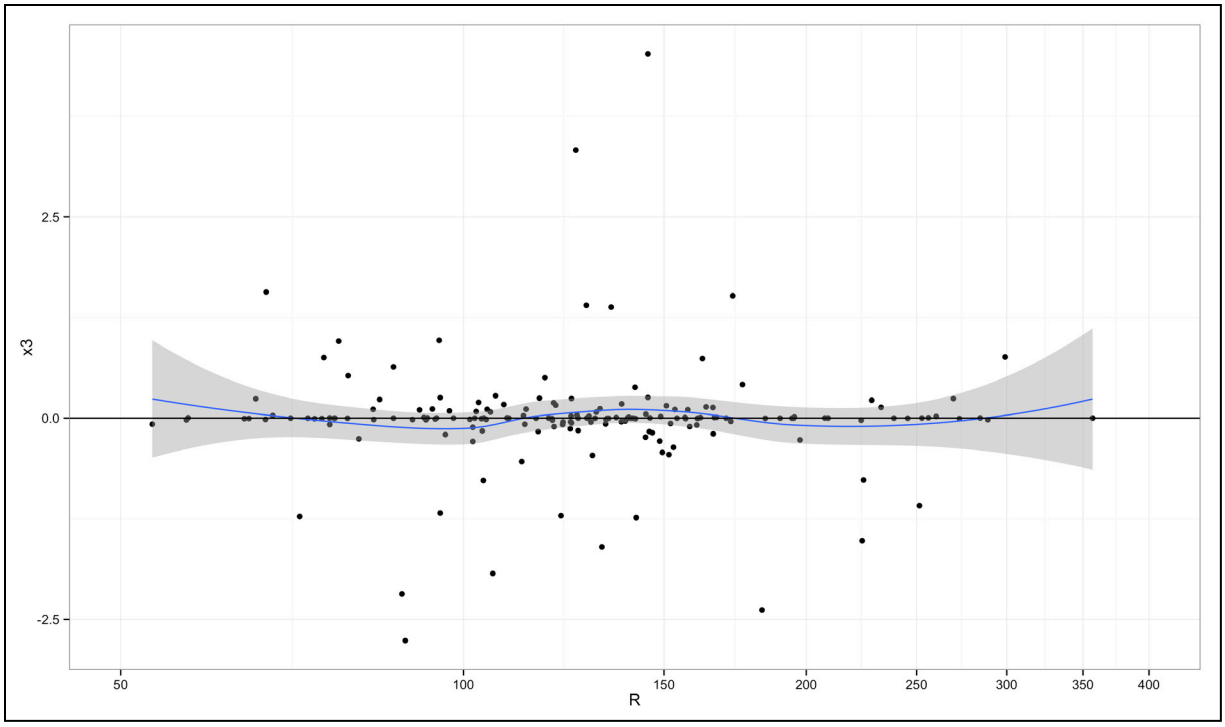

Figure 9.11. (contd) (b) $6.5 < M \leq 7.0$, interface earthquakes.

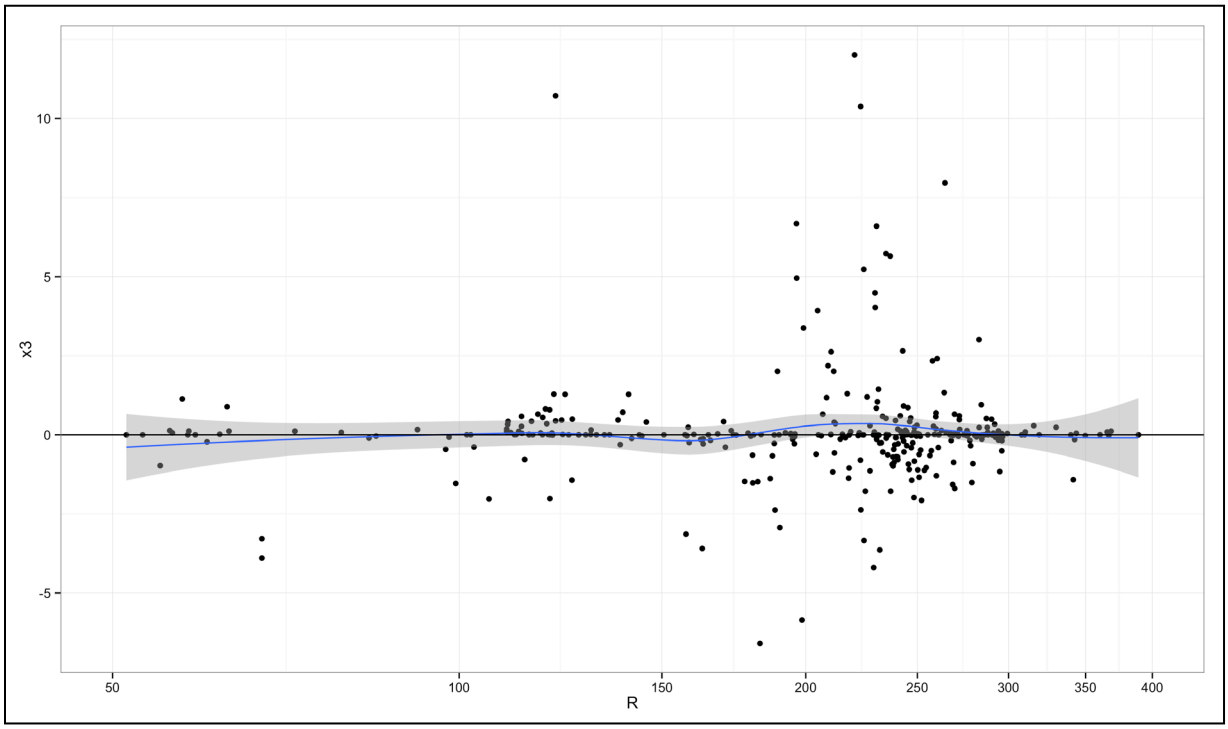

Figure 9.11. (contd) (c) $7 < M \leq 7.5$, interface earthquakes.

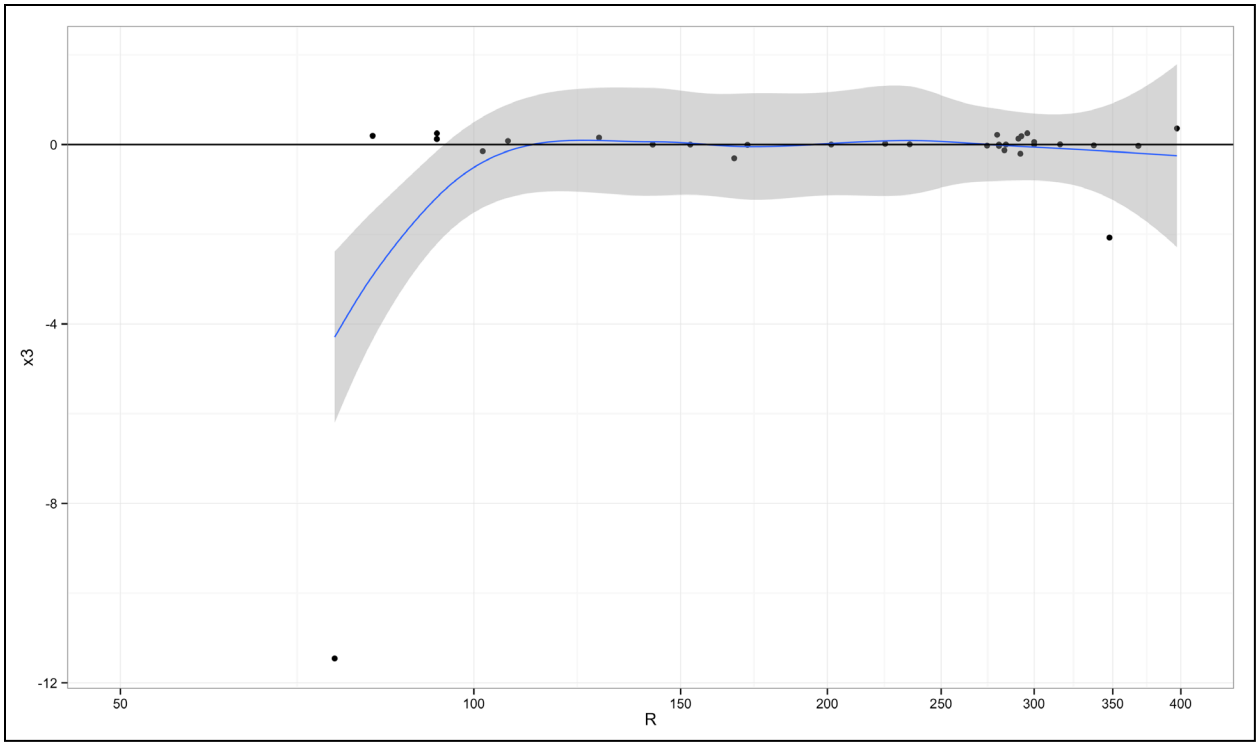

Figure 9.11. (contd) (d) 7.5 < M ≤ 8, interface earthquakes.

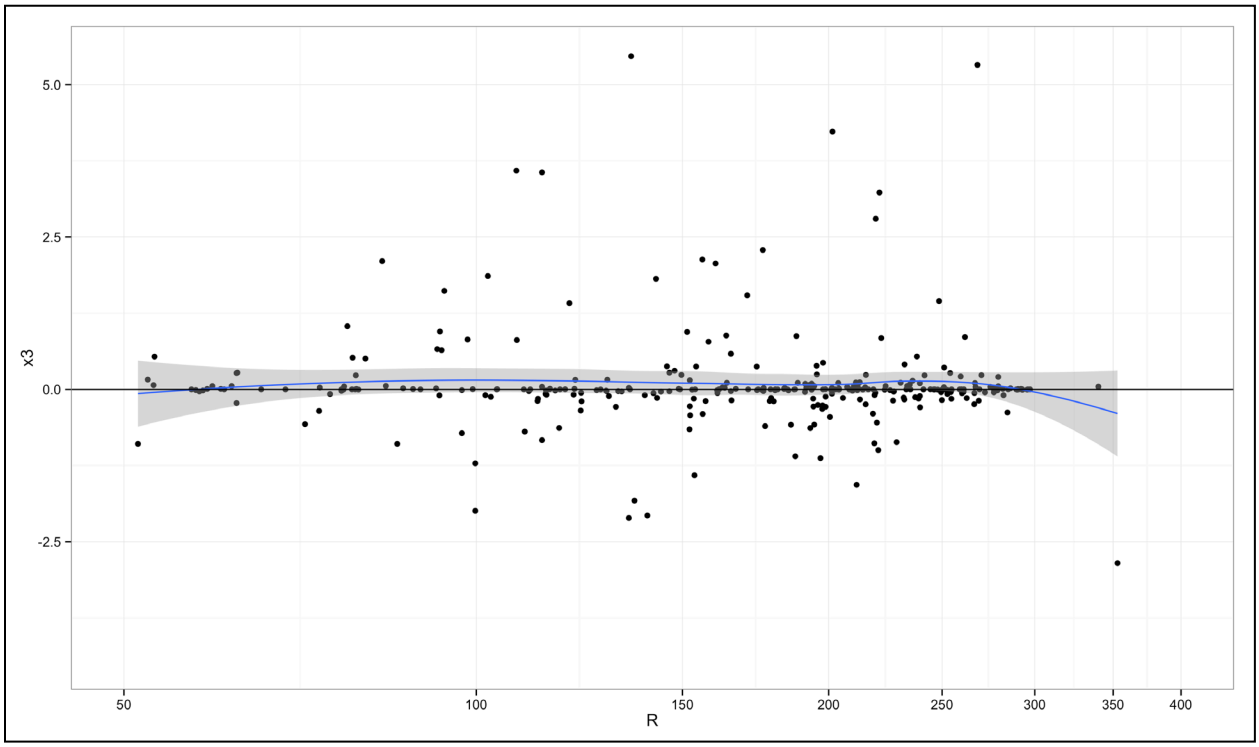

Figure 9.11. (contd) (e) 8 < M ≤ 8.5, interface earthquakes.

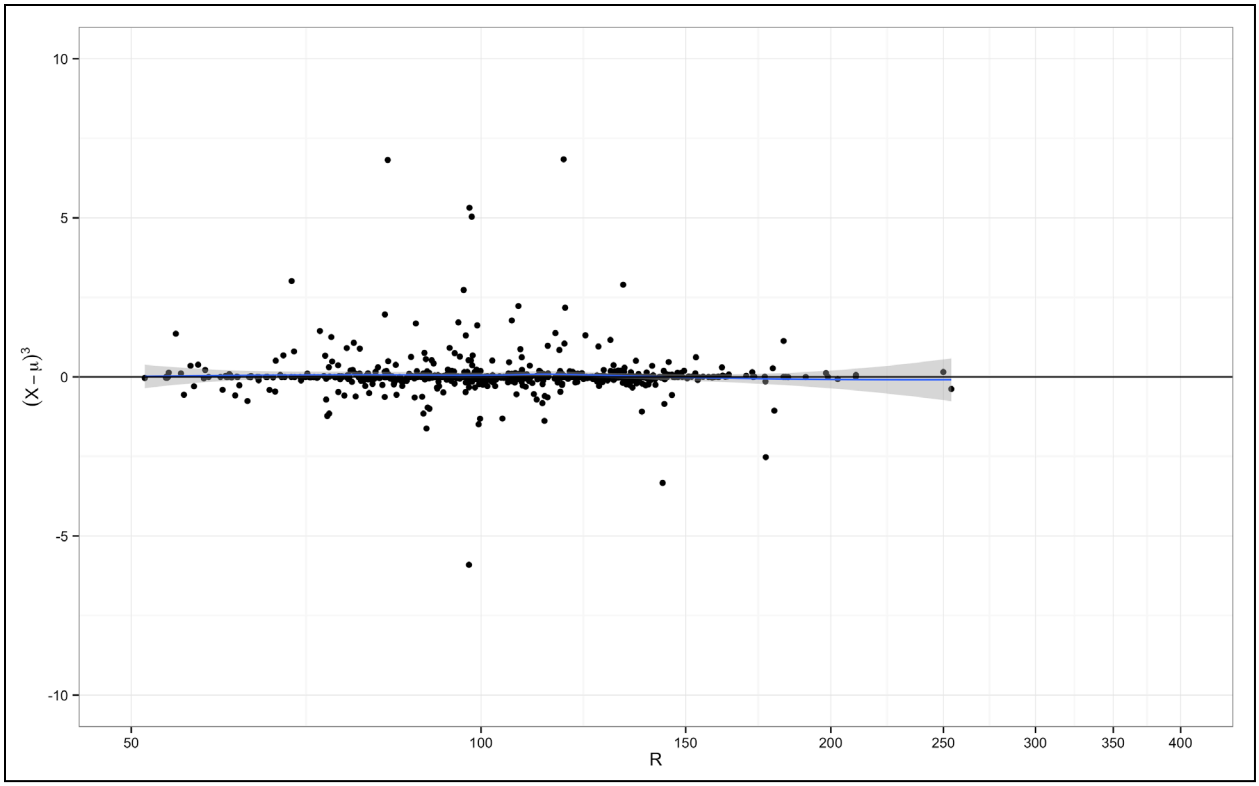

Figure 9.11. (contd) (f) $5 < M \leq 5.5$, intraslab earthquakes.

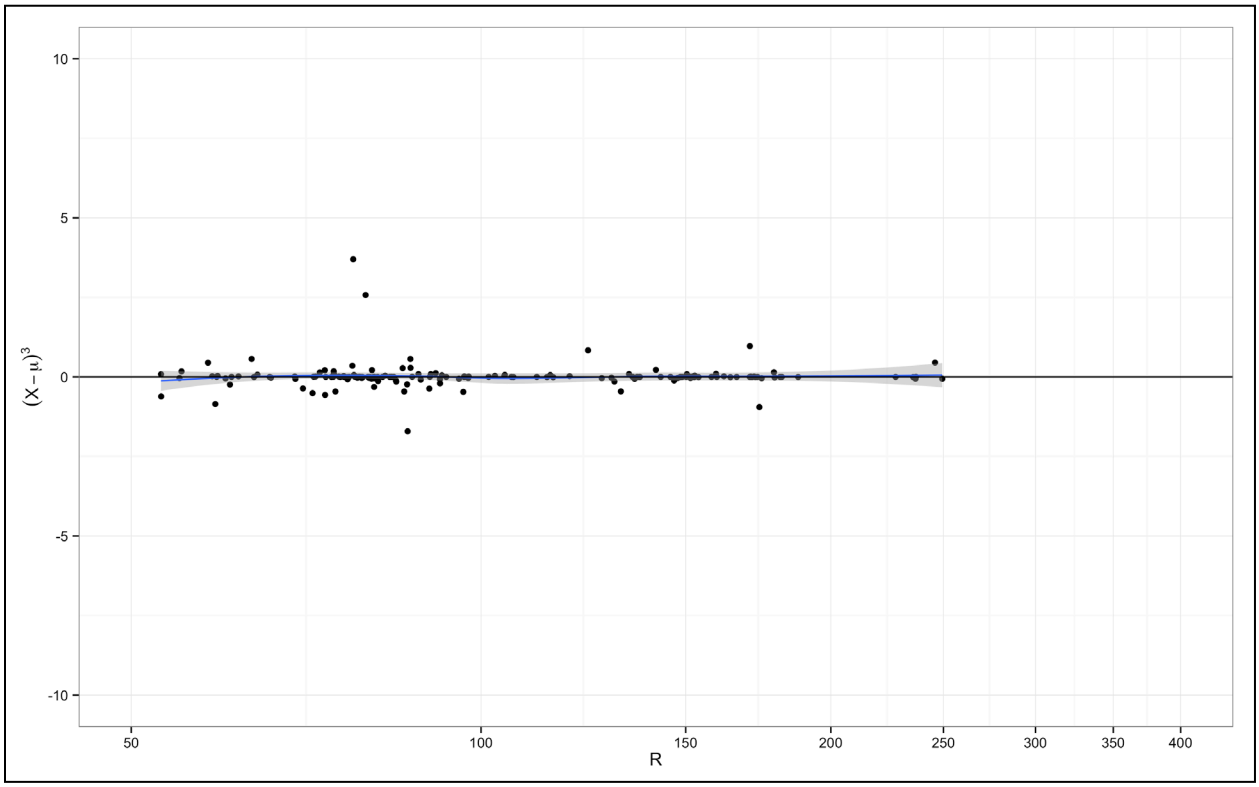

Figure 9.11. (contd) (g) $5.5 < M \leq 6$, intraslab earthquakes.

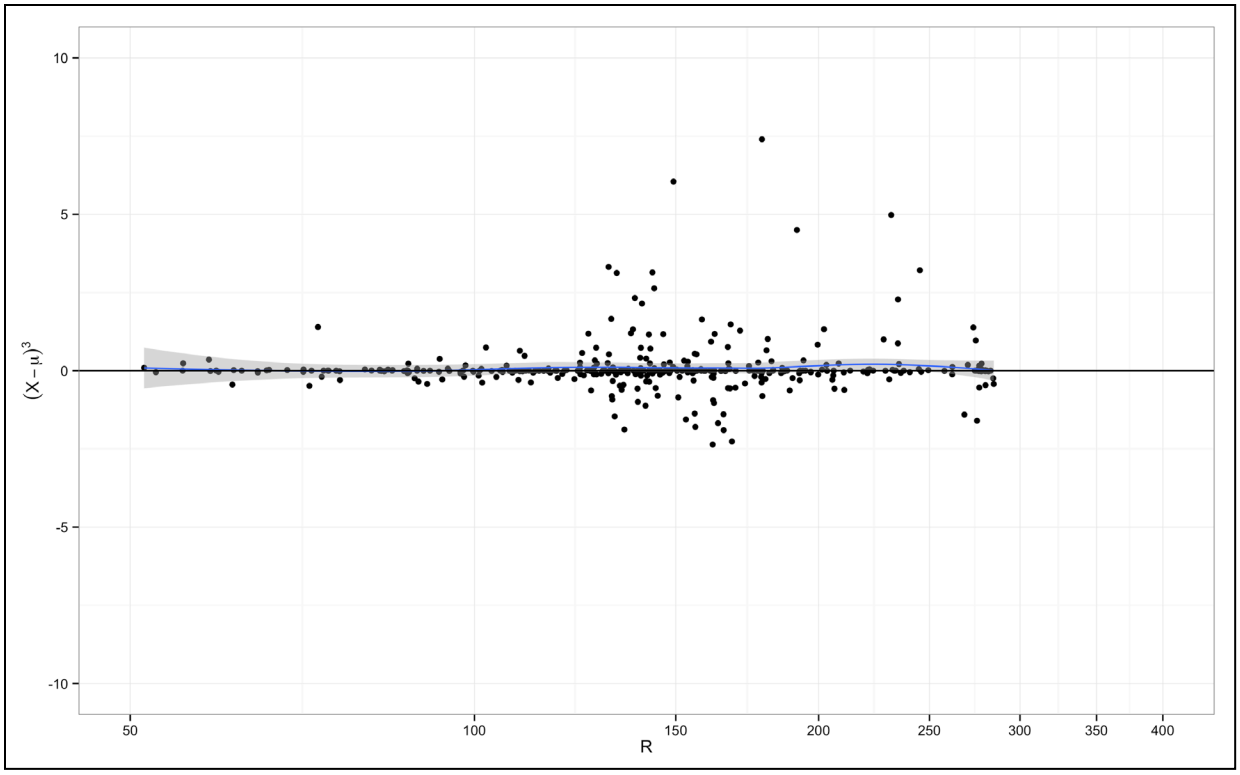

Figure 9.11. (contd) (h) $6 < M \leq 6.5$, intraslab earthquakes

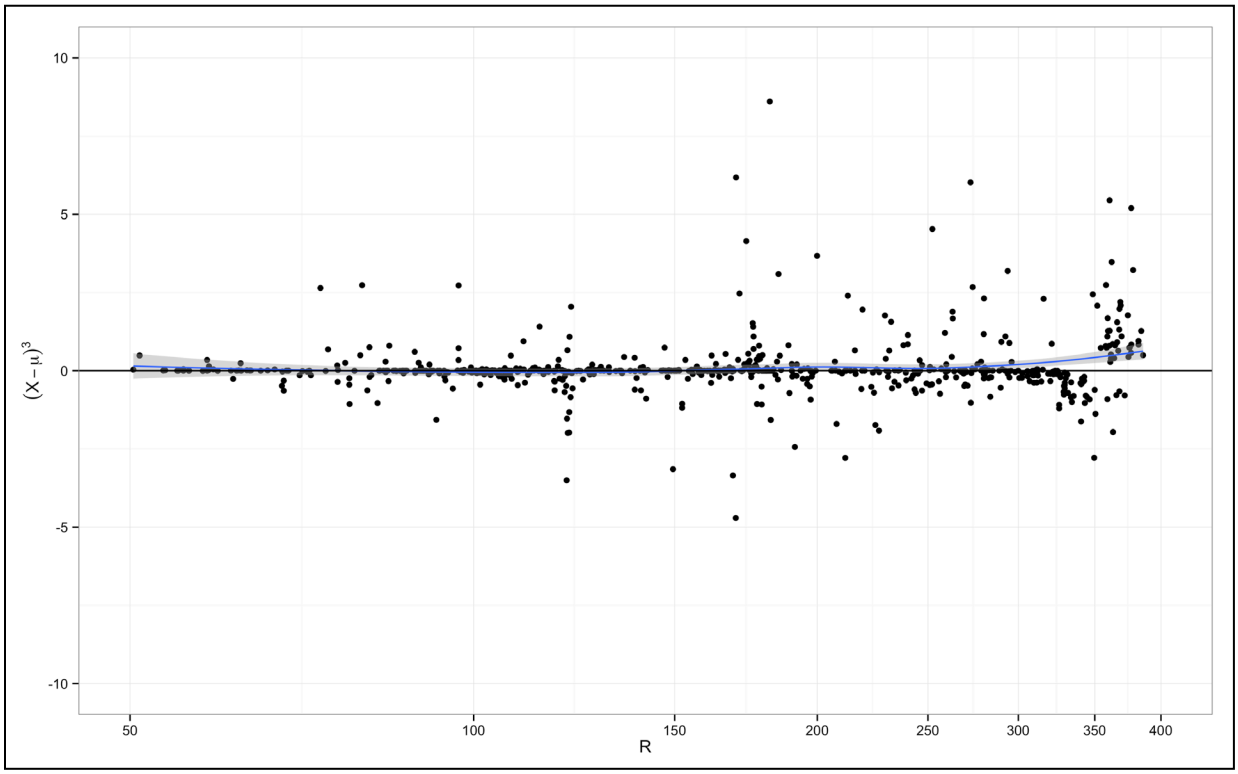

Figure 9.11. (contd) (i) $6.5 < M \leq 7$, intraslab earthquakes.

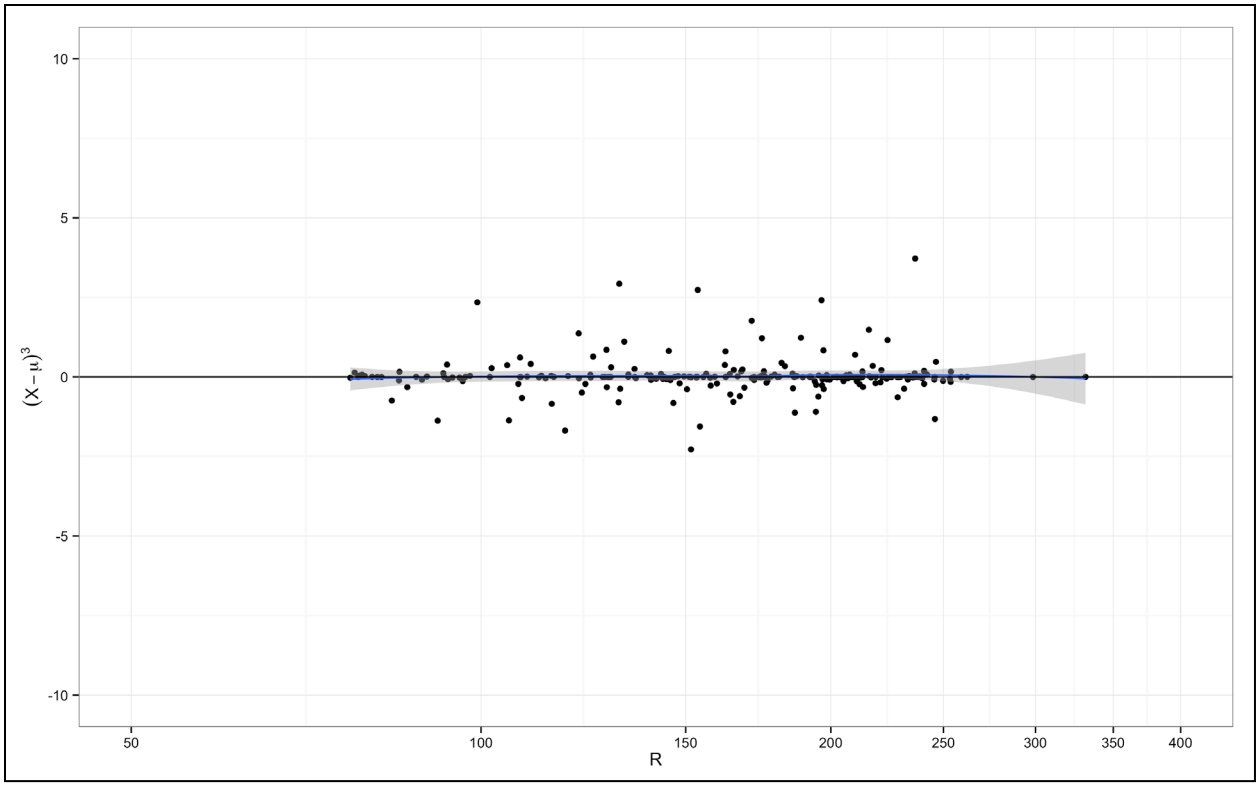

Figure 9.11. (contd) (j) $7 < M \leq 7.5$, intraslab earthquakes.

The censoring distance for interface earthquakes (400 km)is significantly larger than the censoring limits used to develop the BC Hydro model. Though the censoring criteria developed here are very different than those used in BC Hydro model, Figure 9.12 shows that slightly lowering the thresholds used in the BC Hydro model will also result in similar censoring criteria.

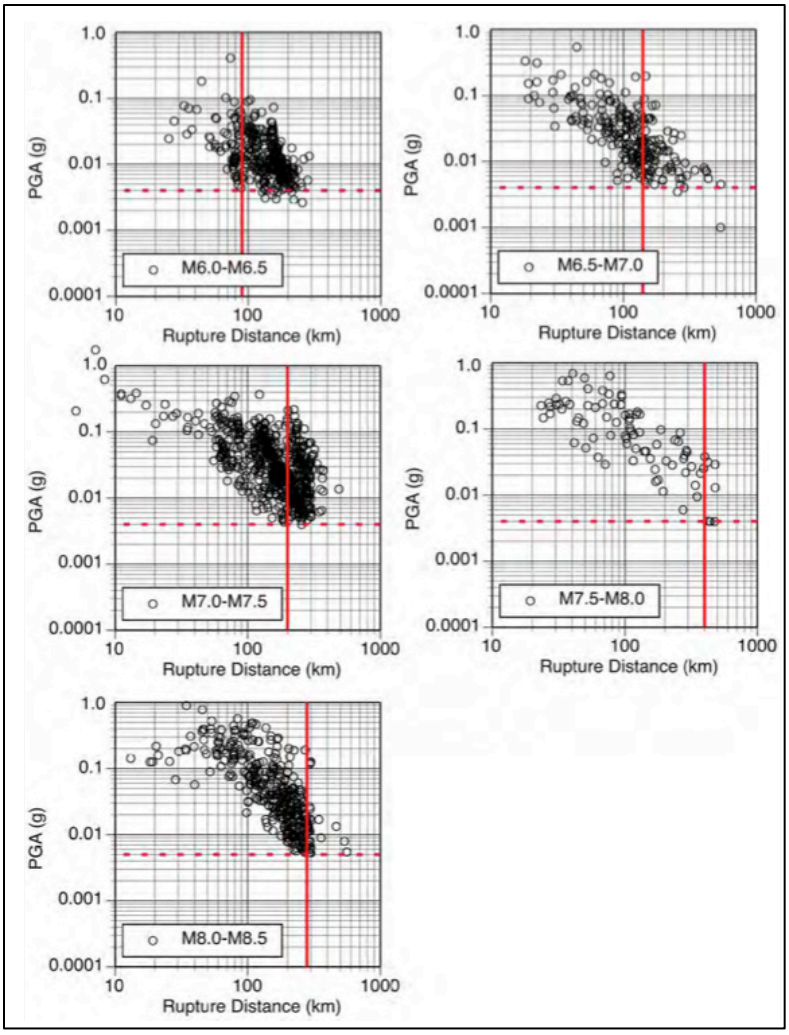

Figure 9.12. The censoring criteria used to censor the interface earthquakes in the BC Hydro model (Abrahamson et al. 2014a). Slightly lowering the PGA threshold will increase the censoring limit to around 400 km in all magnitude bins as used here.

9.2.2.2 Functional Form

The functional form used by the BC Hydro model was adopted with minor modification of the forearc/backarc scaling term. The BC Hydro model used the following functional form to model the difference between forearc and backarc scaling:

$$f_{faba} = \begin{cases} \theta_7 + \theta_8 \ln\left(\frac{\max[R,85]}{40}\right) * F_{faba} & \text{for intraslab} \\ \theta_{15} + \theta_{16} \ln\left(\frac{\max[R,100]}{40}\right) * F_{faba} & \text{for interface} \end{cases} \quad (9.5)$$

where R represents the rupture distance for interface earthquakes and hypocentral distance for intraslab earthquakes, and F_{faba} is 0 for forearc or unknown sites and 1 for sites in the backarc region. This equation allows the regression fit to predict higher spectral acceleration in the backarc region than in the forearc region at close distances. This behavior is not expected and is caused by overfitting to the data.

Overfitting generally occurs when the model is excessively complex and has too many parameters. To avoid overfitting the model we constrain the functional form to make physically valid extrapolations. The new functional form for forearc/backarc scaling is as follows:

$$f_{faba} = \begin{cases} \theta_8 \ln\left(\frac{\max[R,40]}{40}\right) * F_{faba} & \text{for intraslab} \\ \theta_{16} \ln\left(\frac{\max[R,40]}{40}\right) * F_{faba} & \text{for interface} \end{cases} \tag{9.6}$$

With this modification, the final functional form used for regression is

$$\begin{aligned} lnSa = \theta_1 + \theta_4 \cdot \Delta C_1 + \left(\theta_2 + \theta_{14} \cdot F_{event} + \theta_3 \cdot (M - 7.8)\right) \cdot \ln(R + C_4 \cdot \exp[(M - 6) \cdot \theta_9]) + \theta_6 \cdot R \\ + \theta_{10} \cdot F_{event} + f_{Mag}(M) + f_{depth}(Z_h) + f_{faba}(R) + f_{site}(PGA_{1000}, Vs_{30}) \end{aligned} \tag{9.7}$$

where
M = moment magnitude
Z_h = hypocentral depth
R = the rupture distance for interface earthquakes, and hypocentral distance for intraslab earthquakes
F_{event} = 0 for interface earthquakes and 1 for intraslab earthquakes, and
F_{faba} = 0 for forearc or unknown sites and 1 for sites in the backarc region.

The model for magnitude scaling is given by

$$f_{Mag}(M) = \begin{cases} \theta_4 \cdot \left(M - (C_1 + \Delta C_1)\right) + \theta_{13} \cdot (10 - M)^2 & \text{for } M \le C_1 + \Delta C_1 \\ \theta_5 \cdot \left(M - (C_1 + \Delta C_1)\right) + \theta_{13}(10 - M)^2 & \text{for } M > C_1 + \Delta C_1 \end{cases} \tag{9.8}$$

where C_1 is 7.8. Values of ΔC_1 capture the epistemic uncertainty in the break in magnitude scaling. The model for depth scaling is given by

$$f_{depth}(Z_h) = \theta_{11} \cdot (Z_h - 60) \cdot F_{event} \tag{9.9}$$

The model for forearc/backarc scaling is given by

$$f_{faba} = \begin{cases} \theta_8 \ln\left(\frac{\max[R,40]}{40}\right) * F_{faba} & \text{for intraslab} \\ \theta_{16} \ln\left(\frac{\max[R,40]}{40}\right) * F_{faba} & \text{for interface} \end{cases} \tag{9.10}$$

The model for site response is the Walling et al. (2008) model and is given by

$$f_{site}(PGA_{1000}, Vs_{30}) = \begin{cases} \theta_{12} \cdot \ln\left(\frac{V_S^*}{V_{lin}}\right) - b \cdot \ln(PGA_{1000} + c) + b \cdot \ln\left(PGA_{1000} + c \cdot \left(\frac{V_S^*}{V_{lin}}\right)^n\right) & \text{for } Vs30 < V_{lin} \\ \theta_{12} \cdot \ln\left(\frac{V_S^*}{V_{lin}}\right) + b \cdot n \cdot \ln\left(\frac{V_S^*}{V_{lin}}\right) & \text{for } Vs_{30} \ge V_{lin} \end{cases} \tag{9.11}$$

where PGA_{1000} is the median PGA at $Vs_{30} = 1000\ m/s$, and

$$V_s^* = \begin{cases} 1000 & \text{for } Vs_{30} > 1000 \\ Vs_{30} & \text{for } Vs_{30} \leq 1000 \end{cases} \quad (9.12)$$

The use of V_{S30} = 1000 m/s as a proxy for PGA at rock is slightly different from the approach of Walling et al. (2008), which used 1130 m/s. This difference was due to a "rounding" choice by the developers of the BC Hydro model (Nick Gregor, personal communication, 2014). This slight difference does not have a significant impact on regression results because the amount of data showing nonlinearity is not large and both V_{S30} values correspond to very stiff materials. The proposed backbone model is hereafter referred to as the modified BC Hydro model.

9.2.2.3 Regression

We use mixed-effects regression to fit the GMPE. Traditional GMPEs are fitted to predict ground motion intensity for several scenarios. Thus, each data point is given equal weight during the regression as the model aims to perform well everywhere. In this case, the model will be used to predict the ground motion intensity at sites located far away from the fault. To improve the predictive power of the GMPE at large distances we decided to give more weight to recordings at larger distances from the fault than those closer to the fault. All recordings within 100 km of the fault are given a weight of one, recordings between 100 km and 200 km away from the fault are given a weight of two, and recordings more than 200 km away from the fault are given a weight of 4. These weights were selected subjectively based on the importance of the different distance scenarios as inferred from preliminary hazard sensitivity studies. We use the *lmer* function in the *lme4* package of the statistical software R to perform the weighted maximum likelihood regression. We note that the site response function and the terms for magnitude scaling were not modified; hence, the only free parameters in the regressions were θ_1, θ_2, θ_6, θ_{10}, and the parameters of the $f_{FABA}(R)$ term (e.g., θ_8 and θ_{16}). Of particular note is the coefficient ΔC_1 (Equation 9.8). This coefficient controls the break in magnitude scaling at large magnitudes. The coefficient was originally constrained using stochastic simulations (Gregor et al. 2006; Atkinson and Macias 2009). After the occurrence of the Tohoku and Maule earthquakes, the epistemic uncertainty of this coefficient was re-evaluated (Abrahamson et al. 2014a). We adopt these revised values in this project.

Because the mixed-effect regression is conducted independently at each period, the predictions may not be constrained well enough to predict a smooth spectral shape. To ensure smooth spectral predictions regression coefficients are generally smoothed after the initial regression. Smoothing is typically done iteratively where first a set of parameters are smoothed and constrained. The regression is then repeated for other coefficients to re-estimate them using the previously smoothed coefficients. The process is then repeated until every coefficient is smooth across periods. Generally, ad-hoc methods are used for smoothing. The drawback to such an approach is that it reduces the reproducibility of the GMPE regression. Though it is difficult to completely remove subjectivity from this process, we present an algorithmic approach to smoothing that can make the regression reproducible. Because smoothing of the coefficients is done to obtain predictions of smooth response spectra, we minimize the following objective function:

$$\int (\hat{\theta}''(t))^2 \, dt + \lambda \sum_T \left(\theta - \hat{\theta}\right)^2 \quad (9.13)$$

where the term $\int (\hat{\theta}''(t))^2 \, dt$ quantifies the roughness of a curve when the smoothed coefficients ($\hat{\theta}$) are plotted against spectral period, and λ is a tuning parameter. A smooth curve will generally have slowly

changing slopes and thus the integral of the squared value of derivative of slope over the entire length of the curve will be smaller than that from a rough curve where slope changes rapidly. The second part of the equation quantifies the sum of squared difference between the coefficient from the original regression (θ) and the smoothed value of the coefficients ($\hat{\theta}$) across the periods of interest. Thus, the optimization algorithm searches for values of the coefficient that change smoothly with respect to the period, while still being close to the original values found by regression. Equation 9.13 was developed by the GMC TI Team to satisfy a multi-objective optimization. In this case, the two objectives are to increase smoothness and to minimize the deviation from the original (unsmooth) values. The exact same formulation is used to fit *smoothing splines*. *Smoothing splines* are used to find the smooth moving average of "unsmooth" data and involves the same tradeoff as smoothing of acceleration response spectra. Details about the formulation we used and more information about *smoothing splines* can be found in Hastie et al. (2009). The parameter λ is a tuning parameter that is choosen by trial and error. We found the appropriate value by bracketing the value of λ by a high and low value and then iteratively tightening the bounds through visual inspection of the resulting spectra. In general, the value of λ depends on the level of discretization chosen to do the numerical integrations (Equation 9.13); hence, generic rules to determine its value do not exist. Moreover, the lack of a clear definition of the "ideal" smooth spectra prevents purely quantitative comparison of different λ values, thus necessitating a manual intermediate check. A value of $\lambda = 100$ was used in this study.

The procedure described above is applied to a single coefficient at a time. After smoothing a coefficient the regression is performed again to estimate new values of the non-smoothed coefficients by keeping the smooth coefficients fixed. This process is repeated several times until every coefficient is smoothed. In addition to the smoothing process, the coefficients for two oscillator periods required for this project were not part of the regressions of the BC Hydro project (T = 0.03 and T = 0.04 sec). The coefficients for these periods were obtained from a log-linear interpolation. The coefficients of the final median model are given in Table 9.3 and Table 9.4.

Table 9.3. Period-independent coefficients for the modified BC Hydro model.

Parameter	Value
θ_3	0.1
θ_4	0.9
θ_5	0.0
θ_9	0.4
n	1.18
c	1.88
C_4	10.0

Table 9.4. Period-dependent coefficients for the modified BC Hydro model.

T (s)	V_{LIN}	b	θ_1	θ_2	θ_6	θ_8	θ_{10}	θ_{11}	θ_{12}	θ_{13}	θ_{14}	θ_{16}	Med ΔC_1 IF	Med ΔC_1 IS
0.01	865.1	-1.186	3.8796	-1.1337	-0.00555	-0.525	2.6929	0.013	0.98	-0.0135	-0.34	-0.2247	0.2	-0.3
0.02	865.1	-1.186	3.8796	-1.1337	-0.00555	-0.525	2.6929	0.013	0.98	-0.0135	-0.34	-0.2247	0.2	-0.3
0.03	944.57	-1.257	4.1844	-1.179	-0.00555	-0.6	2.392	0.013	1.116	-0.0136	-0.263	-0.2450	0.2	-0.3
0.04	1009.12	-1.307	4.4006	-1.211	-0.00555	-0.653	2.1786	0.013	1.213	-0.0137	-0.208	-0.2600	0.2	-0.3
0.05	1053.5	-1.346	4.5683	-1.236	-0.00555	-0.694	2.013	0.013	1.288	-0.0138	-0.166	-0.2711	0.2	-0.3
0.075	1085.7	-1.471	4.8415	-1.2298	-0.006070	-0.705	1.7517	0.013	1.483	-0.0142	-0.108	-0.2811	0.2	-0.3
0.1	1032.5	-1.624	4.9937	-1.215	-0.006446	-0.696	1.5244	0.013	1.613	-0.0145	-0.0681	-0.2787	0.2	-0.3
0.15	877.6	-1.931	5.0793	-1.1804	-0.0067	-0.652	1.1536	0.013	1.882	-0.0153	-0.0165	-0.2514	0.2	-0.3
0.2	748.2	-2.188	5.0182	-1.1468	-0.006678	-0.597	0.876	0.0129	2.076	-0.0162	0.0152	-0.2114	0.2	-0.3
0.3	587.1	-2.518	4.7475	-1.091	-0.0064	-0.49	0.52418	0.0128	2.348	-0.0183	0.0548	-0.1342	0.2	-0.3
0.4	503	-2.657	4.429	-1.0455	-0.006203	-0.401	0.33841	0.0127	2.427	-0.0206	0.0744	-0.0785	0.1437	-0.3
0.5	456.6	-2.669	4.1181	-1.0061	-0.00605	-0.328	0.24017	0.0125	2.399	-0.0231	0.0823	-0.0406	0.1	-0.3
0.75	410.5	-2.401	3.4397	-0.92773	-0.005773	-0.197	0.20044	0.012	1.993	-0.0296	0.0651	-0.0144	0.04157	-0.3
1	400	-1.955	2.9005	-0.86825	-0.005576	-0.114	0.28493	0.0114	1.47	-0.0363	0.0305	-0.0128	0	-0.3
1.5	400	-1.025	2.1062	-0.78125	-0.005298	-0.029	0.47641	0.01	0.408	-0.0493	-0.0291	-0.0105	-0.0585	-0.3
2	400	-0.299	1.5317	-0.72143	-0.005102	0	0.62135	0.0085	-0.401	-0.061	-0.0685	-0.0089	-0.1	-0.3
3	400	0	0.69726	-0.63711	-0.004824	0	0.77231	0.0054	-0.673	-0.0798	-0.106	-0.0067	-0.2	-0.3
5	400	0	-0.4776	-0.53089	-0.004474	0	0.827	0.0005	-0.596	-0.098	-0.12	-0.0039	-0.2	-0.3
7.5	400	0	-1.5093	-0.44657	-0.004196	0	0.827	-0.0033	-0.528	-0.098	-0.12	-0.0016	-0.2	-0.3
10	400	0	-2.2565	-0.38675	-0.004	0	0.827	-0.006	-0.504	-0.098	-0.12	0.0000	-0.2	-0.3

9.2.2.4 Regression Results

The median prediction of the modified BC Hydro model is shown in Figure 9.13, Figure 9.14, and Figure 9.15 (at the end of this section). For comparison, the original BC Hydro model is also shown (comparisons with other models are made in Section 9.4.3). For interface earthquakes, the difference between the forearc and backarc models disappears at about 1 sec. For short oscillator periods, the proposed models at large distances plot in between the forearc and backarc predictions of the BC Hydro model. At intermediate periods, the predictions of the proposed model become closer than the forearc attenuation, and at longer periods the proposed model has much lower attenuation than the BC Hydro model. For intraslab earthquakes, the two models are very similar.

Figure 9.15 plots the spectral shapes of the proposed model and those of the original BC Hydro model. As indicated before, the models coincide for intraslab earthquakes. For interface earthquakes, the proposed model is close to the forearc BC Hydro model at distances less than about 200 km. For a distance of 400 km (the limit of applicability of this model, and beyond the limit of applicability of the BC Hydro model), the proposed model fits the backarc model at short periods and predicts larger motions than the BC Hydro model at long periods. For both intraslab and interface earthquakes, the proposed models have smoother spectral shapes at long distances.

Ground motion residuals were computed using the proposed relationship. Figure 9.16 shows the between-event residuals (e.g., the event term) plotted as a function of magnitude. The data are in general unbiased. At some periods, however, some subsets of the data show different attenuation. For example, the Arango et al. (2011) data at T = 0.01 sec appear to attenuate faster than the rest of the data. The KiK-net data from Dawood et al. (2014) appear to be biased at T = 0.1 sec for intraslab earthquakes. Also, note that there is a negative bias at T = 10 sec.

Figure 9.17 shows the average inter-event residuals for each region. Note that in general there are systematic region-to-region deviations in the data. One important note about these figures is that the event terms within the regression were computed with the weighting scheme described in the previous section (higher weight to long-distance data). Figure 9.18, however, shows the event terms computed without any weighting, hence the overall event terms are not necessarily unbiased. The deviation from zero-mean is particularly noticeable for the Cascadia data. This deviation is discussed in more detail in Section 9.4.3.

Figure 9.18 shows the intra-event residuals as a function of distance. The data in general do not appear to be biased. One observation, however, is that data with "unknown" locations with respect to the volcanic arc show biases at some periods. These data were assumed to be located in the forearc region in the regression. The same data are plotted in Figure 9.19 as the average (with 95% confidence interval) over non-overlapping distance bins. These figures illustrate that the intraslab data have well-behaved residuals across all distances. A possible exception is backarc data for T = 0.01 and T = 0.1 sec, where the residuals are erratic at very large distances.

The interface data do show some clear trends. The stations that do not have a backarc or forearc classification have strongly biased residuals. The regression treated these data as forearc data. The residuals would have been even more strongly biased if they had been assumed to belong to backarc earthquakes, because the backarc model has more attenuation at longer distances and short periods. In general, however, the "unclassified" data are not as abundant as the data with a backarc/forearc

classification. In general, forearc residuals have slightly stronger biases, likely because these data were averaged with the "non-classified" data in the regression.

The modified BC Hydro model was proposed to overcome some shortcomings of the BC Hydro model, in particular, the lack of predictive ability for the large distances at which the sites are located in this project. To evaluate the predictive ability of the model at large distances, Figure 9.20 shows the moving average (loess average) of the expected value of the square of the intra-event residuals versus distance. This is an estimate of the variance as a function of distance. The new model is clearly better at short periods (T < 1 sec) but the differences are trivial at periods of 1 to 3 sec. At T = 10 sec the BC Hydro model appears to perform better at distances less than 300 km.

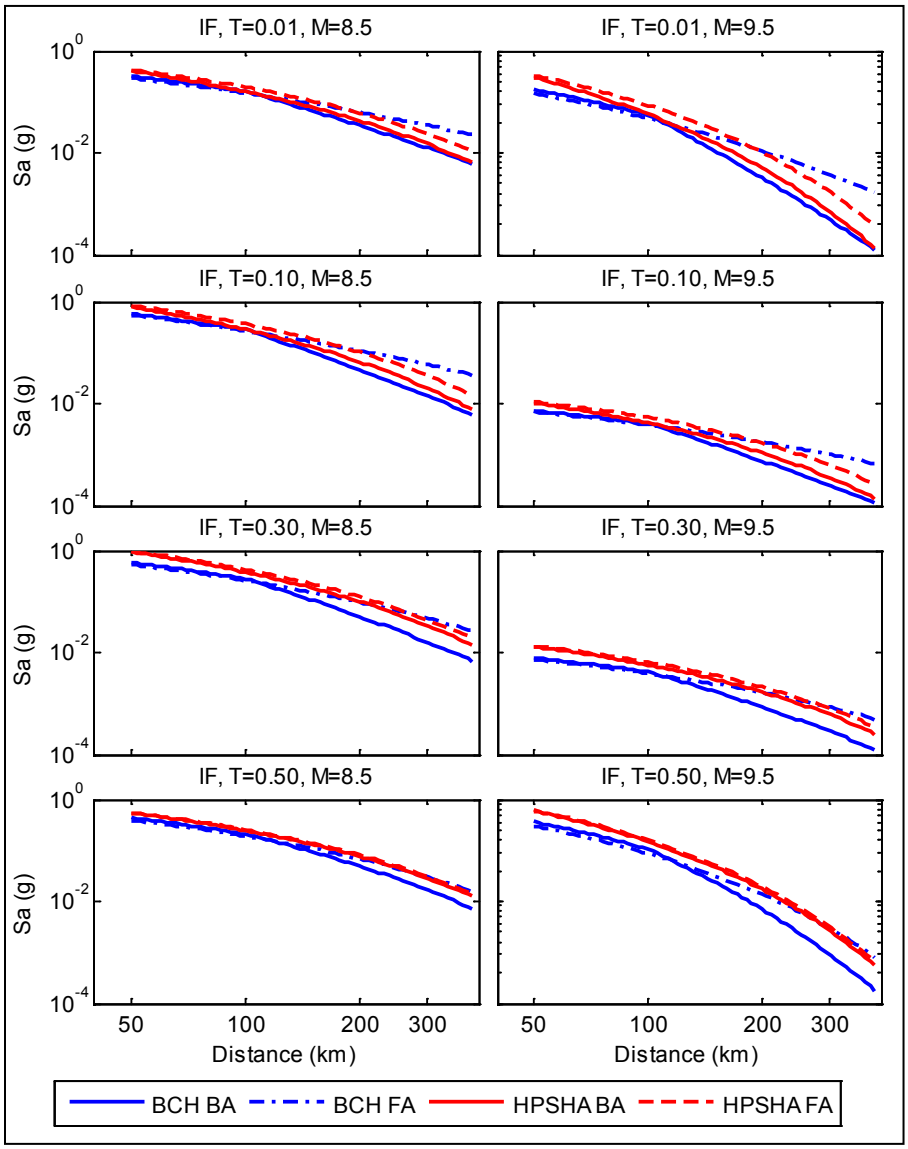

Figure 9.13a. Distance scaling of the modified BC Hydro model (HPSHA) for **interface** earthquakes (backarc [BA] and forearc [FA]) and selected periods. Each column corresponds to a different magnitude. The BC Hydro model is shown for comparison.

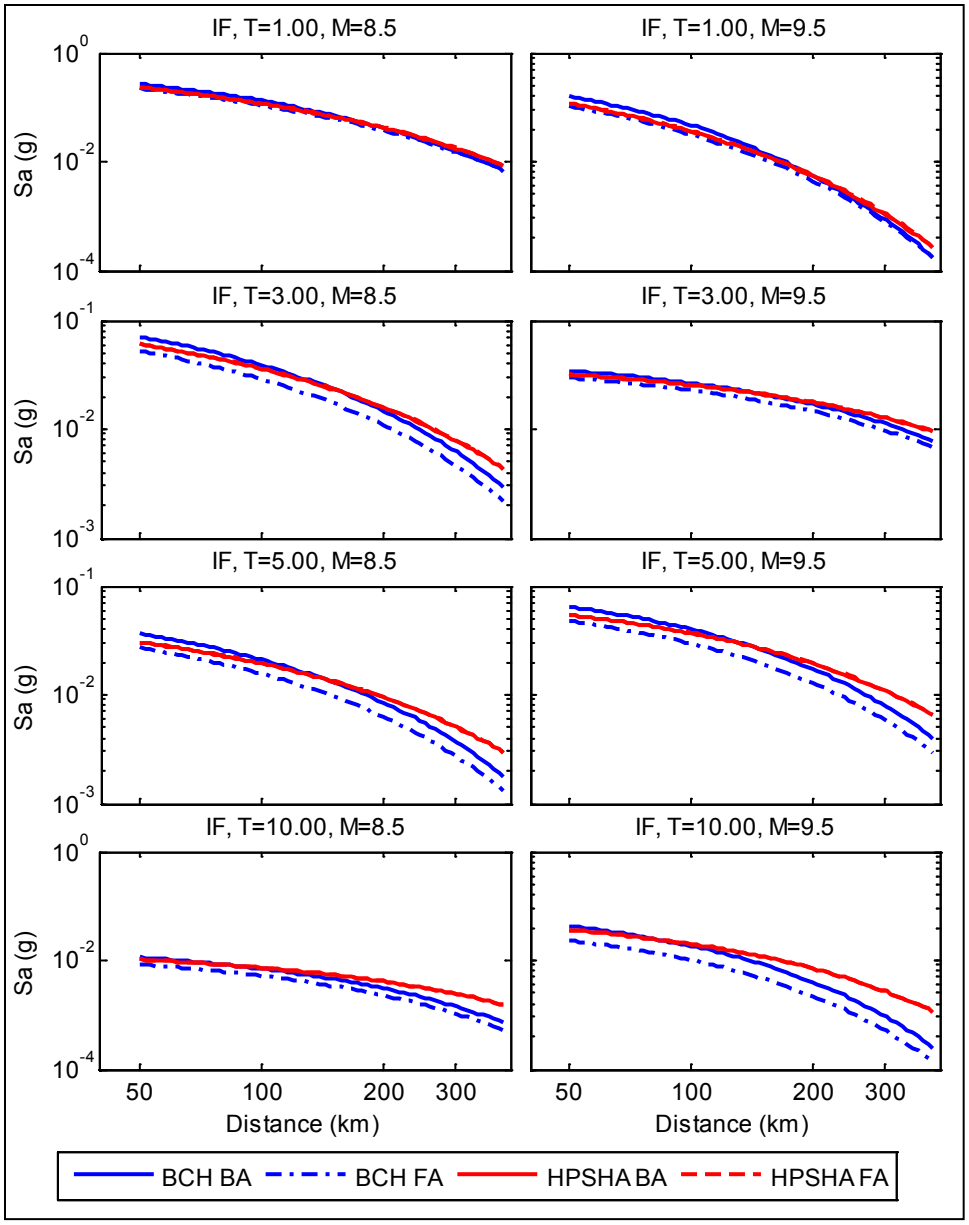

Figure 9.13b. (contd)

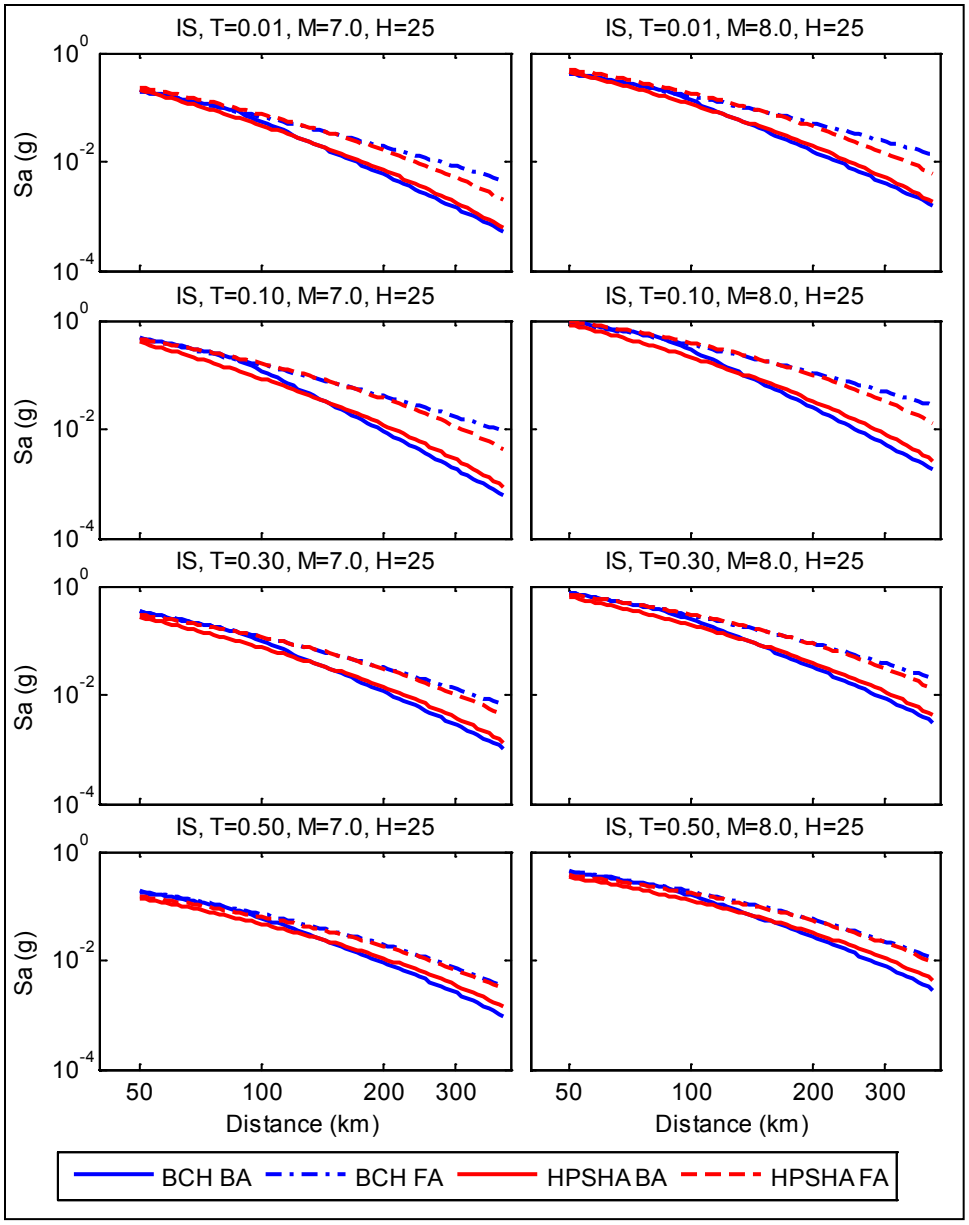

Figure 9.14a. Distance scaling of the modified BC Hydro model (HPSHA) for **intraslab** earthquakes (backarc [BA] and forearc [FA]) and selected periods. Each column corresponds to a different magnitude. The BC Hydro model is shown for comparison.

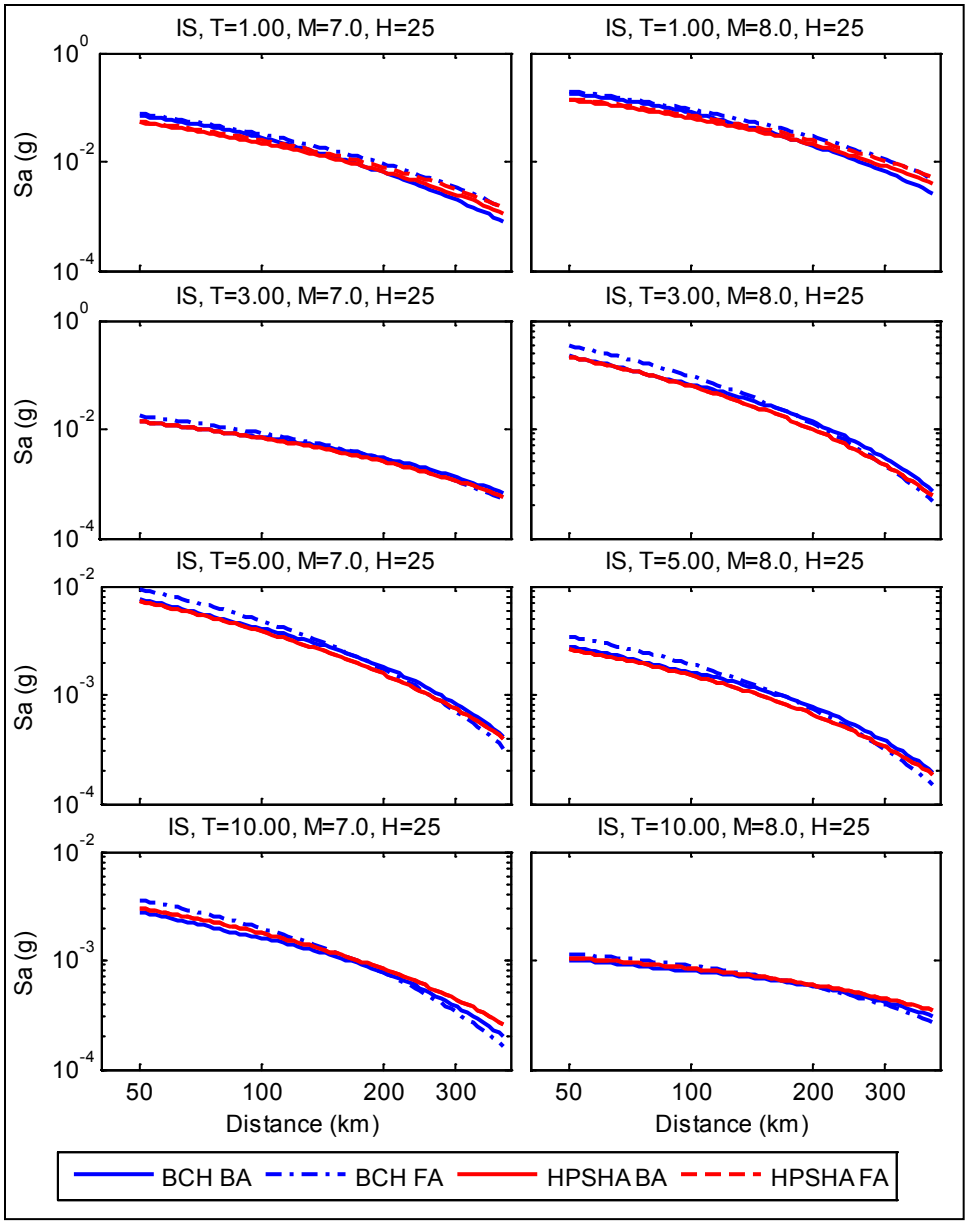

Figure 9.14b. (contd)

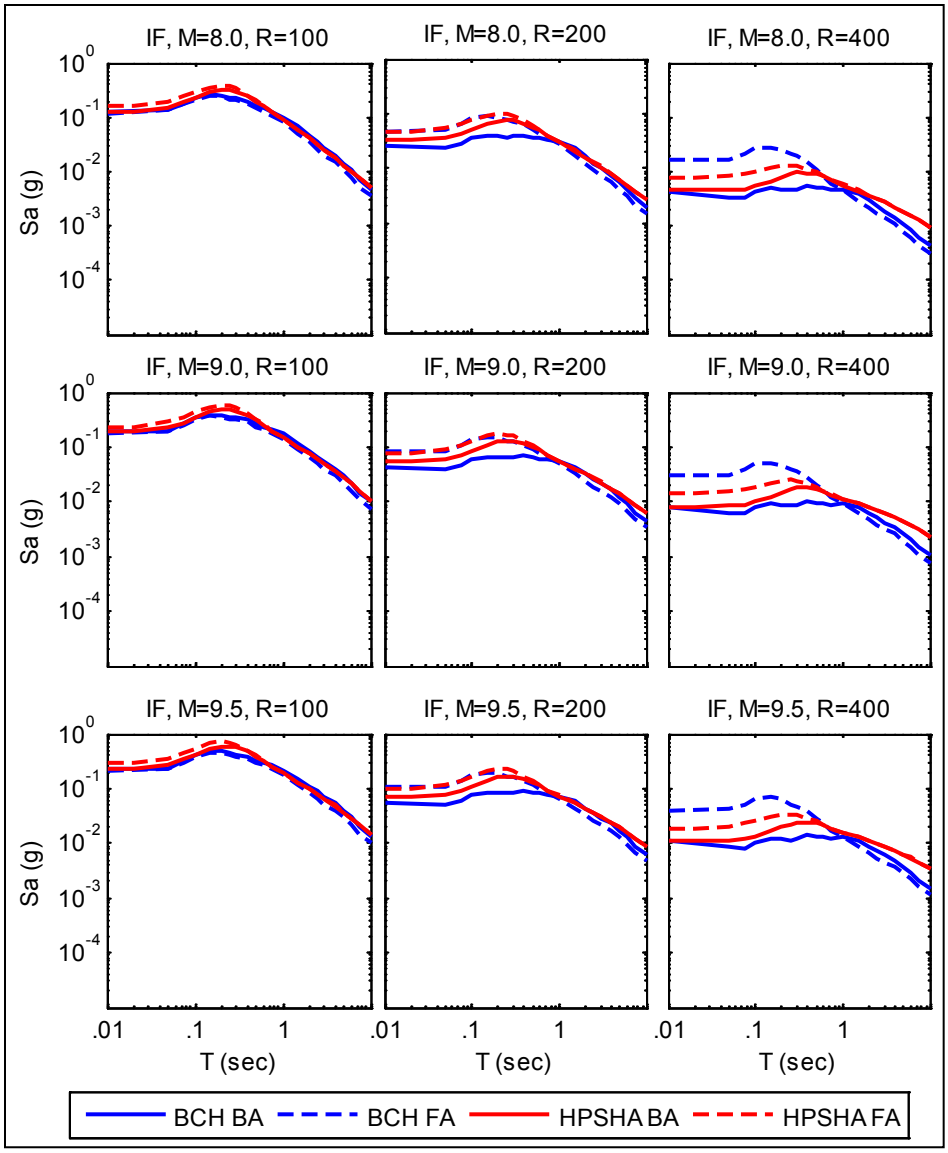

Figure 9.15a. Model predictions for interface earthquakes at selected distances and magnitudes for the proposed model (HPSHA) for forearc (FA) and backarc (BA) cases. The BC Hydro model is shown for comparison.

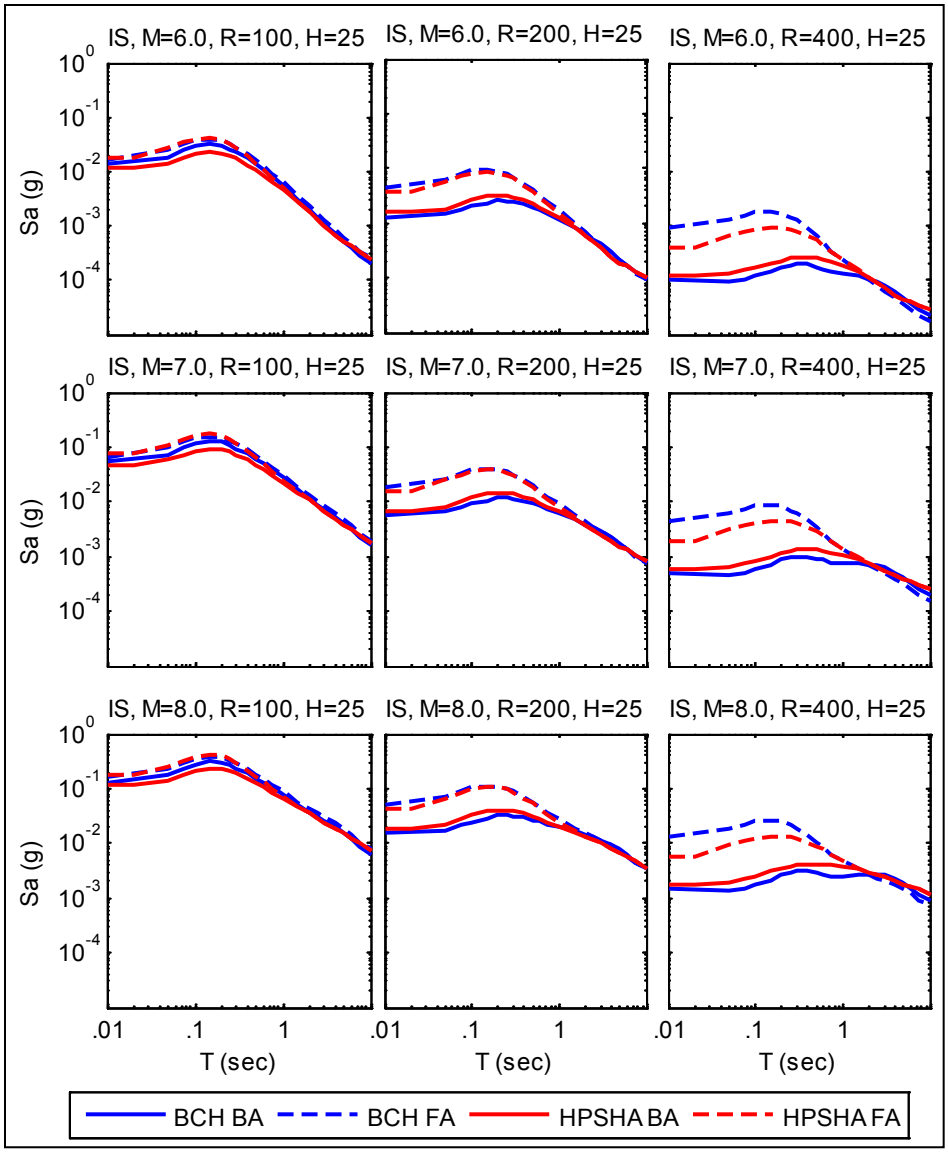

Figure 9.15b. (contd)

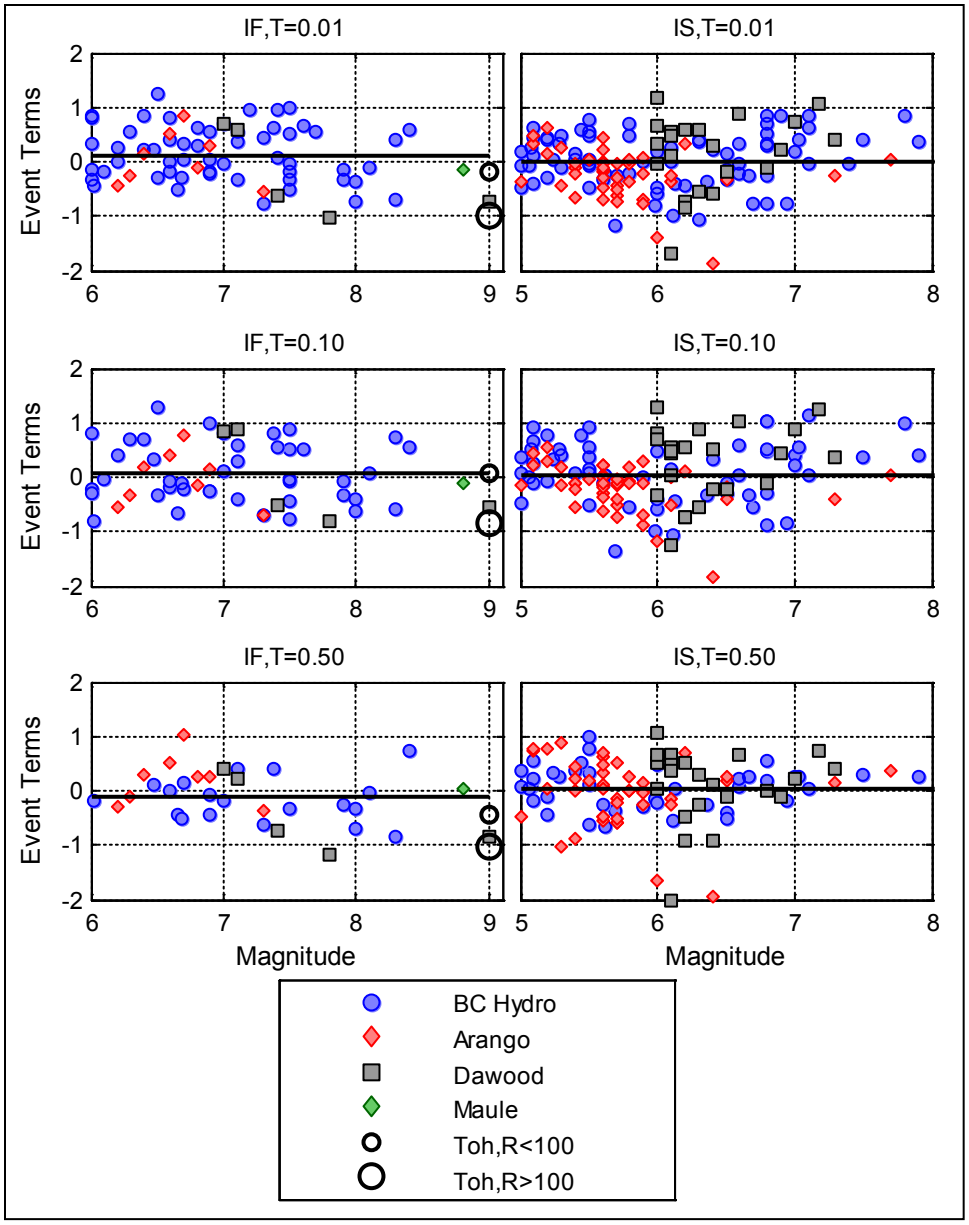

Figure 9.16a. Event terms computed at selected periods. The column on the left shows interface data (IF), the right column shows intraslab data (IS). The data are differentiated by their source. The Tohoku data are included, but were not used in the regression analyses. The solid line is the mean of all the data for each period.

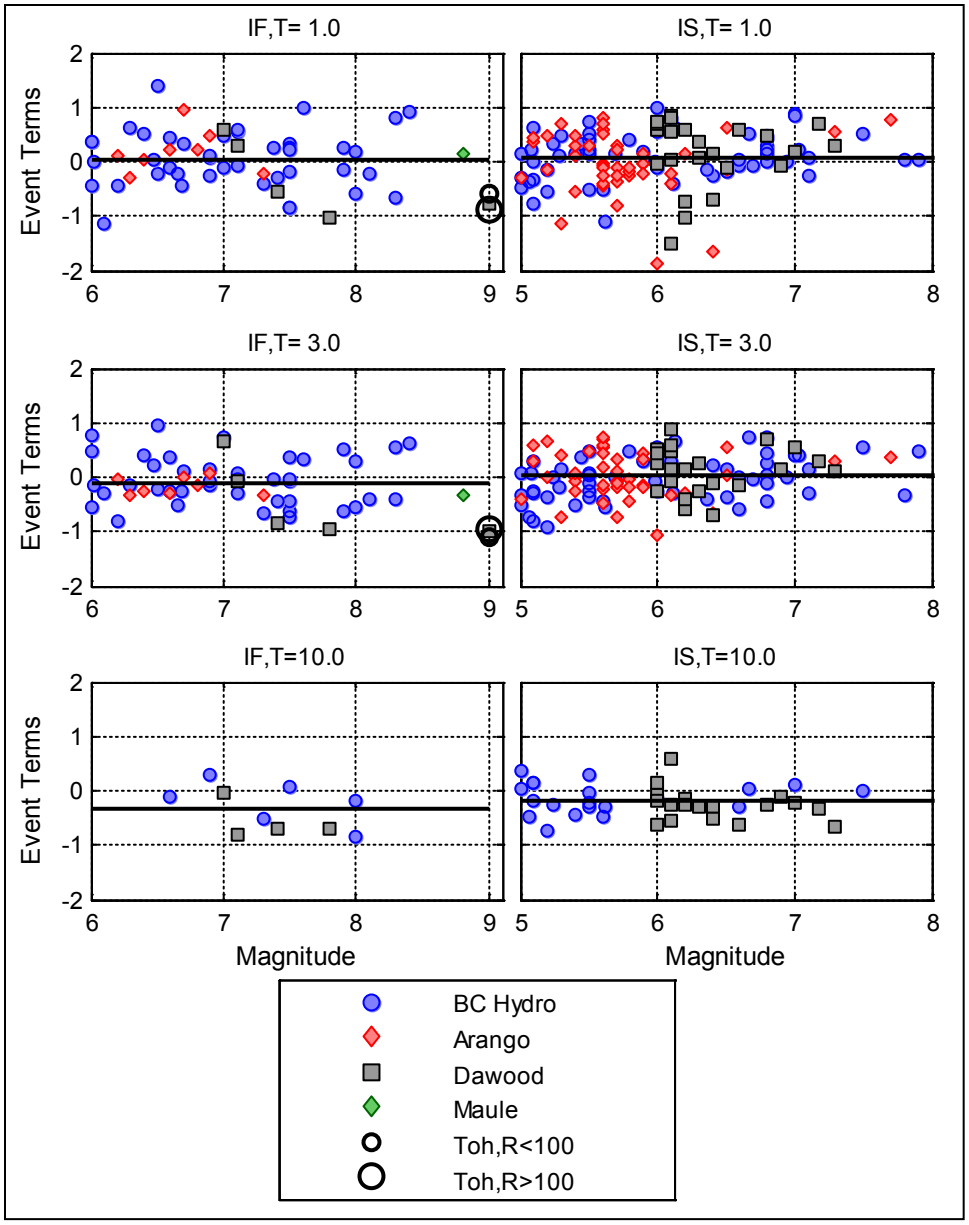

Figure 9.16b. (contd)

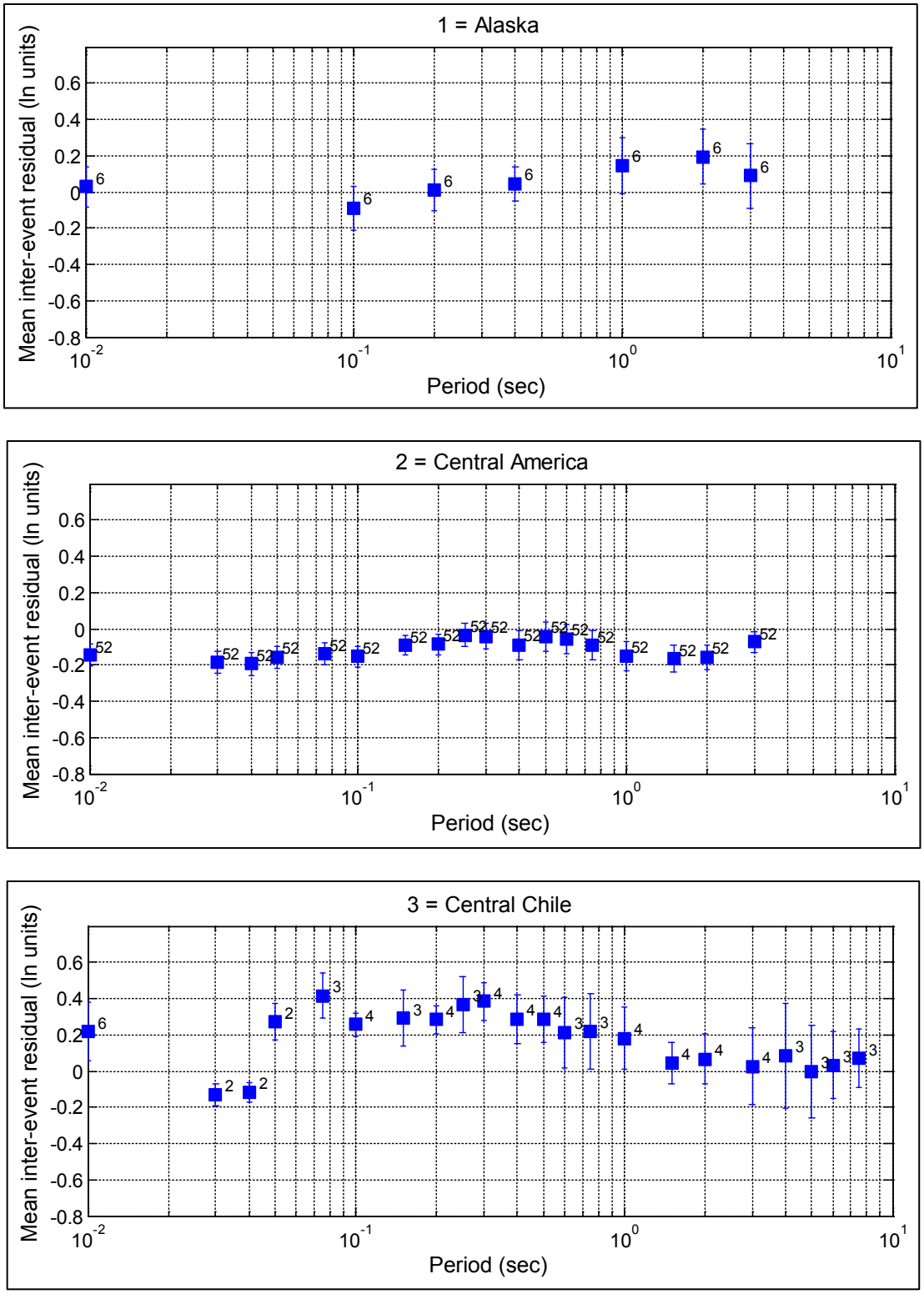

Figure 9.17a. Event terms by region. The number next to the data indicates the number of earthquakes per point. The error bars are a one standard error of the mean range.

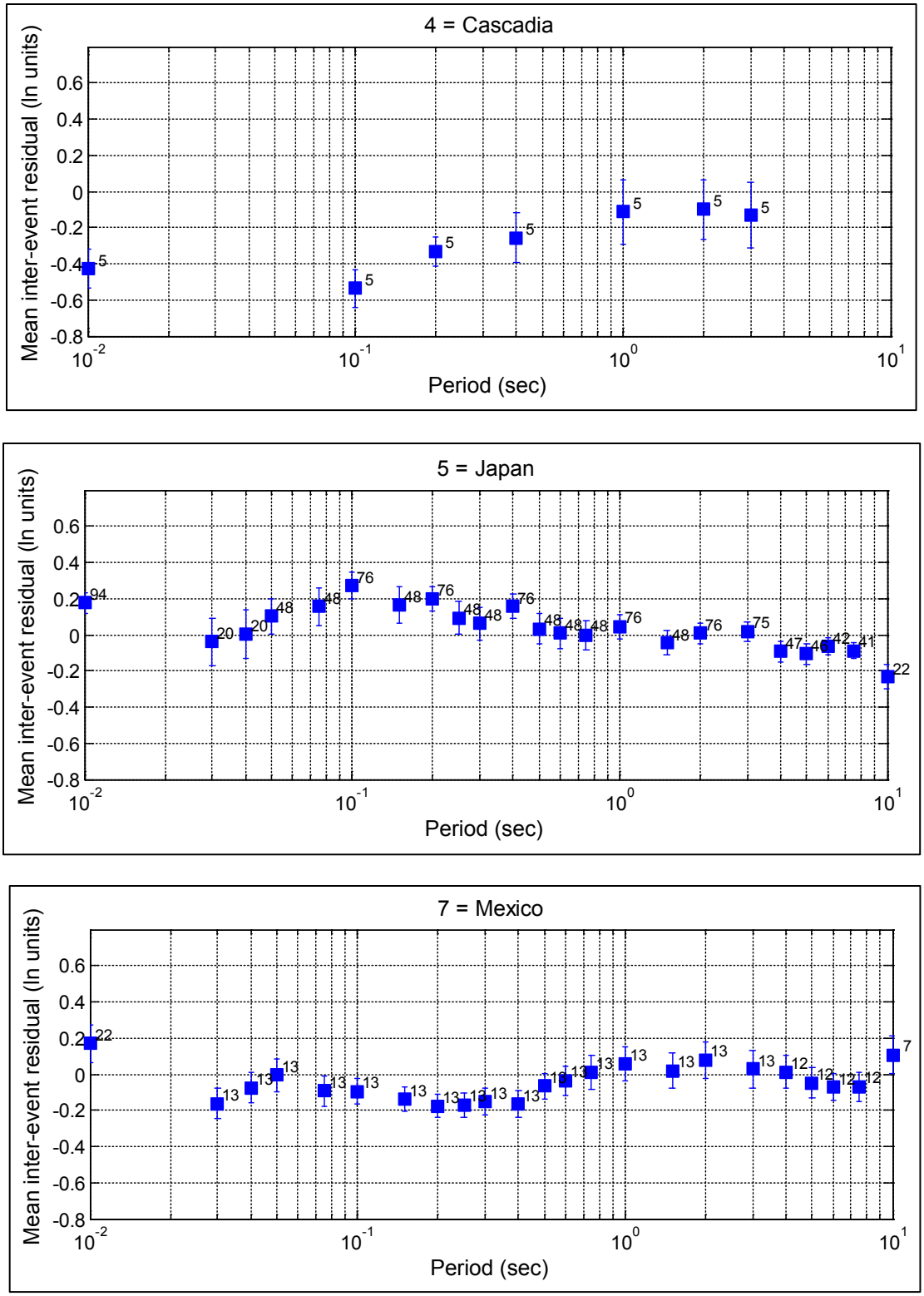

Figure 9.17b. (contd)

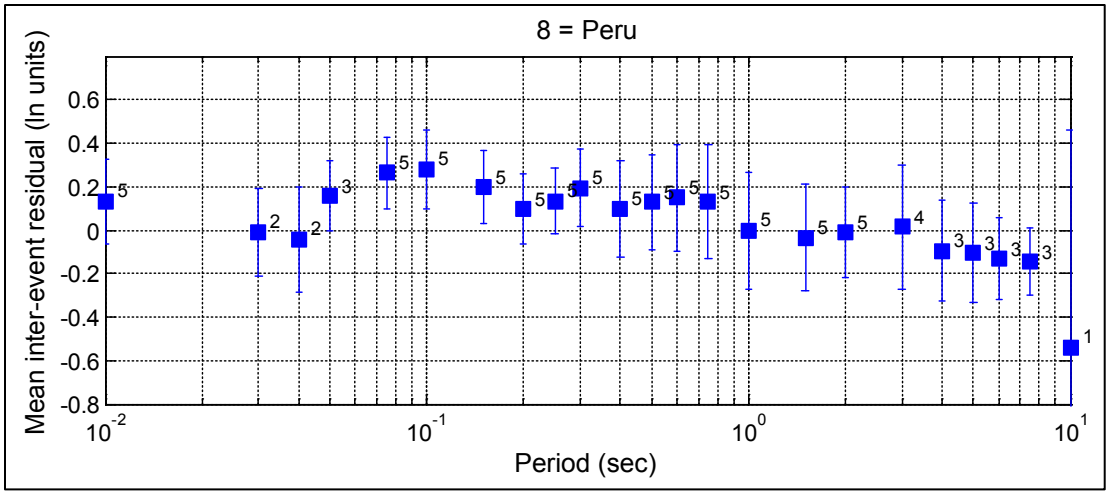

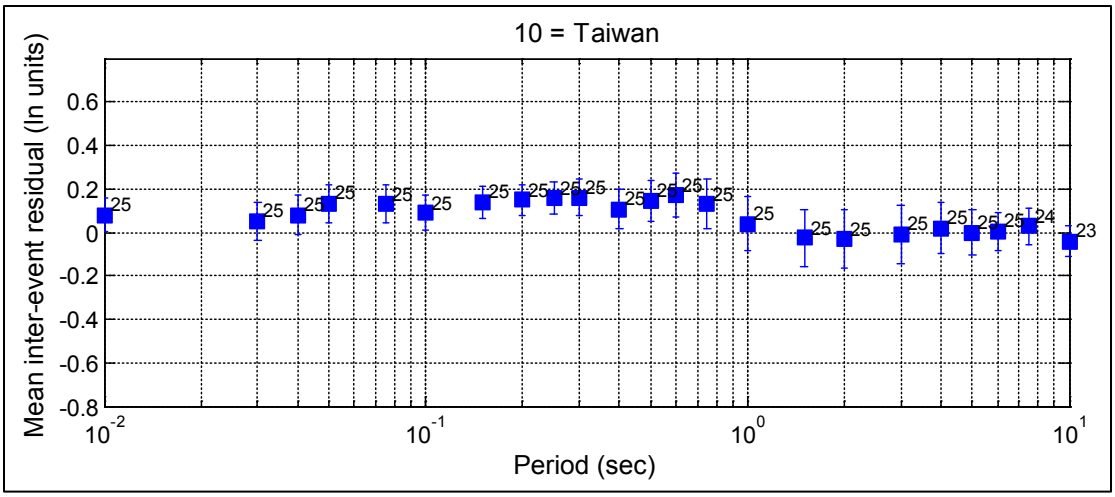

Figure 9.17c. (contd)

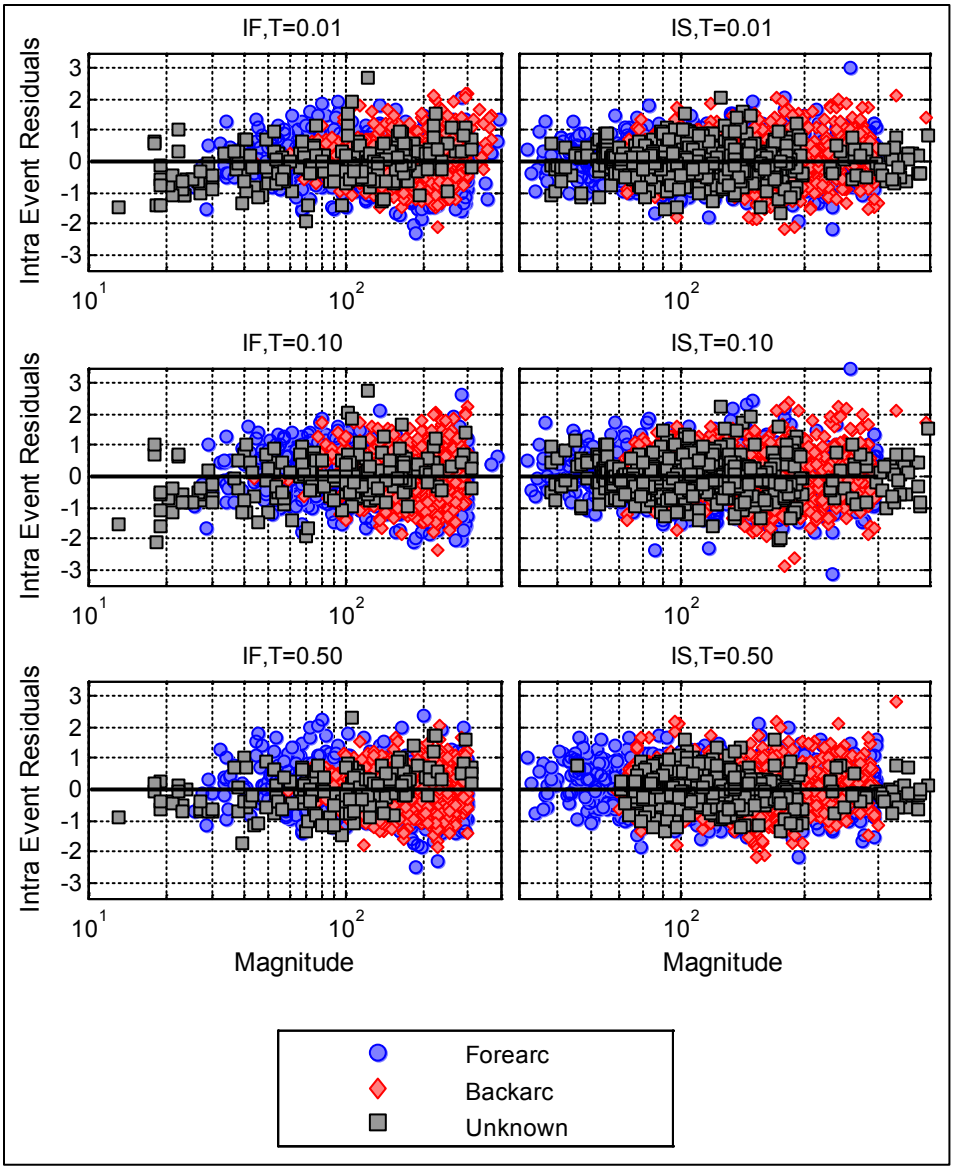

Figure 9.18a. Intra-event residuals for selected periods. The left column and right columns are for interface and intraslab earthquakes, respectively.

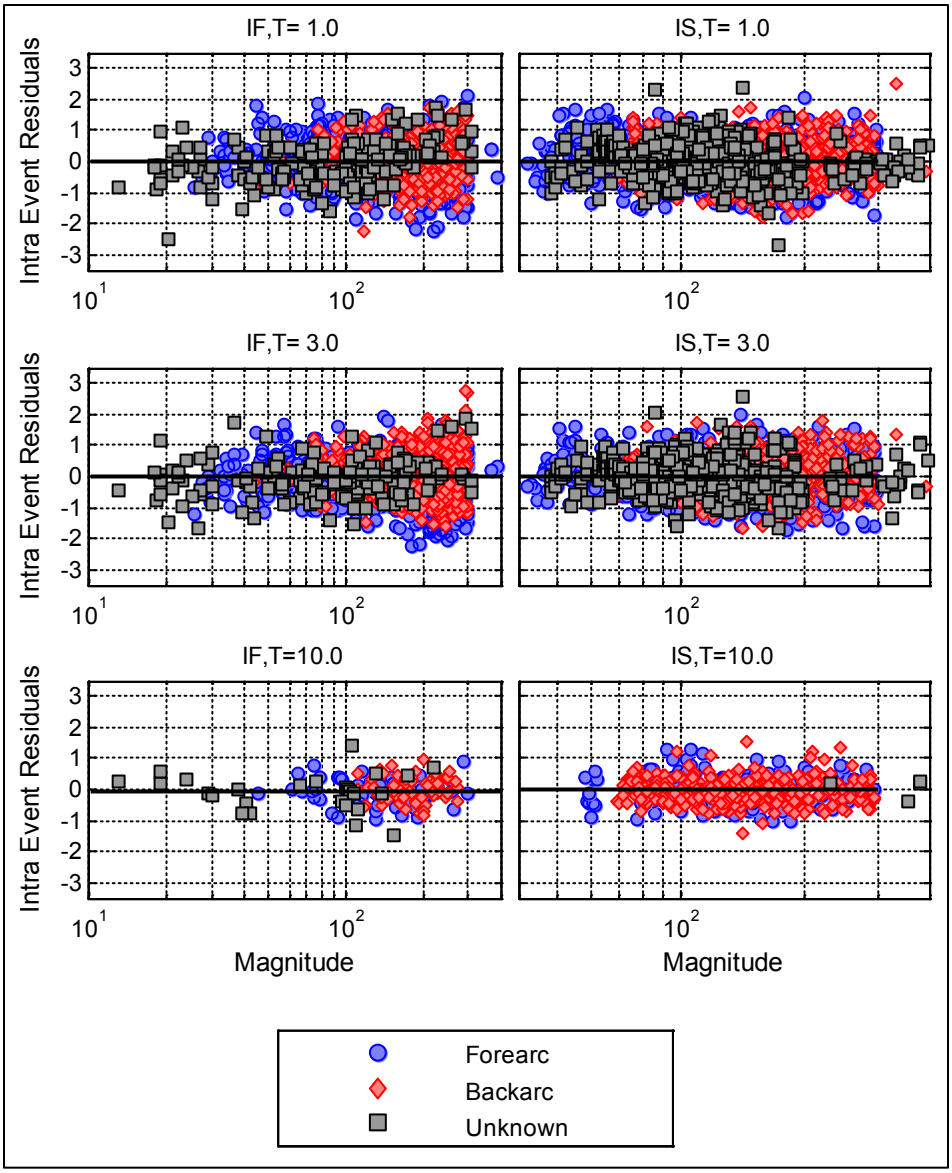

Figure 9.18b. (contd)

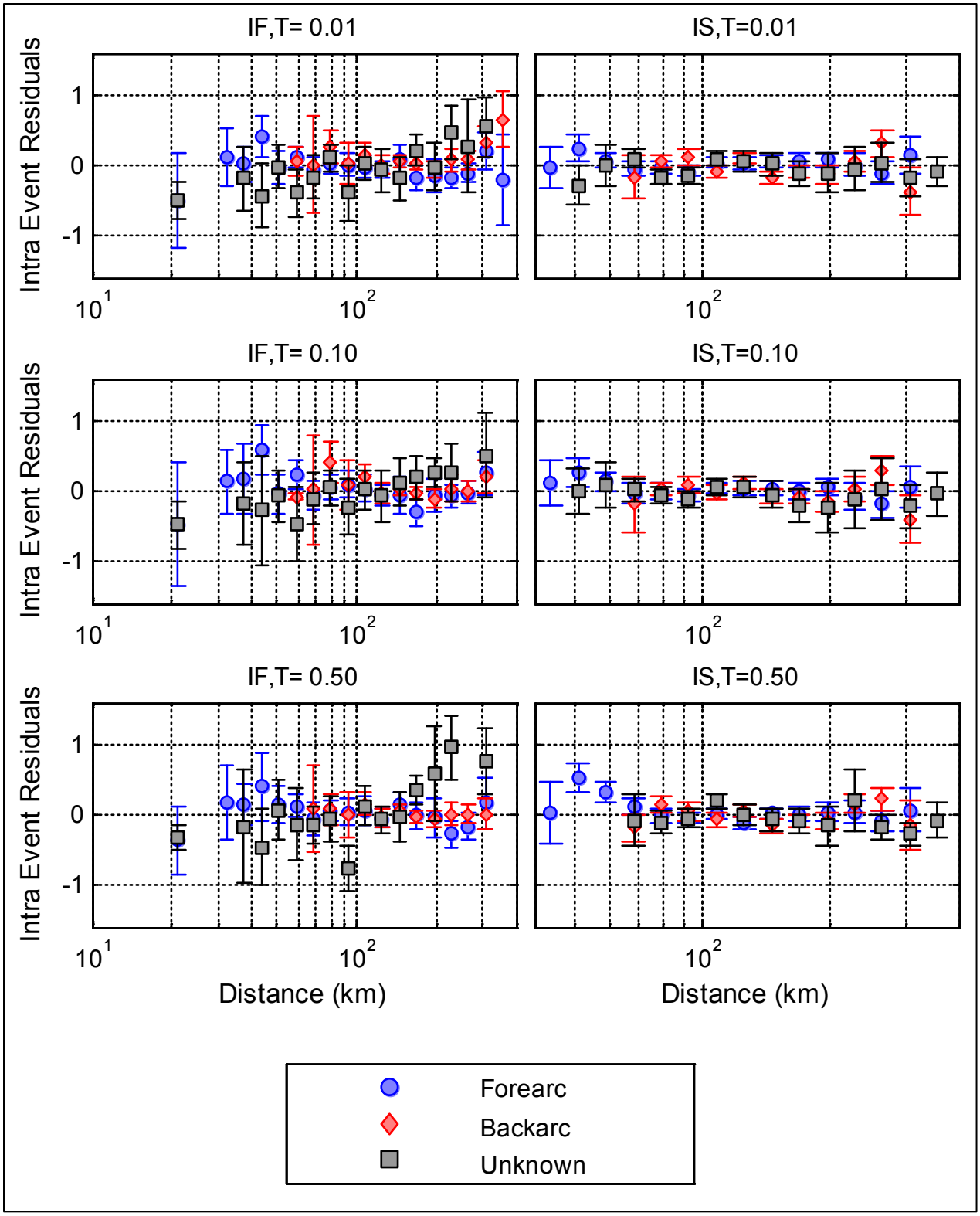

Figure 9.19a–b. Intra-event residuals for selected periods average over distance bins. The left column and right columns are for interface and intraslab earthquakes, respectively. The error bars correspond to a 95% confidence interval of the data within each bin.

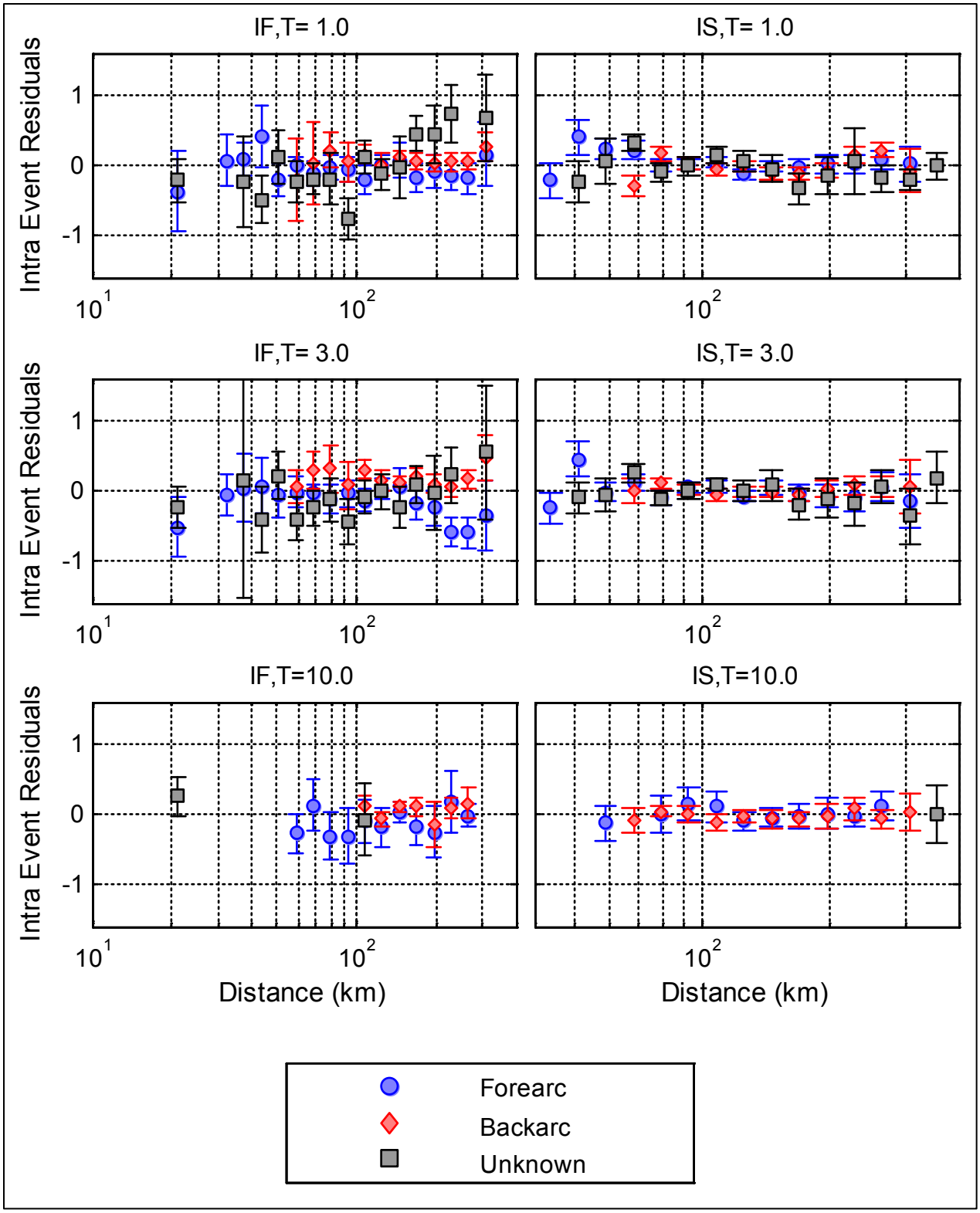

Figure 9.19b. (contd)

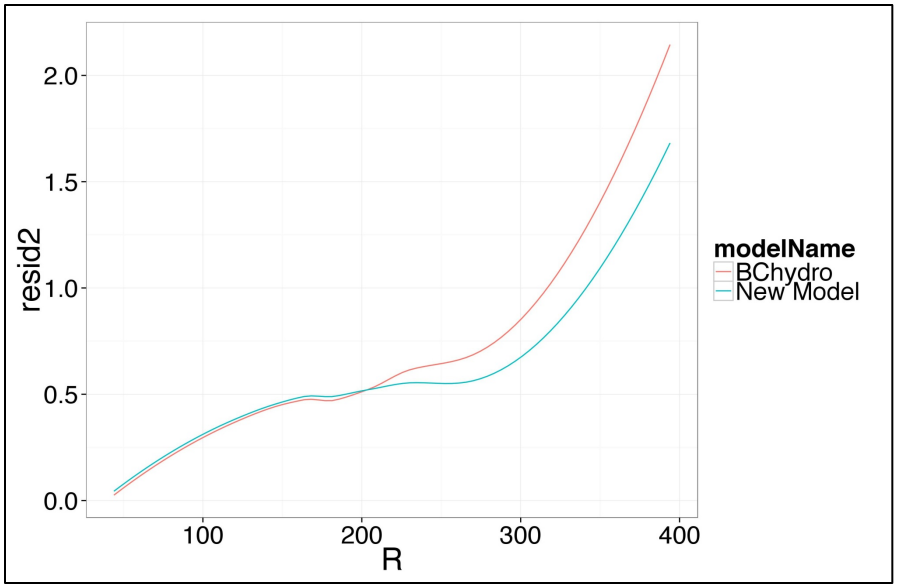

Figure 9.20a−f. Moving average (loess) of the expected value of the square of intra-event residuals. This is an estimate of the variance as a function of distance. The "New Model" refers to the proposed model. Data shown for T = 0.01 sec.

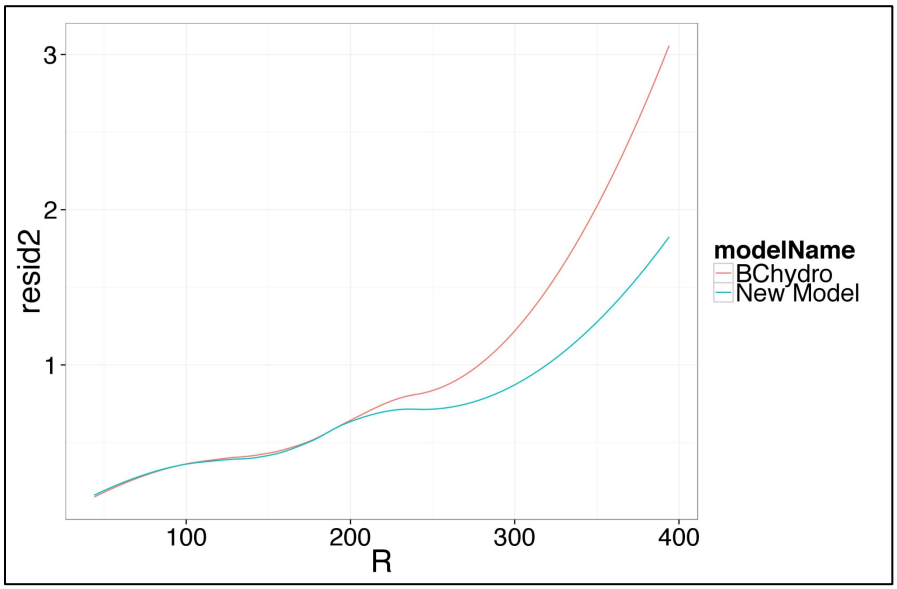

Figure 9.20b. (contd) Data shown for T = 0.2 sec.

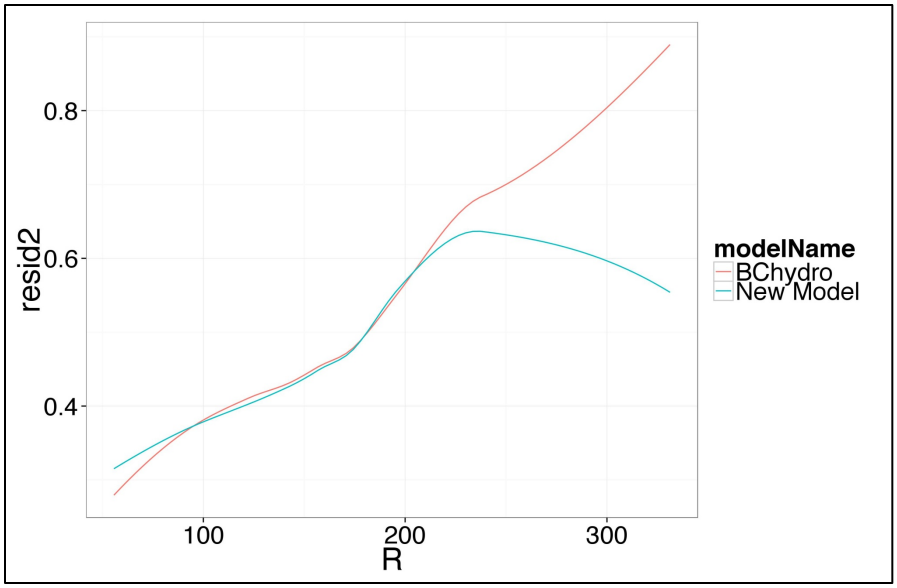

Figure 9.20c. (contd) Data shown for T = 0.3 sec.

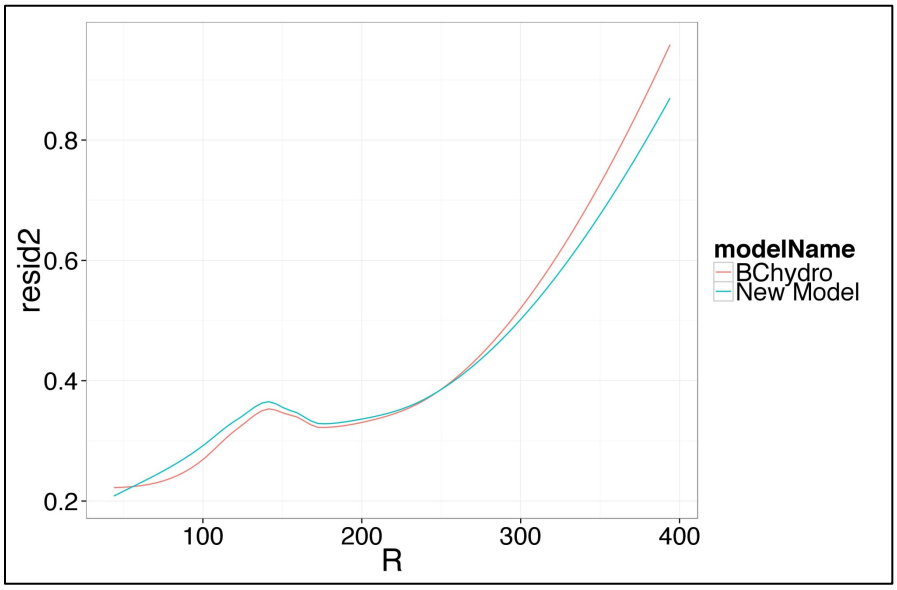

Figure 9.20d. (contd) Data shown for T = 1.0 sec.

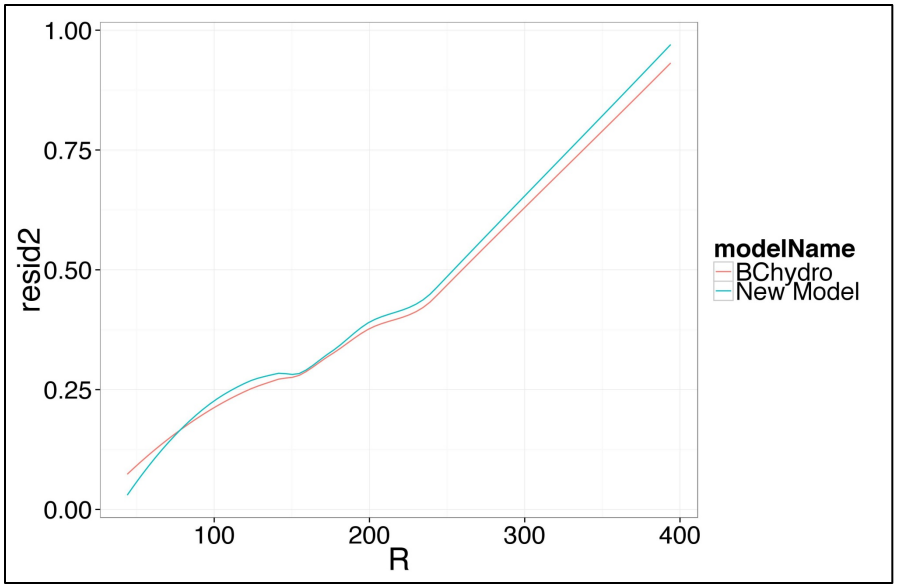

Figure 9.20e. (contd) Data shown for T = 3.0 sec.

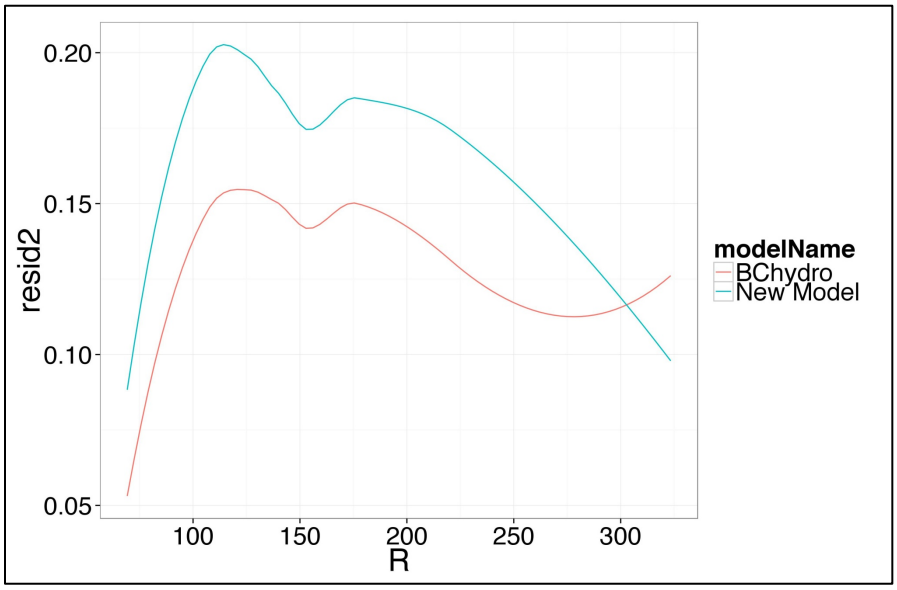

Figure 9.20f. (contd) Data shown for T = 10 sec.

9.3 Site (V_S-Kappa) Adjustments of Backbone GMPEs

Selected backbone GMPEs for the crustal region (Chiou and Youngs 2014, hereafter referred to as CY14) and the subduction region (modified BC Hydro) were adjusted for differences in site conditions (V_S profiles and kappa) between the host and the target regions. The inverse random vibration theory (IRVT) approach (Al Atik et al. 2013) was used to derive GMPE site adjustment factors. The target region is defined as the reference baserock horizon at the five hazard calculation sites—Sites A through E—at Hanford. Target V_S profiles and target $\kappa_{baserock}$ are presented in Section 7.3. This section describes the host V_S profiles and kappa values for the backbone GMPEs, the adjustment methodology, and the derived adjustment factors.

9.3.1 Methodology

The V_S and V_S-kappa scaling factors for the crustal and subduction GMPEs were derived using the IRVT approach described by Al Atik et al. (2013). This approach relies upon deriving GMPE response spectra-compatible Fourier amplitude spectra (FAS) using the IRVT as implemented in the computer program STRATA (Kottke and Rathje 2008). Input to STRATA consists of the GMPE response spectra and ground motion duration estimates for the scenarios considered.

Figure 9.21 presents a flowchart outlining the steps followed to derive kappa adjustment factors for GMPEs. GMPE host kappa values are estimated using the high-frequency slope of the response spectra-compatible FAS according to the Anderson and Hough (1984) method for short-distance scenarios. To decouple kappa from site amplification effects, the FAS are first divided by the host site amplification factors before estimating host kappa. Multiplying the FAS by $\exp[-(\kappa_{target}-\kappa_{host})\pi f]$ results in kappa-adjusted FAS. FAS are multiplied by the ratio of target to host site amplification factors to correct for V_S profile differences between the host and the target regions. The V_S, kappa, and V_S-kappa-adjusted FAS are then converted to response spectra using the random vibration theory (RVT) as implemented in STRATA. Ratios of scaled response spectra to original GMPE response spectra are averaged for the scenarios considered to define the GMPE adjustment factors.

The IRVT approach has the advantage of applying V_S-kappa scaling in the Fourier domain as opposed to the response spectra domain and thus does not rely on the assumption that response spectra scale in a similar fashion to FAS. This approach does not require a full seismological model for the stochastic parameters of the host and target regions and does not assume that the response spectral shape of the GMPE is consistent with that of the point-source stochastic model. As discussed by Al Atik et al. (2013), response spectra with strong high-frequency attenuation such as the Western United States (WUS) spectra are subject to saturation effects resulting from the increased contribution of Fourier amplitudes at lower frequencies to the high-frequency spectral accelerations. This makes it difficult to resolve the FAS at high frequencies (greater than about 30 to 35 Hz for WUS GMPEs) resulting in potentially inaccurate values at these frequencies. Saturation has a more pronounced effect for spectra with stronger high-frequency damping than for those with lower host kappa.

V_S-kappa scaling factors are derived using GMPE response spectra for scenarios at short distances and on stiff soil or rock. Scenarios with short distances are used to minimize the impact of anelastic attenuation (Q) on the high-frequency part of the response spectra and FAS. Relatively high V_{S30} values are used to avoid overwhelming the rock kappa with soil damping. No distance limitation applies when deriving only V_S adjustment factors.

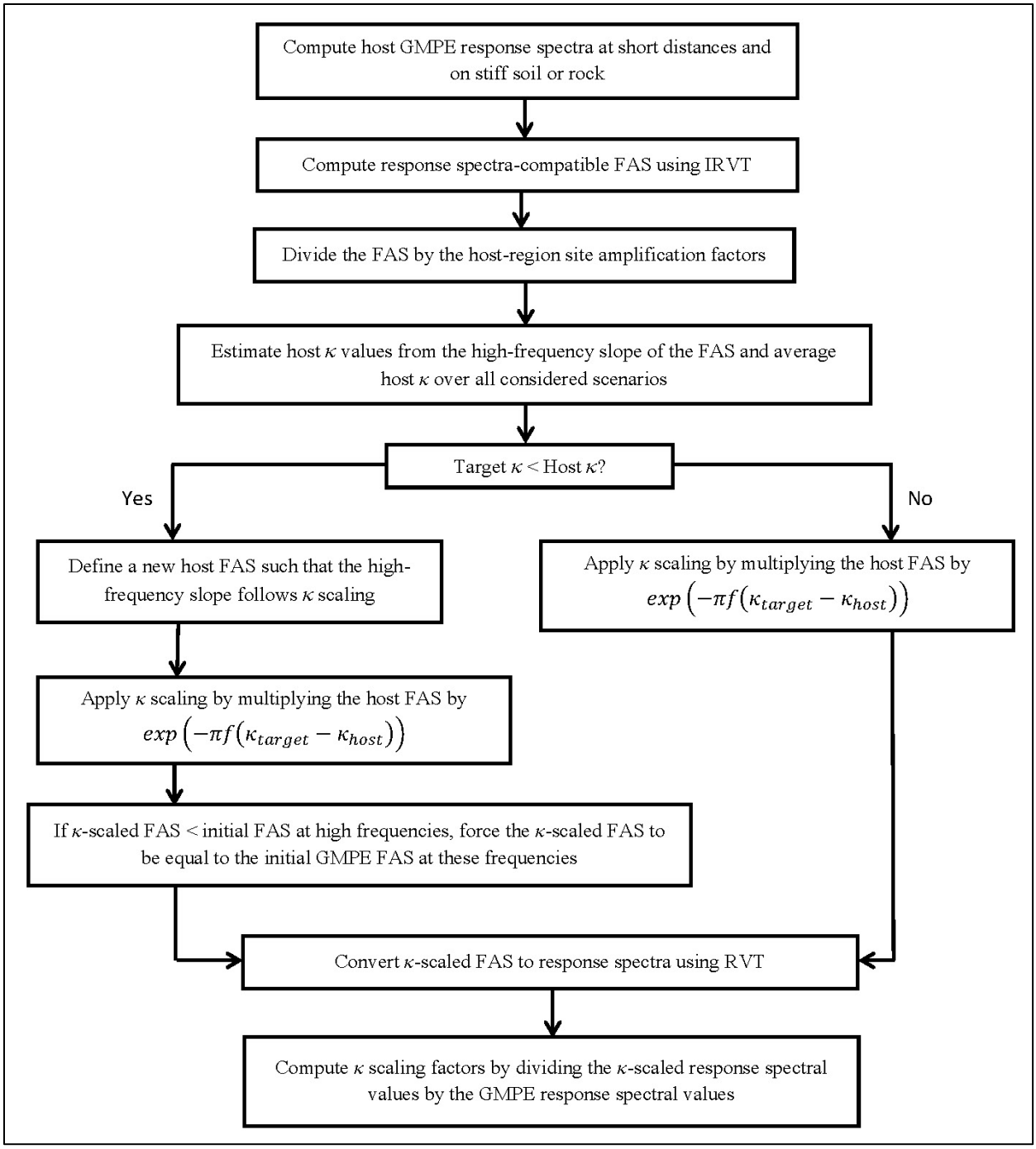

Figure 9.21. Steps for deriving kappa scaling factors using the IRVT approach.

9.3.2 V_S-Kappa Adjustments of Crustal Backbone GMPE

V_S-kappa adjustment factors were derived for CY14 to adjust for V_S profile and kappa differences between the WUS host region and the five hazard calculation sites at Hanford. Target V_S profiles (candidate Profiles 1 and 2) at the five hazard calculation sites and their corresponding site amplification factors are shown in Figures 7.28 and 7.29, respectively. Target $\kappa_{baserock}$ values are listed in Table 7.25 for the target kappa logic tree shown in Figure 7.61.

Adjustment factors were derived and averaged for CY14 strike-slip scenarios with magnitudes 5.5, 6.5, and 7.5 and Joyner-Boore distances (R_{JB}) of 5, 10, and 20 km with V_{S30} of 760 m/sec. These magnitude and distance scenarios were considered because of their significant contribution to the hazard from crustal sources at the Hanford Site while also limiting the Q attenuation effects on the spectra. CY14 response spectra were calculated assuming a dip of 90 degrees with the rupture width calculated according to Wells and Coppersmith (1994). The depth-to-top of rupture (Z_{TOR}) was assumed to be equal to 3 km for magnitude 5.5 scenarios, and zero for the magnitude 6.5 and 7.5 scenarios. Ground motion duration was estimated by adding the source and path durations, which were calculated according to the WUS stochastic model parameters of Campbell (2003) with a stress drop of 100 bars. The resulting adjustment factors are not very sensitive to small changes in the ground motion durations.

9.3.2.1 Host V_S Profiles for Crustal GMPE

It is generally desirable to have a reference host V_S profile that represents an average profile for the region for which the GMPE was developed; having a V_{S30} value that is well sampled in the GMPE data set and that is relatively large to avoid nonlinear soil effects. The WUS V_S profile of Kamai et al. (2013) with a V_{S30} of 760 m/sec was used as a representative V_S profile for the host WUS region. While a V_{S30} of 760 m/sec is not the best sampled value in the CY14 ground motion data set, this profile was selected because of its use in the NGA-West2 site response study and because it satisfies the general criteria for selecting a reference V_S profile. Figure 9.22 shows the host WUS V_S profile along with the target V_S profiles at the Hanford hazard calculation sites.

Linear site amplification factors for the host V_S profile were developed using the square-root impedance (SRI) or quarter wavelength (QWL) method (Boore 2005) as described in Section 7.3.1 for the target V_S profiles. Amplification factors were derived at the surface of the profile with respect to the half-space located at a depth of around 9.6 km with a V_S of 3.5 km/sec. Default densities based on WUS V_S-density relationships built into the QWL program were used. An angle of incidence at the source of zero degrees was adopted. Figure 9.23 presents the QWL linear site amplification factors for the host V_S profile compared to the target V_S profiles at the five hazard calculation sites at Hanford. Figure 9.23 shows that the difference between host and target site amplification factors is large compared to the relative difference in site amplification factors between candidate target Profiles 1 and 2.

The sensitivity of the V_S adjustment factors to deriving the host and target site amplification factors using the full resonant method as implemented in the RATTLE program (Boore 2005) was assessed. A comparison of the CY14 V_S adjustment factors derived for Site A using the QWL method and RATTLE is shown in Figure 9.24. The difference in the V_S adjustment factors is small, and the QWL method leads to slightly more conservative results. Moreover, the QWL method is generally considered to be standard practice (e.g., Boore et al. 2013; Boore and Joyner 1997; Cotton et al. 2006; Renault et al. 2010; Bommer et al. 2014) and was therefore adopted by the TI Team. The sensitivity of the V_S

adjustment factors to using an angle of incidence at the source of 30 degrees instead of zero degrees in the development of the host and target site amplification factors was also evaluated. The resulting impact on the CY14 V_S adjustment factors at Site A is shown in Figure 9.25. While an angle of incidence of 30 degrees is considered to be more appropriate for deep earthquake sources, the difference in the V_S adjustment factors resulting from using zero versus 30 degrees angle of incidence is very small. Moreover, an angle of incidence of zero degrees is considered to be generally more consistent with 1-D site response analyses and was therefore adopted by the TI Team.

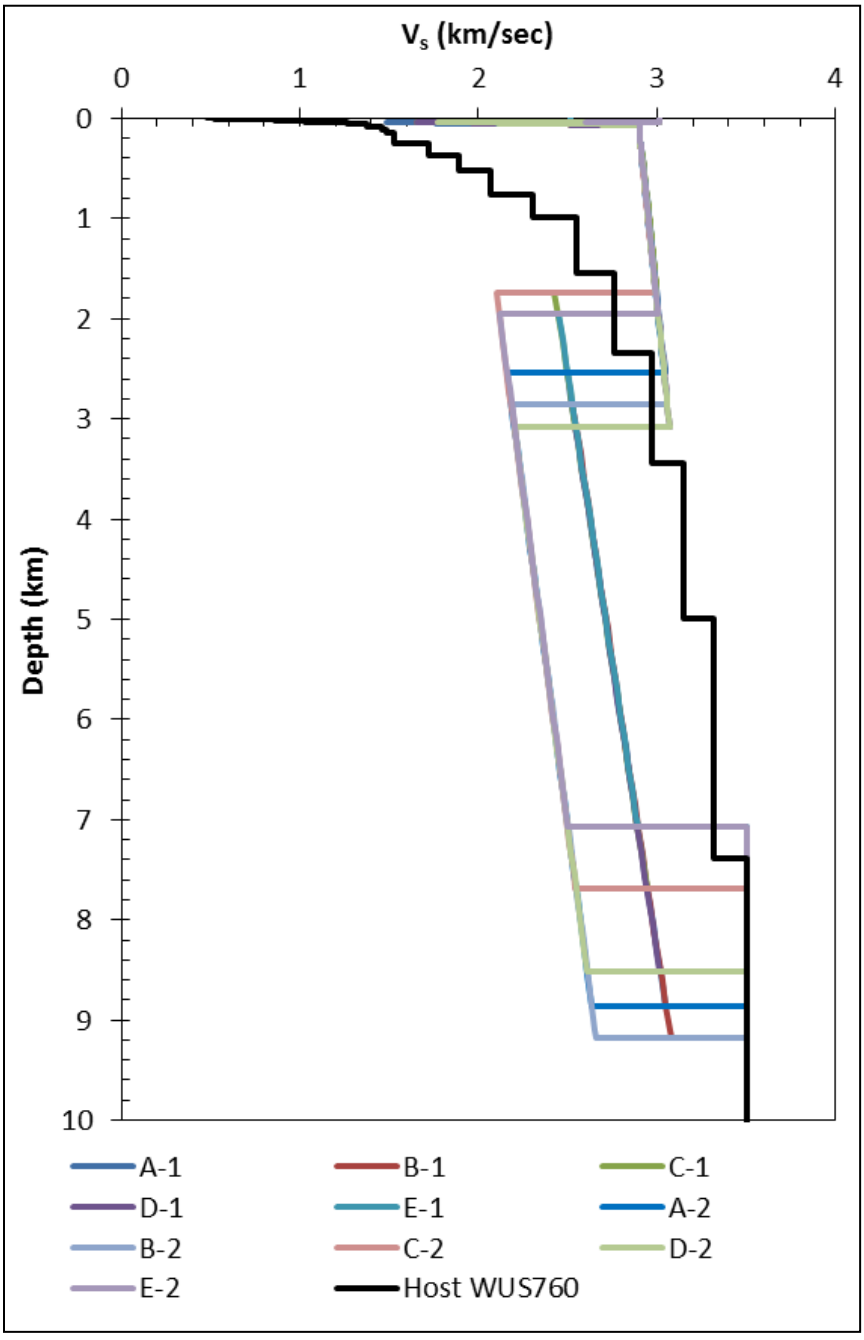

Figure 9.22. Host WUS V_S profile with V_{S30} of 760 m/sec based on Kamai et al. (2013) compared to target V_S profiles at the Hanford hazard calculation sites.

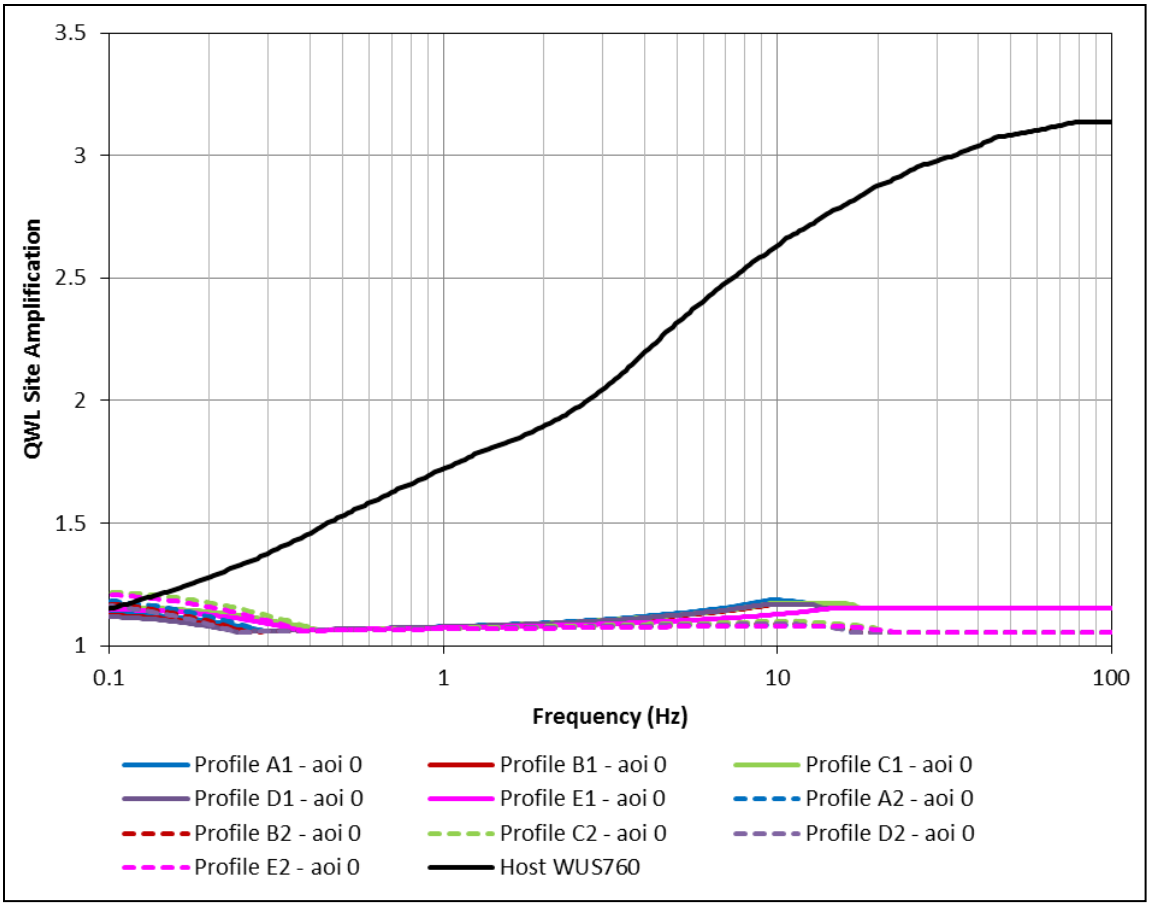

Figure 9.23. QWL linear site amplification factors for the host WUS V_S profile with V_{S30} of 760 m/sec compared to target site amplification factors at the Hanford hazard calculation sites.

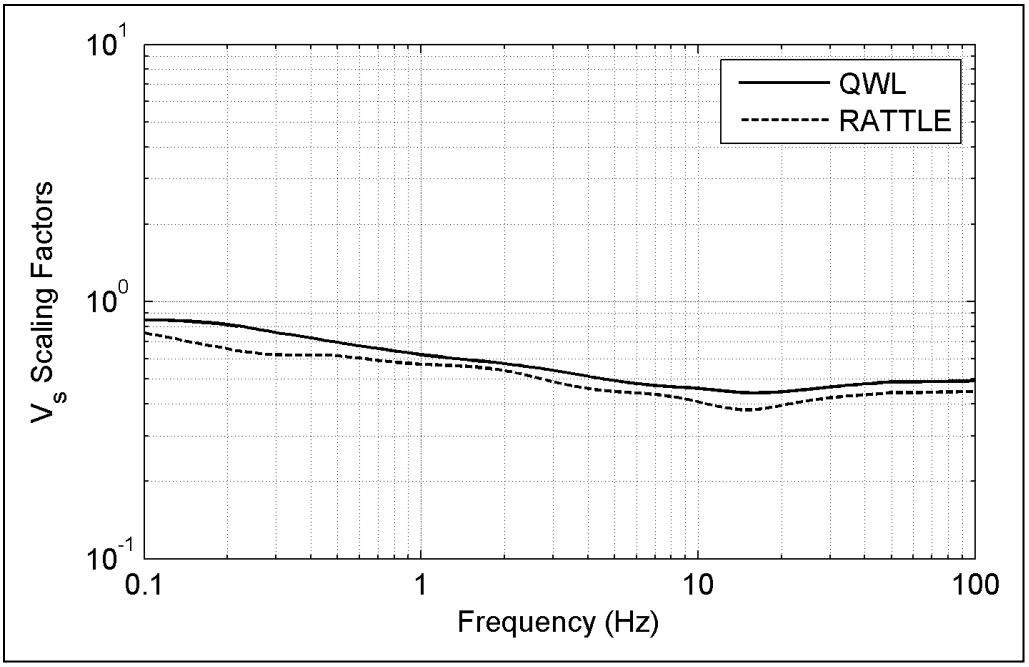

Figure 9.24. Comparison of V_S adjustment factors at Site A using the QWL method versus RATTLE for deriving site amplification factors for the host WUS V_S profile (Kamai et al. 2013) and target Profile 1.

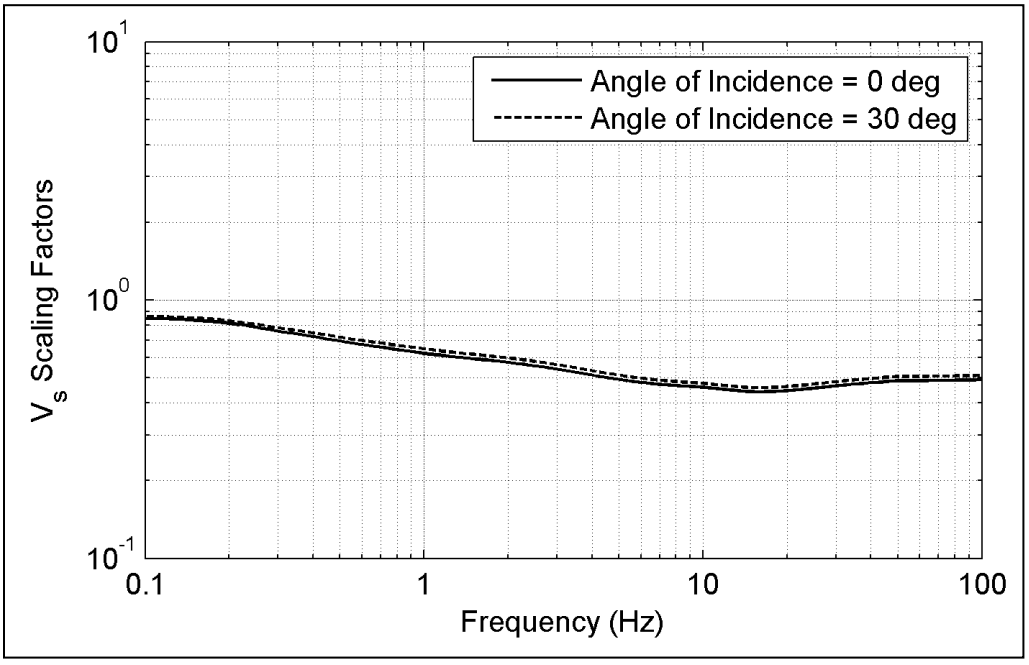

Figure 9.25. Comparison of V_S adjustment factors at Site A Profile 1 using an angle of incidence of zero versus 30 degrees.

9.3.2.2 Host Kappa Values for Crustal GMPE

Host kappa values for CY14 were estimated using the IRVT approach. The GMPE response spectra-compatible FAS were first divided by the host site amplification factors described in Section 9.3.2.1 to decouple the site amplification from kappa effects at high frequency. The resulting FAS were inspected to select the start and end frequencies (f1 and f2) over which log(FAS) versus frequency is linear. Kappa for each of the nine scenarios considered (**M** 5.5, 6.5, and 7.5 and R_{JB} 5, 10, and 20 km) was estimated by fitting the Anderson and Hough (1984) exponential kappa scaling function to the FAS between f1 and f2. Estimated kappa values were averaged for the nine scenarios considered to define the host kappa for CY14. Note that kappa derived using the IRVT approach (κ_1) is not equal to the zero-distance kappa, $\kappa(0)$. However, for the short-distance scenarios considered, the anelastic attenuation effects are considered negligible and κ_1 approximates $\kappa(0)$. Assuming that the source contribution to kappa is negligible, κ_1 also approximates κ_{site}.

Kappa estimates are sensitive to the choice of f1 and f2. After careful visual inspection of the high-frequency FAS slopes, three alternatives for f1 and f2 were considered. The first alternative consists of f1 being selected at the largest frequency corresponding to a Fourier amplitude at 25% below the peak of the FAS after dividing it by the host site amplification factors. f2 was defined as the frequency corresponding to 1.5 times PGA and was not allowed to exceed 20 Hz to avoid saturation effects and because the FAS display curvature beyond 20 Hz. The second and third alternatives consist of a frequency bandwidth of 10 Hz to the left of f2 and to the right of f1, respectively. Figure 9.26 shows an example of the Anderson and Hough (1984) kappa fits to the high-frequency site amplification-corrected CY14 FAS for a scenario with **M** 6.5 and R_{JB} of 10 km. As shown in Figure 9.26, all three alternative f1 and f2 definitions result in excellent kappa fits to the FAS. They also sample the range of kappa values in the linear high-frequency part of the FAS without exceeding the high-frequency limit where the spectra might be affected by saturation and have a sufficient bandwidth (minimum of 10 Hz) to get reliable kappa estimates. The central kappa value (plot a) has the largest frequency range for the Anderson and Hough (1984) kappa fit and was therefore given a slightly higher weight (0.4) compared to the upper and lower kappa estimates with weights of 0.3. Table 9.5 presents the derived kappa values for the nine scenarios considered and for the three alternative f1 and f2 definitions along with the resulting candidate host kappa values. For each host kappa branch, the standard deviation of kappa over the nine scenarios considered is small as shown in Table 9.5.

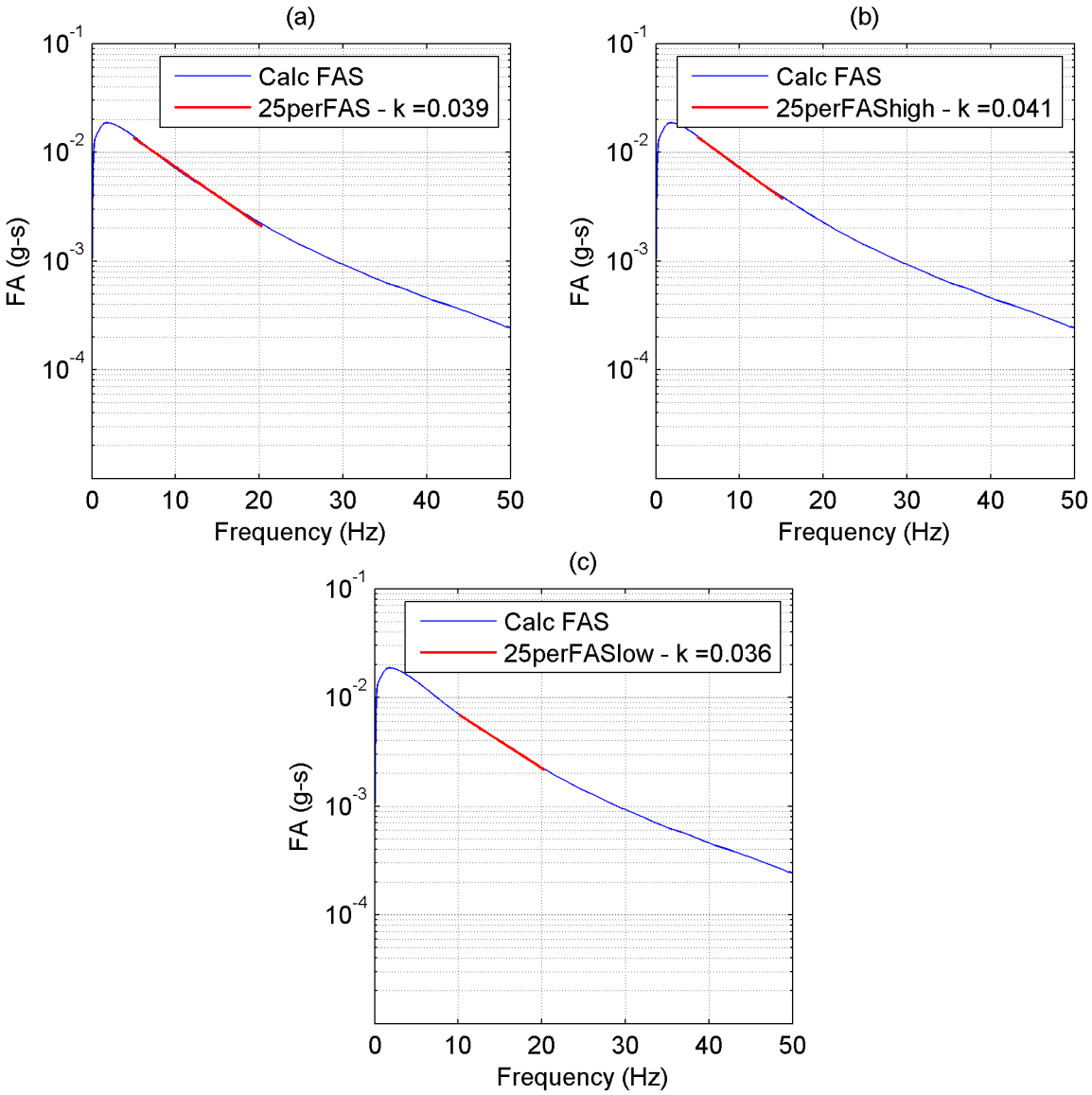

Figure 9.26. Host kappa values for CY14 derived using the IRVT approach for a scenario with **M** 6.5, R_{JB} of 10 km, and V_{S30} of 760 m/sec. (a) f1 selected at 25% below the peak of site amplification-corrected FAS and f2 at minimum of 1.5*PGA or 20 Hz. (b) f1 is the same as in (a) and f2 is at f1 plus 10 Hz. (c) f2 is the same as in (a) and f1 is at f2 minus 10 Hz.

Table 9.5. Host kappa estimates for CY14 estimated using the IRVT approach for the 3 f1-f2 definitions for scenarios with **M** 5.5, 6.5, 7.5 and R_{JB} of 5, 10, and 20 km.

M	R_{JB} (km)	Lower Kappa (sec) (weight 0.3)	Central Kappa (sec) (weight 0.4)	Upper Kappa (sec) (weight 0.3)
5.5	5	0.0384	0.0411	0.0431
5.5	10	0.0379	0.0406	0.0425
5.5	20	0.0368	0.0397	0.0419
6.5	5	0.0369	0.0398	0.0420
6.5	10	0.0363	0.0390	0.0410

Table 9.5. (contd)

M	R_{JB} (km)	Lower Kappa (sec) (weight 0.3)	Central Kappa (sec) (weight 0.4)	Upper Kappa (sec) (weight 0.3)
6.5	20	0.0354	0.0379	0.0398
7.5	5	0.0366	0.0396	0.0418
7.5	10	0.0359	0.0387	0.0407
7.5	20	0.0350	0.0377	0.0395
Average		0.0366	0.0393	0.0414
Standard Deviation		0.0010	0.0011	0.0011

9.3.2.3 V_S-Kappa Adjustment Factors and Sensitivity of Adjustments

Two candidate V_S profiles below the reference baserock horizon are available at each hazard calculation site at Hanford along with their derived site amplification factors. As shown in Figure 9.23, the difference in the site amplification factors for the two candidate V_S profiles at any site is small compared to the difference between the host and target site amplification factors. The sensitivity of the derived V_S-kappa adjustment factors to the use of the two candidate target V_S profiles was examined for Site A. Figure 9.27 (all figures mentioned here follow at the end of this section) shows a comparison of the V_S-kappa adjustment factors for CY14 for three target kappa values of 0.0036, 0.0278, and 0.0666 sec that represent upper, lower, and central kappa values for Site A using candidate Profiles 1 and 2. The resulting difference in the V_S-kappa scaling factors using Profile 1 versus 2 is small (less than 10%), and Profile 1 leads to slightly more conservative factors. Therefore, one target site-specific V_S profile (Profile 1) was used at the Hanford hazard calculation sites to derive V_S-kappa adjustment factors for CY14.

One host WUS V_S profile (Kamai et al. 2013) with a V_{S30} of 760 m/sec was adopted for deriving the CY14 V_S-kappa adjustment factors. The sensitivity of the derived V_S-kappa adjustment factors to using a different WUS V_S profile with a V_{S30} of 760 m/sec obtained by interpolating the Boore and Joyner (1997) V_S profiles according to Cotton et al. (2006) was explored. A comparison of the candidate WUS V_S profiles and their corresponding site amplification factors is shown in Figure 9.28. Derived V_S-kappa scaling factors for CY14 using the two host V_S profiles are shown in Figure 9.29 at Site A for target $\kappa_{baserock}$ values of 0.0036, 0.0278, and 0.0666 sec. The difference in the derived V_S-kappa scaling factors using the two host V_S profiles is small; the maximum is on the order of 7 to 10% at low frequency. Therefore, only one host V_S profile was used in deriving the CY14 V_S-kappa adjustment factors. The logic tree for host and target V_S profiles is shown in Figure 9.21.

Figure 9.30 presents the host and target kappa logic-tree structure. The host kappa logic-tree branches and their associated weights were discussed in Section 9.3.2.2. Target kappa logic tree was discussed extensively in Chapter 7.0 (Section 7.3.5.3) and is briefly summarized here with different target kappa values calculated for the five hazard calculation sites according to Equation (7.13). Two V_S profiles were constructed for the PSHA sites: Profile 1 based on the V_S values from downhole measurements and V_S in the sub-basalt sediments layer assigned according to a V_P/V_S ratio of 1.73 and Profile 2 based on the V_S values from the PS logging and V_S values in the sub-basalt sediments using a V_P/V_S ratio of 2. Weights of 0.67 and 0.33 were assigned to Profile 1 and 2, respectively, based on the discussion of the two V_S measurement methods presented in Section 7.3.5.3. γ values were derived using the kappa values estimated at the recording stations using the inversion approach and the Anderson and Hough (1984) approach. Given the fact that the Anderson and Hough (1984) method is more affected by

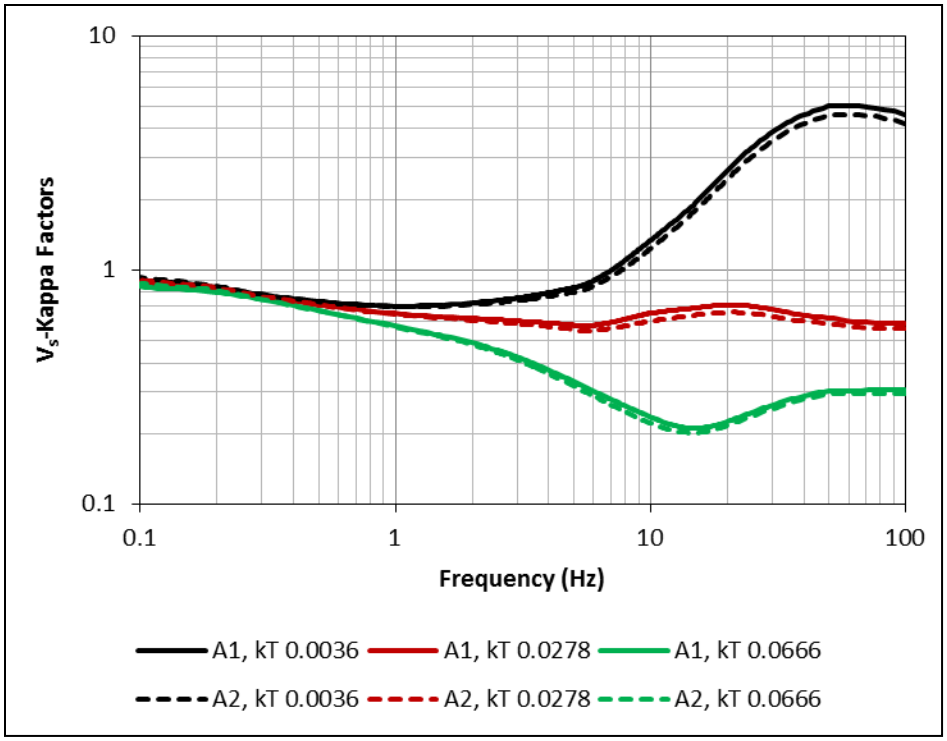

Figure 9.27. Comparison of derived V_S-kappa adjustment factors for CY14 at Site A using Profiles 1 and 2 and target $\kappa_{baserock}$ values of 0.0036, 0.0278, and 0.0666 sec.

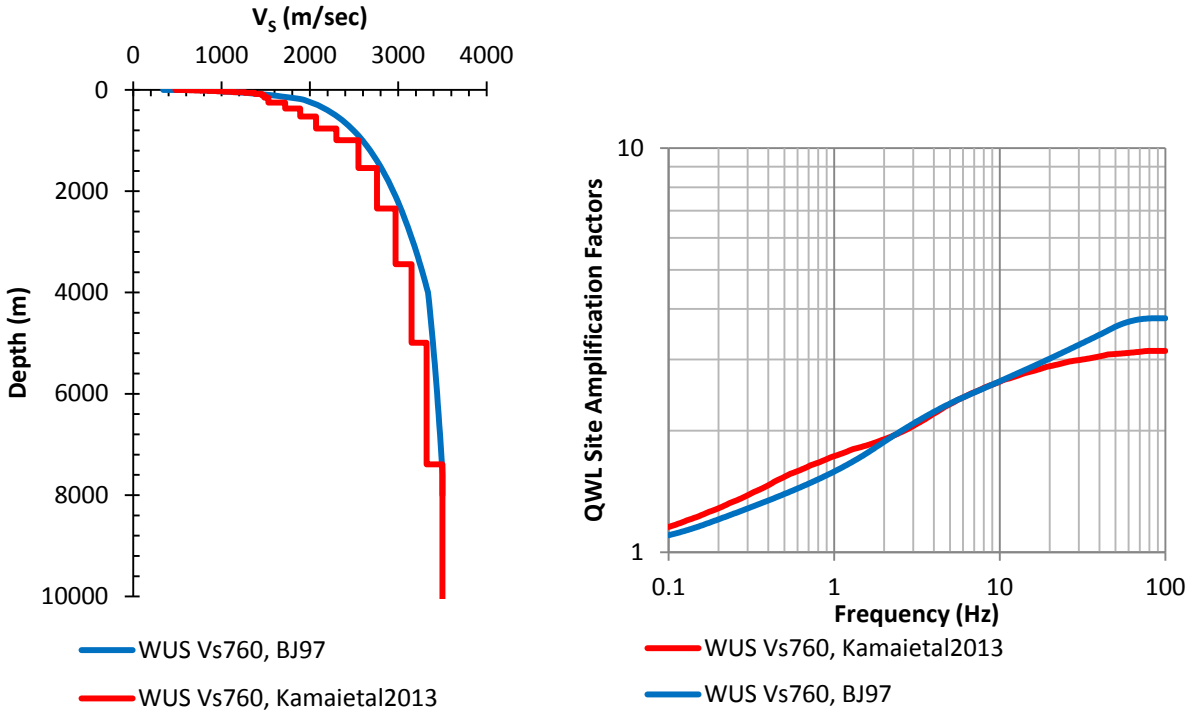

Figure 9.28. Comparison of candidate WUS host V_S profiles (left) with V_{S30} of 760 m/sec and corresponding QWL site amplification factors (right).

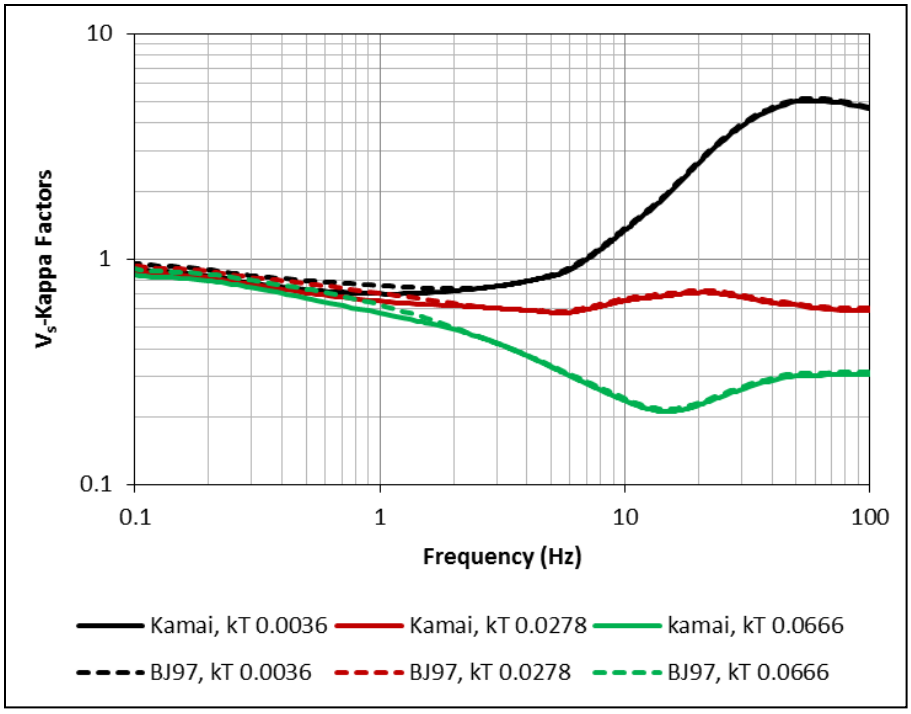

Figure 9.29. Comparison of V_S-kappa adjustment factors derived for CY14 at Site A using the Kamai et al. (2013) WUS host V_S profile and the Boore and Joyner (1997) host V_S profile. Target $\kappa_{baserock}$ is 0.0036, 0.0278, and 0.0666 sec.

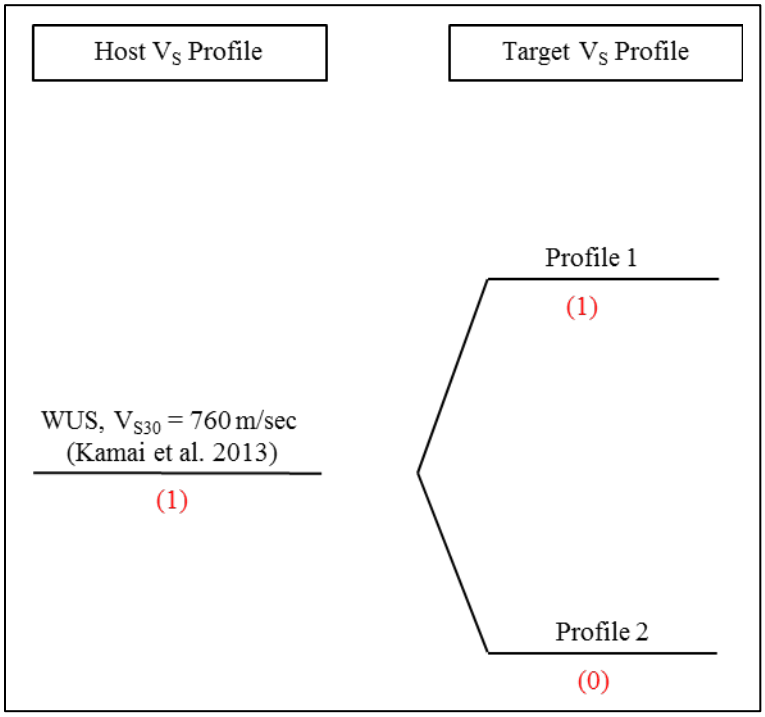

Figure 9.30. Host and target V_S profile logic tree for the CY14 V_S-kappa adjustment factors.

the limited-frequency bandwidth of the recordings and results in different inferred average Q values at the different stations, the inversion method was considered more reliable and given double the weight of the Anderson and Hough (1984) method. Epistemic uncertainty on κ_{site} derived using the inversion approach was considered by adopting the γ values derived using the inversions' best estimates, upper and lower estimates of κ_{site} at the stations. Because the inversions used a fixed frequency-dependent Q that is larger than Q estimated by Phillips et al. (2014) for the Hanford Site, the inversions' best estimates of κ_{site} at the stations were not considered to be representative of the median of the κ_{site} distribution and weights of 0.1, 0.5, and 0.4 were given to the γ values obtained from the upper, best, and lower κ_{site} estimates at the stations. The upper and lower branches of κ_{site} derived by the Anderson and Hough (1984) approach were developed assuming a lognormal distribution of kappa with weights on the branches corresponding to a discrete three-point representation of the assumed continuous distribution. Given the lack of knowledge on the depth of profile that would contribute to kappa for the depth distribution of future earthquakes, the TI Team adopted three branches for the profile depth: entire thickness of sub-basalt sediments layer, half of the sub-basalt sediments layer, and no sub-basalt sediments with almost equal weights of 0.33, 0.34, and 0.33, respectively. Target $\kappa_{baserock}$ values at the five hazard calculation sites are presented in Table 7.25 for the target kappa logic-tree branches in Figure 9.31.

A total of 108 V_S-kappa adjustment factors were derived at each site. For each host and target kappa values, scaling factors were derived using the nine scenarios described above (**M** 5.5, 6.5, 7.5 and R_{JB} of 5, 10, and 20 km) and averaged. Figure 9.32 through Figure 9.35 show sensitivities of the CY14 V_S-kappa adjustment factors at Site A to the alternative branches at each level of the logic tree. For the host kappa branches, Figure 9.32 shows that the V_S-kappa adjustment factors are generally larger for the upper host kappa branch than for the central and lower host kappa branches because $\exp[-(\kappa_{target}-\kappa_{host})\pi f]$ increases when κ_{host} is larger. Comparing the V_S-kappa adjustment factors resulting from using Profile 1 versus Profile 2 in calculating target $\kappa_{baserock}$, Figure 9.33 shows that the adjustment factors are generally smaller for the Profile 2 branch because it results in larger target $\kappa_{baserock}$ values than Profile 1. The largest impact on the V_S-kappa adjustment factors comes from the profile depth branches as shown in Figure 9.34. The smallest profile depth with no contribution from the sub-basalt sediments results in the smallest target $\kappa_{baserock}$ values; hence the largest V_S-kappa adjustment factors. The Anderson and Hough (1984) approach generally resulted in smaller target $\kappa_{baserock}$ values compared to the inversion approach and therefore leads to larger V_S-kappa adjustment factors as shown in Figure 9.26.

The 108 V_S-kappa adjustment factors derived for each site were re-sampled using seven branches according to Miller and Rice (1983) to simplify the hazard calculations. Figure 9.36 to Figure 9.40 present the 7 sets of V_S-kappa adjustment factors at the five hazard calculation sites compared to the 108 sets of factors and show that the 7 branches sample well the V_S-kappa adjustment factors distribution at each site. The seven sets of adjustment factors at Sites A, B, and D are generally similar, while Sites C and E have larger V_S-kappa adjustment factors.

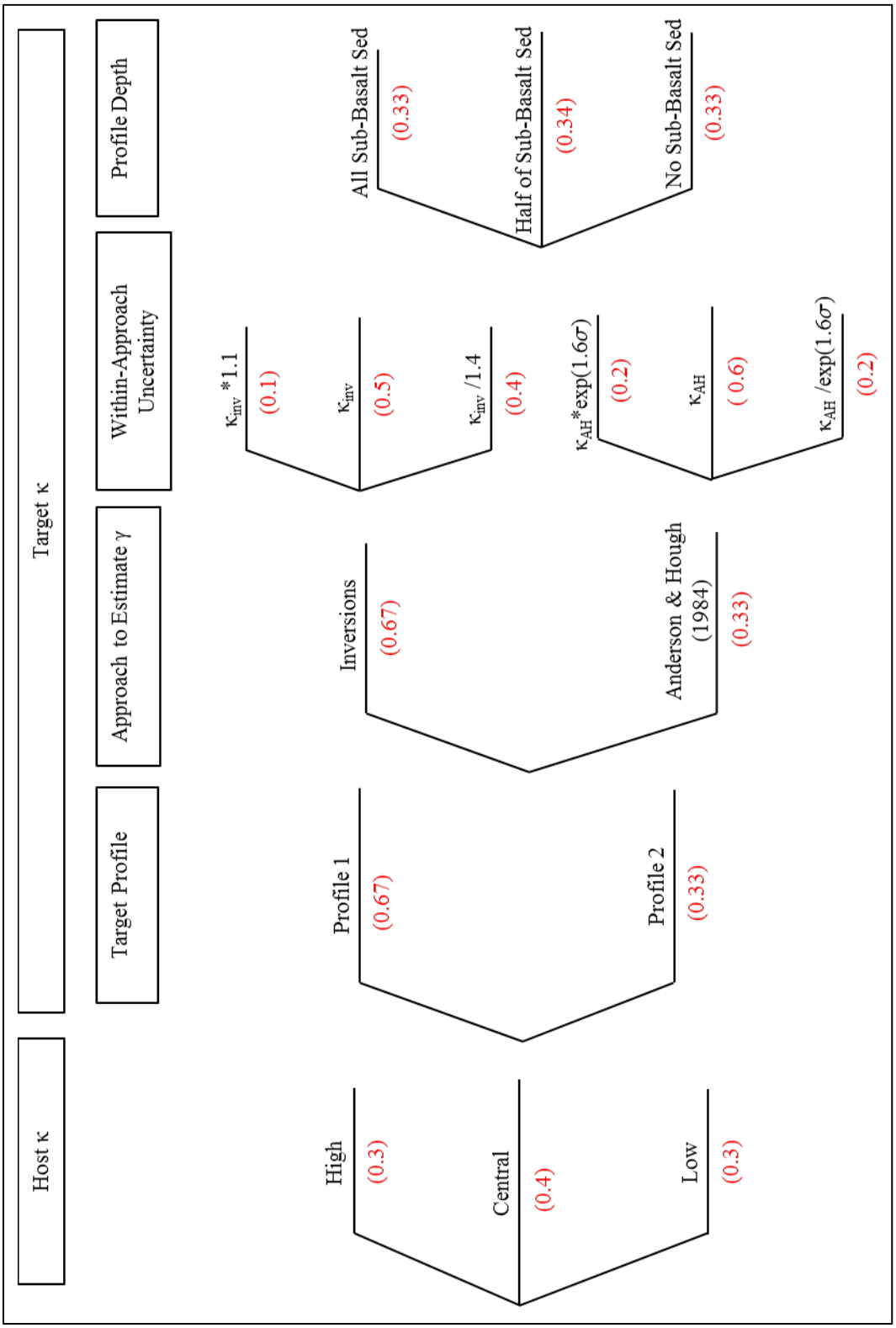

Figure 9.31. Host and target kappa logic tree for the CY14 V_S-kappa adjustment factors.

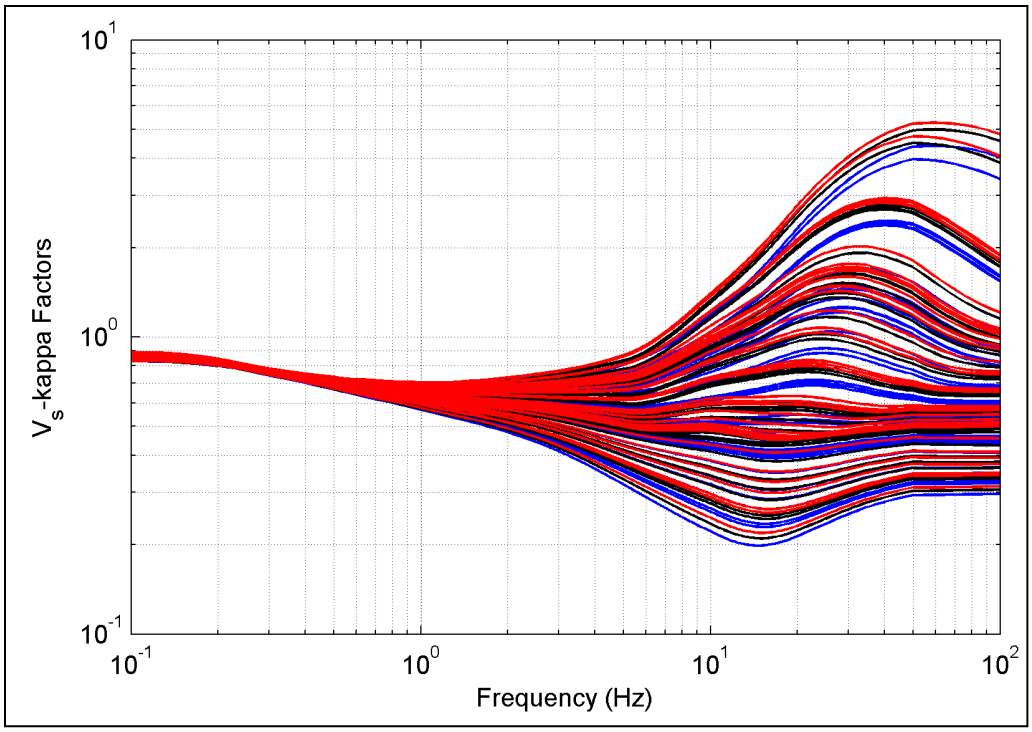

Figure 9.32. Sensitivity of V_S-kappa adjustment factors at Site A to host kappa branches. Blue is for the low host kappa branch, black is for the central branch, and red is for the upper branch.

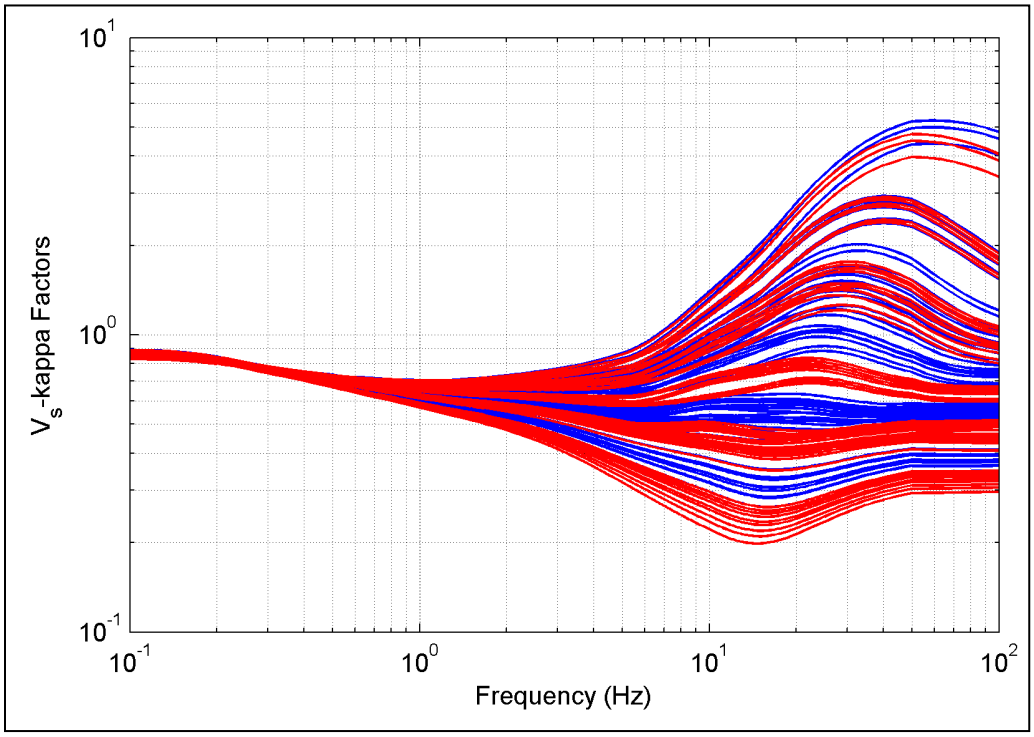

Figure 9.33. Sensitivity of V_S-kappa adjustment factors at Site A to V_S profiles used in computing target $\kappa_{baserock}$. Blue is for Profile 1 and red is for Profile 2.

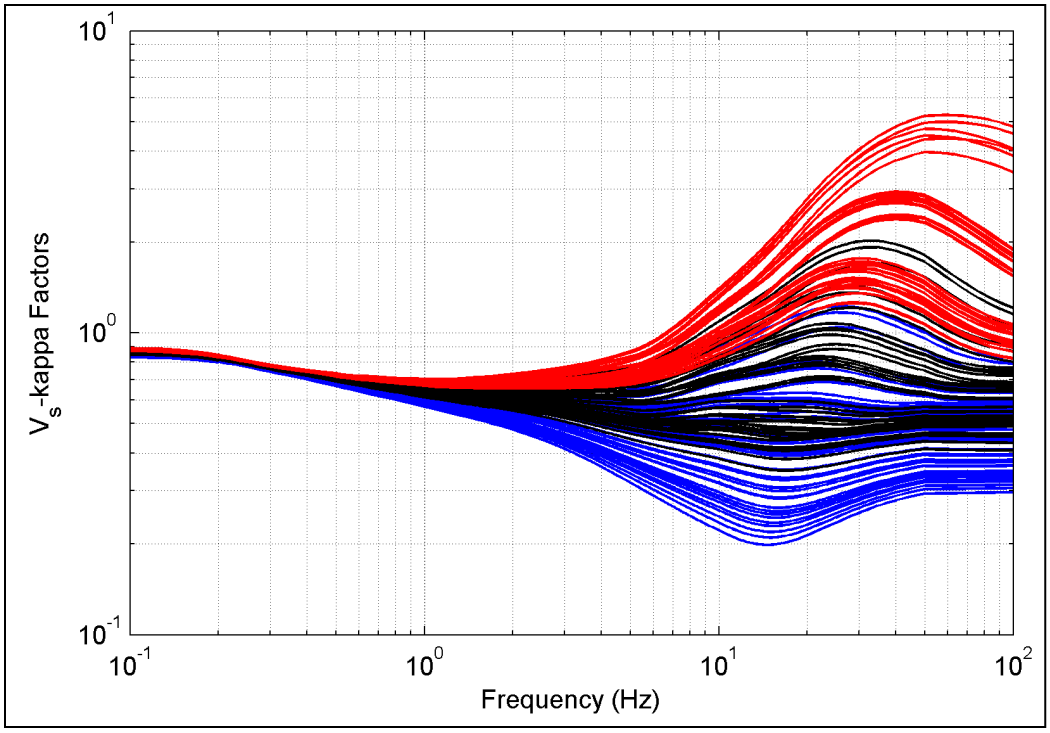

Figure 9.34. Sensitivity of V_S-kappa adjustment factors at Site A to profile depth used to calculate target $\kappa_{baserock}$. Blue is for the all sub-basalt sediments branch, black is for half of the sediments, and red is for the no sediments branch.

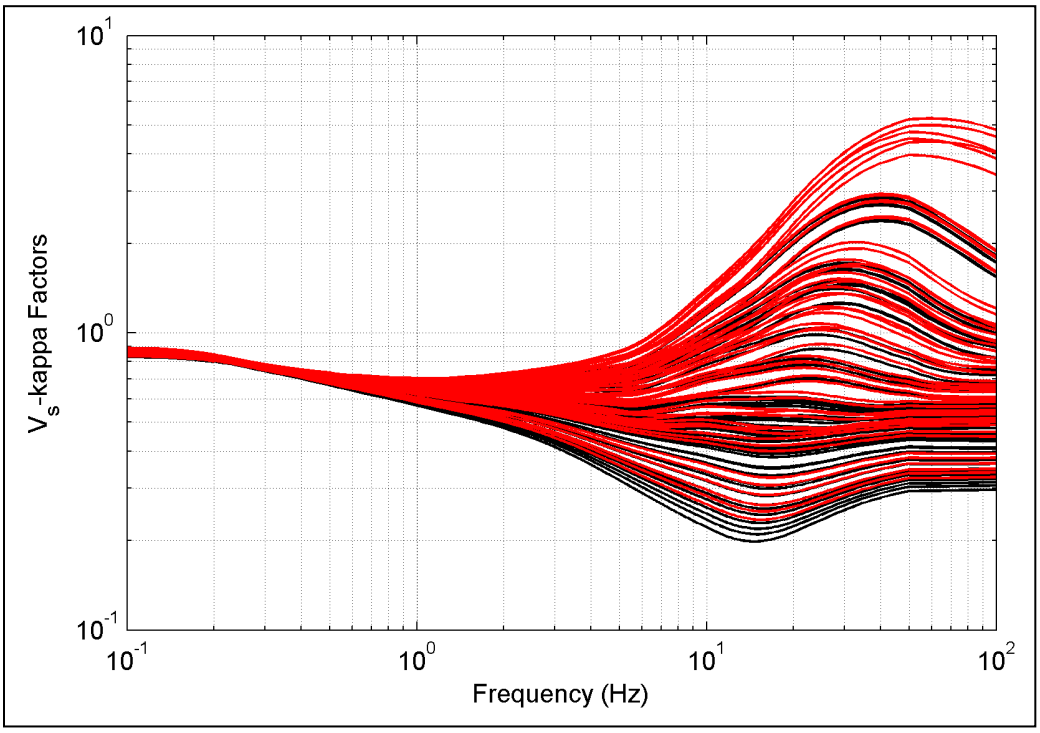

Figure 9.35. Sensitivity of V_S-kappa adjustment factors at Site A to the approach used to compute target $\kappa_{baserock}$. Black is for the inversion branch and red is for the Anderson and Hough (1984) branch.

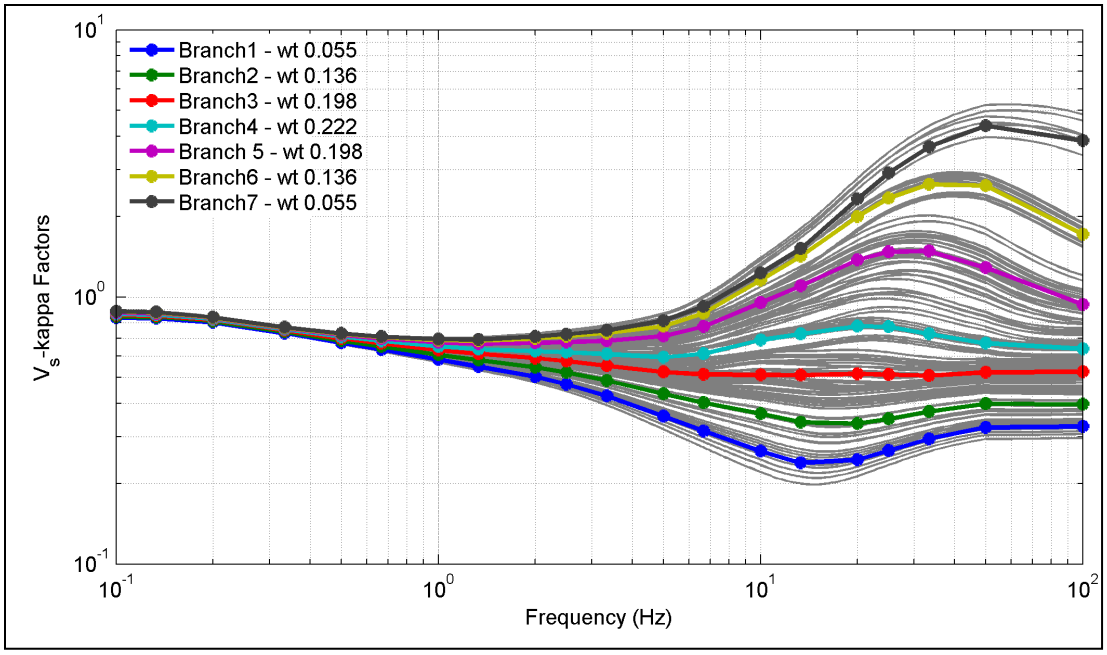

Figure 9.36. V_S-kappa adjustment factors at Site A re-sampled using seven branches.

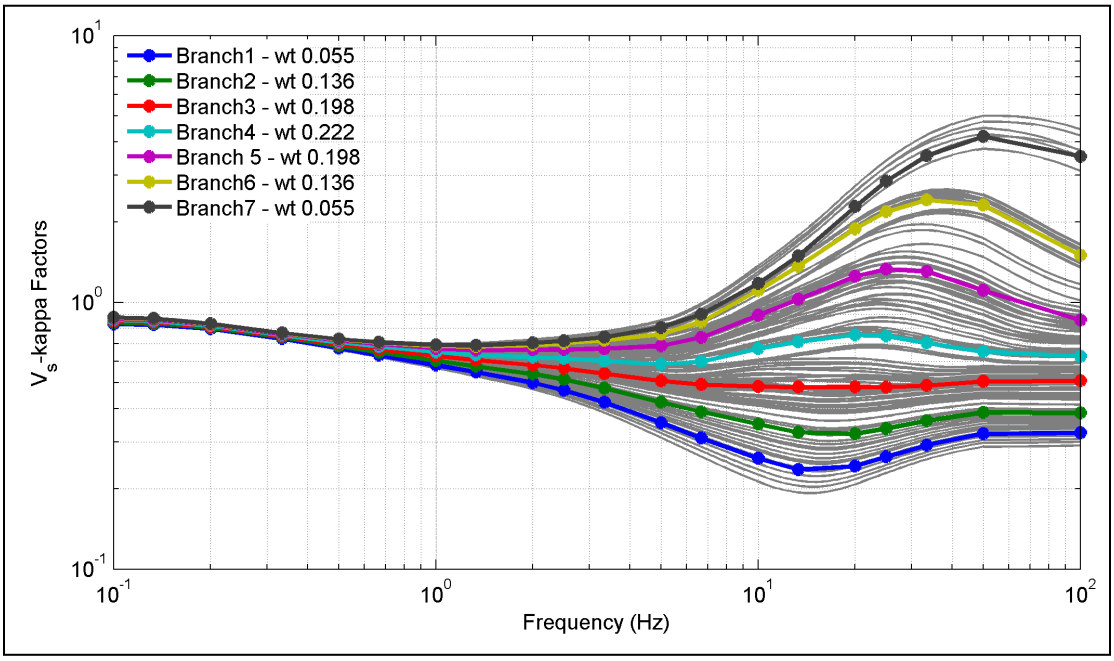

Figure 9.37. V_S-kappa adjustment factors at Site B re-sampled using seven branches.

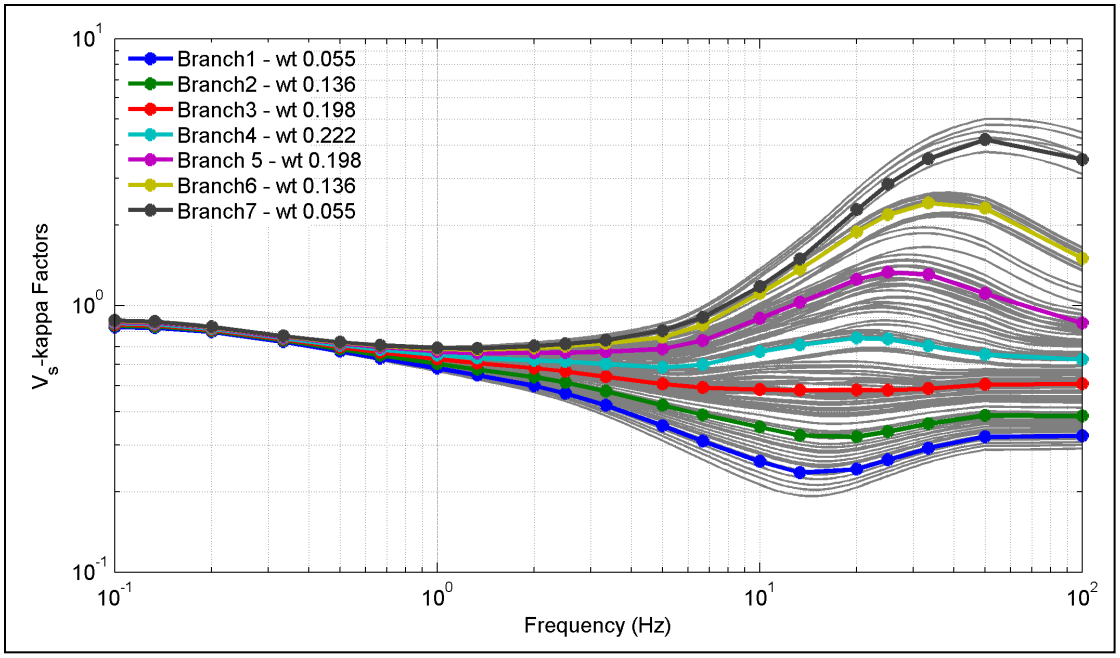

Figure 9.38. V_S-kappa adjustment factors at Site C re-sampled using seven branches.

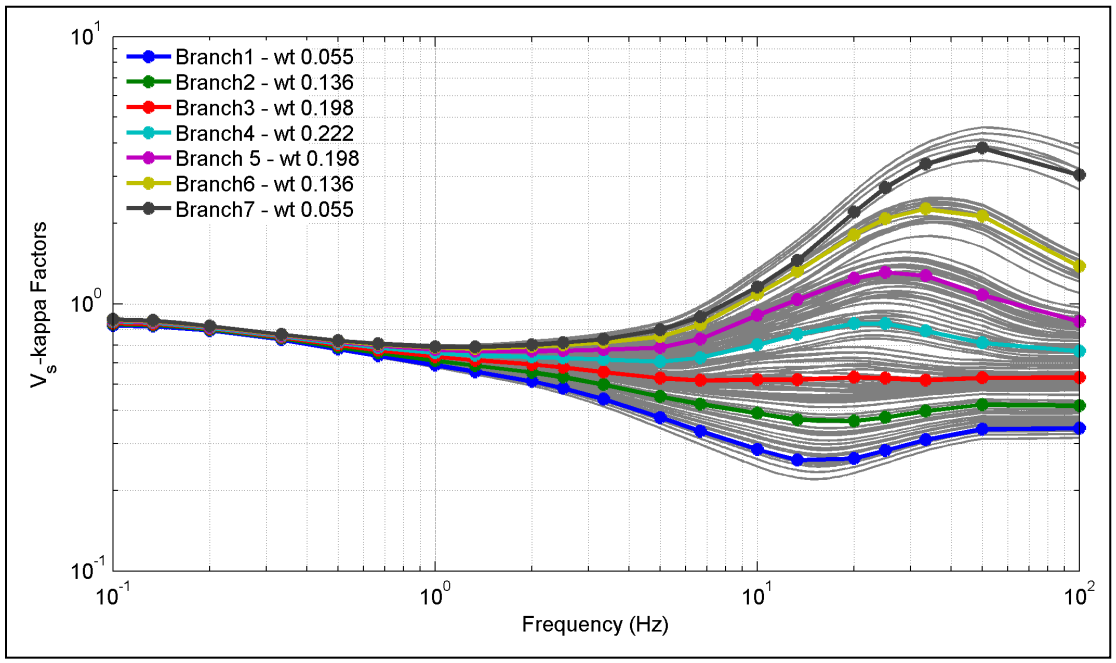

Figure 9.39. V_S-kappa adjustment factors at Site D re-sampled using seven branches.

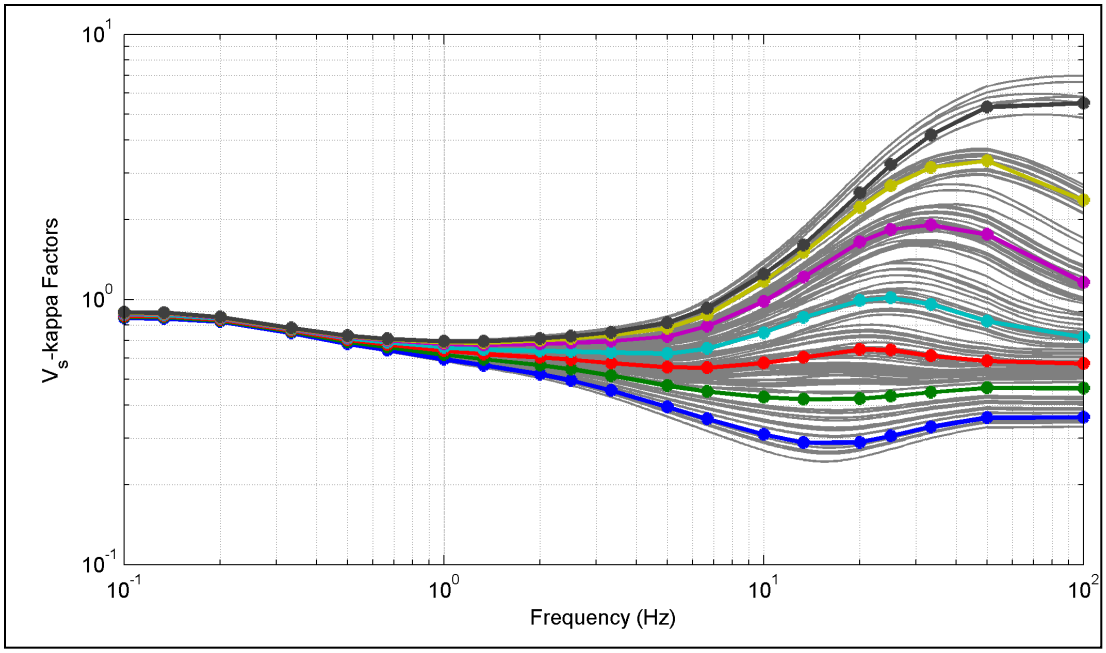

Figure 9.40. V_S-kappa adjustment factors at Site E re-sampled using seven branches.

9.3.3 V_S Adjustments of the Subduction Backbone GMPE

V_S adjustment factors were derived for the modified BC Hydro GMPE using the IRVT approach to adjust for V_S profile differences between the GMPE host region and the five hazard calculation sites at Hanford. Target V_S profiles (Profiles 1 and 2) at the five hazard calculation sites and their corresponding site amplification factors are shown in Figures 7.28 and 7.29, respectively.

Adjustment factors were derived and averaged for interface backarc scenarios with magnitudes 8 and 9 and distances of 200 and 250 km and applied to all subduction scenarios in the hazard calculations. These scenarios were selected because of their significant contribution to the hazard from subduction sources at the Hanford Site. Ground motion duration was estimated for the four scenarios considered using the Abrahamson and Silva (1996) model for the prediction of the 5−75% horizontal significant duration on rock.

The GMC TI Team investigated the need to apply kappa adjustment factors to correct for differences in kappa between the host and the Hanford target regions. Hazard sensitivity results showed that subduction sources with significant contributions to the hazard are at long distances (200 to 250 km) where the anelastic attenuation effects are more dominant than the kappa effects. Moreover, host kappa values for subduction GMPEs are difficult to constrain because these GMPEs are generally derived from and applicable to relatively long-distance scenarios. The TI Team therefore opted for a V_S host-to-target adjustment for the modified BC Hydro GMPE without the kappa adjustment.

9.3.3.1 Host V_S Profiles for Subduction GMPE

Candidate host V_S profiles with a V_{S30} of 760 m/sec were evaluated for the modified BC Hydro GMPE such that they represent an average profile for the data source regions. Figure 9.41 shows the histogram of the data set used in the development of the original BC Hydro model by region. The biggest

contributors to the data set are Japan and Taiwan. Moreover, for the magnitude and distance range of interest for the hazard at the Hanford hazard calculation sites (**M** 8 to 9 and distance of 200 to 250 km), only Japanese data were available to constrain the GMPE.

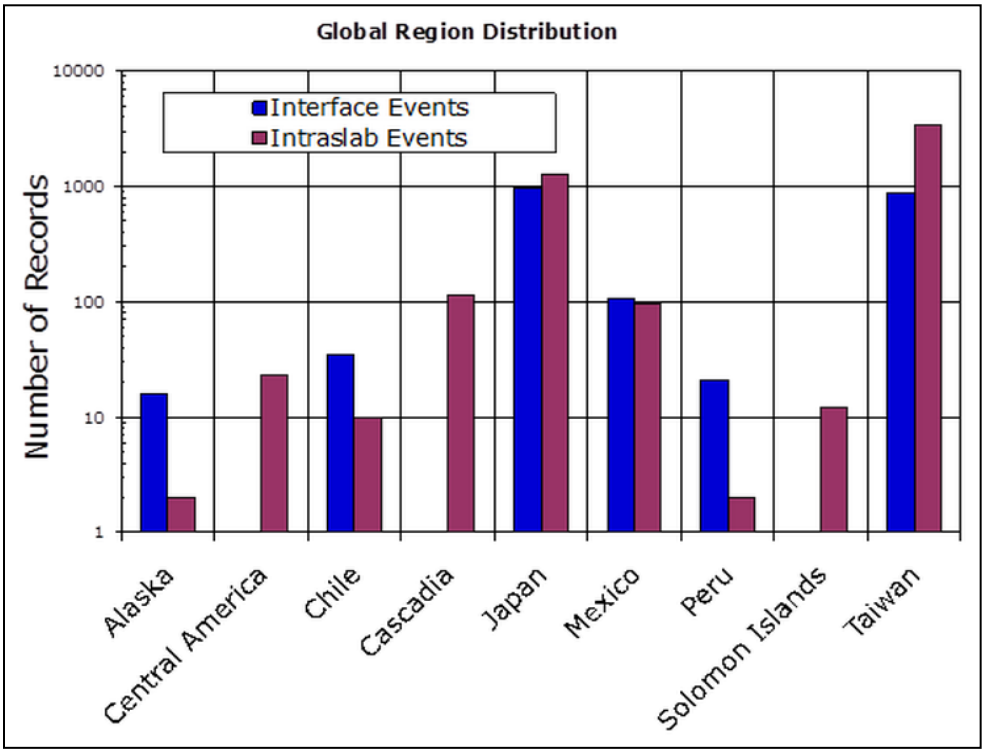

Figure 9.41. Histogram of the number of recordings by region used in the development of the original BC Hydro GMPE (Source: Gregor 2012).

The GMC TI Team reviewed several published Japanese reference V_S profiles. Atkinson and Casey (2003) developed generic site amplifications for 31 typical K-Net stations with National Earthquake Hazards Reduction Program (NEHRP) C, D, and E site conditions. However, they did not have V_S profiles or site amplifications for B/C site conditions with the desired reference V_{S30} of 760 m/sec. Atkinson and Macias (2008, 2009) established regional site models for Japan, Chile, Mexico, and Alaska for B/C site conditions. For Japan, site information for the K-Net stations that lie between B and C categories were used to develop the V_S profile. Ghofrani et al. (2013) characterized site conditions in Japan using surface and downhole KiK-net data. They derived an empirical site amplification model for V_{S30} of 760 m/sec based on horizontal-to-vertical (H/V) ratios at the borehole level. Their site amplification model was published for frequencies of 0.11 to 13.5 Hz and does not cover the entire period vector for the Hanford PSHA. Poggi et al. (2013) developed a model to estimate kappa and site amplifications for generic Japanese reference rock conditions. However, their reference V_S profile had a V_{S30} of 1,350 m/sec, which is larger than the desired V_{S30} of 760 m/sec for the host V_S profile.

Based on the literature search as well as looking into other Japanese V_S profiles collected by the TI Team, two candidate Japanese host V_S profiles with a V_{S30} of 760 m/sec were adopted for the host-to-target V_S adjustment of the modified BC Hydro GMPE. The first profile is based on the K-Net stations reported by Atkinson and Macias (2008, 2009). Both V_S and density profiles were published. The second profile is based on the KiK-net station profiles with a V_{S30} between 600 and 900 m/sec. This profile was developed by the TI Team averaging a total of 109 profiles and extended to a depth of 300 m.

For depths greater than 300 m, the deeper part of the V_S profile reported by Atkinson and Macias (2008, 2009) was adopted. Densities were not available for the KiK-net stations and were assigned to the KiK-net reference profile based on the density profile of Atkinson and Macias (2008, 2009). The GMC TI Team also evaluated the Japanese V_S profiles collected for the NGA-West2 project (Dr. Tadahiro Kishida, personal communication). The NGA-West2 V_S profiles for the K-Net stations were limited to a depth of 20 m and were discarded for being too shallow. The KiK-net station profiles with a V_{S30} between 600 and 900 m/sec were also not used given the availability of a representative V_S profile for the KiK-net stations developed by the TI Team.

The two candidate Japanese V_S profiles are shown in Figure 9.42 and compared to the target V_S profiles at the five hazard calculation sites at Hanford. Site amplification factors were developed for the two profiles with respect to the half-space at a depth of 9.6 km using the QWL/SRI method (Boore 2005) with an angle of incidence of zero degrees. Figure 9.43 shows the candidate host site amplification factors compared to the target site amplification factors. The host site amplification factors are similar for frequencies less than 1 Hz due to using the same deep V_S profile. Equal weights were given to the two candidate host V_S profiles.

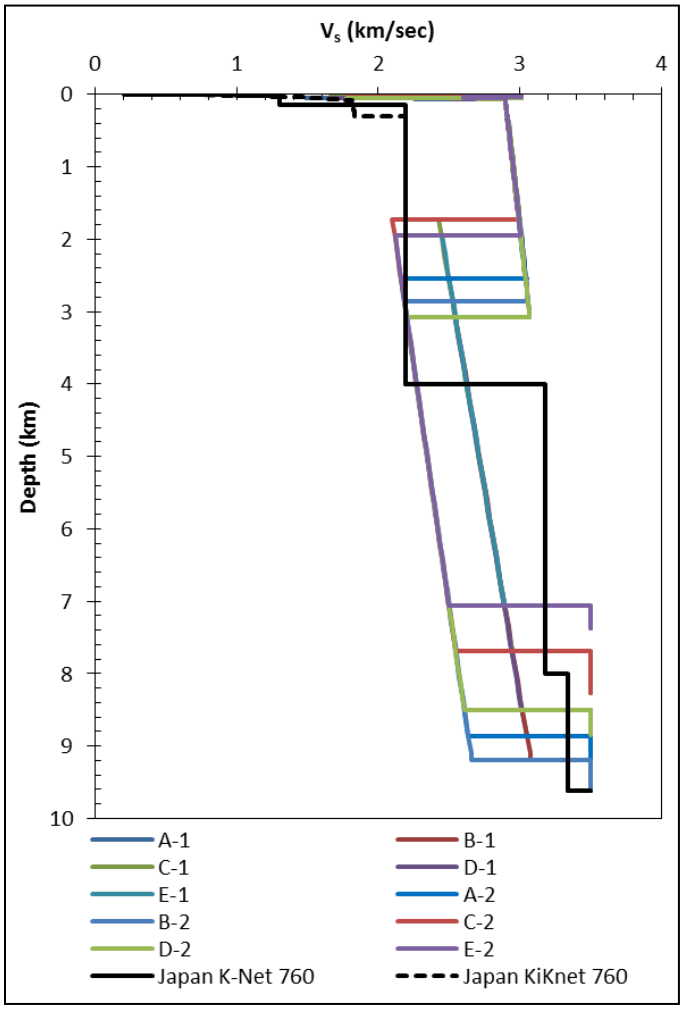

Figure 9.42. Candidate host Japanese V_S profiles compared to the target V_S profiles at the Hanford hazard calculation sites.

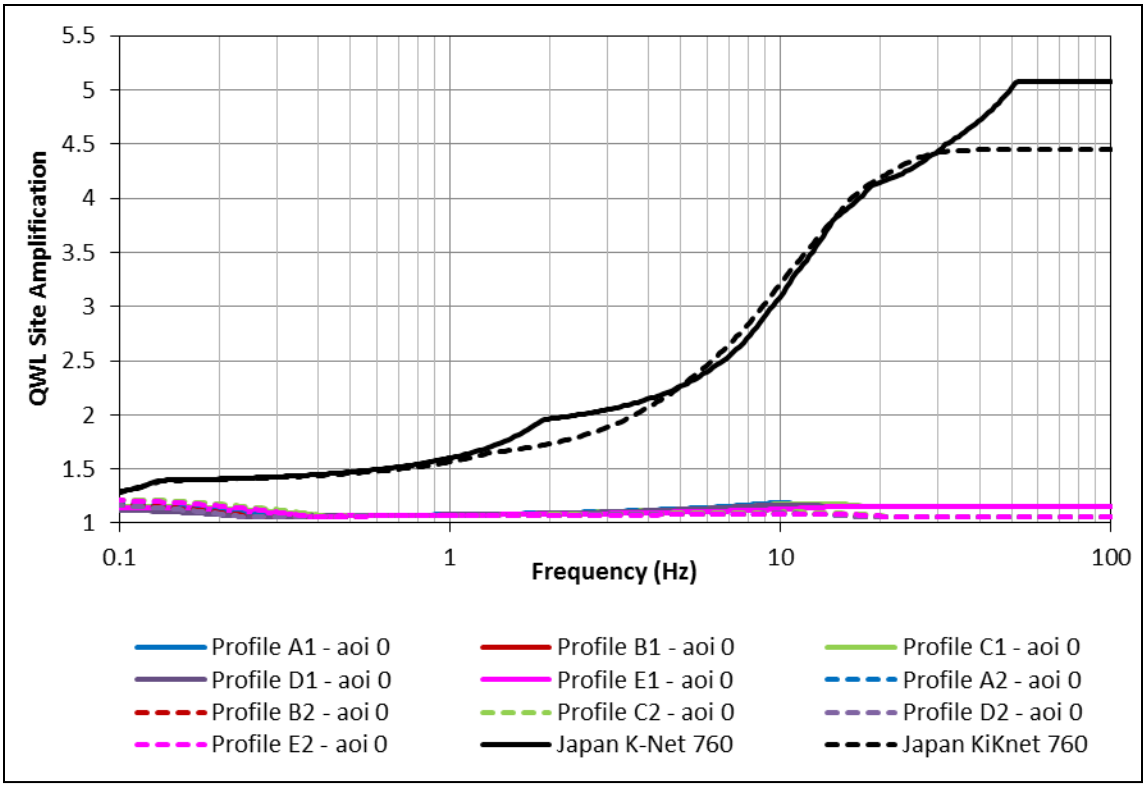

Figure 9.43. QWL site amplification factors for the candidate host Japanese V_S profiles compared to those of the target V_S profiles at the Hanford hazard calculation sites.

9.3.3.2 V_S Adjustment Factors and Sensitivity of Adjustments

Figure 9.44 presents the host-to-target V_S adjustment logic tree for the modified BC Hydro GMPE. Host V_S profiles were given equal weights and the development of the target V_S profiles, their site amplification factors, and their assigned weights are discussed in Chapter 7.0. The same logic-tree structure applies to all five hazard calculation sites at Hanford but site-specific site amplification factors were used. Figure 9.45 shows the median subduction model logic tree. The branches and associated weights for all levels of this logic tree, expect for the host-to-target V_S adjustment level, are discussed in Section 9.4.3. The host-to-target V_S adjustment factors are placed at the last level of the logic tree and are conditioned on both the anelastic attenuation and magnitude scaling branches because these branches produce differences in the median spectral shapes that lead to differences in the resulting V_S adjustment factors.

The sensitivity of the derived V_S adjustment factors at Site A to the two host and two target V_S profiles is shown in Figure 9.46 for the central $\Delta C1$ magnitude scaling branch and the θ_6 anelastic attenuation branch. The maximum difference in the V_S scaling factors resulting from the two target and two host V_S profiles is on the order of 6% and 12%, respectively. The impact of the two anelastic attenuation term scaling branches on the resulting V_S adjustment factors is shown in Figure 9.47 and is less than 4%. Figure 9.48 shows the difference in the V_S adjustment factors for the three magnitude scaling branches. There is no difference in the scaling factors between the central and the lower $\Delta C1$ branches because the difference in the response spectra for these two branches is close to being a constant across the entire frequency range. A difference of about 3% at high frequencies is observed between the

central and upper ΔC1 adjustment factors. Figure 9.49 through Figure 9.53 present the V_S scaling factors for the modified BC Hydro GMPE at Hanford Sites A through E and show that the differences in the factors among the five sites are minimal.

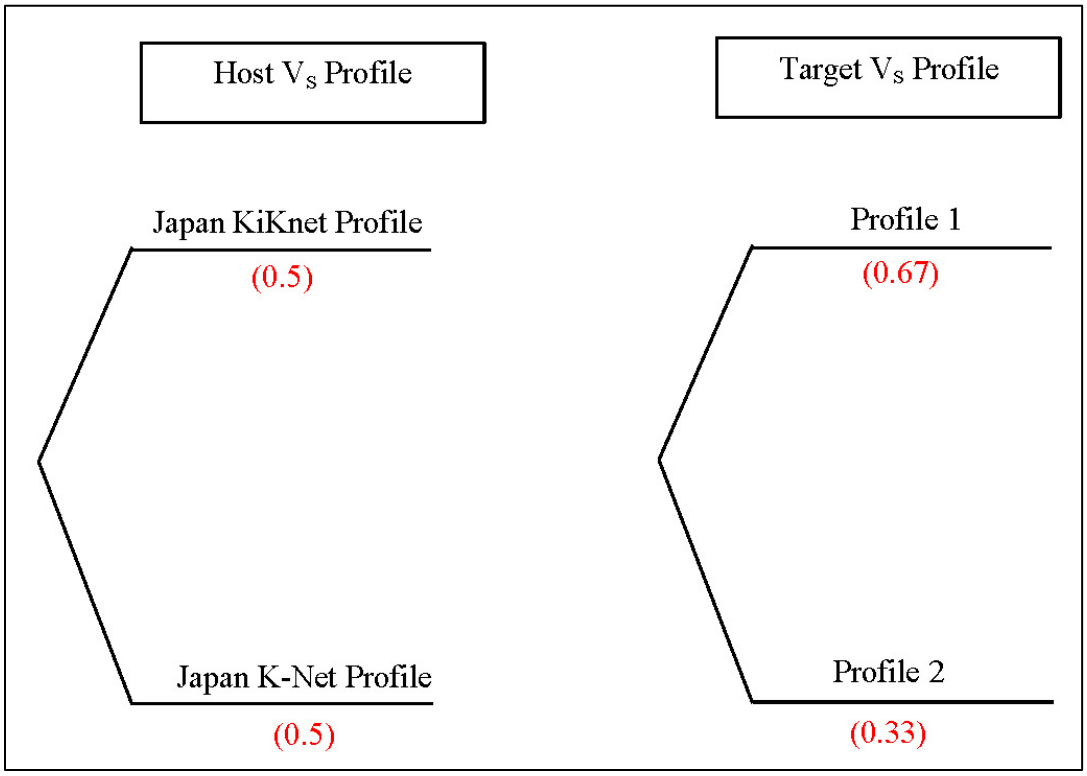

Figure 9.44. V_S adjustment factor logic tree for the modified BC Hydro GMPE.

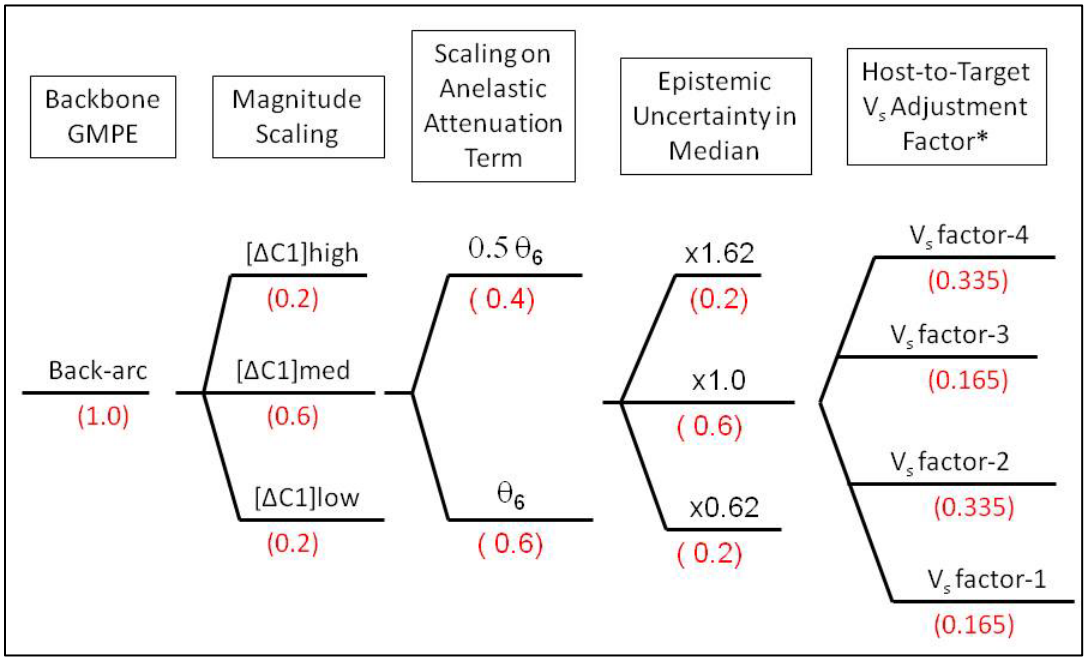

Figure 9.45. Logic tree for the median subduction model.

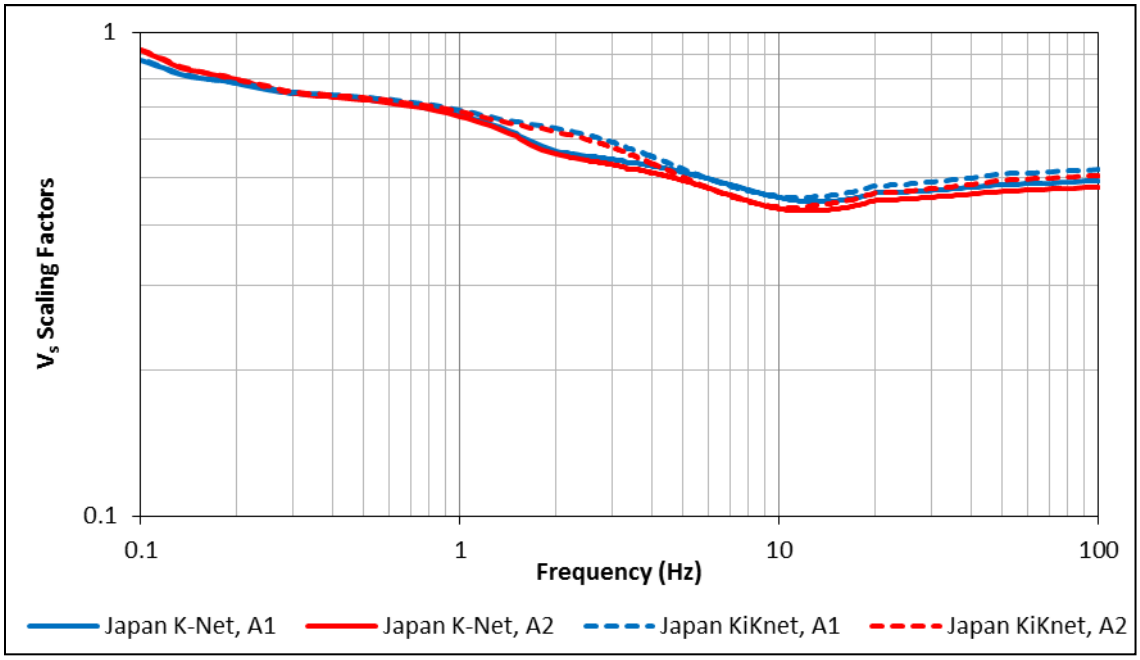

Figure 9.46. Comparison of the V_S adjustment factors for the two host and two target V_S profile branches at Site A for the central ΔC1 branch and the θ_6 branch.

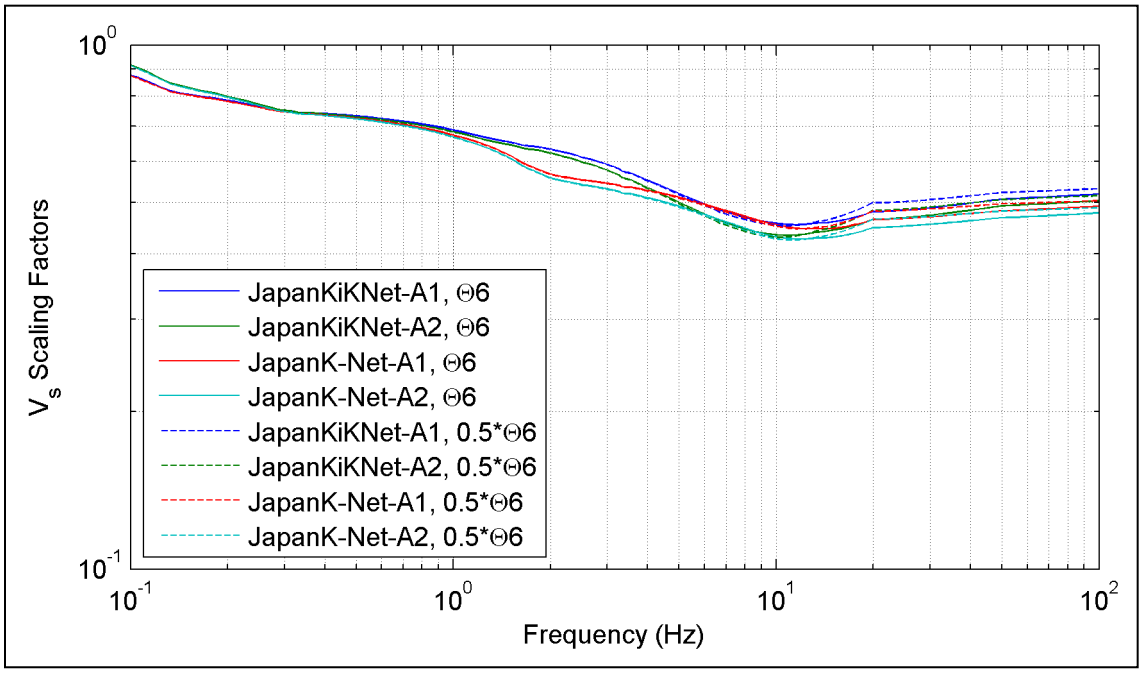

Figure 9.47. Comparison of the V_S adjustment factors at Site A for the θ_6 and the $0.5\theta_6$ branches. Factors derived for the central ΔC1 magnitude scaling branch.

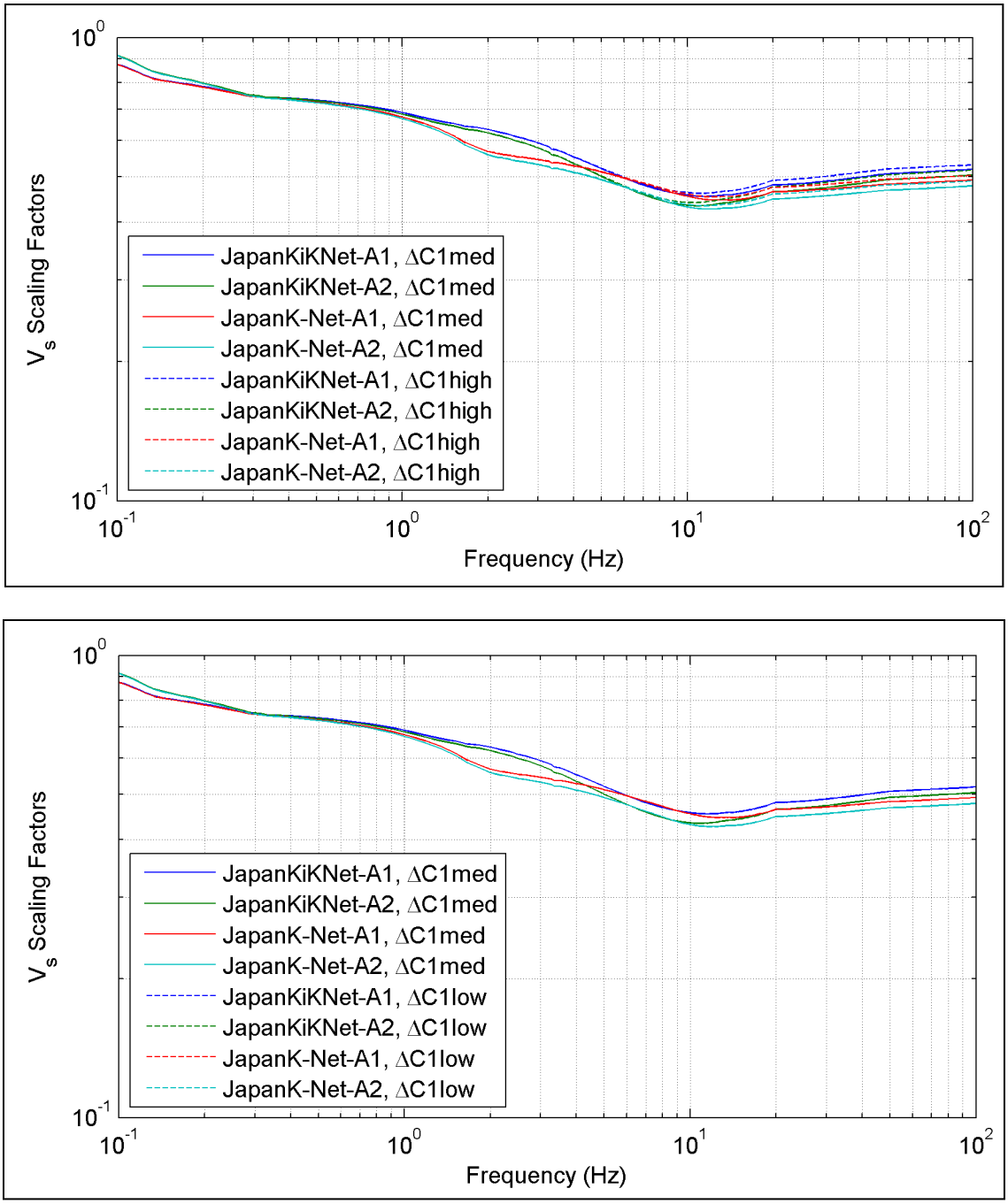

Figure 9.48. Comparison of V_S adjustment factors at Site A for the three ΔC1 branches. Factors derived for the θ_6 anelastic attenuation scaling branch. Top plot shows factors derived for ΔC1 median and high branches. Bottom plot compares factors derived for ΔC1 median and low branches.

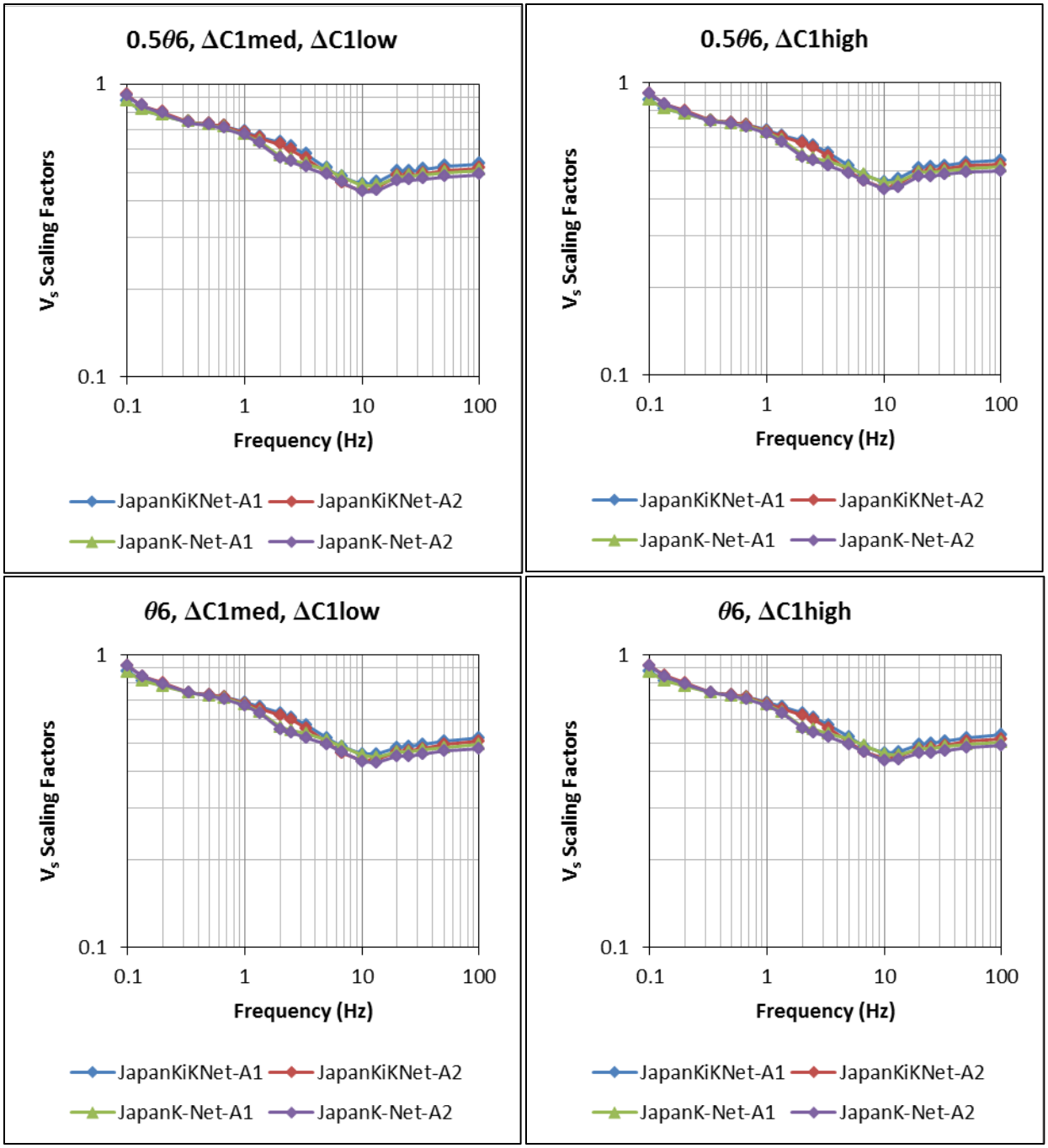

Figure 9.49. V_S adjustment factors for the modified BC Hydro GMPE at Site A.

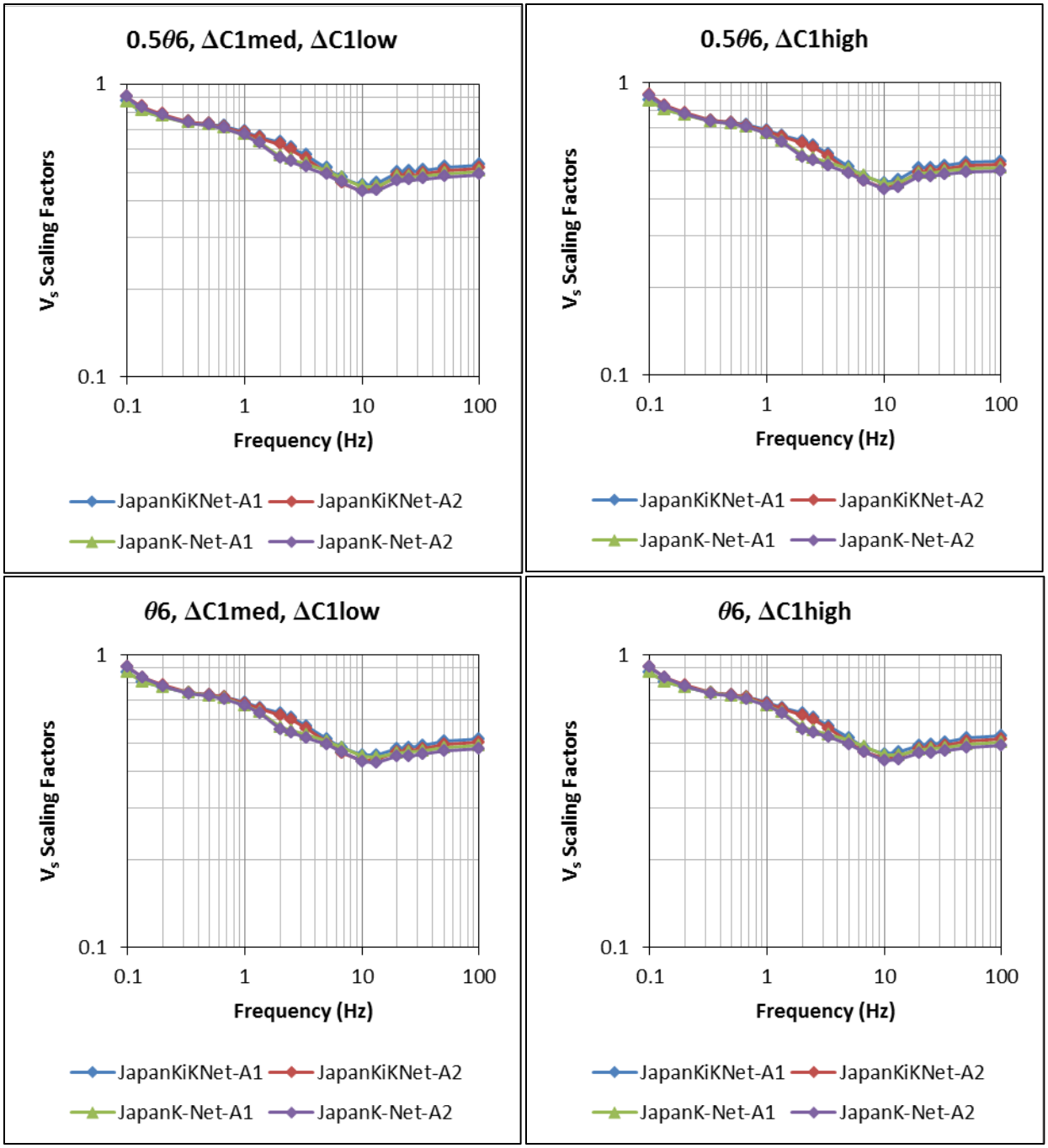

Figure 9.50. V_S adjustment factors for the modified BC Hydro GMPE at Site B.

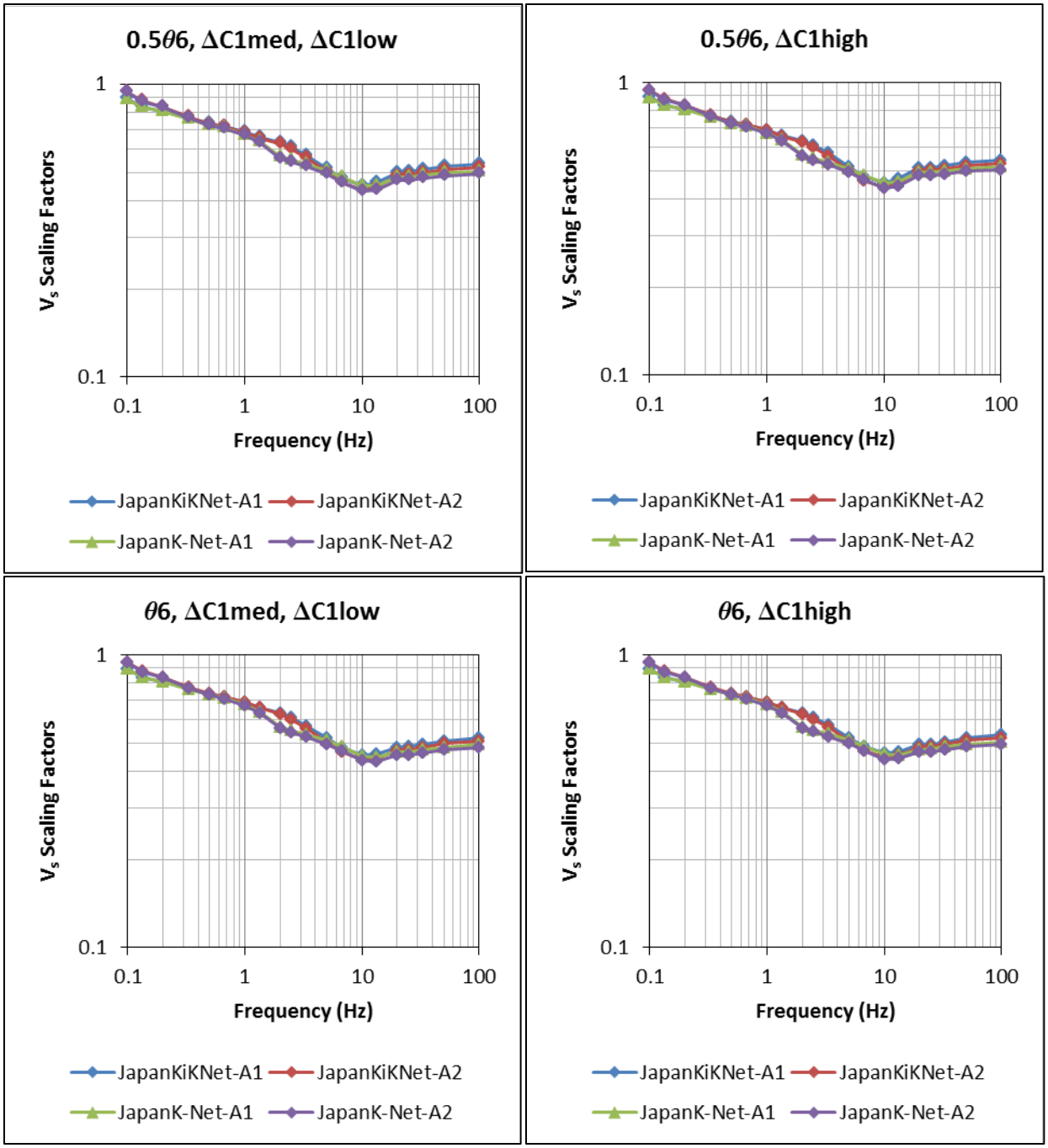

Figure 9.51. V_S adjustment factors for the modified BC Hydro GMPE at Site C.

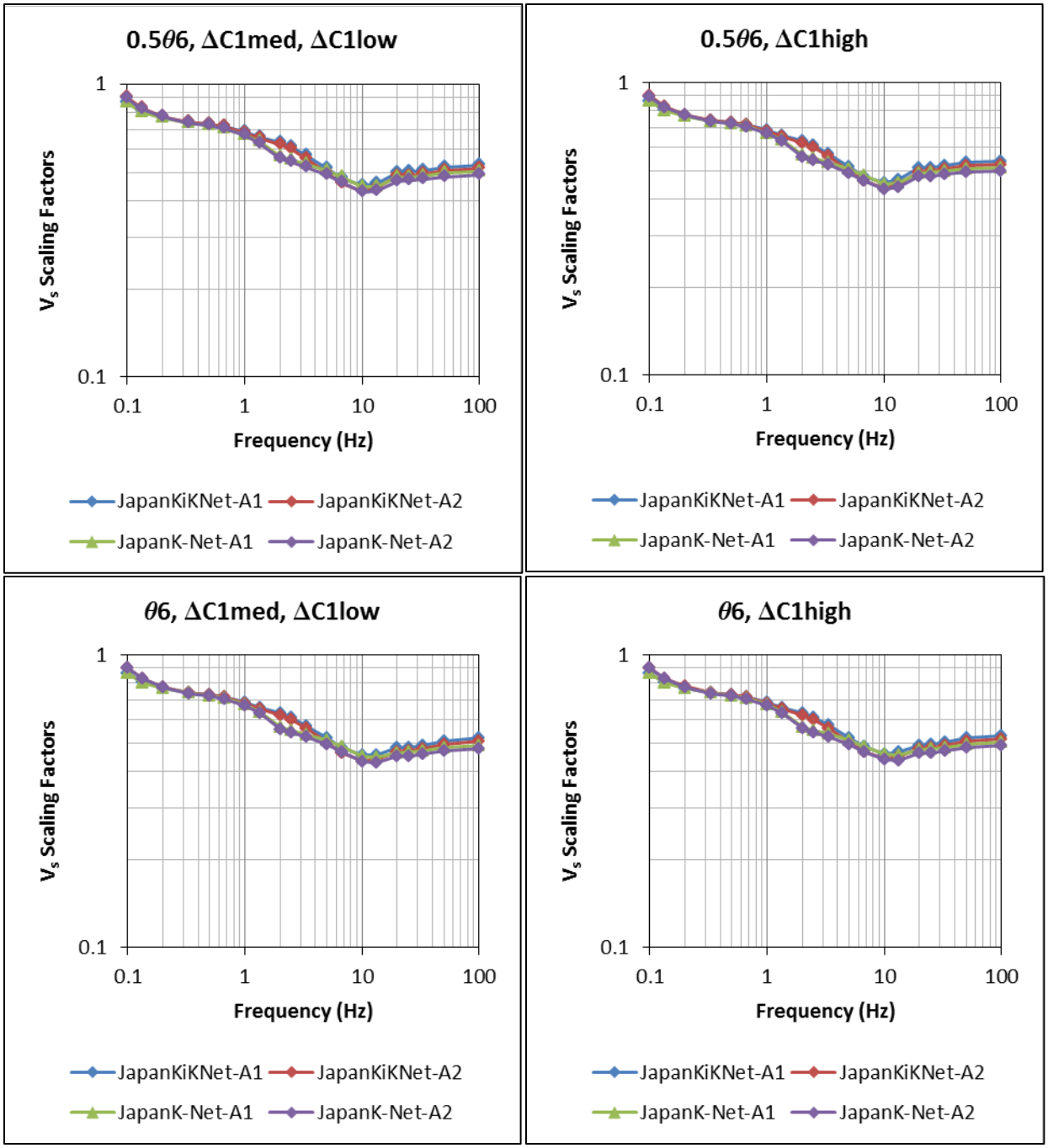

Figure 9.52. V_S adjustment factors for the modified BC Hydro GMPE at Site D.

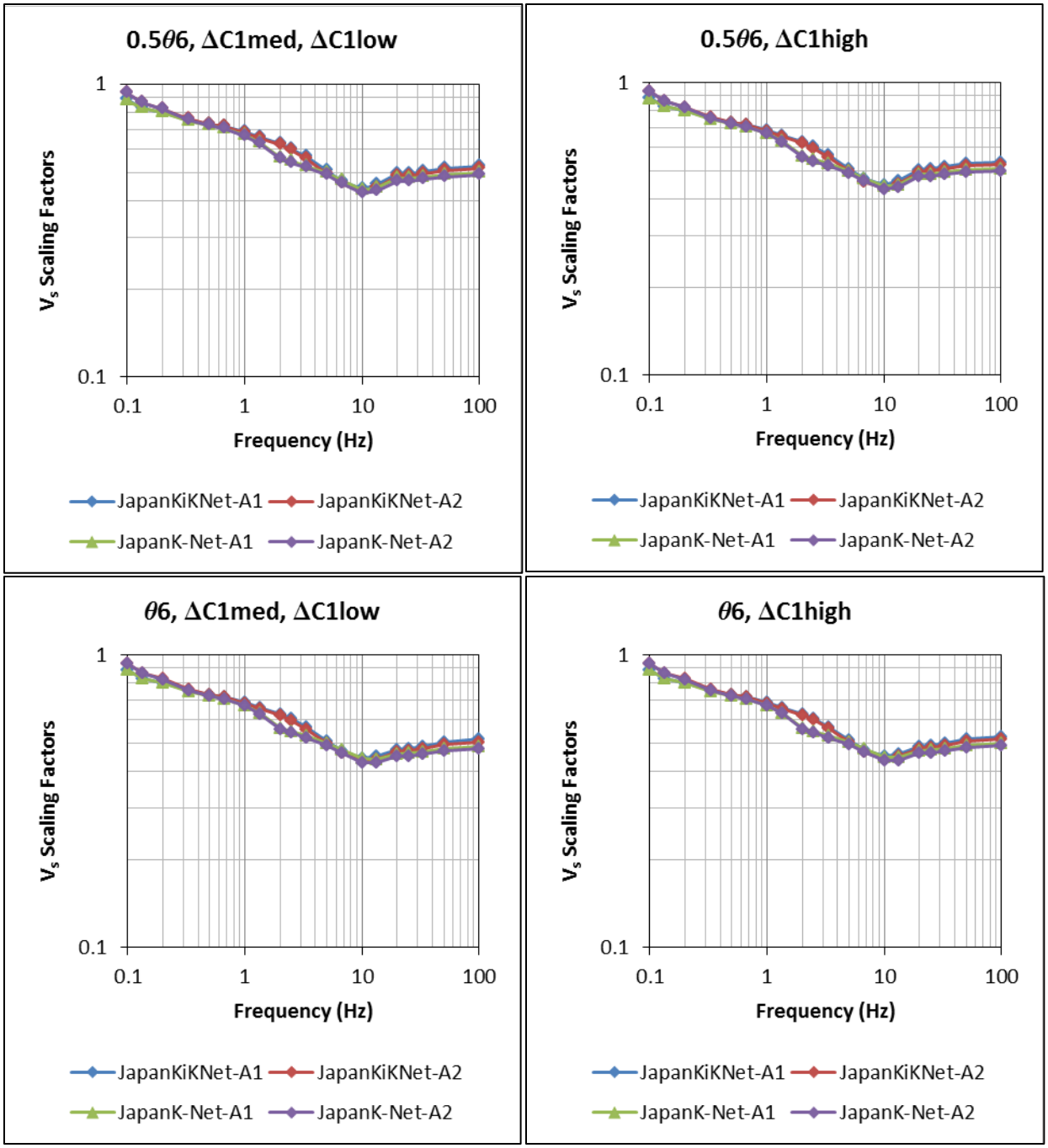

Figure 9.53. V_S adjustment factors for the modified BC Hydro GMPE at Site E.

9.4 Scaling of Backbone GMPEs for Median Logic-Tree Branches

This section describes how the selected and adjusted backbone GMPEs are transformed into the full suite of models for the prediction of median ground motions that form the branches of the GMC logic tree.

9.4.1 Criteria for Scaling Factors

The models selected as the preferred backbones for the prediction of motions due to crustal and subduction earthquakes in Section 9.2 are each transformed into multiple models through the application of site-specific adjustments (Section 9.3). These adjustments transform the equations from the representative site conditions (near-surface and upper crustal structure) in the host region corresponding to the equations to those of the target region of the Hanford Site in eastern Washington. Because there is some uncertainty in the characterization of both the host and target region site conditions, multiple alternative adjustment factors, each with a relative weighting assigned, are applied, in effect creating multiple versions of the original backbone GMPE.

The ultimate objective in the construction of the GMC logic tree, in keeping with the goals of the SSHAC process, is to capture the center, the body, and the range of possible levels of median motions due to potential future earthquakes that might affect the Hanford Site. This means that the most highly weighted branch or branches of the logic tree should correspond to the best estimate predictions, and be as well calibrated to the target region and site as possible. The full set of branches should capture the epistemic uncertainty associated with these predictions. For an application such as this, one way to view the full range of epistemic uncertainty is to see it as consisting of two components, because neither of the selected backbones was derived originally for eastern Washington or for the Hanford Site. The first element of epistemic uncertainty is that corresponding to the inherent uncertainty in the predictions within the host region, which arise from two factors. Firstly, the nature of the available data, both in terms of the number of records and their distribution with respect to the predictor variables (magnitude, distance, style of faulting, etc.), that multiple interpretations, all equally defensible, are possible. This is clearly illustrated by the differences among the predictions from suites of equations such as the NGA-West (Abrahamson et al. 2008) and NGA-West2 (Gregor et al. 2014) GMPEs. Secondly, the data sets from which the empirical models are derived do not include all of the combinations of predictor variables that will necessarily be considered when they are applied in the PSHA calculations. This particularly applies to the larger magnitude values. For example, even though the NGA database contains recordings from earthquakes with magnitudes greater than **M** 7.2, with the exception of a single recording from the 1952 Kern County earthquakes, they are all from outside California and the contiguous United States. There is, therefore, epistemic uncertainty regarding whether these earthquakes and their recorded ground motions are representative of what may be expected from future large-magnitude earthquakes in California.

The second element of epistemic uncertainty in the median ground motion predictions arises from differences between the host and target regions. These differences arise from the uncertainties in the systematic differences in the host- and target-region distributions of parameters that exert a direct influence on the median amplitudes of earthquake ground motions. An example of such a host-to-target difference is the median value of the stress drop for earthquakes in the magnitude range considered in the hazard integrations. Because this distribution is imperfectly known even in the host region of California, for the case of crustal earthquakes, and much less well determined in the target region of eastern Washington, there is inevitably appreciable uncertainty in the scaling factors that need to be applied to transform the backbone model from its original region to the application at Hanford.

The site adjustments—V_S-kappa for crustal earthquakes (Section 9.3.2) and V_S for subduction earthquakes (Section 9.3.3)—provide an improved best estimate model by rendering the predictions applicable to the site characteristics encountered at the Hanford Site. By virtue of using multiple values for these adjustments with associated weights, their application also captures the epistemic uncertainty in

this part of the host-to-target adjustment. In the following sections, the process of developing alternative scaled models for both crustal and subduction earthquakes to capture the center, body, and range, is explained.

9.4.2 Development of Backbone GMPEs for Shallow Crustal Earthquakes

The SSC model developed in Chapter 8.0 indicates predominantly reverse and reverse-oblique fault earthquakes in the immediate site vicinity will be important to the hazard. An important aspect of characterization of ground motions in close proximity to dip slip earthquakes is incorporation of hanging-wall effects. Hanging-wall effects refer to ground motion above the rupture surface of dipping earthquake ruptures that are enhanced compared to what would be expected for equivalent rupture distances on the footwall side of ruptures. The effect was first described by Somerville and Abrahamson (1995) and Abrahamson and Somerville (1996) based on data from the 1994 Northridge, California earthquake. Hanging-wall effects were first introduced into GMPEs by Abrahamson and Silva (1997) and Campbell and Bozorgnia (2003). Chiou et al. (2000) also identified hanging-wall effects from analyses of empirical and numerical modeling data for reverse fault ruptures and demonstrated that they could be accounted for as a geometric effect using a root mean squared distance measure. Ground motion simulations conducted for the PEER NGA project by Somerville et al. (2006) also demonstrated hanging-wall effects and these effects were incorporated in the NGA models of Abrahamson and Silva (2008), Campbell and Bozorgnia (2008), and Chiou and Youngs (2008). More recently, simulations conducted for the PEER NGA-West2 project further demonstrated the presence of hanging-wall effects (Donahue and Abrahamson 2014) and these effects were incorporated in the ASK14, CB14, and CY13 NGA-West2 GMPEs.

As has been suggested by Donahue and Abrahamson (2014) and demonstrated by the use of root mean square distance by Chiou et al. (2000), the hanging-wall effect can be considered the result of the inability of the use of the minimum distance to rupture, R_{RUP}, as the sole distance metric to capture the difference in path effect between sites on the hanging-wall and footwall sides of dipping ruptures, The other commonly used distance metric is the Joyner-Boore distance (Joyner and Boore 1981), R_{JB}, the minimum horizontal distance to the surface projection of the rupture. Joyner and Boore (1981) introduce the use of R_{JB} instead of the use of R_{RUP} because they included a depth parameter h "which makes allowance, among other things, for the fact that the source of the peak motion may lie at some depth below the surface" and they did not want to account for this effect twice by using rupture distance. As indicated by Boore et al. (1997), use of the R_{JB} distance metric "leads automatically to higher ground motion values over the hanging wall of dipping faults than over the footwall" and thus can be argued to implicitly account for hanging-wall effects (Abrahamson et al. 2008; Boore et al. 2014; Donahue and Abrahamson 2014). However, this implicit capture of the effect only occurs in an average sense. This aspect is illustrated in Figure 9.54. Shown are three example **M** 6.5 reverse-faulting earthquake rupture scenarios: one a steeply dipping (67 degree) rupture extending from the surface to a depth of 12 km, one a shallow dipping (30 degree) rupture that is located at a shallow depth (Z_{TOR} = 0 km), and one a shallow dipping rupture at depth (Z_{TOR} = 8.5 km). Two sites are considered: Site 1 is near the up dip tip of the steeply dipping rupture, which is above about the midpoint of the shallowly dipping ruptures, and Site 2 is located directly above the down dip edge of all three ruptures. The R_{JB} distance to all three ruptures for both sites is 0. As a result, the expected ground motions at both sites for all three ruptures are identical. Although the limited available empirical data are insufficient to constrain the details of ground motion variations directly above the hanging wall of dip slip ruptures, the numerical simulations described by Chiou et al. (2000) and Donahue and Abrahamson (2014) clearly show variations in the average motions

among $R_{JB} = 0$ sites for different rupture geometries. Because the Hanford sites are exposed to dip slip ruptures with a wide range of geometries, capturing these differences in the characterization of ground motion from shallow crustal earthquakes is considered important.

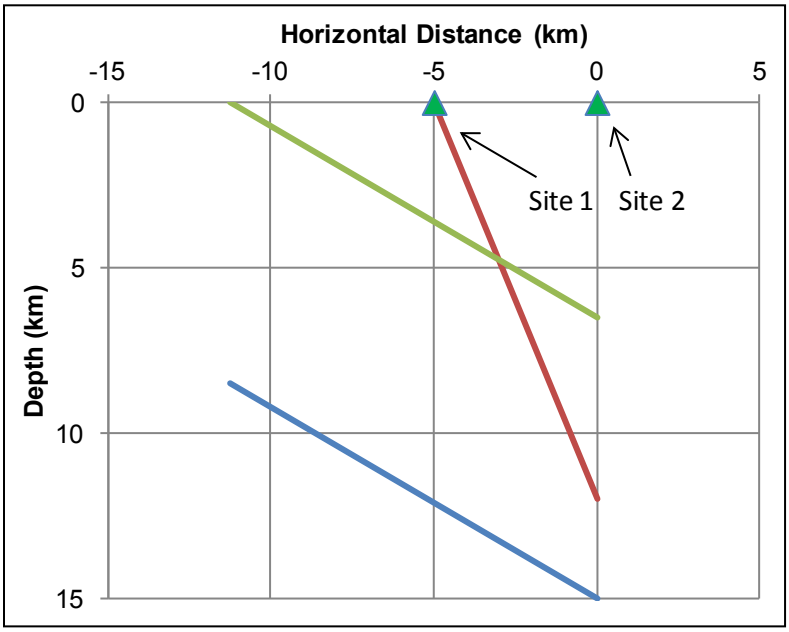

Figure 9.54. Examples of M 6.5 reverse-faulting rupture scenarios.

As discussed in Section 9.1.3, the scaled backbone approach is used to characterize the ground motions from shallow crustal earthquake sources. The intent of the backbone approach is to represent the central estimate of median ground motions using a single functional form and to represent the epistemic distribution of median ground motion with a set of weighted adjustment factors to capture the range in amplitude, range in magnitude scaling, and range in distance scaling, including hanging-wall effects, that is appropriate for the seismic sources important to the hazard assessment. The estimate of the center and epistemic uncertainty of the median ground motions of interest is obtained from a weighed combination of the predictions of from the selected GMPEs. The GMPEs that pass the exclusion criteria are considered equally viable and are given equal weight in developing the central estimate. The epistemic distribution of median ground motions is characterized by treating the set of candidate GMPEs as a sample of possible GMPEs and using this sample to develop a distribution for the scaling factors. The resulting distribution is then captured by a discrete representation that is not bounded by the range of ground motion predictions from the selected candidate GMPES.

Section 9.2.1 presents the process used to select the candidate GMPEs used to characterize shallow crustal earthquake ground motions. The ASK14, CB14, and CY14 GMPEs meet the criteria for use of extensive data from larger magnitude reverse-faulting earthquakes and explicit modeling of hanging-wall effects. Among these three GMPEs the CY14 GMPE form was selected for the backbone model for the shallow crustal earthquake GMPEs, though the process followed could have as easily been done using either of the other two GMPE forms. Because of the importance of hanging-wall effects to the ground motion assessment, R_{JB}-based models were not considered candidates for the backbone form for the reasons given above. However, the BSSA14 NGA-West 2 GMPE also passed all of the exclusion criteria except explicit treatment of hanging-wall effects. The Hanford hazard calculation sites are located in both

the hanging wall and the footwall of reverse-faulting earthquakes and the BSSA14 GMPE contains relevant information about the amplitude, magnitude scaling, and distance scaling of ground motions in the footwall where the differences in R_{JB} and R_{RUP} distance measures are relatively small. Therefore, to capture this information and to explicitly treat uncertainty in hanging-wall effects rather than mixing it with general uncertainty in magnitude and distance scaling, the crustal GMPE scaled backbone model was developed in two steps. The first step was to develop the model for footwall conditions. This allowed for development of appropriate factors to center the backbone model and capture the range in magnitude and distance scaling needed to capture the epistemic uncertainty distribution. The scaling factor uncertainty distribution was generated using the predictions from the four GMPEs that pass all of the exclusion criteria except explicit hanging-wall modeling: ASK14, BSSA14, CB14, and CY14. The second step was to develop a separate distribution of hanging-wall effects using the hanging-wall factors from the ASK14, CB14, and CY14 GMPEs as samples. The hanging-wall effects model was then combined with the footwall model to produce the complete shallow crustal GMPE.

9.4.2.1 Footwall Crustal GMPE

The purpose of the crustal GMPE is to represent the center, body, and range of ground motion estimates. The first step is to develop a centered backbone using the CY14 GMPE. The center was defined as the geometric mean of ground motions predicted by the four candidate models over the range of earthquake rupture scenarios important to the hazard at the Hanford hazard calculation sites. The ASK14, BSSA14, CB14, and CY14 GMPEs were used to predict median ground motions for the following range of rupture scenarios:

1. magnitude **M** 5.5, 6, 6.5, 7, and 7.5 reverse-faulting earthquakes
2. R_X distances of -1, -2, -3, -5, -7.5, -10, -15, -20, -25, -30, -40, and -50 km
3. fault dips of 20, 30, 40, 50, 60, 70, and 80 degrees
4. expected Z_{TOR} for each magnitude and dip based on depth to top of rupture distributions developed for crustal thickness of 13, 16, and 20 km. These values are computed using the depth distributions developed in Section 8.3.2.4. Table 9.6 lists the resulting values of Z_{TOR} for each case.
5. default site parameters for V_{S30} equal to 760 m/s.

For each rupture scenario, the geometric mean of the ground motions predicted by the four GMPEs was divided by the prediction of the CY14 model to compute a footwall scaling factor. Figure 9.55 shows the resulting value of the natural log of the scaling factor. Several observations can be made from these results.

First, with the exception of the magnitude **M** 5.5 results, the scaling factors are approximately constant over the period range of 0.01 to about 3 sec. This indicates that the NGA-West2 GMPEs have similar spectral shapes. More importantly, it indicates that a V_S-κ correction based on the CY14 spectral shape is appropriate for the average ground motions predicted by the NGA-West2 GMPEs. At longer periods there is a strong trend in the scaling factor with period indicating that CY14 has significantly different amplitudes that the other NGA-West2 GMPEs.

Second, the adjustment from CY14 to the average of the NGA-West2 predictions is magnitude-dependent. This indicates that there may be important differences in magnitude scaling among the

selected candidate GMPEs that need to be represented in characterizing the uncertainty in median ground motions in active tectonic regions.

Table 9.6. Expected values of Z_{TOR} used for development of median backbone adjustment factors.

Crustal Thickness (km)	Rupture Dip (deg)	Z_{TOR} (km) for Magnitude:				
		5.5	6.0	6.5	7.0	7.5
13	20	4.4	3.9	3.2	2.1	0.9
13	30	4.1	3.5	2.1	0.3	0
13	40	3.8	2.9	1	0	0
13	50	3.7	2.4	0	0	0
13	60	3.5	2	0	0	0
13	70	3.3	1.6	0	0	0
13	80	3.2	1.4	0	0	0
16	20	5.7	5.3	4.7	3.6	2.3
16	30	5.5	4.9	3.6	1.8	0
16	40	5.3	4.4	2.5	0	0
16	50	5.1	3.8	1.5	0	0
16	60	4.9	3.4	0.7	0	0
16	70	4.7	3	0	0	0
16	80	4.6	2.8	0	0	0
20	20	7.3	7.1	6.5	5.4	4.2
20	30	7.1	6.7	5.4	3.6	1.8
20	40	7	6.2	4.3	2	0
20	50	6.9	5.7	3.3	0.5	0
20	60	6.7	5.3	2.5	0	0
20	70	6.6	4.9	2	0	0
20	80	6.5	4.7	1.6	0	0

Figure 9.56 shows the values from Figure 9.55 averaged over dip for various distance intervals. These results indicate that the effect of distance on the scaling factor from CY14 to the average of the four NGA-West2 predictions is about ± 0.1 natural log units over the distance range of 5 to 50 km.

The remaining factor is the effect of dip. Figure 9.57 shows the values from Figure 9.55 averaged over distance for individual dip values. As indicated in the figure, fault dip has minimal effect on ground motion estimation on the footwall side of the ruptures.

On the basis of the comparisons shown in Figure 9.56 and Figure 9.57, it was concluded that an average scaling factor over the period range of 0.01 sec to 2 sec can be used to center the CY14 GMPE for **M** 6.5 and larger earthquakes. Smaller magnitude earthquakes show some period dependence in the scaling factor within this period range. However, the smaller earthquakes do not contribute significantly to hazard at longer periods. Examination of the results of hazard sensitivity analyses indicates that the contribution from **M** 6 earthquakes is primarily at periods of less than about 1 sec and the contribution from **M** 5.5 earthquakes is primarily at periods of less than about 0.3 sec. Accordingly, period-independent scaling factors were developed for each magnitude by averaging the values shown in Figure 9.55 over periods of 0.01 to 0.3 sec for magnitude **M** 5.5, 0.01 to 1.0 sec for magnitude **M** 6, and

0.01 to 2.0 sec for magnitude **M** 6.5 and larger. The scaling factors were averaged over all dips and all distances. Because of the small variability in scaling over distance, distance-dependent adjustment factors were not included in the model and the variability in median motions was accounted for in the epistemic uncertainty in the scaling factors. Figure 9.58 shows the resulting scaling factors, along with the period-dependent scaling factors. The dotted lines indicate how the scaling factors for **M** 5.5 and 6.0 were extended beyond the period range used for averaging. For periods larger than 2 sec, the period-dependent scaling factors are nearly the same for all magnitudes. Figure 9.59 shows the magnitude dependence of the centering scaling factors.

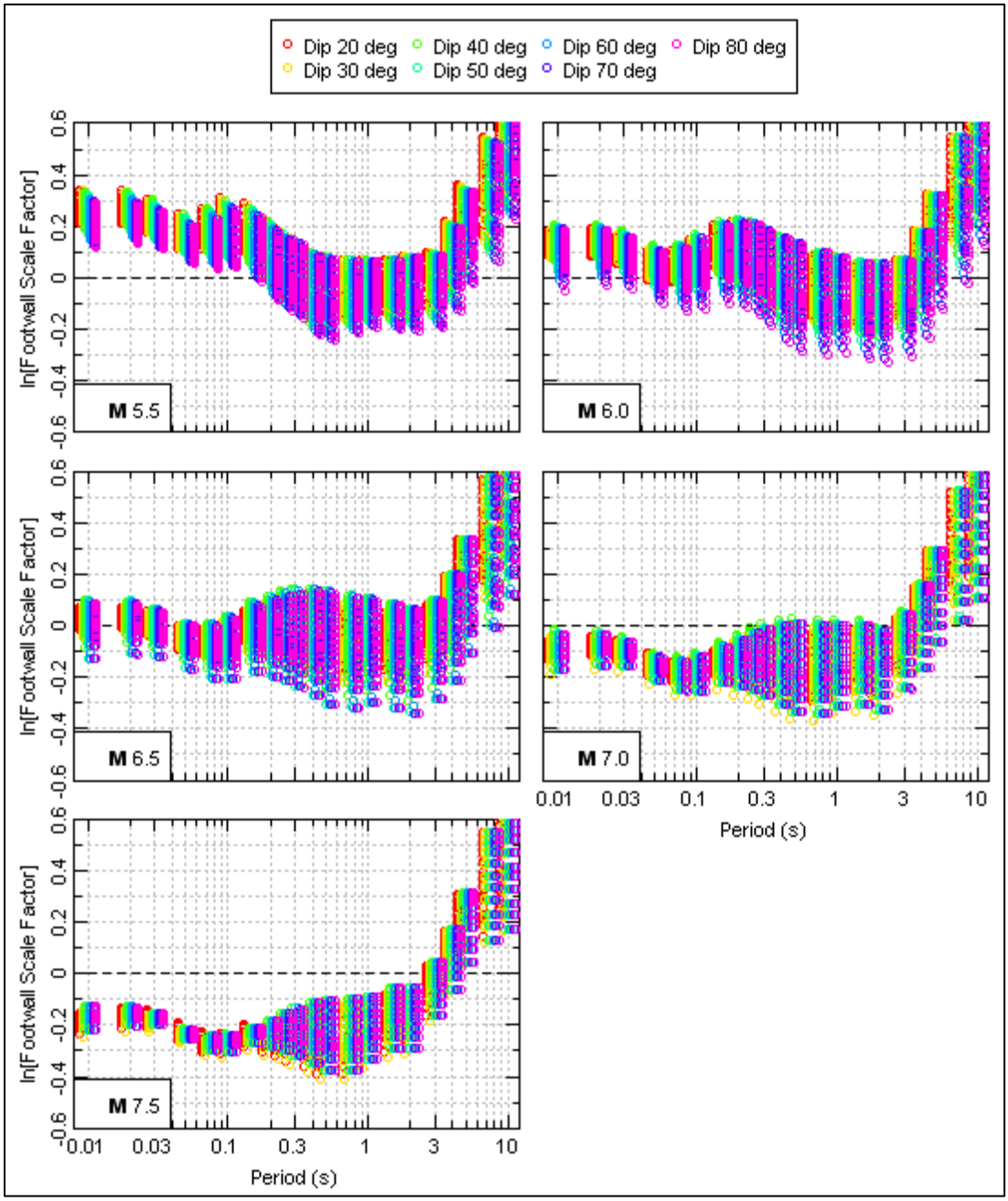

Figure 9.55. Distribution of factors to scale CY14 to the geometric mean of footwall ground motion predictions from the ASK14, BSSA14, CB14, and CY14 GMPEs.

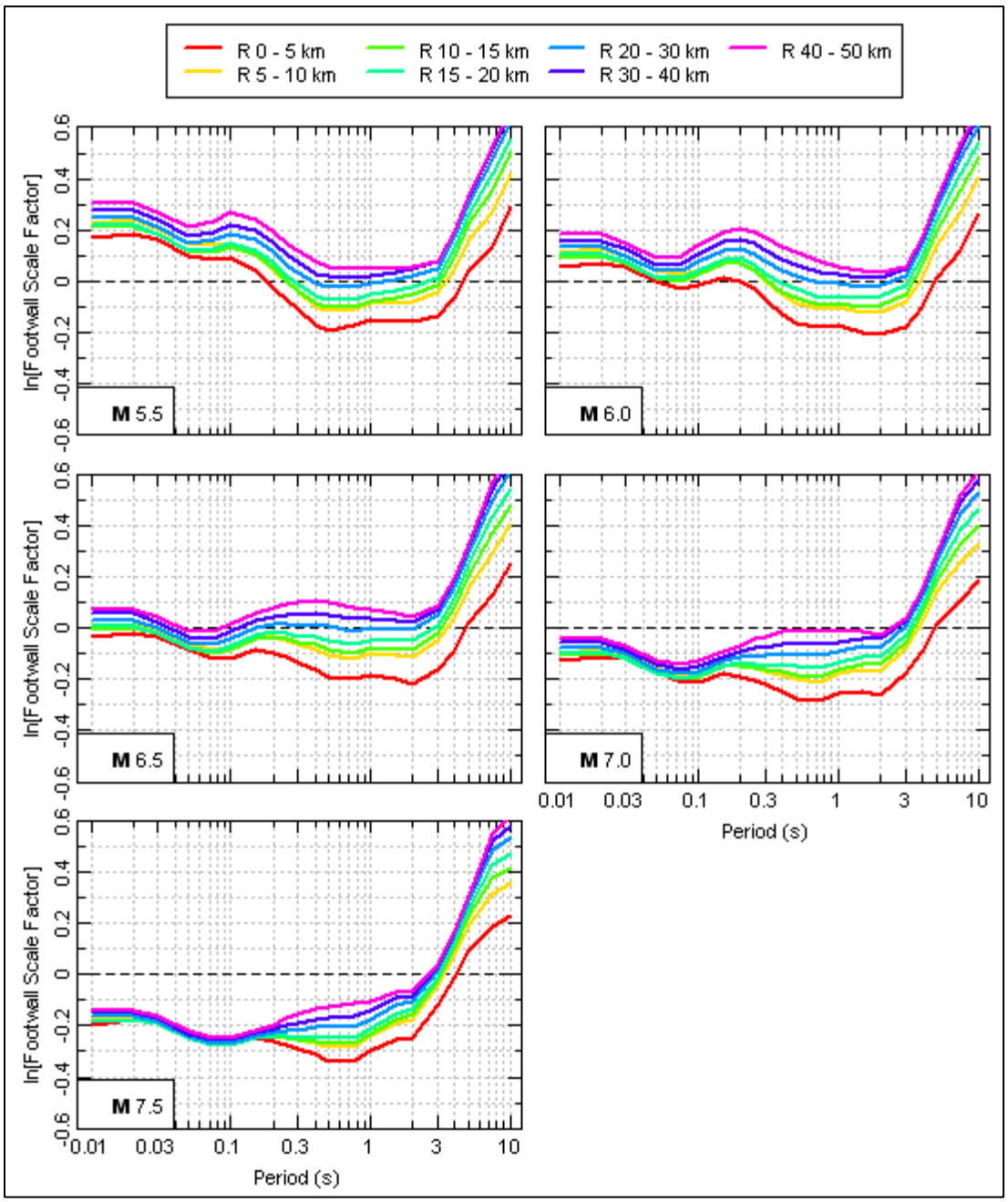

Figure 9.56. Effect of distance on average factor to scale CY14 to the geometric mean of footwall ground motion predictions from the ASK14, BSSA14, CB14, and CY14 GMPEs.

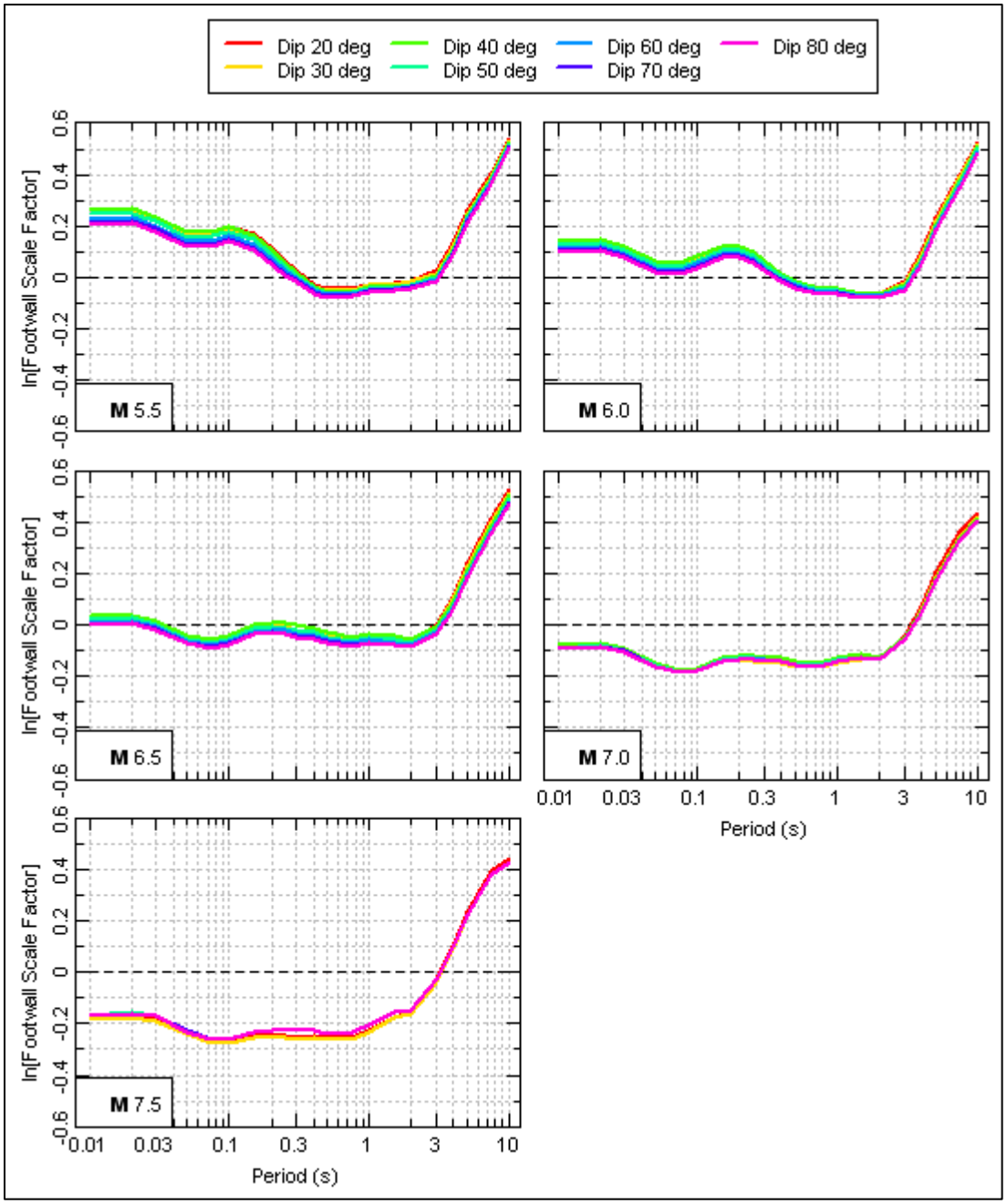

Figure 9.57. Effect of rupture dip on average factor to scale CY14 to the geometric mean of footwall ground motion predictions from the ASK14, BSSA14, CB14, and CY14 GMPEs.

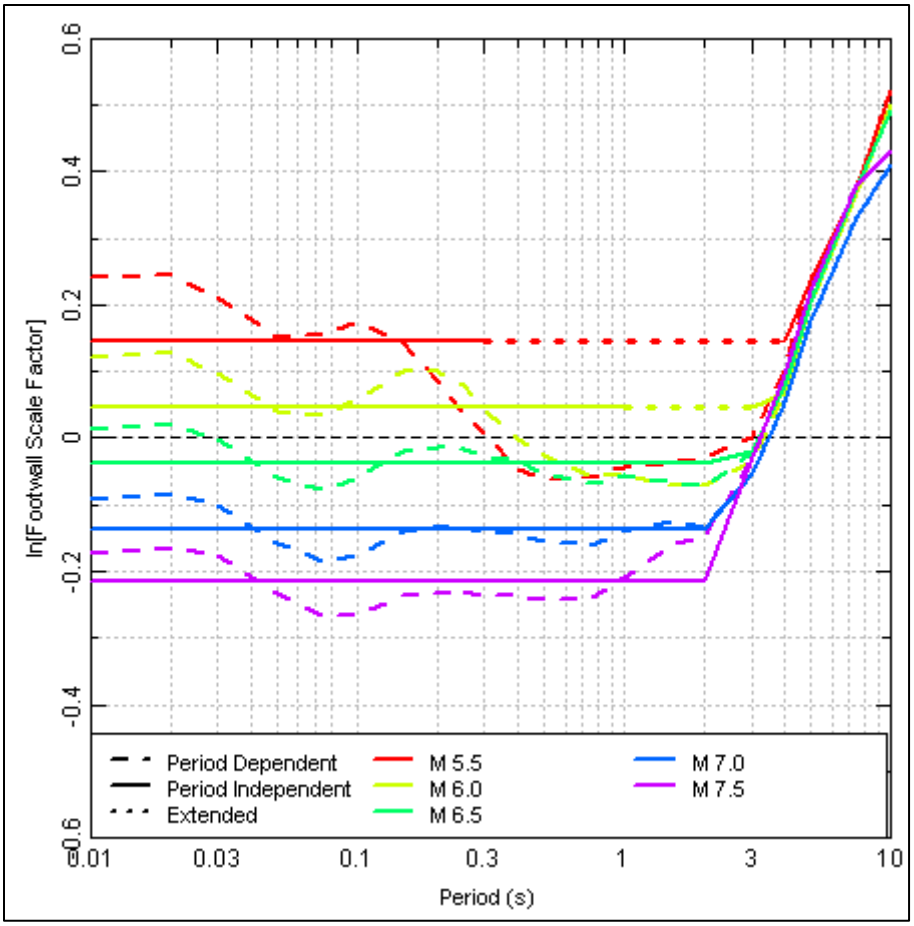

Figure 9.58. Magnitude-dependent scaling factors to center the CY14 GMPE on the geometric mean of footwall ground motion predictions from the ASK14, BSSA14, CB14, and CY14 GMPEs.

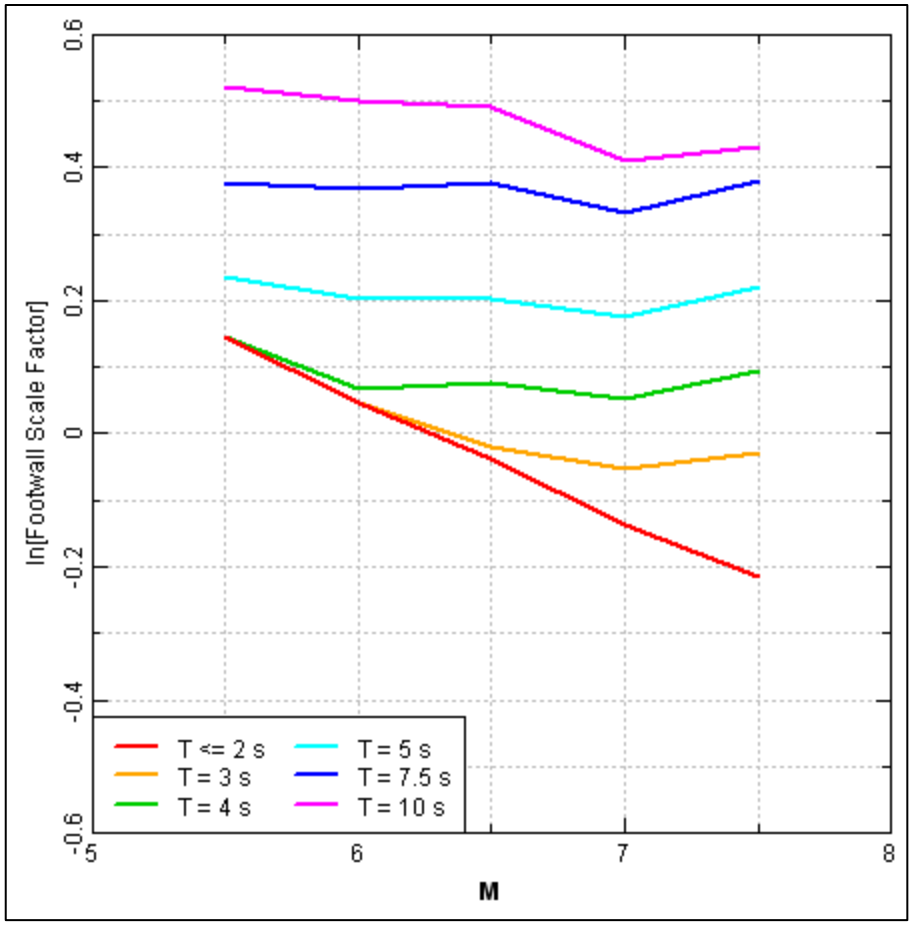

Figure 9.59. Magnitude dependence of scaling factors to center the CY14 GMPE on the geometric mean of footwall ground motion predictions from the ASK14, BSSA14, CB14, and CY14 GMPEs.

The comparisons presented above indicate that magnitude-dependent adjustments of the CY14 GMPE are needed to develop a centered backbone GMPE. The fact that the candidate models have magnitude scaling different from CY14 also indicates that epistemic uncertainty in magnitude scaling should be incorporated into the characterization of ground motions from crustal earthquakes. The process used to capture the epistemic uncertainty in magnitude scaling and centering the crustal backbone GMPE is as follows.

First, a set of ground motion prediction residuals is computed for each of the four candidate GMPEs. These prediction residuals are defined by

$$\Delta \ln(y)_i = \ln(PSA|\text{GMPE}_i) - \ln(PSA|\text{CY14}) \tag{9.14}$$

where the values of $\Delta\ln(y)_i$ represent the difference in ground motion prediction between each candidate GMPE and the prediction from CY14. The average of $\Delta\ln(y)_i$ over the four GMPEs is the scale factor to center CY14 on the geometric mean prediction from the four NGA-West2 GMPEs. For high-frequency motions, the values of $\Delta\ln(y)_i$ were averaged over the period ranges described above (0.01 to 0.3 s for **M** 5.5, 0.01 to 1 sec for **M** 6, 0.01 to 2 sec for **M** $\geq$ 6.5). For periods longer than 2 sec, the values of

$\Delta\ln(y)_i$ were computed for individual periods using only values for **M** 6 and larger earthquakes. The values of $\Delta\ln(y)_i$ were fit with the mixed effects model:

$$\Delta \ln(Y) = c_{1F} + c_{2F}\{M - 6.5\} + \varepsilon_{1R} + \varepsilon_{2R}\{M - 6.5\}$$
$$(\varepsilon_{1R}, \varepsilon_{2R}) \sim N\left(0, \begin{bmatrix} c_{1R}^2 & \rho \\ \rho & c_{2R}^2 \end{bmatrix}\right) \quad (9.15)$$

where the coefficients c_{1F} and c_{2F} are the fixed effects that define the relationship to center the CY14 model on the geometric mean of ground motions predicted by the four NGA-West2 GMPEs. Terms ε_{1R} and ε_{2R} are the random intercept adjustment and a random magnitude scaling adjustment that model the variability in scaling from CY14 among the various GMPEs. Their standard deviations, c_{1R} and c_{2R}, and correlation coefficient ρ are estimated by treating the individual GMPEs as the effect. The correlation between ε_{1R} and ε_{2R} captures the correlation between amplitude and magnitude scaling inherent in each GMPE. The coefficients were estimated for the individual periods and then smoothed to maintain a relatively constant spectral shape for periods up to about 3 sec. Table 9.7 lists the final smoothed coefficients. The values of used in the model c_{1R} were set equal to the square root of the sum of the variances from the random effect for the constant term, the residual variance in fitting the values of $\Delta\ln(y)_i$ and the average mean squared error between the values at the individual periods and the smoothed model.

The standard deviations c_{1R} and c_{2R} and the correlation coefficient ρ provide a 2-D Gaussian covariance matrix representing the uncertainty in crustal ground motions in terms of scaling factors from CY14. This uncertainty distribution was represented by the 9-point discrete distribution presented by Cools and Rabinowitz (1993). For uncorrelated variables, the 9-point discrete distribution is listed in Table 9.8, where ε_X and ε_Y are the number of standard deviations in the two component directions. This discrete representation of a 2-D Gaussian distribution was chosen because it reproduces the marginal mean and standard deviation in both directions and along the 45 degree diagonals. More generally, the degree of this discretization is 5, which means that it reproduces the expected values of so-called monomials of the form $(x^i)*(y^j)$ for which I + j <= 5. This discretization is superior in accuracy to the application of well-known 3-point one-dimensional discretization to each variable (e.g., Keefer and Bodily 1983), which would result in a 5-point discrete distribution; and is superior in efficiency to application of the well-known 5-point discretization to each variable (e.g., Miller and Rice 1983), which would result in a 24-point discrete distribution. Viewed in a marginal sense, the discrete distribution becomes a 5-point distribution with weights of 0.0625, 0.125, 0.625, 0.125, and 0.0625 on the marginal ε values of -2, $-\sqrt{2}$, 0, $\sqrt{2}$, and 2, respectively. The distribution is illustrated marginally in Figure 9.60 along with the 1-D discrete 3-point distribution of Keefer and Bodily (1983) and the 1-D general 5-point discrete distribution of Miller and Rice (1983) applied to the normal distribution. In 1-D, the marginal sense of Cools and Rabinowitz's 9-point distribution has greater range than the other two distributions and reproduces the standard deviation and 4th moment (kurtosis) exactly.

If the error terms are correlated with correlation coefficient $\rho_{X,Y}$, then the second random variable is scaled by

$$\varepsilon'_Y = \varepsilon_Y \sqrt{1 - \rho_{X,Y}^2} + \varepsilon_X \rho_{X,Y} \quad (9.16)$$

Table 9.7. Coefficients of mixed-effects crustal backbone scaling model.

Period (sec)	c_{1F}	c_{2F}	c_{1R}	c_{2R}	ρ
0.01	-0.03	-0.19	0.15	0.15	0.3
0.02	-0.03	-0.19	0.15	0.15	0.3
0.03	-0.03	-0.19	0.15	0.15	0.3
0.04	-0.03	-0.19	0.15	0.15	0.3
0.05	-0.03	-0.19	0.15	0.15	0.3
0.075	-0.03	-0.19	0.15	0.15	0.3
0.1	-0.03	-0.19	0.15	0.15	0.3
0.15	-0.03	-0.19	0.15	0.15	0.3
0.2	-0.03	-0.19	0.15	0.15	0.3
0.25	-0.03	-0.19	0.15	0.15	0.3
0.3	-0.03	-0.19	0.15	0.15	0.3
0.4	-0.03	-0.173	0.15	0.15	0.243
0.5	-0.03	-0.16	0.15	0.15	0.198
0.75	-0.03	-0.137	0.15	0.15	0.117
1	-0.03	-0.12	0.15	0.15	0.06
1.5	-0.03	-0.108	0.165	0.141	-0.021
2	-0.03	-0.099	0.176	0.135	-0.079
3	-0.03	-0.087	0.191	0.126	-0.16
4	0.07	-0.078	0.202	0.12	-0.217
5	0.2	-0.071	0.21	0.115	-0.262
7.5	0.365	-0.059	0.29	0.106	-0.343
10	0.474	-0.05	0.34	0.1	-0.4

Table 9.8. Nine-point discrete representation of a 2-D Gaussian distribution (from Cool and Rabinowitz 1993)

Point	ε_X	ε_Y	Weight
1	2	0	0.0625
2	$\sqrt{2}$	$\sqrt{2}$	0.0625
3	0	2	0.0625
4	$-\sqrt{2}$	$\sqrt{2}$	0.0625
5	0	0	0.5
6	-2	0	0.0625
7	$-\sqrt{2}$	$-\sqrt{2}$	0.0625
8	0	-2	0.0625
9	$\sqrt{2}$	$-\sqrt{2}$	0.0625

The fixed and random effects values listed in Table 9.7 were used to develop a set of nine scaling factors to scale CY14 ground motion estimates. As part of this calculation, the value of c_{1R} was modified by summing corresponding variances to include the within-model epistemic uncertainty for the NGA-West2 GMPEs developed by Al Atik and Youngs (2014). The Al Atik and Youngs (2014) within-model epistemic uncertainty standard deviation is given by

$$\sigma_{\mu} = 0.083 + 0.056 \max\{M - 7,0\} + 0.0171 \max\{\ln(T),0\} \tag{9.17}$$

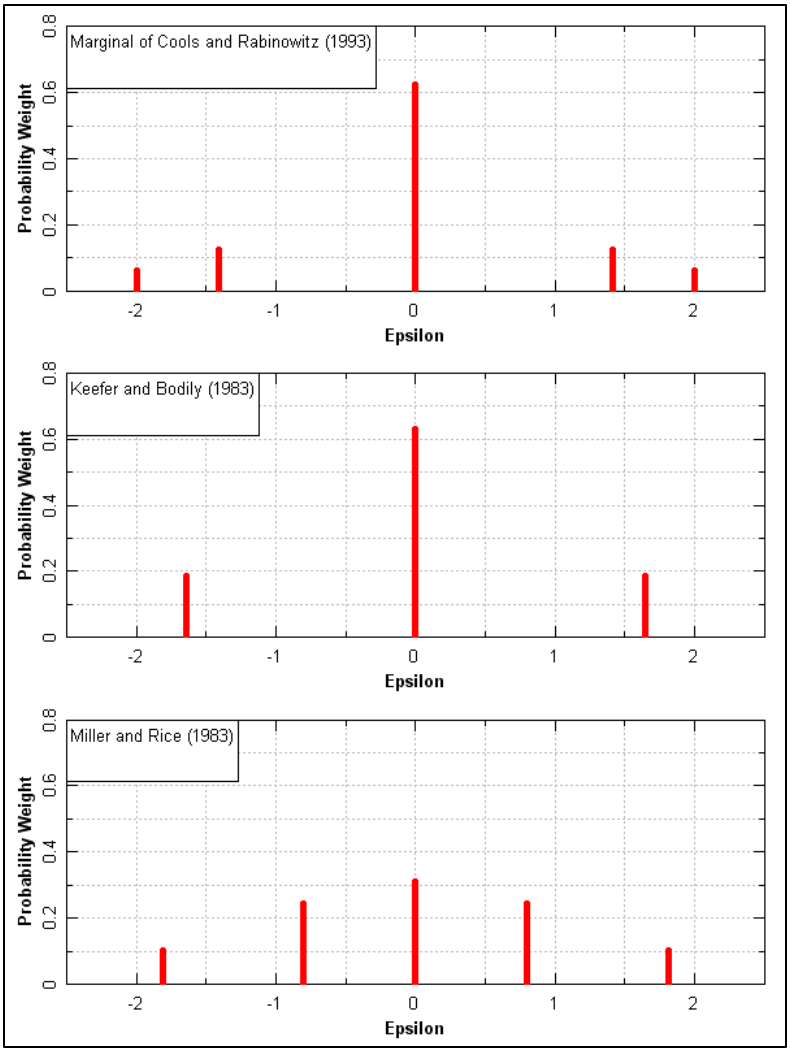

Figure 9.60. Comparison of marginal representation of the Cools and Rabinowitz (1993) 9-point 2-D discrete distribution with the 1-D discrete distributions of Keefer and Bodily (1983) and Miller and Rice (1983).

The scaling factors were applied to median ground motion values given by the CY14 GMPE to produce ground motion estimates. Figure 9.61 shows response spectra predicted by the resulting crustal GMPEs for footwall locations at R_X of -5 and -20 km. Figure 9.62 shows the corresponding response spectral shapes. The spectral shapes are nearly constant over the period range of 0.01 to 3 sec. This allows application of a single set of V_S-κ corrections to scale the full suite of nine crustal GMPEs to the Hanford hazard calculation sites' baserock conditions.

Figure 9.63 shows the range of magnitude scaling relationships resulting from the suite of nine crustal GMPEs for PGA (100-Hz pseudo-spectral acceleration [PSA]) and PSA at periods from 0.05 to 10 sec for a range of distances from R_X of -2 to -50 km. Each figure also shows the predictions from the four NGA-West2 GMPEs used to develop the crustal backbone models. The predictions from the four NGA-West2 GMPEs lie within the range of the predictions from the epistemic crustal models.

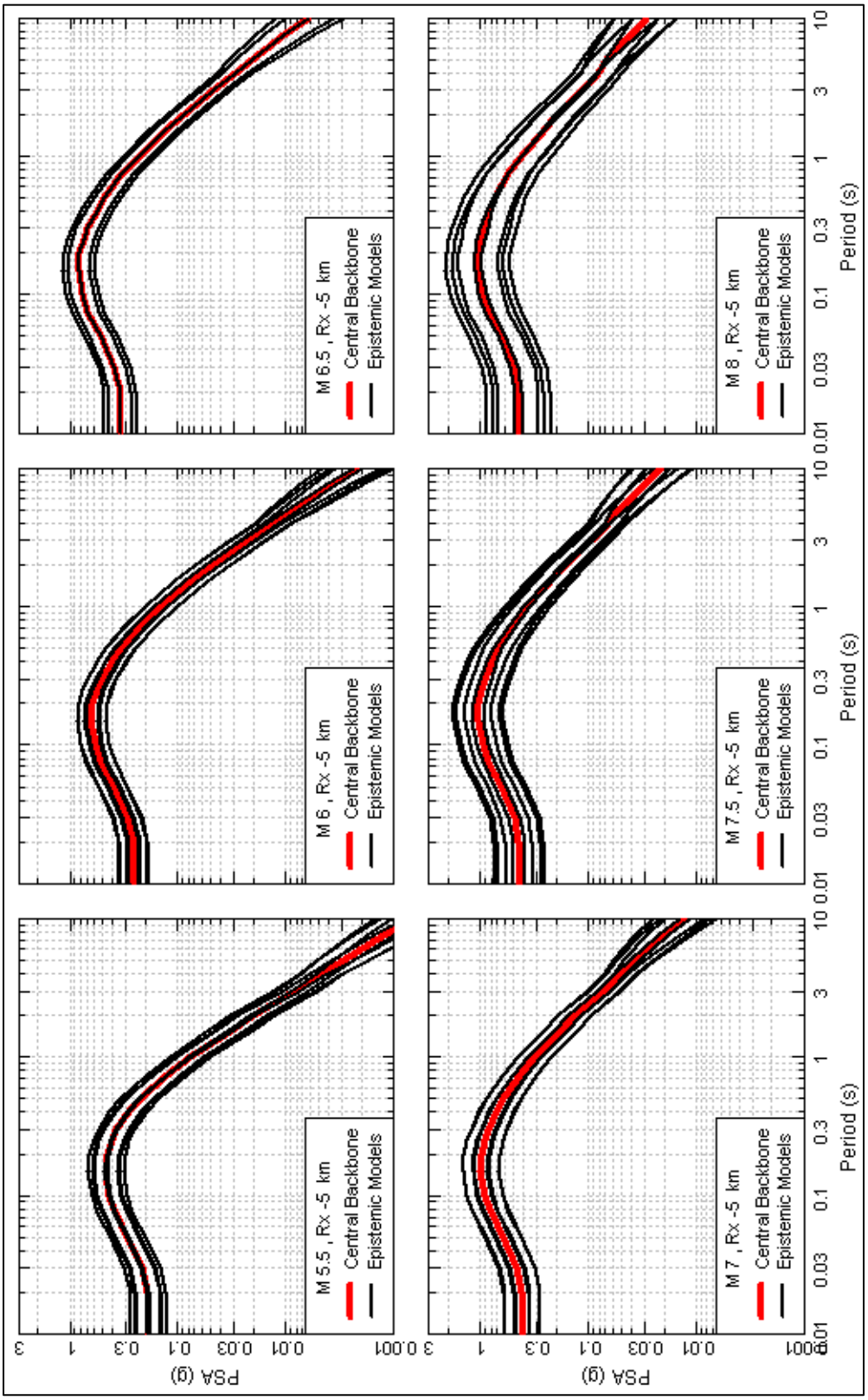

Figure 9.61. Response spectra computed using crustal footwall GMPEs (1 of 2).

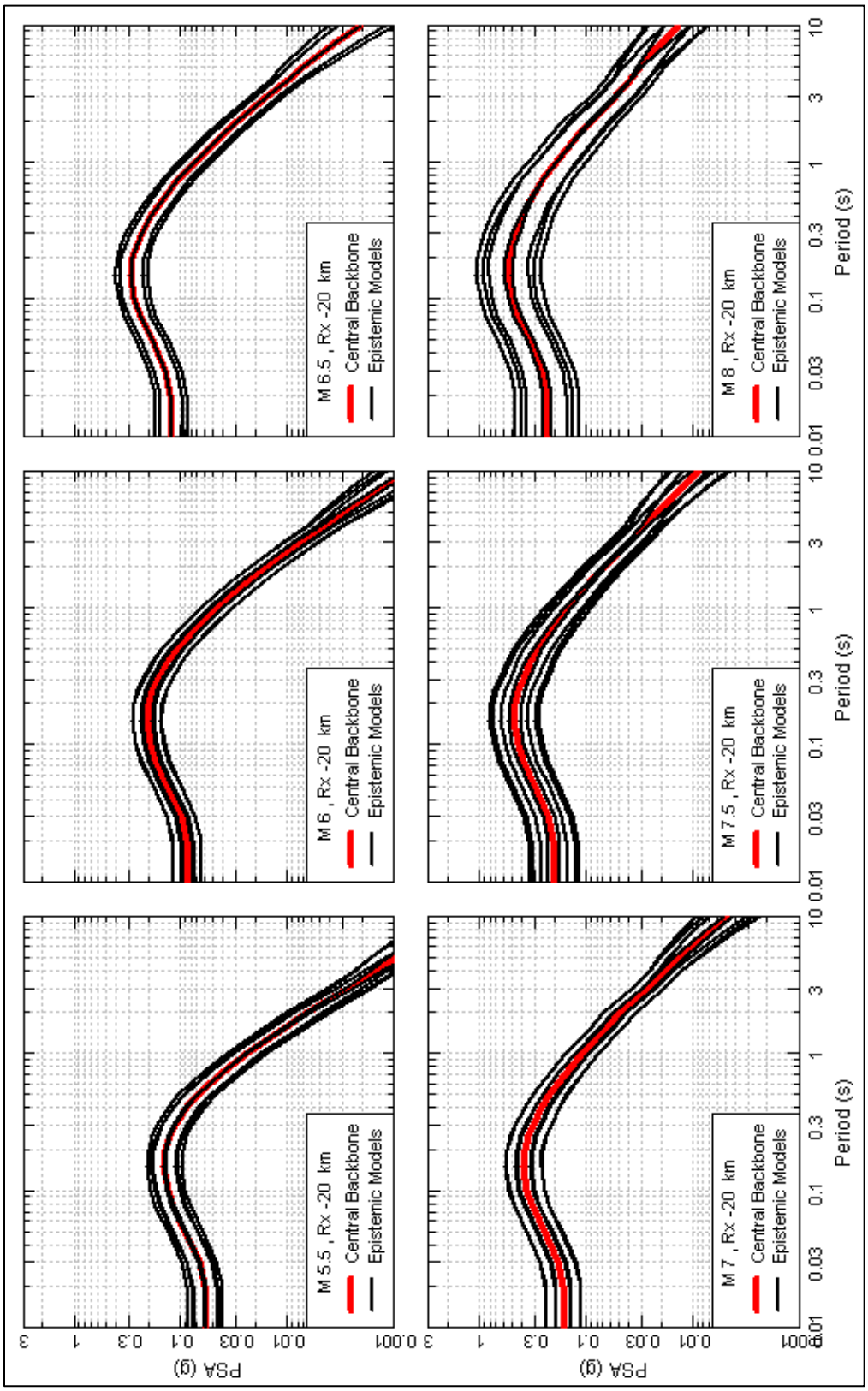

Figure 9.61. (contd; 2 of 2)

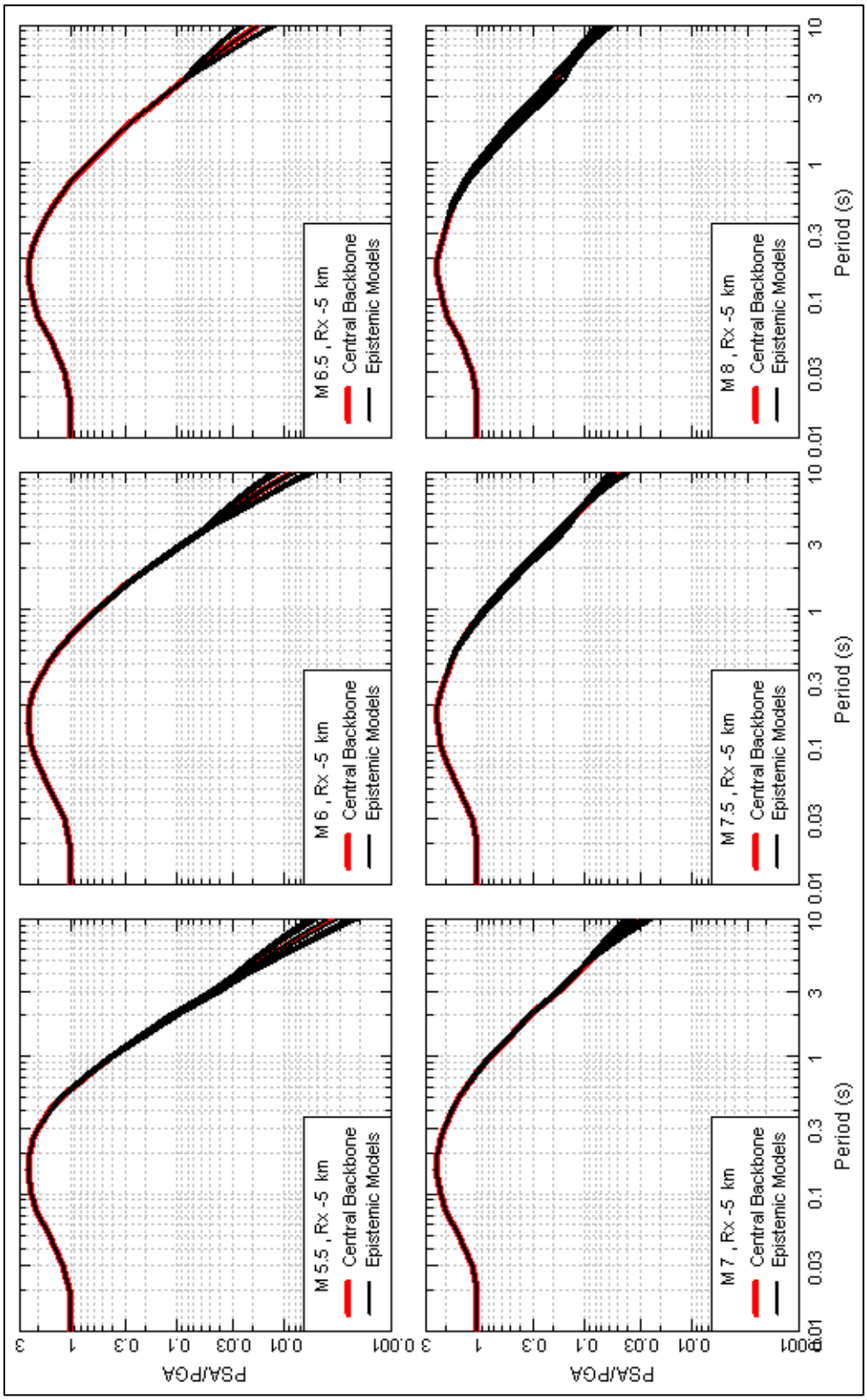

Figure 9.62. Response spectral shapes computed using crustal footwall GMPEs (1 of 2).

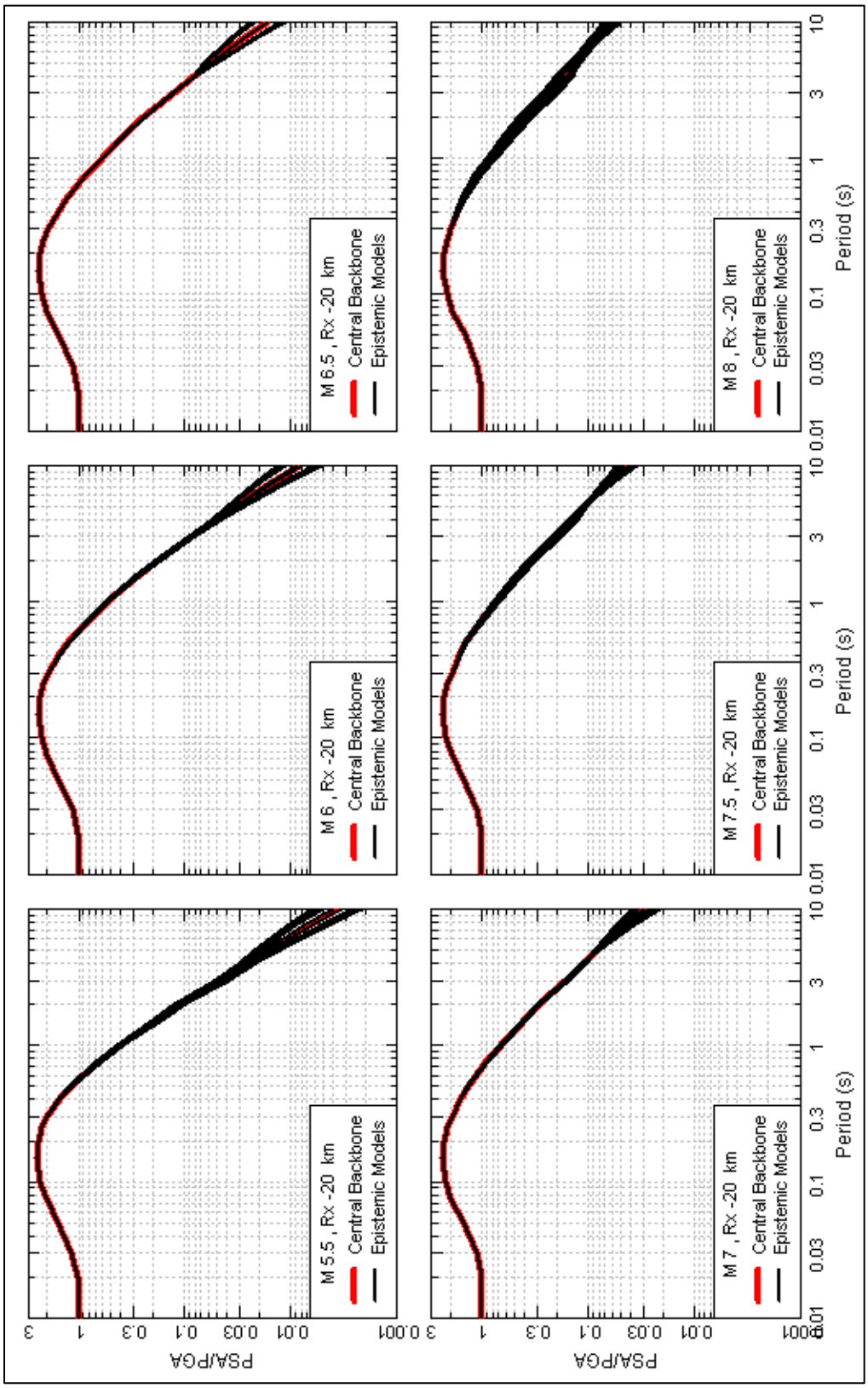

Figure 9.62. (contd; 2 of 2)

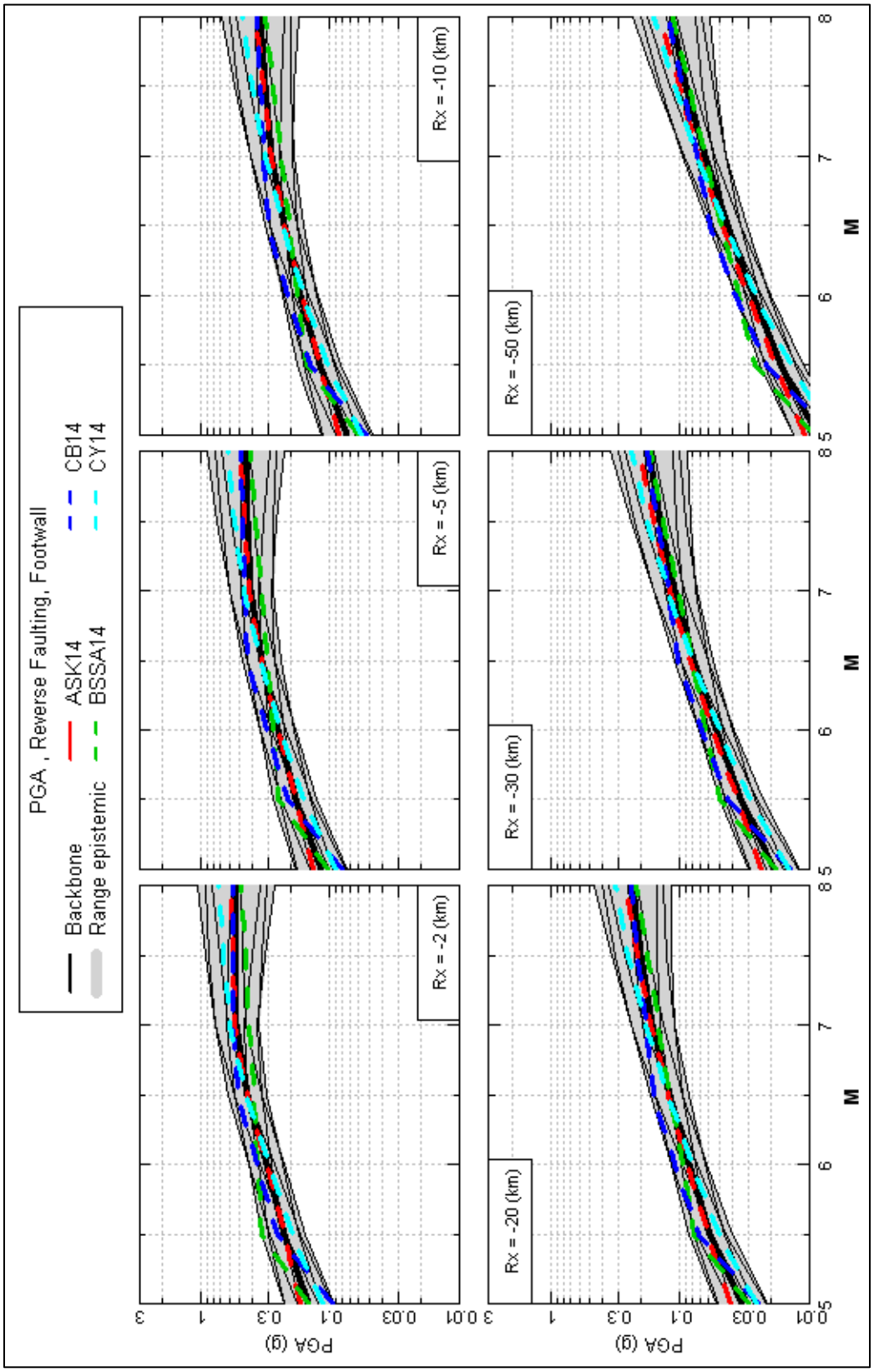

Figure 9.63. Range of magnitude scale produced by crustal footwall GMPEs (1 of 6).

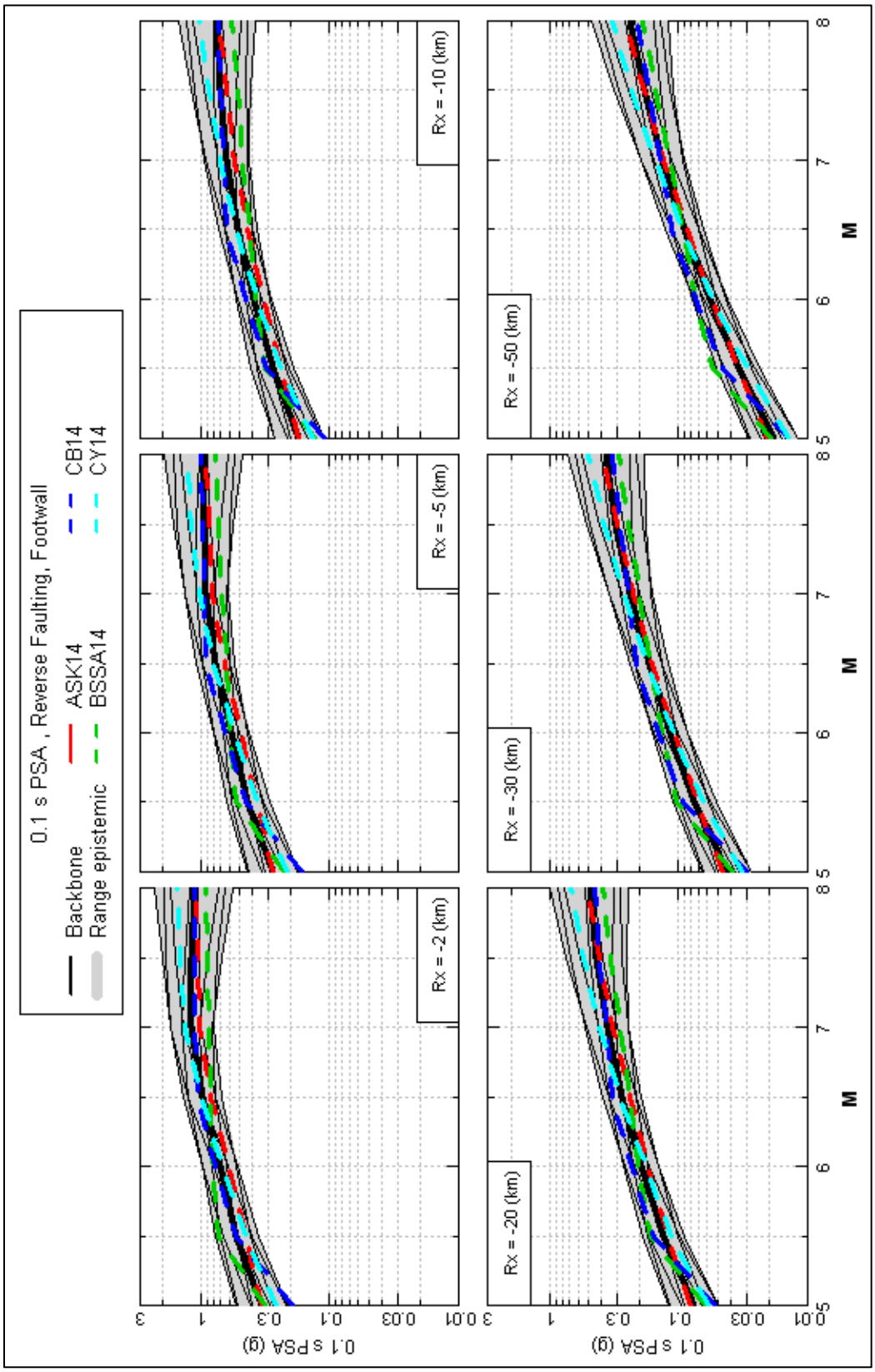

Figure 9.63. (contd; 2 of 6)

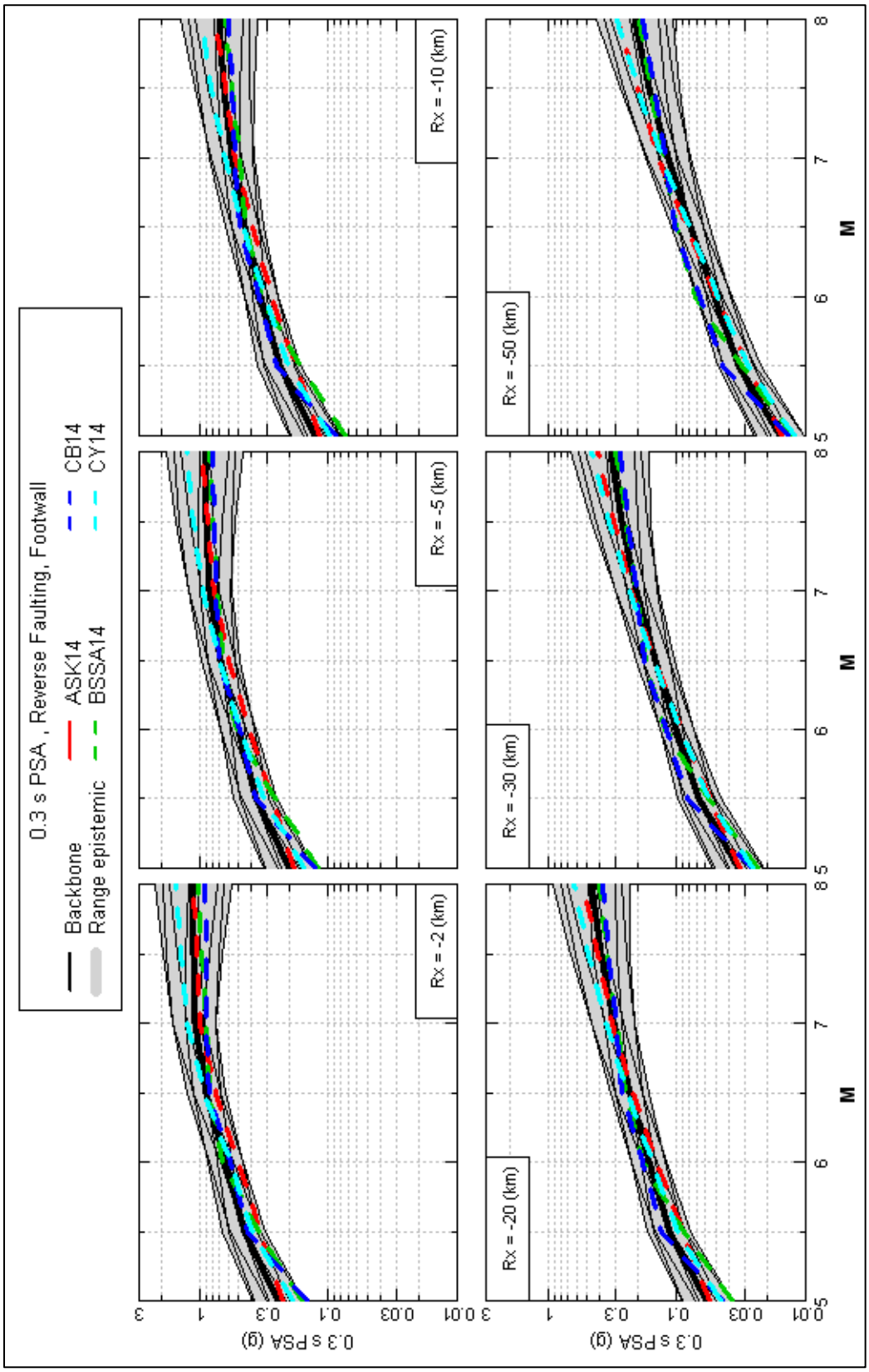

Figure 9.63. (contd; 3 of 6)

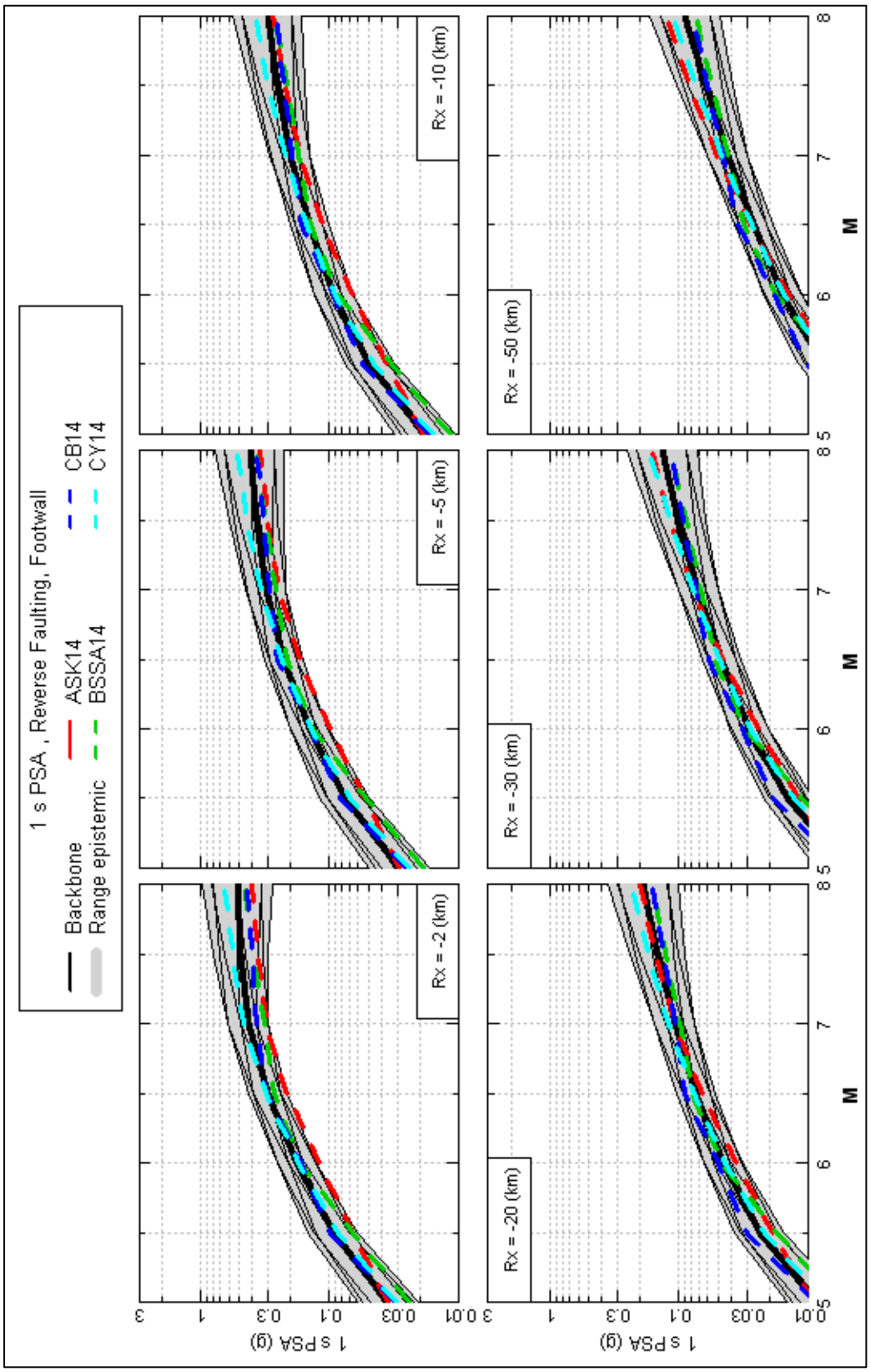

Figure 9.63. (contd; 4 of 6)

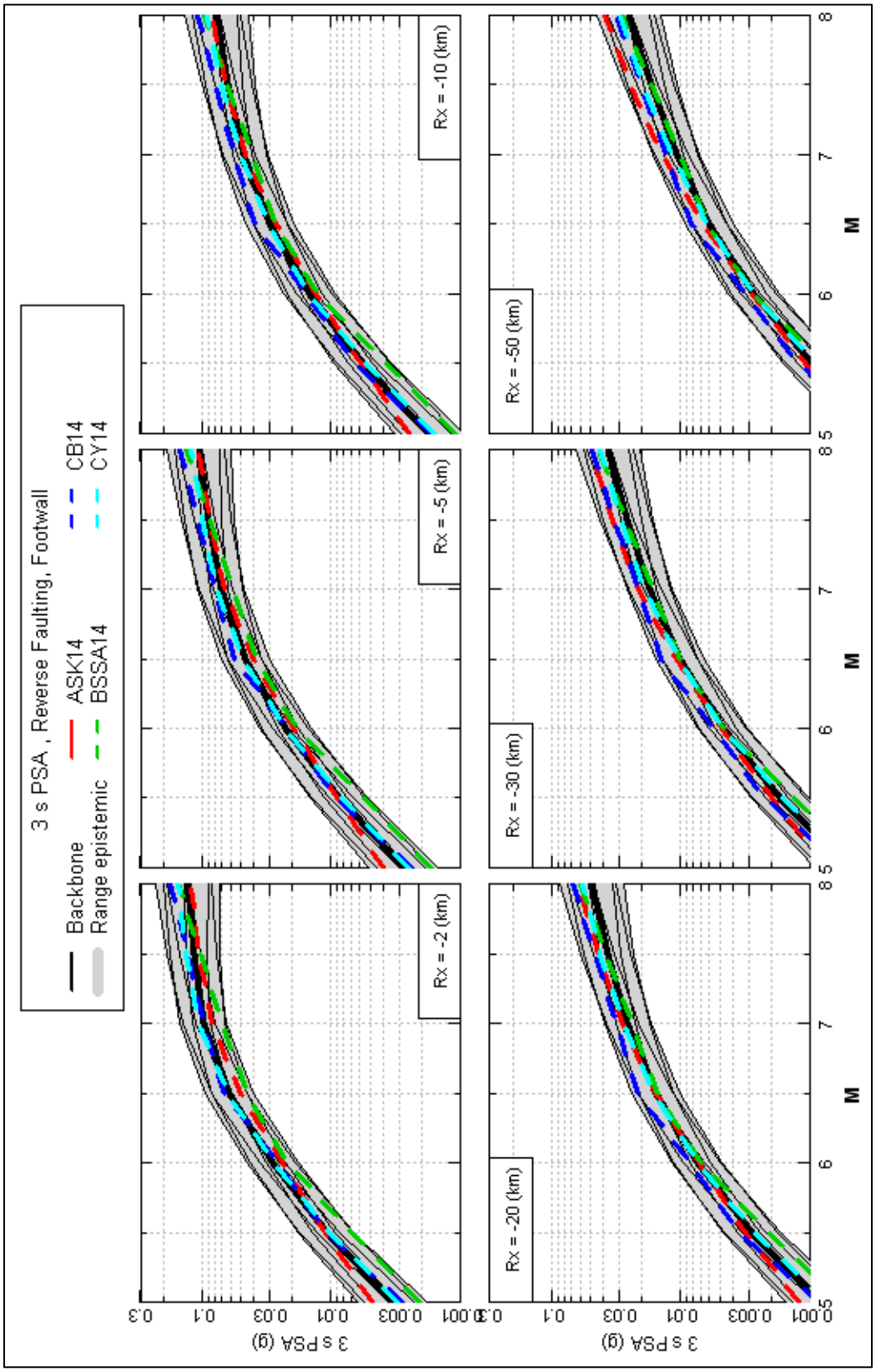

Figure 9.63. (contd; 5 of 6)

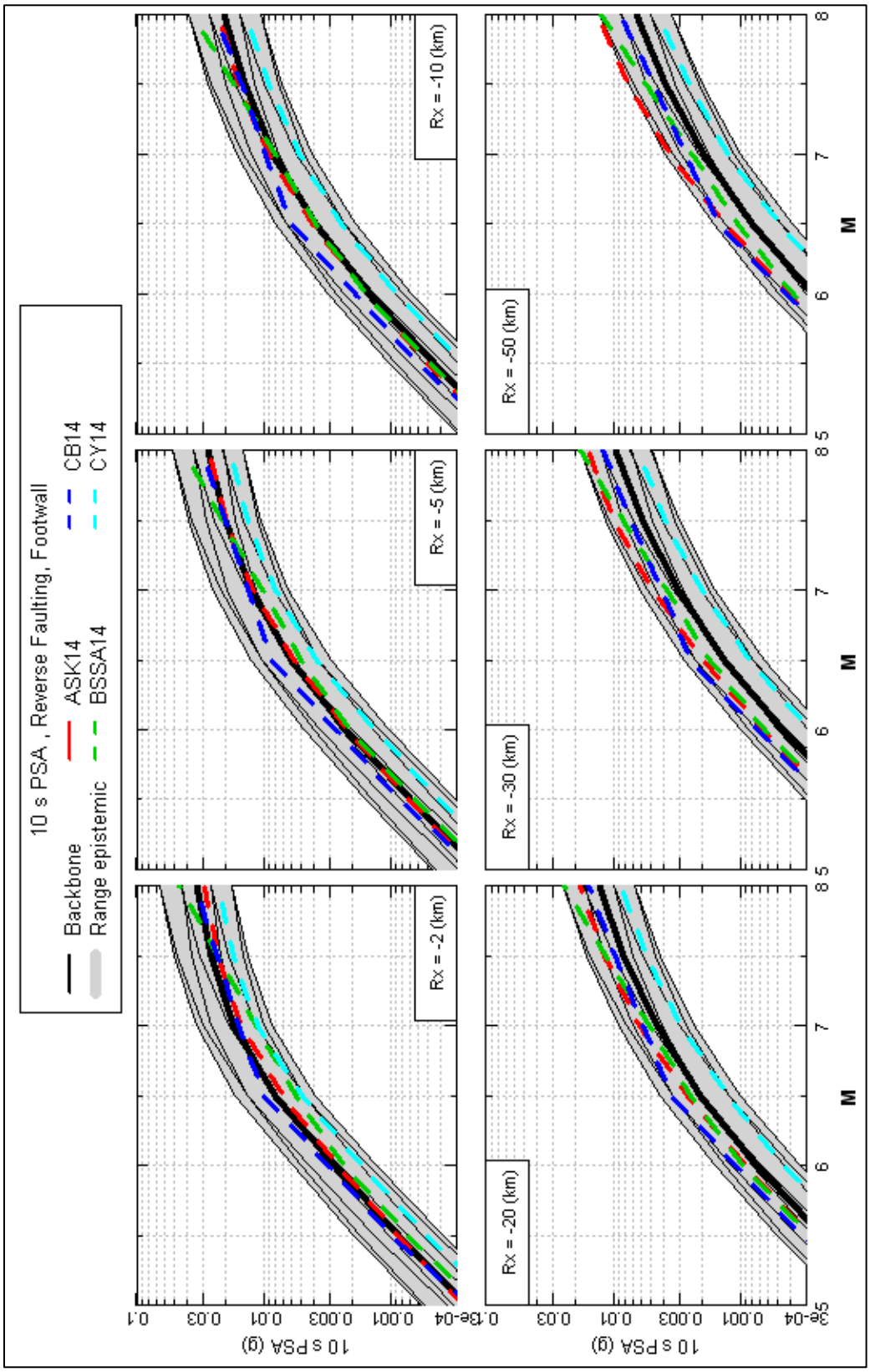

Figure 9.63. (contd; 6 of 6)

At shorter distances, two or three of the nine epistemic models show some degree of oversaturation at magnitudes above **M** 7. This is a consequence of the increasing epistemic uncertainty with increasing magnitude above **M** 7. The GMC TI Team considers this effect to be a proper result of increased uncertainty at large magnitudes. It should be noted that most of the nine models do not show oversaturation and it clearly is not the expected result.

To complete the footwall crustal GMPE characterization, the nine sets of footwall scaling factors were fit with the following functional form:

$$\Delta \ln(y) = p_1 + p_2(M - 6.5) + p_3 \max\{M - 7,0\} \tag{9.18}$$

The third term in Equation (9.18) was introduced to capture the increased epistemic uncertainty for magnitudes greater than **M** 7 introduced by incorporating the epistemic uncertainty model for an individual NGA-West 2 GMPE given above in Equation (9.17). The coefficients of Equation (9.18) are listed in Table 9.9. As indicated in the table, coefficient p_3 is zero for the central model (model 5) and takes on small positive or negative values for the other models to represent the increased epistemic uncertainty at large magnitudes given by the Al Atik and Youngs (2014) model.

9.4.2.2 Hanging-Wall Crustal GMPE

The second step in the development of the crustal GMPE was to model the hanging-wall effect. A range of rupture scenarios was defined for the hanging-wall side of earthquakes consisting of the following:

1. magnitude **M** 5.5, 6, 6.5, 7, and 7.5 reverse-faulting earthquakes
2. R_X distances of 1, 2, 3, 5, 7.5, 10, 15, 20, 25, 30, 40, and 50 km
3. fault dips of 20, 30, 40, 50, 60, 70, and 80 degrees
4. expected Z_{TOR} for each magnitude and dip based on depth to top of rupture distributions developed for crustal thickness of 13, 16, and 20 km. Values are listed in Table 9.6.
5. default site parameters for V_{S30} equal to 760 m/s.

For each rupture scenario, the hanging-wall (HW) factor in the ASK14, CB14, and CY14 GMPEs was computed. Figure 9.64 shows the HW factors for dips of 20, 40, 60, and 80 degrees. For earthquakes of magnitude **M** 6.5 and greater, the HW factors in the three NGA-West2 GMPEs show very similar behavior, differing primarily in amplitude. Both the ASK14 and CB14 models have explicit magnitude tapers that reduce the HW effect to zero over the magnitude interval from **M** 6.5 to **M** 5.5, while the CY14 GMPE has a more gradual reduction in the HW effect with decreasing magnitude. At locations beyond the top of rupture (sites with $R_{JB} > 0$), the HW factors attenuate rapidly for the three GMPEs.

The comparisons shown in Figure 9.64 indicate that an additive factor can be used to scale the CY14 HW term to center it on the average of the HW terms for the three NGA-West2 GMPEs. Figure 9.65 shows the mean HW adjustments as a function of magnitude, distance, and rupture dip for sites above the rupture ($R_{JB} = 0$). For each rupture scenario, the mean HW adjustment is defined as the average of the HW factors for the three NGA-West2 GMPEs minus the CY14 HW factor. The values are relatively

constant for distances up to R_X of about 10 km, and increase with increasing distance beyond 10 km. The mean HW adjustment is proportional to rupture dip, but magnitude has a weak effect for magnitudes of **M** 6.5 and greater. Figure 9.66 shows the standard deviation of the HW adjustments.

The standard deviation has a behavior similar to the mean adjustment. Based on the trends shown in Figure 9.65 and Figure 9.66, the mean and sigma of the HW adjustments were fit with the following functional form:

$$HW_{adjustment} = \left[1 + p_4 \cos(\delta)\right] \times \ln\left[p_5 \cosh\left\{p_6 \max(\ln(R_X / p_7), 0\right\}\right] \tag{9.19}$$

For sites beyond the bottom edge of the rupture ($R_{JB} > 0$) the HW mean HW adjustment attenuates rapidly to zero, as shown in Figure 9.67.

Following the procedure used to develop the footwall crustal model, a set of nine scaling factors was developed to scale CY14 ground motion estimates. The scaling factors consisted of the fixed and random coefficients given in Table 9.7 plus the HW adjustments. The mean HW adjustment was added to the c_{1F} term in Table 9.7 and the standard deviation in the HW adjustment was added to the c_{1R} term by summing variances along with the standard error in fitting the HW adjustment. As was done for the footwall case, the within-model epistemic uncertainty from Al Atik and Youngs (2014) was also included. The scaling factors were applied to median ground motion values given by the CY14 GMPE to produce ground motion estimates for the HW site of ruptures. Figure 9.68 shows response spectra predicted by the resulting crustal GMPEs for footwall locations at R_X of 5 km. Figure 9.69 shows the corresponding response spectral shapes. As was the case for the footwall models, the spectral shapes are nearly constant over the period range of 0.01 to 3 sec.

Figure 9.70 shows the range of distance scaling relationships resulting from the suite of nine crustal GMPEs for PGA (100 Hz PSA) and PSA at periods from 0.05 to 1 sec for **M** 6.5, 7.0, and 7.5 earthquakes. Each figure also shows the predictions from the three NGA-West2 GMPEs used to develop the HW adjustments for the crustal backbone models. The predictions from the three NGA-West2 GMPEs lie within the range of the predictions from the epistemic crustal models. Also shown are the predictions for the BSSA14 model, which used the R_{JB} distance metric. As indicated, the BSSA14 predictions also generally lie within the range of the crustal backbone GMPEs.

The final step to complete the crustal GMPE characterization was to fit the nine sets of HW scaling factors to provide a complete model. The process used was to first subtract the corresponding footwall scaling factors defined by Equation (9.18) from the HW scaling factors. The differences represent the HW adjustments for each of the nine models. These HW adjustments were fit with the function form of Equation (9.19). The resulting parameters are listed in Table 9.9. The complete crustal backbone GMPE is then defined by the following model to adjust the median ground motion predictions from CY14:

$$\begin{aligned} \Delta \ln(Y) = {} & p_1 + p_2 (M - 6.5) + p_3 \max(M - 7, 0) + \\ & F_{HW} \left\{1 + p_4 \cos(\delta)\right\} \times \ln\left[p_5 \cosh\left\{p_6 \max(\ln(R_X / p_7), 0)\right\}\right] \times \\ & \exp(p_8 R_{JB}) \times \max[0, \min(M, 6.5) - 5.5] \end{aligned} \tag{9.20}$$

The parameter F_{HW} is 1 for $R_X \geq 0$, and 0 otherwise. The term $\exp(p_8 R_{JB})$ produces a rapid attenuation of the HW adjustment, as shown in Figure 9.67. The final term attenuates the HW adjustment to zero as the magnitude goes from **M** 6.5 to 5.5. The net effect is to maintain the CY14 HW factors for smaller magnitudes rather than zero HW factors as in ASK14 and CB14.

Table 9.9 Parameters for the adjustments to CY14 (Equation 9.20) used to create the crustal median GMPEs.

Period (sec)	Backbone Adjustment Model	p_1	p_2	p_3	p_4	p_5	p_6	p_7	p_8
0.01	1	0.3129	-0.1	0.0063	3.348	1.0473	0.2538	9	-0.2
0.01	2	-0.3729	-0.28	-0.0063	1.9104	1.014	0.1303	9	-0.2
0.01	3	-0.03	0.0962	0	3.0239	1.0305	0.2017	9	-0.2
0.01	4	-0.03	-0.4762	0	3.0239	1.0305	0.2017	9	-0.2
0.01	5	-0.03	-0.19	0	3.0239	1.0305	0.2017	9	-0.2
0.01	6	0.2124	0.076	0.0044	3.2983	1.0422	0.2392	9	-0.2
0.01	7	0.2124	-0.3287	0.0044	3.2983	1.0422	0.2392	9	-0.2
0.01	8	-0.2724	-0.0513	-0.0044	2.6115	1.018	0.1516	9	-0.2
0.01	9	-0.2724	-0.456	-0.0044	2.6115	1.018	0.1516	9	-0.2
0.02	1	0.3129	-0.1	0.0063	3.348	1.0473	0.2538	9	-0.2
0.02	2	-0.3729	-0.28	-0.0063	1.9104	1.014	0.1303	9	-0.2
0.02	3	-0.03	0.0962	0	3.0239	1.0305	0.2017	9	-0.2
0.02	4	-0.03	-0.4762	0	3.0239	1.0305	0.2017	9	-0.2
0.02	5	-0.03	-0.19	0	3.0239	1.0305	0.2017	9	-0.2
0.02	6	0.2124	0.076	0.0044	3.2983	1.0422	0.2392	9	-0.2
0.02	7	0.2124	-0.3287	0.0044	3.2983	1.0422	0.2392	9	-0.2
0.02	8	-0.2724	-0.0513	-0.0044	2.6115	1.018	0.1516	9	-0.2
0.02	9	-0.2724	-0.456	-0.0044	2.6115	1.018	0.1516	9	-0.2
0.03	1	0.3129	-0.1	0.0063	3.348	1.0473	0.2538	9	-0.2
0.03	2	-0.3729	-0.28	-0.0063	1.9104	1.014	0.1303	9	-0.2
0.03	3	-0.03	0.0962	0	3.0239	1.0305	0.2017	9	-0.2
0.03	4	-0.03	-0.4762	0	3.0239	1.0305	0.2017	9	-0.2
0.03	5	-0.03	-0.19	0	3.0239	1.0305	0.2017	9	-0.2
0.03	6	0.2124	0.076	0.0044	3.2983	1.0422	0.2392	9	-0.2
0.03	7	0.2124	-0.3287	0.0044	3.2983	1.0422	0.2392	9	-0.2
0.03	8	-0.2724	-0.0513	-0.0044	2.6115	1.018	0.1516	9	-0.2
0.03	9	-0.2724	-0.456	-0.0044	2.6115	1.018	0.1516	9	-0.2
0.04	1	0.3129	-0.1	0.0063	3.348	1.0473	0.2538	9	-0.2
0.04	2	-0.3729	-0.28	-0.0063	1.9104	1.014	0.1303	9	-0.2
0.04	3	-0.03	0.0962	0	3.0239	1.0305	0.2017	9	-0.2
0.04	4	-0.03	-0.4762	0	3.0239	1.0305	0.2017	9	-0.2
0.04	5	-0.03	-0.19	0	3.0239	1.0305	0.2017	9	-0.2
0.04	6	0.2124	0.076	0.0044	3.2983	1.0422	0.2392	9	-0.2
0.04	7	0.2124	-0.3287	0.0044	3.2983	1.0422	0.2392	9	-0.2
0.04	8	-0.2724	-0.0513	-0.0044	2.6115	1.018	0.1516	9	-0.2

Table 9.9. (contd)

Period (sec)	Backbone Adjustment Model	p_1	p_2	p_3	p_4	p_5	p_6	p_7	p_8
0.04	9	-0.2724	-0.456	-0.0044	2.6115	1.018	0.1516	9	-0.2
0.05	1	0.3129	-0.1	0.0063	3.348	1.0473	0.2538	9	-0.2
0.05	2	-0.3729	-0.28	-0.0063	1.9104	1.014	0.1303	9	-0.2
0.05	3	-0.03	0.0962	0	3.0239	1.0305	0.2017	9	-0.2
0.05	4	-0.03	-0.4762	0	3.0239	1.0305	0.2017	9	-0.2
0.05	5	-0.03	-0.19	0	3.0239	1.0305	0.2017	9	-0.2
0.05	6	0.2124	0.076	0.0044	3.2983	1.0422	0.2392	9	-0.2
0.05	7	0.2124	-0.3287	0.0044	3.2983	1.0422	0.2392	9	-0.2
0.05	8	-0.2724	-0.0513	-0.0044	2.6115	1.018	0.1516	9	-0.2
0.05	9	-0.2724	-0.456	-0.0044	2.6115	1.018	0.1516	9	-0.2
0.075	1	0.3129	-0.1	0.0063	3.348	1.0473	0.2538	9	-0.2
0.075	2	-0.3729	-0.28	-0.0063	1.9104	1.014	0.1303	9	-0.2
0.075	3	-0.03	0.0962	0	3.0239	1.0305	0.2017	9	-0.2
0.075	4	-0.03	-0.4762	0	3.0239	1.0305	0.2017	9	-0.2
0.075	5	-0.03	-0.19	0	3.0239	1.0305	0.2017	9	-0.2
0.075	6	0.2124	0.076	0.0044	3.2983	1.0422	0.2392	9	-0.2
0.075	7	0.2124	-0.3287	0.0044	3.2983	1.0422	0.2392	9	-0.2
0.075	8	-0.2724	-0.0513	-0.0044	2.6115	1.018	0.1516	9	-0.2
0.075	9	-0.2724	-0.456	-0.0044	2.6115	1.018	0.1516	9	-0.2
0.1	1	0.3129	-0.1	0.0063	3.348	1.0473	0.2538	9	-0.2
0.1	2	-0.3729	-0.28	-0.0063	1.9104	1.014	0.1303	9	-0.2
0.1	3	-0.03	0.0962	0	3.0239	1.0305	0.2017	9	-0.2
0.1	4	-0.03	-0.4762	0	3.0239	1.0305	0.2017	9	-0.2
0.1	5	-0.03	-0.19	0	3.0239	1.0305	0.2017	9	-0.2
0.1	6	0.2124	0.076	0.0044	3.2983	1.0422	0.2392	9	-0.2
0.1	7	0.2124	-0.3287	0.0044	3.2983	1.0422	0.2392	9	-0.2
0.1	8	-0.2724	-0.0513	-0.0044	2.6115	1.018	0.1516	9	-0.2
0.1	9	-0.2724	-0.456	-0.0044	2.6115	1.018	0.1516	9	-0.2
0.15	1	0.3129	-0.1	0.0063	3.348	1.0473	0.2538	9	-0.2
0.15	2	-0.3729	-0.28	-0.0063	1.9104	1.014	0.1303	9	-0.2
0.15	3	-0.03	0.0962	0	3.0239	1.0305	0.2017	9	-0.2
0.15	4	-0.03	-0.4762	0	3.0239	1.0305	0.2017	9	-0.2
0.15	5	-0.03	-0.19	0	3.0239	1.0305	0.2017	9	-0.2
0.15	6	0.2124	0.076	0.0044	3.2983	1.0422	0.2392	9	-0.2
0.15	7	0.2124	-0.3287	0.0044	3.2983	1.0422	0.2392	9	-0.2
0.15	8	-0.2724	-0.0513	-0.0044	2.6115	1.018	0.1516	9	-0.2
0.15	9	-0.2724	-0.456	-0.0044	2.6115	1.018	0.1516	9	-0.2
0.2	1	0.3129	-0.1	0.0063	3.348	1.0473	0.2538	9	-0.2
0.2	2	-0.3729	-0.28	-0.0063	1.9104	1.014	0.1303	9	-0.2
0.2	3	-0.03	0.0962	0	3.0239	1.0305	0.2017	9	-0.2

Table 9.9. (contd)

Period (sec)	Backbone Adjustment Model	p_1	p_2	p_3	p_4	p_5	p_6	p_7	p_8
0.2	4	-0.03	-0.4762	0	3.0239	1.0305	0.2017	9	-0.2
0.2	5	-0.03	-0.19	0	3.0239	1.0305	0.2017	9	-0.2
0.2	6	0.2124	0.076	0.0044	3.2983	1.0422	0.2392	9	-0.2
0.2	7	0.2124	-0.3287	0.0044	3.2983	1.0422	0.2392	9	-0.2
0.2	8	-0.2724	-0.0513	-0.0044	2.6115	1.018	0.1516	9	-0.2
0.2	9	-0.2724	-0.456	-0.0044	2.6115	1.018	0.1516	9	-0.2
0.3	1	0.3129	-0.1	0.0063	3.4722	1.0461	0.2518	8.33	-0.2
0.3	2	-0.3729	-0.28	-0.0063	1.8763	1.0142	0.1282	8.33	-0.2
0.3	3	-0.03	0.0962	0	2.9408	1.0311	0.2035	8.33	-0.2
0.3	4	-0.03	-0.4762	0	2.9408	1.0311	0.2035	8.33	-0.2
0.3	5	-0.03	-0.19	0	2.9408	1.0311	0.2035	8.33	-0.2
0.3	6	0.2124	0.076	0.0044	3.3981	1.0413	0.2377	8.33	-0.2
0.3	7	0.2124	-0.3287	0.0044	3.3981	1.0413	0.2377	8.33	-0.2
0.3	8	-0.2724	-0.0513	-0.0044	2.4588	1.0188	0.1529	8.33	-0.2
0.3	9	-0.2724	-0.456	-0.0044	2.4588	1.0188	0.1529	8.33	-0.2
0.4	1	0.3129	-0.1001	0.0063	3.7943	1.0427	0.2461	7.374	-0.2
0.4	2	-0.3729	-0.2459	-0.0063	1.3585	1.0176	0.1337	7.374	-0.2
0.4	3	-0.03	0.118	0	3.0013	1.0307	0.2022	7.374	-0.2
0.4	4	-0.03	-0.464	0	3.0013	1.0307	0.2022	7.374	-0.2
0.4	5	-0.03	-0.173	0	3.0013	1.0307	0.2022	7.374	-0.2
0.4	6	0.2124	0.0843	0.0044	3.6377	1.0389	0.2336	7.374	-0.2
0.4	7	0.2124	-0.3272	0.0044	3.6377	1.0389	0.2336	7.374	-0.2
0.4	8	-0.2724	-0.0188	-0.0044	2.1145	1.0211	0.157	7.374	-0.2
0.4	9	-0.2724	-0.4303	-0.0044	2.1145	1.0211	0.157	7.374	-0.2
0.5	1	0.3129	-0.1006	0.0063	4.0102	1.0406	0.2427	6.708	-0.2
0.5	2	-0.3729	-0.2194	-0.0063	1.05	1.0204	0.1361	6.708	-0.2
0.5	3	-0.03	0.1341	0	2.9892	1.0308	0.2025	6.708	-0.2
0.5	4	-0.03	-0.4541	0	2.9892	1.0308	0.2025	6.708	-0.2
0.5	5	-0.03	-0.16	0	2.9892	1.0308	0.2025	6.708	-0.2
0.5	6	0.2124	0.0899	0.0044	3.8064	1.0374	0.2311	6.708	-0.2
0.5	7	0.2124	-0.3259	0.0044	3.8064	1.0374	0.2311	6.708	-0.2
0.5	8	-0.2724	0.0059	-0.0044	1.8712	1.023	0.16	6.708	-0.2
0.5	9	-0.2724	-0.4099	-0.0044	1.8712	1.023	0.16	6.708	-0.2
0.75	1	0.3129	-0.1019	0.0063	4.5051	1.0366	0.2352	5.649	-0.2
0.75	2	-0.3729	-0.1721	-0.0063	0.6947	1.0249	0.1363	5.649	-0.2
0.75	3	-0.03	0.1609	0	3.0666	1.0302	0.2007	5.649	-0.2
0.75	4	-0.03	-0.4349	0	3.0666	1.0302	0.2007	5.649	-0.2
0.75	5	-0.03	-0.137	0	3.0666	1.0302	0.2007	5.649	-0.2
0.75	6	0.2124	0.0985	0.0044	4.1661	1.0346	0.2257	5.649	-0.2
0.75	7	0.2124	-0.3229	0.0044	4.1661	1.0346	0.2257	5.649	-0.2
0.75	8	-0.2724	0.0489	-0.0044	1.5581	1.0261	0.163	5.649	-0.2

Table 9.9. (contd)

Period (sec)	Backbone Adjustment Model	p_1	p_2	p_3	p_4	p_5	p_6	p_7	p_8
0.75	9	-0.2724	-0.3725	-0.0044	1.5581	1.0261	0.163	5.649	-0.2
1	1	0.3129	-0.102	0.0063	3.2435	1.0373	0.237	5	-0.2
1	2	-0.3729	-0.138	-0.0063	0.9883	1.0118	0.1635	5	-0.2
1	3	-0.03	0.1795	0	2.5543	1.0255	0.2019	5	-0.2
1	4	-0.03	-0.4195	0	2.5543	1.0255	0.2019	5	-0.2
1	5	-0.03	-0.12	0	2.5543	1.0255	0.2019	5	-0.2
1	6	0.2124	0.1045	0.0044	3.1145	1.0337	0.2264	5	-0.2
1	7	0.2124	-0.319	0.0044	3.1145	1.0337	0.2264	5	-0.2
1	8	-0.2724	0.079	-0.0044	1.6933	1.016	0.1725	5	-0.2
1	9	-0.2724	-0.3445	-0.0044	1.6933	1.016	0.1725	5	-0.2
1.5	1	0.3198	-0.0963	0.0066	2.0942	1.0359	0.2429	3.333	-0.2
1.5	2	-0.3798	-0.0837	-0.0066	0.8717	0.9837	-0.1692	3.333	-0.2
1.5	3	-0.03	0.2099	0	2.9735	1.0057	0.1753	3.333	-0.2
1.5	4	-0.03	-0.3899	0	1.9605	1.019	0.2002	3.333	-0.2
1.5	5	-0.03	-0.09	0	2.3908	1.0117	0.1884	3.333	-0.2
1.5	6	0.2173	0.1176	0.0046	2.4035	1.023	0.2205	3.333	-0.2
1.5	7	0.2173	-0.3065	0.0046	1.9551	1.0345	0.2349	3.333	-0.2
1.5	8	-0.2773	0.1265	-0.0046	2.3265	0.993	0.1511	3.333	-0.2
1.5	9	-0.2773	-0.2976	-0.0046	1.856	1.0004	0.1618	3.333	-0.2
2	1	0.3249	-0.0917	0.0067	1.4618	1.0367	0.2437	2.5	-0.2
2	2	-0.3849	-0.0443	-0.0067	0.0624	0.9404	0.2044	2.5	-0.2
2	3	-0.03	0.2311	0	2.5456	0.9936	0.1711	2.5	-0.2
2	4	-0.03	-0.3671	0	1.5059	1.0135	0.1997	2.5	-0.2
2	5	-0.03	-0.068	0	1.9675	1.002	0.1854	2.5	-0.2
2	6	0.221	0.1267	0.0048	1.8138	1.0163	0.2188	2.5	-0.2
2	7	0.221	-0.2962	0.0048	1.3665	1.036	0.2359	2.5	-0.2
2	8	-0.281	0.1602	-0.0048	0.7622	0.961	0.1901	2.5	-0.2
2	9	-0.281	-0.2627	-0.0048	1.6518	0.9874	0.1604	2.5	-0.2
3	1	0.3325	-0.0818	0.007	0.7542	1.043	0.2401	1.667	-0.2
3	2	-0.3925	0.0058	-0.007	-0.121	0.8859	0.203	1.667	-0.2
3	3	-0.03	0.2325	0	1.2662	0.9781	0.1832	1.667	-0.2
3	4	-0.03	-0.3085	0	0.9969	0.9951	0.1932	1.667	-0.2
3	5	-0.03	-0.038	0	1.1395	0.9861	0.1877	1.667	-0.2
3	6	0.2264	0.1223	0.0049	0.9045	1.0162	0.2224	1.667	-0.2
3	7	0.2264	-0.2603	0.0049	0.7699	1.033	0.2291	1.667	-0.2
3	8	-0.2864	0.1843	-0.0049	0.1401	0.9134	0.2036	1.667	-0.2
3	9	-0.2864	-0.1983	-0.0049	0.5019	0.9447	0.1849	1.667	-0.2
5	1	0.6746	-0.0639	0.0059	0.0051	0.9633	0.2269	1	-0.2
5	2	-0.2746	0.0639	-0.0059	-0.0162	0.9326	0.1703	1	-0.2
5	3	0.2	0.2355	0	0.0001	0.9386	0.2	1	-0.2
5	4	0.2	-0.2355	0	0.0001	0.9578	0.2	1	-0.2

Table 9.9. (contd)

Period (sec)	Backbone Adjustment Model	p_1	p_2	p_3	p_4	p_5	p_6	p_7	p_8
5	5	0.2	0	0	0.0002	0.9482	0.2	1	-0.2
5	6	0.5356	0.1213	0.0041	0.0044	0.952	0.2192	1	-0.2
5	7	0.5356	-0.2117	0.0041	0.0036	0.9657	0.2193	1	-0.2
5	8	-0.1356	0.2117	-0.0041	-0.0108	0.9305	0.1794	1	-0.2
5	9	-0.1356	-0.1213	-0.0041	-0.0045	0.9442	0.1791	1	-0.2
7.5	1	0.9908	-0.0748	0.0048	0.0041	0.9686	0.2213	1	-0.2
7.5	2	-0.2608	0.0748	-0.0048	-0.0093	0.9447	0.1769	1	-0.2
7.5	3	0.365	0.2048	0	0	0.9527	0.2	1	-0.2
7.5	4	0.365	-0.2048	0	0.0002	0.9608	0.2	1	-0.2
7.5	5	0.365	0	0	0.0004	0.9567	0.2	1	-0.2
7.5	6	0.8075	0.0919	0.0034	0.0022	0.9622	0.2153	1	-0.2
7.5	7	0.8075	-0.1977	0.0034	0.003	0.968	0.2153	1	-0.2
7.5	8	-0.0775	0.1977	-0.0034	-0.0038	0.9455	0.1838	1	-0.2
7.5	9	-0.0775	-0.0919	-0.0034	-0.0038	0.9512	0.1838	1	-0.2
10	1	1.1967	-0.08	0.0043	0.0035	0.9727	0.2188	1	-0.2
10	2	-0.2487	0.08	-0.0043	-0.0049	0.9536	0.1797	1	-0.2
10	3	0.474	0.1833	0	-0.0003	0.9632	0.2	1	-0.2
10	4	0.474	-0.1833	0	-0.0003	0.9632	0.2	1	-0.2
10	5	0.474	0	0	-0.0003	0.9632	0.2	1	-0.2
10	6	0.985	0.073	0.003	0.0025	0.9699	0.2134	1	-0.2
10	7	0.985	-0.1862	0.003	0.0025	0.9699	0.2134	1	-0.2
10	8	-0.037	0.1862	-0.003	-0.0031	0.9564	0.1858	1	-0.2
10	9	-0.037	-0.073	-0.003	-0.0031	0.9564	0.1858	1	-0.2

The hanging-wall formulation given in ASK14 includes an additional variable, R_Y, that results in attenuation of the hanging-wall effect with increasing R_{JB} distance off of the top of the rupture in the strike parallel direction. The HW formulation of CY14 shown in Equation (9.1) includes the multiplicative distance attenuation term $\left\{1-\frac{\sqrt{R_{JB}^2+Z_{TOR}^2}}{R_{RUP}+1}\right\}$. This term produces attenuation of the HW effect as R_{JB} increases in both the R_X (strike normal) and R_Y (strike parallel) directions. The attenuation is more rapid near the top of the rupture (small R_X), where R_{JB} and R_{RUP} are more similar, than near the bottom of the rupture. The attenuation behavior captures the trends of the ASK14 and CB14 formulations that also have more rapid attenuation of the HW effect in the R_Y direction at small R_X compared to at large R_X.

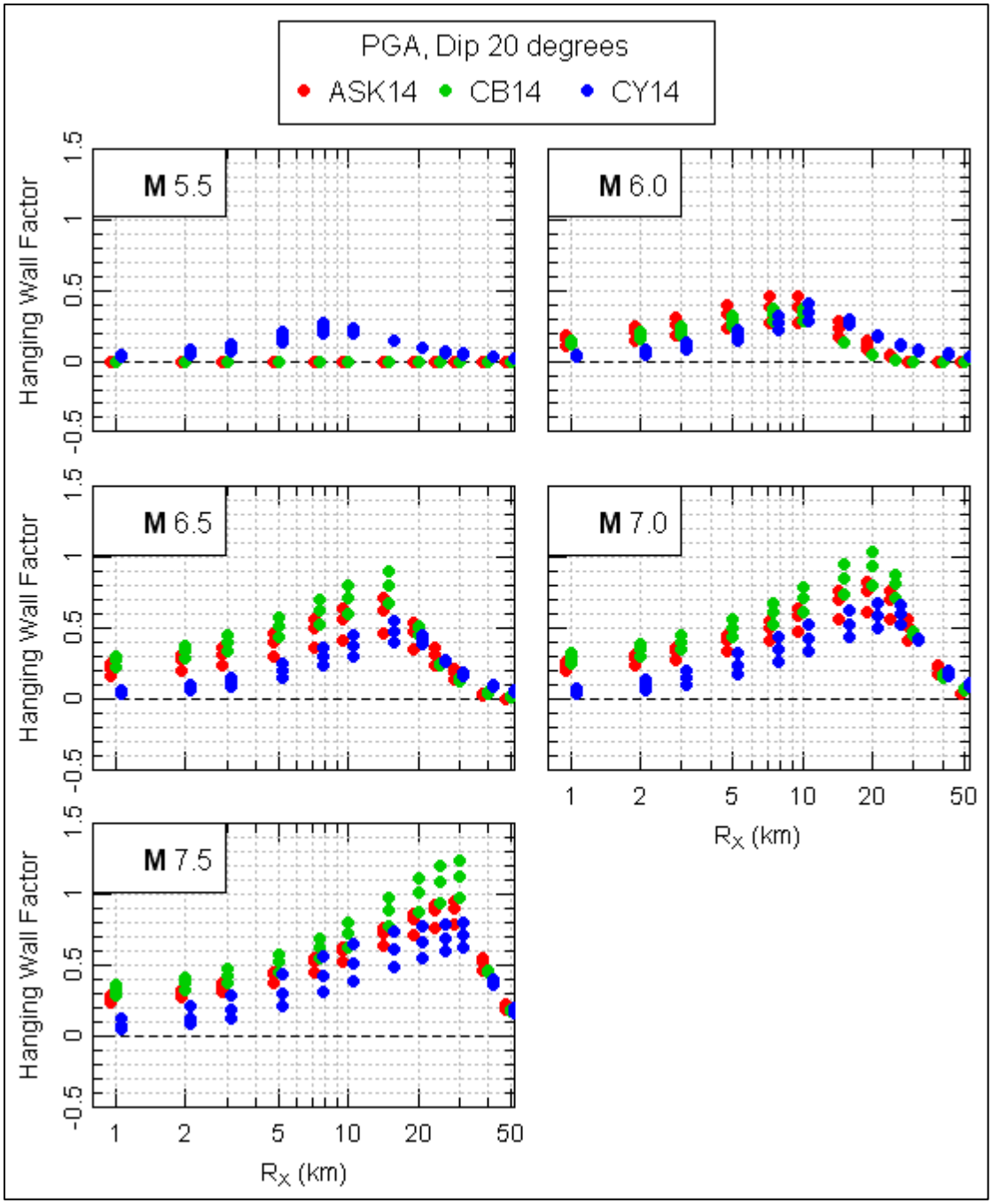

Figure 9.64. Hanging-wall scaling factor for PGA from ASK14, CB14, and CY14 (1 of 4).

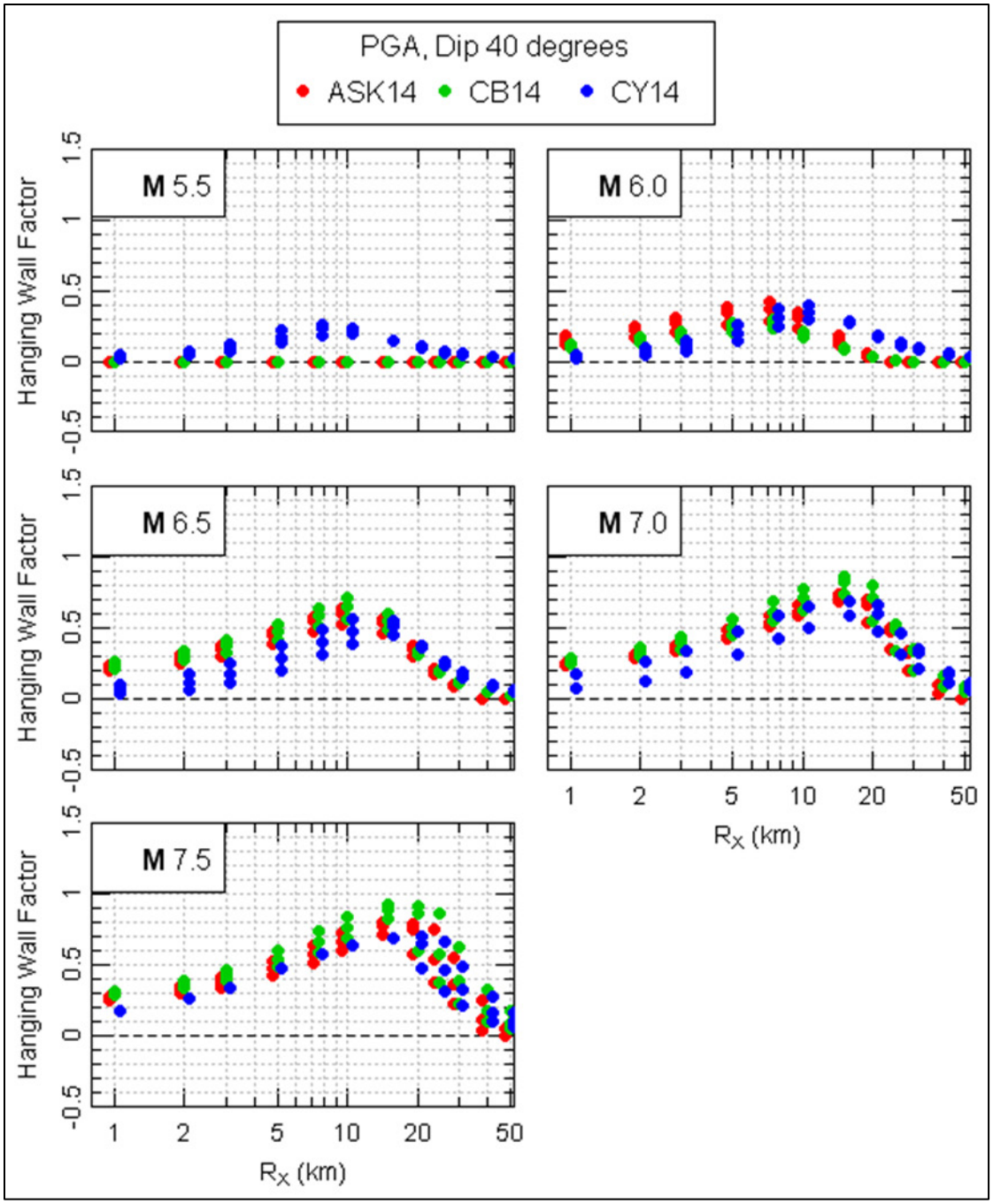

Figure 9.64. (contd; 2 of 4)

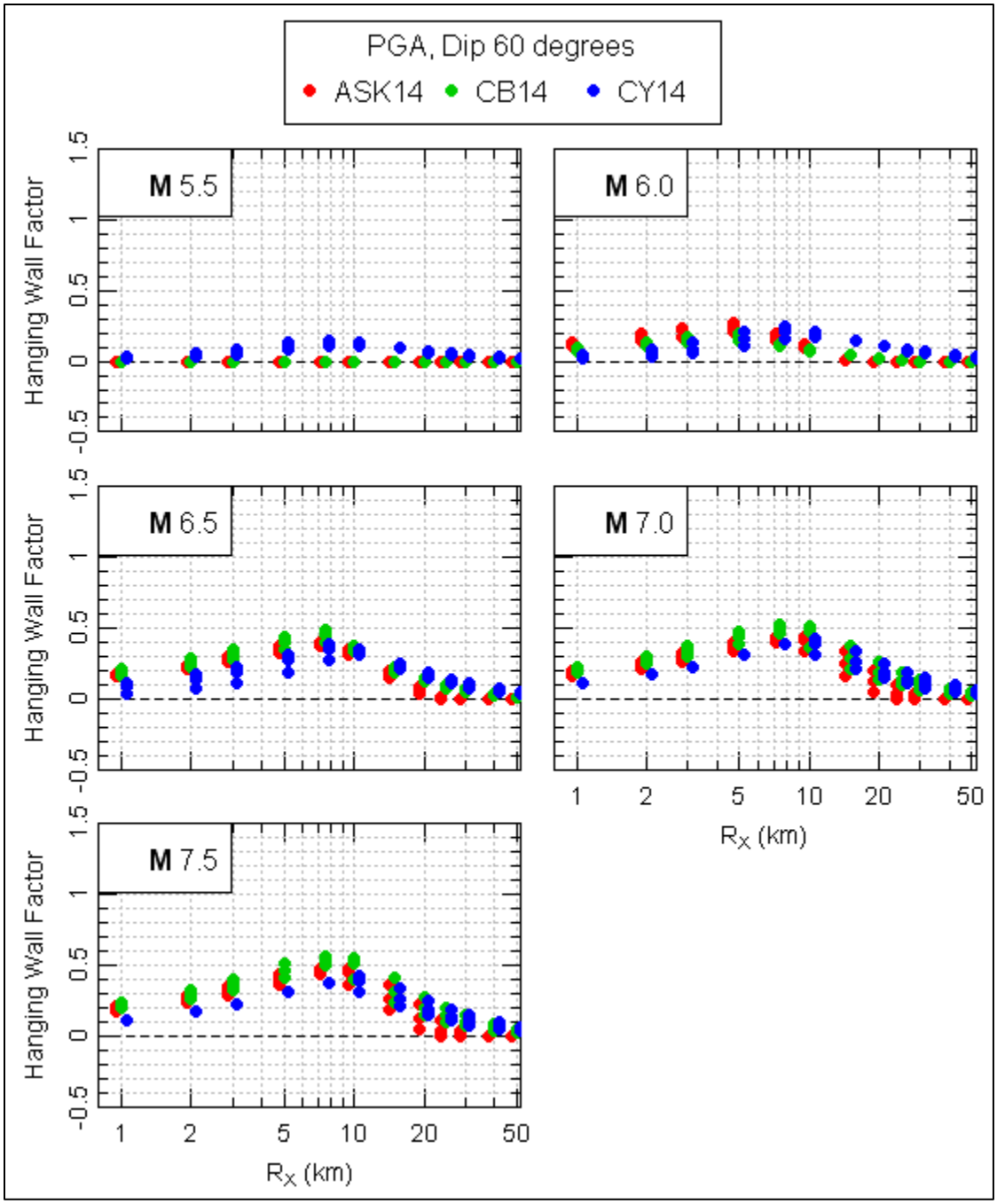

Figure 9.64. (contd; 3 of 4).

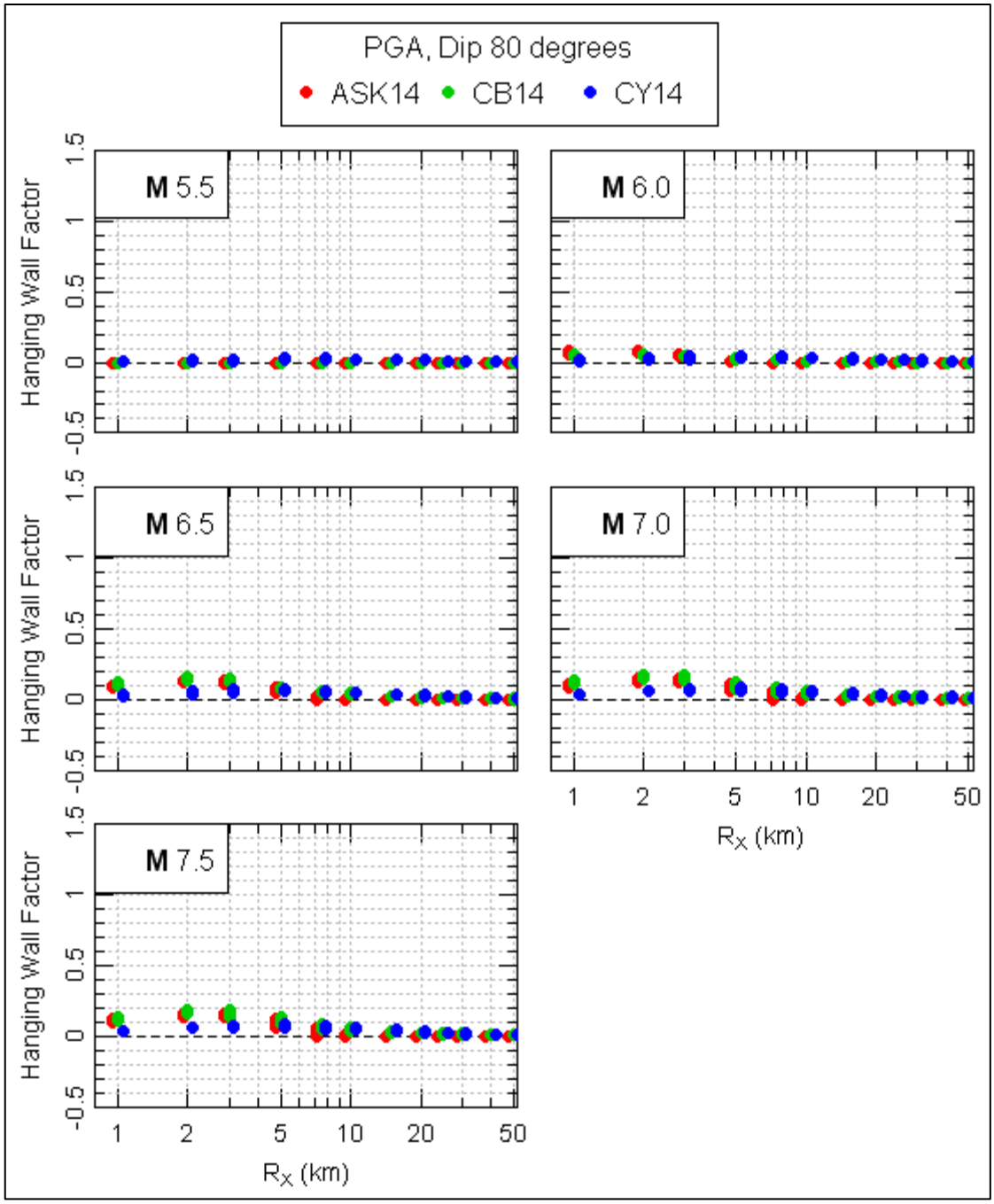

Figure 9.64. (contd; 4 of 4).

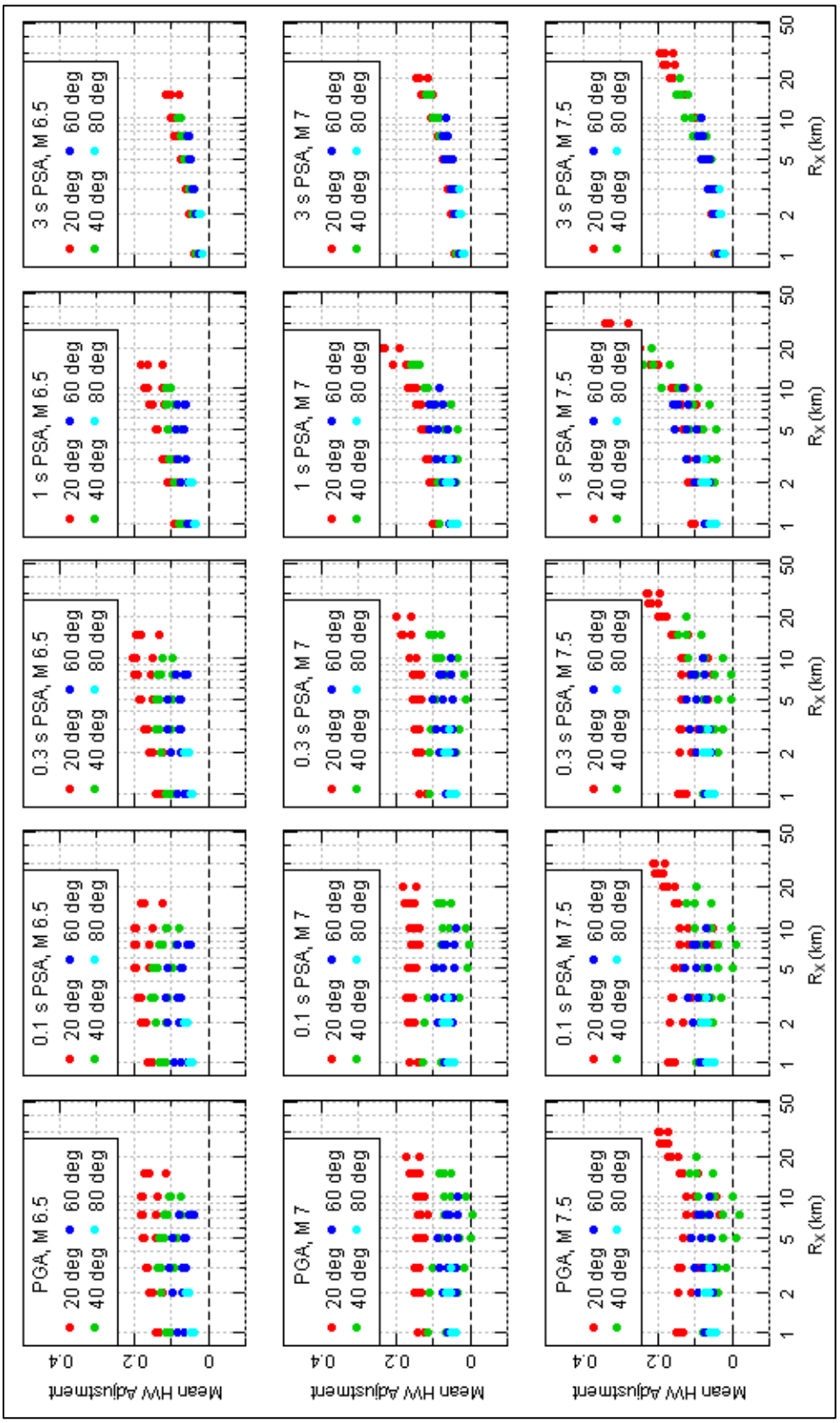

Figure 9.65. Mean hanging-wall adjustment.

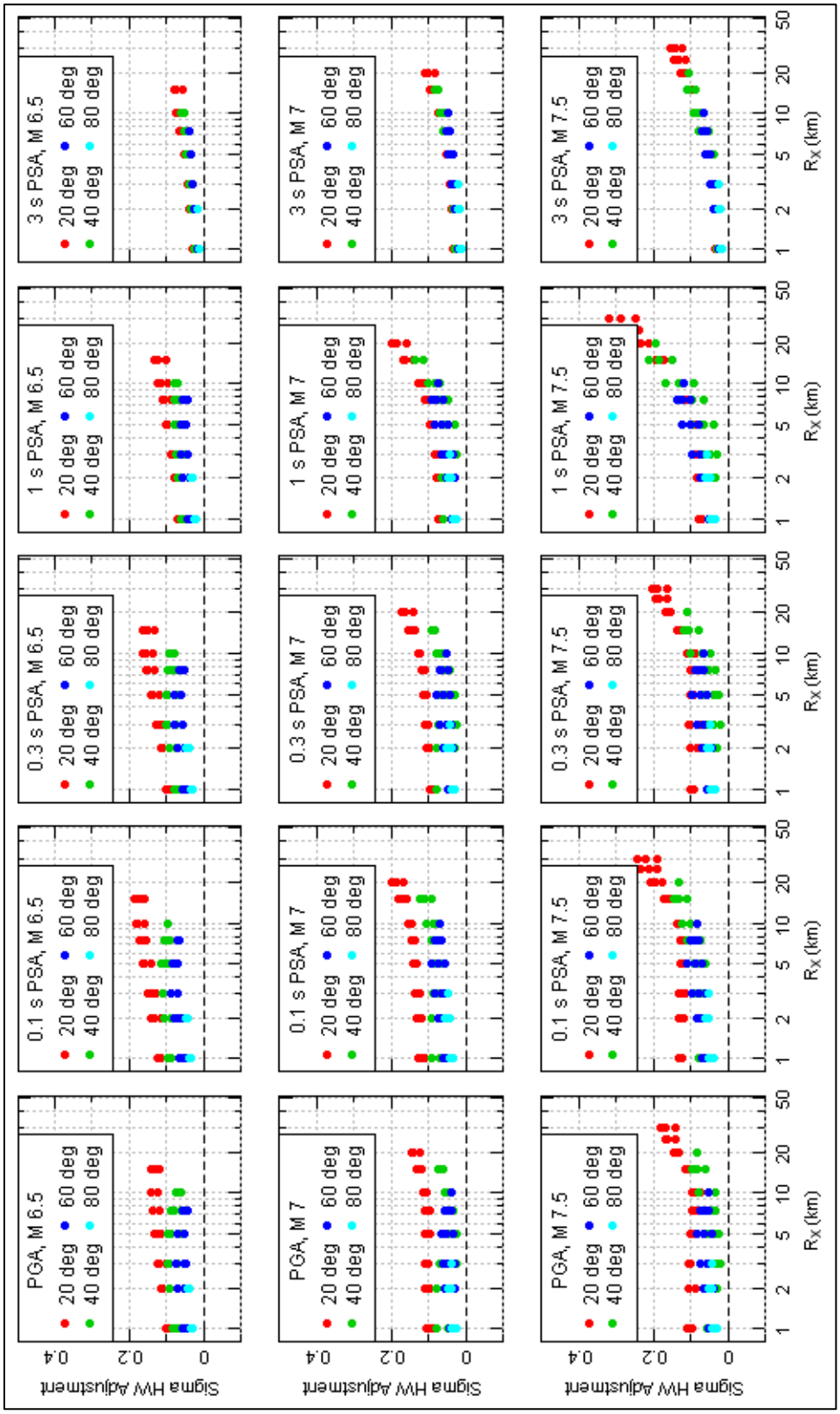

Figure 9.66. Standard deviation of the hanging-wall adjustment.

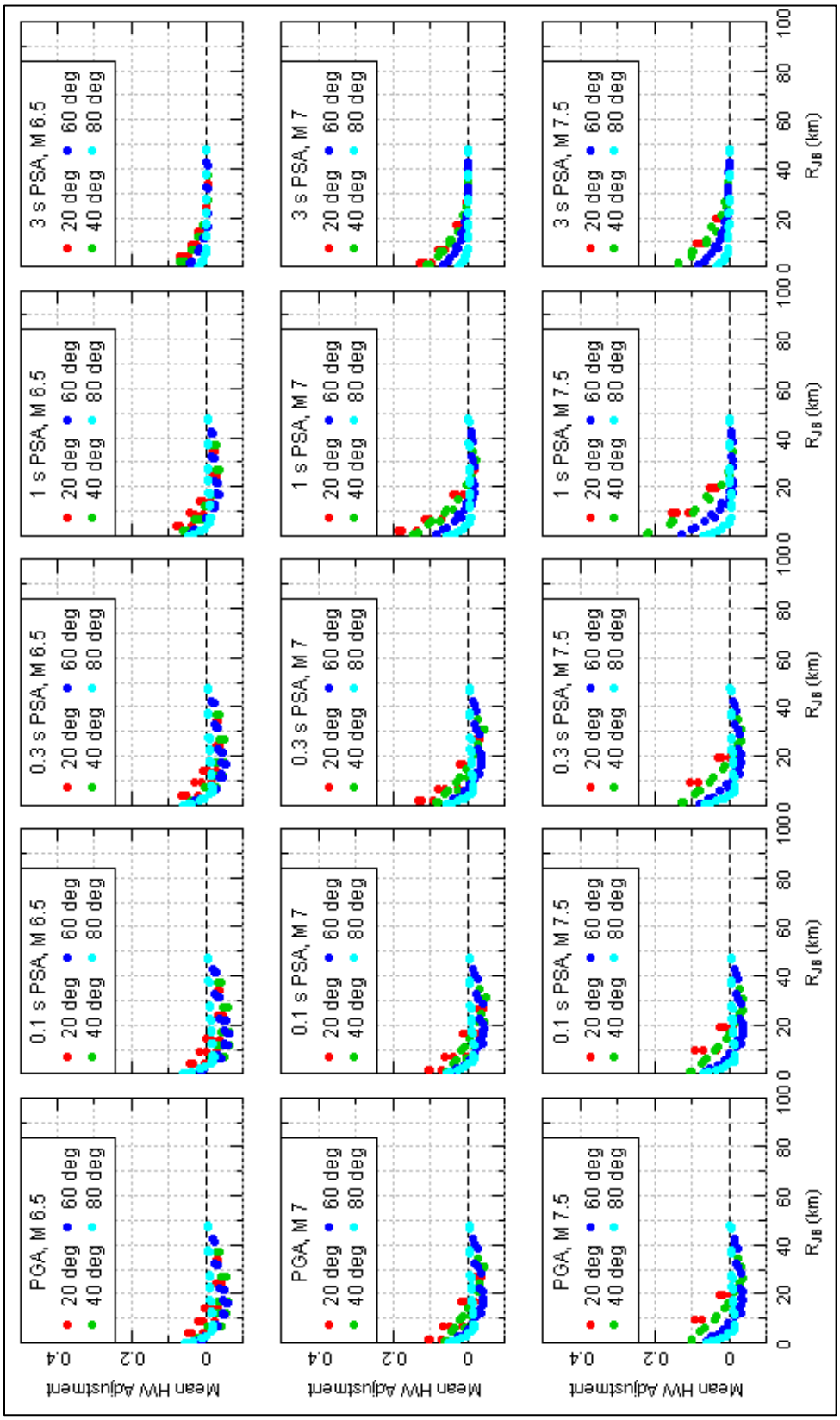

Figure 9.67. Mean hanging-wall adjustment for sites with R_{JB} greater than zero.

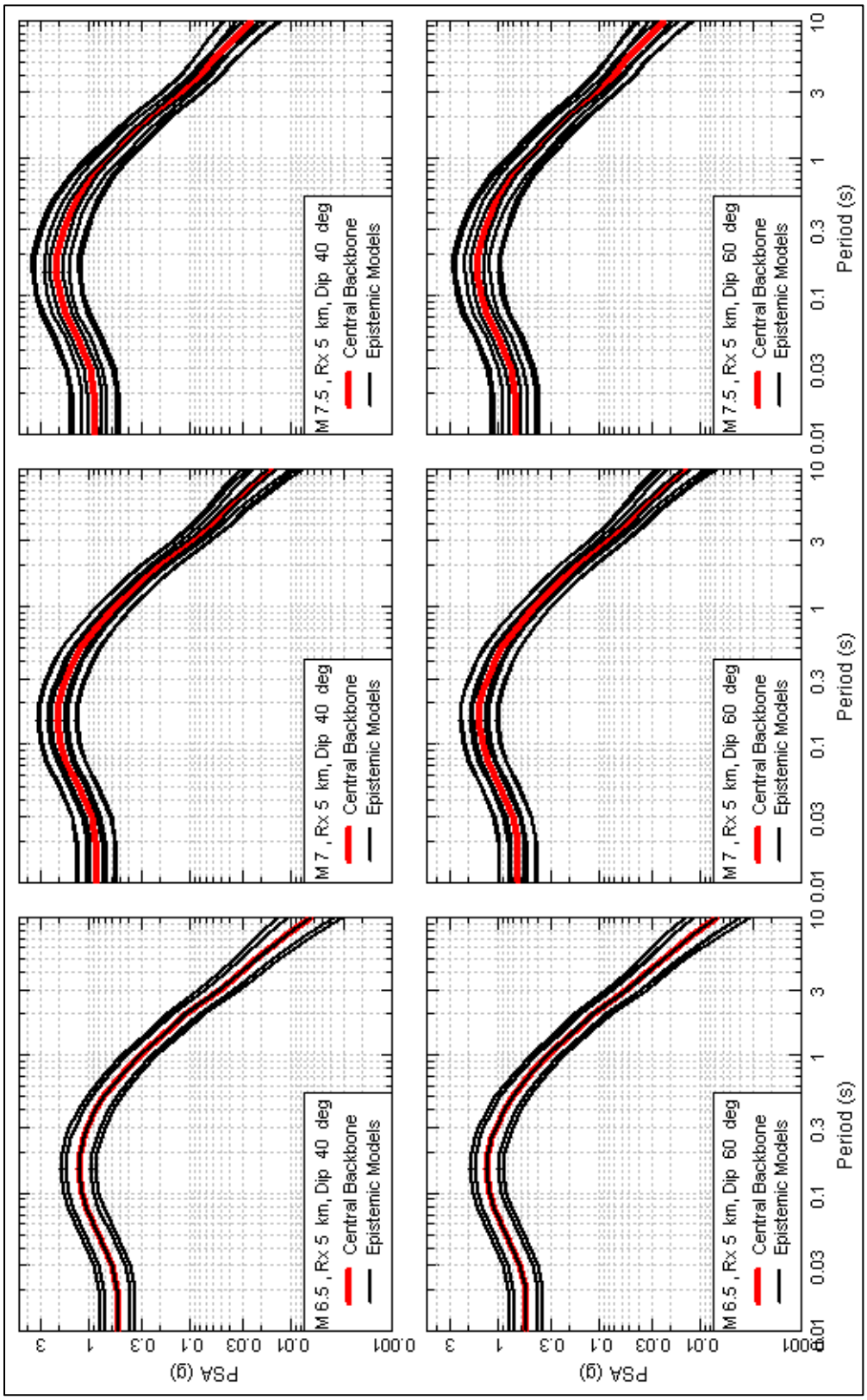

Figure 9.68. Response spectra computed using crustal hanging-wall GMPEs.

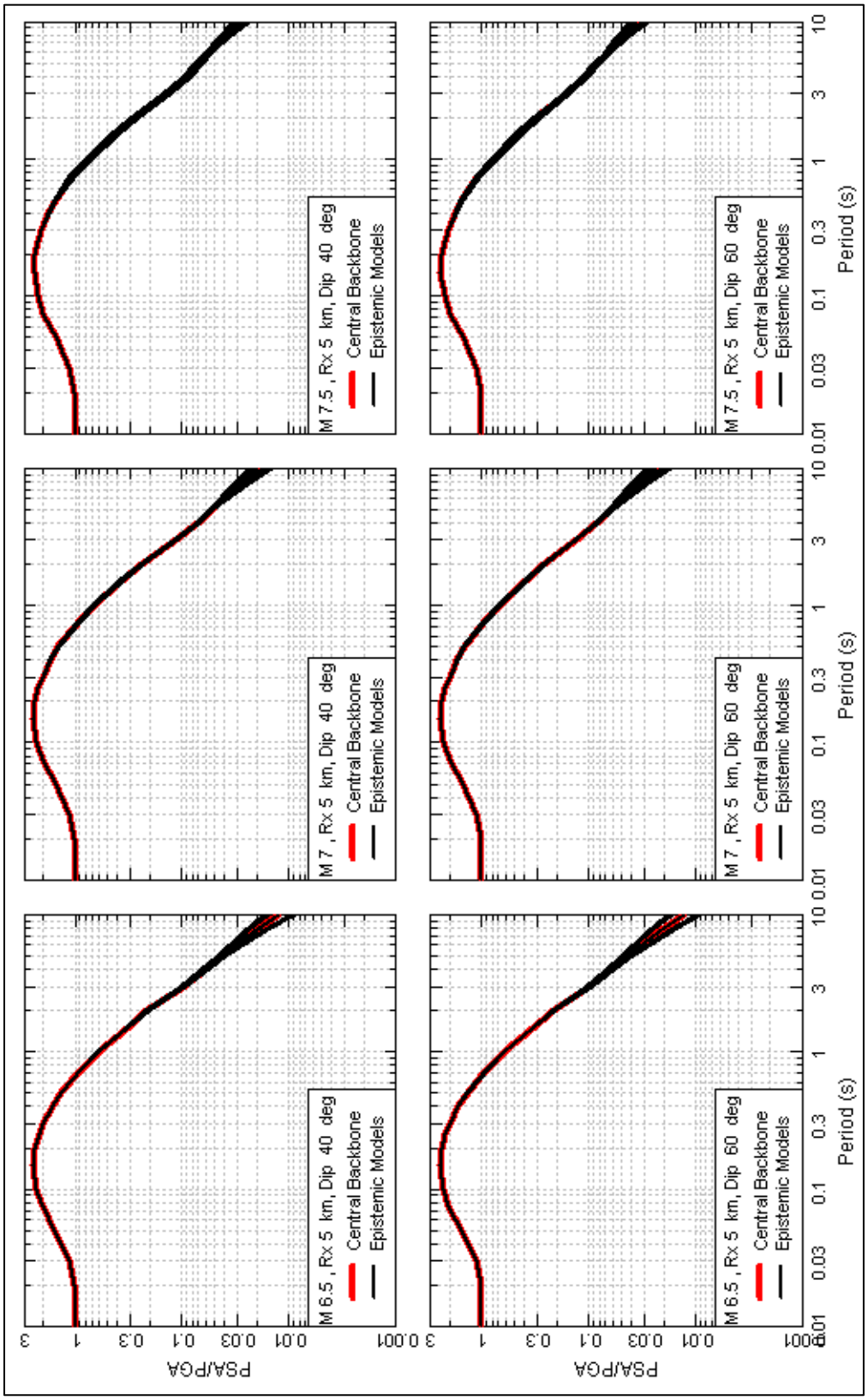

Figure 9.69. Response spectral shapes computed using crustal hanging-wall GMPEs.

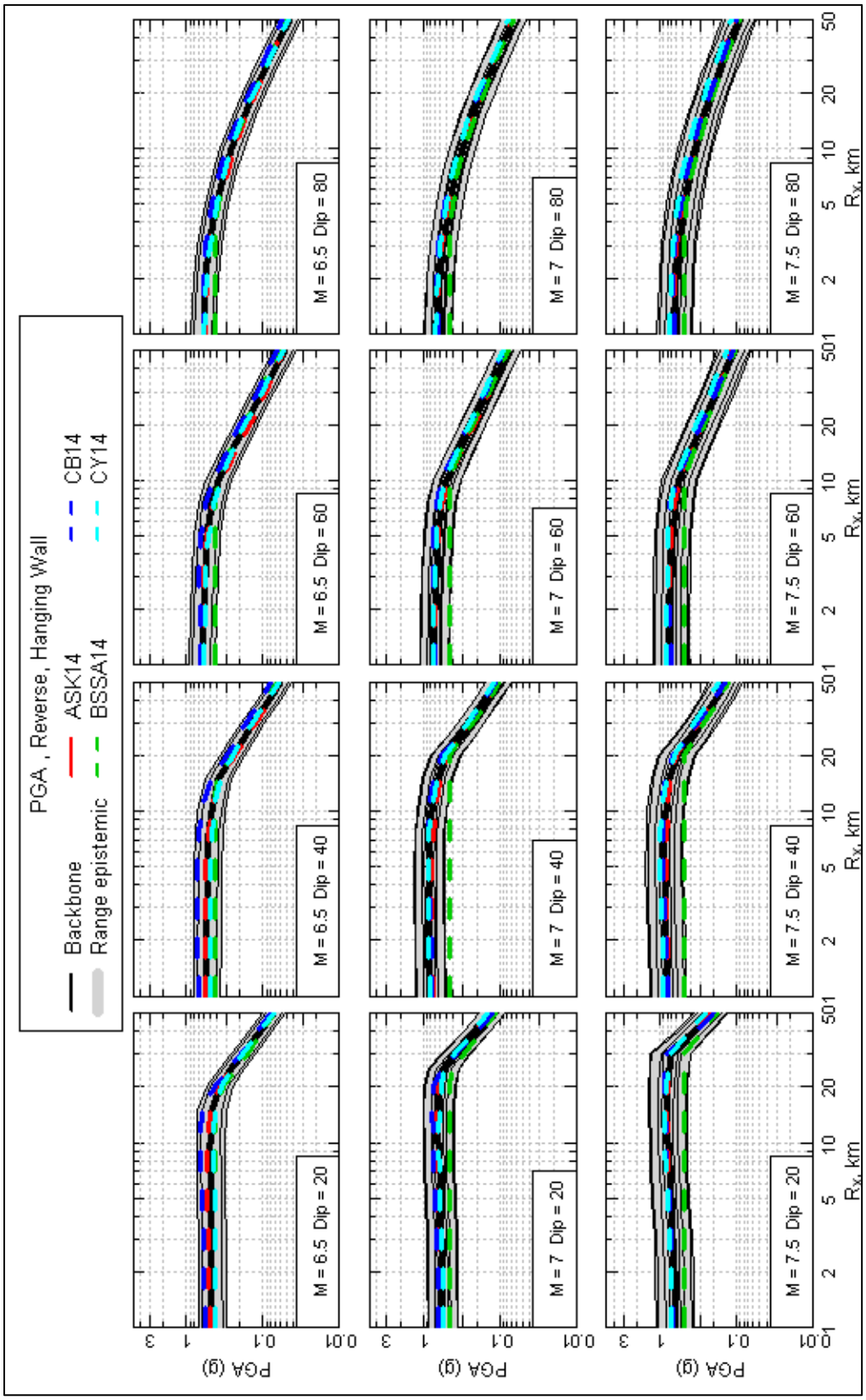

Figure 9.70. Distance scaling of the crustal hanging-wall GMPEs (1 of 4).

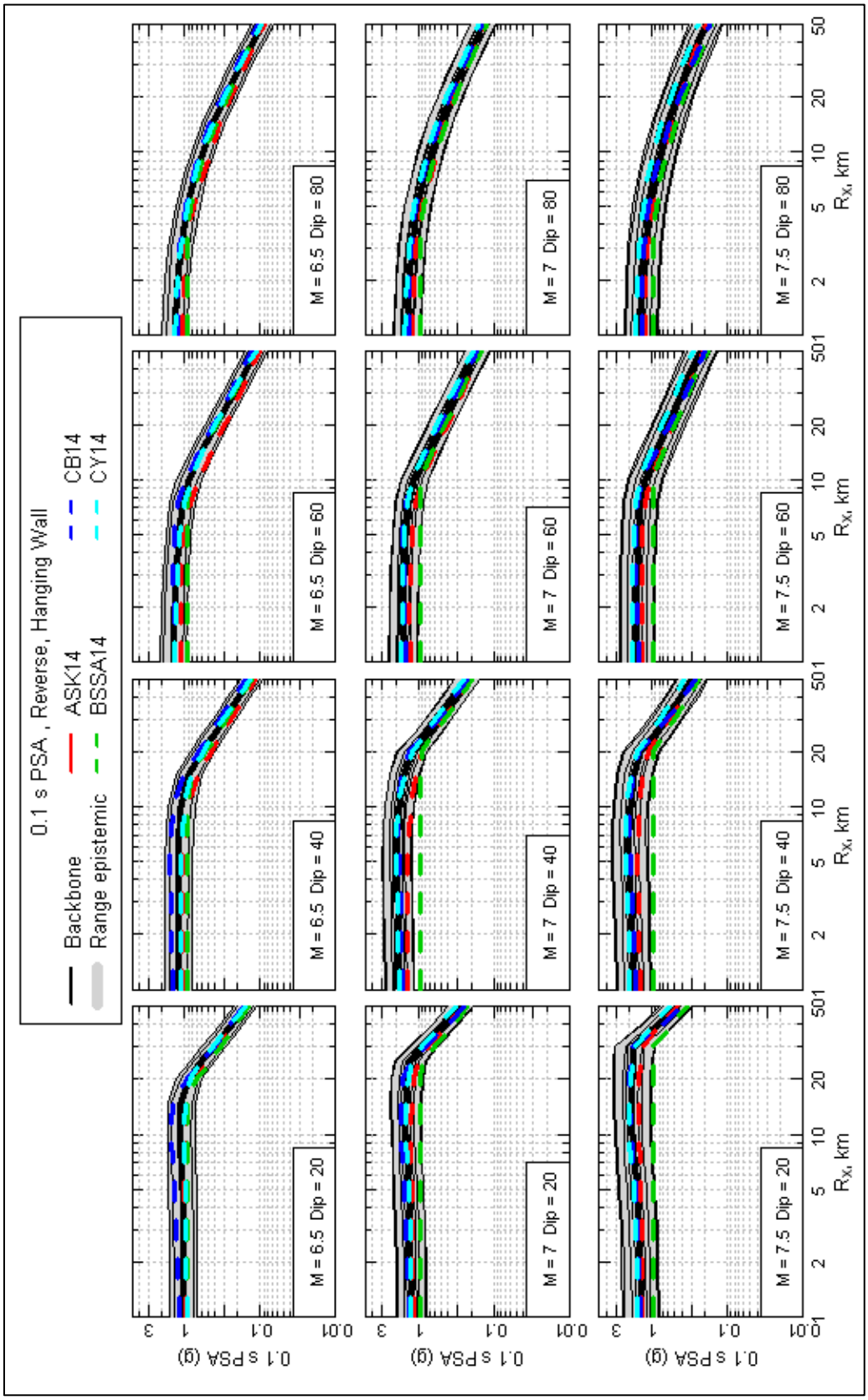

Figure 9.70. (contd; 2 of 4).

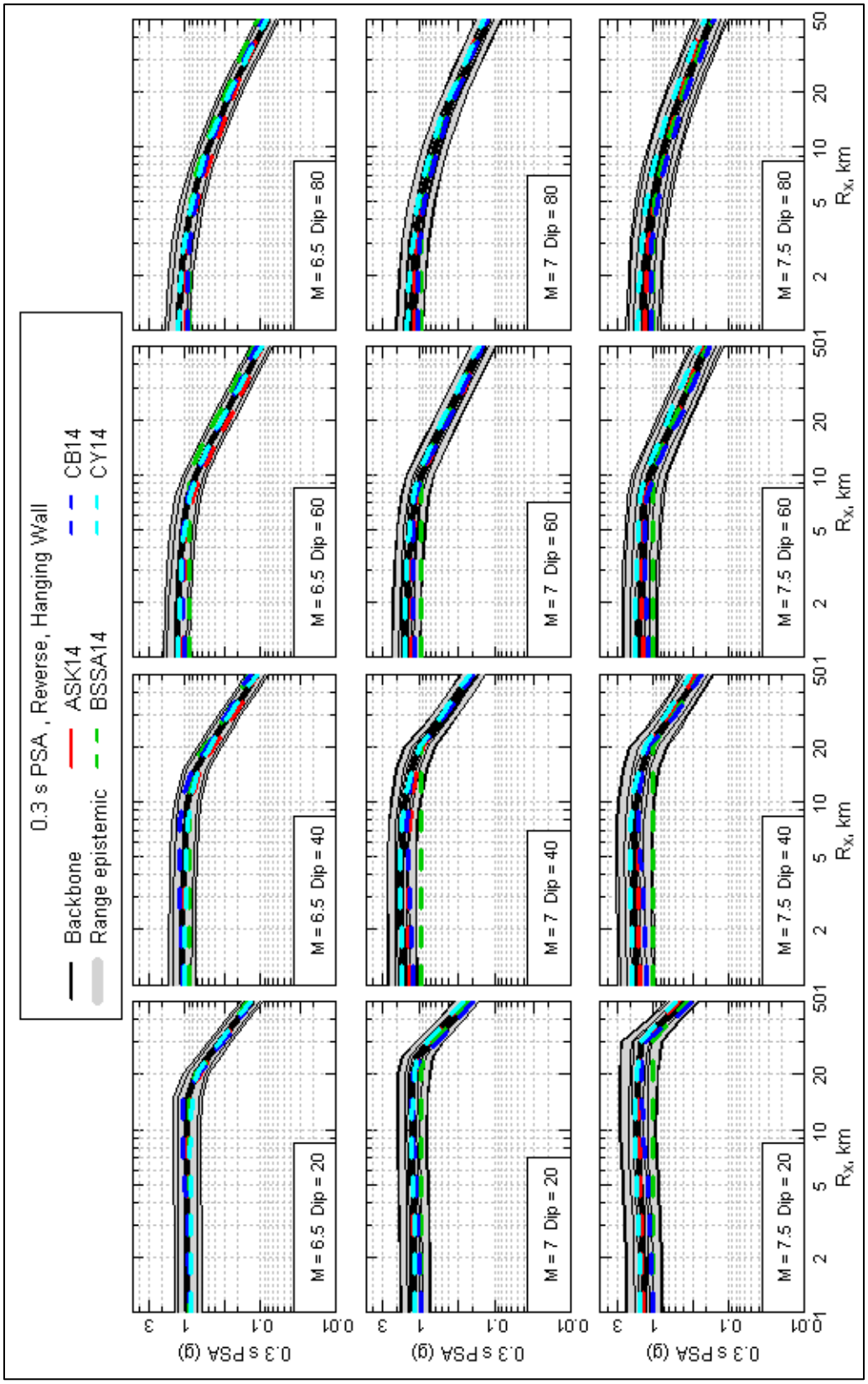

Figure 9.70. (contd; 3 of 4)

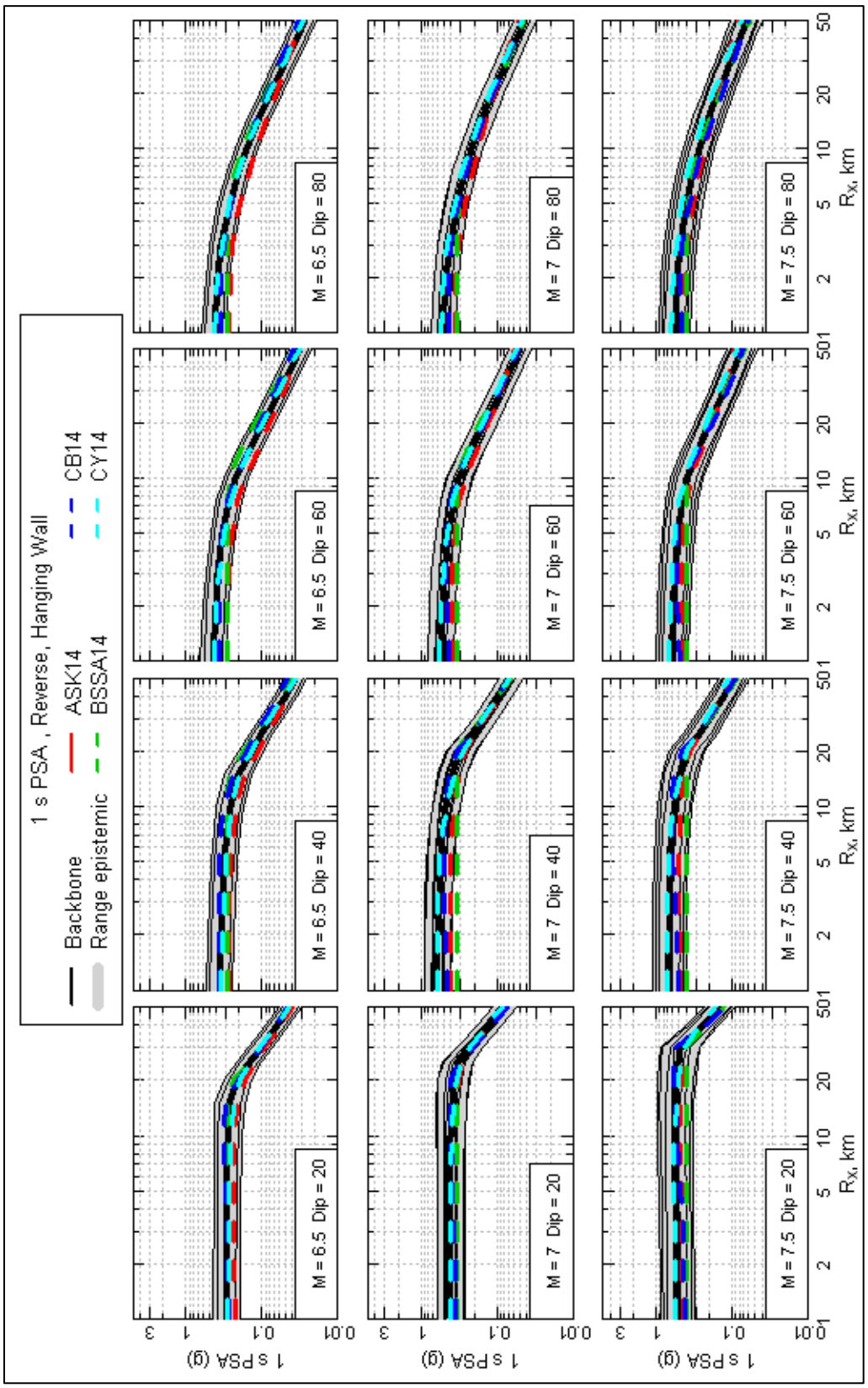

Figure 9.70. (contd; 4 of 4)

9.4.2.3 Comparison with Ground Motion Data

The approach used to develop the crustal backbone GMPEs is based on the assessment that the selected NGA-West2 GMPEs provide the best sample of ground motion estimates to define the center, body, and range of median ground motions because they combine analyses of a large empirical database with evaluations of numerical simulations and the extensive experience of the developers in evaluations of shallow crustal earthquake ground motions. The crustal GMPEs developed for this project were compared to recorded ground motion data contained in the NGA-West2 database. The data selected for comparison were records from magnitude **M** 5.5 and greater earthquakes at distances from 0 to 50 km on sites with V_{S30} of 400 m/s and higher. Figure 9.71 shows the magnitude-distance distribution of the selected data. The selected data consist of approximately 320 recordings from 18 earthquakes. At periods longer than 2 sec, the available data decrease with increasing period, becoming 194 recordings from 11 earthquakes for a period of 10 sec.

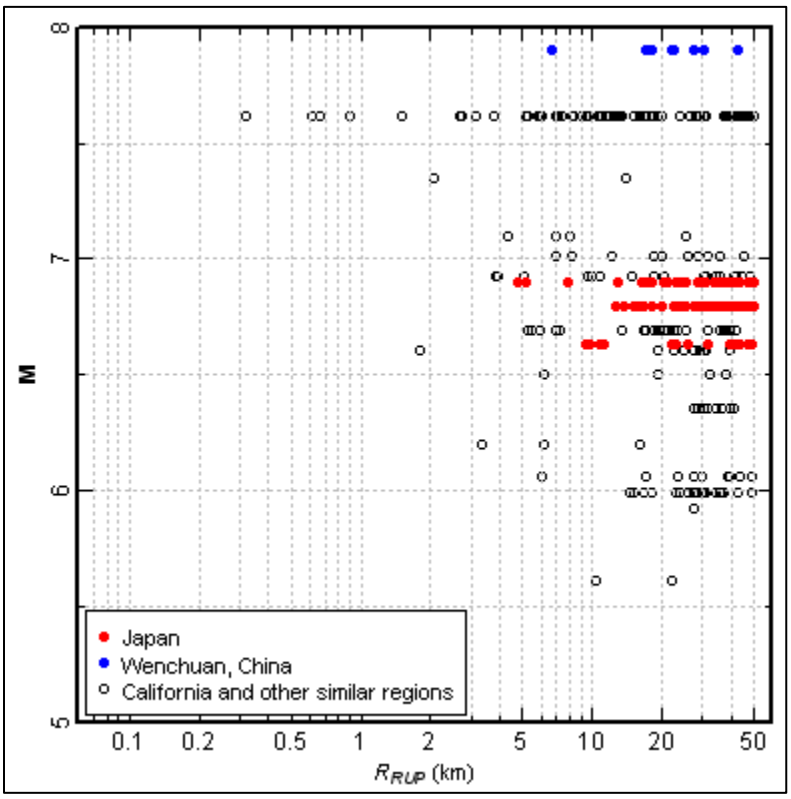

Figure 9.71. Magnitude-distance distribution of recordings of ground motion from reverse-faulting earthquakes used for comparison with developed crustal GMPEs.

The ground motion recordings were adjusted to a site V_{S30} of 760 m/sec using the site response model contained within the CY14 GMPE. Ground motion residuals were then computed with each of the nine crustal GMPEs created using the adjustments to CY14 from Equation (9.20) and Table 9.9. These residuals were fit with a mixed-effects model to compute the mean residual. The mean residuals and their 95% confidence intervals are plotted in Figure 9.72. The central crustal model (Model 5) has a mean positive residual of approximately 0.1, with a 95% confidence interval that encompasses 0 for most periods. The mean residual across all nine backbone models and all periods up to 2 sec is also approximately 0.1. The value of the event to event variability, τ, developed for crustal earthquakes in

Section 9.5 is approximately 0.4. For a set of 18 earthquakes, the variability in the mean residual would be $\pm 0.4/18^{-1/2}$, or ± 0.09. These results indicate that the overall crustal GMPE model, which is centered with respect to the ground motion predictions of the selected NGA-West 2 GMPEs, is also reasonably centered with respect to the available recorded data, at least for periods up to 2 sec. At periods of 3 sec and longer the mean residual increases to 0.3 to 0.4. The longer period empirical data are generally more variable and the amount of data is decreasing. In addition, the crustal models are consistent with the underlying NGA-West2 GMPEs. Therefore, the larger mean errors at longer periods are not considered important.

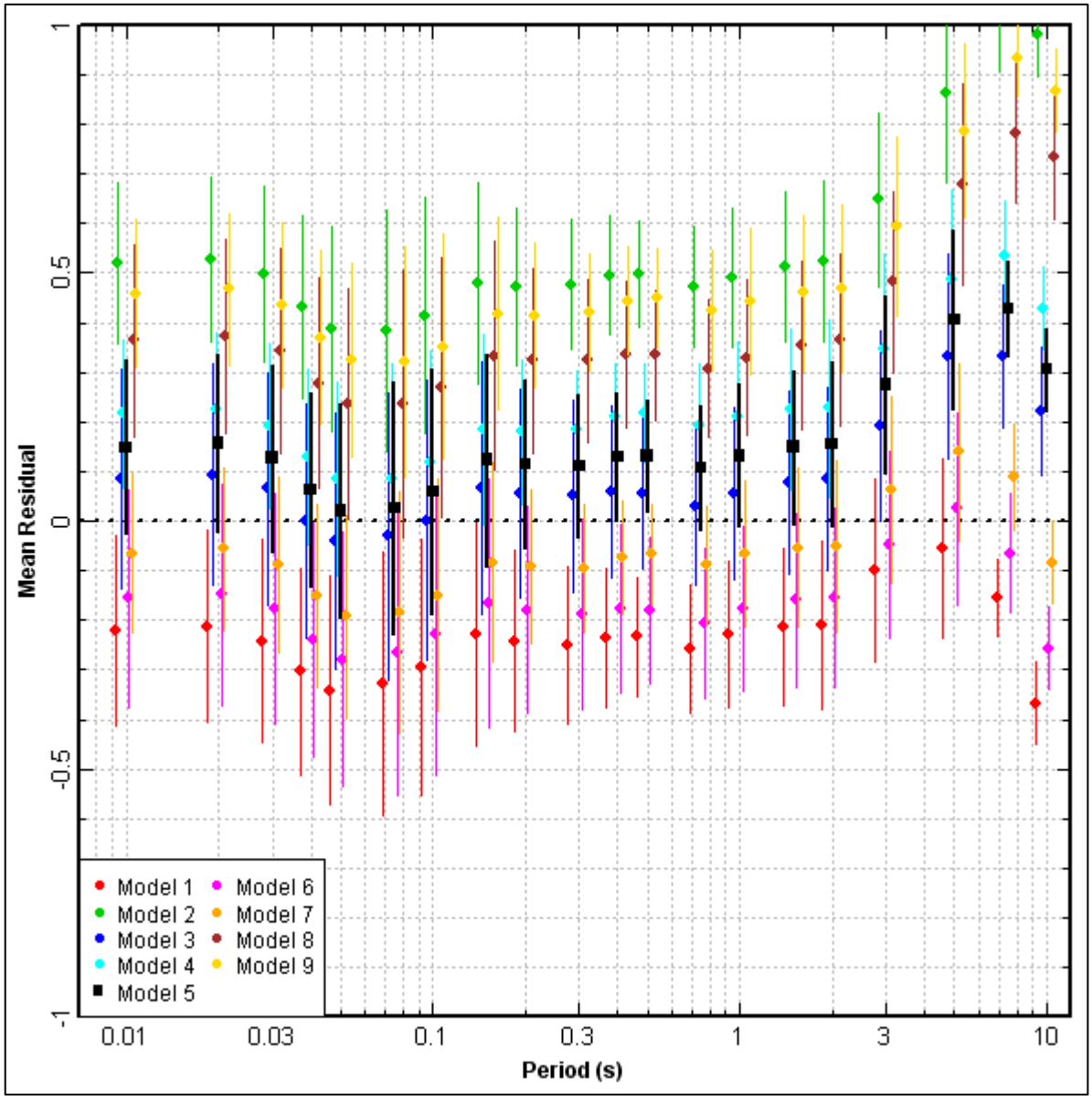

Figure 9.72. Mean residuals of fits to reverse-faulting data for each of the nine crustal GMPEs. Vertical bars denote 95% confidence intervals on the mean residual.

9.4.2.4 Additional Epistemic Uncertainty and Comparisons with Models from Other Regions

The crustal model presented in Sections 9.4.2.1 and 9.4.2.2 is intended to represent the epistemic uncertainty in ground motion predictions for reverse-faulting earthquakes in active tectonic regions, such as those that supplied the data used to develop the NGA-West2 GMPEs. The Hanford Site is located in a region (eastern Washington State) that might be considered active tectonically or at the margin of active tectonics. Analyses performed by BC Hydro (2012) concluded that the 2008 NGA GMPEs were consistent with the available data from western Washington State and southwestern British Columbia, but no data from eastern Washington were available for that comparison. The available ground motion data from the Hanford Site are described in Section 7.1.2. The available data from crustal earthquakes are for magnitudes generally too small to make meaningful comparisons with the crustal GMPEs developed for the project. Therefore, there is some epistemic uncertainty in using the crustal model developed above from data recorded primarily in California and other active regions to the Hanford Site region. This uncertainty may represent factors such that the model may not be centered on the median stress parameter for crustal earthquakes in the Hanford region.

The epistemic uncertainty in applying the active tectonic region crustal GMPEs to the Hanford region was addressed in two parts. First, three of the four NGA-West2 GMPEs used to develop the crustal models contain terms for increasing ground motions as the depth of the earthquake increases. It is assumed that this increase may be related to effects such as increasing stress drop with depth or increasing crustal rigidity with depth. The Hanford hazard calculation sites are underlain by the CRBs such that crustal velocities reach high values (V_S ~ 3 km/s) at much shallower depths than is typical in active tectonic regions. The effect of difference in shear-wave velocity profiles on site amplification is accounted for by the V_S-κ corrections described in Section 9.3, but this does not account for potential differences in source properties. To account for the higher-velocity crustal rocks at shallow depths at Hanford compared to other active regions, the parameter Z_{TOR} was limited to a minimum of 3 km when calculating the effect of depth on ground motions in the CY14 model. This was applied only to the term containing the coefficients c_7 and c_{7b}. The minimum value of 3 km was chosen as a typical depth where the crustal shear-wave velocity in active tectonic regions reaches the value of ~3 km/s found at shallow depth in the CRBs. The effect of this adjustment is to increase the median ground motions of large-magnitude earthquakes that rupture to the surface by about 10 percent and the ground motions for **M** 5 earthquakes that rupture to the surface by about 25 percent.

Second, epistemic host-to-target uncertainty factors were applied to the crustal GMPEs. The factors essentially represent the potential differences between median ground motions in the host region (coastal California) and the target region (eastern Washington), which is interpreted as being mainly due to differences in median stress drop values between the two regions. On the basis of work carried out for the SSHAC Level 3 PSHA of the Thyspunt site in South Africa (Bommer et al. 2014), it was noted that for a given change in stress drop, the ratios of response spectral ordinates are fairly stable for a wide range of combinations of magnitude and response period. The one exception to this is found for small magnitudes and longer response periods, but because small earthquakes generally do not contribute appreciably to the hazard at long oscillator periods, it was assumed that constant scaling factors could be applied across the full response spectrum. Three branches were constructed to capture this range of uncertainty in the form of different scaling factors, the central branch carrying a neutral factor of unity. The lower and upper branches could be interpreted as representing median stress drops in the target region of slightly less than a half and a little less than twice the host value, respectively, if the latter is assumed to be 100 bars. The

three factors are 1.0 [wt 0.6], 1.3 [wt 0.3], and 0.8 [wt 0.1]. The highest weight is given to a scale factor of 1.0—no difference from active tectonic regions—because the analysis of ground motion data for the adjacent western Washington and southwestern British Columbia regions found no significant difference from California data (BC Hydro 2012) and because the NGA-West2 developers did not identify significant regional differences in source effects among the active tectonic regions contributing data. Preference is given to an increase (factor of 1.3) over a decrease (factor of 0.8) because it is considered more likely that if different, the average stress parameter would be higher rather than lower as the site region is approaching more stable continental regions.

The effect of including the host-to-target uncertainty factors is to broaden the epistemic uncertainty in the crustal GMPEs. This effect is illustrated in Figure 9.73, where the light gray band is the range of the models from Figure 9.63, and the dark gray bands show the extension of that range due to the inclusion of the host-to-target uncertainty factors. Also shown in Figure 9.73 are additional GMPEs that define ground motions for reverse-faulting earthquakes, but were not considered good candidate GMPEs for the reasons given in Section 9.2. The Akkar et al. (2014a,b) and Bindi et al. (2014a,b) GMPEs are based on European data and contain a limited amount of recordings from reverse-faulting earthquakes. The Idriss (2014) model is a NGA-West2 GMPE that does not address HW effects. The Zhao and Lu (2011) model is based on their proposed modification to the magnitude scaling of Zhao et al. (2006). Zhao and Lu (2011) find that magnitude scaling for crustal earthquakes becomes very weak, and in some cases transitioning to an actual decrease of amplitude with increasing earthquake magnitude, at magnitudes above about **M** 7. They do not provide an actual model in their paper. However, examination of their results suggests that the Zhao and Lu (2011) concept can be modeled by capping the ground motion predictions from Zhao et al. (2006) at **M** 7.3, and that is what was done to generate the curves shown in Figure 9.73. The results shown in Figure 9.73 indicate that for the most part, the models from other regions are captured with the range of epistemic uncertainty of the crustal GMPE developed for the Hanford region.

The results shown in Figure 9.73 indicate the ranges of the ground motion models in the crustal GMPE logic tree prior to the application of the V_S-κ adjustments. The alternative models and their associated weights can be used to compute distributions of predicted median ground motions to further illustrate the epistemic uncertainty in the crustal GMPE model. Figure 9.74 displays the 10%−90% range and the 0%−100% range of predicted ground motions for the same cases shown in Figure 9.73. The GMPEs from other regions are again shown in the plots. These comparisons indicate that to a large degree, the models are captured within the 10%−90% uncertainty intervals. The results also show that the oversaturation at short distances shown in Figure 9.63 has low weight in the composite uncertainty distribution for median motions.

The limited excursions outside of the range of crustal models defined for the Hanford region are not considered significant for two reasons. First, the GMPEs with excursions are those that are not considered appropriate for defining the center, body, and range of ground motions associated with reverse-faulting earthquakes in the active crustal region based on the assessments presented in Section 7.4.1. Thus, the fact that some of the excluded models produce limited excursions is not unexpected. The second reason relates to representation of the continuous distribution of backbone adjustment factors developed above by a discrete distribution. The discrete distributions shown in Figure 9.60 are all intended to represent the continuous normal distribution extending from $-\infty$ to ∞. However, because of their discrete nature, each representation has a finite range, capturing the effects of the missing tails on the distribution moments (e.g., the variance) through the assigned weights. As a result, the 0%−100% range

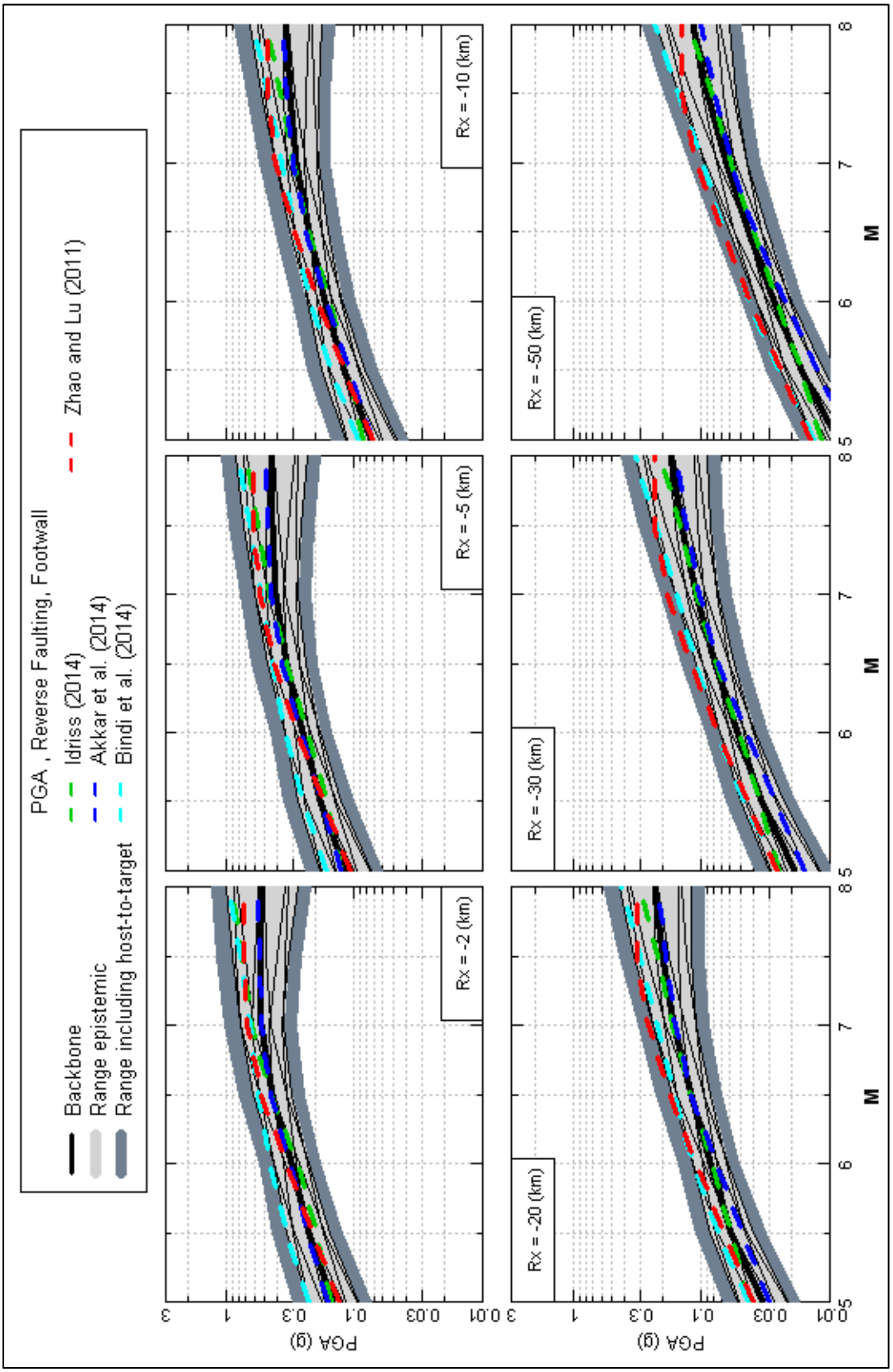

Figure 9.73. Full range of magnitude scaling produced by crustal footwall GMPEs (1 of 4).

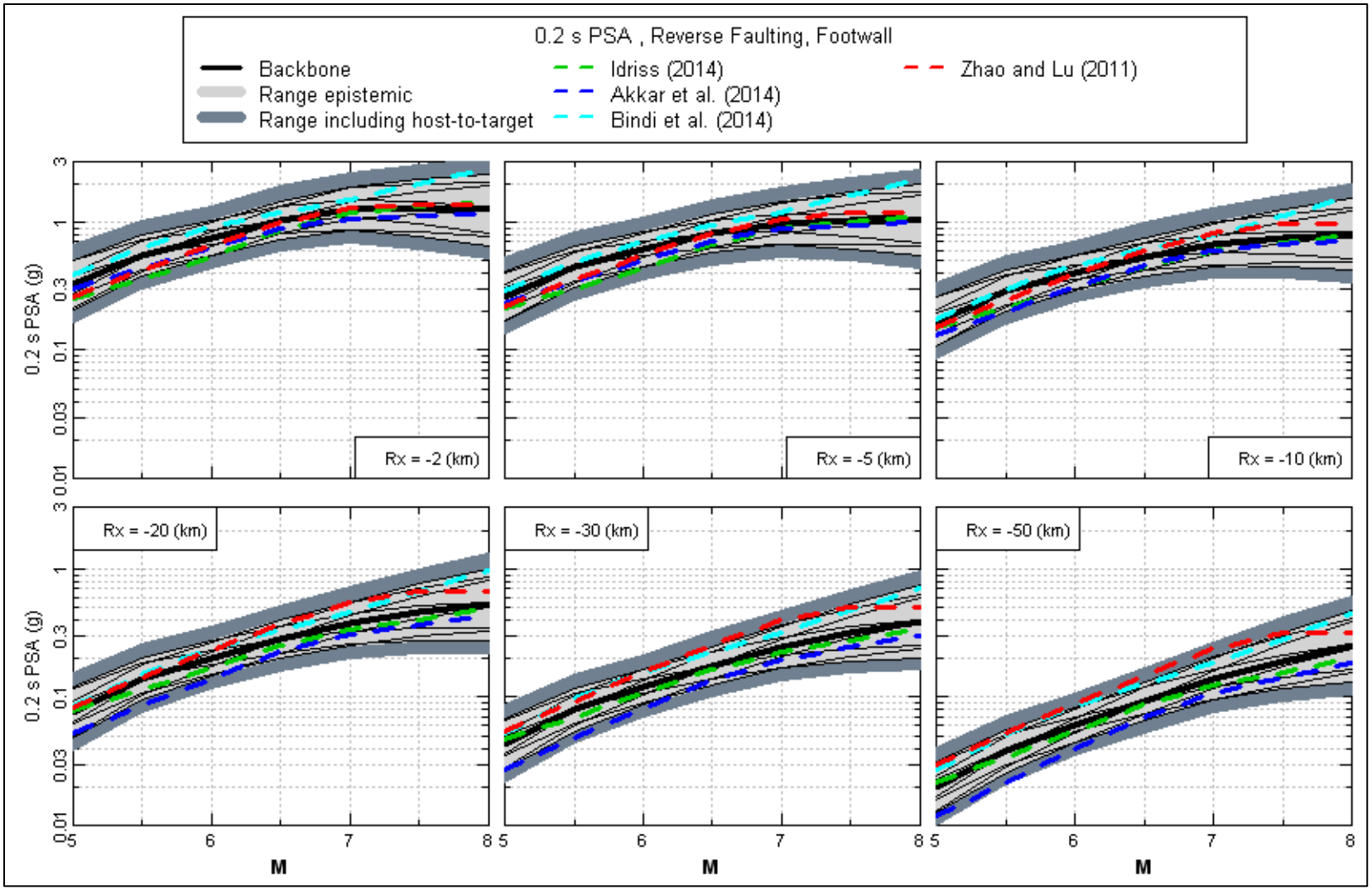

Figure 9.73. (contd; 2 of 4)

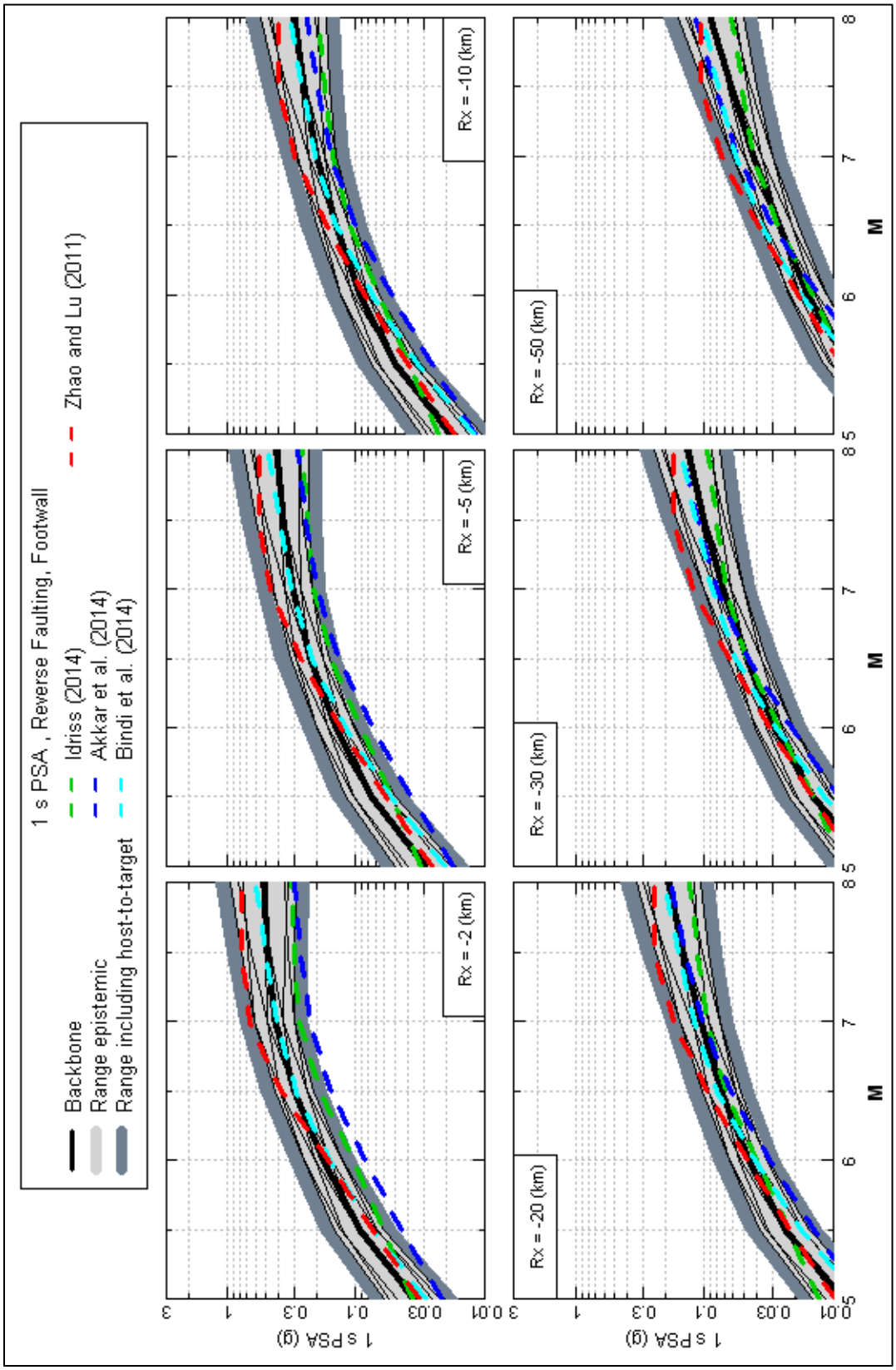

Figure 9.73. (contd; 3 of 4)

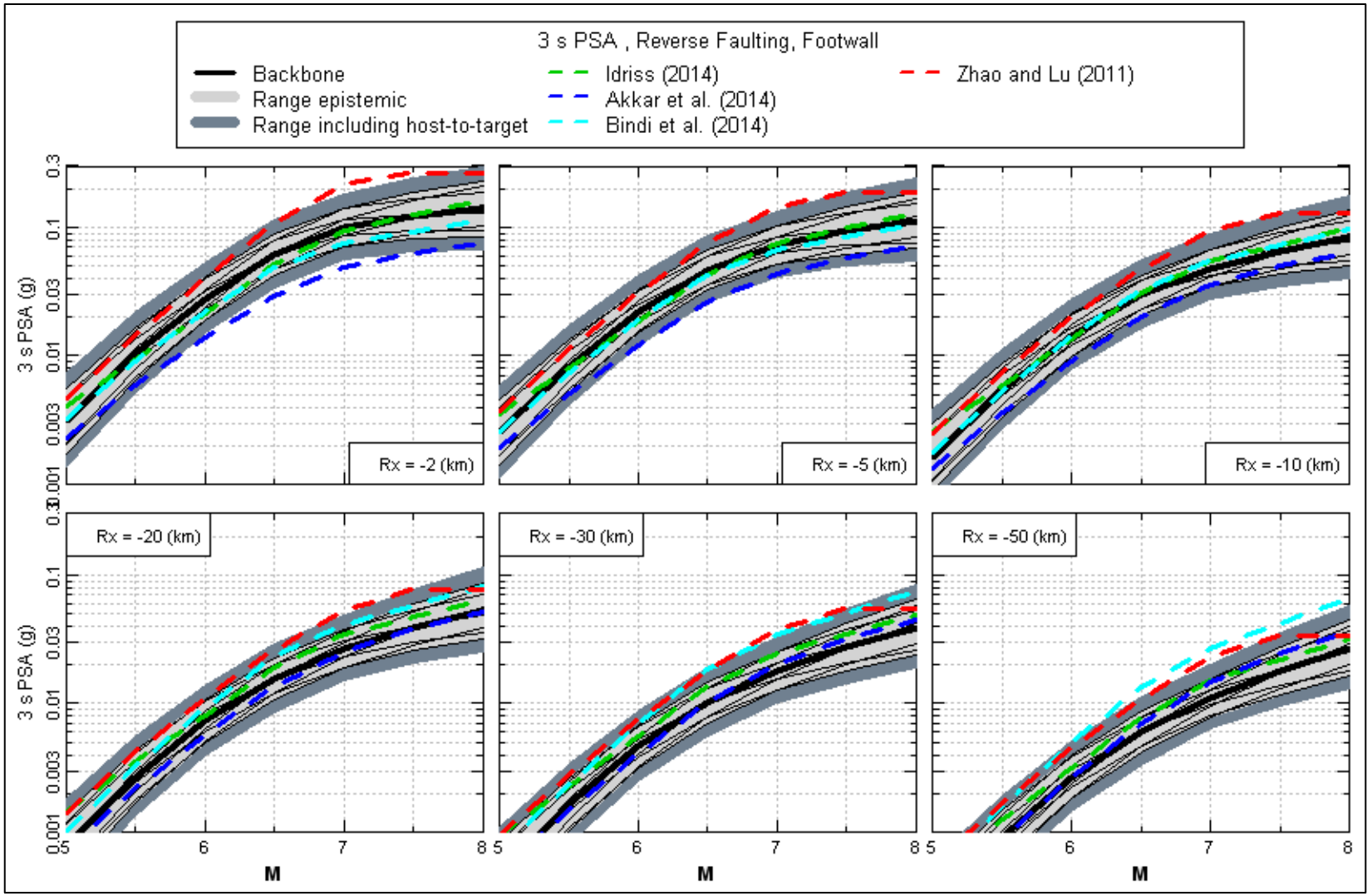

Figure 9.73. (contd; 4 of 4)

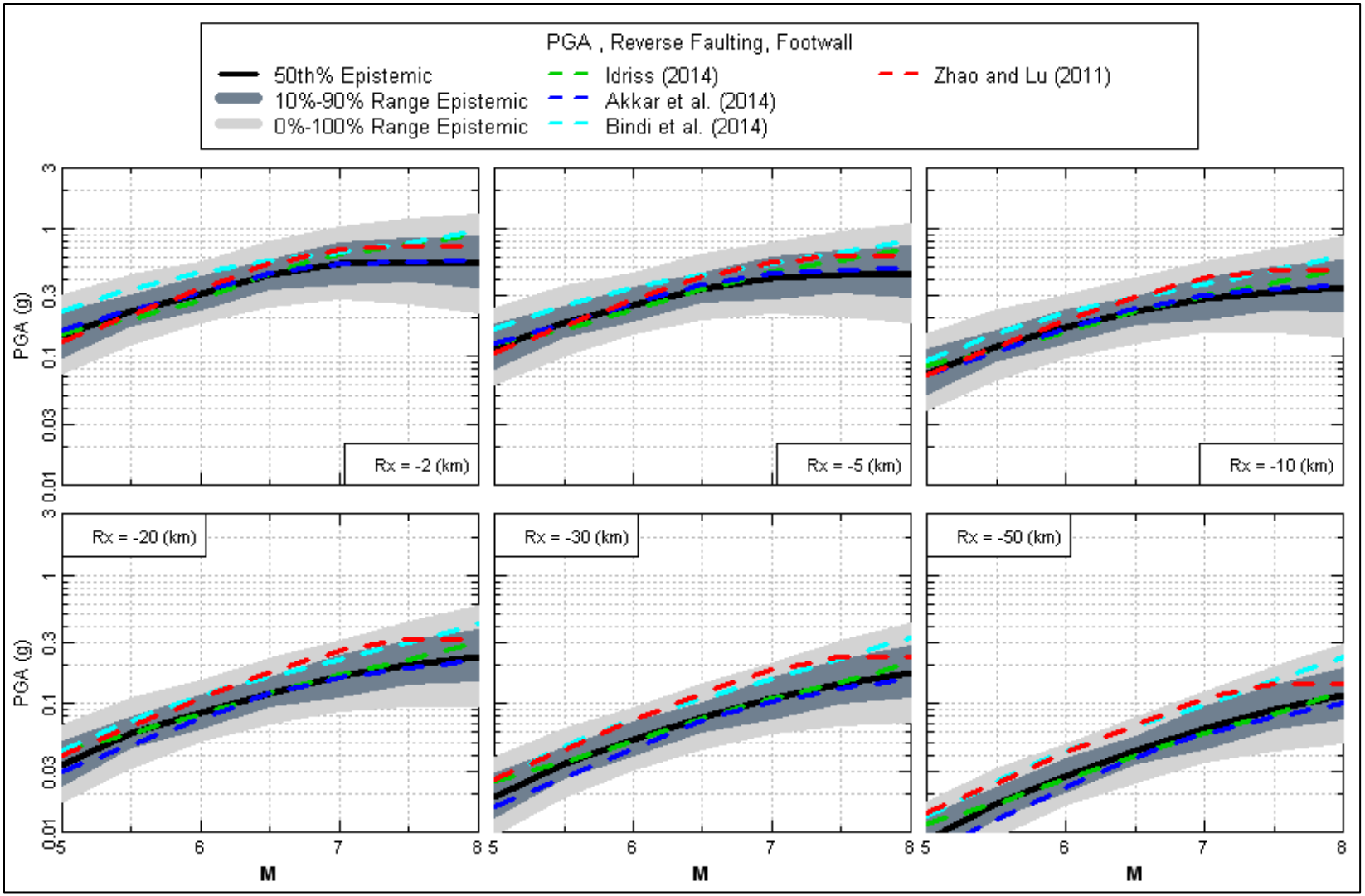

Figure 9.74. Epistemic distribution for magnitude scaling produced by crustal footwall GMPEs (1 of 4).

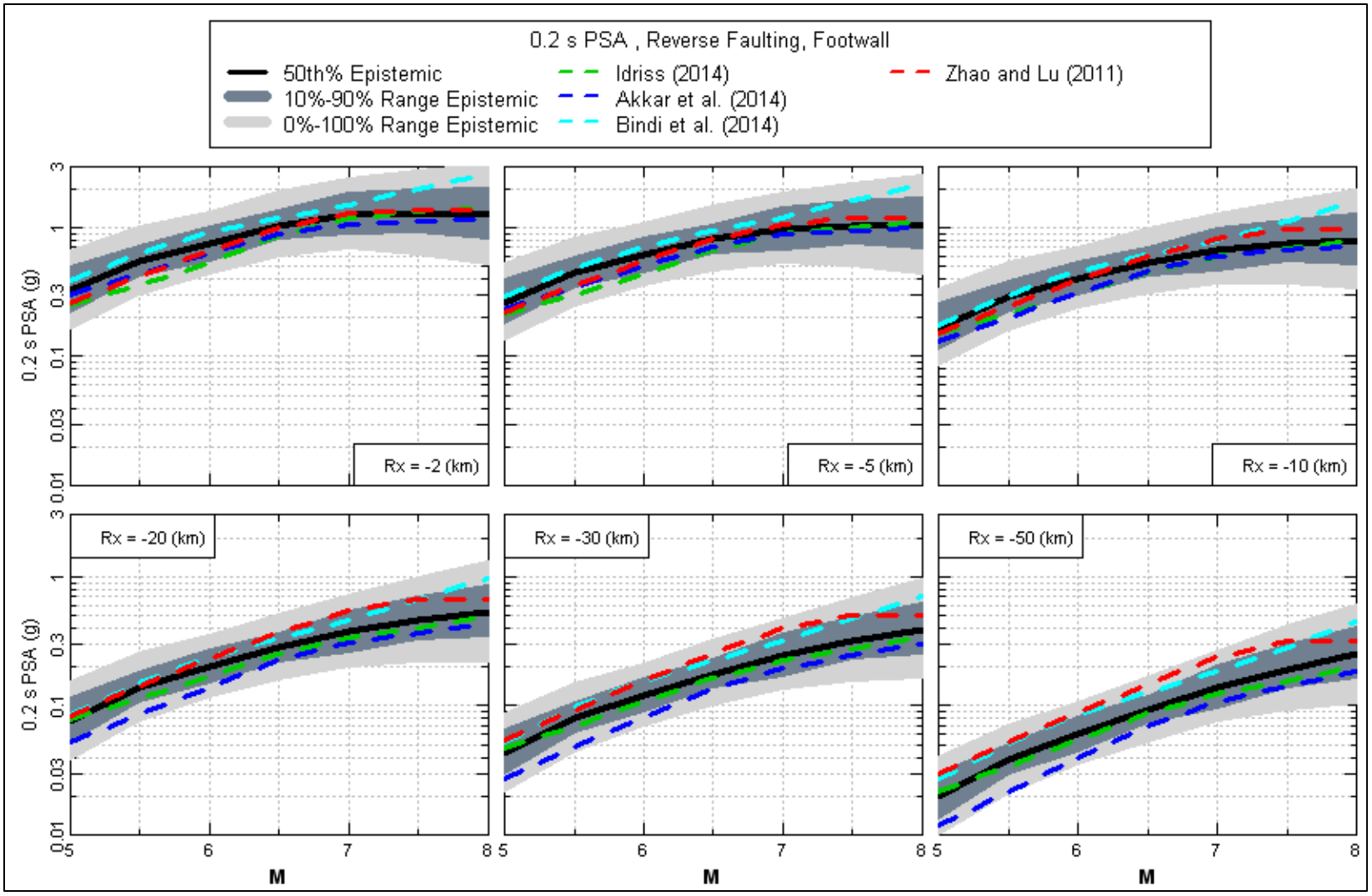

Figure 9.74. (contd; 2 of 4).

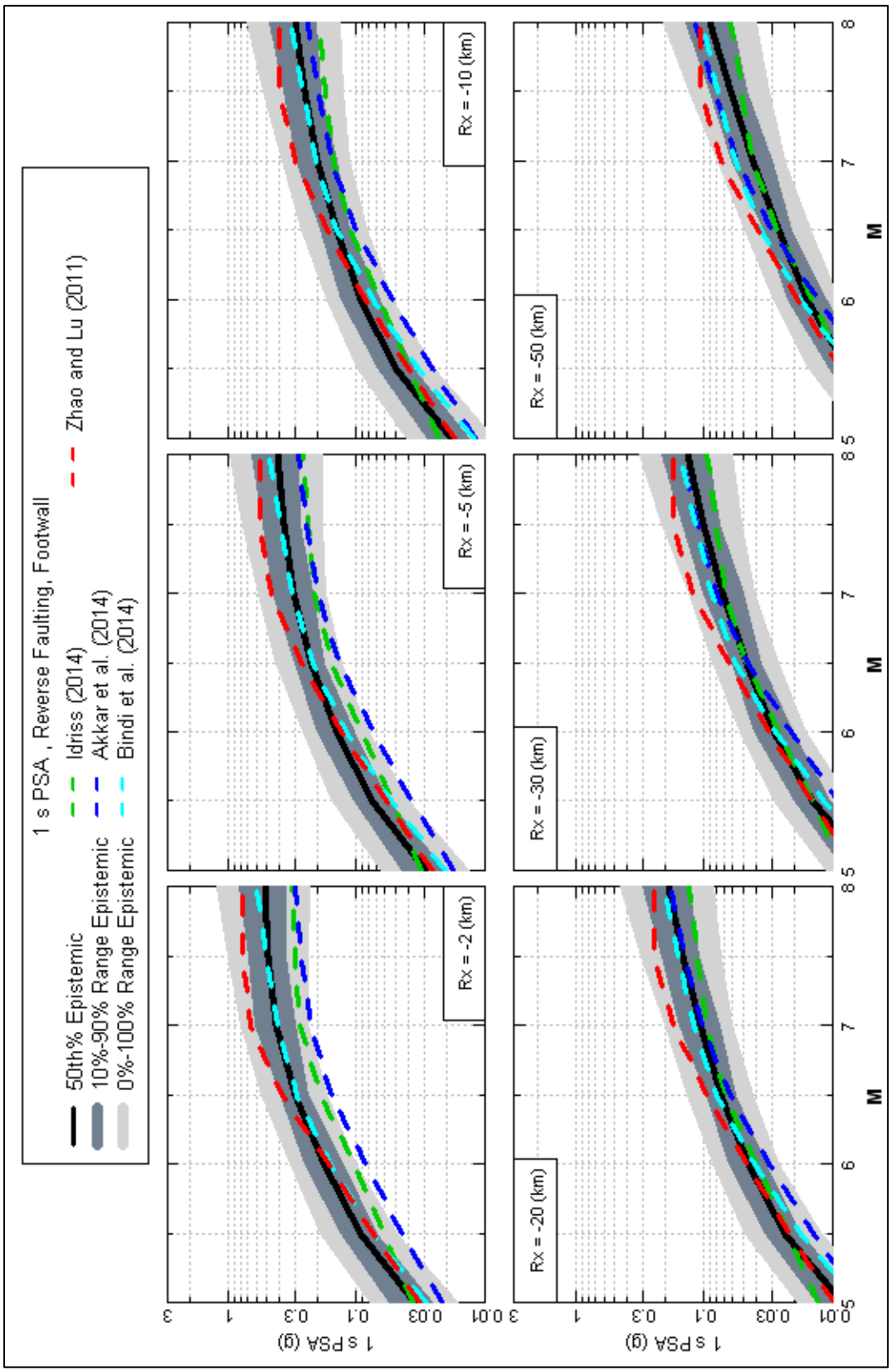

Figure 9.74. (contd; 3 of 4)

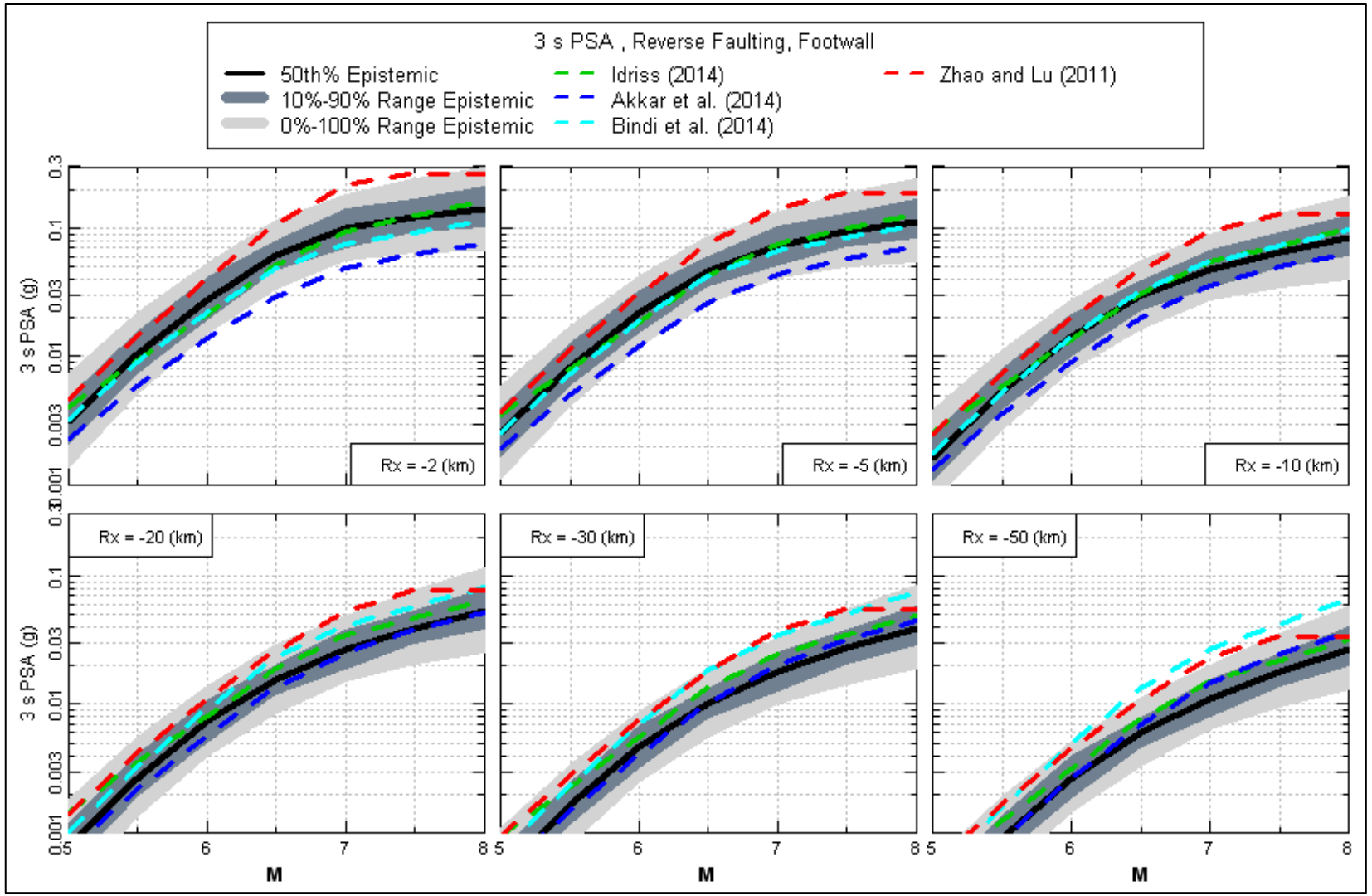

Figure 9.74. (contd; 4 of 4)

of the discrete distributions, such as shown in Figure 9.60 and in Figure 9.74, will be narrower than the range of the underlying continuous distribution they are representing. However, the discrete distributions do represent the width of the continuous distribution by have the same variance, and in the case of the selected Cools and Rabinowitz (1993) 9-point distribution, capture the distribution shape by having the same kurtosis. Therefore, the limited excursions outside of the range of the discrete backbone models are considered to be the results of ground motion predictions with low probability resulting from some GMPEs that are considered to be unlikely to provide appropriate assessments for the seismic sources of interest to the site hazard.

9.4.3 Scaling Factors for Subduction GMPE Branches

A suite of ground motion models for subduction earthquakes is created from a single backbone. Existing GMPEs for subduction zones are discussed in Section 7.4.2. The GMC TI Team considered that the only viable model for consideration for the backbone model was the BC Hydro model (Abrahamson et al. 2014a). The philosophy for scaling the backbone model is discussed in Section 9.4.2 for crustal earthquakes. Namely, we incorporate two elements of epistemic uncertainty. The first element reflects the inherent uncertainty of predictions within the data used for constraining the backbone GMPE. The second element reflects the uncertainty in how the selected GMPE would apply to eastern Washington State.

Prior to discussing the scaling factors per se, we must consider the fact that the BC Hydro relationship embodies in essence two different relationships: one for forearc sites and one for backarc sites, the difference between both being simply the degree of anelastic attenuation (Equation 9.6). Anelastic attenuation will be treated as a separate source of epistemic uncertainty, and for this reason, it is easier to simply choose one of the two models (backarc or forearc) as the starting point for the scaling exercise. The following arguments are made in favor of the adoption of the backarc model:

1. The Hanford Site is located entirely in the backarc region of the Cascadia subduction zone
2. While there is a general lack of ground motion data in the Cascadia subduction zone, in particular in the backarc region, the Hanford stations recorded the **M**6.8 2001 Nisqually earthquake, an intraslab earthquake in the Cascadia subduction zone. Figure 9.75 plots the residuals from recordings of this earthquake. The residuals are computed using both the backarc and forearc models (e.g., assuming all stations are either in the backarc or in the forearc) for periods up to 1 second (beyond this period the attenuation in the forearc and backarc models are identical). Observe that the forearc model does not have enough attenuation and results in negative residuals at the distances of interest for this project (200 to 400 km). On the other hand, the backarc model has residuals that are approximately zero at the distance of interest. Figure 9.76 shows the recorded spectra at stations within the Hanford Site, which lies entirely in the backarc region. Figure 9.77 shows the location of these stations within the Hanford Site. In nearly all cases, the backarc model predictions are closer to the recorded motions at these sites. Also note that since most of the recordings shown in Figure 9.75 are in the forearc region, the good fit of the backarc model may indicate that anelastic attenuation might be the same in the forearc and backarc regions in this part of the Cascadia subduction zone.

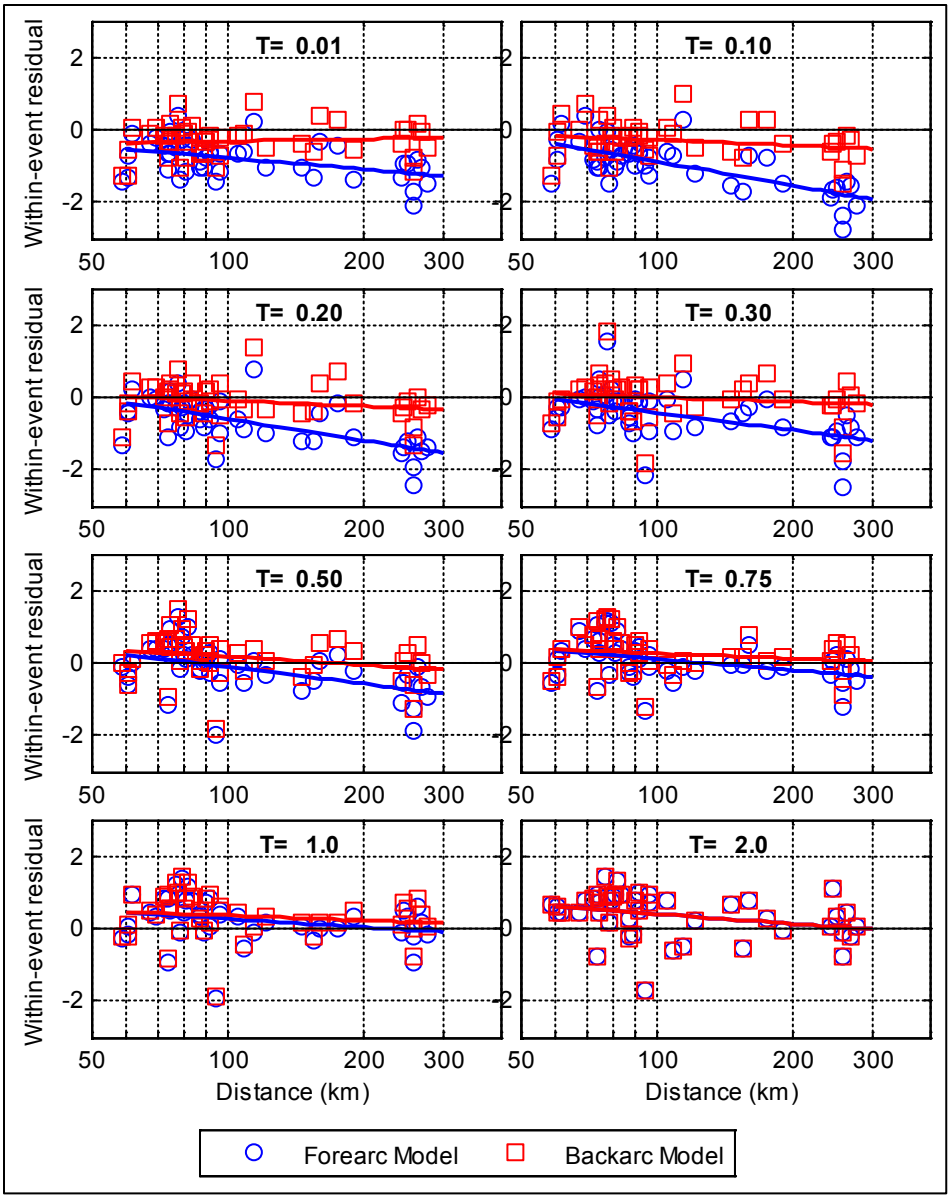

Figure 9.75. Within-event residuals recorded during the Nisqually earthquake. Residuals are computed separately using the modified BC Hydro forearc and backarc models (with the median ΔC_1 value). The solid line is a linear trend through the residuals.

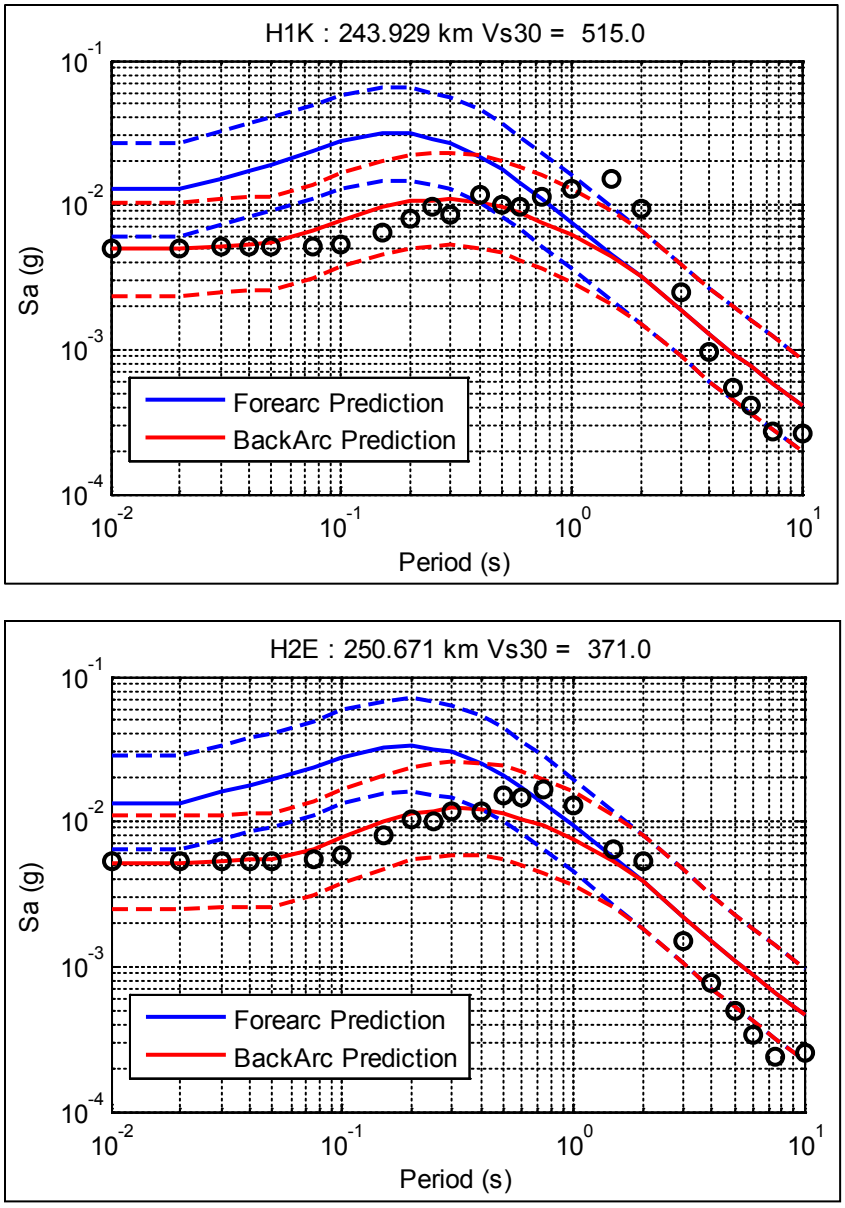

Figure 9.76. Recorded ground motions at stations in the Hanford Site area from the 2001 Nisqually earthquake, along with predictions from the modified BC Hydro model (using the median ΔC_1 value), both assuming forearc and backarc conditions. The dashed lines are a ± one standard deviation band (1 of 4).

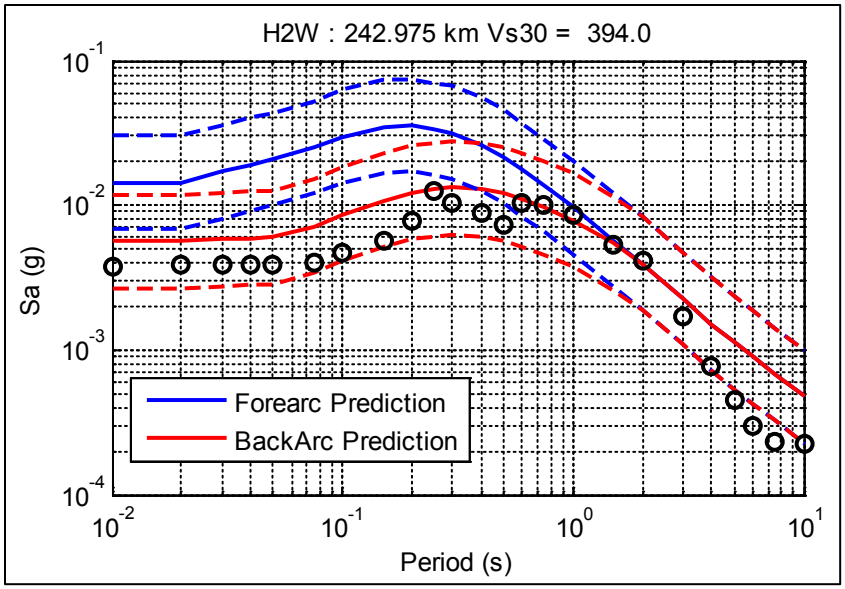

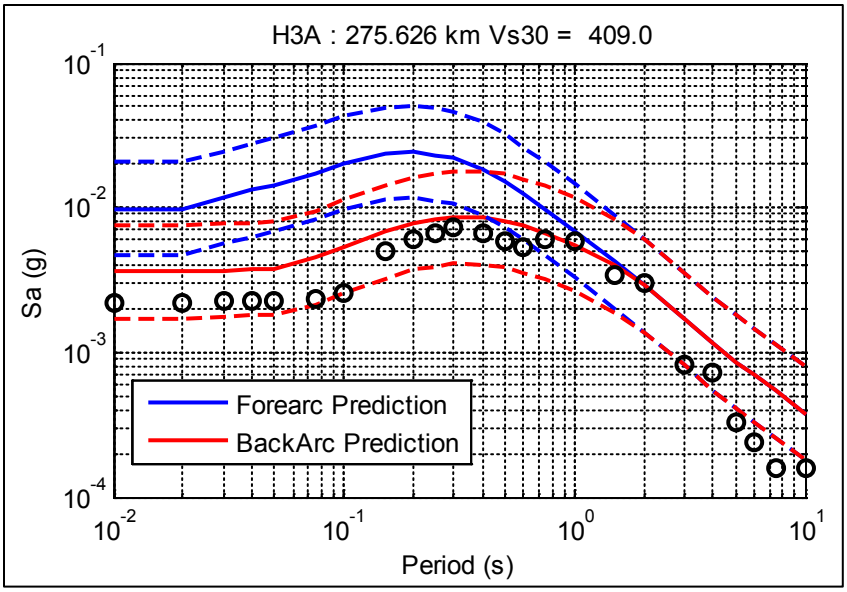

Figure 9.76. (contd) (2 of 4).

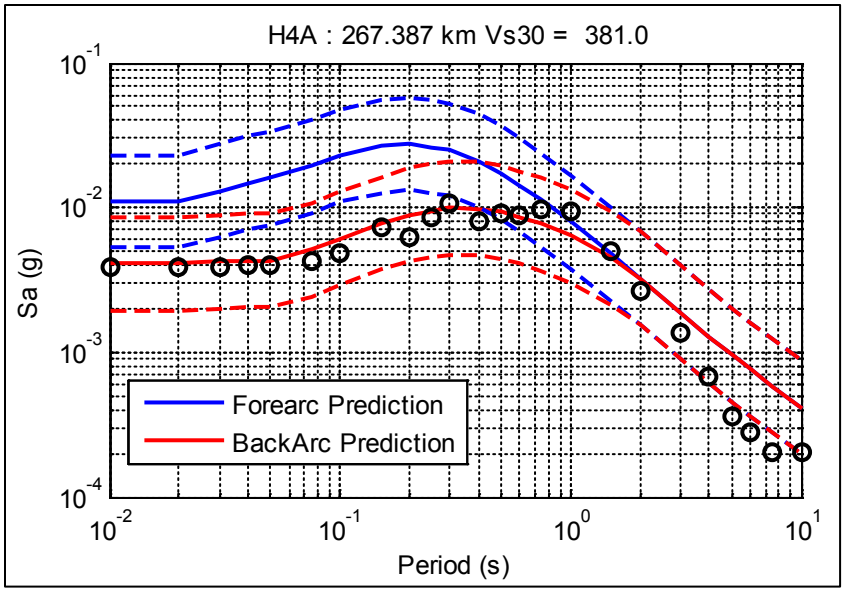

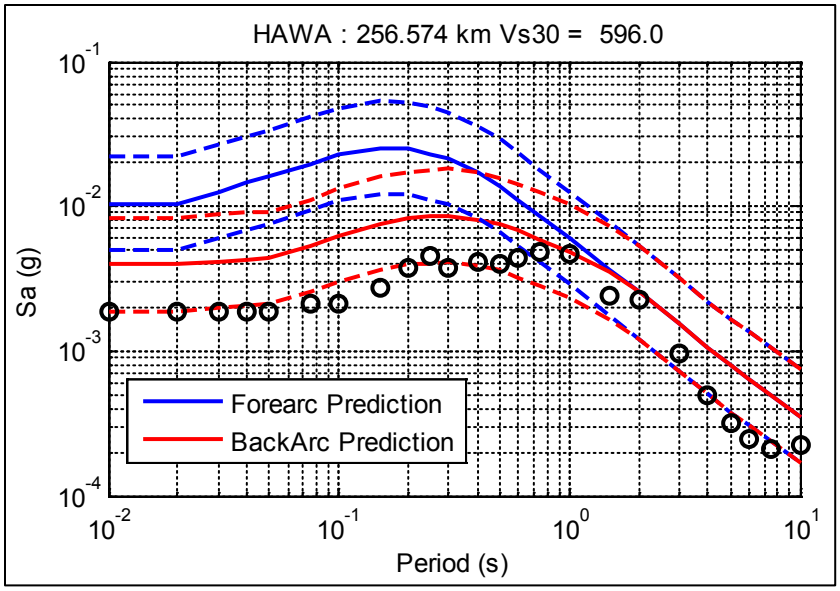

Figure 9.76. (contd) (3 of 4).

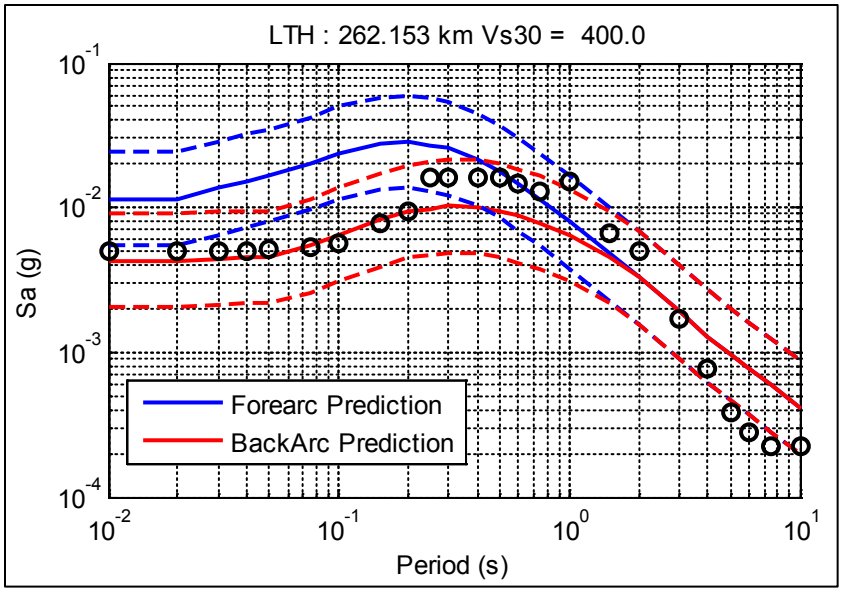

Figure 9.76. (contd) (4 of 4)

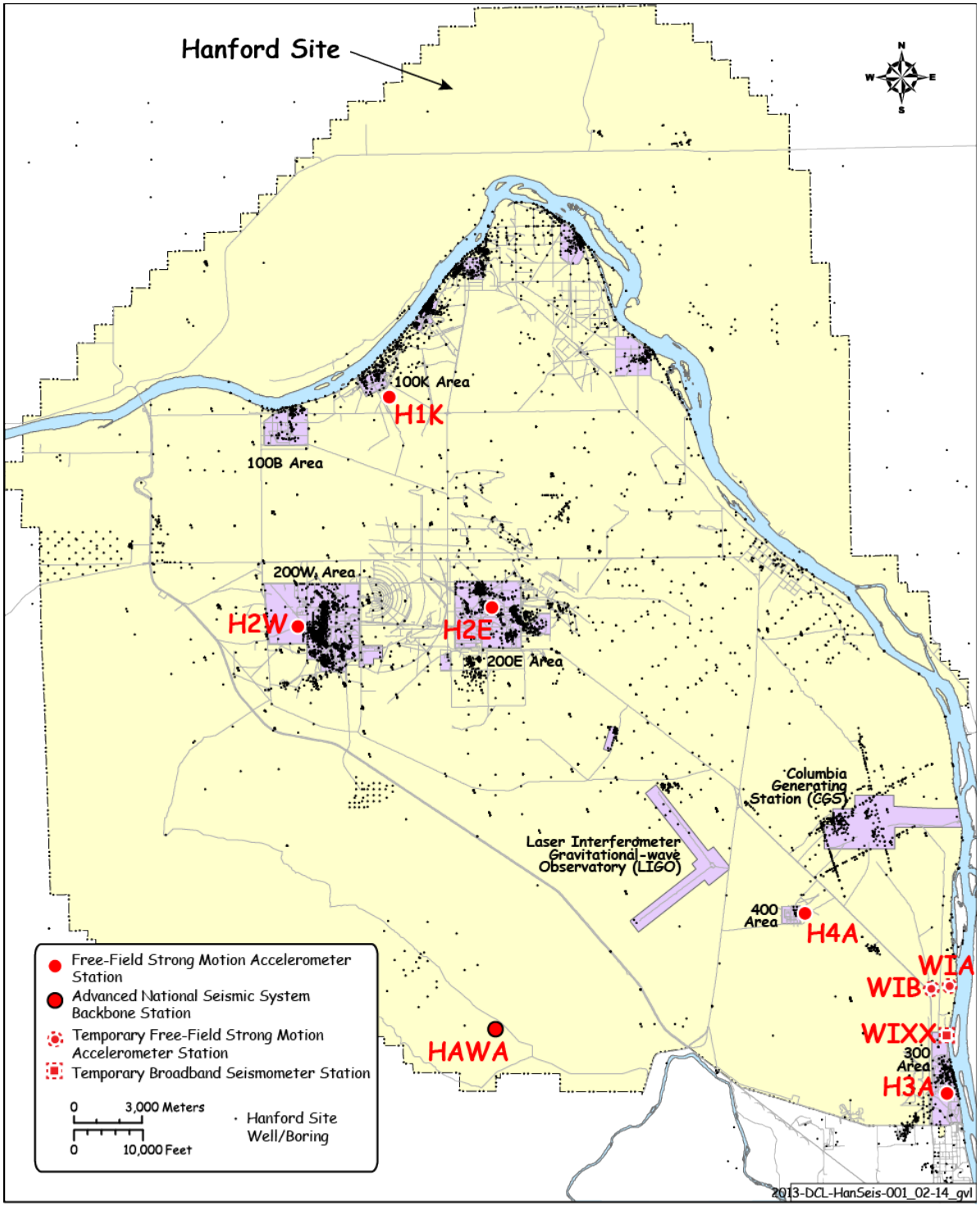

Figure 9.77. Hanford Site map showing the location of strong motion accelerometers.

The suite of scaled backbone models for subduction earthquakes will be created by consideration of the following sources of epistemic uncertainty: a) large-magnitude scaling, b) anelastic attenuation, and c) uncertainty on the median. Each of these is discussed separately below. It is important to note that an additional source of epistemic uncertainty not considered in the discussion below is the uncertainty in host-to-target V_S adjustment factors. This uncertainty is discussed in Section 9.3.3.

9.4.3.1 Large-Magnitude Scaling

Only a few earthquakes are recorded for magnitudes higher than 8.0 for interface earthquakes (Figure 9.8). For this reason, it is reasonable to expect that the epistemic uncertainty at large magnitudes would be higher than that at smaller magnitudes. In the BC Hydro SSHAC Level 3 PSHA project, this uncertainty was quantified by introducing epistemic uncertainty into the magnitude at which the magnitude scaling changes (BC Hydro 2012). This is illustrated in Figure 9.78 for a distance of 100 km and a period of 1 second. The break in magnitude scaling is controlled by the parameters $(C_1 + \Delta C_1)$ in Equation 9.8, where the value of C_1 is 7.8. The value of ΔC_1 was calibrated using the event terms of the Tohoku (**M** = 9.0) and Maule (**M** = 8.8) earthquakes (Abrahamson et al. 2014a). The event terms for these two earthquakes without the large-magnitude correction are plotted in Figure 9.79 (for the original BC Hydro data and setting ΔC_1 to zero). The Tohoku earthquake data exhibit strong distance attenuation, which could bias the magnitude scaling. For this reason, the data from the Tohoku earthquake are shown separately for distances less than 100 km, and distances between 100 and 200 km. Note that for the Maule earthquake and for Tohoku data for less than 100 km, the event terms are positive at short periods and negative at long periods. These events terms were used in the BC Hydro project to calibrate the ΔC_1 term. The period dependence of the correction implies a correction to the spectral shape for large-magnitude interface earthquakes. Note, however, that the correction proposed by the BC Hydro project would not completely lead to zero-event terms for these two earthquakes (e.g., the correction does not fully fit the data in Figure 9.79); such a strong modification would not be warranted for only two earthquakes. Moreover, the data from the Tohoku earthquake for distances between 100 and 200 km indicate much lower event terms at short periods, even when the stronger backarc attenuation model is used (Figure 9.78). We also note that Ghofrani *et al*. (2011) ascribe the large ground motions observed in the Tohoku earthquake at periods around 0.1 seconds to site effects The GMC TI Team decided to adopt the same correction for this project as that used in the BC Hydro (2012) project.

The GMC TI Team also decided to adopt the epistemic uncertainty that was adopted for the ΔC_1 term in the BC Hydro project. This model assigns three branches to ΔC_1, a median branch with the proposed median value (Table 9.4), a high branch with a value of $\Delta C_1 + 0.2$, and a low branch with a value of $\Delta C_1 - 0.2$. The branches have weights of 0.6 for the central branch and 0.2 for the outer branches. These weights imply that the three branches are a discrete representation of a normal distribution (where the low and high branches are the 5th and 95th percentile of the distribution).

9.4.3.2 Distance Scaling Correction

In the introduction to this section, arguments were made indicating that the Nisqually data are matched well by the distance attenuation in the modified BC Hydro backarc model. However, a large degree of epistemic uncertainty exists about this attenuation. One source of uncertainty is the degree of region-to-region variation in the data themselves. This is demonstrated by the results of an analysis performed by the GMC TI Team where the term that scales with distance in Equation 9.7 (i.e., the anelastic attenuation term, θ_6) is allowed to have regional variations by including a random-effect term

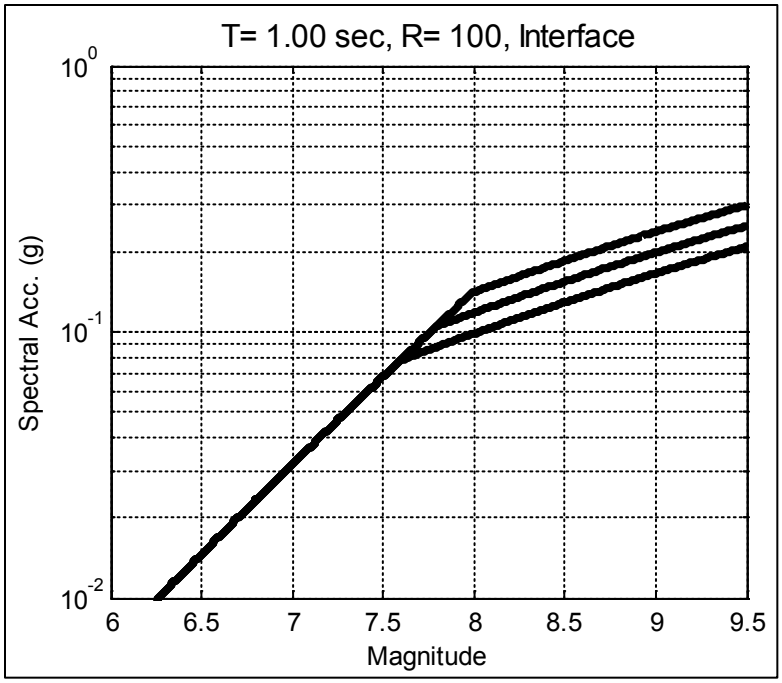

Figure 9.78. Predicted spectral accelerations for the modified BC Hydro model including epistemic uncertainty for C_1.

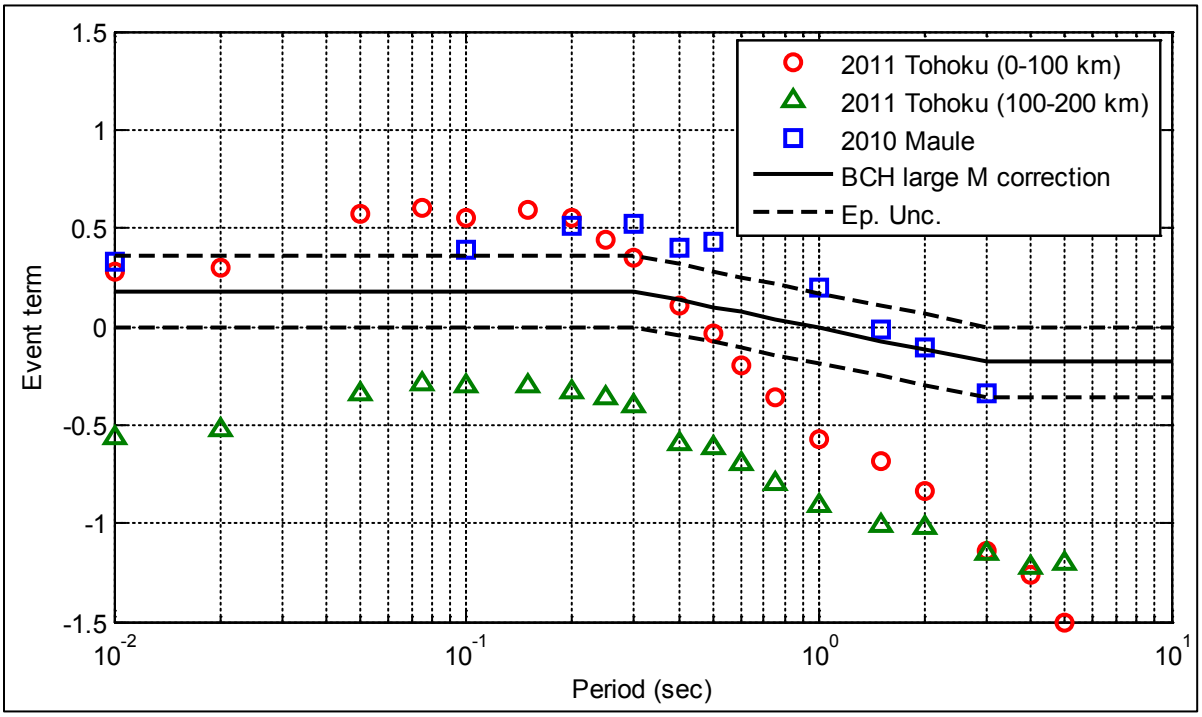

Figure 9.79. Event terms for the 2011 Tohoku and 2010 Maule earthquakes. The event terms were computed using the original BC Hydro equation and setting $\boldsymbol{\Delta C_1 = 0}$. The $\boldsymbol{\Delta C_1}$ correction ($\boldsymbol{\theta_4 \Delta C_1}$) at large magnitudes is also shown, along with its epistemic uncertainty.

($\delta\theta_6$) in the distance scaling term. This random-effect term differentiates the anelastic attenuation by regions. Not all of the regional attenuation terms could be constrained. Those regions for which the term could be constrained are shown in Figure 9.80. Note that the average term is controlled by Japanese data. For other regions, the regional attenuation term differs by as much as 50% of the overall term.

An additional source of uncertainty for distance scaling is related to the complete absence of data for large interface earthquakes in the Cascadia region. The alternative is the use of simulation-based attenuation, which is reviewed in Section 7.4.2. The conclusion of this review was that two models are worth of consideration (Gregor et al. 2002, Atkinson and Macias 2009). Neither of these models is directly applicable to the Cascadia region. However, these models can be used for constraining anelastic attenuation for spectral ordinates at long response periods. For this purpose, the absolute values of spectral acceleration predicted by these equations may not be particularly important because the focus would be on the relative decay of these accelerations over distance.

The model by Atkinson and Macias (2009; referred to as AM09) includes geometrical spreading proportional to R^{-1} (spherical) up to 40 km and $R^{-0.5}$ (cylindrical) at greater distances. The Q-model has a value for Q_0 of 180 and η=0.45. These values compare well with values from Philips et al. (2013) averaged over the source-to-site azimuths that would predominate for interface earthquakes at the Hanford Site (Figure 9.81). In particular, the AM09 Q-model is closer to the values of Philips et al. (2013) than the one used in Gregor et al. (2002). The Phillips et al. (2013) model also uses an $R^{-0.5}$ geometrical spreading model. Hence, the AM09 model was selected as a guide to constrain the long-distance attenuation.

Figure 9.82 shows plots of distance attenuation for the modified BC Hydro model for interface earthquakes. Two magnitudes and multiple periods are shown. The modified BC Hydro model with an anelastic attenuation term (θ_6) reduced by half is also shown. For comparison, the AM09 model (Atkinson and Macias 2009) is also shown. Two important observations can be made. First, the low-attenuation branch always has lower attenuation than the modified BC Hydro model for forearc sites. Second, the low-attenuation branch mimics well the attenuation predicted by the AM09 model. Figure 9.83 shows the same plots for intraslab earthquakes. The low-attenuation branch mimics the forearc behavior for intraslab earthquakes (except at short periods, but for these short periods the intraslab earthquakes do not contribute to hazard). This comparison is valid because a possible hypothesis is that the backarc attenuation is Japan-specific, hence a valid model for Cascadia would be one with forearc attenuation. This hypothesis is partially supported by the plots shown in Figure 9.84. Figure 9.84a shows the event-corrected residuals for Central America at two periods; although the forearc/backarc classification of these stations is unknown, the forearc model works well for all stations. Figure 9.84b shows the same plot for Mexican records; note that the few backarc stations have positive residuals, indicating that the backarc model over-attenuates for this region. Figure 9.84c shows the same plot for Taiwan; for this region backarc residuals are positive, indicating that the backarc model over-attenuates for this region. The comparison of the low-attenuation branch with the modified BC Hydro forearc model (Figure 9.82 and Figure 9.83) shows that the low-attenuation branch covers the possibility that forearc attenuation is applicable to Cascadia. Only periods up to T = 0.5 seconds are shown because for higher periods the forearc and backarc models are almost identical.

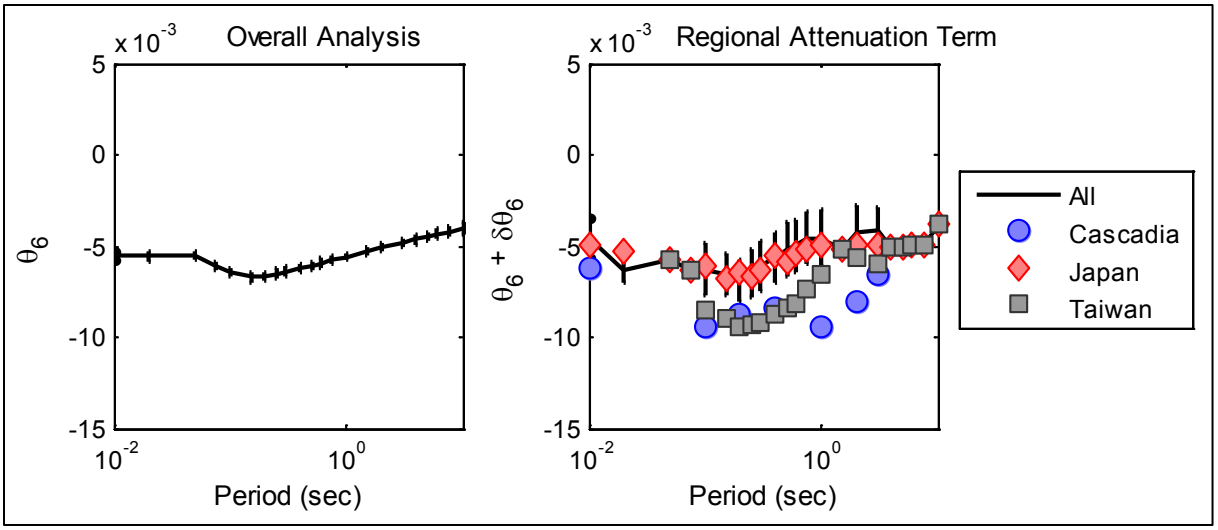

Figure 9.80. Anelastic attenuation term. The left plot shows the term computed using all of the data. The right plot shows the term computed when allowing for regional attenuation terms within a random effects analysis. A preliminary version of the modified BC Hydro model was used to compute these regional attenuation terms.

Azimuth	Average Q	Average η
ALL	237	0.44
22.5	498	0.35
67.5	512	0.33
112.5	236	0.41
157.5	198	0.43
202.5	191	0.48
247.5	180	0.53
292.5	193	0.53
337.5	219	0.48

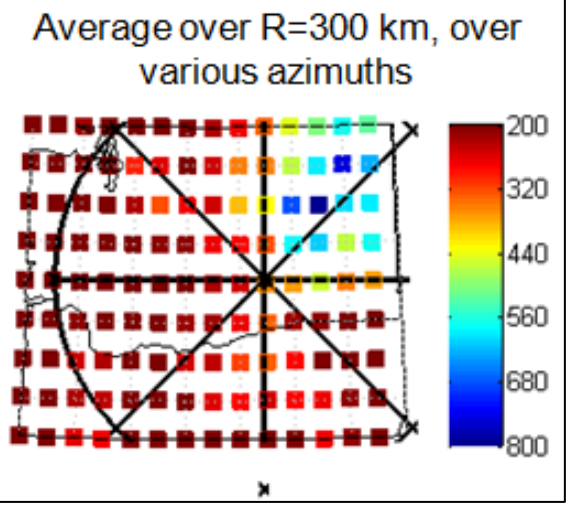

Figure 9.81. Q-model from Philips et al. (2013) (on right). The Hanford Site is located at the center of the circle. The circle has a radius of 300 km. The table on the left shows the values of Q_o and η averaged over different azimuths.

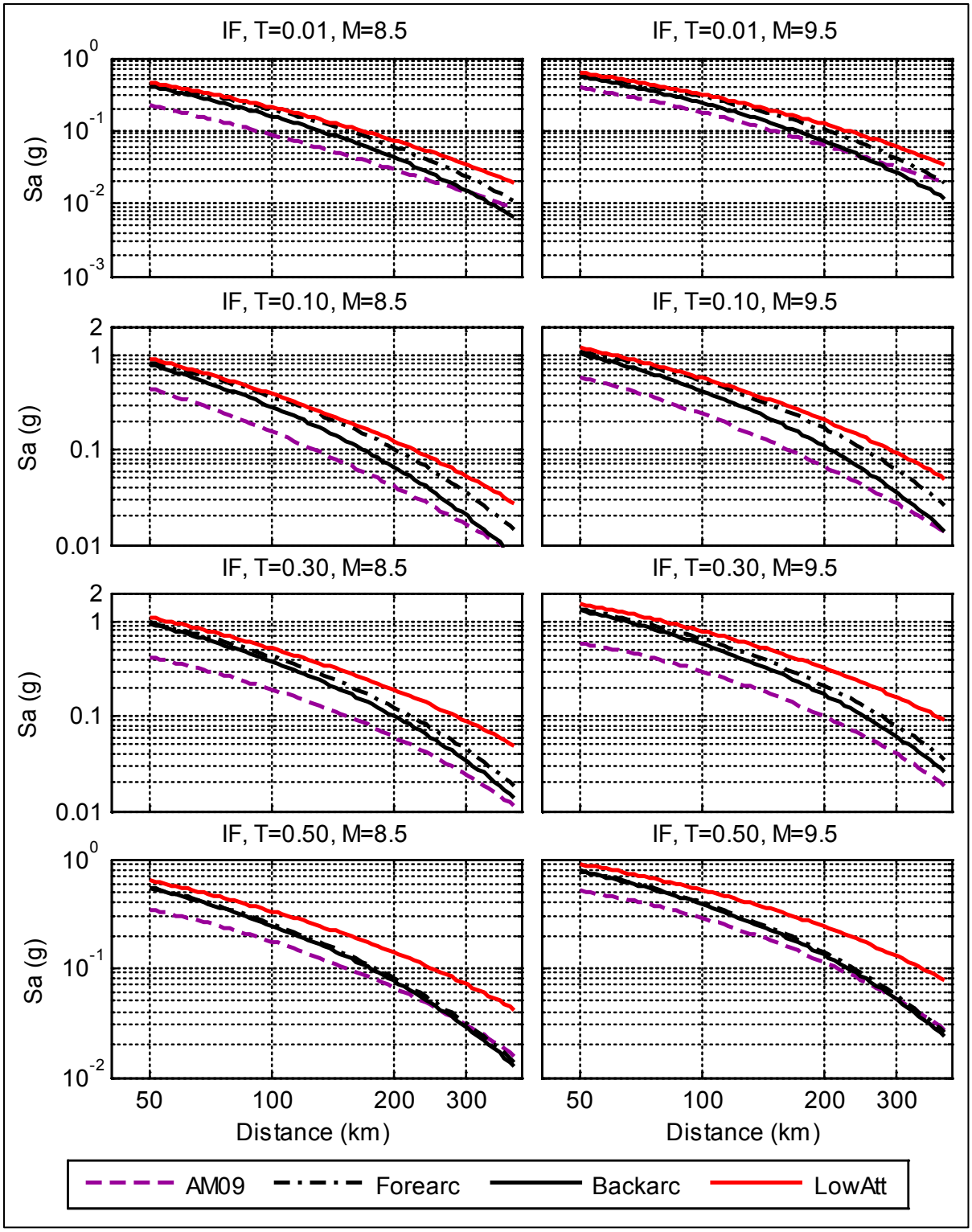

Figure 9.82. Distance attenuation of the modified BC Hydro model for interface earthquakes (forearc and backarc), and the low-attenuation branch obtained by scaling $\boldsymbol{\theta_6}$ by 0.5. For comparison, the Atkinson and Macias (2009; AM09) model is also shown. (1 of 2)

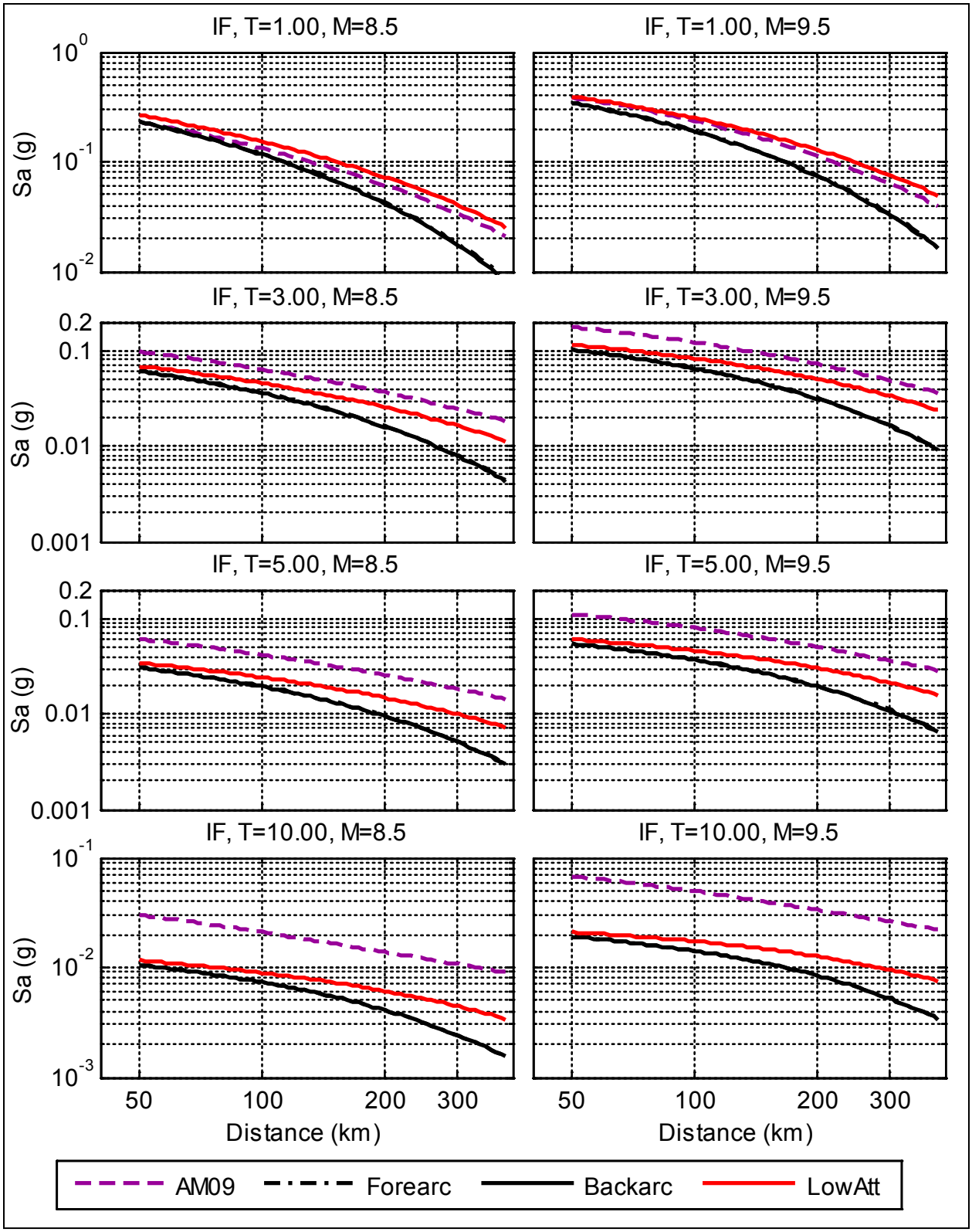

Figure 9.82. (contd) (2 of 2)

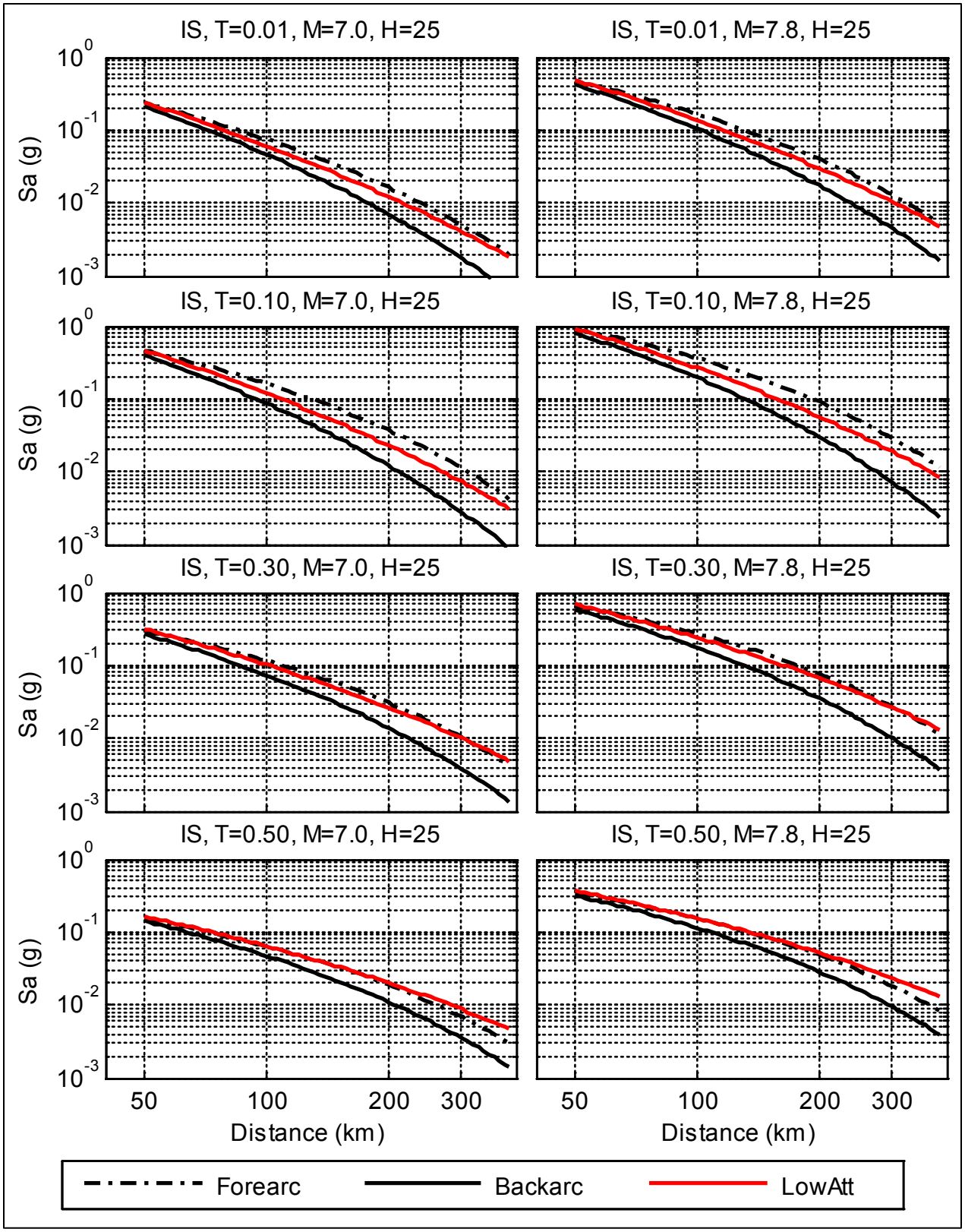

Figure 9.83. Distance attenuation of intraslab modified BC Hydro model (forearc and backarc), and the low-attenuation branch obtained by scaling $\boldsymbol{\theta_6}$ by 0.5.

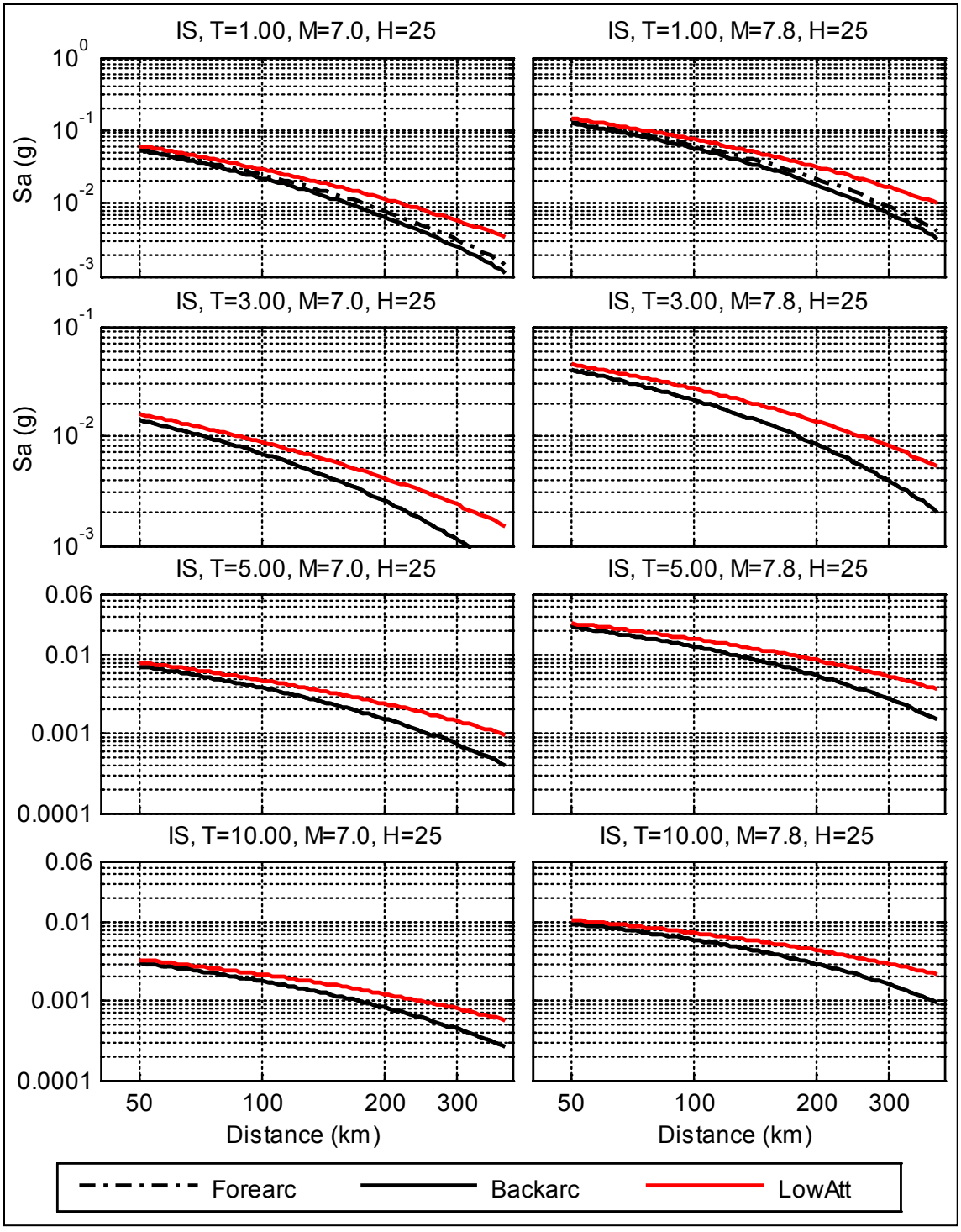

Figure 9.83. (contd)

For the reasons described above, GMC TI Team chose two branches to capture epistemic uncertainty in distance attenuation. One branch is the modified BC Hydro model for backarc conditions, and second branch is the modified BC Hydro model for backarc conditions with the parameter θ_6 replaced by $0.5\theta_6$ (the low-attenuation branch). The team applied a weight of 0.6 to the backarc branch and a weight of 0.4 to the low-attenuation branch. The higher weight for the backarc branch is because of the fact that the

Nisqually data match well the backarc attenuation model. Moreover, the regional Cascadia attenuation is, in general, higher (the θ_6 parameter is more negative) than the average attenuation of the modified BC Hydro model (Figure 9.80). However, a relatively high weight was maintained for the low-attenuation branch because of uncertainties in the attenuation of the target region and the fact the AM09 model predicts such low attenuation.

9.4.3.3 Epistemic Uncertainty on the Median

The epistemic uncertainty branch for the median model was quantified by a standard deviation value, which is the combination of two components: a component that quantifies the epistemic uncertainty intrinsic to the BC Hydro model, and another component that quantifies the region-to-region variations. Hence, the epistemic uncertainty of the median is given by:

$$\sigma_{epi} = \sqrt{\left(\sigma_{Region}\right)^2 + \left(\sigma_{\mu}\right)^2} \tag{9.21}$$

where σ_{Region} is the region-to-region standard deviation and σ_{μ} is the inherent epistemic uncertainty of the model.

The region-to-region standard deviation is computed from the regional event terms shown in Figure 9.8. The standard deviation at each period of the average event terms from each region (e.g., those shown in Figure 9.8) is shown in Figure 9.85. We adopted the period-averaged value of 0.159 for the region-to-region standard deviation. It is important to note that the average event terms for Cascadia (Figure 9.8) show strong period dependence. Atkinson and Adams (2013, see also Atkinson and Casey 2003) claim that these differences are mostly differences in site response between Cascadia and Japan, and use computed differences in event term to propose a "Cascadia correction" to global subduction GMPEs. The GMC TI Team considered that the V_S scaling corrections (Section 9.3.3, Figure 9.46) will effectively introduce this correction. For this reason, there is no need to include period-dependent region-to-region uncertainty.

The epistemic uncertainty in the median (σ_{μ}) was computed using the methodology of Al Atik and Youngs (2014). The computation of the epistemic uncertainty included Tohoku data with distance less than 100 km because these data were used in the BC Hydro project (BC Hydro 2012) to constrain the ΔC_1 term of the equation. The epistemic uncertainty computed for interface earthquakes and a distance of 250 km for various magnitudes is shown in Figure 9.86. Interface earthquakes are used because they control the hazard and because the epistemic uncertainty for these earthquakes is higher. The average value of σ_{μ} for **M** = 9 (0.2589) was adopted for the computation of the epistemic uncertainty of the median. The epistemic uncertainty was assumed to be represented by a normal distribution with a standard deviation (σ_{epi}) equal to the combination of the region-to-region standard deviation (0.159) and the epistemic uncertainty on the median (0.2589; Equation 9.21). Hence, the period-independent value of σ_{epi} is 0.3033. We used a three-point distribution with weights of 0.2, 0.6, and 0.2 for the lower, central, and upper branches respectively, with the following scaling factors:

Upper: $\exp\left(\sigma_{epi} * 1.581\right) = 1.62$
Central: $\exp(0) = 1$
Lower: $\exp\left(-\sigma_{epi} * 1.581\right) = 0.62$.

For a normal distribution (i.e., for the distribution of $\ln[\sigma_{epi}]$), this discretization is nearly identical to the 'extended Pearson-Tukey' discretization recommended by Keefer and Bodily (1983; it is expressed in terms of mean and σ rather than fractiles, the off-center weights differ by less than 10 percent, and the masses are moved towards the mean to compensate for this difference). It is easy to verify that this discretization preserves the mean and standard deviation of the normal distribution.

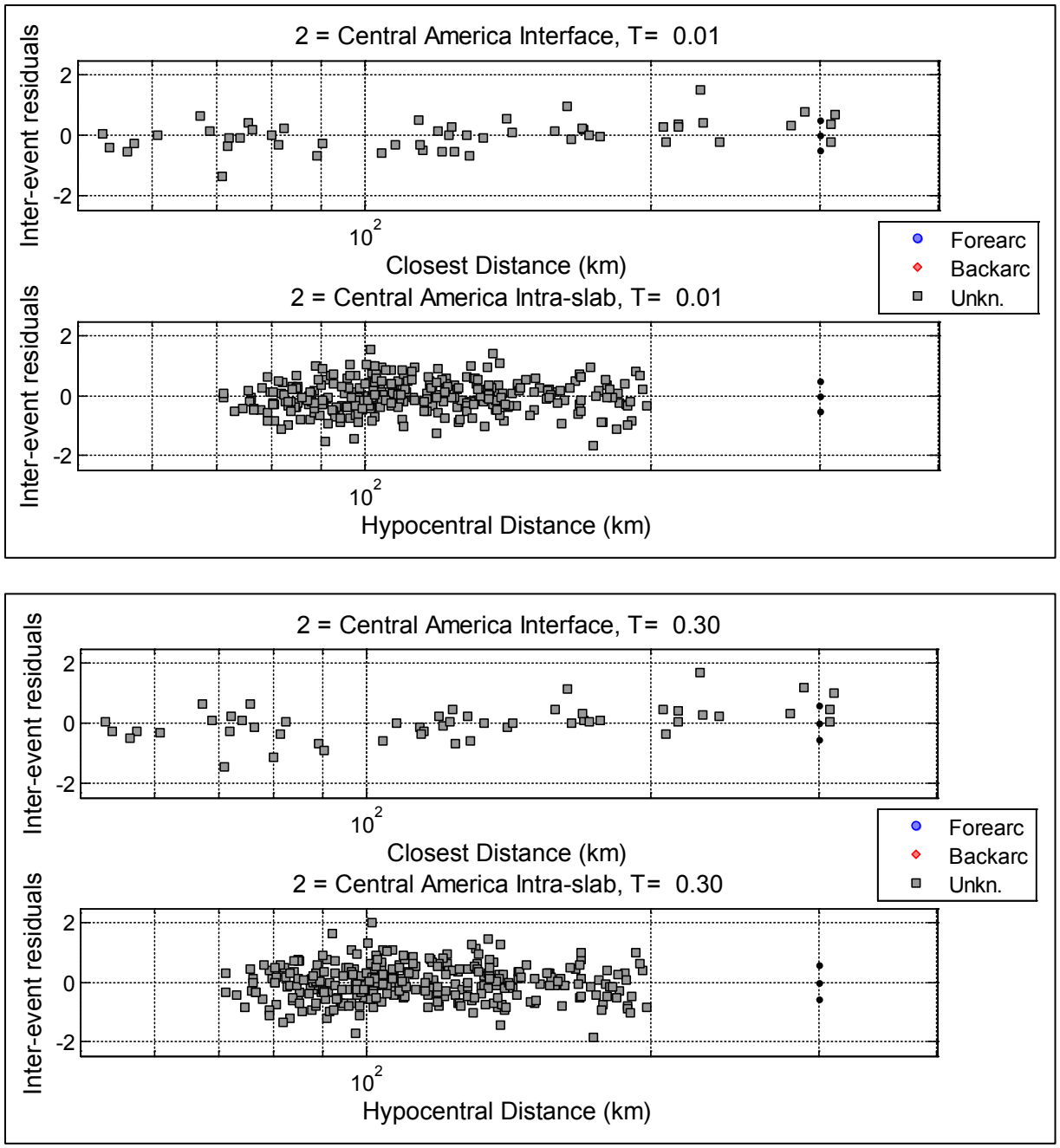

Figure 9.84a. Event-corrected residuals for selected regions and selected periods. Residuals are computed using the modified BC Hydro model using the median branch for ΔC_1.

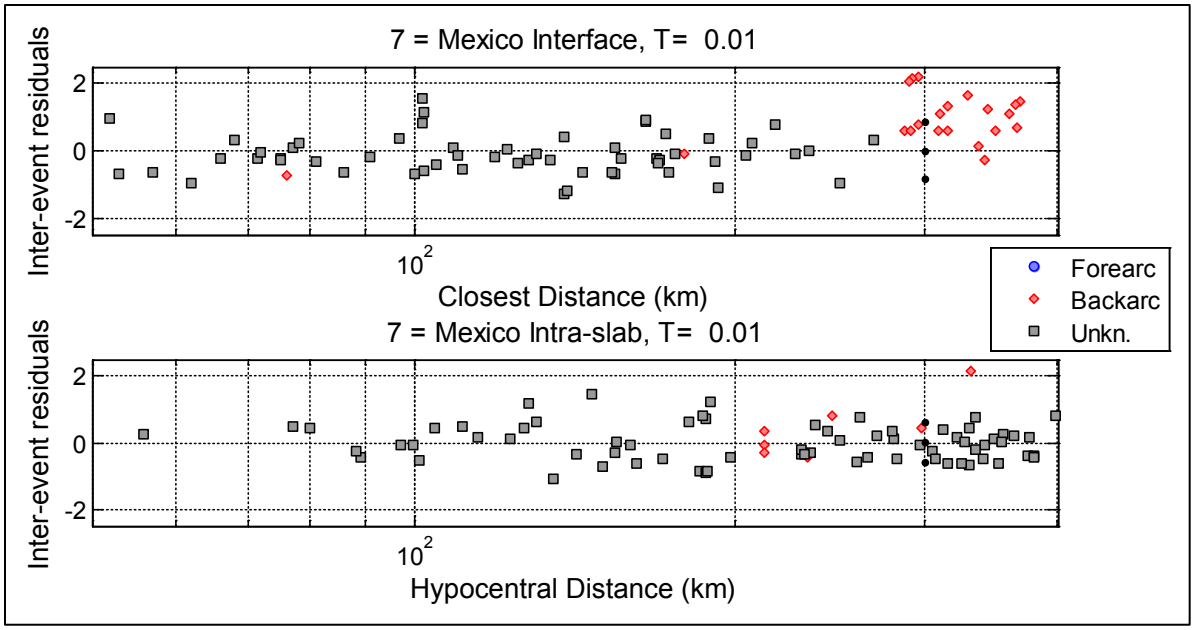

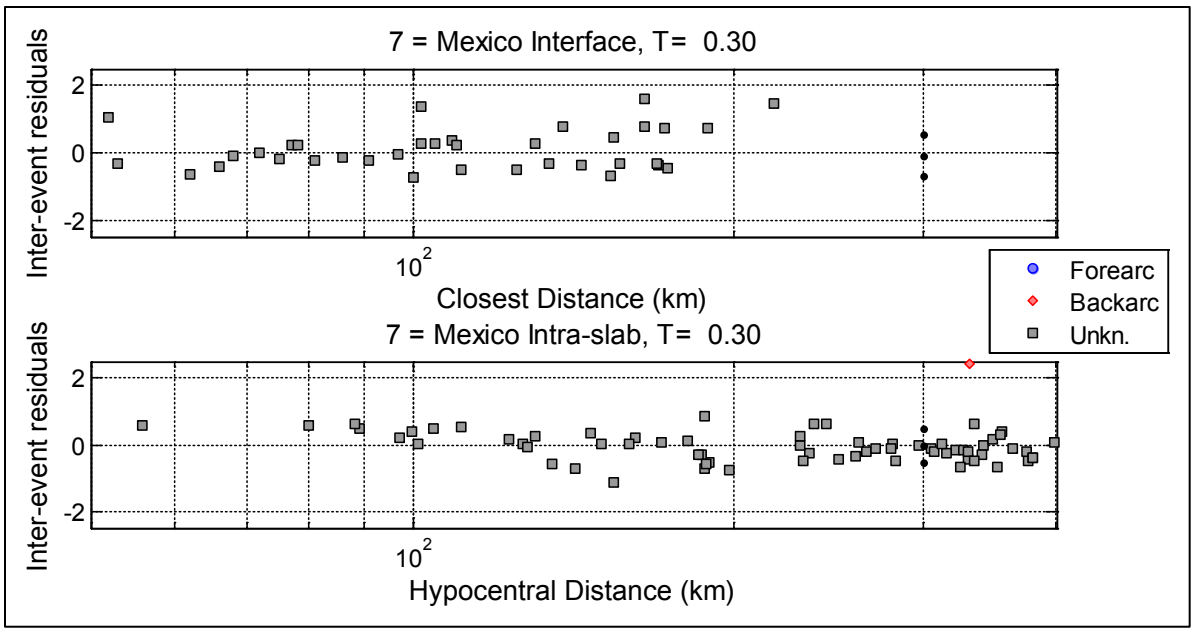

Figure 9.84b. (contd)

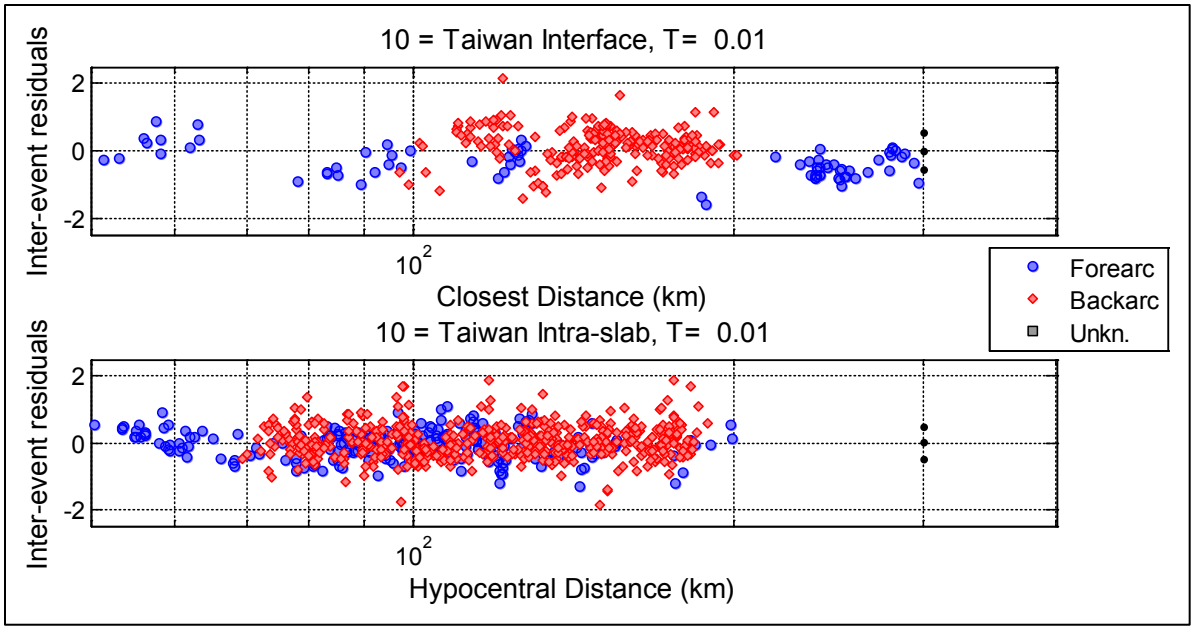

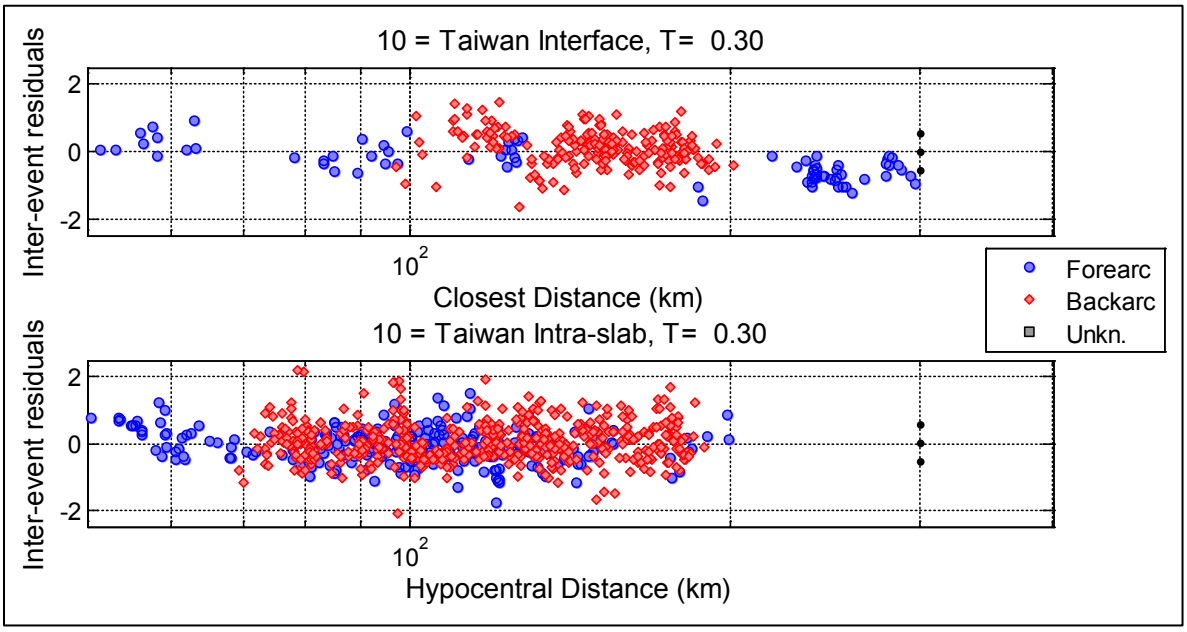

Figure 9.84c. (contd)

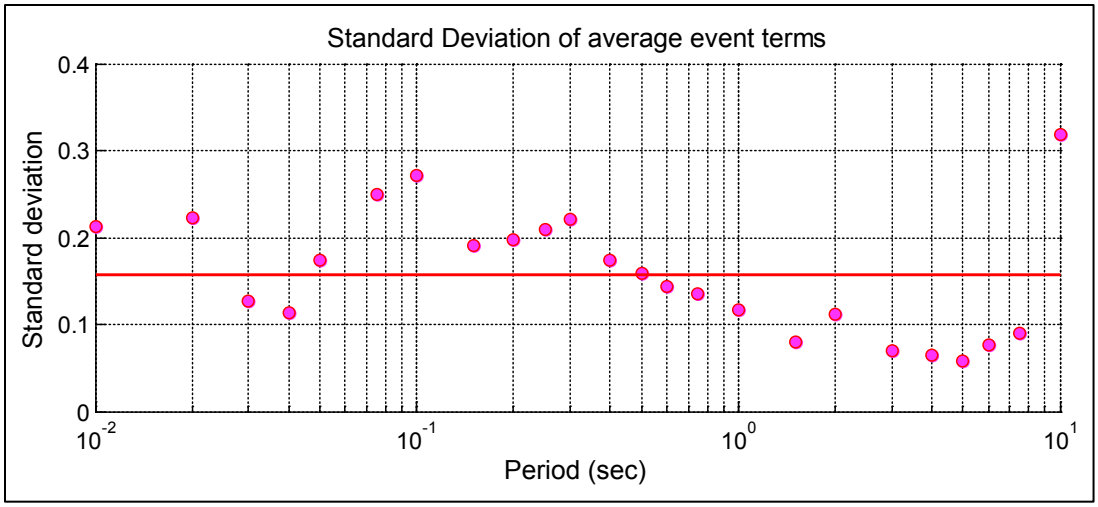

Figure 9.85. Standard deviation of the average event terms. The red line is the average standard deviation across periods.

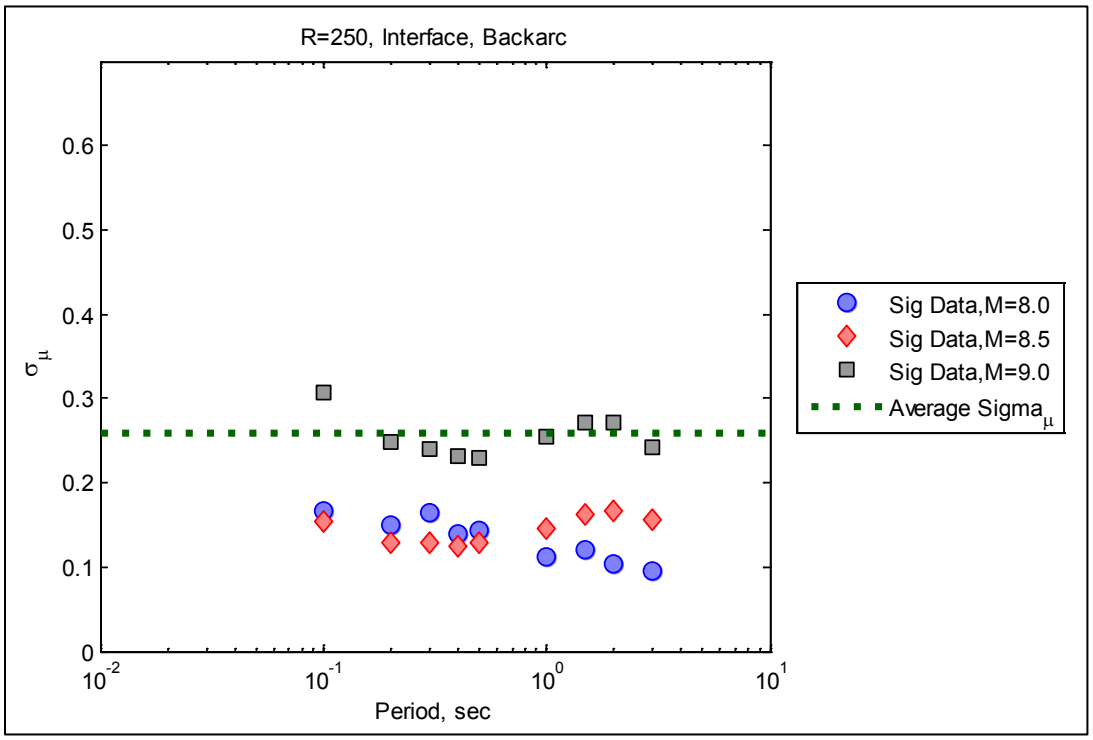

Figure 9.86. Epistemic uncertainty in the median computed for the modified BC Hydro model for a distance of 250 km, interface earthquakes, and three different magnitudes. The average for M = 9 is (0.2589) is also shown.

9.4.3.4 Logic Tree for Subduction Motions

The final logic tree for subduction motions is shown in Figure 9.87. The first four branches were discussed in this section. The fifth branch (V_S scaling adjustments) is discussed in Section 9.3.3. It is interesting to explore the implicit epistemic uncertainty in the subduction logic tree. This uncertainty (excluding the Vs correction factors) is plotted in Figure 9.88. The epistemic uncertainty has a very slight magnitude dependence, because of the epistemic uncertainty in ΔC_1, and a somewhat stronger period dependence. The period dependence results from the period dependence of θ_6. Observe that the epistemic uncertainty is close to that recommended for the Canadian Building Code by Atkinson and Adams (2013). At larger distances, the epistemic uncertainty in the logic tree exceeds that of the Canadian Building Code (Figure 9.89).

Figure 9.90 plots the range of models implied in the subduction logic tree for interface earthquakes (without host-to-target V_S conversion) and compares this to the pre-selected models in Table 7.28. Also plotted in this figure are the central backbone model and the central low-attenuation branch. Both the forearc and backarc BC Hydro models are plotted. This figure (along with Figure 9.91 to Figure 9.93) has to be interpreted with caution, because all of the existing models (except for the BC Hydro model) were considered to have problems for applicability to the Hanford Site (Section 7.4.2). However, for almost all cases the proposed range of models covers all of the other models. An exception is the Arroyo et al. (2010) model, which plots low at short periods and high for long periods. This model also has a linear magnitude scaling up to a magnitude of 9.5, which is incompatible with observed data (most data strongly support different magnitude scaling at large magnitudes; see also Zhao 2011). The Arroyo et al. (2012) model uses only regional data and hence the fact that it does not agree with the range proposed by the logic-tree models is of no great significance. For a period of 10 seconds, the only applicable models are the BC Hydro model and the AM09 model. The former shows an excessive amount of attenuation at long distances, and hence plots low with respect to the proposed range. On the other hand, the latter model predicts a level of ground motion that is incompatible with all recorded data.

Figure 9.91 repeats the same exercise for intraslab models. The forearc BC Hydro model tends to plot high with respect to the other models at short periods. This model, however, was much higher than the only observed large-magnitude earthquake in the Cascadia region (the 2001 Nisqually earthquake). Moreover, for reasons discussed before, the forearc attenuation model is not likely to be applicable to eastern Washington State. The other model that deviates from the range covered by the logic tree is the Atkinson and Boore (2003) model for T = 3 seconds. The AB03 model predicts much stronger magnitude scaling. For the magnitudes that control hazard at these periods ($M \geq 7$), the AB03 predictions are in the range covered by the logic-tree models.

Figure 9.92 and Figure 9.93 show the same information as for the previous two figures, except that they also show the distance-dependence of the models. The same observations made for the previous figures are applicable; namely, that the proposed range of models covers the range of existing models, with the same exceptions noted above. It is also important to note that for interface earthquakes (Figure 9.92) the AB03 model predicts much lower attenuation with distance, in particular for long periods. This attenuation in the AB03 model is partly controlled by earthquakes in Mexico with data from soft soils in Mexico City (Gail Atkinson, personal communication, 2014). The high amplification of motion by these deposits contributes to an apparent lack of attenuation.

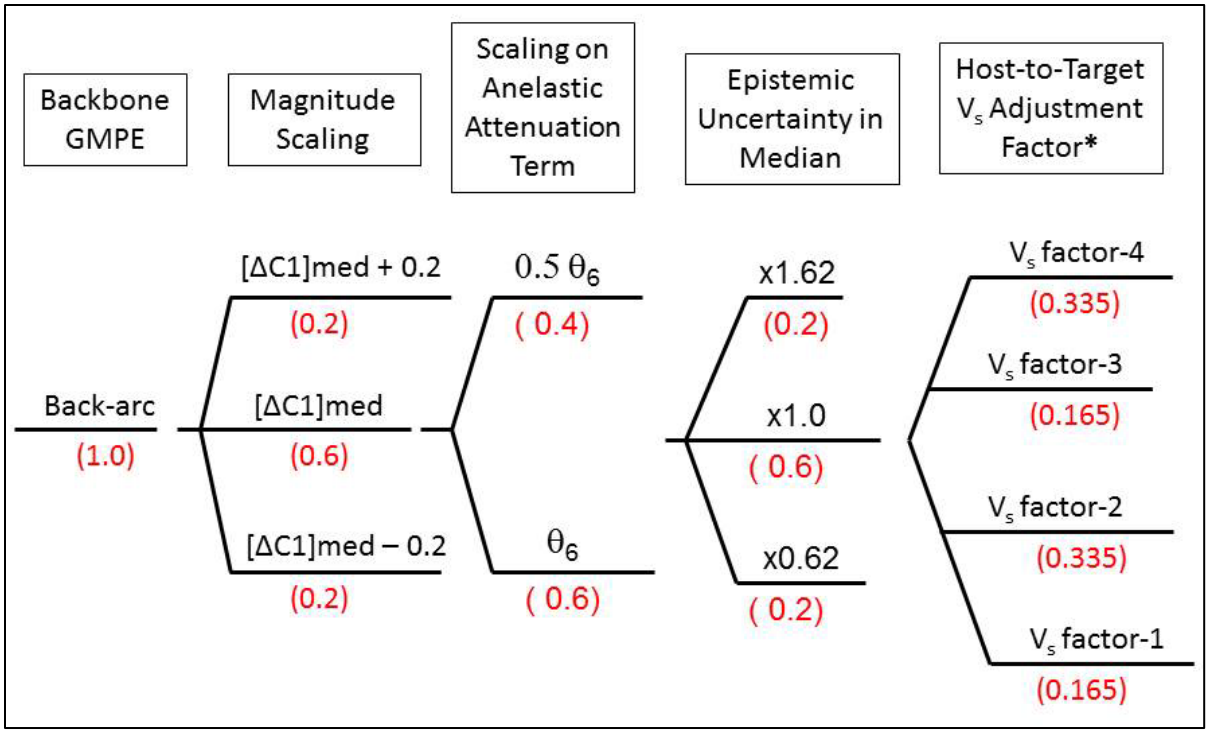

Figure 9.87. Logic tree for the subduction ground motion model. The host-to-target V_S adjustment factors are conditioned on ΔC_1 and θ_6, hence they are different for every branch.

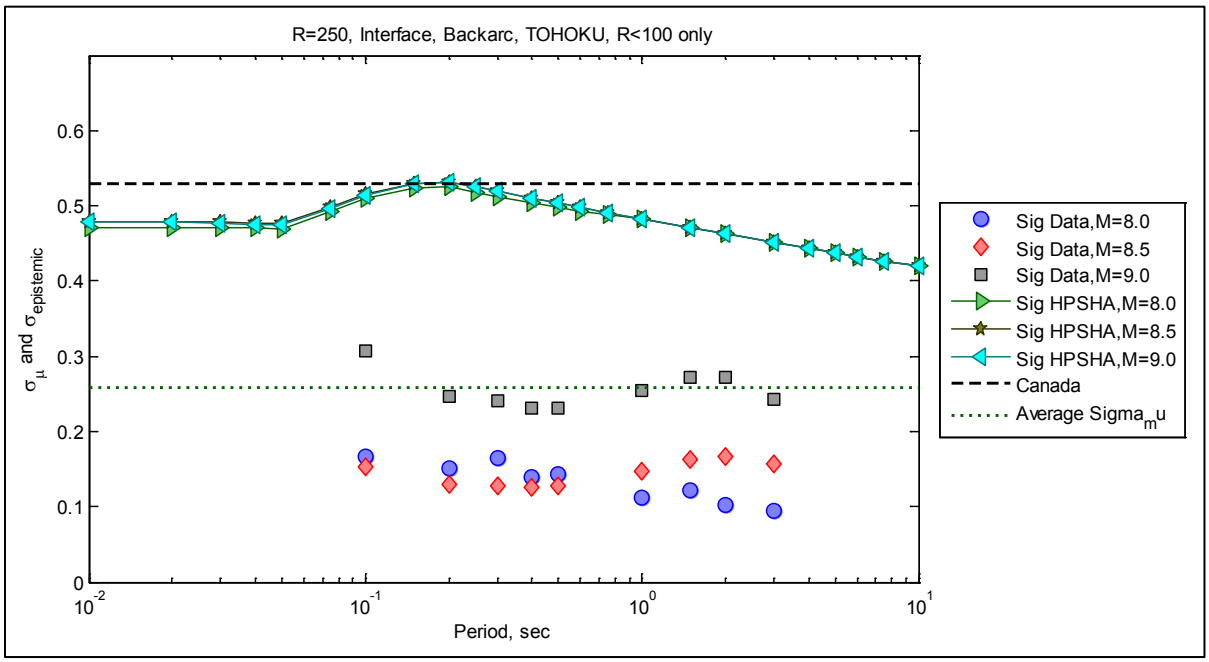

Figure 9.88. Epistemic uncertainty in the subduction logic tree (without considering host-to-target V_S factors). For comparison, the epistemic uncertainty suggested for subduction motions for the Canadian Building Code (Atkinson and Adams 2013) is also shown.

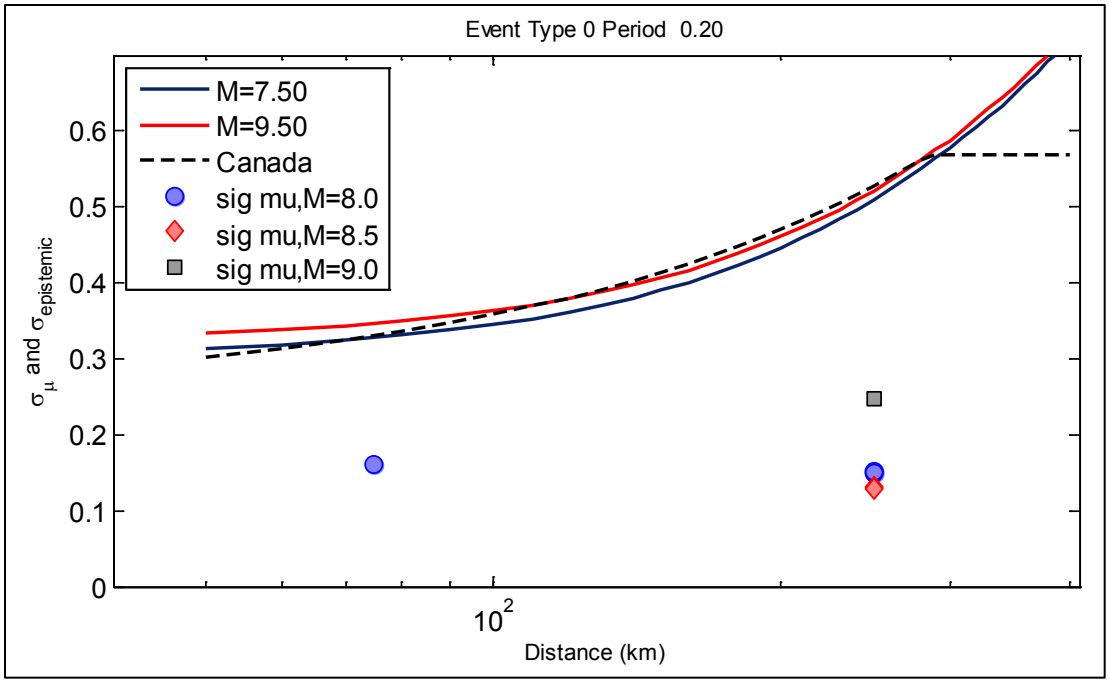

Figure 9.89. Epistemic uncertainty in the subduction logic tree (without considering host-to-target V_S factors) for a period of 0.2 seconds. For comparison, the epistemic uncertainty suggested for subduction motions for the Canadian Building Code (Atkinson and Adams 2013) is also shown.

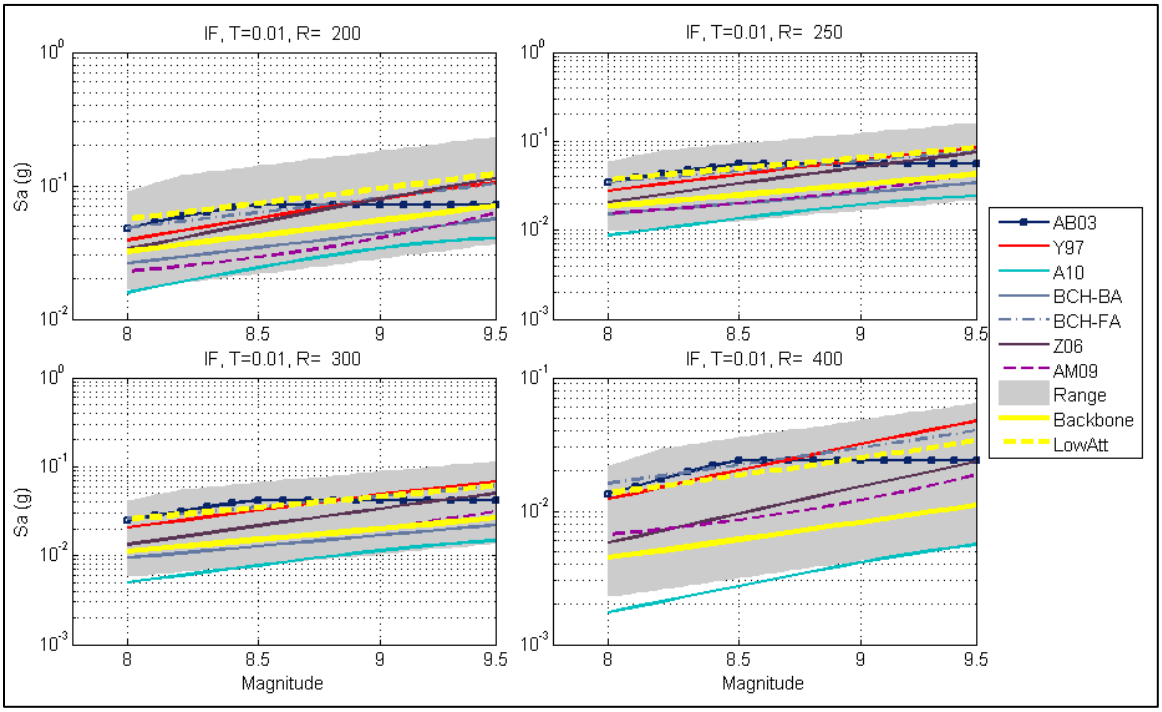

Figure 9.90. Proposed range of predicted values from the suite of GMPEs represented by the subduction logic tree for interface earthquakes. The central backbone model and the central low-attenuation branch are also plotted. The model abbreviations are given in Table 7.28. (1 of 5)

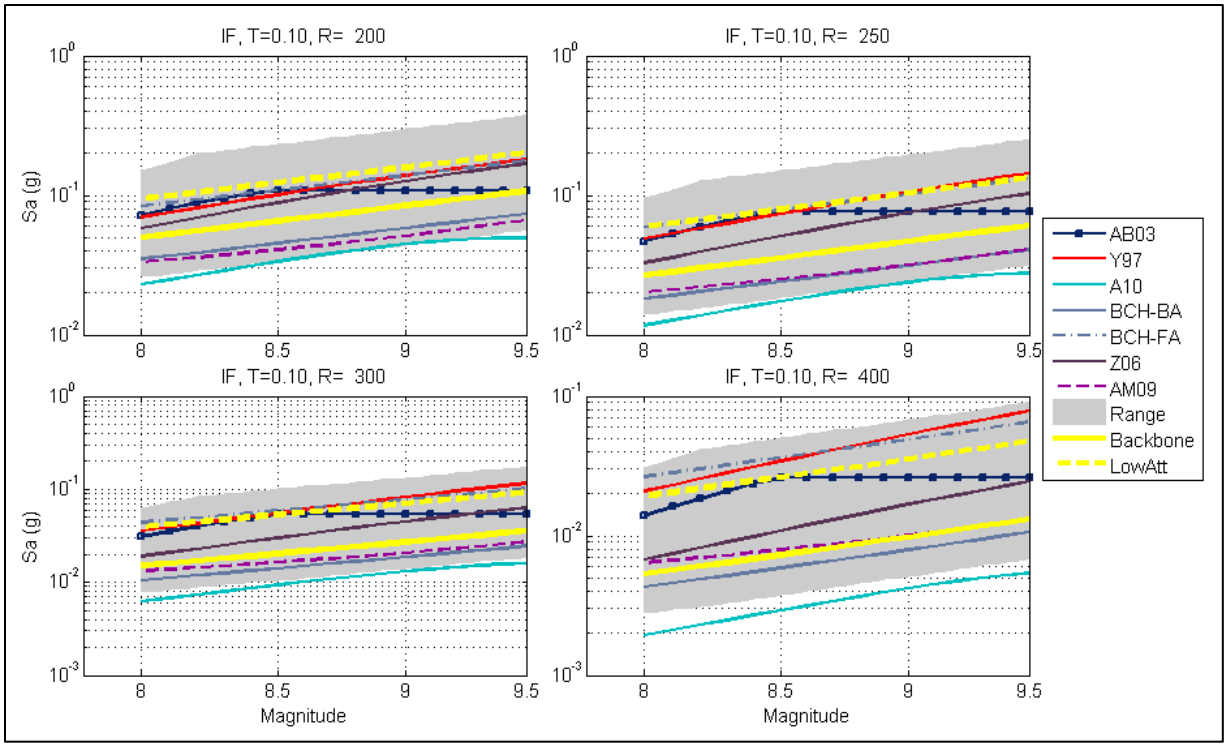

Figure 9.90. (contd) (2 of 5)

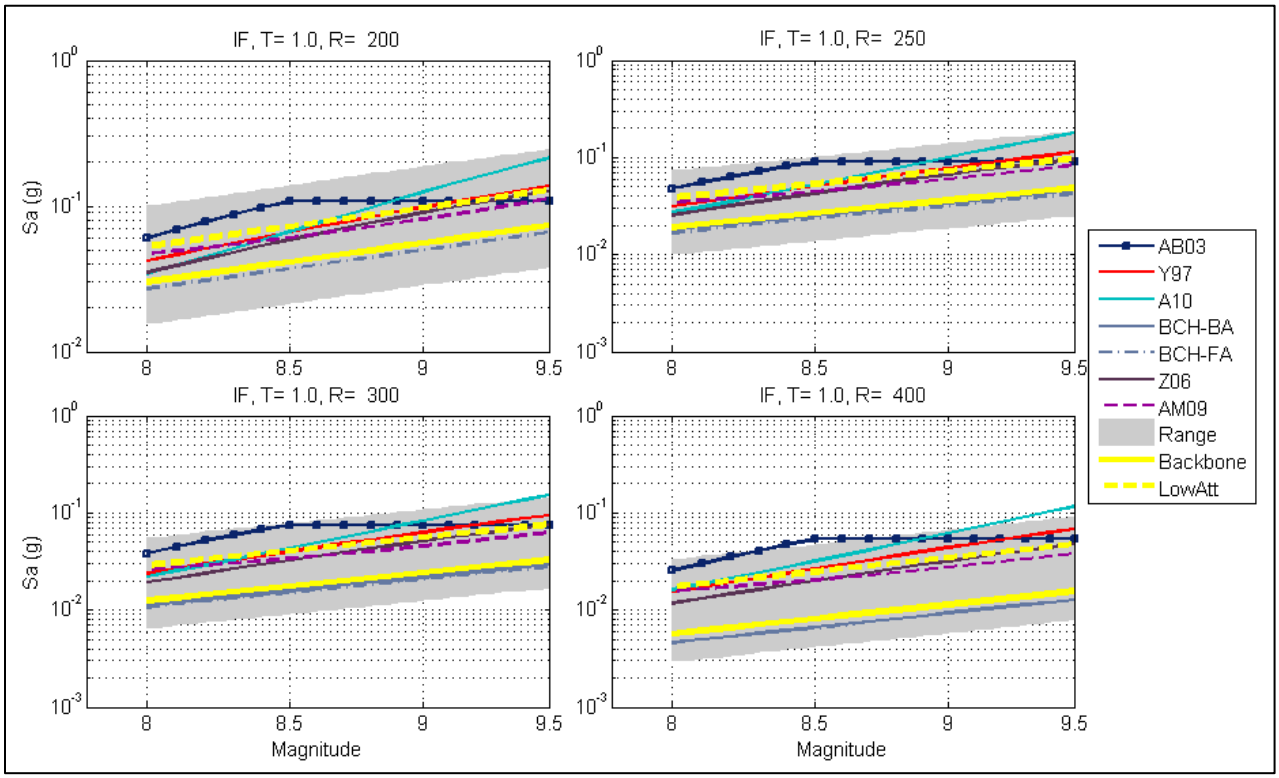

Figure 9.90. (contd) (3 of 5)

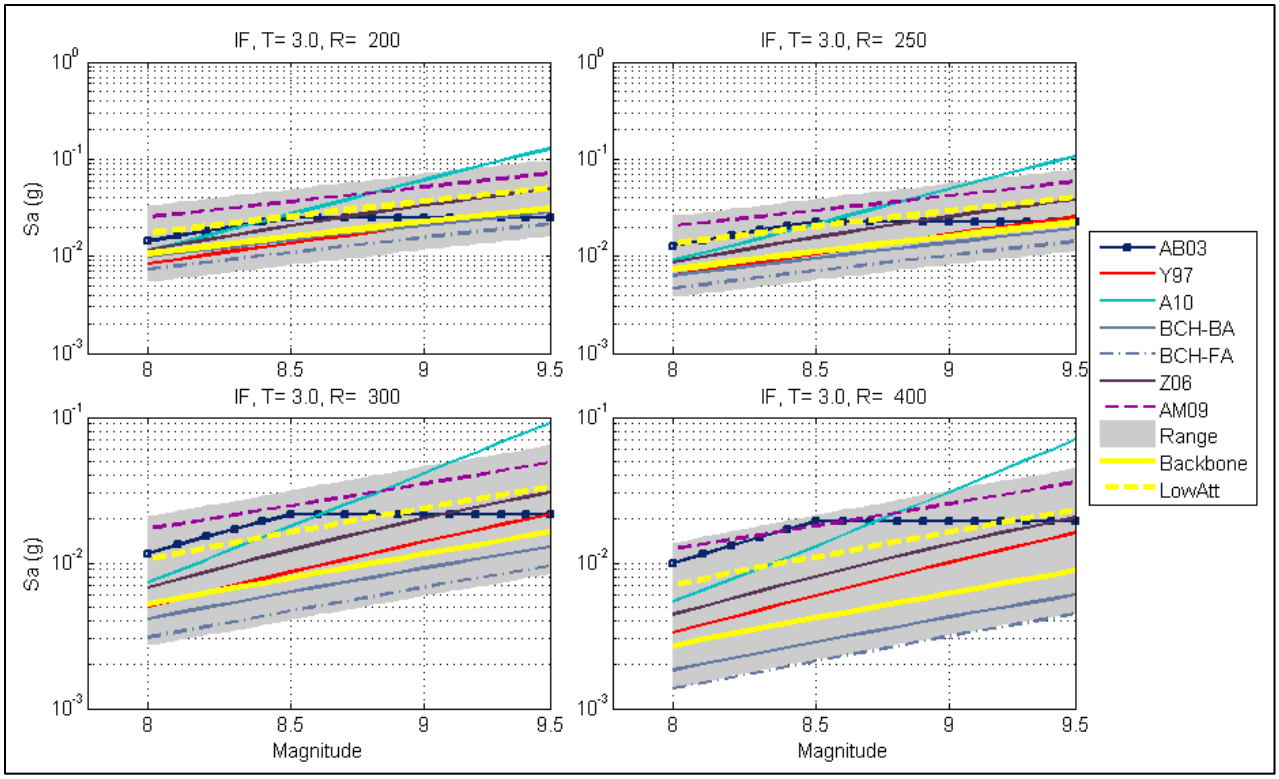

Figure 9.90. (contd) (4 of 5)

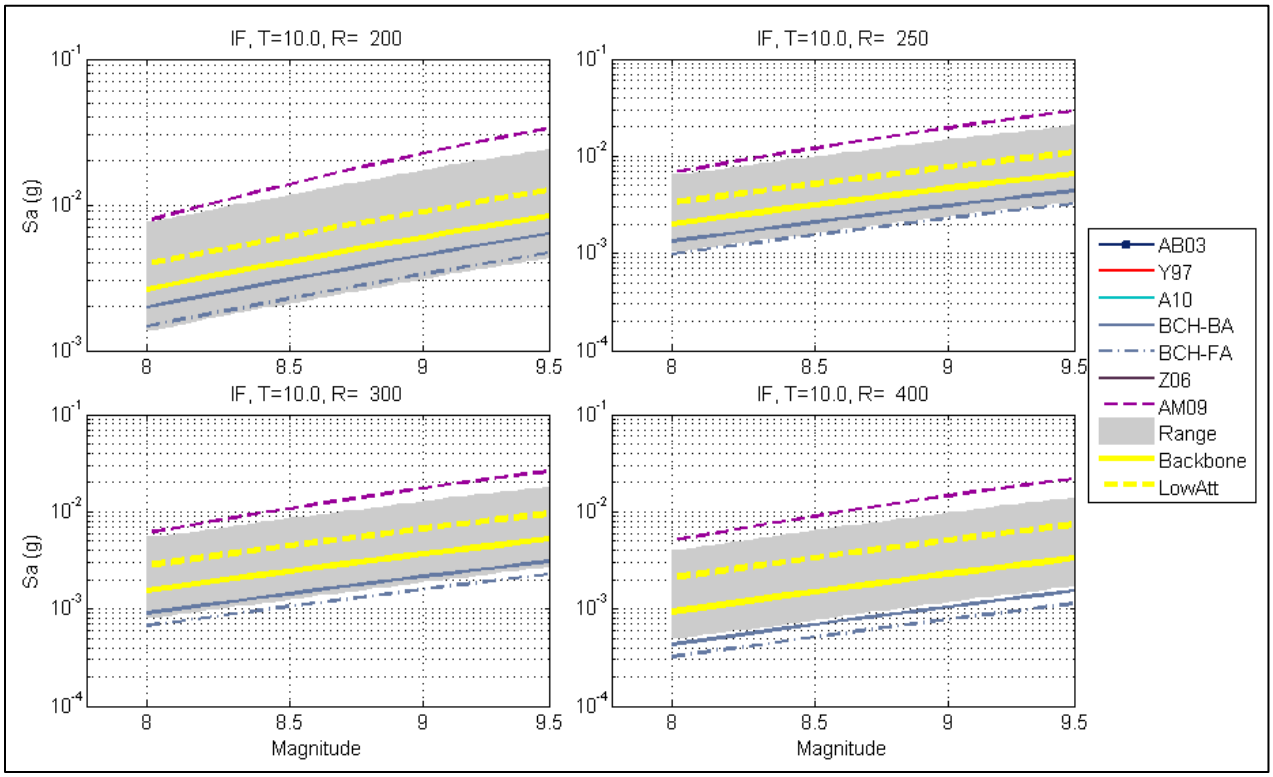

Figure 9.90. (contd) (5 of 5)

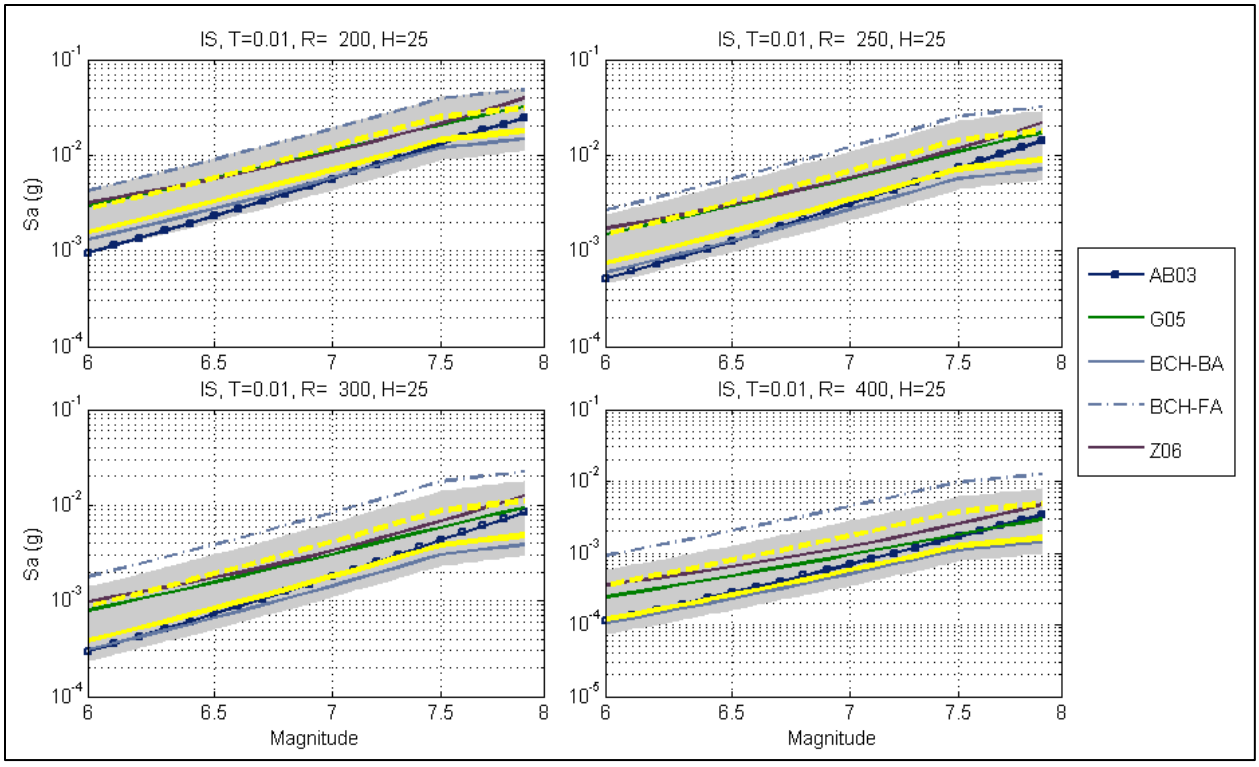

Figure 9.91. Proposed range of predicted values from the suite of GMPEs represented by the subduction logic tree for intraslab earthquakes. The central backbone model and the central low-attenuation branch are also plotted. The model abbreviations are given in Table 7.28. (1 of 5)

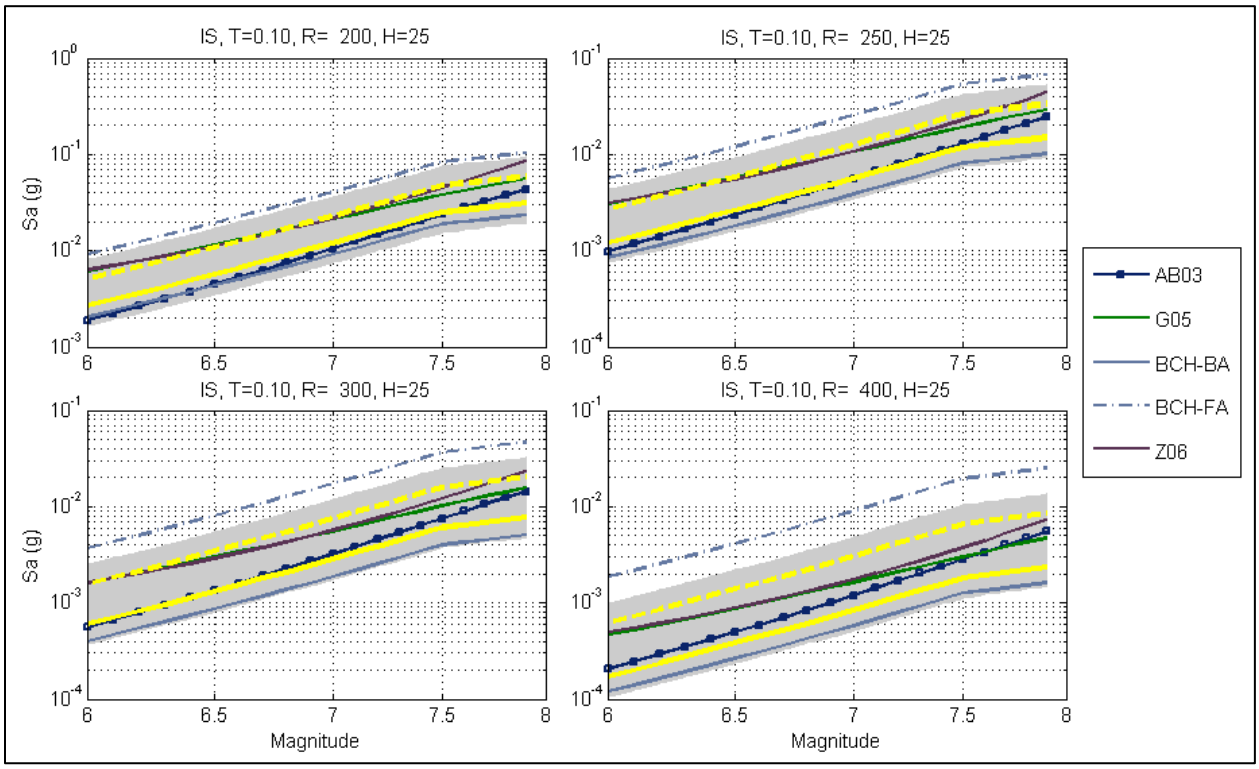

Figure 9.91. (contd) (2 of 5)

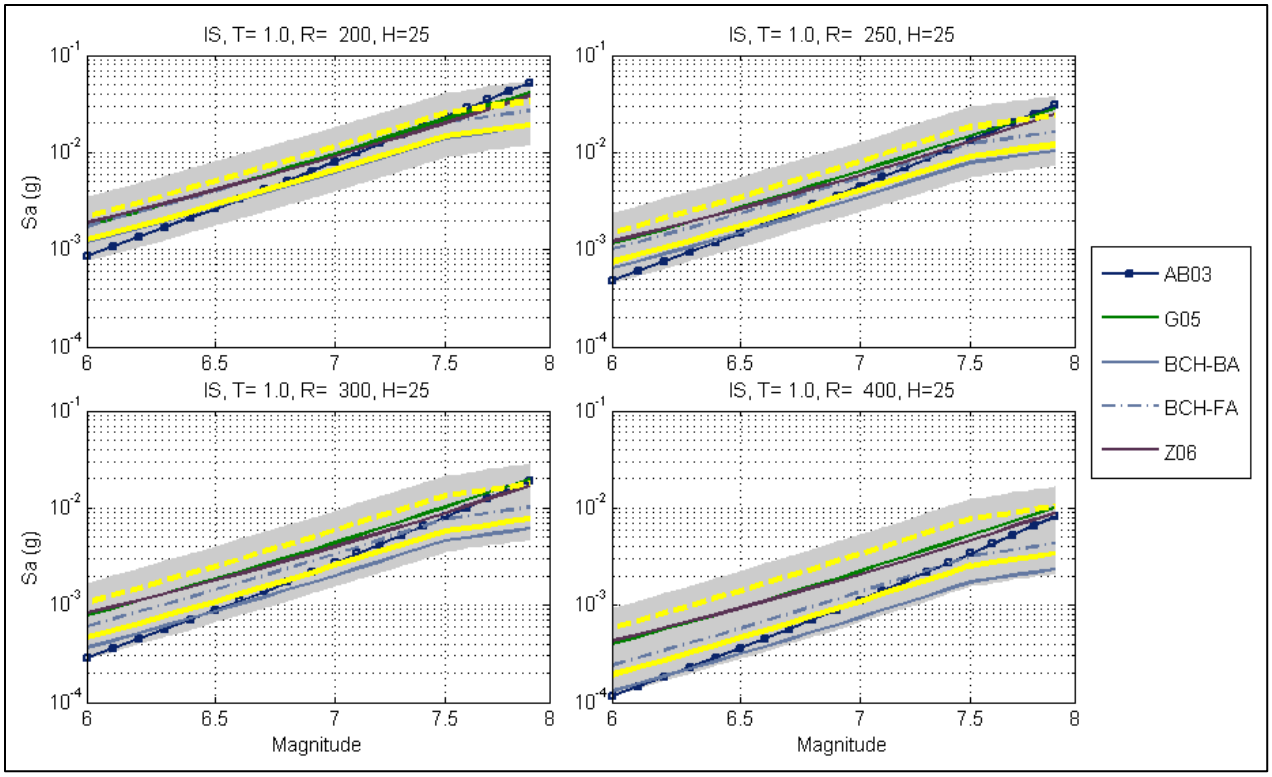

Figure 9.91. (contd) (3 of 5)

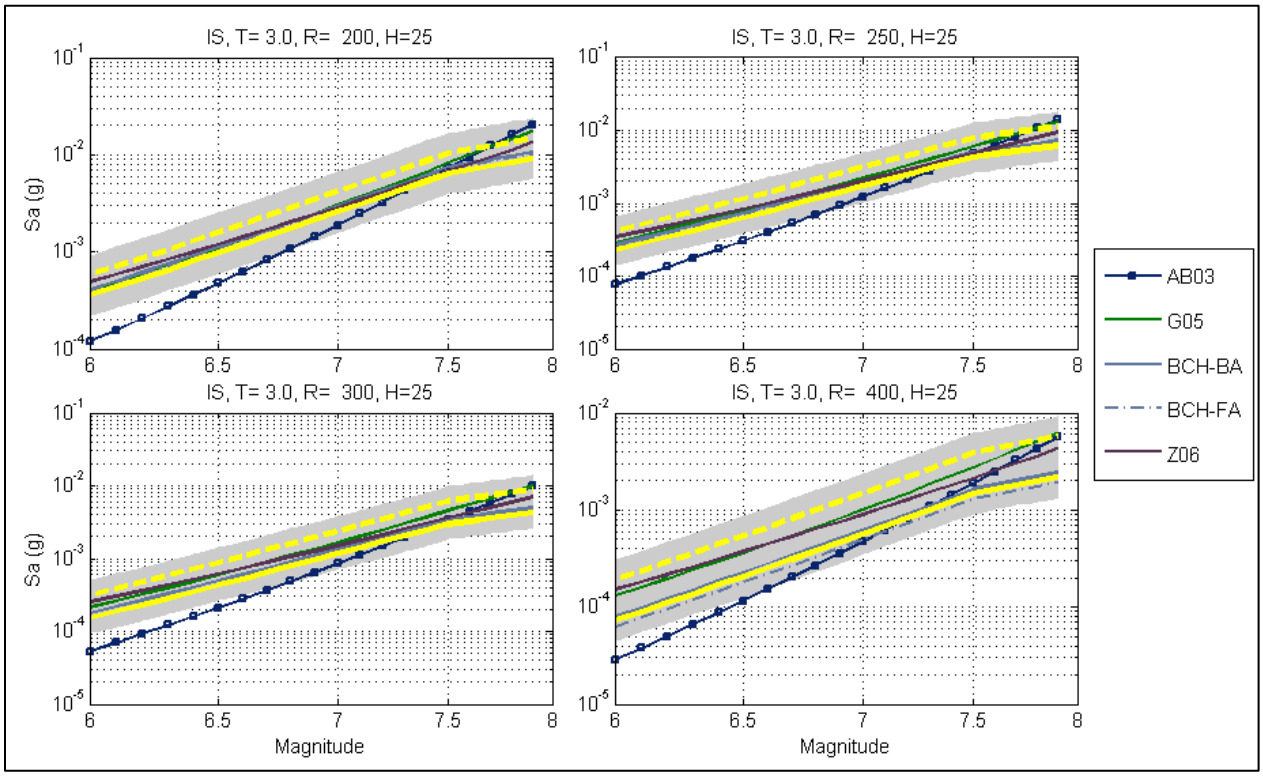

Figure 9.91. (contd) (4 of 5)

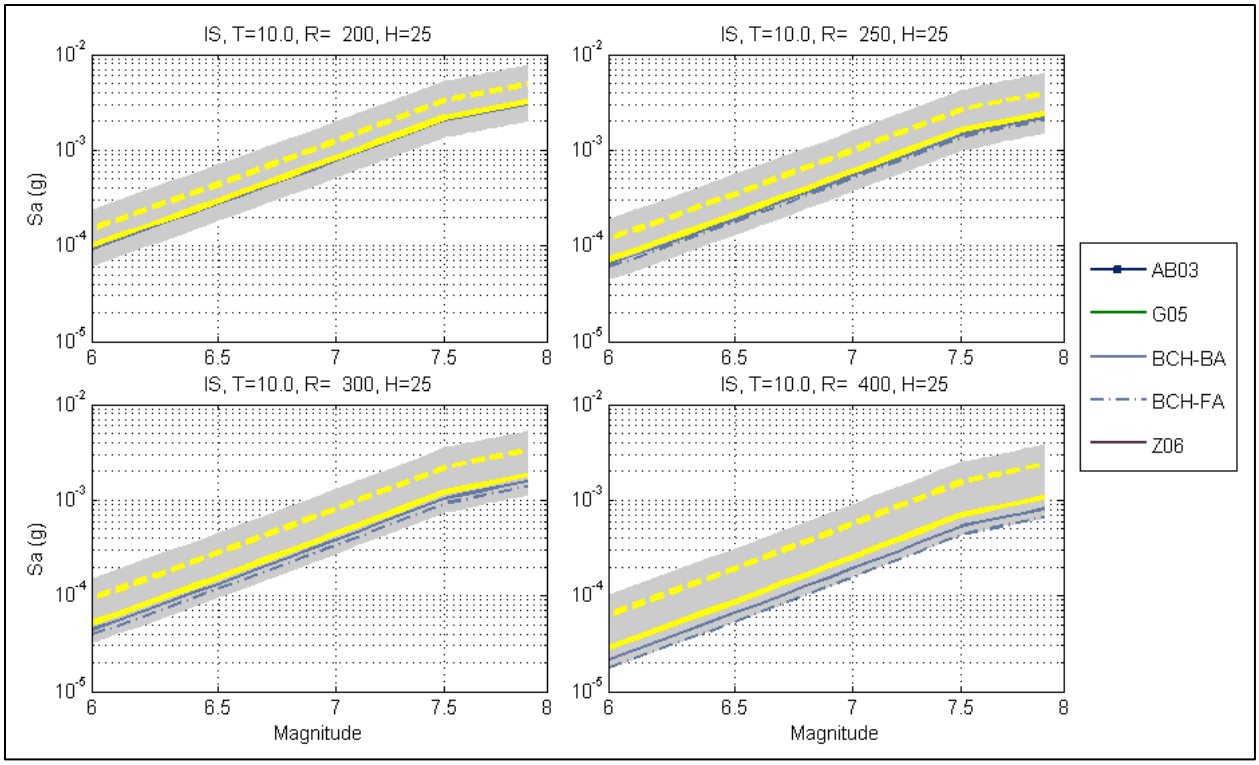

Figure 9.91. (contd) (5 of 5)

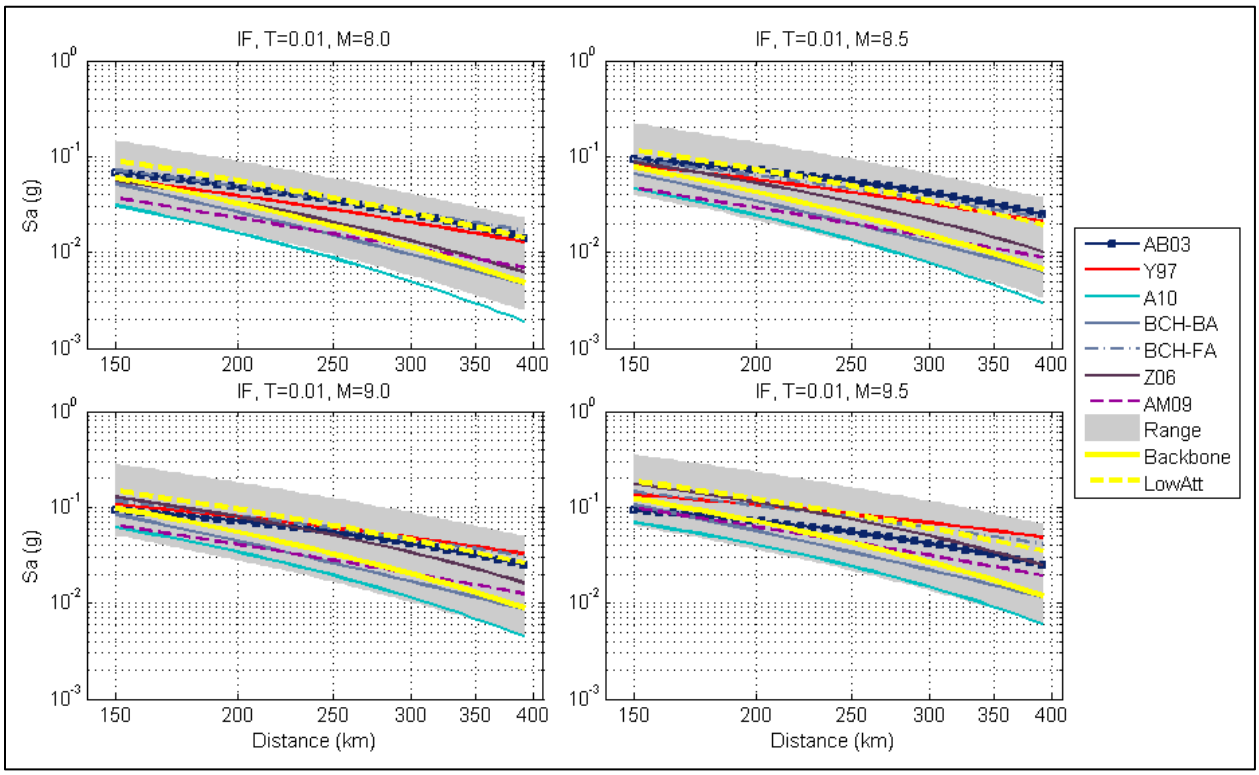

Figure 9.92. Proposed range of predicted values from the suite of GMPEs represented by the subduction logic tree for interface earthquakes. The central backbone model and the central low-attenuation branch are also plotted. The model abbreviations are given in Table 7.28. (1 of 5)

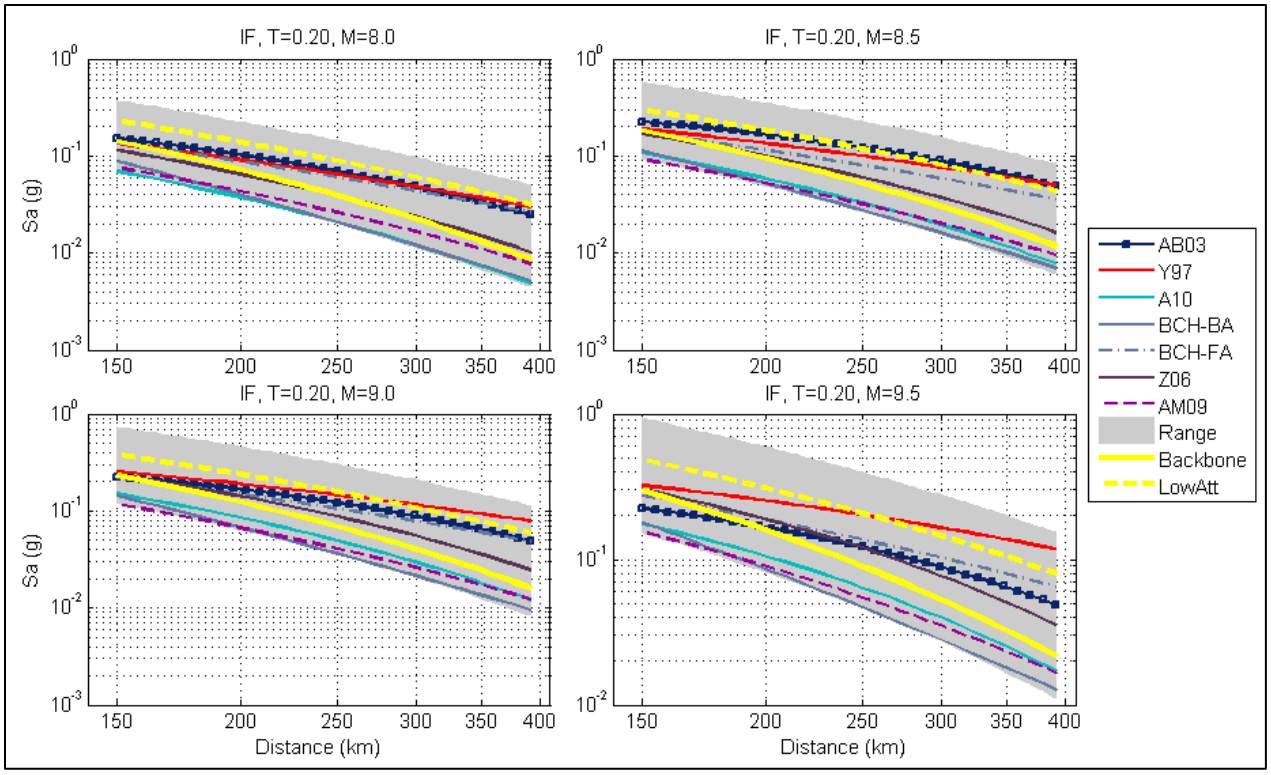

Figure 9.92. (contd) (2 of 5)

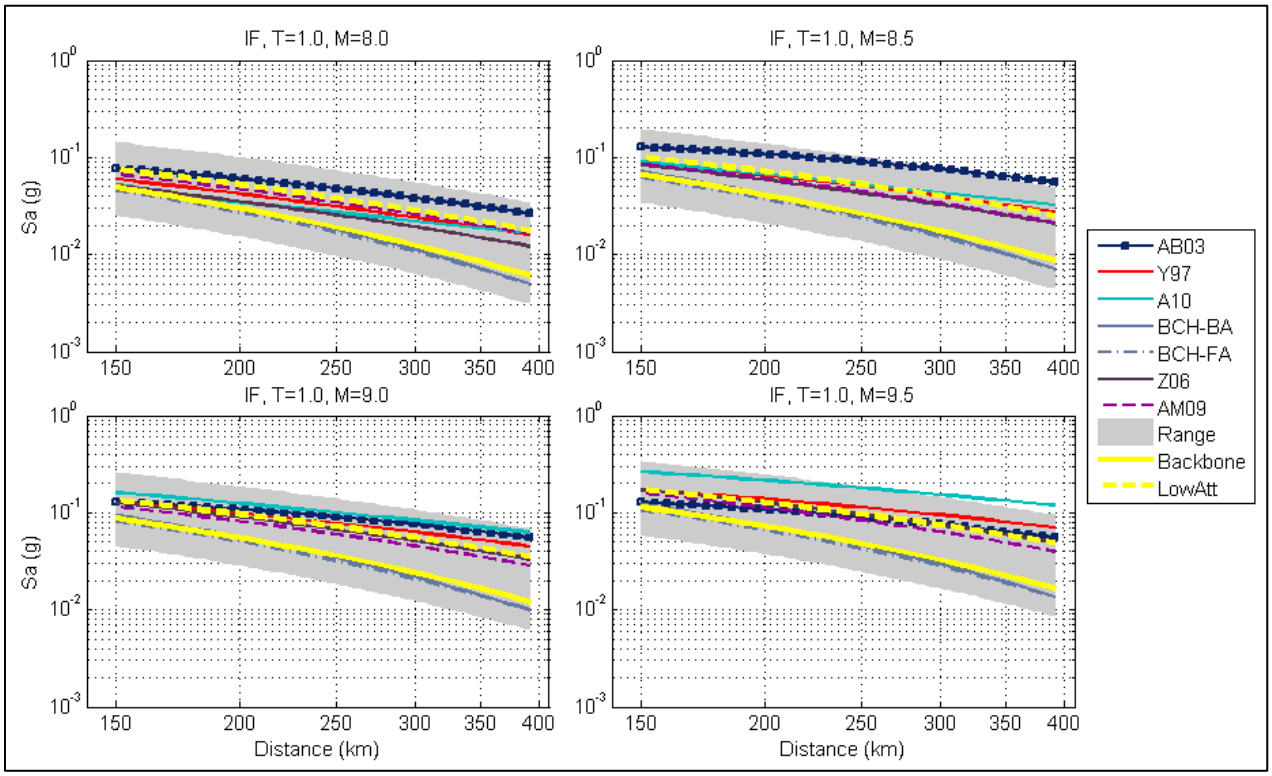

Figure 9.92. (contd) (3 of 5)

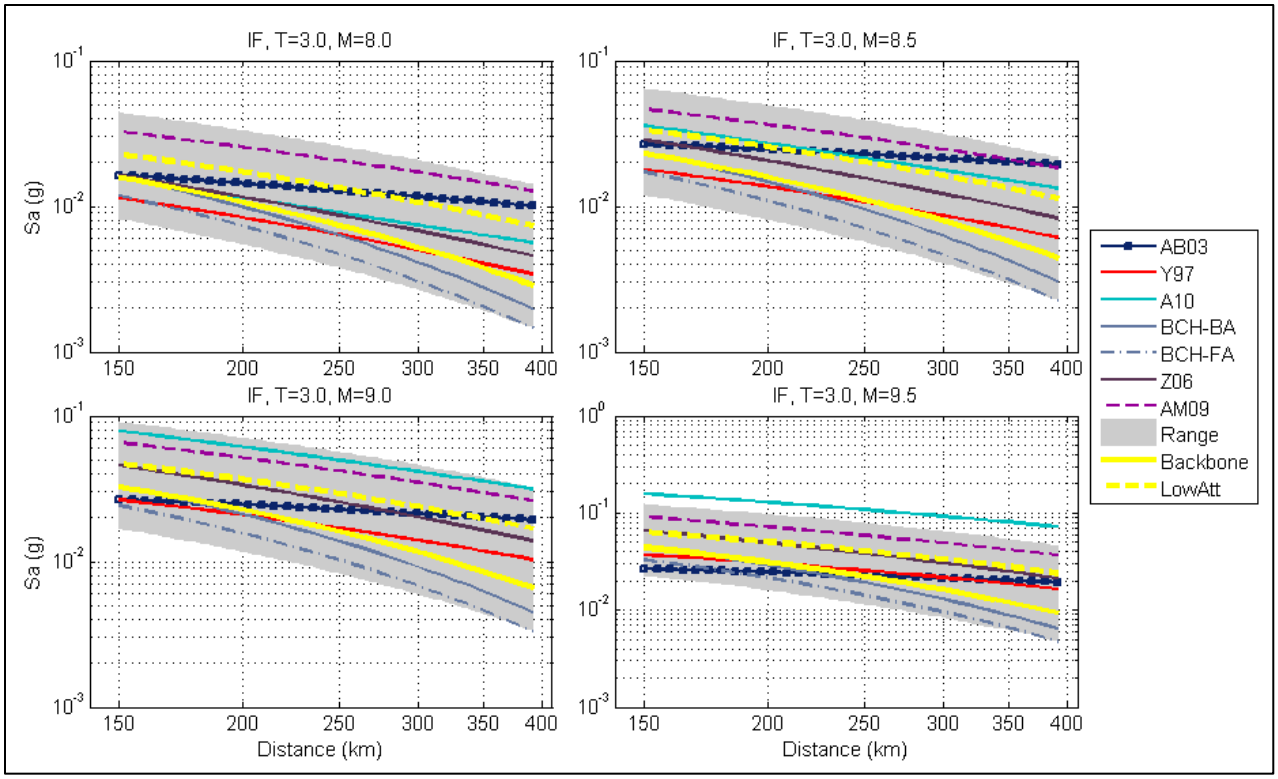

Figure 9.92. (contd) (4 of 5)

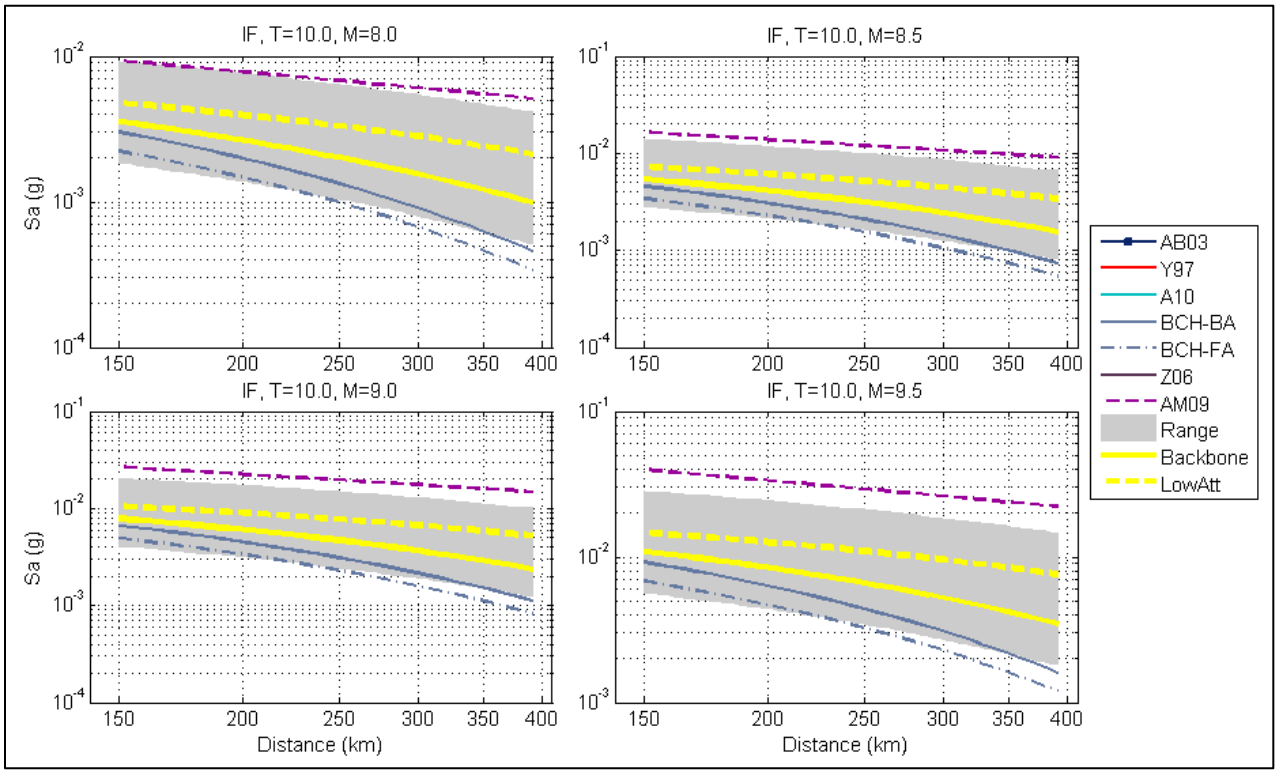

Figure 9.92. (contd) (5 of 5)

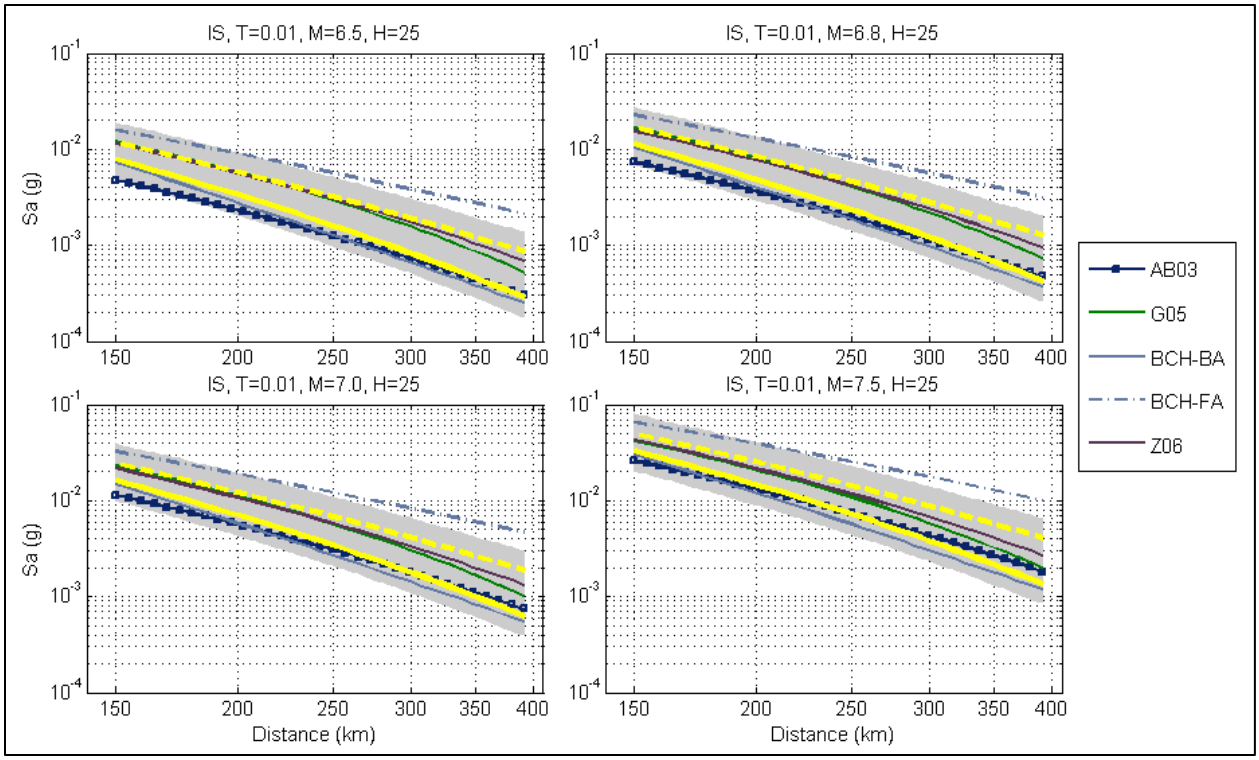

Figure 9.93. Proposed range of predicted values from the suite of GMPEs represented by the subduction logic tree for intraslab earthquakes. The central backbone model and the central low-attenuation branch are also plotted. The model abbreviations are given in Table 7.28. (1 of 5)

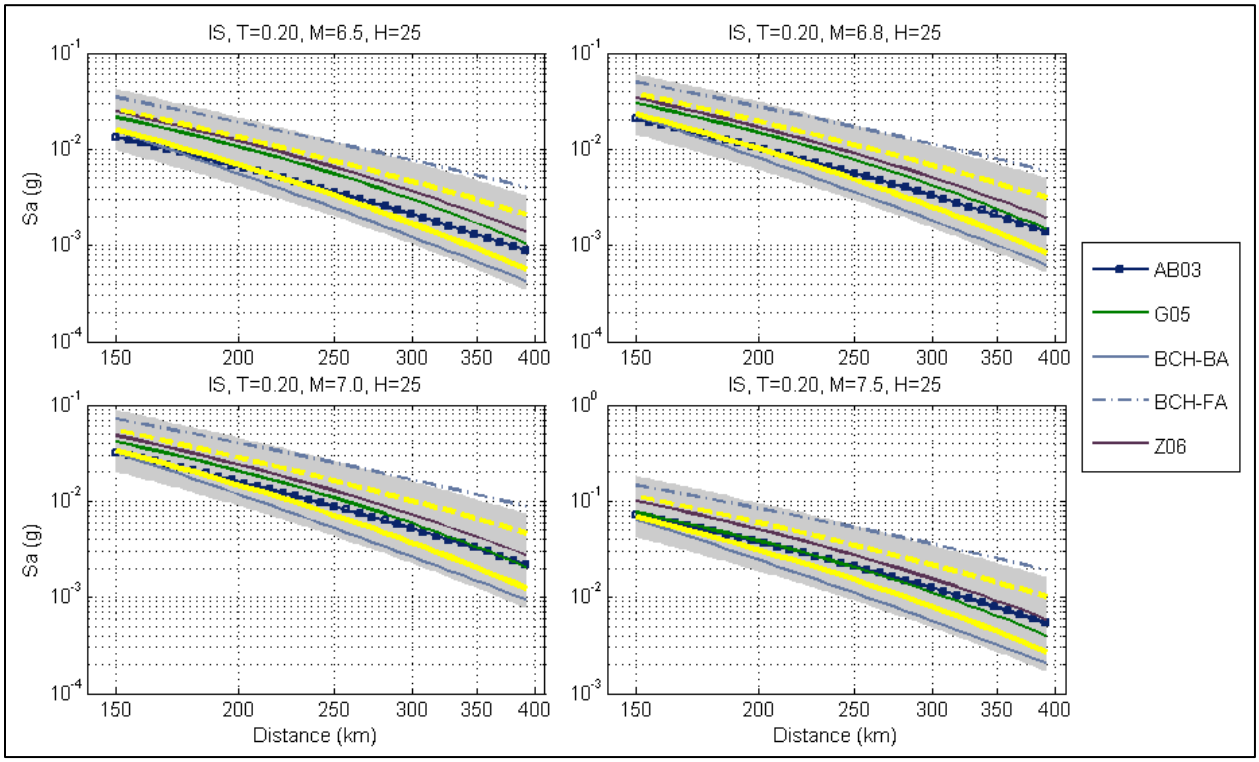

Figure 9.93. (contd) (2 of 5)

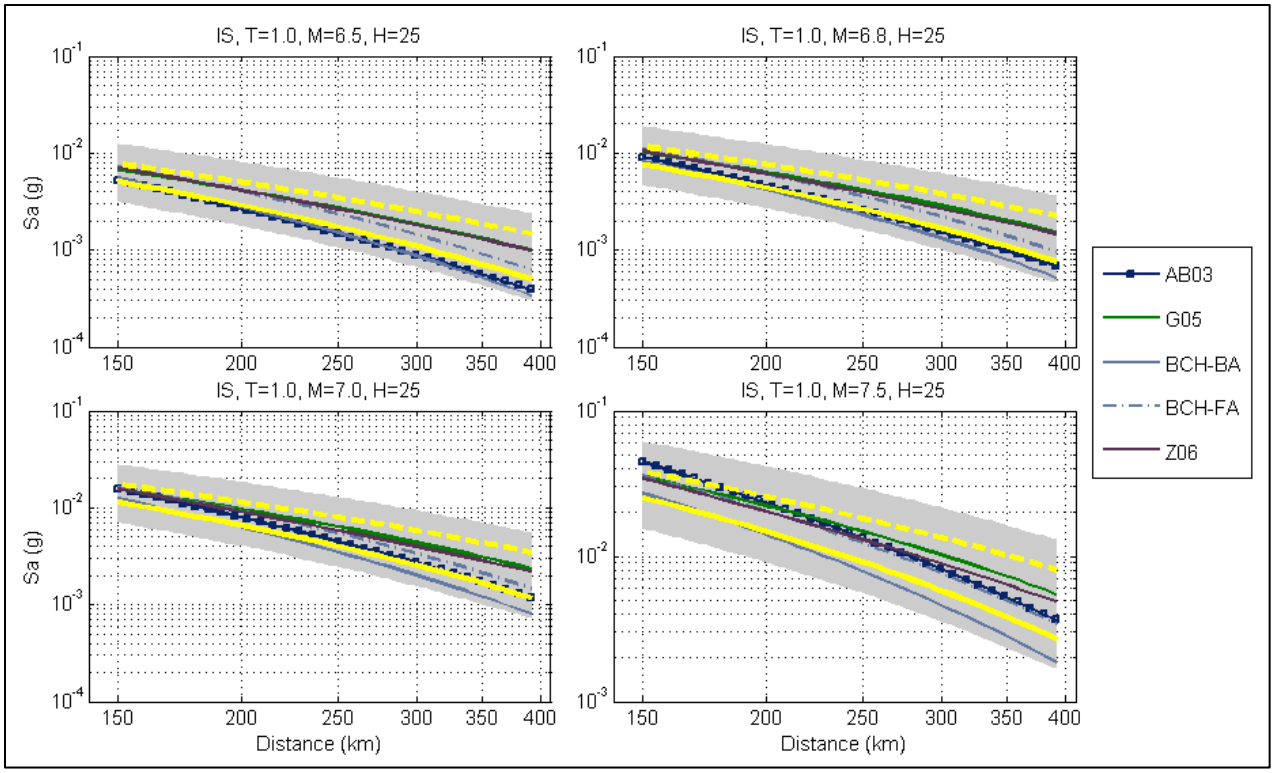

Figure 9.93. (contd) (3 of 5)

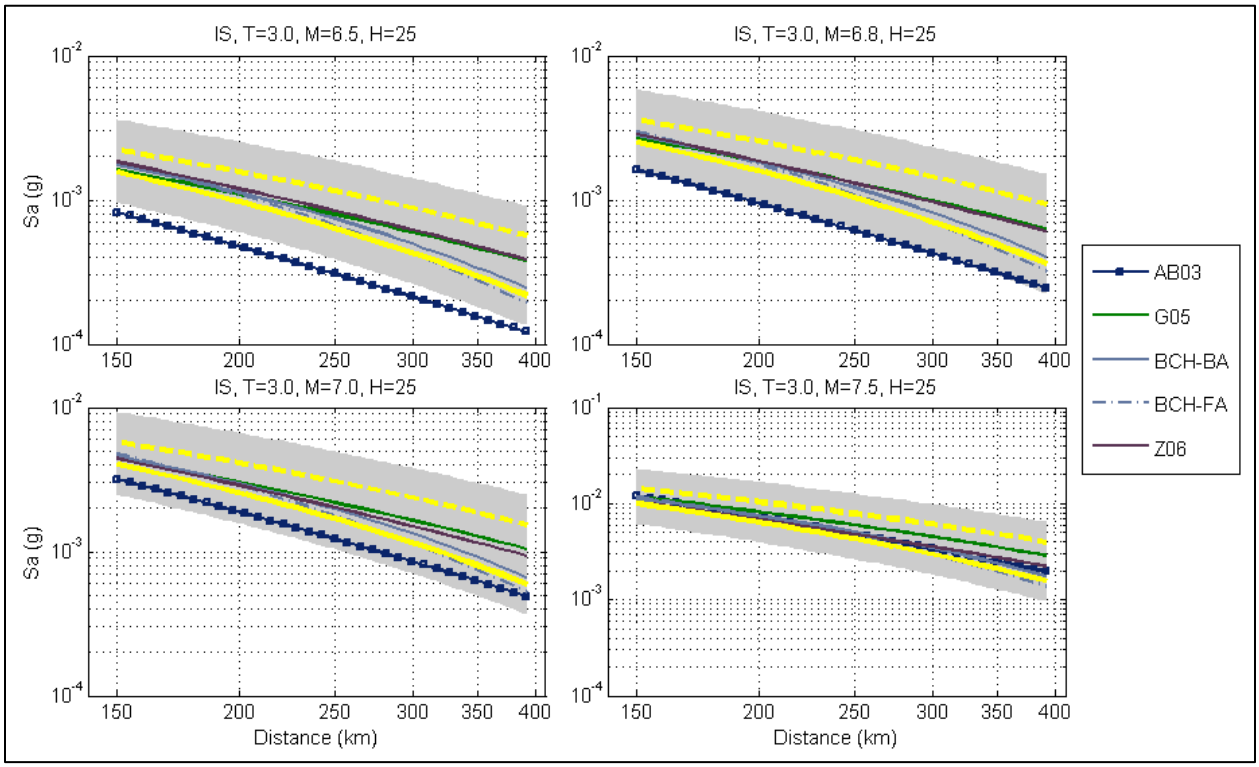

Figure 9.93. (contd) (4 of 5)

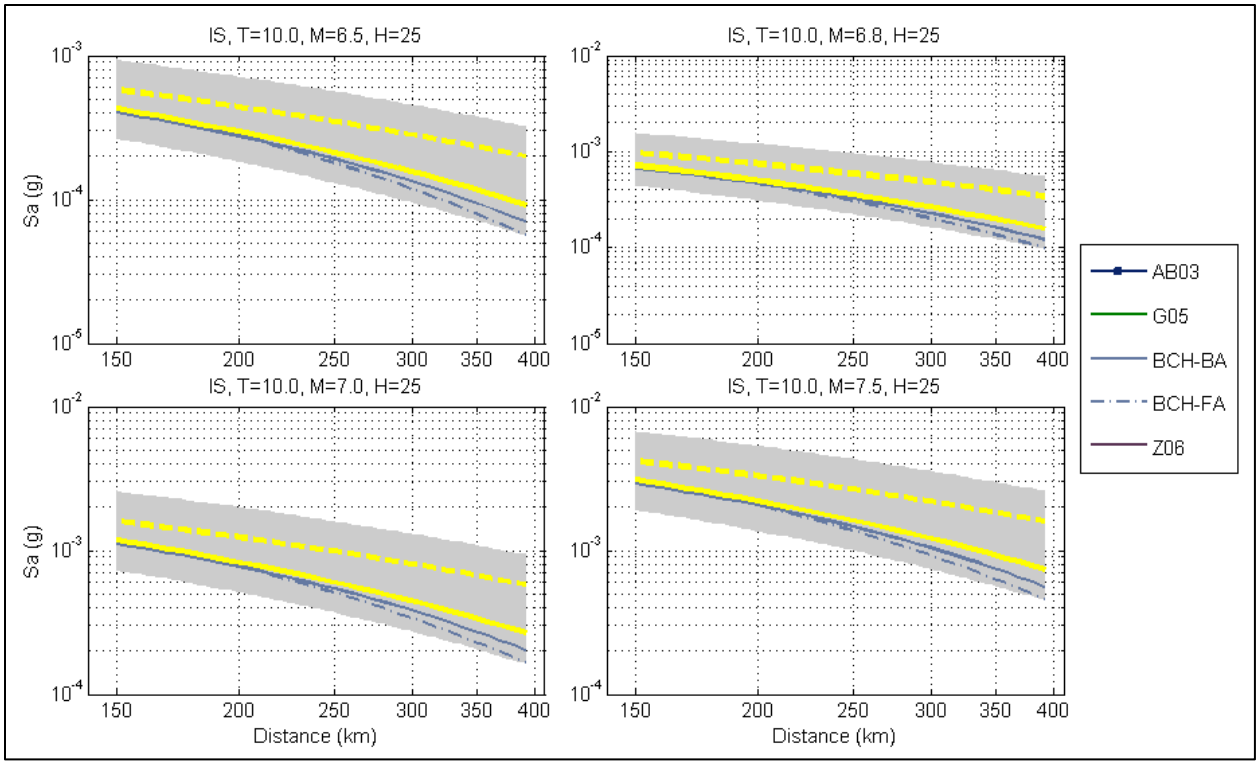

Figure 9.93. (contd) (5 of 5)

9.5 Sigma Models for Baserock Motions

The ground motion models constructed from the backbone models in Section 9.4 represent models for the median ground motion. In PSHAs, however, it is necessary to capture the full distribution of ground motions that may be generated by any given earthquake scenario. Most studies in the past have assumed that the distribution of spectral accelerations follows a lognormal distribution, which implies that the distribution is fully defined by the mean and the standard deviation (sigma) of the logarithm of spectral acceleration. More recent observations of dense data sets have indicated the possibility that the lognormal distribution does not fit well at large deviations from the mean; in these cases, we show that the distribution is better fit with a mixture model.

The sigma model for this project is built around the concept of partially non-ergodic seismic hazard analyses (Anderson and Brune 1999), which implies the use of a single-station sigma model. Section 9.5.1 introduces the concept of partially non-ergodic PSHA. This is followed by a discussion of the general framework of the sigma model (Section 9.5.2). The following two sections present the sigma model for crustal (Section 9.5.3) and subduction (Section 9.5.4) earthquakes. Section 9.5.5 presents the mixture model along with a justification for using this model. Finally, Section 9.5.6 discusses the minimum epistemic uncertainty that is needed in the site term computed in the downstream site response analyses. This is needed because the adoption of a single-station sigma is subject to certain conditions that for this project are not met at intermediate and long periods; because these reasons are related to site response issues, it was considered appropriate that this variability be captured in the site response calculations.

9.5.1 Background on Partially Non-Ergodic Sigma

In applying a GMPE to the assessment of seismic hazard at a specific location, the interest is in the variation of motions at this site due to different earthquakes that could occur over time. It is rare to have a recording from the location under study, and even in the few cases where such recordings exist they will cover at most a few decades. Therefore, PSHA generally invokes what is referred to as the ergodic assumption (Anderson and Brune 1999). The ergodic assumption essentially states that variability over space can be used as a substitute for variation over time, and it is invoked in practice because the sigma values calculated from regression analyses to develop GMPEs represent the variability across many different sites (and sometimes many regions). Where there are multiple recordings from individual sites, they display lower variability than indicated by the sigma values of GMPEs (e.g., Atkinson 2006), the reason being that there are components of the behavior at an individual site that are repeated in all cases and therefore do not contribute to variability. The effect is even more pronounced when multiple recordings from a single site of earthquakes are associated with a single seismogenic source because in that case there are repeatable effects of both the path and the site.

If the repeatable contributions to the seismic motion at the site of interest can be modeled through an appropriate adjustment to the median predictions, then the sigma value can be reduced—to a value referred to as "single-station sigma" (Atkinson 2006)—by an amount that reflects the variability of the site term. The single-station sigma concept can also be invoked if epistemic uncertainty in the site term is incorporated into the logic tree for the PSHA. In such a case, the net effect on the mean hazard is expected to be zero because the increased epistemic uncertainty balances the decreased aleatory variability, but it does mean that the division between randomness and uncertainty is being applied more completely. The ergodic assumption effectively folds the epistemic uncertainty regarding individual site terms into the sigma value of the GMPE, representing it as aleatory variability.

Single-station sigma is an important facet of the GMC logic tree for sigma; for that reason, some background for the concept is presented here. We follow the notation of Al Atik et al. (2010). Total residuals (Δ_{es}) are defined as the difference between recorded ground motions and the values predicted by a GMPE (in natural log units). Total residuals are separated into a between-event term (δB_e) and a within-event term (δW_{es}):

$$\Delta_{es} = \delta B_e + \delta W_{es} \tag{9.22}$$

where the subscripts denote an observation for event e at station s. The between-event and the within-event residuals have standard deviations τ and ϕ, respectively, and are assumed to be uncorrelated. The within-event residuals can in turn be separated into:

$$\delta W_{es} = \delta S2S_s + \delta WS_{es} \tag{9.23}$$

where $\delta S2S_s$ represents the systematic deviation of the observed ground motion at site s (e.g., the "site term") from the median event-corrected ground motion predicted by the GMPE, and δWS_{es} is the site- and event-corrected residual. The standard deviation of the $\delta S2S_s$ and δWS_{es} terms are denoted by ϕ_{S2S} and ϕ_{ss}, respectively. Table 9.10 lists the components of the total residual, their respective standard deviations, and the terminology used for each standard deviation component. Figure 9.94 graphically illustrates this breakdown of residuals.

Table 9.10. Terminology used for residual components and their standard deviations. *SD*( ) denotes the standard deviation operator.

Residual Component	Residual Notation	Standard Deviation Component	Definition of Standard Deviation Component
Total residual	Δ_{es}	Total or ergodic standard deviation	$\sigma_{ergodic} = SD(\Delta_{es})$
Event term	δB_e	Between-event (or inter-event) standard deviation (τ)	$\tau = SD(\delta B_e)$
Event-corrected residual	δW_{es}	Within-event (or intra-event) standard deviation (phi)	$\phi = SD(\delta W_{es})$
Site term	$\delta S2S_s$	Site-to-site variability	$\phi_{S2S} = SD(\delta S2S_s)$
Site- and event-corrected residual	δWS_{es}	Event-corrected single-station standard deviation (single-station phi)	$\phi_{ss} = SD(\delta WS_{es})$

The sigma model for this project is developed within the paradigm of a "partially non-ergodic" PSHA approach (also called a *single-station sigma* approach). In traditional (e.g., ergodic) PSHA, all of the residual components are considered as part of the aleatory variability, such that:

$$\sigma_{ergodic} = \sqrt{\tau^2 + \phi_{ss}^2 + \phi_{S2S}^2} \tag{9.24}$$

In the partially non-ergodic approach, the site term ($\delta S2S_s$) is assumed to be known (or knowable) and hence its standard deviation (ϕ_{S2S}) is excluded from Equation 9.24. In this case, the standard deviation is known as the *single-station standard deviation* and is given by:

$$\sigma_{ss} = \sqrt{\tau^2 + \phi_{ss}^2} \tag{9.25}$$

The principal motivation for adopting a single-station sigma approach for this project is to avoid double counting uncertainty. This double counting would result if the site-to-site variability (ϕ_{S2S}) is included in the total sigma (see Equation 9.24) and in addition the site term is assigned an epistemic uncertainty. The latter epistemic uncertainty results from epistemic uncertainty assigned to parameters of the V_S-kappa correction and the uncertainty in the site amplification factor. The epistemic uncertainty in V_S-kappa correction factors is generally accounted for in the median logic tree and the uncertainty in the site amplification factor is generally captured through randomization of the properties of the site response analyses.

An additional motivation for the adoption of a single-station sigma approach is that the value of single-station phi (ϕ_{ss}) has proven to be relatively constant across different regions and tectonic environments. Figure 7.70 shows a comparison of the values of single-station phi and ergodic phi for five different regions. Observe that the variability of the ergodic values across tectonic regions is higher than the variability observed in the single-station values. The lack of regional dependence of the single-station phi implies that they are more readily "exportable" to different regions, and that global data sets can be used to estimate their values.

The basic requirements to apply a partially non-ergodic PSHA are as follows:

1. The median value of the site term ($\delta S2S_s$) must be properly estimated for the site under analysis.
2. The epistemic uncertainty on the value of the site term must be fully accounted for.
3. The epistemic uncertainty on the single-station sigma must be accounted for.

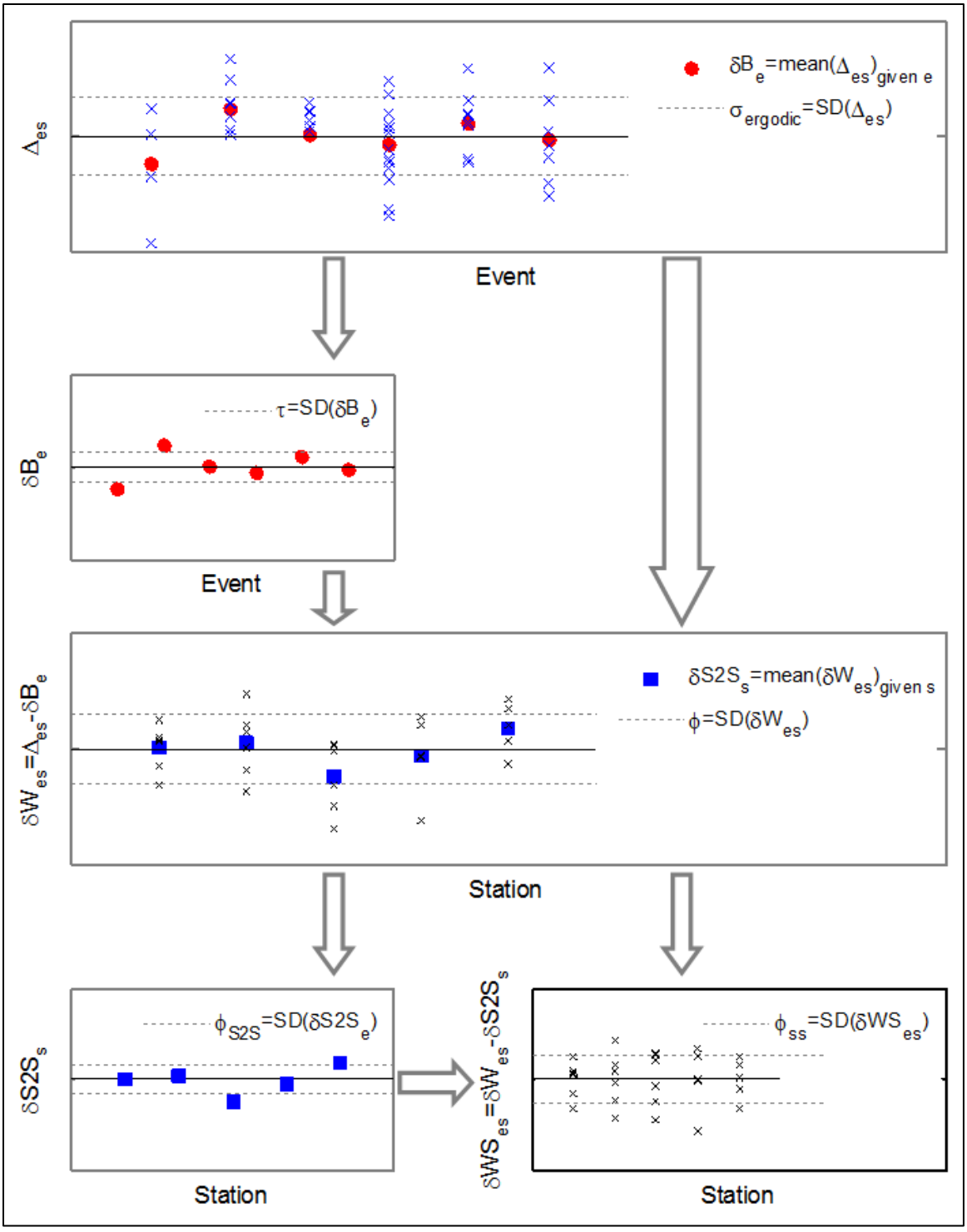

Figure 9.94. Schematic representation of the breakdown of residuals leading to the single-station phi ($\boldsymbol{\phi_{ss}}$).

For the Hanford PSHA project, Requirement 1 is satisfied because a site-specific correction is applied to the backbone GMPEs. In particular, the site term is estimated through the V_S-kappa correction and the site response calculations. The epistemic uncertainty in the site term (Requirement 2) is accounted for

through the use of branches in the median logic tree for the V_S-kappa correction factors (Section 9.3) and by the inclusion of variability of the site amplification factor. The latter is accounted for by including uncertainty in the characterization of the SMB stack (Section 9.6) and in the characterization of the suprabasalt sediments in the downstream site response analyses. To ensure that enough uncertainty is captured in the site amplification factors, a minimum level of uncertainty is prescribed (Section 9.5.6). Requirement 3 will be accounted for by including branches to the sigma logic-tree model that will represent the epistemic uncertainty in the sigma model.

9.5.2 Framework for the Sigma Model

A separate sigma model is constructed for crustal and subduction earthquakes. Both models have two main branches in the logic tree, each representing different assumptions about the shape of the distribution of spectral accelerations residuals: one branch for a normal distribution (normal distribution of the logarithm of spectral accelerations, which imply a lognormal distribution of spectral accelerations), and one branch for a mixture model. A second level of the sigma logic tree represents the epistemic uncertainty in the standard deviations with three branches (high, central, and low). As discussed in the previous section, the incorporation of the epistemic uncertainty in the single-station standard deviation is a necessary requirement for the use of single-station sigma. Figure 9.95 shows the sigma logic tree applicable to both crustal and subduction earthquakes.

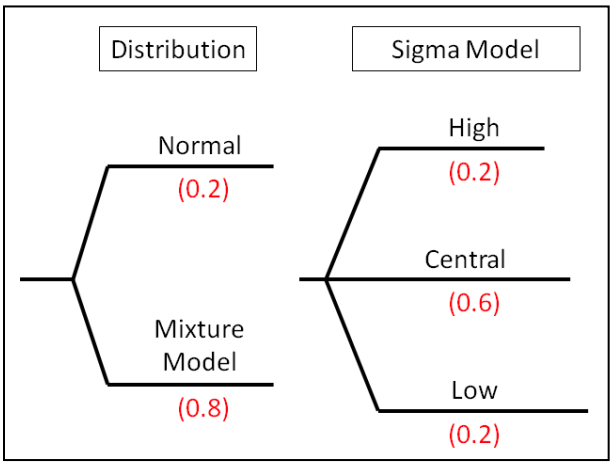

Figure 9.95. Logic tree for sigmas.

Single-station sigma is adopted for the sigma model. Single-station sigma is built from a model for between-event standard deviation (also known as inter-event standard deviation, or simply τ) and a model for event- and site-corrected standard deviation (heretofore referred to as single-station phi or ϕ_{ss}; see Equation 9.25). The models for crustal earthquakes are discussed in Section 9.5.3, and those for subduction earthquakes are discussed in Section 9.5.4. Each of these sections presents separately a model for τ and a model for ϕ_{ss}. The mixture model is based on the sigmas of the normal models and is discussed in Section 9.5.5.

The models for the high, central, and low branches (Figure 9.95) are obtained by assuming that the variance of ground motion residuals (σ^2) follows a scaled chi-squared distribution (Ang and Tang 2007) with mean given by σ^2 and standard deviation given by σ_{σ^2}. The standard deviation of the variance of

the total residuals (σ_{σ^2}) is in turn built from the standard deviation of the variance of between-event residuals (σ_{τ^2}) and the standard deviation of the variance of site- and event-corrected residuals ($\sigma_{\phi_{ss}^2}$):

$$\sigma_{\sigma^2} = \sqrt{\left[\sigma_{\phi_{ss}^2}\right]^2 + [\sigma_{\tau^2}]^2} \tag{9.26}$$

The models for the standard deviation of τ^2 and ϕ_{ss}^2 are discussed for the crustal and subduction models in Sections 9.5.3 and 9.5.4, respectively. The central branch is the mean value of σ. The high and low branches are obtained by first computing the 95th and 5th percentile of a scaled Chi-square distribution with mean σ^2 and standard deviation σ_{σ^2}, and then taking the square root of these values. This is expressed mathematically as follows:

$$\begin{aligned} \sigma_{High} &= \sqrt{c\ \chi_{2,k}^{-1}(0.95)} \\ \sigma_{Low} &= \sqrt{c\ \chi_{2,k}^{-1}(0.05)} \end{aligned} \tag{9.27}$$

where $\chi_{2,k}^{-1}(x)$ is the inverse of the Chi-square distribution with *k* degrees of freedom and *c* is a scaling parameter; *k* and *c* are given by

$$\begin{aligned} c &= \frac{(\sigma_{\sigma^2})^2}{2\sigma^2} \\ k &= \frac{2\sigma^4}{(\sigma_{\sigma^2})^2} \end{aligned} \tag{9.28}$$

The use of Equation 9.26 assumes that the uncertainties in ϕ_{ss}^2 and τ^2 are uncorrelated; analyses of the CY14 residuals proved this to be a valid assumption. The sigma logic tree (Figure 9.95) includes the weights assigned by the GMC TI Team. The weights on the normal and mixture models (0.2 and 0.8, respectively) reflect the observation that the residuals in the NGA and other databases are better fit by the mixture model at large values of epsilon (at other values the model is no different from a model that assumes a normal distribution). This is discussed further in Section 9.5.5. The weights for the high, central, and low models reflect the weights corresponding to a discrete three-point representation of the assumed continuous distribution.

9.5.3 Model for Crustal Ground Motions

The sigma model for crustal ground motions is presented in this section. The model is built from the components of Equation 9.5.1-4 (ϕ_{ss} and τ). This section presents both the median model and the model for the standard deviation of the τ^2 (σ_{τ^2}). The latter is needed to build the branches of the sigma logic tree using Equations 9.26 through 9.28.

9.5.3.1 Tau Model

9.5.3.1.1 Central Tau Model

The model for the median value of τ (the Central Tau model) was built from four of the NGA-West2 models for τ (Abrahamson et al. 2014b; Boore et al. 2014; Campbell and Bozorgnia 2014, Chiou and Youngs 2014). These equations were judged by the GMC TI Team to be mature relationships using a large and uniformly processed data set and hence are a good representation of the values of inter-event variability for crustal earthquakes.

To define an average τ model from the four selected models, it is convenient to adopt a functional form for the magnitude dependence of the model and for the shape of the smoothing function across periods. To inform the magnitude dependence of τ, the four selected models were plotted for various magnitudes in Figure 9.96 (shown for T = 1 sec, similar plots were made for other oscillator periods) along with the mean of the four models. The τ values shown in Figure 9.96a for the CB14 and the BSSA14 models are the published values. For the ASK14 and the CY14 models, the τ values prior to smoothing across periods were plotted (these values were obtained from Bob Youngs, from the GMC TI Team, and Ronnie Kamai, personal communication 2014, both developers of these models). An important consideration is that all statistics on the τ values are conducted on the square of τ (i.e., the variance), because it is mathematically appropriate to average variances and not standard deviations. The results, however, are plotted as τ for simplicity.

All four selected NGA-West2 models are heteroskedastic (i.e., the value of τ varies with magnitude). Moreover, all four models have a bilinear shape in the magnitude range of interest to this project (Figure 9.96a). The magnitude at which there are breaks in the magnitude dependence of τ (e.g., τ goes from varying linearly with **M** to constant) changes for each of the models. As a result, the mean of the four models has four linear segments (Figure 9.96a). To simplify the final model into a bilinear model, two magnitude breakpoints were selected: **M** = 5.0 and **M** = 7.0; however, the model parameters were selected by fitting the bilinear model to the average of the four NGA models at **M** = 5.25 and **M** = 7.0. Using **M** = 5.25 in place of **M** = 5 to fit the model minimizes the differences between the proposed bilinear model and the mean model from the four selected GMPEs. The selected model is slightly conservative (i.e., overestimates the average τ from the four NGA models) for magnitudes between 5.25 and 7.0 and is slightly unconservative for **M** < 5.25, a magnitude range that, according to the hazard sensitivity analyses, does not contribute significantly to hazard. Hence, the final τ model is a bilinear model that is expressed as follows:

$$\tau(M) = \begin{cases} \tau_1 + \frac{M-5}{2}(\tau_2 - \tau_1) & for\ M < 7 \\ \tau_2 & for\ M \geq 7 \end{cases} \quad (9.29)$$

where τ_1 and τ_2 are parameters of the model that corresponds to the value of τ at **M** = 5 and **M** = 7, respectively. These parameters are period-dependent (the period dependence is not shown in Equation 9.29 for simplicity).

The parameter τ_2 can be directly calibrated from the mean of the four selected models for **M** = 7 (after smoothing across periods). As indicated before, for computing the parameter τ_1, instead of directly

computing the average of the selected models at **M** = 5 we chose to compute an intermediate parameter at **M** = 5.25. Computing the average τ at this magnitude avoids over-estimating the value of τ for 5.0 < **M** < 7.0 (Figure 9.96b). While the model is constrained at **M** = 5.25, the parameters of the model (Equation 9.29) are, for simplicity, given for **M** = 5 (e.g., τ_1 is defined at **M** = 5).

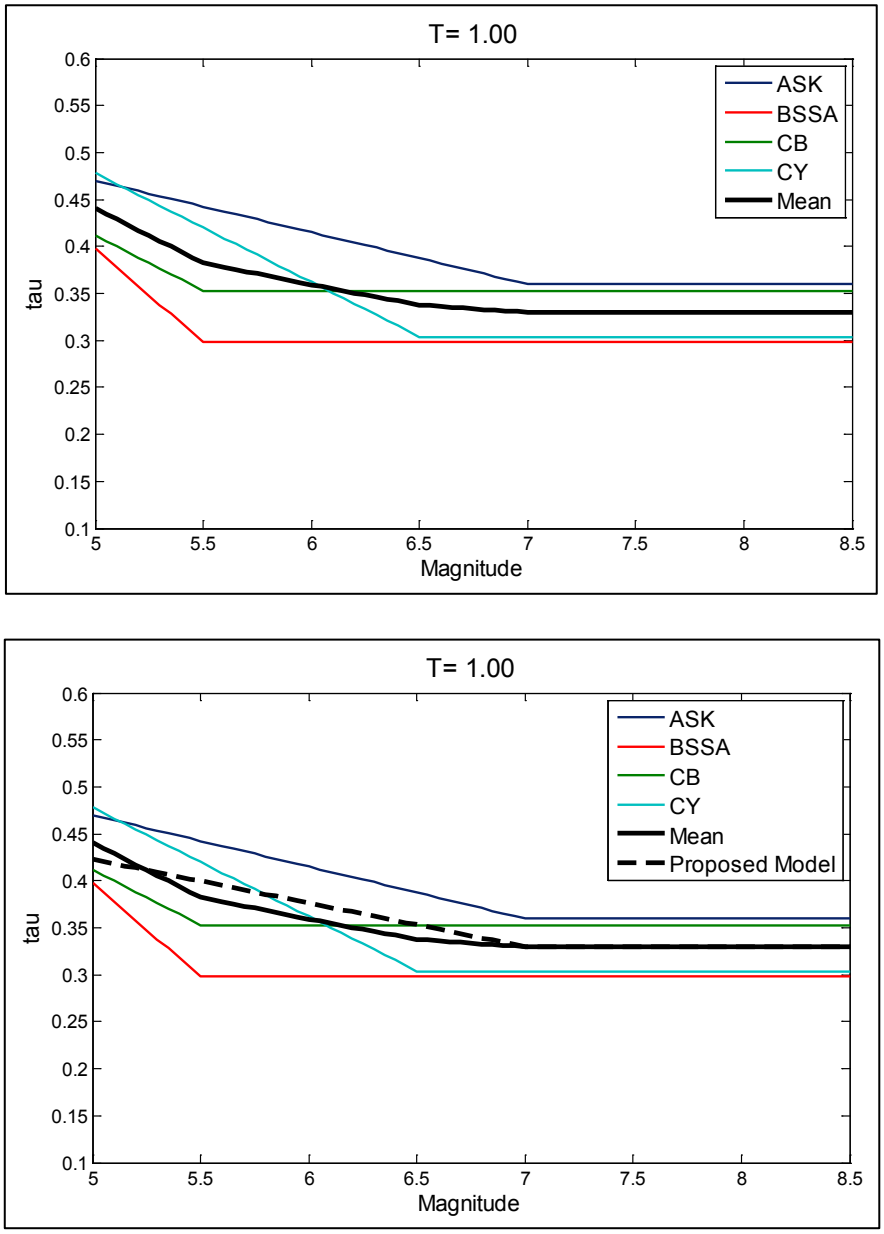

Figure 9.96. The four selected NGA-West2 τ models along the computed mean τ values (top plot), and the same including the proposed τ model (bottom plot).

Figure 9.97 shows the plots of the four selected τ models at **M** = 5.25 and **M** = 7, along with the computed mean τ values. A noticeable characteristic of all four NGA τ models is a *bump* around a period of 0.1 sec. This bump deserves special attention, because a possible explanation for its presence is that regional differences in kappa are mapped into τ. To test this hypothesis, we conducted 250 point-source

simulations for an average stress drop of 50 (with a logarithmic standard deviation of 0.5). Motions were computed for 50 sites per earthquake using a lognormal distribution of kappa with median kappa of 0.035 and a standard deviation of 0.3 (in natural log units). WUS amplification factors (Boore and Joyner 1997) were used with a frequency independent site factor that is log-normally distributed around zero with a standard deviation of 0.4 (natural log units). The variance of residuals was then partitioned into within-event (ϕ) and between-event (τ) terms. The resulting standard deviations are shown in Figure 9.98. Note that in this case there is a bump in ϕ but not in τ. Other simulations with different distributions of kappa and with frequency-dependent site factors were computed with similar results (the bump is more noticeable for frequency-dependent site factors).

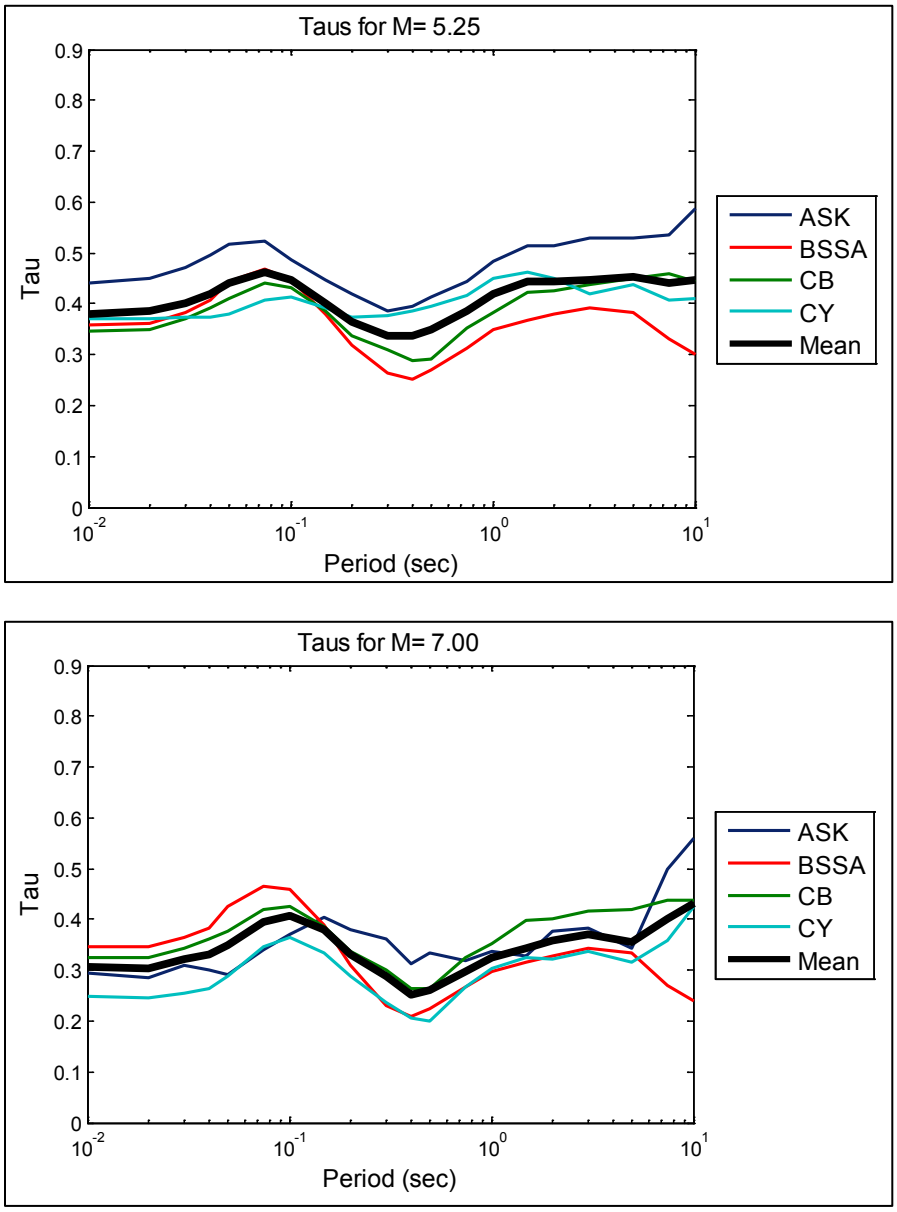

Figure 9.97. Values of τ from the four selected NGA-West2 models for M = 5.25 (top) and M = 7 (bottom), along with the computed mean of τ.

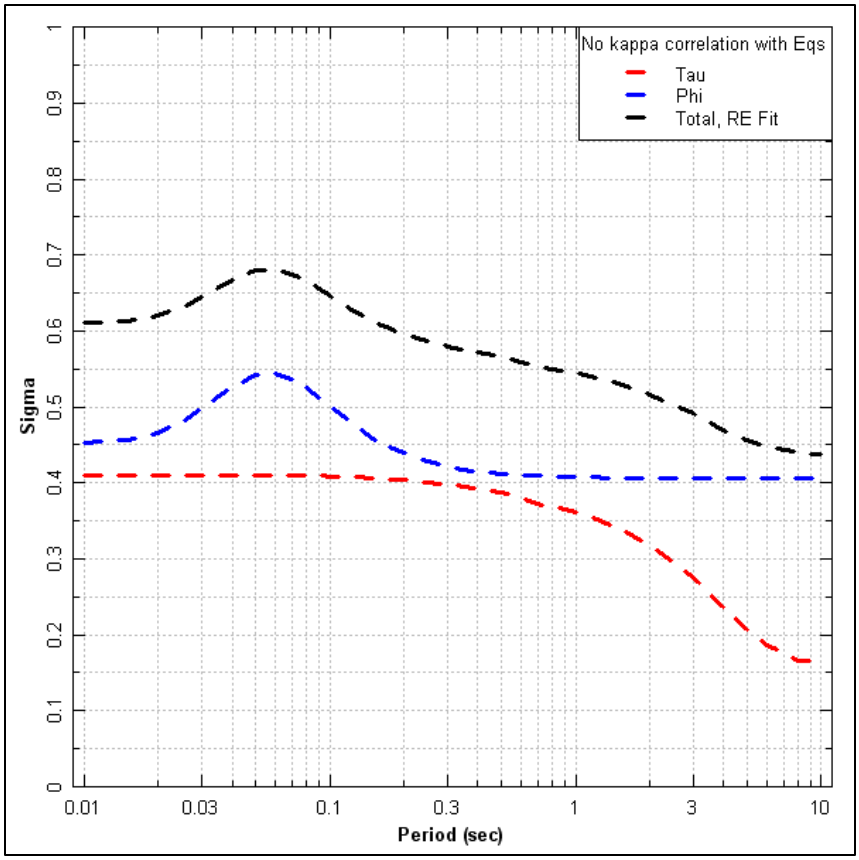

Figure 9.98. Standard deviations computed from point-source stochastic simulations with random kappa values.

A second set of simulations were conducted by allowing for correlation between earthquakes and kappa values. This correlation would result if there are regional kappa differences; in this case, an earthquake would sample preferentially some range of kappa values. The uncertainty in kappa was divided between a median value for each earthquake and a within-earthquake distribution, preserving the total variance of kappa. All other parameters were kept the same. The resulting standard deviations are shown in Figure 9.99. Observe that in this case the bump occurs both in ϕ and in τ. Additional evidence for the fact that the bump in τ maybe due to kappa comes from performing regressions analyses including both event and site terms. Figure 9.100 shows standard deviations computed from the KiK-net data (Rodriguez-Marek et al. 2011). The total (ergodic) sigma at the surface shows a region of high values over a wide range of periods (e.g., a wide bump) that peak around 0.1 sec. A similar bump is seen for the total sigma at borehole stations; however, the peak is narrower and occurs at a higher frequency (which would be consistent with the lower kappa values at the borehole depth). When the site-to-site variability is removed (i.e., in the single-station sigma), the bump is no longer observed.

Similar results were obtained for California data. Figure 9.101 shows estimates of τ for two magnitude ranges using the residuals from Chiou and Youngs (2014). Two cases are shown, one in which τ is estimated using only random effects for each earthquake and one in which a random effect for each earthquake and a random effect for each recording station are both included, separating the total ϕ into ϕ_{S2S} and ϕ_{ss}. In both analyses, only residuals for earthquakes with at least five recordings are included to provide a better estimate of τ. For the $3 < \mathbf{M} < 5.5$ data set, inclusion of random effects for

individual stations translates the peak in τ near T = 0.1 sec into a peak in ϕ_{S2S} at this period. For the **M** $\geq$ 5.5 data, there is little difference in the estimates of τ for the two cases, although the peak in τ is much less pronounced for the California large-magnitude data than it is for the analyses of the global data sets shown earlier. It should be noted that for the large-magnitude California data set there are very few stations that have recorded five or more earthquakes. As a result, ϕ_{S2S} is not well estimated. In the mixed-effects formulation, when a particular class (i.e., recording station) has very limited data, its average effect is shifted away from the mean residual toward zero (see discussion by Abrahamson and Youngs 1992). This can be seen in the plots of the estimated values of ϕ, where ϕ_{S2S} is much smaller than ϕ_{ss} for the large-magnitude data set, while they are comparable for the small magnitude data set.

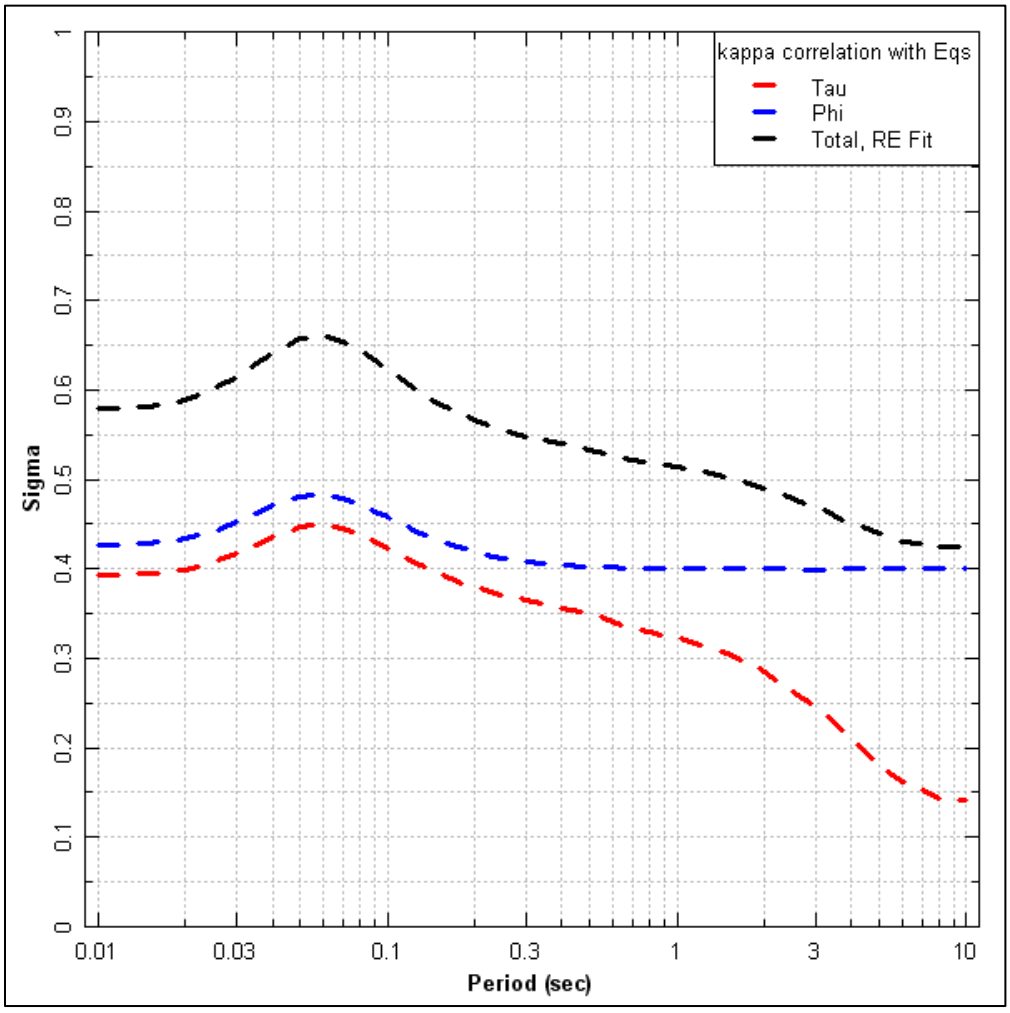

Figure 9.99. Standard deviations computed from point-source stochastic simulations with correlated kappa values.

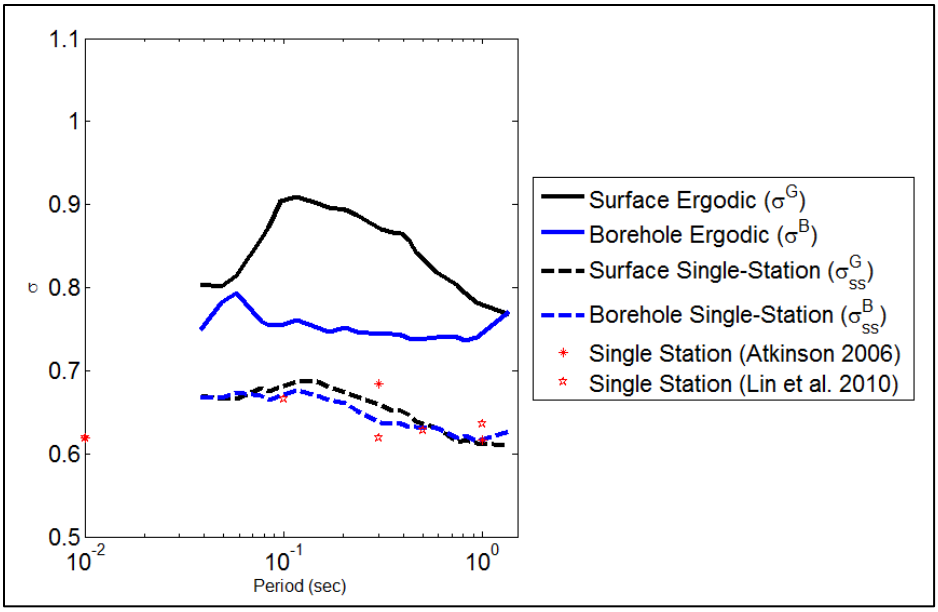

Figure 9.100. Standard deviation values computed from the Japanese KiK-net data (from Rodriguez-Marek et al. 2011). Different components of sigma are shown.

In summary, the bump seen at T = 0.1 sec in the mean τ values (Figure 9.97) is very likely an artifact of kappa and should not remain as a component of τ, in particular because for this project we are computing site-specific V_S-kappa corrections and the effects of kappa will be captured by this correction. Moreover, the epistemic uncertainty in the V_S-kappa corrections are large at these periods (see Figure 9.26 to Figure 9.30). For this reason, the GMC TI Team chose to smooth the mean τ values in Figure 9.97. The selected functional form for smoothing the τ values is as follows:

$$\tau(T) = \tau_{VLP}(T) + \frac{[\tau_{PGA} - \tau_{VLP}]}{\cosh\left[0.4 \ln\left(\frac{T}{0.01}\right)\right]} \qquad (9.30)$$

where $\tau_{VLP}(T)$ and $\tau_{PGA}(T)$ are parameters that correspond to the values of τ at very long periods and PGA, respectively. This is the same functional form used by Chiou and Youngs (2014) to produce a smooth τ model. The smoothed models for **M** = 5.25 and **M** = 7 are shown in Figure 9.102. Observe that an artifact of the selected functional form for τ (Equation 9.30) is that the model also smoothes across the "dip" in τ at about 0.3 sec. There are no physical models to explain this dip, and the smooth model represents a conservative choice. This figure also includes the statistical uncertainty (one standard deviation band) in the τ values from each of the four NGA models, which was estimated by computing the COV of the CY14 model and using it for all the other models (the computations were done, as discussed earlier, on the variance, but the plots are shown on the standard deviation). The parameter τ_{PGA} is obtained from the average τ from the four models at T = 0.01 sec. For **M** = 5.25, the parameter τ_{VLP} is computed from the highest value of τ for long periods (T ≥ 2 sec). For **M** = 7.0, the parameter τ_{VLP} is set such that the resulting model becomes equal to 0.4 at T ≥ 7 sec. The resulting fit overestimates τ values for periods less than 7 sec, but underestimates τ values for longer periods. For these longer periods the data are scarce. The proposed model is essentially an extrapolation of values of τ to periods longer than 7 sec. The resulting model achieves the objective of smoothing the bump in τ and represents a good match to the average τ values from the four selected NGA models. Note also that the model is always within the one uncertainty band of the four selected NGA models.

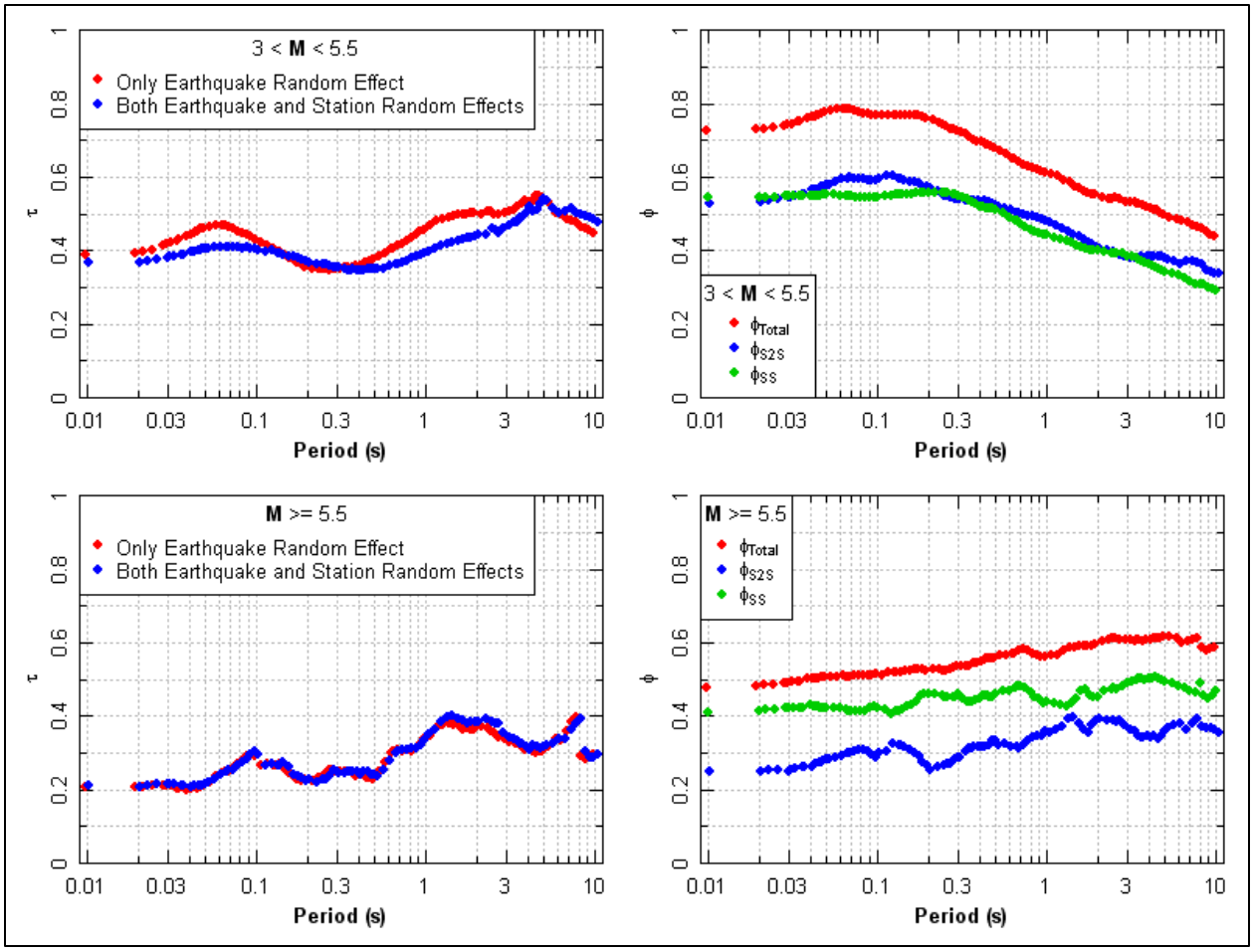

Figure 9.101. Values of standard deviation components computed from different regression analyses for California data. The red line shows results of a regression that considers event terms as random effects. The blue and green lines show results of a regression that considers both event terms and site terms as random effects. (EQID = earthquake ID; STID = station ID.) The top two plots are for $3 < M < 5.5$, and the bottom plots are for $M \geq 5.5$.

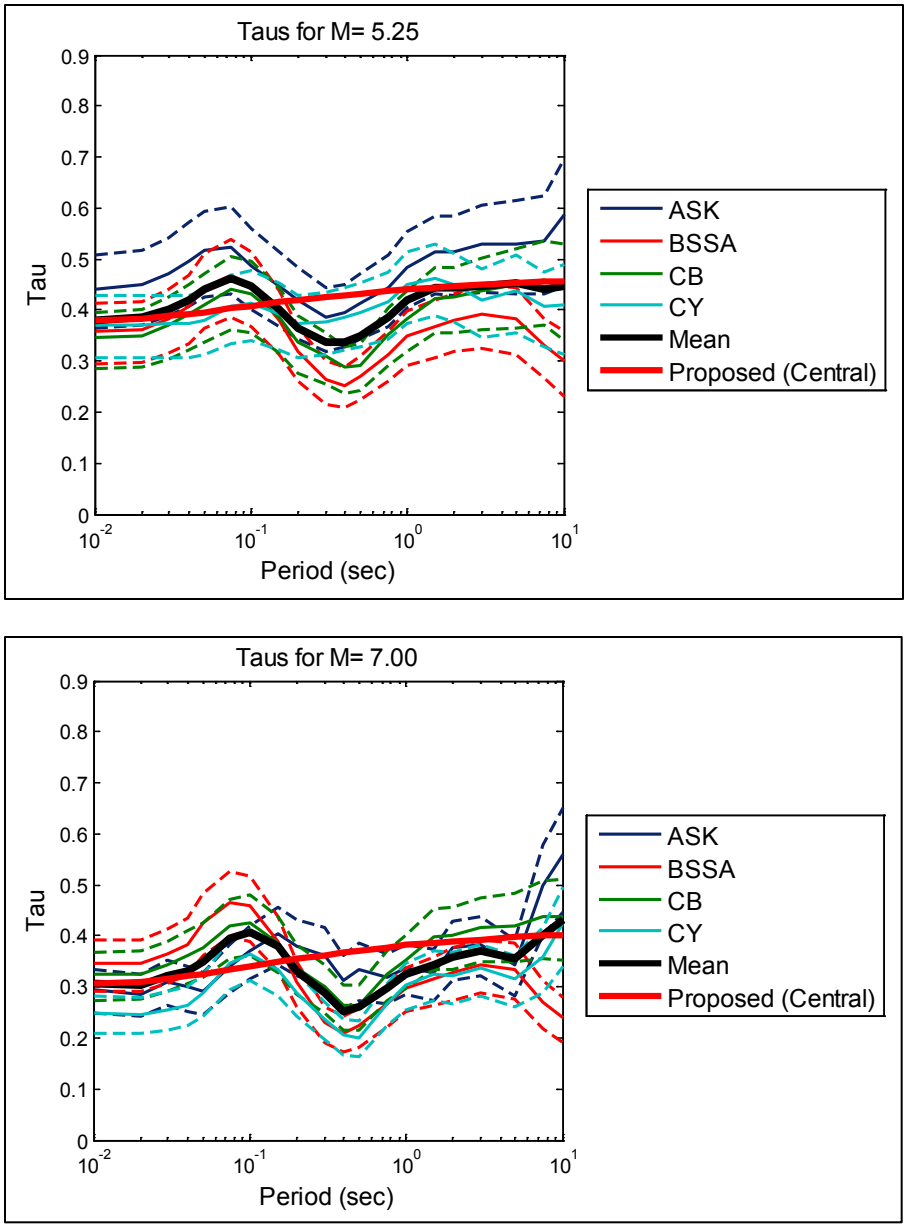

Figure 9.102. Proposed model for τ. Also shown are the values of t from the four selected NGA-West2 models along with the one standard deviation band reflecting the statistical uncertainty in the models.

9.5.3.1.2 Model for the Standard Deviation of τ^2 (σ_{τ^2})

The model for the standard deviation of τ^2 is build from two components, the within-model variability ($\sigma_{\tau_W^2}$) and the between-model variability ($\sigma_{\tau_B^2}$):

$$\sigma_{\tau^2} = \sqrt{\left(\sigma_{\tau_B^2}\right)^2 + \left(\sigma_{\tau_W^2}\right)^2} \tag{9.31}$$

The within-model variability was computed by a member of the GMC TI Team as part of the regressions conducted for the CY14 model (). The between-model variability is computed by obtaining the standard deviation of τ^2 from the four selected NGA-West2 models. The same process as for the median τ model was used to constrain the magnitude dependence. The between-model and within-model standard deviations of τ^2 for **M** = 5.25 and **M** = 7 are shown in Figure 9.103.

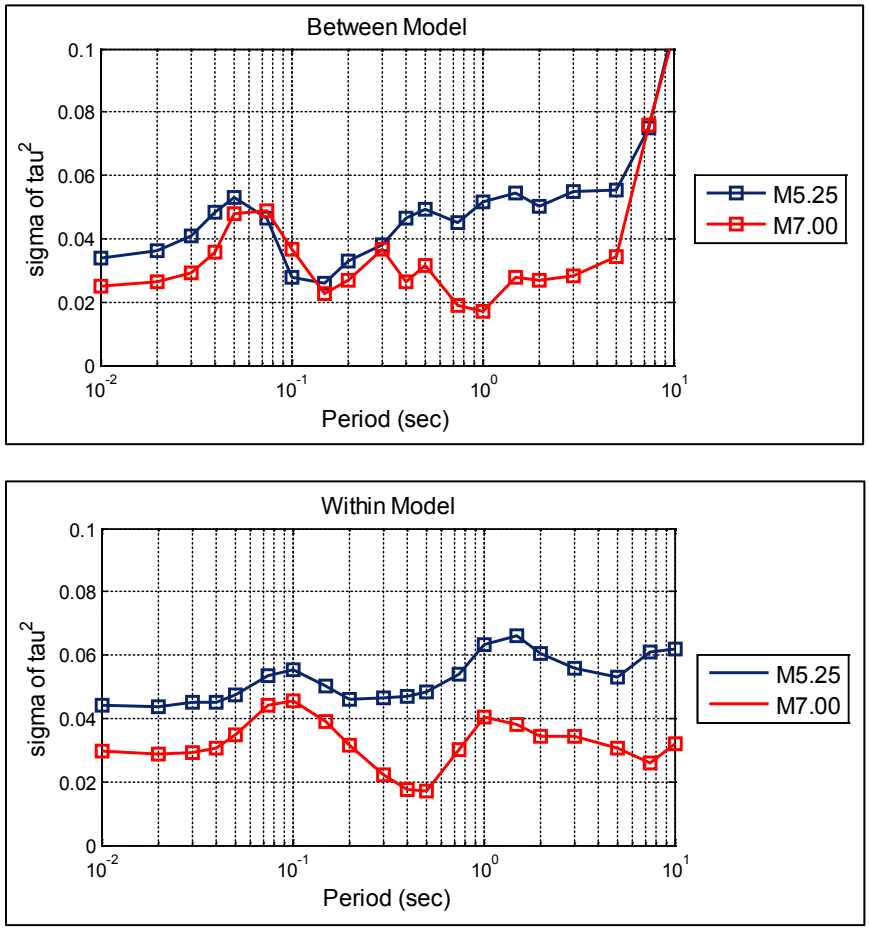

Figure 9.103. Between-model (top) and within-model (bottom) uncertainty for τ^2.

The standard deviation of τ^2 was computed using Equation 9.31. The resulting values were smoothed across the period using the same functional form as for the median τ model (Equation 9.30) and are shown in Figure 9.104. The value of the parameter τ_{VLP} was selected by visual inspection to envelope the values for T ≤ 7. The GMC TI Team decided to smooth across the large values of σ_{τ^2} at periods longer than 7 sec. The data at these periods are scarce and the large epistemic uncertainty in τ at long periods is likely the result of different extrapolation choices of the NGA developers (see Figure 9.102). There are no physical explanations for why source variability should suddenly increase so much at long periods. The choice of the GMC TI Team is to use the data at periods from 1 to 5 sec to extrapolate for the epistemic uncertainty at longer periods.

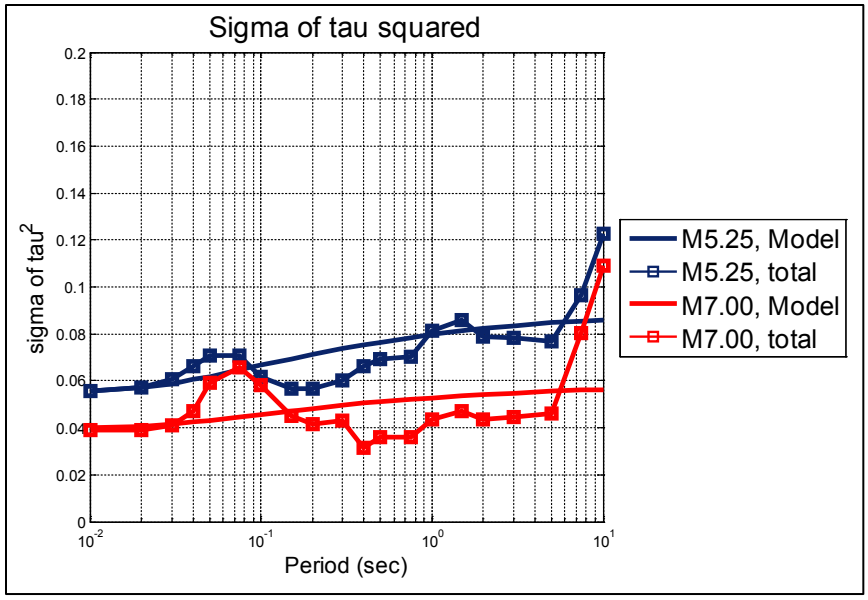

Figure 9.104. Proposed model for σ_{τ^2} for M = 5.25 and M = 7.

9.5.3.2 Single-Station Phi (ϕ_{ss}) Model

The selected model for ϕ_{ss} is a slight modification of the heteroskedastic ϕ_{ss} model developed for the Thyspunt Nuclear Siting Project (TNSP; Bommer et al. 2014; Rodriguez-Marek et al. 2014). (The data used to derive this model are discussed in Section 7.4.3). The TNSP model was derived from data from multiple regions that were compiled within the PEGASOS Refinement Project (PRP; Renault et al. 2010; Rodriguez-Marek et al. 2013), and is explained in detail by Rodriguez-Marek et al. (2014). Rodriguez-Marek et al. (2013) highlight the homogeneity of single-station phi estimates across regions, which implies that the model can be extrapolated with some confidence to other regions (see also Figure 7.70). Moreover, the absence of ground motion data in Cascadia precludes the development of a region-specific model; hence, the GMC TI Team opted for using the TNSP data because it is based on multiple regions, rather than using a model simply from the NGA data set (which is dominated by California data). In any case, the estimates of single-station phi (ϕ_{ss}) using the PRP data are similar to those obtained using the NGA data (Figure 9.105). The TNSP sigma model includes both a homoskedastic and a heteroskedastic model. In this project, the GMC TI Team chose to adopt only the latter (heteroskedastic) because the view of the scientific community has shifted toward the use of heteroskedastic models in GMPEs for crustal earthquakes, as demonstrated by the fact that the recent NGA-West2 models all have heteroskedastic models for ϕ.

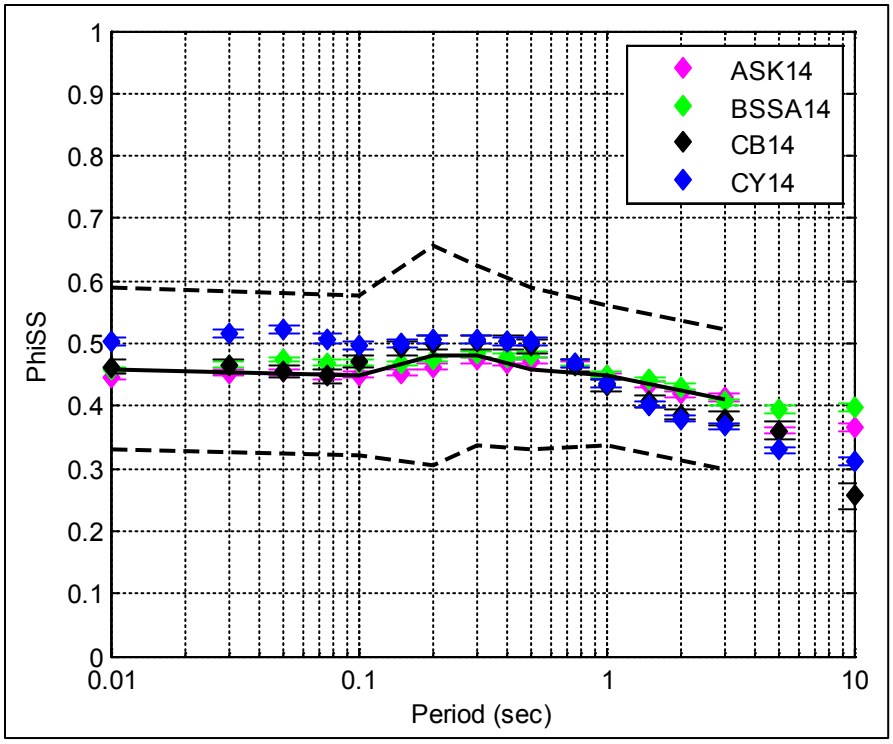

Figure 9.105. Estimates of single-station phi (ϕ_{ss}) from the PEGASOS Refinement Project (dark lines) and selected NGA-West2 relationships. The solid line is the median ϕ_{ss} model dashed lines correspond approximately to the 5th and 95th percentile values.

9.5.3.2.1 Central ϕ_{ss} Model

The selected ϕ_{ss} model is chosen to be 80% of the model for intra-event standard deviation (ϕ) by Abrahamson and Silva (2008). The choice of scaling the Abrahamson and Silva (2008) ϕ did not respond to any particular preference for that model; it simply reflected the fact that the ϕ_{ss} values computed using the PRP data matched very well the Abrahamson and Silva (2008) model scaled by 0.8 (Figure 7.73). Additional discussion on this topic is presented in Section 7.4.3.1.2. The only modification to the model was at long periods. At periods higher than 1.0 sec, the TNSP model is not well constrained because the PRP data extend only up to T = 3.0 sec, and the data are limited at this period. However, the single-station sigma model at long periods has no effect on the hazard because the minimum epistemic uncertainty for the amplification factors (Section 9.5.6) will be prescribed in such a manner that the resulting sigma after the application of the site effects calculations is equal to the ergodic sigma. For this reason, the simplifying assumption was made that the value of ϕ_{ss} at T = 1.5 sec applies to longer periods. The original TNSP model and the model for ϕ_{ss} adopted for this project are shown in Figure 9.106.

The magnitude dependence of the proposed ϕ_{ss} model is identical to that of the τ model:

$$\phi_{ss}(M) = \begin{cases} \phi_{ss1} + \frac{M-5}{2}(\phi_{ss2} - \phi_{ss_1}) & for\ M < 7 \\ \phi_{ss2} & for\ M \geq 7 \end{cases} \quad (9.32)$$

where ϕ_{ss1} and ϕ_{ss2} are parameters that correspond to the values of ϕ_{ss} at **M** = 5 and **M** = 7, respectively. These values are plotted in Figure 9.106.

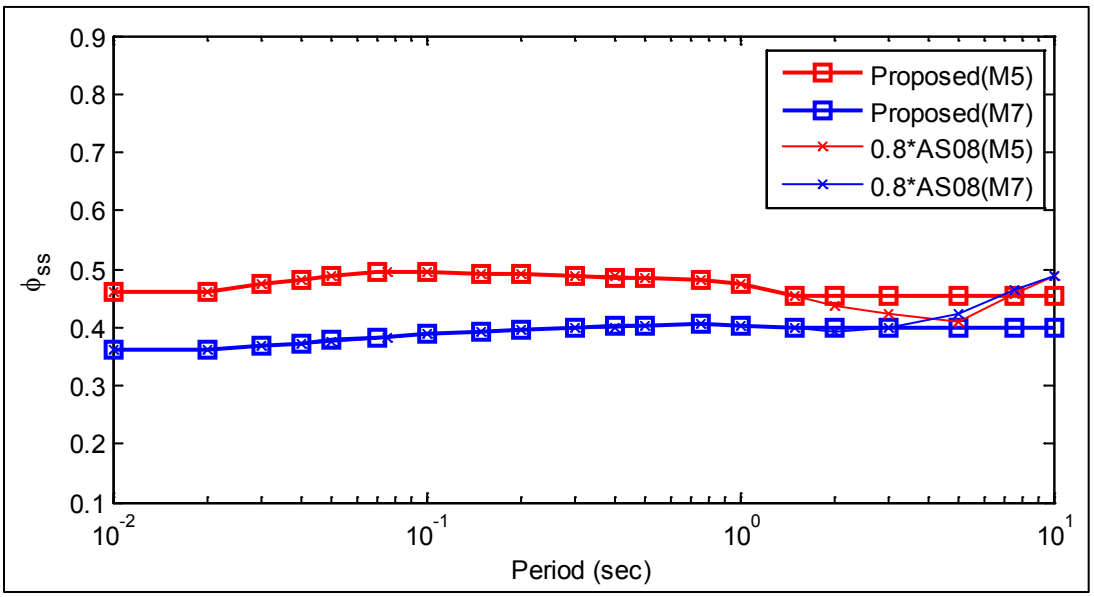

Figure 9.106. Proposed ϕ_{ss} model, shown along with the Abrahamson and Silva (2008) model scaled by 0.8.

9.5.3.2.2. Epistemic Uncertainty Model for ϕ_{ss}^2

The value of ϕ_{ss} at a given station is, in principle, a quantity that can be measured; hence its uncertainty is epistemic in nature. The quantification of this epistemic uncertainty is one of the requisites for the use of a single-station sigma approach (Section 9.5.1). As indicated in the previous section, the median value of ϕ_{ss} was estimated using the PRP database. Similarly, the epistemic uncertainty of ϕ_{ss} can be estimated using the site-to-site variability of this parameter across sites from the PRP database. This is akin to adopting an ergodic approach on the standard deviation.

For simplicity of notation, we will let the estimate of ϕ_{ss} at a single station be denoted by $\phi_{ss,s}$. The standard deviation (SD) of $\phi_{ss,s}$ across all the PRP stations (for different numbers of records per station) is given in Table 9.11. These estimates, however, are affected by sampling error. To quantify the effect of sampling error, we estimated the sampling error from a simulated ground motion database with the same number of stations as the PRP database, but where all stations were assigned the same value of $\phi_{ss,s}$. We then computed the standard deviation of $\phi_{ss,s}$ using multiple realizations of the ground motion database. This standard deviation is not zero solely due to sampling error. The corresponding coefficient of variation ($COV = SD(\phi_{ss,s})/mean(\phi_{ss,s})$) is shown in Figure 9.107. Observe that the COV approaches zero as the number of records per station increases (e.g., the sampling error goes to zero with a larger number of records per station). The COV of the PRP database for selected stations with more than 20 records per station is also shown in Figure 9.107. The difference between the COV for the PRP data and those for the simulated database corresponds to the true variability of the PRP data. To estimate what this variability is, the simulation exercise was repeated by simulating a database where the SD($\phi_{ss,s}$) was increased so to match a target COV. These results are shown in Figure 9.108. A target COV of 0.1 envelopes the PRP data. This target value was selected by the GMC TI Team. The selected value of

$COV(\phi_{ss,s}) = 0.1$ was obtained assuming a homoskedastic ϕ_{ss}. However, it is reasonable to adopt this variation also for the chosen heteroskedastic model. It can be easily shown that the COV of the variance (ϕ_{ss}^2) is twice the COV of the standard deviation (ϕ_{ss}), hence, the standard deviation of ϕ_{ss}^2 can be computed as follows:

$$\sigma_{\phi_{ss}^2} = 0.2\phi_{ss}^2 \tag{9.33}$$

where ϕ_{ss} is computed using Equation 9.32.

Table 9.11. Mean and standard deviation of $\boldsymbol{\phi_{ss,s}}$ in the PRP database for different values of the minimum number of records per station, $\boldsymbol{N}$. All records with $\boldsymbol{M \geq 4.5}$ and $\boldsymbol{R_{rup} \leq 200}$ km are used.

	$N \geq 10$			$N \geq 15$			$N \geq 20$		
Period (sec)	Mean	Std. Dev.	Stations	Mean	Std. Dev.	Stations	Mean	Std. Dev.	Stations
0.01	0.43	0.10	326	0.44	0.09	133	0.44	0.08	32
0.1	0.45	0.12	316	0.45	0.10	133	0.45	0.08	32
0.2	0.47	0.12	50	0.52	0.10	13	0.56	0.11	5
0.3	0.46	0.11	326	0.47	0.10	133	0.47	0.09	32
0.5	0.46	0.11	316	0.47	0.09	133	0.46	0.08	32
1	0.44	0.10	326	0.43	0.08	133	0.43	0.07	32
3	0.41	0.10	245	0.42	0.08	89	0.41	0.07	16

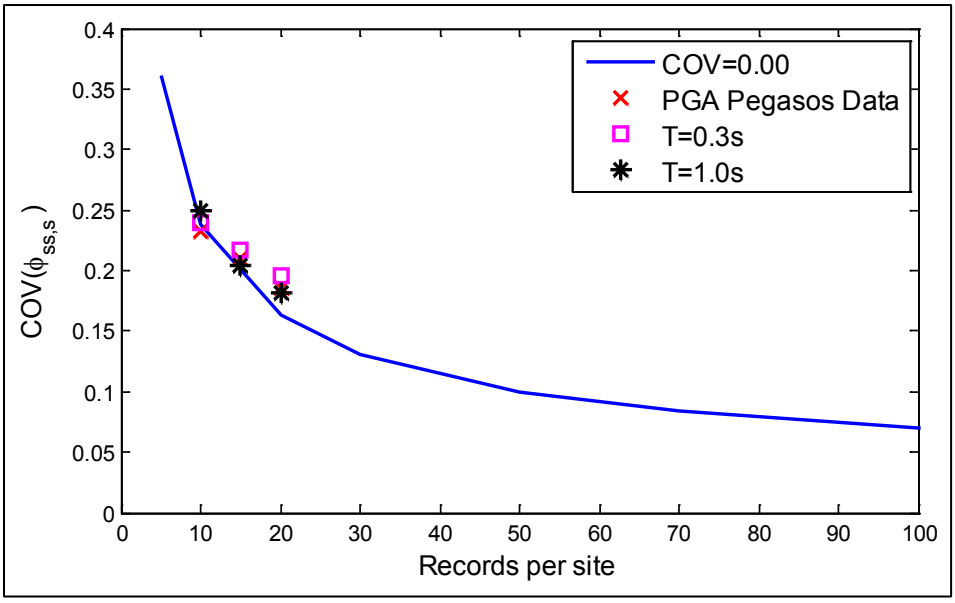

Figure 9.107. Coefficient of variation (COV) from the PRP data for stations with at least 10 records per site. The blue line represents the COV from a simulated ground motion for which the values of $\boldsymbol{\phi_{ss,s}}$ were identical for all stations; hence the COV of the blue line represents pure sample error on the estimate of $\boldsymbol{SD(\phi_{ss,s})}$. The simulations were run on a ground motion set of 32 stations (the average number of stations in the Kik-Net database). A total of 3,000 simulations were run to obtain stable estimates of the COV.

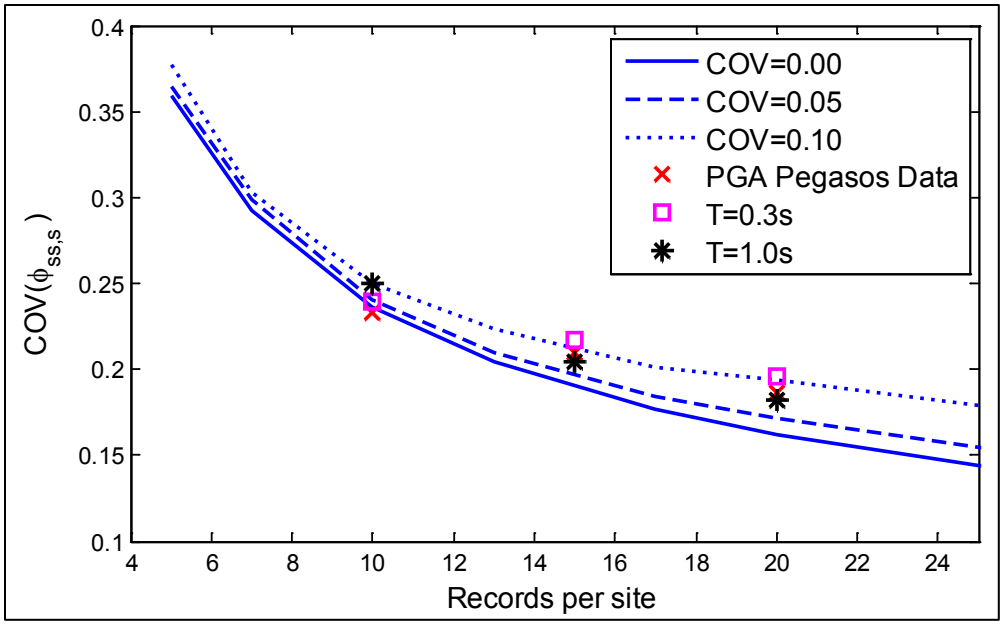

Figure 9.108. Coefficient of Variation (COV) from the PRP data for stations with at least 10 records per sites. The blue lines represent the COV for simulated ground motion data sets for which the values of $\boldsymbol{\phi_{ss,s}}$ were varied to obtain the target COVs shown in the legend. Details of the simulations are given in the caption for Figure 9.107.

9.5.3.2.3. Proposed Sigma Model for Crustal Earthquakes

Because the magnitude dependence of the τ and ϕ_{ss} models is identical, the two models can be combined at the two reference magnitudes (**M** = 5 and **M** = 7) using

$$\sigma = \sqrt{\phi_{ss}^2 + \tau^2} \tag{9.34}$$

The final sigma models are computed using

$$\sigma(M) = \begin{cases} \sigma_1 + \frac{M-5}{2}(\sigma_2 - \sigma_1) & for\ M < 7 \\ \sigma_2 & for\ M \geq 7 \end{cases} \tag{9.35}$$

where σ_1 and σ_2 are the values of sigma computed at **M** = 5 and **M** = 7, respectively (Table 9.12). The final sigma models (high, central, and low) for crustal earthquakes are shown in Figure 9.109 and Figure 9.110.

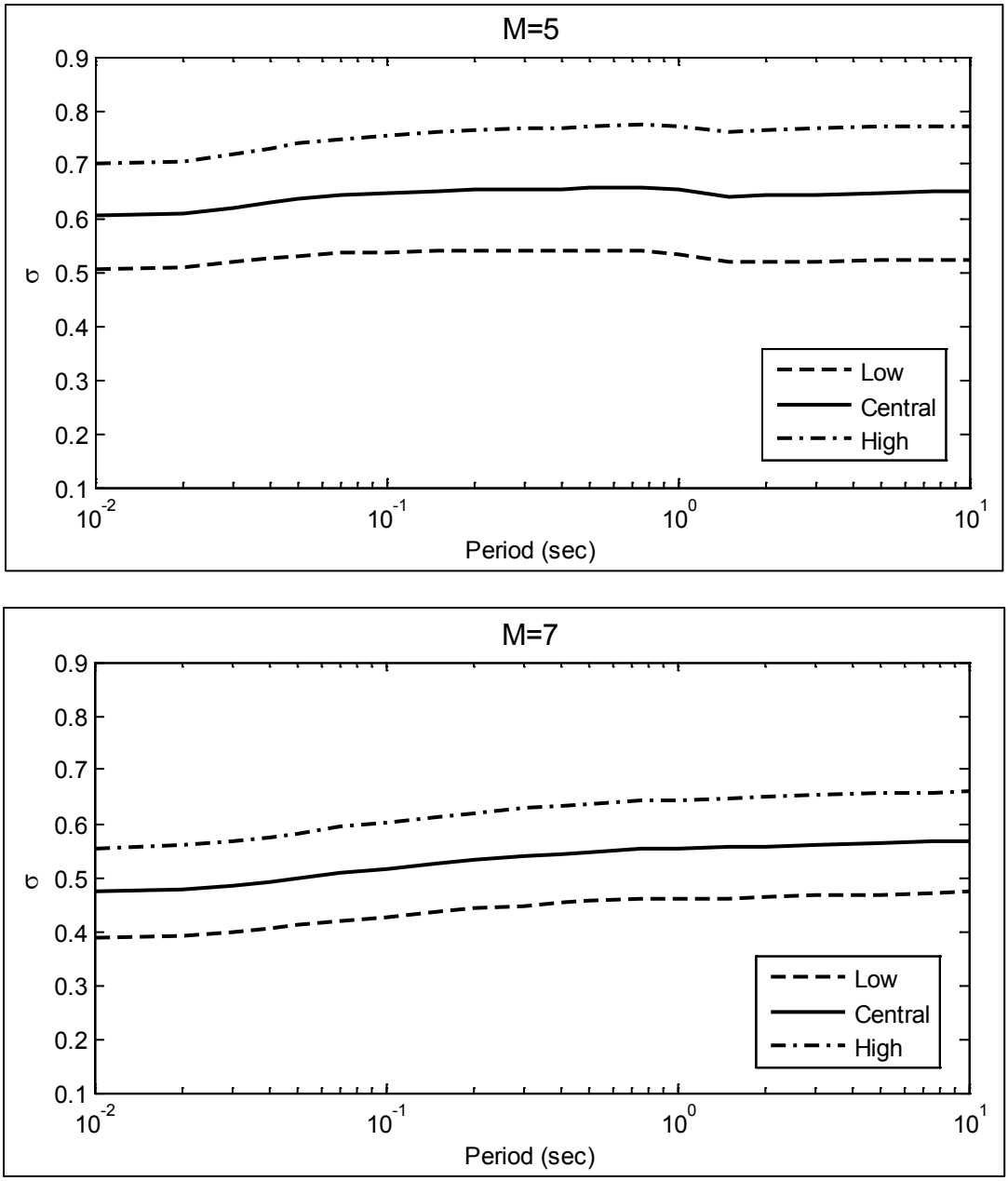

Figure 9.109. Proposed sigma model for M = 5 and M = 7.

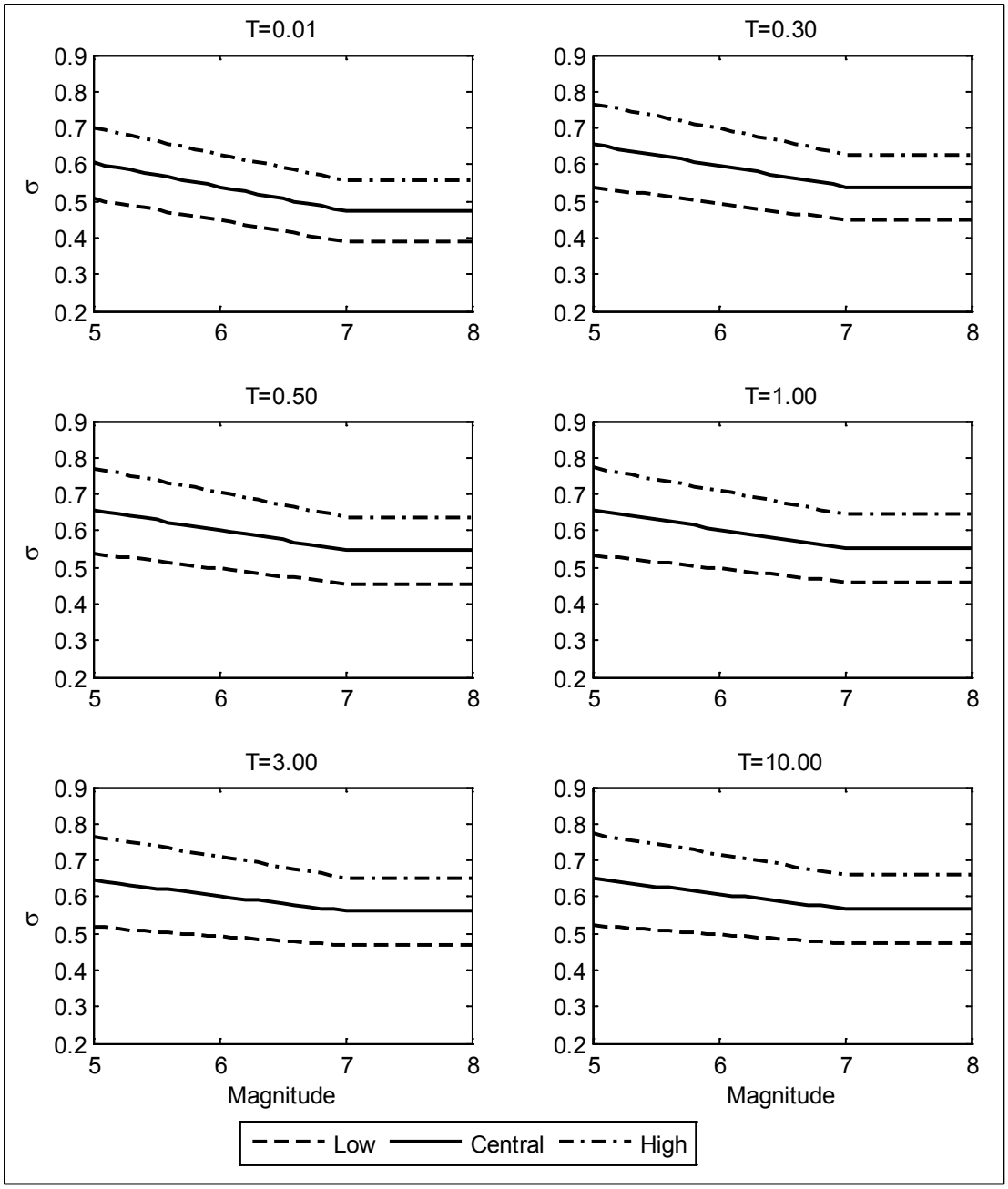

Figure 9.110. Proposed sigma models for selected periods.

Table 9.12. Parameters for the proposed sigma models.

	Central		Low		High	
T	σ_1	σ_2	σ_1	σ_2	σ_1	σ_2
0.01	0.605	0.473	0.506	0.389	0.701	0.555
0.02	0.607	0.477	0.508	0.392	0.704	0.559
0.03	0.619	0.485	0.517	0.399	0.718	0.569
0.04	0.628	0.492	0.525	0.405	0.729	0.576
0.05	0.635	0.498	0.530	0.412	0.738	0.582
0.07	0.644	0.508	0.537	0.420	0.748	0.594
0.1	0.647	0.516	0.538	0.427	0.754	0.602
0.15	0.651	0.526	0.539	0.437	0.760	0.612
0.2	0.652	0.532	0.538	0.442	0.763	0.619
0.3	0.655	0.539	0.539	0.448	0.767	0.628
0.4	0.655	0.544	0.538	0.452	0.769	0.634
0.5	0.656	0.548	0.539	0.456	0.771	0.637
0.75	0.657	0.554	0.538	0.462	0.773	0.644
1	0.654	0.554	0.533	0.461	0.772	0.645
1.5	0.641	0.556	0.518	0.462	0.760	0.647
2	0.643	0.558	0.520	0.465	0.763	0.649
3	0.644	0.561	0.519	0.467	0.766	0.653
5	0.647	0.564	0.521	0.469	0.769	0.656
7.5	0.649	0.566	0.522	0.471	0.772	0.658
10	0.649	0.567	0.523	0.473	0.772	0.659

9.5.4 Model for Subduction Ground Motions

The structure for the sigma model for subduction ground motions is identical to that of the sigma model for crustal ground motions (Section 9.5.3), except that both ϕ_{ss} and τ are magnitude independent (e.g., homoskedastic) and period-independent. The choice of a homoskedastic model reflects two facts: 1) all of the existing models for subduction ground motions are homoskedastic, and 2) the heteroskedastic models that exist for crustal ground motions are all constant for magnitudes greater than 7 (e.g., the magnitudes that control subduction earthquakes). The choice of a period-independent model will be justified as each of the model components is discussed. A particularity of the proposed model is that τ is different for intraslab and interface earthquakes.

The components of the sigma model are the median models for ϕ_{ss} and τ (Equation 9.36) and the models for the standard deviation of the variance ($\sigma_{\phi_{ss}^2}$ and σ_{τ^2}). These are discussed in the sections below.

9.5.4.1 Median Model for τ, and ϕ_{ss}

9.5.4.1.1. Tau Model

The inter-event standard deviation (τ) was computed from the regression analyses discussed extensively in Section 9.2.2. Separate values of τ for interface and intraslab events were computed from the residuals of the regression analyses. The resulting values are shown in Figure 9.111. Note that the intraslab and interface residuals are different over different period ranges. Observe also that the *bump* at a period of about 0.1 sec (see discussion in Section 9.5.3.1) is also present in these data. Other than the bump, the only other clear period dependence is a decrease in τ for intraslab earthquakes at long periods, and a more erratic pattern at long periods for the interface earthquakes. Because the data at long periods are less abundant, the GMC TI Team opted to simply smooth all data for $T \leq 5$ sec. The choice of 5 sec is because for this period the interface τ values become lower than the average (Figure 9.111). The average τ values are 0.496 for interface earthquakes and 0.507 for intraslab earthquakes.

The GMC TI Team also noted that the τ values contain some measure of region-to-region variability. This region-to-region variability was considered to be part of the epistemic uncertainty of the median (Section 9.4.3), and for this reason it was not considered appropriate to include it as part of the aleatory variability (e.g., as part of τ). Hence, the values of τ were corrected by

$$\tau_{corrected} = \sqrt{\tau^2 - \sigma_{reg}^2} \tag{9.36}$$

where σ_{reg} represents the region-to-region variability, which was computed as 0.158 in Section 9.4.3. Hence, the selected values of τ for the subduction model are 0.471 for interface earthquakes and 0.482 for intraslab earthquakes.

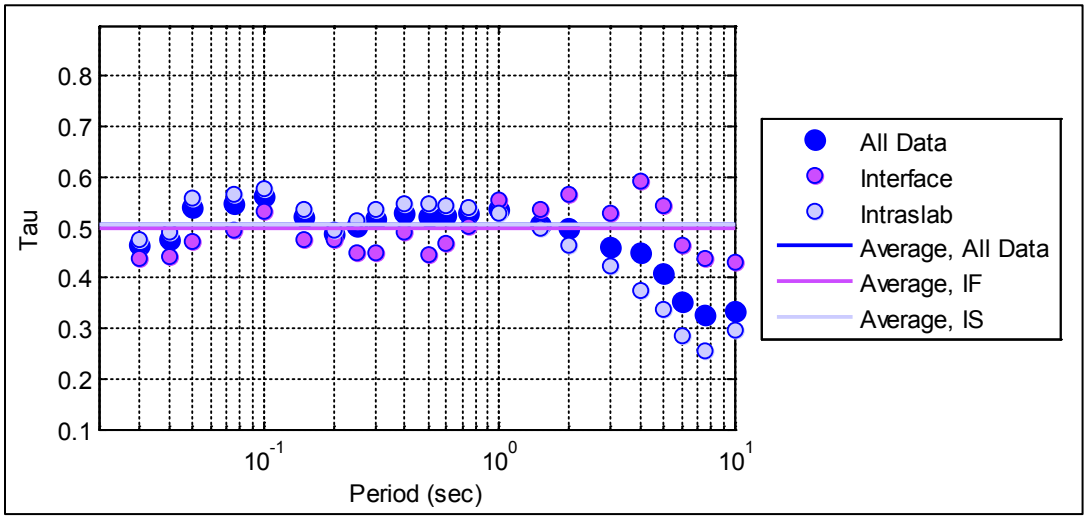

Figure 9.111. Computed values of τ from the residuals of the GMPE developed for subduction zone earthquakes (Section 9.2.2).

9.5.4.1.2. Phi Model

The values of ϕ computed from the regression analyses (Section 9.2.2) are shown in Figure 9.112. Separate values of ϕ for intraslab and interface events were computed from an analysis of the residuals from the regression. The value of ϕ averaged across all periods less than or equal than 5 sec is 0.670 and 0.591 for interface and intraslab earthquakes, respectively. The difference between interface and intraslab events is more marked at long periods, with significantly lower values for intraslab earthquakes.

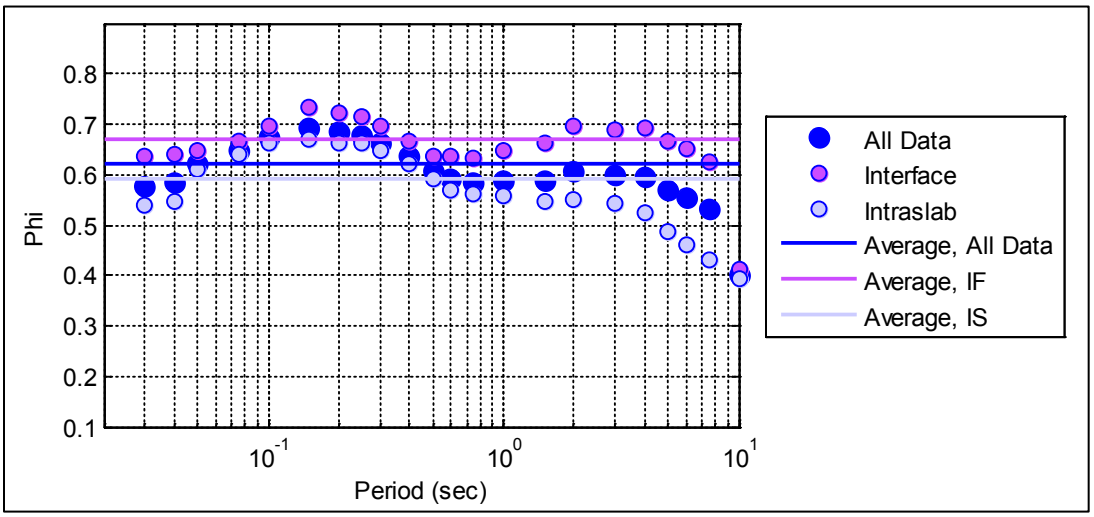

Figure 9.112. Computed values of ϕ from the residuals of the GMPE developed for subduction zone earthquakes (Section 9.2.2).

9.5.4.1.3. Single-Station Phi (ϕ_{ss}) Model

The model for ϕ_{ss} for subduction earthquakes was developed by performing a mixed-effects regression using the modified BC Hydro model discussed in Section 9.2.2. The mixed-effects regression included both site terms and event terms as random effects. Only stations with five or more recordings were used. The resulting values, which are not very different for interface and intraslab earthquakes, are shown in Figure 9.113. Note that the values for ϕ_{ss} drop for periods longer than T = 4 sec. Because at these periods the ϕ_{ss} model is not important (for reasons discussed previously and discussed further in Section 9.5.6), the GMC TI Team opted to not include these periods in the averaging of ϕ_{ss}. Hence, the proposed model is the average of ϕ_{ss} values from the modified BC Hydro model for periods equal to and less than 4 sec. This value is 0.45 and is plotted in Figure 9.113. For comparison purposes, Figure 9.113 also includes the ϕ_{ss} values computed by Abrahamson et al. (2014a; e.g., the original BC Hydro model). These values are slightly lower than the ones adopted for this project.

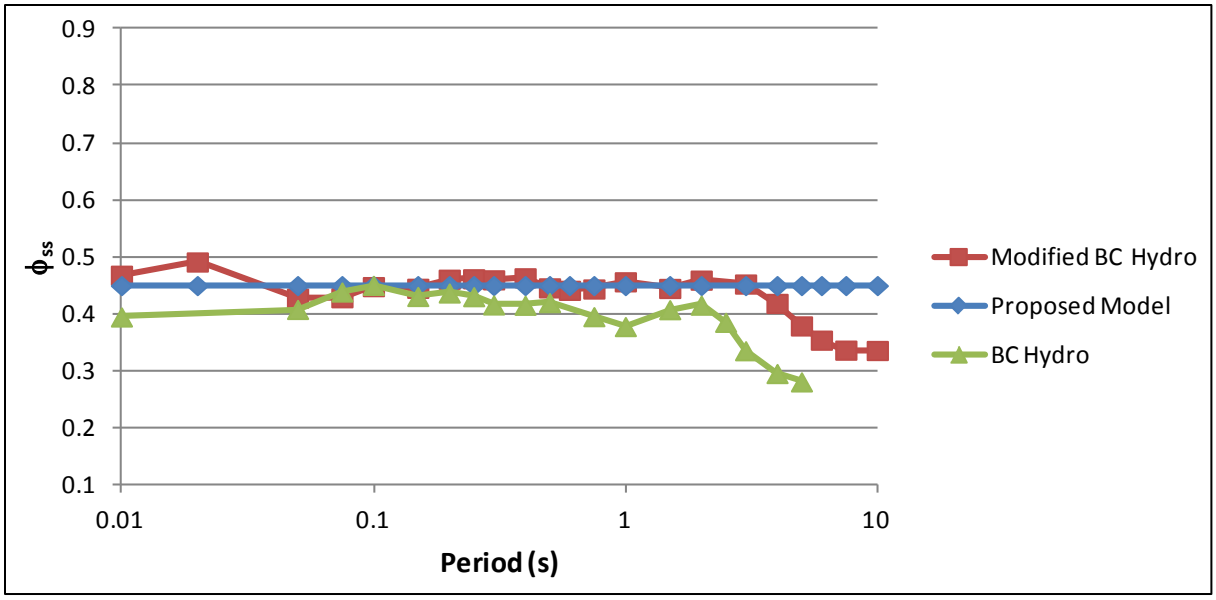

Figure 9.113. Proposed ϕ_{ss} model for subduction earthquakes. For comparison, the ϕ_{ss} values from the modified BC Hydro model (Section 9.2.2) and the original BC Hydro model (Abrahamson et al. 2014b) are also shown.

9.5.4.2 Uncertainty Models

Models for the standard deviation of τ^2 and ϕ_{ss}^2 are needed (Equation 9.26). As for the crustal models, the model for the standard deviation of τ^2 includes both within-model and between-model uncertainty (Equation 9.31). The between-model uncertainty could not be computed for subduction earthquakes because only one model was identified as viable (Abrahamson et al. 2014b; see Section 7.4.2). For this reason, the between-model standard deviation for τ^2 from the crustal events for **M** = 7 was considered (Figure 9.103). A smoothed value across periods ($\sigma_{\tau_B^2}$ =0.03) was used.

To compute the standard deviation of the variance component ($\sigma_{\tau_W^2}$) we used the profile likelihood approach (McCullagh and Nelder 1989) to estimate a confidence interval. The profile likelihood is computed by systematically varying the variance component under consideration and computing the log-likelihood of the model fitted with the fixed parameter ($l(\sigma_0)$), and comparing this to the log-likelihood of the unrestricted model ($l(\hat{\sigma})$). From the likelihood ratio test we know that $2(l(\hat{\sigma}) - l(\sigma_0))$ has a chi-squared distribution. This information is used to construct the confidence interval of the variance components. We used the profile likelihood implementation in the R package *lme4* for the computation. The confidence intervals were used to estimate the within-model uncertainty for τ^2. The analyses were conducted without differentiating between interface and intraslab earthquakes. The total epistemic uncertainty for $\tau^2(\sigma_{\tau^2})$ is shown in Figure 9.114. A smoothed value across periods (0.054) was used. The epistemic uncertainty on ϕ_{ss}^2 was obtained as for the crustal model (Section 9.5.3.2).

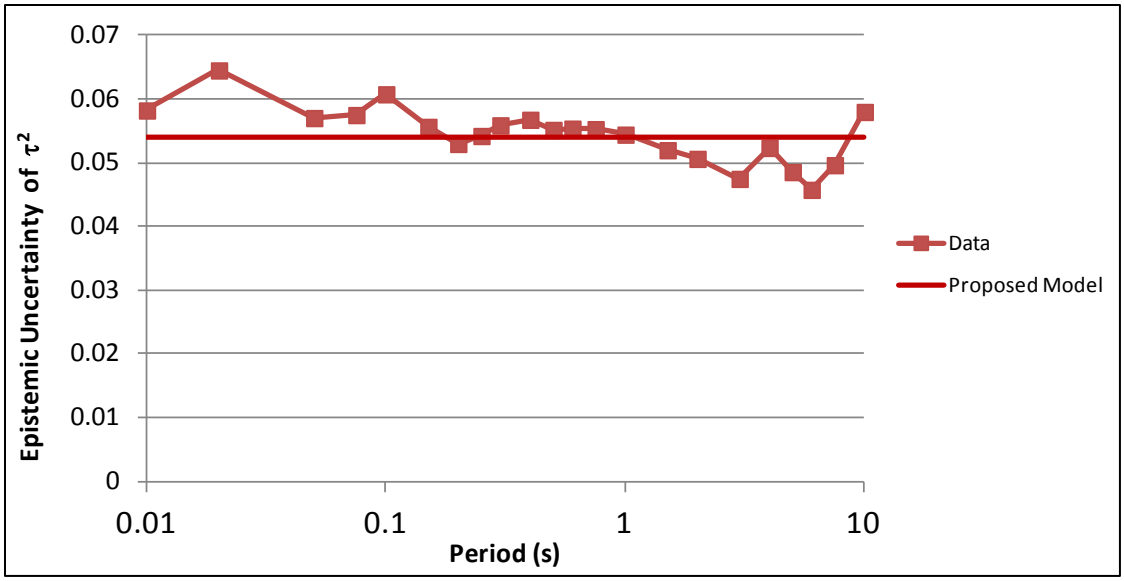

Figure 9.114. Epistemic uncertainty of $\boldsymbol{\tau^2}$ ($\boldsymbol{\sigma_{\tau^2}}$). The values were obtained using Equation 9.31 with $\boldsymbol{\sigma_{\tau^2,B} = 0.03}$ and $\boldsymbol{\sigma_{\tau^2,W}}$ values obtained from the regression analyses.

9.5.4.3 Proposed Model

The proposed sigma model for subduction earthquakes is given in Table 9.13.

Table 9.13.Values for the subduction sigma model.

	Interface	IntraSlab
τ	0.471	0.482
$\phi_{ergodic}$	0.670	0.591
ϕ_{ss}	0.450	0.450
σ_{τ^2}	0.054	0.054
$\sigma_{\phi_{ss}^2}$	0.0405	0.0405

9.5.5 Mixture Model

The traditional assumption regarding the shape of the distribution of ground motion residuals (in log-space) is that these residuals follow a normal distribution. Recent analyses of large ground motion data sets have shown that the normal assumption is not valid at large values of epsilon (where epsilon is the residual in natural log-space normalized by the standard deviation). In this section, we present first the analyses of several data sets that show that this deviation from normality is rather pervasive, and then present a mixture model to account for this deviation. Finally, we present the arguments for the weights assigned to the logic tree shown in Figure 9.95.

9.5.5.1 Analysis of Large Ground Motion Data Sets: Deviations from Normality at Large Epsilon

The GMC TI Team conducted an analysis of the intra-event residuals for the Abrahamson et al. (2014b; [ASK14]) NGA relationship; the results are shown in Figure 9.115. The residuals are shown in

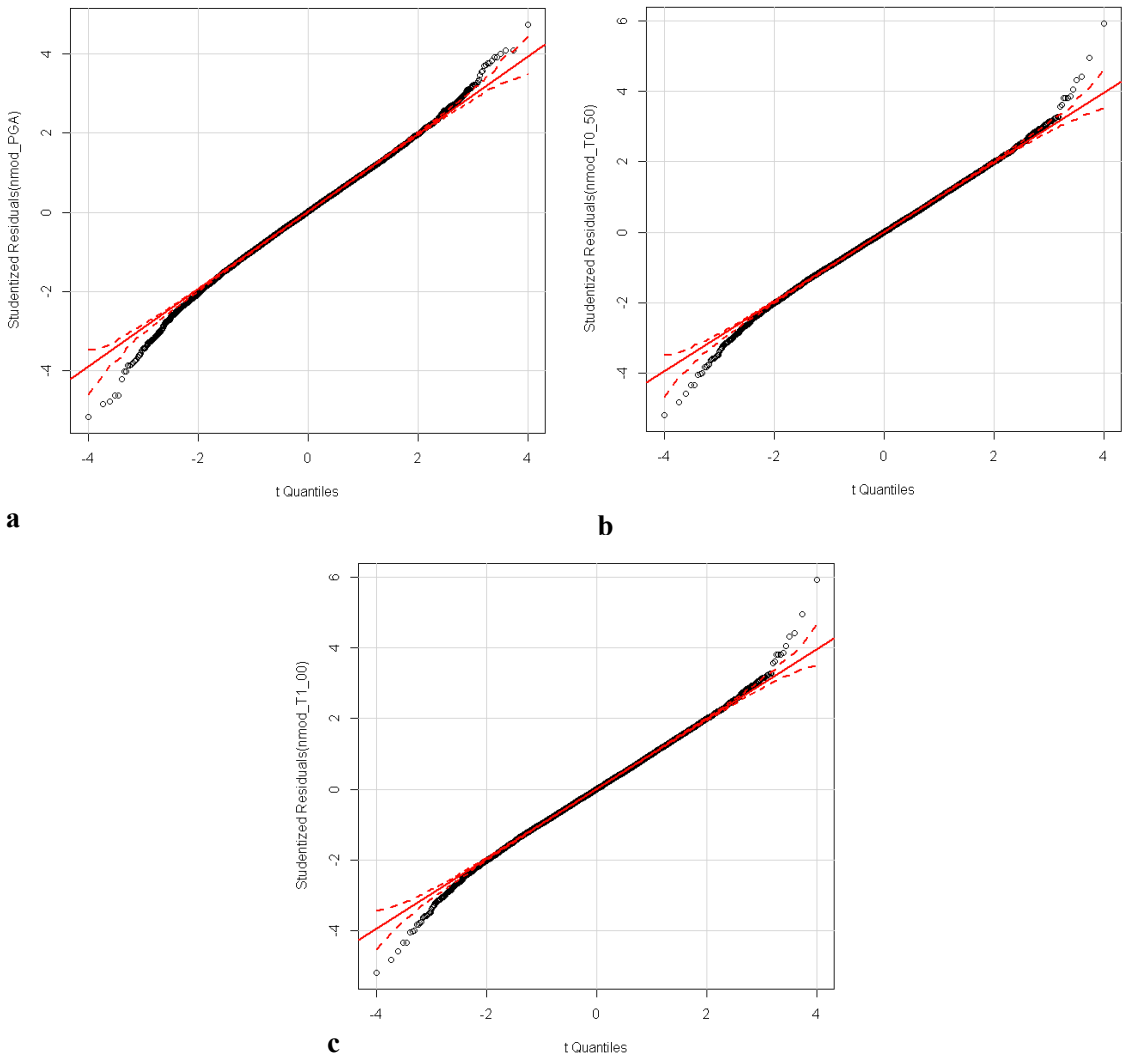

Figure 9.115. Q-Q plots for ASK14 intra-event normalized residuals for M ≥ 5. a) PGA, b) T = 2 sec, c) T = 1 sec.

terms of a quantile plot (Q-Q plot), which compares the observed data density at various values of epsilon (vertical axis) with what is expected from the assumed distribution, in this case normal, on the horizontal axis. A normal distribution would fit along the 1:1 line. The dashed lines show a 95% confidence interval on the normal distribution. A departure of the residuals from these lines indicates a departure from the normal distribution. The deviation from normality in this case is described as a "heavy tailed" because there is a higher probability of extremes (at both high and low epsilon) than provided by the normal distribution. Heavy tails are observed in the ASK14 data for a wide range of oscillator periods at values of epsilon higher than 2. The same deviation from normality is observed for site- and event-corrected residuals (e.g., for single-station sigma; see Figure 9.116). Similar results are seen when magnitudes are restricted to **M** ≥ 5.5. The same deviations from normality are not seen in the between-event terms.

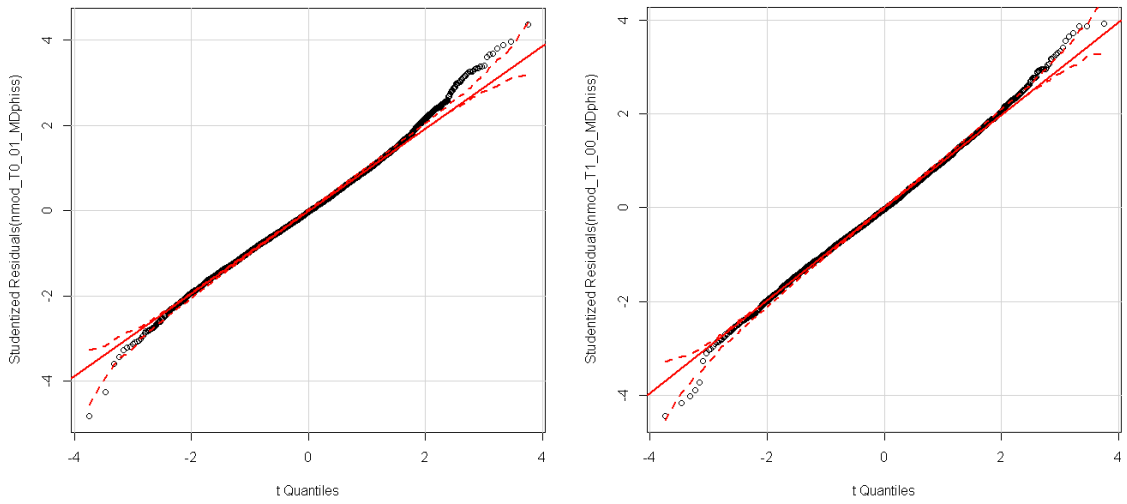

Figure 9.116. Q-Q plots for normalized site- and event-corrected residuals for the ASK database for two periods.

Similar analyses to those presented in Figure 9.115 and Figure 9.116 were conducted by the GMC TI Team on the Chiou and Youngs (2014 [CY14]) residuals. The results of these analyses are similar to those conducted on the ASK14 data. A statistical test was also conducted on these residuals. The statistic tested was the number of residuals that exceed a given epsilon level. For a normal distribution, the null distribution would be a binomial distribution. The results for the CY14 residuals are shown in Table 9.14 for the within-event residuals, and Table 9.15 for the between-event residuals. Note that the deviation from normality is pervasive at nearly all periods for epsilons greater than 2.5 for the within-event term. On the other hand, the normality assumption holds for between-event residuals with the exception of very long periods and an epsilon of 3.5 (the highest epsilon tested).

The same tests were also conducted by the GMC TI Team on the KiK-net data for crustal earthquakes (Dawood et al. 2014) and results are shown in Figure 9.117 for one period only (T = 0.2 sec), both for the within-event residuals (δW_{es}) and the site- and event-corrected residuals (δWS_{es}) (the y-axis is not normalized in these plots, hence the line for the normal distribution is not a 1:1 line). The heavy tails appear in the within-event residuals but are much stronger in the site- and event-corrected residuals. The between-event residuals (not shown) fit the normal distribution well and do not show heavy tails. The same results were obtained for other periods.

A final set of tests was conducted by the GMC TI Team on the subduction data compiled for this study (Section 7.1.3) using the GMPE developed during this study (Section 9.2.2). The results are shown in terms of the statistical tests described above in Table 9.16 and Table 9.17 for within-event and between-event residuals, respectively. The conclusions are similar to those above: the within-event residuals deviate from normality at high epsilons (2 to 2.5 for this data set). For the subduction data set, the between-event residuals deviate from normality at an epsilon of 3.5. However, at this large epsilon the data are very scarce.

Table 9.14. Statistical significance analysis test for CY14 within-event residuals. Cells highlighted in red are those that have statistically significant heavy tails (i.e., deviation from normality).

Periods	ε=1	ε= 1.5	ε= 2	ε= 2.5	ε= 3	ε= 3.5
0.01	0.999205	0.982823	0.602911	0.009359	0.004127	0.000591
0.02	0.999649	0.962289	0.694656	0.016367	0.00057	0.000591
0.03	0.997444	0.948244	0.480993	0.009359	0.0022	6.77E-06
0.04	0.999759	0.939817	0.775933	0.001398	2.7E-05	0.002208
0.05	0.999982	0.984362	0.480993	0.000689	4.98E-06	0.002208
0.075	0.999941	0.968051	0.896384	0.002734	0.0022	0.002208
0.1	0.996509	0.959106	0.153204	0.016367	0.089673	0.299099
0.12	0.99453	0.85733	0.295458	0.085747	0.089673	0.061627
0.15	0.807709	0.873444	0.295458	0.151058	0.022437	0.007486
0.17	0.986562	0.585823	0.167931	0.085747	0.000131	0.002208
0.2	0.999334	0.939817	0.046199	0.002734	0.000131	0.002208
0.25	0.987415	0.919808	0.530105	0.069653	0.000277	0.022792
0.3	0.947058	0.977023	0.406672	0.035073	0.002192	0.000589
0.4	0.964093	0.869348	0.645676	0.021032	0.089212	0.007458
0.5	0.959844	0.836442	0.350523	0.402039	0.001107	0.002183
0.75	0.988907	0.968783	0.618475	0.017622	0.003676	1.19E-06
1	0.989859	0.971626	0.848569	0.005424	3.98E-05	0.0005
1.5	0.975808	0.905059	0.668582	0.16491	0.026618	0.001234
2	0.806934	0.985334	0.600183	0.002277	0.01781	0.00063
3	0.845986	0.782553	0.218903	0.020892	6.63E-05	1.63E-05
4	0.818945	0.888188	0.046376	0.007101	0.000576	3.53E-06
5	0.815955	0.767781	0.191394	0.002477	4.43E-05	6.63E-05
7.5	0.972834	0.874671	0.214937	0.024911	5.5E-06	0.004302
10	0.993585	0.975522	0.188072	0.00441	0.00097	0.000329

Table 9.15. Statistical significance analysis test for CY14 between-event residuals. Cells highlighted in red are those that have statistically significant heavy tails (i.e., deviation from normality).

Periods	$\varepsilon = 1$	$\varepsilon = 1.5$	$\varepsilon = 2$	$\varepsilon = 2.5$	$\varepsilon = 3$	$\varepsilon = 3.5$
0.01	0.551997	0.786246	0.521846	0.554591	0.332284	0.0672
0.02	0.488879	0.786246	0.676131	0.844713	0.332284	0.0672
0.03	0.488879	0.438605	0.521846	0.844713	0.332284	0.0672
0.04	0.168181	0.62232	0.676131	0.554591	0.332284	0.0672
0.05	0.209595	0.530566	0.676131	0.554591	0.332284	0.0672
0.075	0.673895	0.203793	0.96702	0.844713	0.332284	0.0672
0.1	0.614178	0.203793	0.909858	0.844713	0.332284	0.0672
0.12	0.36603	0.272014	0.371508	0.844713	0.332284	0.0672
0.15	0.36603	0.786246	0.371508	0.554591	0.332284	0.0672
0.17	0.42639	0.786246	0.243763	0.554591	0.332284	0.0672
0.2	0.551997	0.351139	0.082693	0.284481	0.332284	0.0672
0.25	0.780715	0.530566	0.082693	0.040132	0.332284	0.0672
0.3	0.893293	0.266766	0.145438	0.002875	0.331381	0.066983
0.4	0.664907	0.14393	0.081233	0.000634	0.331381	0.066983
0.5	0.77339	0.266766	0.009152	0.011474	0.331381	0.066983
0.75	0.542076	0.345317	0.0421	0.552784	0.331381	0.066983
1	0.655802	0.194827	0.143283	0.550972	0.330478	0.066766
1.5	0.187989	0.25639	0.51126	0.841784	0.329573	0.066548
2	0.209262	0.642906	0.479039	0.83266	0.321372	0.064592
3	0.346529	0.921472	0.224262	0.210441	0.290437	0.057382
4	0.740154	0.720729	0.067655	0.050101	0.03646	0.050118
5	0.893942	0.422427	0.034613	0.033688	0.230533	0.044132
7.5	0.763384	0.359282	0.045929	0.222994	0.175655	0.032722
10	0.93686	0.587918	0.446472	0.489689	0.135745	0.024814

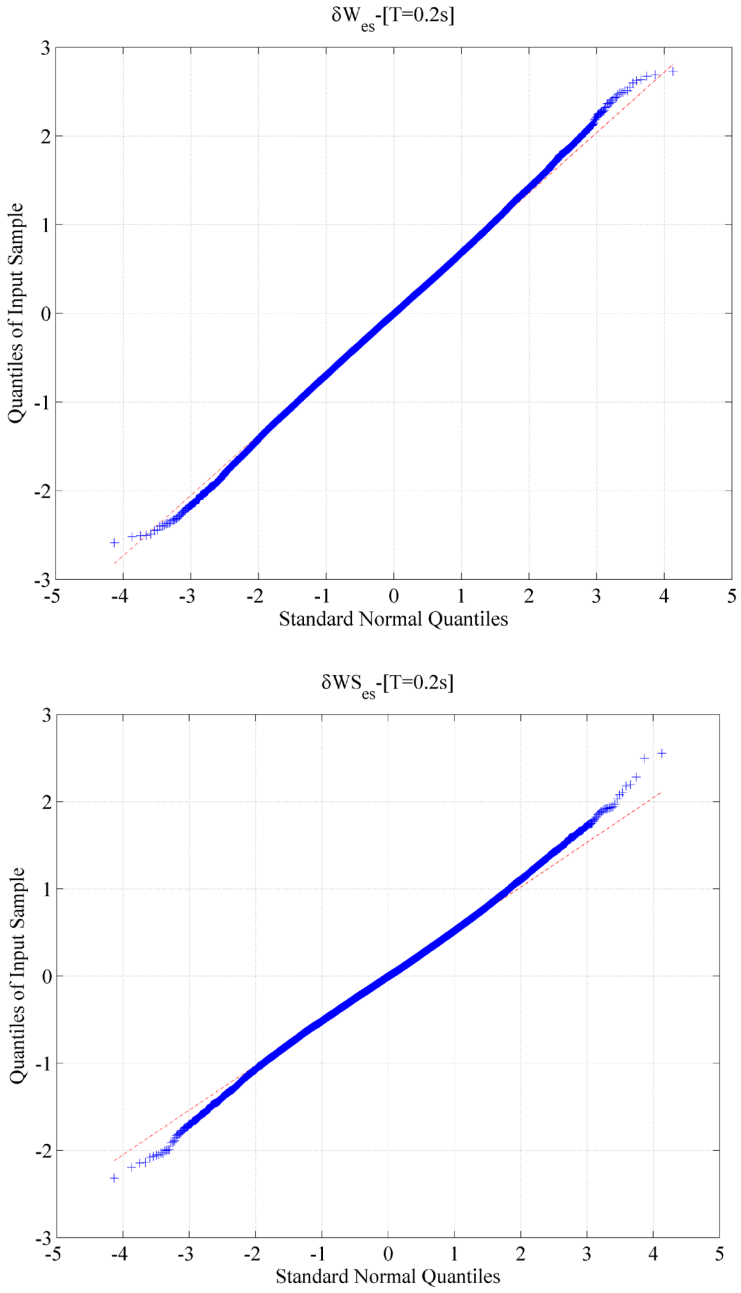

Figure 9.117. Q-Q plots of residuals from the KiK-net crustal database of Dawood et al. (2014). The top plot shows within-event residuals, the bottom plot shows site-corrected within-event residuals. The y-axis is not normalized.

Table 9.16. Statistical significance analysis test for the within-event residuals of the subduction GMPE developed in this study. Cells highlighted in red are those that have statistically significant heavy tails (i.e., deviation from normality).

Periods	$\varepsilon = 1$	$\varepsilon = 1.5$	$\varepsilon = 2$	$\varepsilon = 2.5$	$\varepsilon = 3$	$\varepsilon = 3.5$
0.01	0.950074	0.268922	0.001239	0.001297	0.000212	0.01145
0.02	0.865997	0.288177	0.021141	0.014393	0.034756	0.174914
0.05	0.973969	0.353214	0.000617	1.27E-05	1.34E-05	0.01989
0.075	0.732848	0.704535	0.081598	0.000184	0.003162	0.020126
0.1	0.919413	0.313368	0.151623	0.001194	8.2E-07	0.005112
0.15	0.995837	0.250865	0.000368	3.45E-06	4.64E-05	0.003945
0.2	0.997958	0.178779	1.52E-06	2.02E-09	8E-07	0.00089
0.25	0.9872	0.19469	5.06E-06	9.74E-10	1.34E-05	0.019875
0.3	0.986496	0.14353	0.000388	1.45E-05	4.72E-05	0.020215
0.4	0.869919	0.460953	0.011601	1.77E-06	0.000262	0.000849
0.5	0.667824	0.190889	0.161686	0.000282	0.001111	8.83E-05
0.6	0.860104	0.246235	0.057358	0.01476	0.002708	0.019007
0.75	0.777803	0.088021	0.177128	0.032099	0.069743	0.018779
1	0.810367	0.944406	0.213167	0.021259	0.023471	0.000796
1.5	0.791988	0.701156	0.423567	0.480598	0.127199	0.018343
2	0.909811	0.5839	0.453919	0.33648	0.003421	1.24E-05
3	0.966486	0.553429	0.020913	0.007987	0.009457	0.002677
4	0.989649	0.070902	4.57E-05	0.001352	0.215992	0.152558
5	0.992355	0.195471	0.000349	3.93E-05	0.000469	0.027054
6	0.999573	0.672974	0.000871	6.9E-08	2.38E-08	0.000209
7.5	0.999947	0.73086	0.002623	4.28E-09	1.91E-07	3.74E-08
10	0.925132	0.864672	0.699625	0.016265	0.001043	0.001032

Table 9.17. Statistical significance analysis test for the between-event residuals of the subduction GMPE developed in this study. Cells highlighted in red are those that have statistically significant heavy tails (i.e., deviation from normality).

Periods	$\varepsilon = 1$	$\varepsilon = 1.5$	$\varepsilon = 2$	$\varepsilon = 2.5$	$\varepsilon = 3$	$\varepsilon = 3.5$
0.01	0.529531	0.497751	0.625497	0.691886	0.225318	0.043019
0.02	0.166534	0.475215	0.725959	0.502247	0.140402	0.025721
0.05	0.387941	0.731804	0.624608	0.584508	0.173425	0.032272
0.075	0.611446	0.367854	0.638712	0.592201	0.176768	0.032947
0.1	0.25873	0.58405	0.41234	0.684113	0.221121	0.042128
0.15	0.521116	0.853085	0.638712	0.225271	0.176768	0.032947
0.2	0.199872	0.466452	0.41234	0.684113	0.221121	0.042128
0.25	0.611446	0.629646	0.638712	0.592201	0.176768	0.032947
0.3	0.784429	0.376449	0.64333	0.594733	0.177879	0.033172
0.4	0.400232	0.697337	0.794257	0.684113	0.221121	0.042128
0.5	0.62504	0.927072	0.844458	0.594733	0.177879	0.033172
0.6	0.521116	0.752707	0.963624	0.592201	0.176768	0.032947
0.75	0.774071	0.924207	0.638712	0.592201	0.176768	0.032947
1	0.711595	0.875749	0.608791	0.109045	0.221121	0.042128
1.5	0.358489	0.637867	0.420145	0.062358	0.016743	0.033172
2	0.559144	0.875749	0.41234	0.109045	0.221121	0.042128
3	0.068744	0.683775	0.600268	0.106456	0.025825	0.041682
4	0.31737	0.373527	0.323862	0.017765	0.112078	0.020266
5	0.503453	0.516919	0.132978	0.100237	0.109676	0.01981
6	0.547675	0.181238	0.117255	0.092534	0.104852	0.018897
7.5	0.389862	0.286106	0.274171	0.392451	0.102431	0.01844
10	0.421019	0.253187	0.323624	0.272165	0.066572	0.011795

9.5.5.2 Proposed Mixture Model

A mixture model is a model in which the distribution of residuals is represented by a weighted mixture of two normal distributions, one with a larger variance, and one with a smaller variance. While there are alternative ways of capturing heavy-tailed distributions, the mixture model is attractive because the only parameters that need to be calibrated are the mixture weights and the standard deviations used for the two distributions. These standard deviations are given as ratios of the standard deviation of the normal distribution, which was already computed in Sections 9.5.3 and 9.5.4. The mixture model was calibrated using the ASK14 residuals. The selected model assigns 50% weight to each of two distributions with sigma ratios of 1.2 and 0.8 (Figure 9.118). For this mixture model, the conditional probability of exceeding a ground motion level Z is given by

$$P(Z > z) = w_{Mix1}\left\{1 - \Phi\frac{(z-\mu)}{\sigma_{Mix1}}\right\} + w_{Mix2}\left\{1 - \Phi\frac{(z-\mu)}{\sigma_{Mix2}}\right\} \quad (9.37)$$

where w_{Mix1} and w_{Mix2} are the mixture weights (0.5 and 0.5), and σ_{Mix1} and σ_{Mix2} are the standard deviations obtained by combining $1.2\phi_{ss}$ and $0.8\phi_{ss}$ with the values of τ, where ϕ_{ss} and τ are the normal models discussed in Sections 9.5.3 and 9.5.4. In the GMC logic tree, the mixture model is assigned a weight of 0.8 and a normal distribution is assigned a weight of 0.2. The mixture model is strongly favored because most of the data sets tested showed statistically significant evidence of heavy tails in the intra-event residuals and improved fits of the residuals were found with very similar mixtures.

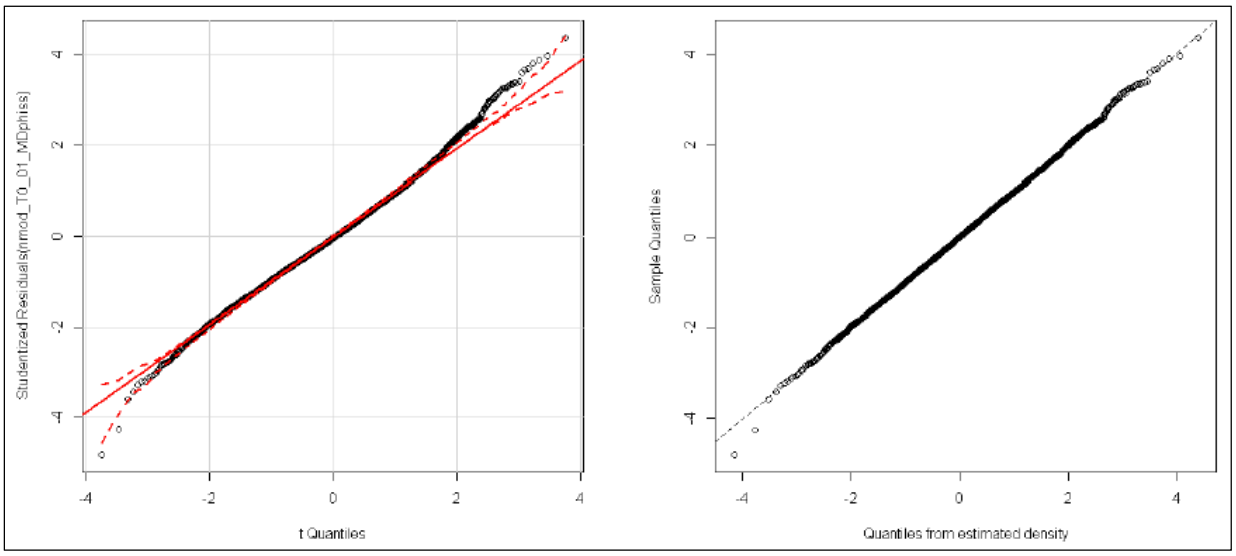

Figure 9.118. The plot on the left shows the event- and site-corrected residuals of the ASK14 relationship using a normal distribution. The plot on the right shows the same residuals fitted to a mixture model that uses two distributions with sigma ratios of 1.2 and 0.8 with 50% weight to each distribution.

9.5.6 Minimum Epistemic Uncertainty on the Site Term

As discussed in Section 9.1.1, at longer response periods, the GMC TI Team concluded that the single-station sigma could not be fully invoked for two reasons: the lack of variability in the site response calculations at long periods (Section 9.6.5) and the possible presence of basin effects at intermediate periods (Section 7.6.3). Because both of these factors are related to the behavior of layers above the baserock elevation, it was not considered appropriate to use ergodic sigma in the baserock for these period ranges. Rather, the effective variability due to the increase above single-station sigma is estimated at the relevant periods and then specified as a minimum level of variability to be associated with the site amplification factors (Section 9.6.6).

The effective variability due to the increase above single-station sigma can be computed from what would be the equivalent site-to-site uncertainty in the models (ϕ_{S2S}). This uncertainty can be derived from Equations 9.24 and 9.25 as

$$\phi_{S2S} = \sqrt{\phi^2 - \phi_{ss}^2} \tag{9.38}$$

where ϕ is the ergodic within-event standard deviation. The values of ϕ for crustal earthquakes can be computed using the NGA-West2 database (as was done for τ in Section 9.5.3.1). The ϕ model for

subduction earthquakes was presented in Section 9.5.4.1, and single-station phi models for crustal and subduction earthquakes were discussed extensively in Sections 9.5.3 and 9.5.4. The computed values of ϕ_{S2S} are shown in Figure 9.119. Note that the estimates of ϕ_{S2S} vary with magnitude and with earthquake type. This is, in part, due to the fact that the ergodic phi (ϕ) and ϕ_{ss} models used in this study

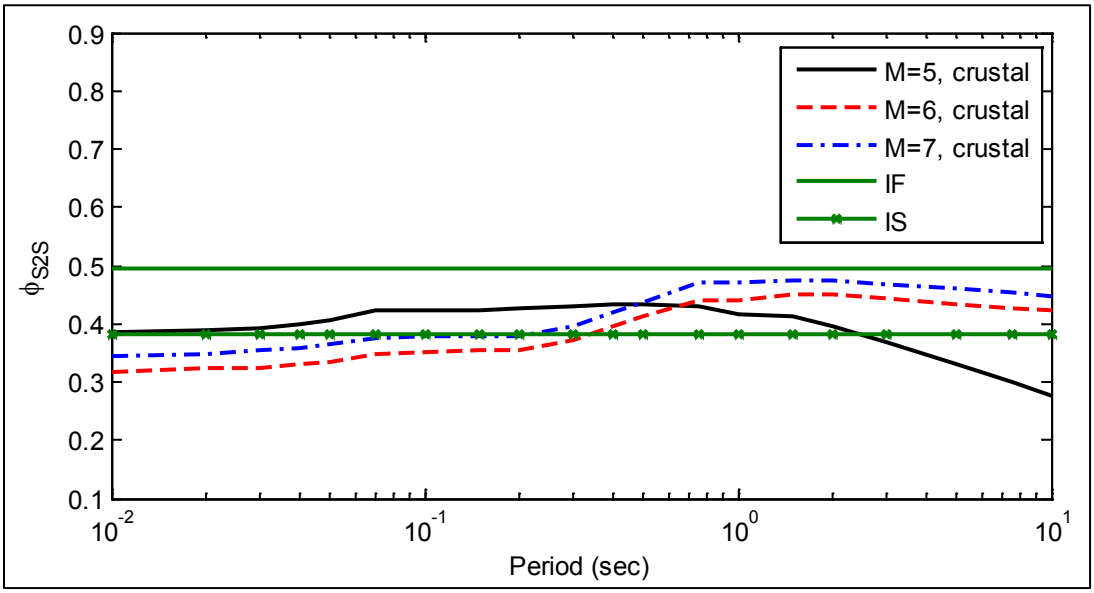

Figure 9.119. Estimated values of ϕ_{S2S} using the ϕ_{ss} models developed for this project, an average ϕ model from the NGA-West2 database for crustal earthquakes, and the ϕ model for subduction earthquakes (Section 9.5.4.1).

are obtained from different data sets. These values are, in general, bounded between 0.4 and 0.5. Estimates of site-to-site variability obtained from the PRP data for T = 1 sec and for different regions are shown in Figure 9.120. Note that these values vary from region to region and are a function of average shear-wave velocity. However, the higher ϕ_{S2S} values can also be reasonably bounded between 0.4 and 0.5. An additional set of data that can inform the choice of ϕ_{S2S} is the subduction data used in this project (Section 9.2.2). The resulting ϕ_{S2S} values from this data set are shown in Figure 9.121. Observe that for intermediate and long periods (T > 0.5 sec), the values of ϕ_{S2S} are also bounded between 0.4 and 0.5.

For the reasons explained in the preceding paragraph, a value of ϕ_{S2S} = 0.45 is proposed for application in this project. This value becomes a minimum epistemic uncertainty ($\sigma_{epi,min}$) that needs to be applied to the site term at intermediate to long periods. These periods are determined by the consideration of potential basin effects (Section 7.6; which start to take effect at T > 0.5 sec) and the fact that the V_S-kappa correction factors have low uncertainty at periods higher than about 1 sec (Section 9.3). For this reason, a taper function is proposed such that the proposed minimum epistemic uncertainty goes from zero at T = 0.5 sec to 0.45 at approximately T = 1 sec. Hence, the proposed minimum epistemic uncertainty is shown in Figure 9.122 and is given by

$$\sigma_{epi,min}(T) = 0.225 * tanh[2.2662 * (\log(T) + 0.3436] + 0.225 \quad (9.39)$$

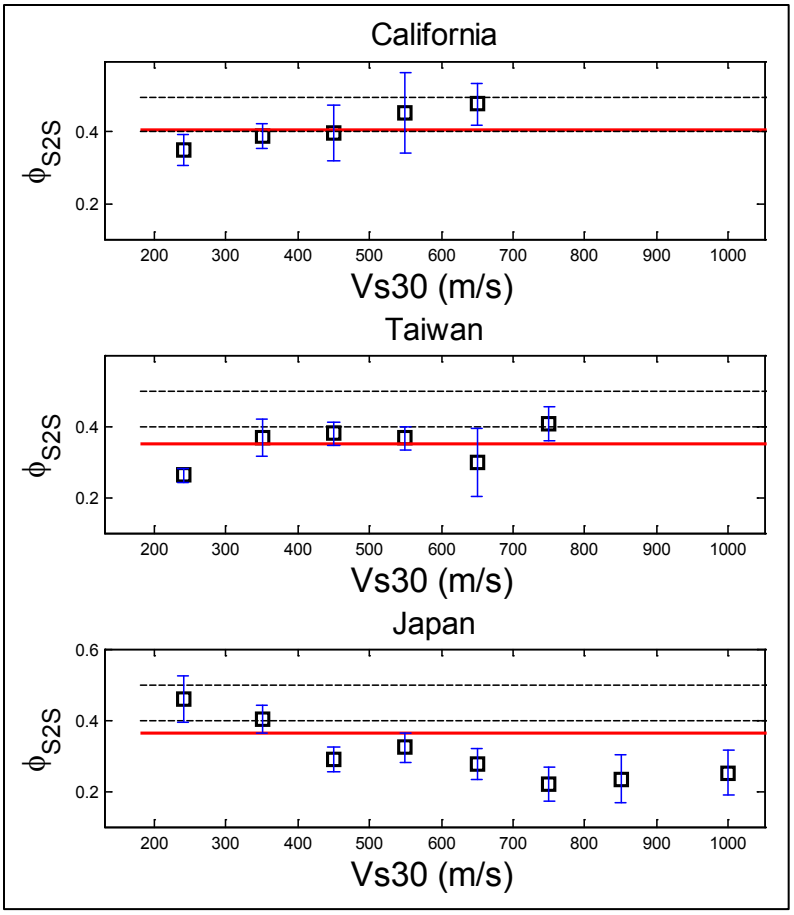

Figure 9.120. Values of ϕ_{S2S} from the PRP database for T = 1 sec. The dashed lines correspond to values of 0.4 and 0.5.

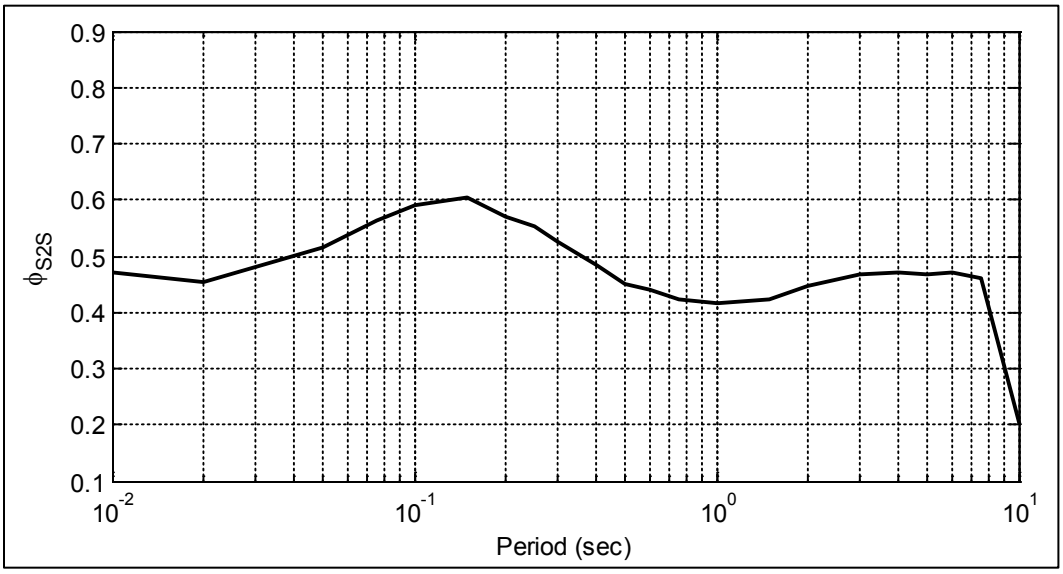

Figure 9.121. ϕ_{S2S} values from the subduction data set used in this study.

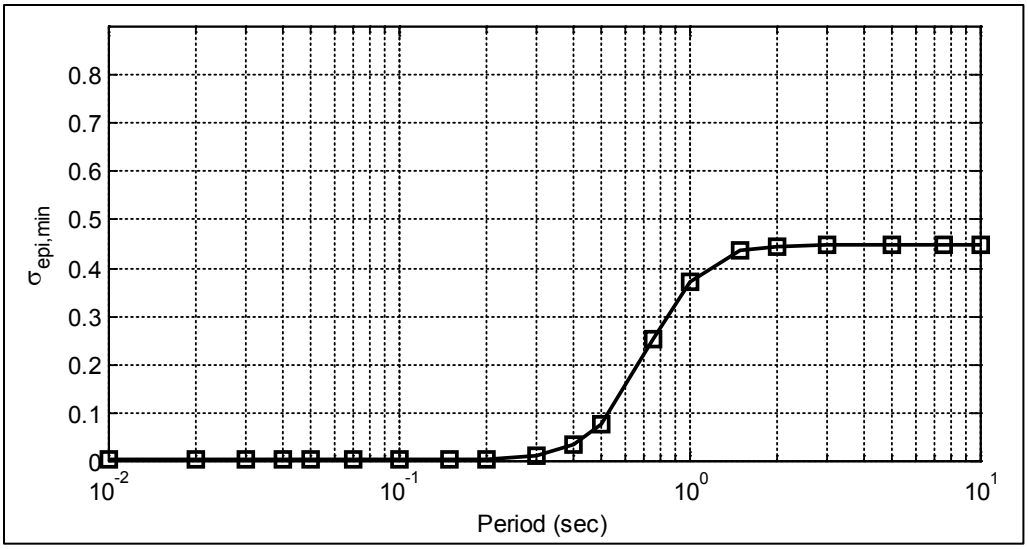

Figure 9.122. Proposed minimum epistemic uncertainty for the site response computations.

9.6 Saddle Mountain Basalt Stack Models for Site Response Analysis

In this section, the complete models of the layers from the baserock to the top of the basalts required as input to the site response calculations are presented for the five selected hazard calculation locations. The digital files containing this information are contained in Appendix J and the associated electronic supplement.

9.6.1 V_S and Density Profiles at Five Hazard Calculation Locations

In Section 7.2, the development of stratigraphic models from the top of basalts to the crystalline basement at the five hazard calculation locations was explained. The available measurements of shear-wave velocity, V_S, and density, ρ, from the WTP site were then used to transform the stratigraphic models into layer models of V_S and ρ. To capture the uncertainties in the velocities resulting from different velocities measured by different techniques, particularly in the basalts, two V_S models were developed for each of the locations, and assigned relative weights. The uppermost part of the V_S and ρ profiles for the five locations, which include the full SMBs stacks, are shown in Figures 7.21 to 7.25. The profile shown in those figures extends well below the top of the baserock (the elevation corresponding to the base of the flowtop of the Lolo flow, which is the uppermost part of the Wanapum basalts) because these were models developed for the complete stratigraphy from the top of the SMB to the crystalline basement. For the handover, only the portion of these profiles above the baserock elevations are required, together with the model for the elastic half-space that will represent the underlying Wanapum and Grande Ronde basalts in the site response analyses. The depths below the top of the SMBs at which the baserock elevation is encountered are summarized in Table 9.18.

Table 9.18. Depths to baserock at the five hazard locations and baserock properties.

Site	Depth Below Top of SMB (m)
A	254.13
B	280.23
C	236.90
D	253.23
E	280.49

The elastic half-space is represented by a shear-wave velocity, V_S, of 3,000 m/s and a mass density of 2.83 g/cm^3, to be used in the site response analyses with both the Profile 1 and Profile 2 models of the SMB stacks. Because the motions in the baserock are calculated taking full account of the baserock, it is not necessary or appropriate to model any significant damping in the elastic half-space, for which reason a nominal value of 0.001 (i.e., 0.1%) is proposed. Figure 9.123 through Figure 9.127 show the stack models, in terms of V_S and ρ, overlying the half-space.

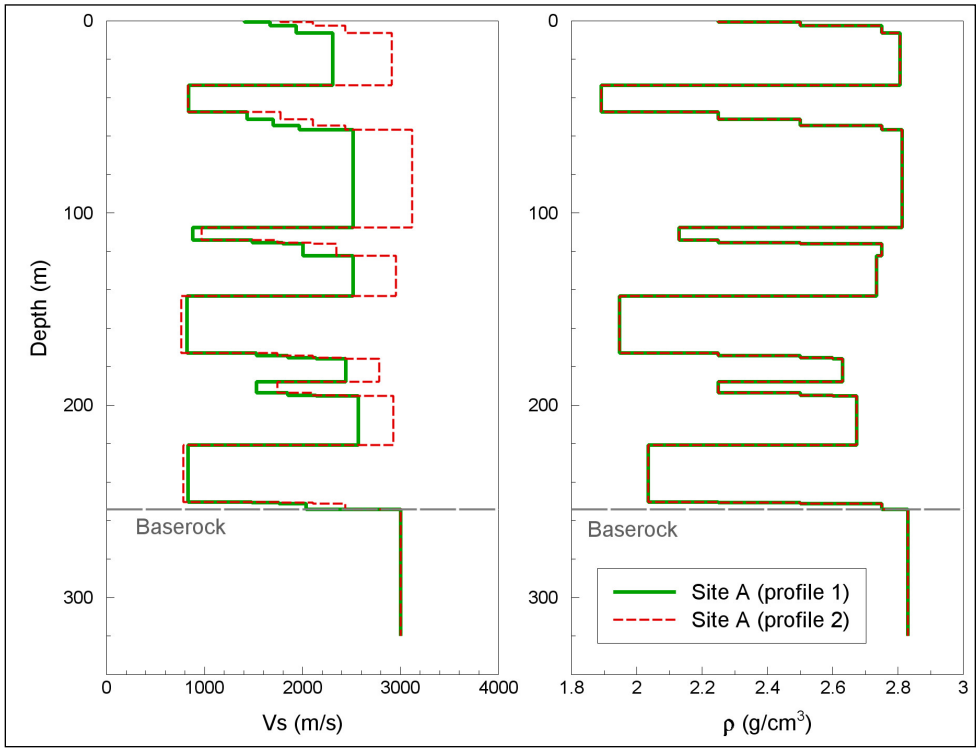

Figure 9.123. Models for SMB stack and elastic half-space at Site A.

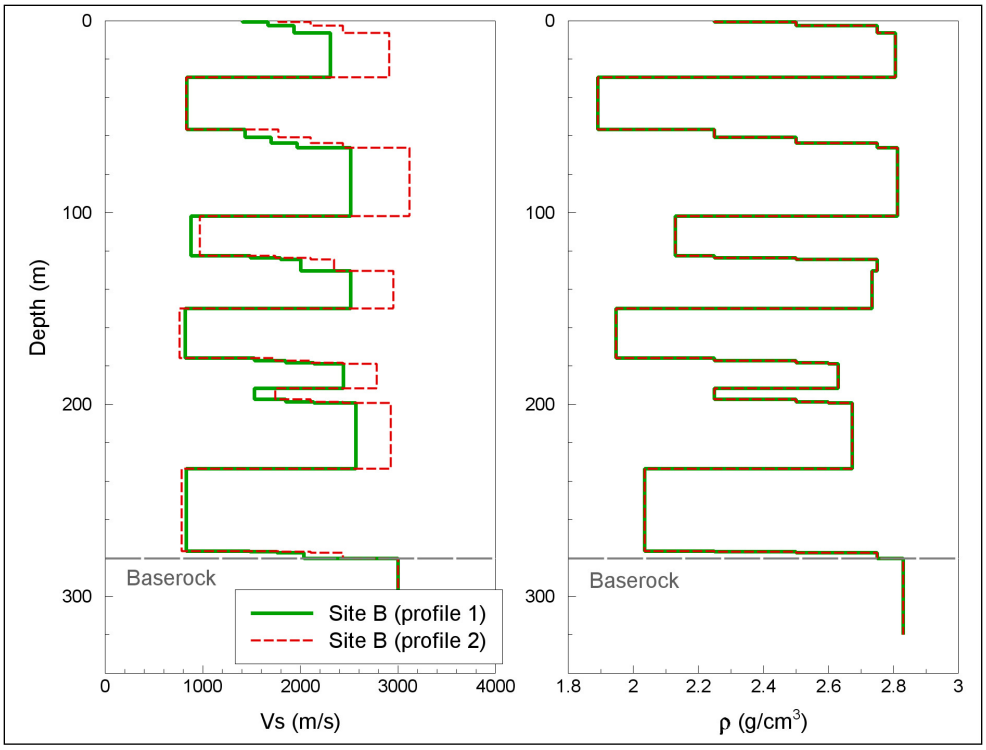

Figure 9.124. Models for SMB stack and elastic half-space at Site B.

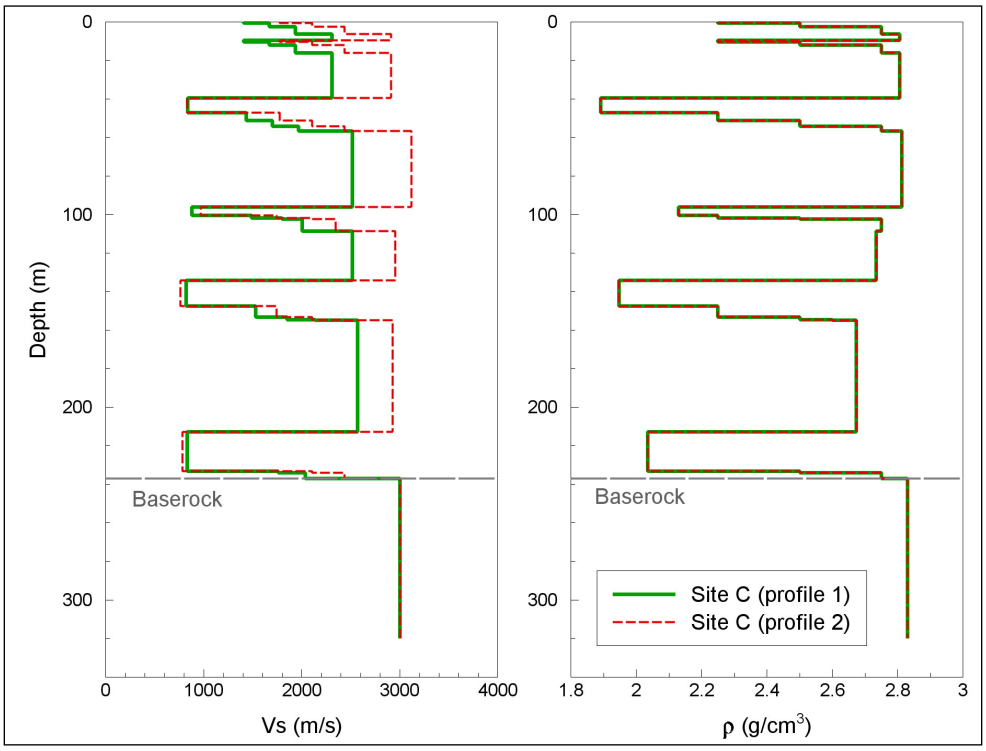

Figure 9.125. Models for SMB stack and elastic half-space at Site C.

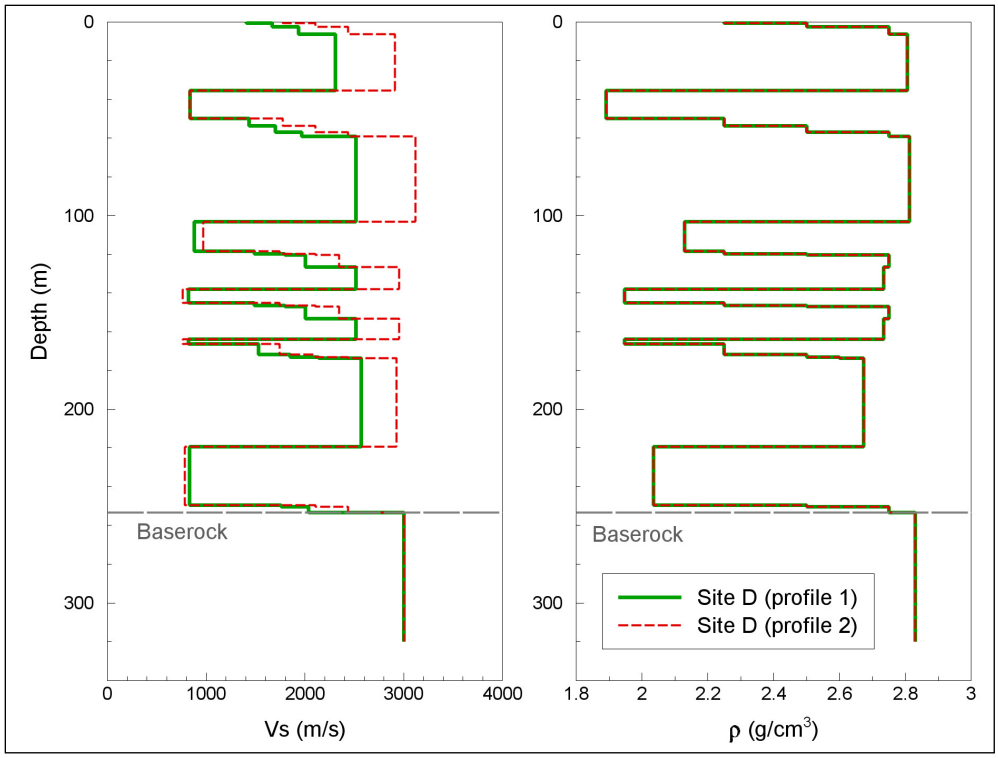

Figure 9.126. Models for SMB stack and elastic half-space at Site D.

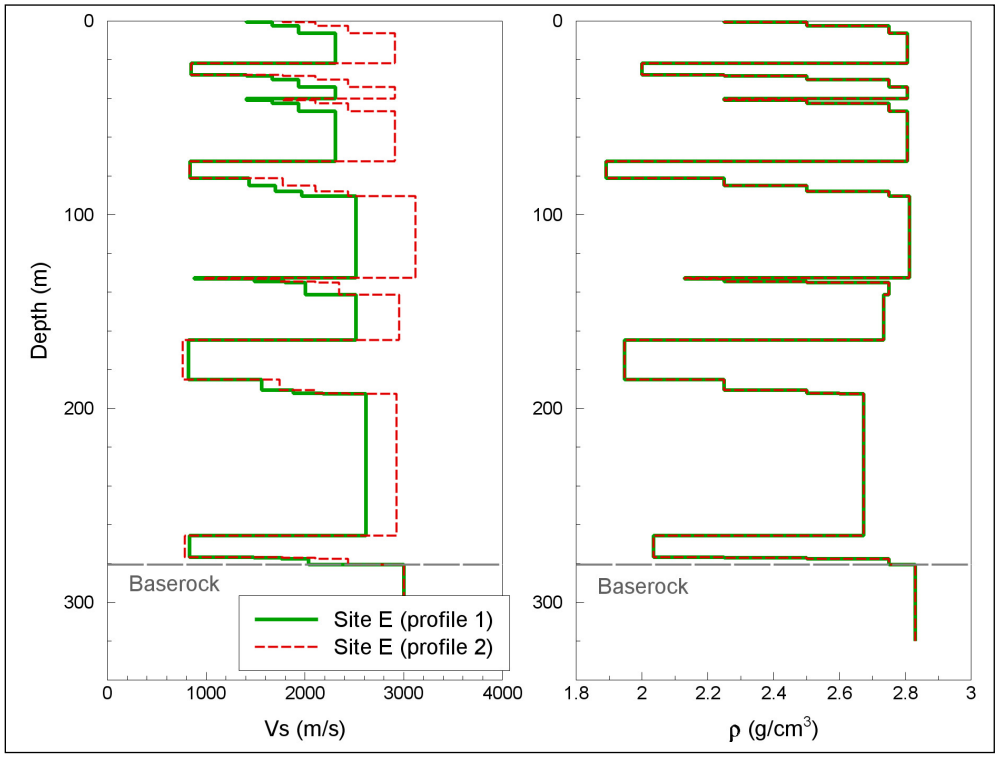

Figure 9.127. Models for SMB stack and elastic half-space at Site E.

9.6.2 Effective Damping of the SMB Stacks and Site Kappa Models

The kappa model for the Hanford Site is discussed in Section 7.3.4 and quantifies the damping effects at the five hazard calculation sites. Estimates of κ_{site} due to damping are presented in Table 7.23. At each hazard calculation site, the difference in κ_{site} between Profiles 1 and 2 is mostly due to the difference in $\kappa_{baserock}$ for the profile depth branches where the sub-basalt sediments contribute to damping. This is due to the large thickness of the sediments layer, where V_S values are different for the two profiles, relative to the entire profile depths. For the no sub-basalt sediments branch, κ_{site} estimates are comparable for Profiles 1 and 2.

Material damping properties in the SMB stack are presented in Table 7.24 for Profiles 1 and 2 at the five hazard calculation sites. These properties were estimated using a fixed γ model ($\gamma = 0.0345$ sec/m) in the stack while transferring the epistemic uncertainty in the SMB damping to the baserock damping. As discussed in Section 7.3.5.4, this approach preserves the κ_{site} estimates and the epistemic uncertainty in κ_{site} while simplifying the downstream site response analysis. A consequence of this approach is that the estimates of $\kappa_{baserock}$ and the resulting hazard at the reference baserock horizon are specific to this application and to the damping assigned to the SMB stack and cannot be used alone.

Scattering is considered to be negligible below the reference baserock horizon as discussed in Section 7.3.5.1. In the SMB stack, scattering kappa is not negligible due to the velocity contrasts in the stack. Table 9.19 presents the damping, scattering, and total kappa estimates in the SMB stack at the five hazard calculation sites for Profiles 1 and 2. Scattering kappa in the SMB stack is estimated following the same SHAKE (Schnabel et al. 1972b) approach used to estimate scattering kappa at the recording stations and discussed in Section 7.3.5.1. Table 9.19 shows that damping kappa in the SMB stack is practically the same for the two profiles. This is because the V_S in the interbeds of the stack are similar for the two profiles and damping in the stack is largely explained by the interbeds where V_S values are significantly lower than in the basalt layers. Because of the larger velocity contrasts in Profile 2 compared to Profile1, scattering kappa is larger for Profile 2 than for Profile 1. Differences in scattering kappa between Profiles 1 and 2 are on the order of 0.0035 to 0.0045 sec. It is important to note that while the GMC TI Team estimated scattering kappa in the SMB stack, these estimates are not part of the handover to the site response analysis. Damping in the stack should be assigned according to the TI Team's estimates, but scattering kappa will result from the stratigraphy and the V_S profiles in the site response analysis.

Given the presence of two V_S profiles for the stack, the GMPEs adjusted to each of the baserock kappa values are used to calculate baserock hazard and these hazard estimates should ideally be kept coupled with the corresponding stack models, with the hazard estimates only being combined at the ground surface. However, this separation is not maintained, and a single model is developed for ground motion prediction in the baserock, providing a single dynamic input into the base of the two different stack models. The decision to decouple the baserock hazard from the stack models was adopted to avoid complexities in the hazard calculations and the downstream site response analysis. The handover to the downstream site response analyses and convolution with the hazard would have become very complicated had the coupling been maintained, and the baserock hazard calculations—which are already remarkably time-consuming—would have become prohibitively demanding in terms of computation.

In terms of damping kappa, decoupling the baserock hazard estimates from the stack models has no impact on the ground motion at the top of SMB because κ_{site} estimates were maintained in the analysis and $\kappa_{damping}$ estimates in the SMB stack are very similar for the two profiles as shown in Table 9.19.

Table 9.19. Kappa (sec) in the SMB stack for Profiles 1 and 2 at the five hazard calculation sites at Hanford.

	Profile 1			Profile 2		
	$\kappa_{damping}$	$\kappa_{scattering}$	κ_{total}	$\kappa_{damping}$	$\kappa_{scattering}$	κ_{total}
Site A	0.0044	0.0075	0.0119	0.0044	0.0120	0.0164
Site B	0.0058	0.0060	0.0118	0.0058	0.0100	0.0158
Site C	0.0030	0.0053	0.0083	0.0029	0.0093	0.0122
Site D	0.0039	0.0080	0.0119	0.0037	0.0120	0.0157
Site E	0.0033	0.0035	0.0068	0.0031	0.0070	0.0101

Differences in scattering kappa between the two profiles are ignored by decoupling the baserock hazard estimates from the stack models. To evaluate the impact of the differences in scattering kappa on the ground motion at the top of SMB, site amplification factors at the top of the SMB stack were computed using the computer program RATTLE (Boore 2005) with respect to the half-space located at the reference baserock horizon using Profile 1 and 2. Smoothing was applied using the Konno and Ohmachi (1998) filter. Figure 9.128 and Figure 9.129 show comparisons of the site amplification factors in the SMB stack for Profiles 1 and 2 at the five hazard calculation sites. The impact of scattering kappa can be observed in the difference in the high-frequency site amplification factors. It is important to note, however, that this observed high-frequency difference in the site amplification factors in the Fourier domain would have a smaller impact in the response spectra domain. Therefore, the difference in site response between the two profiles due to differences in scattering kappa is considered small compared to the range of epistemic uncertainty in κ_{site} and $\kappa_{baserock}$ and the resulting range of V_S-kappa adjustment factors derived for CY14.

The modified BC Hydro subduction GMPE was not adjusted for host-to-target differences in kappa due to the dominance of distant scenarios on the hazard for subduction sources as discussed in Section 9.3.3. For such distant scenarios (distance of 200 to 250 km), the effect of anelastic attenuation is expected to cause significant decay in the high-frequency energy of Fourier and response spectra. As a result, the same difference in kappa causes a significantly smaller impact on the high-frequency ground motion for long-distance scenarios than for short-distance scenarios. Therefore, relatively small differences in scattering kappa between Profiles 1 and 2 in the SMB are expected to have a negligible effect on the ground motion at the top of SMB from subduction scenarios with significant contribution to the hazard at Hanford and can be ignored.

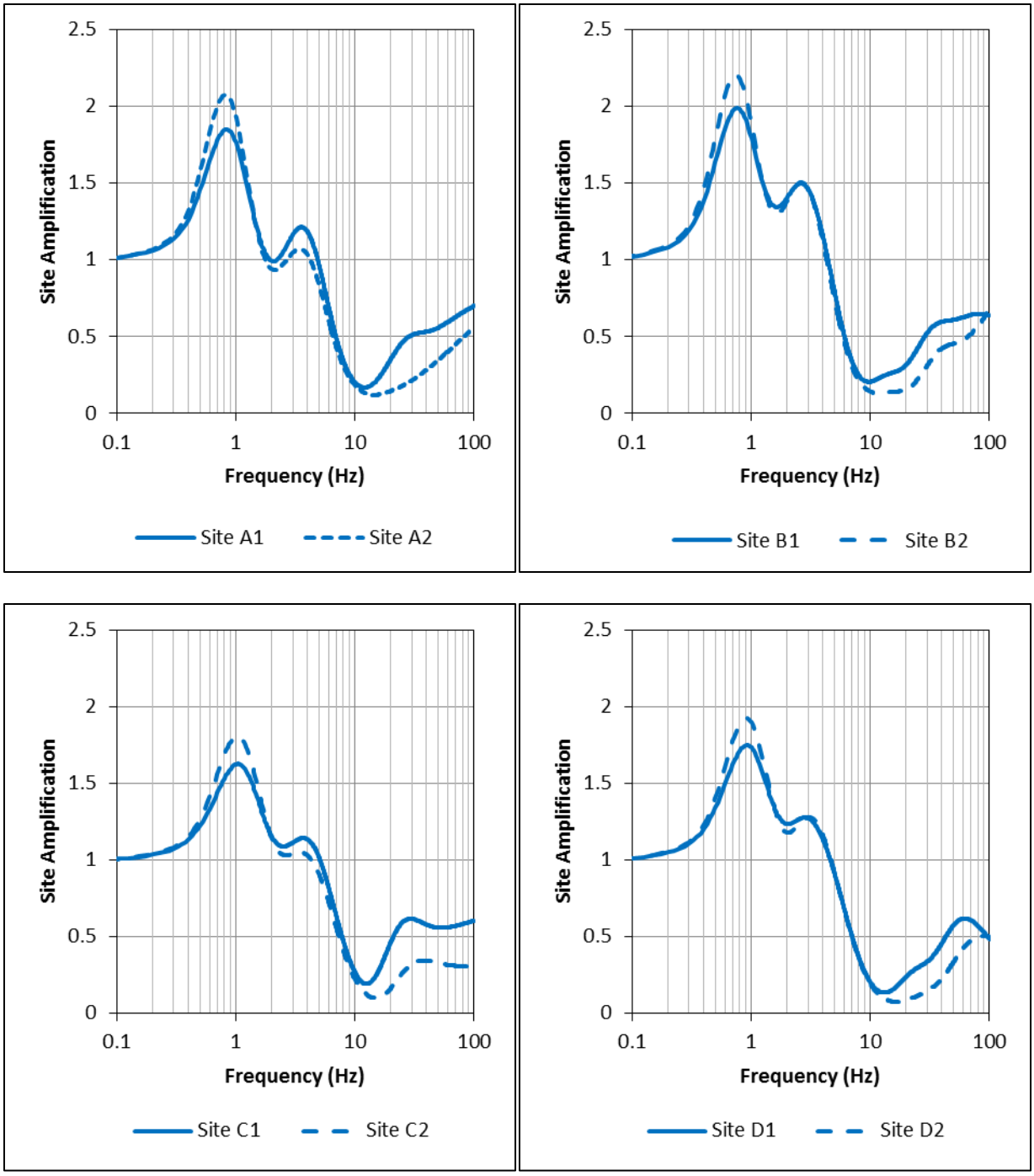

Figure 9.128. Comparison of site amplification factors in the SMB stack between Profiles 1 and 2 at Sites A, B, C, and D.

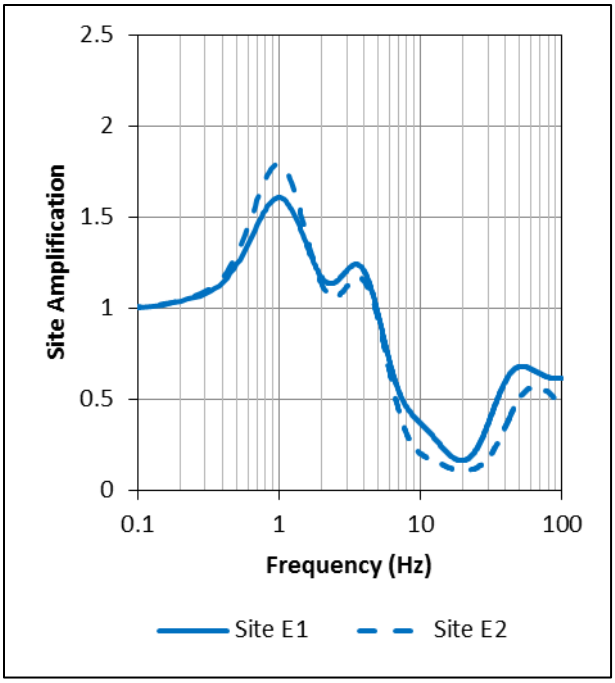

Figure 9.129. Comparison of site amplification factors in the SMB stack between Profiles 1 and 2 at Site E.

9.6.3 Recommendations Regarding Nonlinearity in the SMB Stack

When the amplitude of the cyclic loads applied on geological materials exceeds a certain threshold, these materials will exhibit nonlinear behavior. Within the equivalent linear approach used to estimate site effects, this nonlinearity is quantified by the relationships between the shear modulus normalized by its elastic value (G/G_{max}) and shear strain, and by the relationship between damping and shear strain. The G/G_{max} curves are usually referred to as modulus reduction curves, which together with the damping curves are referred to as the material nonlinearity curves. In this section we first investigate whether material nonlinearity has an effect on site response at the Hanford Site, and then recommend a set of material nonlinearity curves for use in the SMB stack.

Two preliminary profiles were used to investigate the effects of nonlinearity in the SMB stack. The first is the WTP profile of Rohay and Brouns (2007), and the second is the CGS profile (Bechtel 2013). Equivalent linear analyses were conducted using SHAKE 2000 (Ordonez, 2012). The input ground motions were selected from the NRC time history library. Eight strong ground motions were selected using modal scenarios evaluated from preliminary hazard sensitivity runs as a guide ($6 < M_w < 7$, $15 < R < 20$ km and $7 < M_w < 7.5$, $R < 20$ km). These motions were scaled to 11 different PGAs ranging from 0.01 g to 1.50 g. The input motions are shown in Table 9.20.

Table 9.20. Input ground motions used in the analyses to evaluate the effects of nonlinearity.

Earthquake	Year	Magnitude (Mw)	File Name	PGA (g)	N_o data points	Δt (sec)
Kocaeli, Turkey	1999	7.4	NGA_no_1165_IZT180	0.152	6000	0.005
Kocaeli, Turkey	1999	7.4	NGA_no_1165_IZT090	0.220	6000	0.005
Cape Mendocino	1992	7.1	NGA_no_825_CPM000	1.497	1500	0.02
Cape Mendocino	1992	7.1	NGA_no_825_CPM090	1.039	1500	0.02
Landers	1992	7.3	LCN260	0.721	9625	0.005
Landers	1992	7.3	LCN345	0.785	9625	0.005
Mammoth Lakes	1980	6.0	NGA_no_238_A-LVL000	0.104	8000	0.005
Mammoth Lakes	1980	6.0	NGA_no_238_A-LVL090	0.0773	8000	0.005

The shear-wave velocity profiles used in the analyses are shown in Figure 9.130 and Figure 9.131. Some simplifying assumptions were made in developing the profiles, because the objective of this exercise was not to capture the response at the site but simply to test the importance of nonlinear effects. Unit weights were obtained from Rohay and Brouns (2007). Two sets of nonlinear curves were used in this evaluation: the curves proposed by Schnabel (1973), which exhibit only limited nonlinear behavior, and the curves proposed by Darendeli (2001), which have a stronger degree of nonlinearity and also account for the effect of confining pressure and soil plasticity. The Darendeli curves were used for all the suprabasalt units except for the Ringold Formation, for which the Schnabel curves were used. Both sets of curves were used for the SMB interbeds to test the effects of different degrees of nonlinearity. The basalt layers in the SMB stack were always assumed to behave linearly.

The results of the analyses for the WTP site are shown in Figure 9.132. In these analyses, the Schnabel curves were assigned to the SMB interbeds. For comparison, an analysis where the interbeds are assumed to remain linear is also shown (in this case, the suprabasalt sediments were still assumed to behave nonlinearly). Note that there is only a slight deviation from linear behavior that is observed only for very high-input PGAs. Figure 9.133 repeats these analyses, but this time the Darendeli curves are used for the SMB interbeds. In this case, the difference between linear and nonlinear behavior becomes evident at an input PGA of about 0.3 g. Figure 9.134 shows the strains that develop in the WTP profile. Observe that the strains are concentrated on the SMB interbeds because of their lower stiffness. The SMBs experience only very low strain levels even for very strong input motions. Results for the CGS site are similar to those of the WTP site and are not shown. These results demonstrate the potential importance of capturing nonlinear behavior in the basalt interbeds.

The previous analyses demonstrated that the potential nonlinear behavior of the SMB interbeds can affect site response results for strong input ground motions. For this reason, the GMC TI Team recommends that nonlinearity be taken into account for these layers. The GMC TI Team also recommends that the basalt layers in the SMB stack be assigned linear properties because it is highly unlikely that these layers will develop high strains during seismic loading.

In the process of selecting nonlinear curves for the SMB interbeds it is important to consider the nature of these deposits. According to Rohay and Brouns (2007), these materials consist of epiclastic and volcanoclastic sedimentary rocks such as sandstones, mudstones, claystones, siltstones, and also tuff with an approximate shear-wave velocity of around 900 m/s.

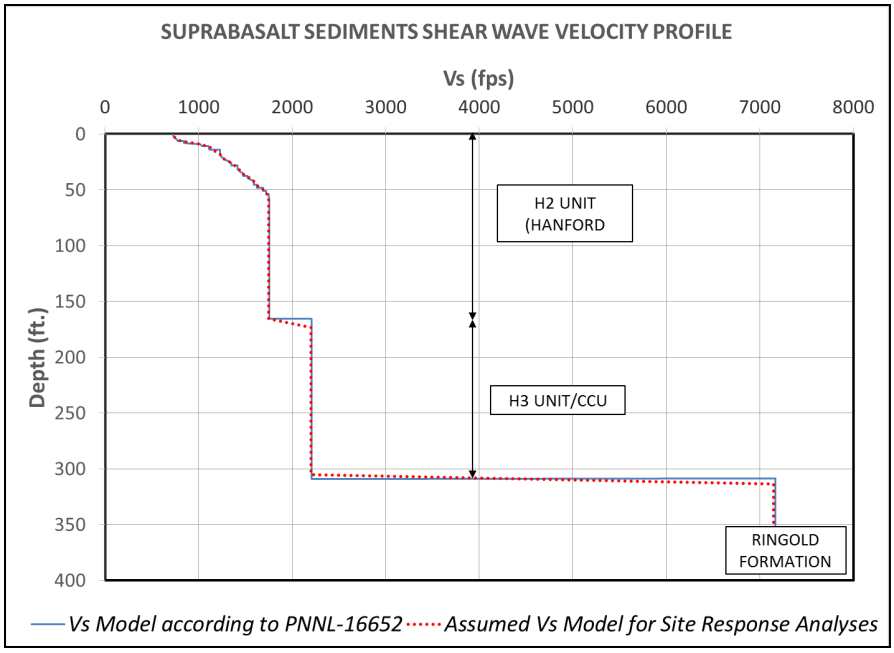

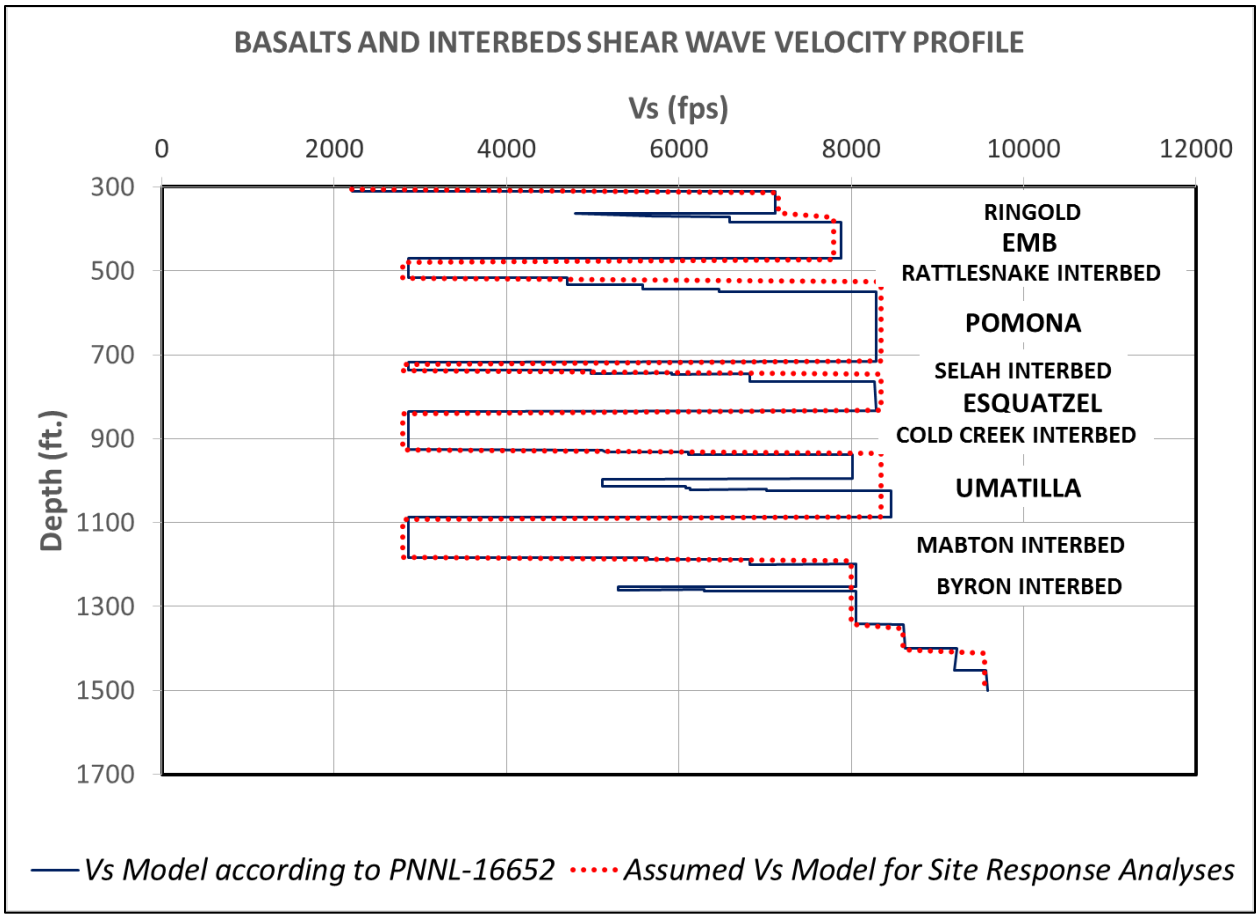

Figure 9.130. Shear-wave velocity profile used in the preliminary analyses for the WTP site. Top: suprabasalt sediments; bottom: Saddle Mountain Basalt stack.

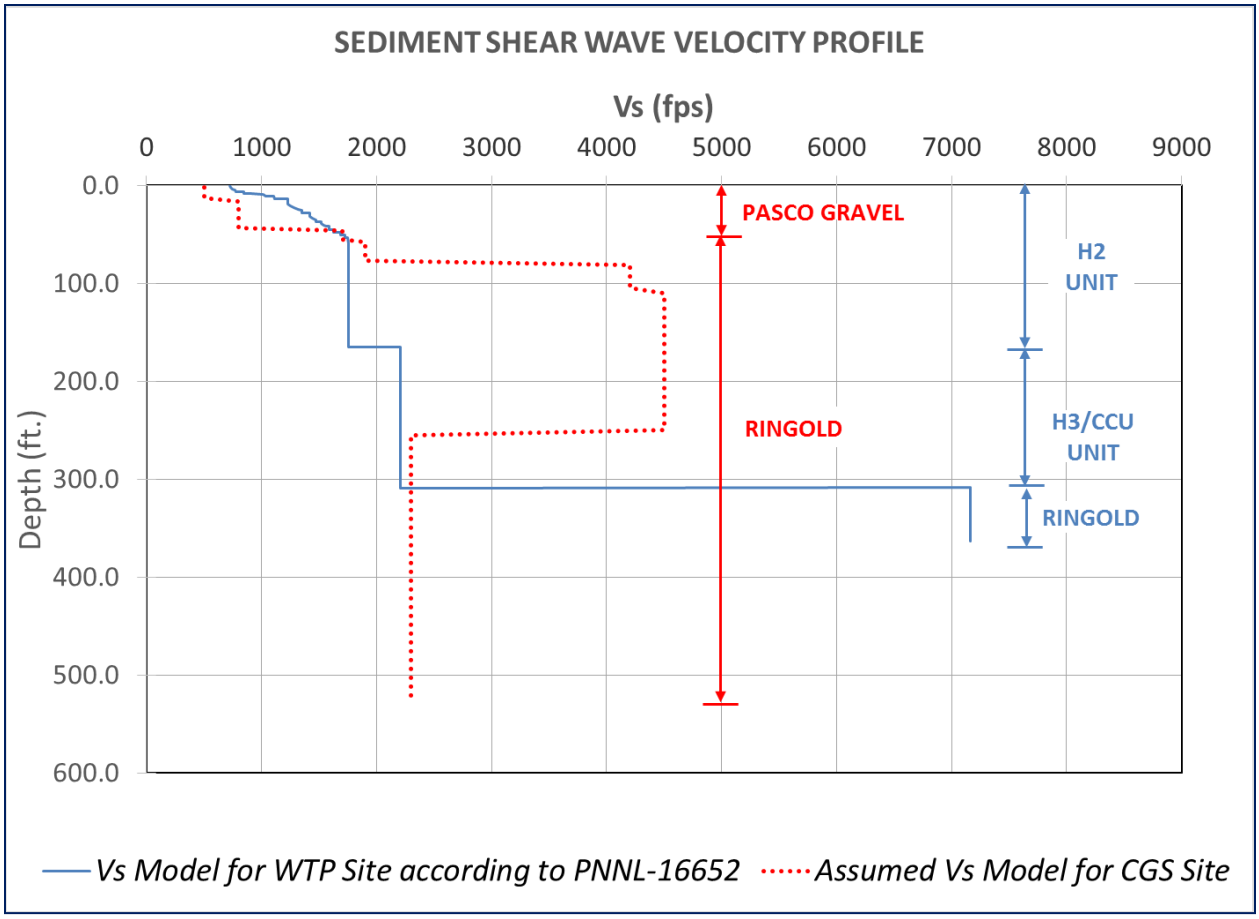

Figure 9.131. Shear-wave velocity profile for the suprabasalt sediments at the CGS site. The same stratigraphy as for the WTP profile was used for the units below the Ringold Formation (Figure 9.130). The V_S profile for the WTP site is also shown for reference.

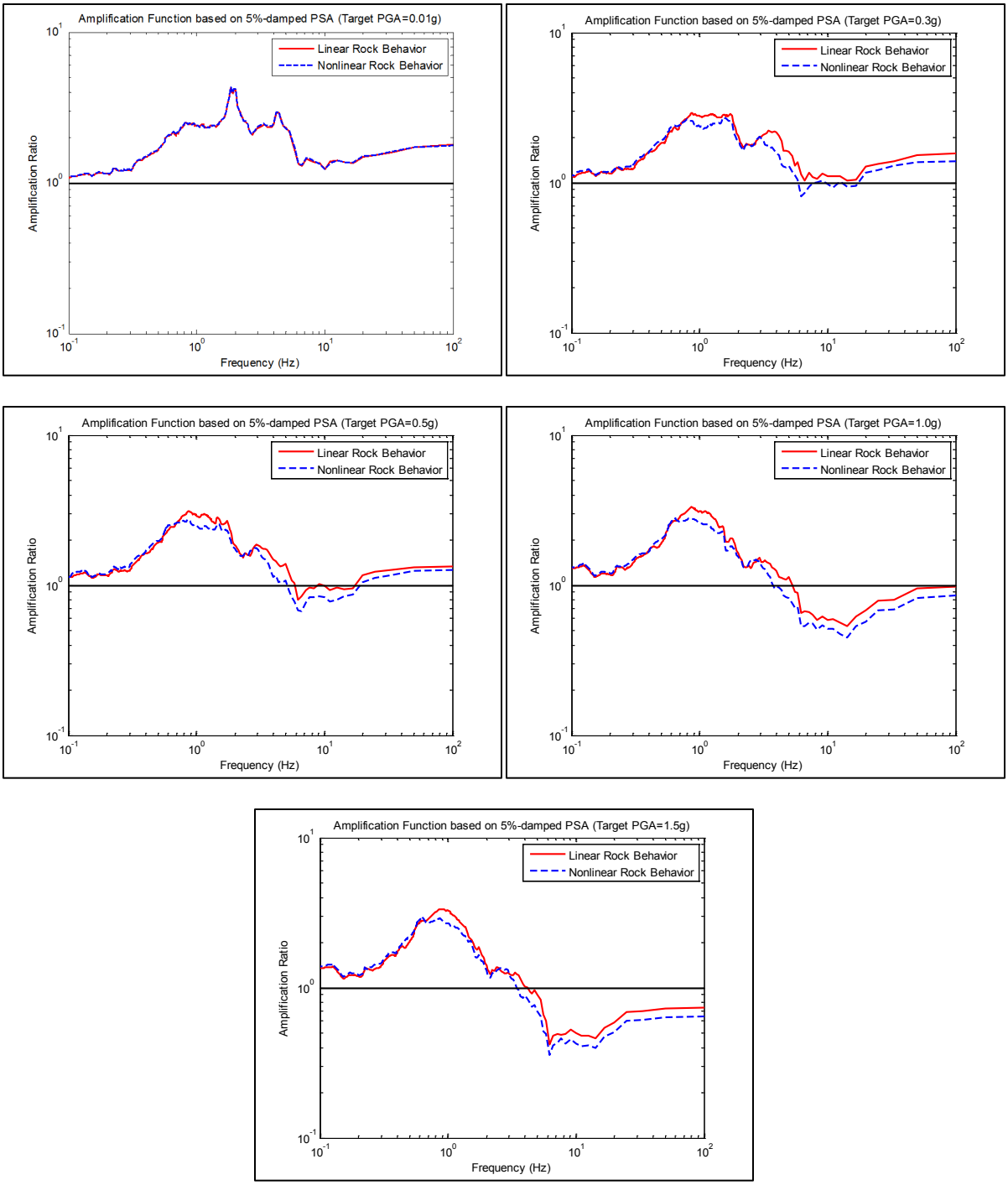

Figure 9.132. Results of site response analyses at the WTP site using the Schnabel curves for the SMB interbeds.

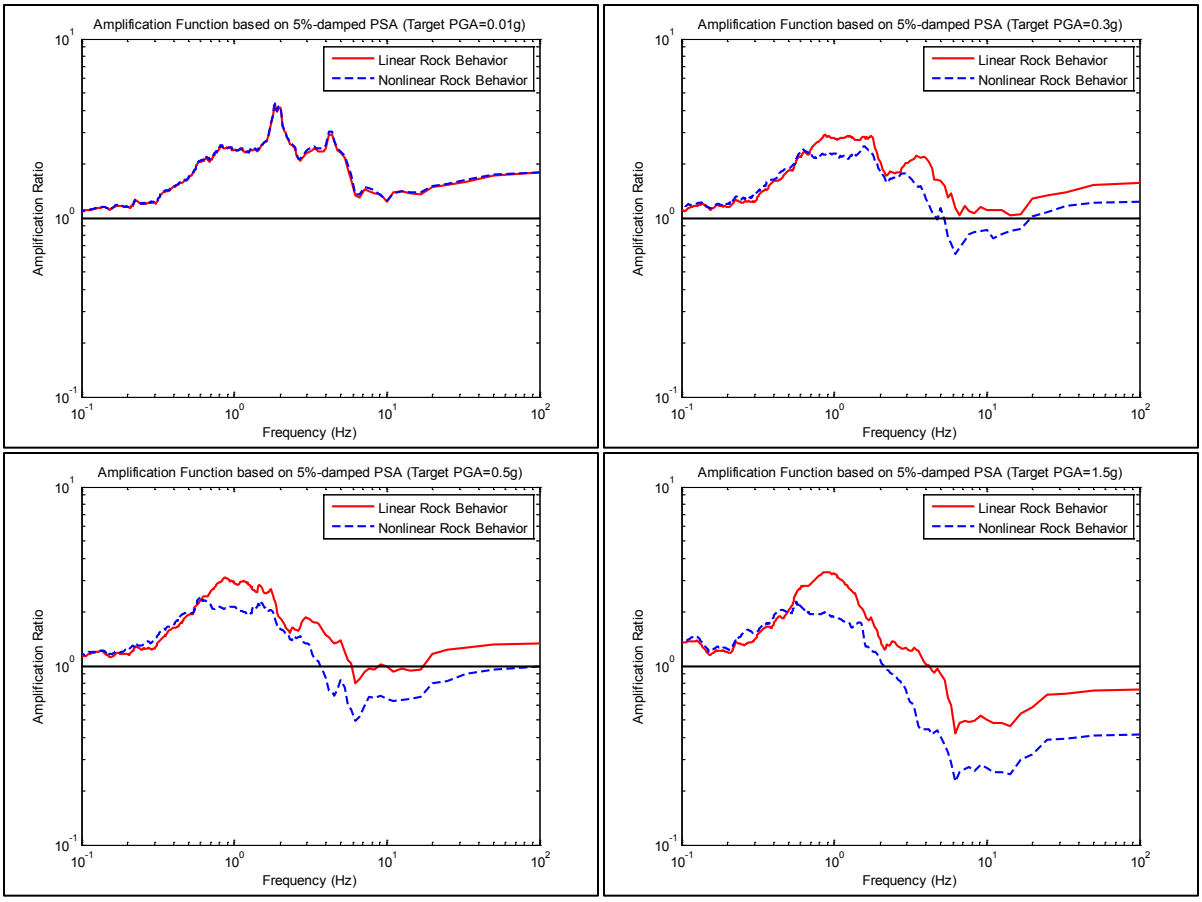

Figure 9.133. Results of site response analyses at the WTP site using the Darendeli curves for the SMB interbeds.

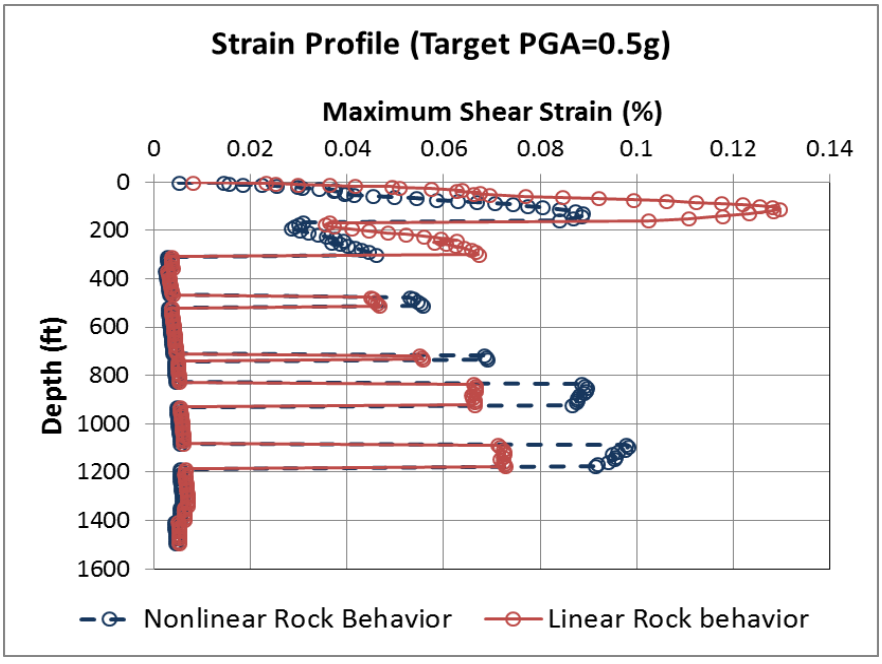

Figure 9.134. Strains in the WTP profile using the Darendeli curves.

Various nonlinear models potentially applicable to the SMB interbeds were considered (Table 9.21). The corresponding modulus reduction and damping curves are shown in Figure 9.135 and Figure 9.136. The Menq (2008) curves were developed for the suprabasalt sediments at the WTP sites. These curves introduce a strong degree of nonlinearity that is unlikely to be applicable to the SMB interbeds, given that the interbeds have large confining stresses and are very stiff materials. The Menq model also results in very high damping at relatively low levels of strain. The Sun et al. (1988) curve used for Mudstone has a very large nonlinear range, which is typical of highly plastic materials but it is unlikely to apply to the SMB interbeds. The Peninsular Range Curves and the Brookhaven National laboratory curves used by Silva are a subset of the EPRI (1993) soil curves. While these curves could be viable alternatives, they were developed for soils and not for the stiff materials that make up the SMB interbeds. The same can be said of the curves developed for tuff by Jeon (2008), and hence this model is also eliminated.

Table 9.21. Material nonlinearity models considered for the SMB interbeds.

Model	Reference	Assumptions and Limitations	Based on…	Empirical?
Schnabel	Schnabel (1973)	No empirical data. Derivations and linear interpolations used with limited data (developed by other authors) at low strains.	Values proposed by Seed and Idriss (1970)	N
Mudstone	Sun et al. (1988)	Curve developed for mudstones with a V_S = 1500 ft/sec	Dynamic Moduli and Damping Ratios for Cohesive Soils.	Y
EPRI Soil	EPRI (1993)	Depth-dependent curves for soils (35 undisturbed samples in California. Gravels, sands, and clays were tested).	Resonant column and torsional shear tests of intact soil specimens carried out at the University of Texas.	Y
EPRI Rock	EPRI (1993)	Curves developed for firm rock (i.e., Cenozoic or Paleozoic sedimentary rocks, such as shale, sandstones, or siltstones).	Assumed "firm rock", (3,000 ft/sec < V_S < 7,000 ft/sec), behaves similarly to gravels as described by EPRI soil curves. Implies more nonlinearity with higher damping than more fine-grained sandy soils.	N
Peninsular Ranges	Silva et al. (1996)	Curves developed for deep cohesionless soils (appropriate for soils comprised of sands, gravels, silts, and low plasticity clays).	EPRI cohesionless soil curves and generic deep soil curves. Subset of the EPRI soil curves.	N
W. Silva	Silva et al. (1996)	Curves for soft rock represent an extrapolation to higher strains of the Comanche Peak claystone curves. The extrapolation was also based on EPRI soil models.	Derived as an attempt to reconcile laboratory testing data and trends in attenuation relationships in rocks.	Y/N
Rollins et al.	Rollins et al. (1998)	Curves used by Rohay and Reidel (2005) and digitized from PNNL-16653 report.	Cyclic triaxial tests performed mostly on reconstituted gravel samples (data taken from 15 previous studies combined with tests by Rollins et al. to find best-fit relationships).	Y
Darendeli	Darendeli (2001)	Accounts for confining pressure and plasticity (only fine-grained soils and sands were used).	Resonant column and torsional shear (RCTS) tests of intact soil specimens	Y
Menq	Menq (2003)	Site-specific curves developed for the H3 and CCU formations at the WTP site. Developed in terms of Cu, D_{50}, and mean effective stress.	RCTS tests for reconstituted samples from the H2, H3, and CCU layers. Test data are well represented by Darendeli (2001) model.	Y
Jeon-Tuff	Jeon (2008)	Empirical curves for tuffs, fitted and extended by using Darendeli and Choi models.	Resonant column and torsional shear tests on 47 tuff specimens.	Y

The above considerations eliminate most of the models in Table 9.21. Of the remaining models, the EPRI rock curves have excessive damping at small strains, which is incompatible with the kappa values

estimated for the SMB stack, and for this reason they are eliminated from consideration. The two models left (Rollins et al. 1998 and Darendeli 2001) are both viable models; however, the Darendeli model offers more flexibility because it accounts for confining stress dependence, which is important for the depths at which the SMB stack interbeds are located. For this reason, the GMC TI Team recommends the use of the Darendeli (2001) curves for the SMB interbeds; while assuming linear behavior for the basalt layers in the stack. These recommendations are summarized in Table 9.22.

Table 9.22. Summary of recommendations for material nonlinearity for the SMB stack.

Geologic Formation	Recommendation for Site Response Analysis Purposes
Basalts	Assume elastic behavior
Interbeds	Darendeli (2001)

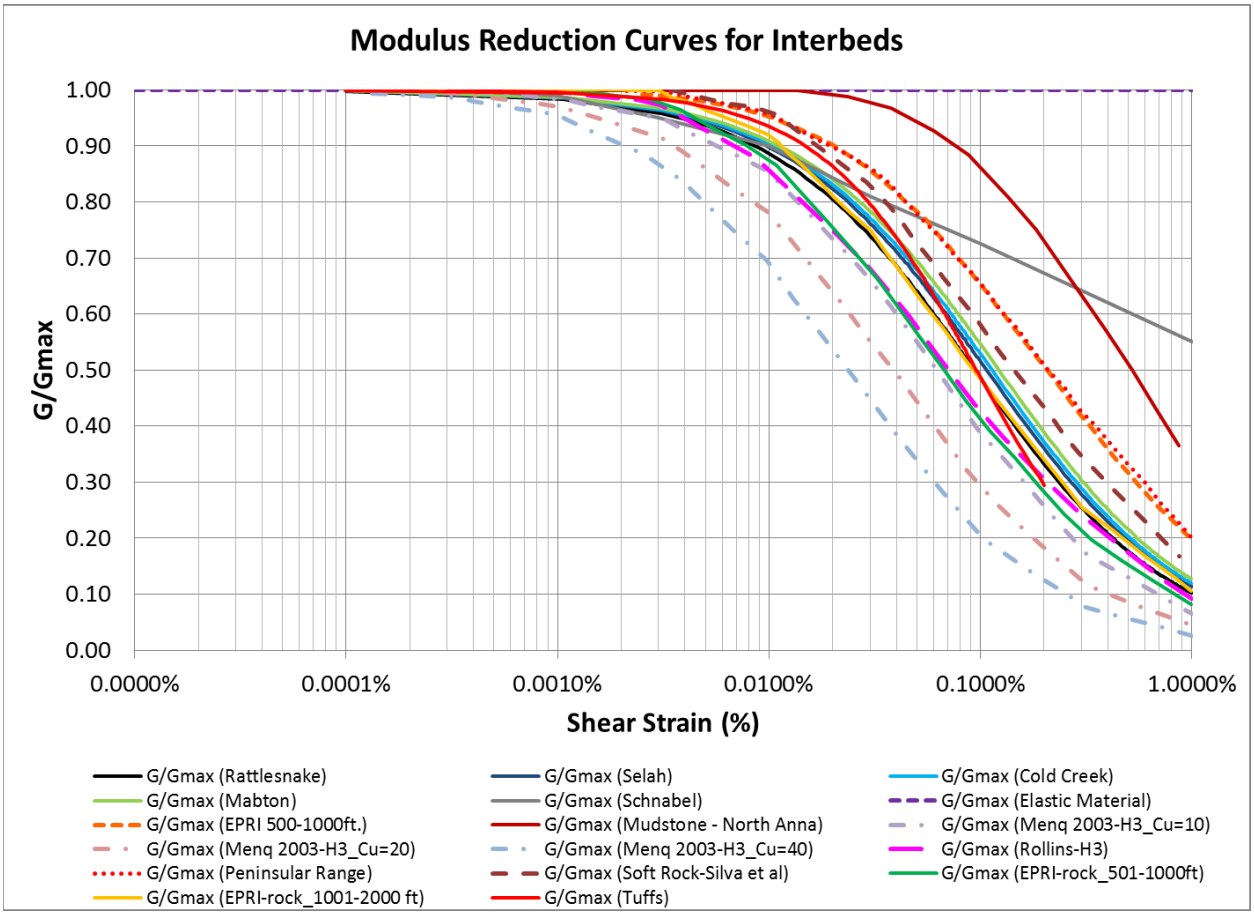

Figure 9.135. Modulus reduction curves for the models identified in Table 9.21. The Darendeli (2001) model is labeled by the SMB interbeds to which it is applied (Rattlesnake, Selah, Cold Creek, and Mabton).

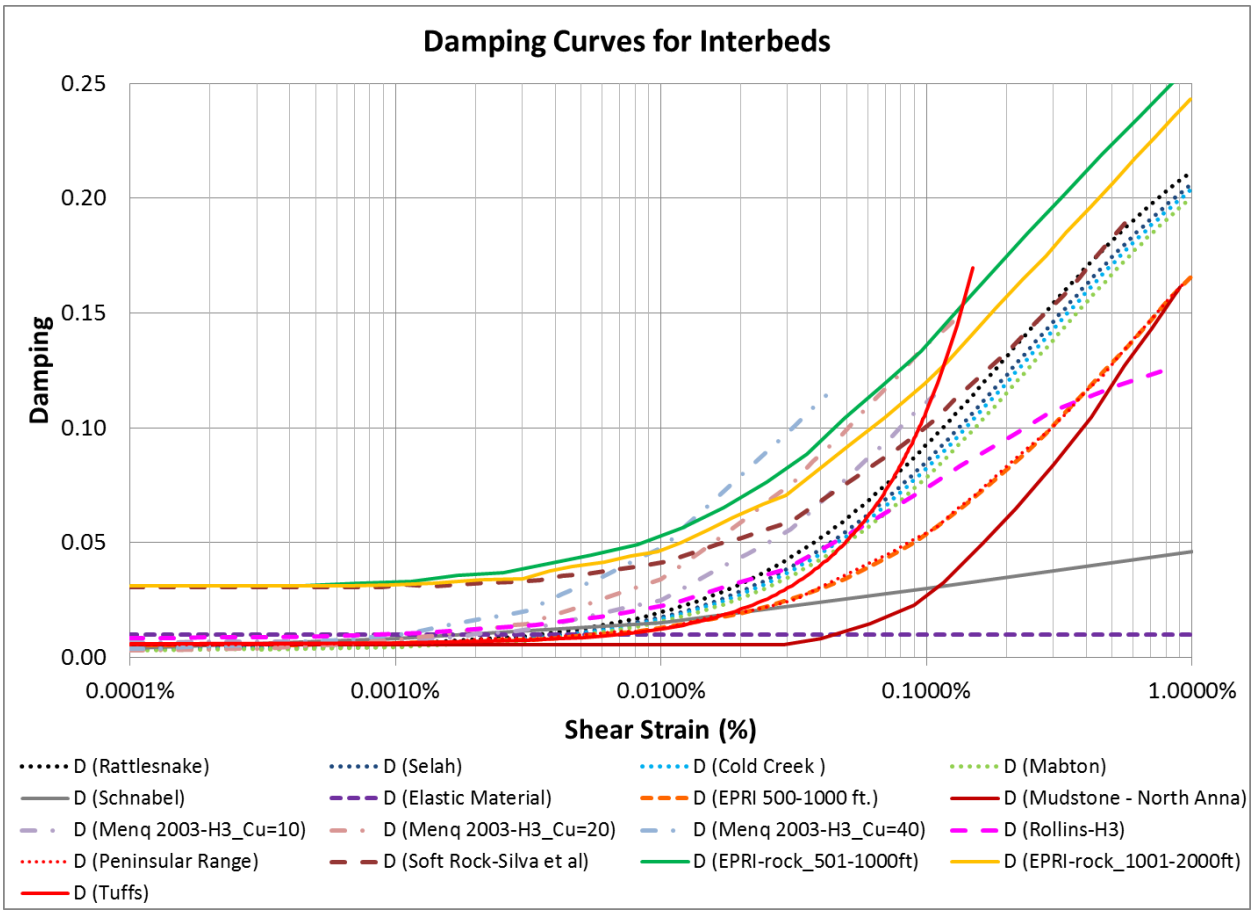

Figure 9.136. Damping curves for the models identified in Table 9.21. The Darendeli (2001) model is labeled by the SMB interbeds to which it is applied (Rattlesnake, Selah, Cold Creek, and Mabton).

The small-strain damping for the SMB stack is specified in Section 7.3.4. These damping values are not necessarily the same as the small-strain damping of the proposed curves. This inconsistency is easy to overcome because the Darendeli (2001) equations for damping have two separate terms. The first term is independent of strain and controls low-strain damping. The second term represents hysteretic damping, is strain-dependent, is negligible at low strains (e.g., 10^{-4}%), and is dominant at high strains. Taking advantage of this separability, the damping curves for the interbeds are then constructed as the sum of the low-strain damping specified in Section 7.3.4 and the Darendeli (2001) hysteretic damping term.

9.6.4 Specification for Site Response Randomizations

This section documents the development of synthetic profiles to represent the dynamic properties of the SMB stack at the five hazard calculation sites, and the associated uncertainty. Separate sets of 60 randomized profiles are developed for Profiles 1 and 2 at each site, resulting in a total of 600 synthetic profiles. These SMB profiles, together with randomized profiles to be developed later by the project sponsors or their contractors, will be used by them to calculate site amplification factors, which will then be convolved with the baserock hazard using the approach described in Section 10.5.

There are several reasons for randomizing the dynamic properties of shear-wave velocity profiles and then using these profiles in site response calculations. The main reasons are as follows:

- To characterize uncertainty about the profile dynamic properties at a reference location. For a site where measurements are available, some of the more common sources of uncertainty include the following:
  - Measurement error.
  - Measurements may only be available some distance away from the reference location.
  - No measurements may be available, as in the case of the degradation properties for the SMB interbeds, requiring the use of generic models.
- To characterize spatial variability within the facility footprint.
- To compensate for simplifications used in conventional site response analysis methodology, such as the assumptions of horizontal layers with uniform dynamic properties and vertically propagating SH waves. Both simplifications may exaggerate the response peaks.

Profile randomization introduces uncertainty in the amplification factor (which is then considered in the development of the ground motion response spectra [GMRS], as described in Section 10.5), and tends to smooth out the peaks of the site-column response. Both effects are necessary and desirable for the realistic calculation of site hazard from baserock hazard. Profile randomization was introduced by EPRI (1993), was refined by Toro (1995, 1997, 2005), and has been used (often with site-specific adjustments) in a number of nuclear projects, including Youngs (2007). The Regulatory Guide 1.208 (NRC 2007), the SPID (screening, prioritization, and implementation details) document (EPRI 2013b), and other regulatory and guidance documents specify the use of profile randomization to characterize uncertainty in site response.

The generation of synthetic profiles consists of three main steps:

1. Randomization of the site stratigraphy. The result from this step is the thickness of each layer in each synthetic profile.
2. Randomization of shear-wave velocity V_S, taking into account the uncertainty in V_S at each depth, as well as possible correlation in V_S between adjacent layers (to avoid unrealistic V_S reversals). The result of this step is a V_S value for each layer in each synthetic profile. Mass density is usually not randomized because its range of variation is smaller than that of V_S.
3. Randomization of the degradation curves (i.e., G/G_{max} and damping). The result of this step is a G/G_{max} curve and a damping curve for each layer in each synthetic profile.

The non-homogeneous random-process based approach for the randomization of stratigraphy by EPRI (1993) and Toro (1995, 1997, 2005) is not appropriate for the SMB randomization; that approach is more applicable to generic applications or to site-specific applications where the base-case profile is relatively smooth. In contrast, the SMB stack contains strong velocity contrasts between well-identified basalt flows, flowtops, and interbeds, as described in Section 9.6.1. The former approach may well be applicable to the randomization of the Hanford suprabasalt stratigraphy, which is not part of the scope of this project.

The approach used for the randomization of SMB stratigraphy takes as inputs the layer thicknesses, V_S values, and densities developed in Section 9.6.1 (which represent the base-case profiles), uncertainties in unit thickness as provided in Last (2013) and summarized in Table 7.7, and other quantities provided in Last (2014) in Section 5.4 or in the plates accompanying that document. When an uncertainty is given as range of values in either of these sources, the greater of the two values is used and is taken to represent the range of a uniform distribution between –range/2 and +range/2. These quantities are summarized in Table 9.23.

Table 9.23. Uncertainties and other quantities used in randomization of stratigraphy.

Site	Base-case thickness of suprabasalt sediments (m; from Last 2014)	Uncertainty (range/2) in elevation of the top of SMB (m; from Table 7.7 unless noted)	Uncertainty (range/2) in unit thickness (m; from Table 7.7)	Uncertainty (range/2) in top of Wanapum Basalt elevation (m; from Last 2014)	Suprabasalt dry confining pressure (g/cm^2; see details later in this section)	Elevation of top of water table, relative to top of basalt (m; from plates in Last 2014)
A	116	1.5	3.5 m down to Selah interbed, 1.85 m below	6.5	4.1E+04	34
B	156	1.5	3.35 m through the Esquatzel Member, 10.5 m below	5.0	4.3E+04	85
C	159	3.5	4.9 m for Elephant Mountain, 13.5 m below[(a)]	5.0	4.2E+04	143
D	199	5.0	3.5	11.5	5.5E+04	177
E	59	1 (from Last 2014)	6.5	9.5	1.8E+04	42

(a) At Site C, the Elephant Mountain unit and flowtops have a combined base-case thickness of 9.75 m, so the half-range of 13.5 m is inappropriate. Instead, a value of ½ the base-case thickness was used.

For the randomization of the thickness of suprabasalt sediments, this thickness is treated as uniformly distributed and independent of other quantities, with mean and half-range values for each site as given in Table 9.23. This thickness is the only property of the suprabasalt sediments that is randomized as part of this project.

For the randomization of the basalt thicknesses, the uncertainties given in Table 9.23 are taken as representing the uncertainty in the total thickness of the basalt unit (including flow tops). Then, the randomized thickness (i.e., base-case total unit thickness + uniformly distributed random term) is divided by the base-case total unit thickness, obtaining a factor that is applied to the thickness of the flow and of the flowtops. For the interbeds, a uniformly distributed + 10% uncertainty is used (this percentage is the same one used by Youngs 2007). These random terms are treated as independent from unit to unit.

Application of the above randomization procedure to each unit results in a total SMB stack thickness with a standard deviation equal to

$$\sigma_{th,SMB_1} = \frac{1}{\sqrt{3}} \sqrt{\sum\nolimits_i \left(\Delta_i / 2\right)^2} \tag{9.40}$$

where the summation extends over all units composing the SMB stack and $\Delta_i / 2$ represents the half-range of uncertainty for the i-th unit (given in Table 9.23 for basalts, and equal to 10% of thickness for interbeds). The quantity $1/\sqrt{3}$ in the above equation is the ratio between the standard deviation and the half-range of a uniform distribution.

On the other hand, considering that the depth to the top of the Wanapum (relative to the ground surface) is the sum of the depth to the top of the SMB and the SMB thickness (both of which are given in Table 9.23), one can also calculate the standard deviation of the latter as

$$\sigma_{th,SMB_2} = \frac{1}{\sqrt{3}} \sqrt{(\Delta_{elev,topWanapum} / 2)^2 - (\Delta_{elev,topSMB} / 2)^2} \tag{9.41}$$

To preserve the standard deviation given by Equation 9.41, the randomized thickness of each unit is multiplied by an adjustment factor equal to

$$\frac{th, SMB_{BaseCase} + (th, SMB_{randomized} - th, SMB_{BaseCase}) \times \sigma_{th,SMB_2} / \sigma_{th,SMB1}}{th, SMB_{randomized}} \tag{9.42}$$

where the term *th* indicates thickness.

This adjustment factor is calculated (and applied) separately for each realization of the synthetic profile. The adjustment factor distorts the uncertainty range in unit thickness, but the distortion is small because the adjustment factors are usually not very different from unity.

For the V_S randomization, V_S is treated as lognormal with a logarithmic standard deviation of 0.1 [1] in the basalt flows and flowtops, and 0.2 in the interbeds. The former value is the same used by Youngs (2007). The latter value is based on the recognition that V_S in the interbeds has higher spatial variability and higher measurement error. Following Youngs (2007), a correlation coefficient of 0.95 is used between a flow and its adjacent flowtop (or between adjacent flowtops) to avoid unrealistic V_S reversals. No correlation is used between an interbed and adjacent flows or flowtops or between two different flows. These assumptions are considered appropriate because the SMB data used by Youngs (2007) are the same data available at present.

As is frequently done in profile randomization, the tails of the underlying normal distributions are truncated at + 2 standard deviations. To achieve the desired standard deviation with the truncated distribution, the underlying standard deviation is multiplied by a factor of 1.16. Note that this form of truncation is preferable to simply setting all values outside the + 2 range to the limiting value. The latter approach results in many realizations having the bounding values, which is unrealistic.

A standard deviation of 0.2 was considered as a candidate value for the basalt and flowtop V_S in sites other than A, in order to take into account that these sites have no V_S measurements in the SMB, but it was found that this value led to unrealistically high V_S values for the A2 through E2 profiles. Considering that a very strong truncation of the upper tails would be required to avoid these values and that the basalts are thought to have high lateral homogeneity, it was decided to use 0.1 at all sites. Another argument favoring this decision is that, as indicated by Youngs (2007), the 0.1 logarithmic standard deviation is higher than the values calculated from measured velocities.

[1] All logarithmic standard deviations in this section are given in natural log units.

Figure 9.137 through Figure 9.147 depict the randomized V_S profiles for the five sites and the two alternative base-case profiles (i.e., Profiles 1 and 2), as well as their summary statistics. It is clear from the plots of logarithmic standard deviations as a function of depth that the main source of variability is the uncertainty in layer thickness. The logarithmic-mean profile from the 60 randomizations (thick black line) is smoother than the corresponding base-case profiles (thick red line). This smoothing effect is unavoidable when there are strong V_S contrasts and the stratigraphy is randomized, even with the more restricted randomization used in this project.

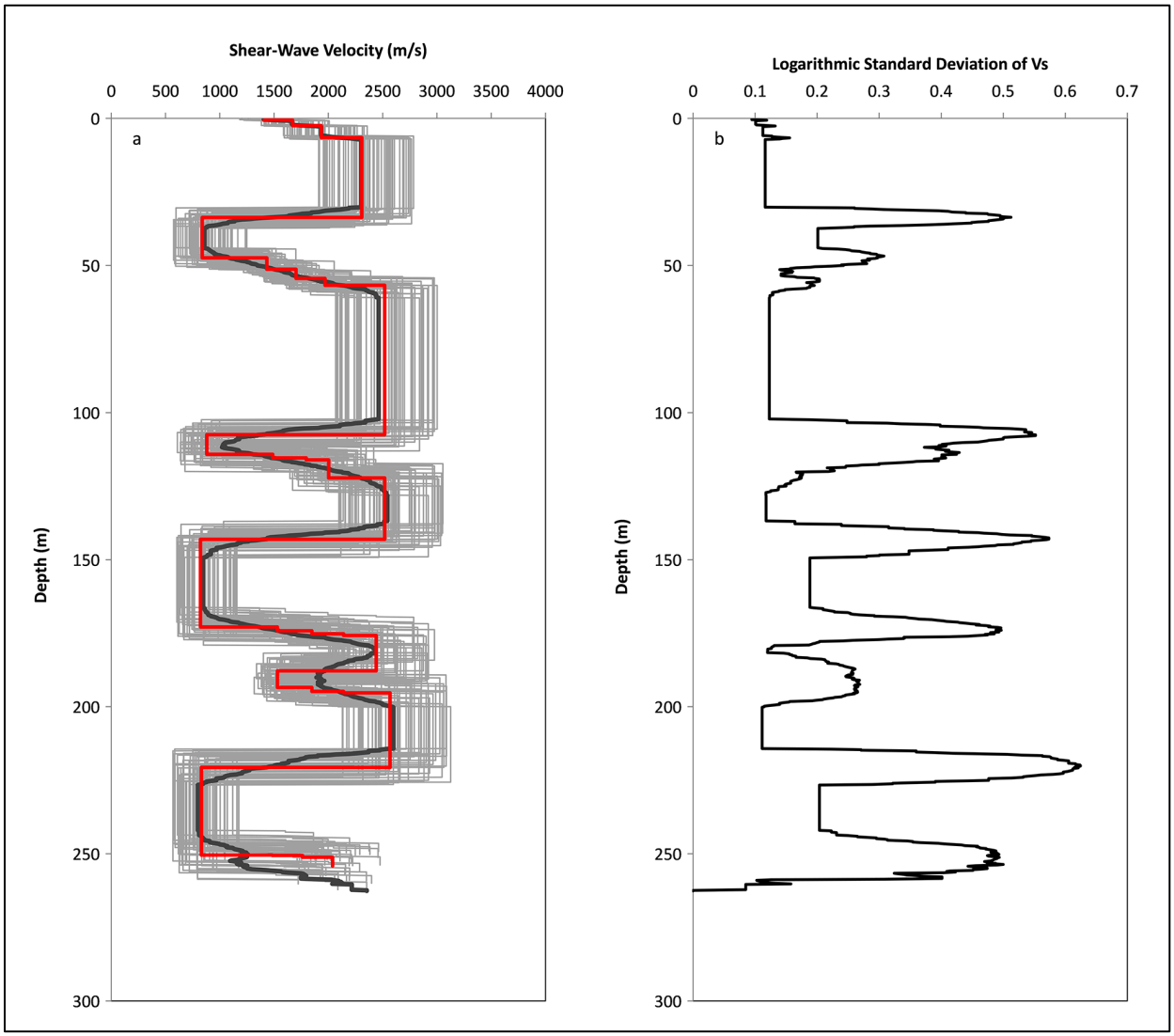

Figure 9.137. Synthetic V_S profiles for Site A, Profile 1 and summary statistics. Left: gray, synthetic profiles; black, logarithmic-mean V_S; red, base-case profile. Right: logarithmic standard deviation of V_S.

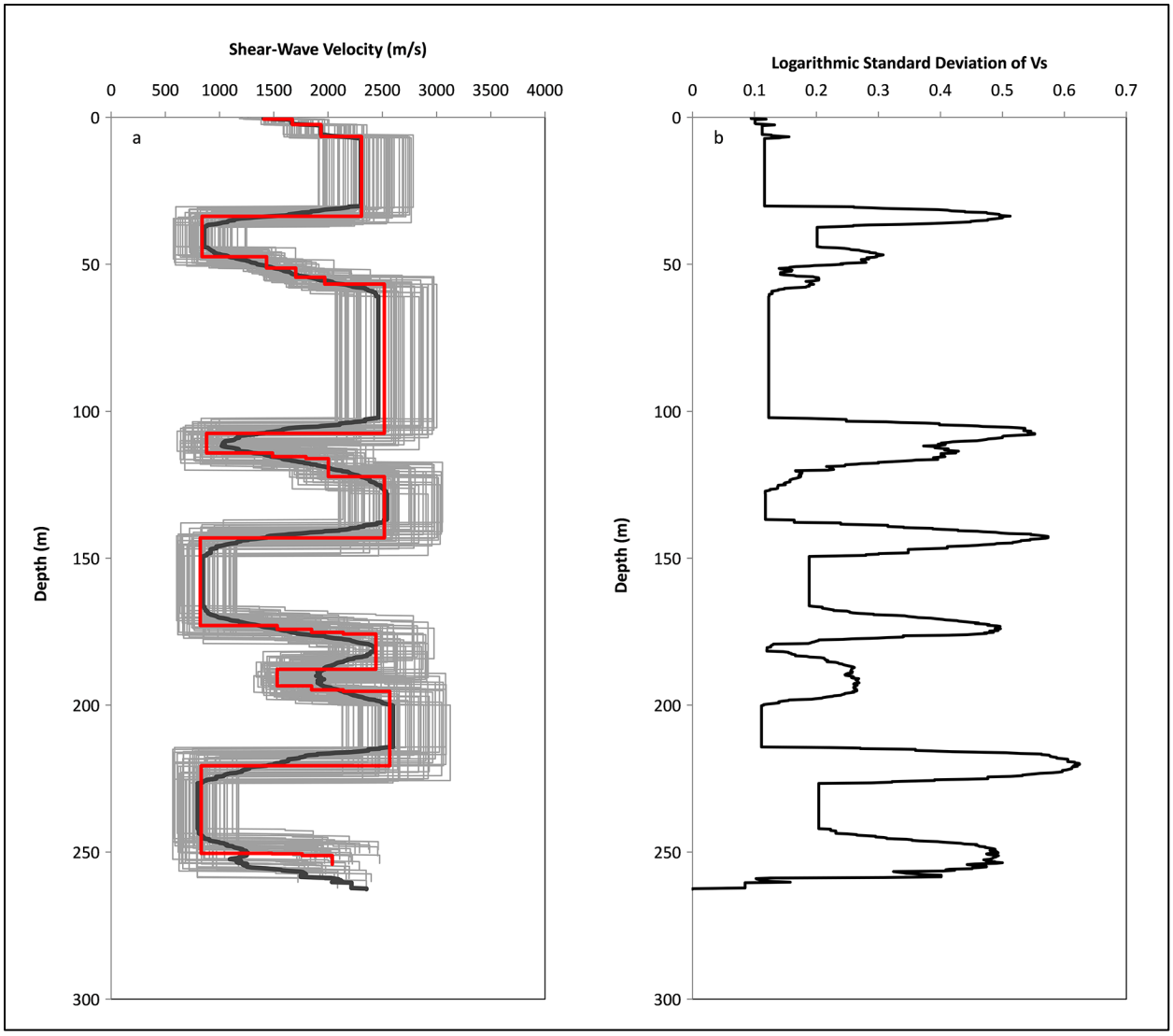

Figure 9.138. Synthetic V_S profiles for Site A, Profile 1 and summary statistics. Left: gray, synthetic profiles; black, logarithmic-mean V_S; red, base-case profile. Right: logarithmic standard deviation of V_S.

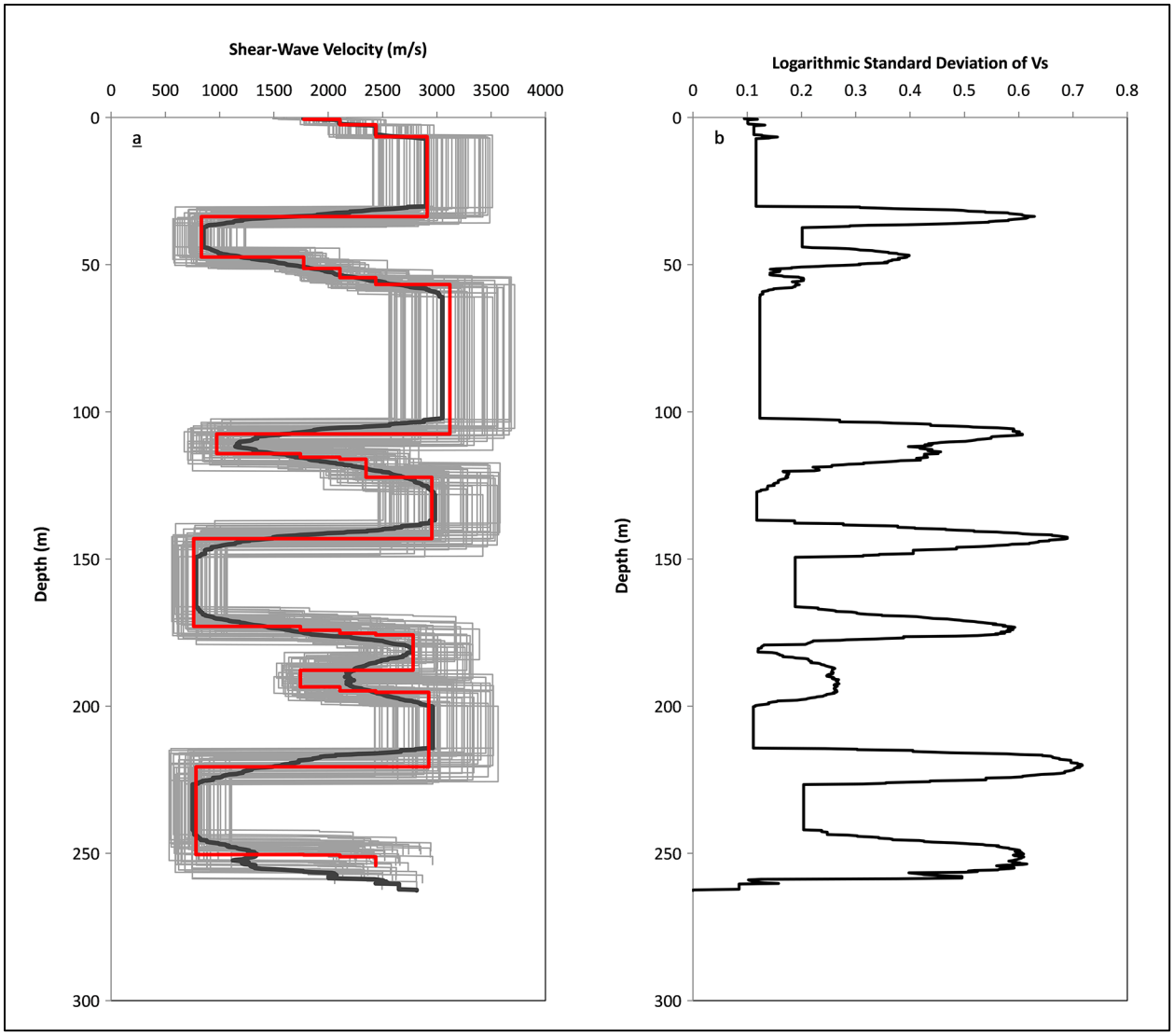

Figure 9.139. Synthetic V_S profiles for Site A, Profile 2 and summary statistics. Left: gray, synthetic profiles; black, logarithmic-mean V_S; red, base-case profile. Right: logarithmic standard deviation of V_S.

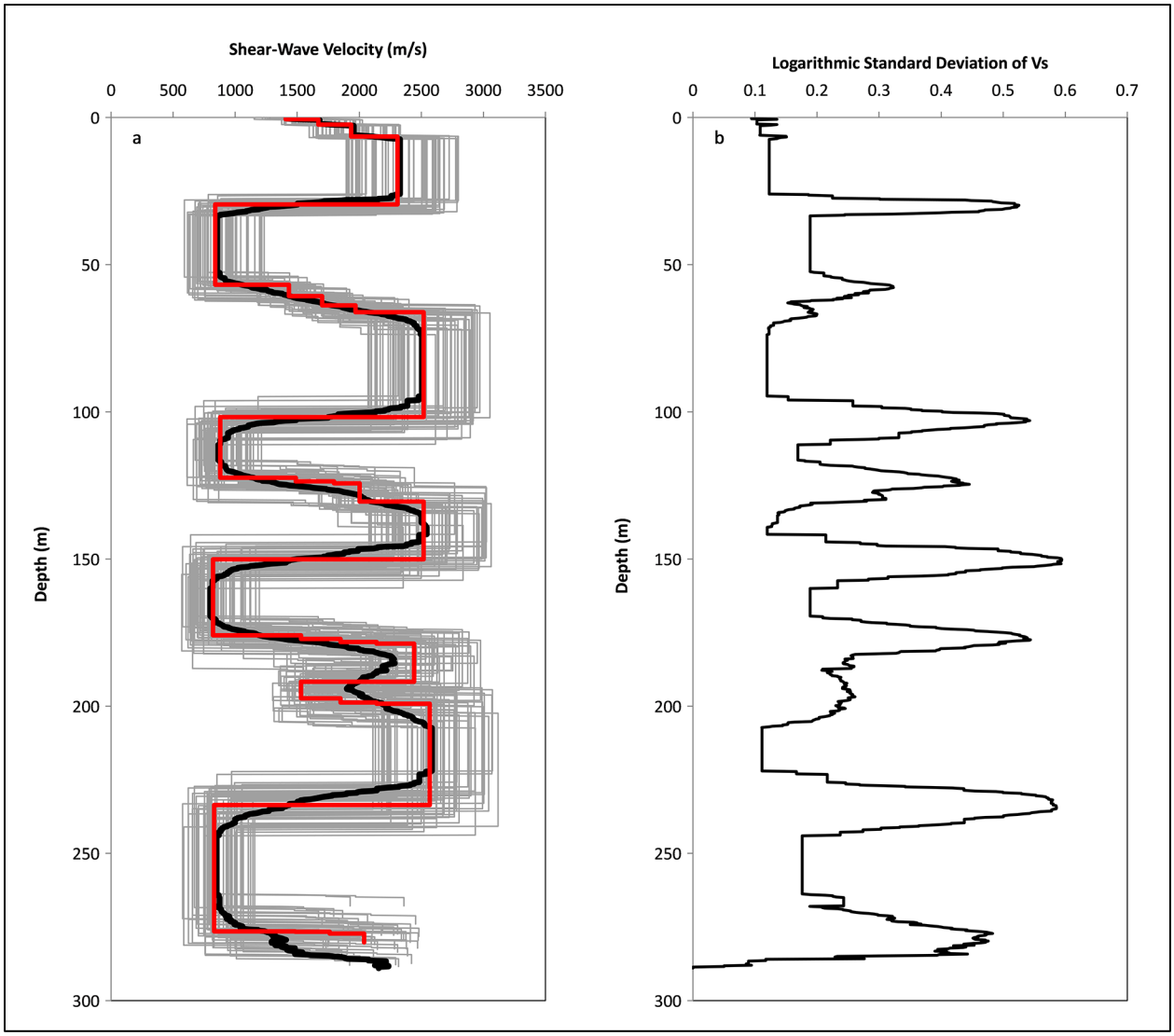

Figure 9.140. Synthetic V_S profiles for Site B, Profile 1 and summary statistics. Left: gray, synthetic profiles; black, logarithmic-mean V_S; red, base-case profile. Right: logarithmic standard deviation of V_S.

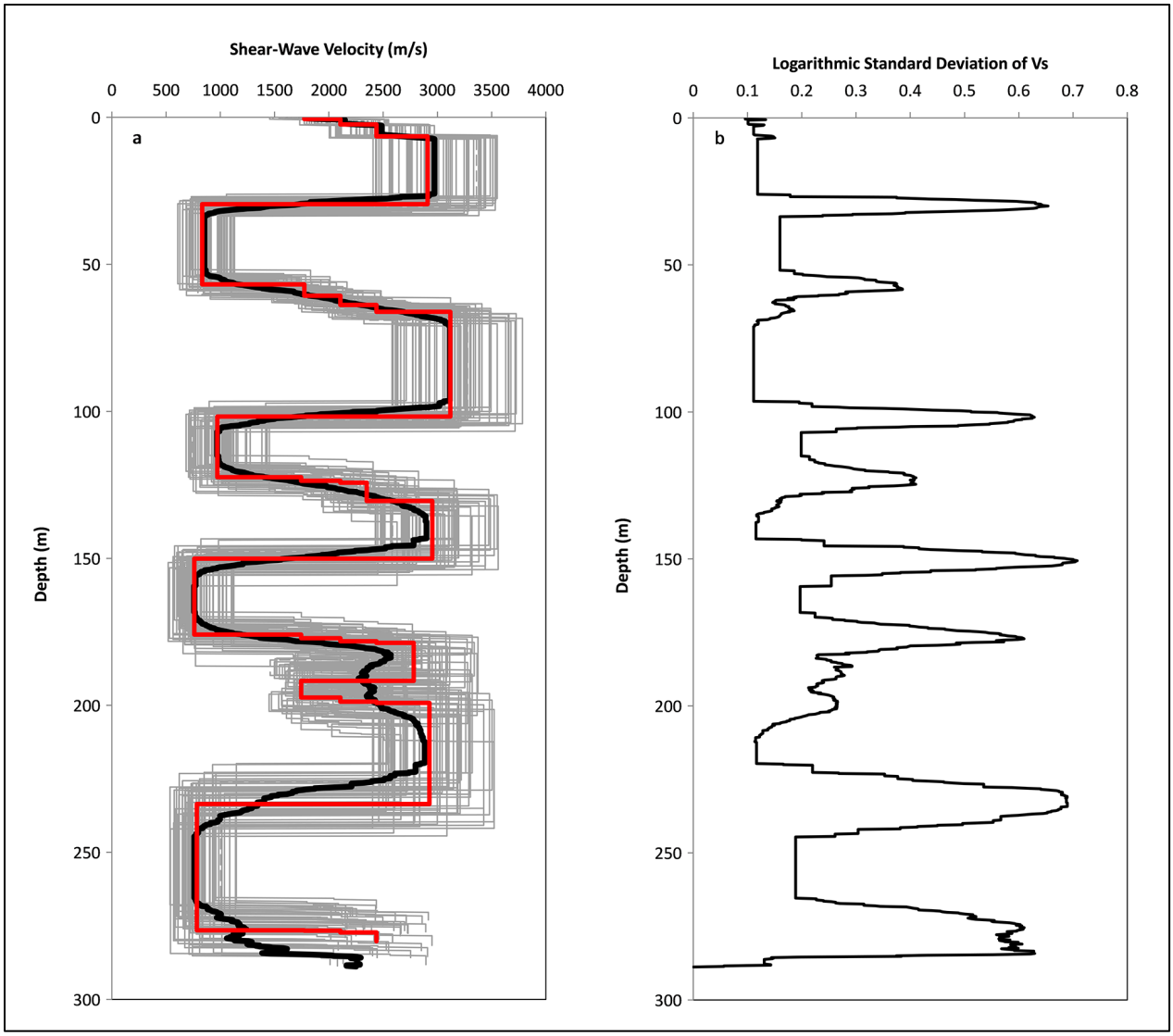

Figure 9.141. Synthetic V_S profiles for Site B, Profile 2 and summary statistics. Left: gray, synthetic profiles; black, logarithmic-mean V_S; red, base-case profile. Right: logarithmic standard deviation of V_S.

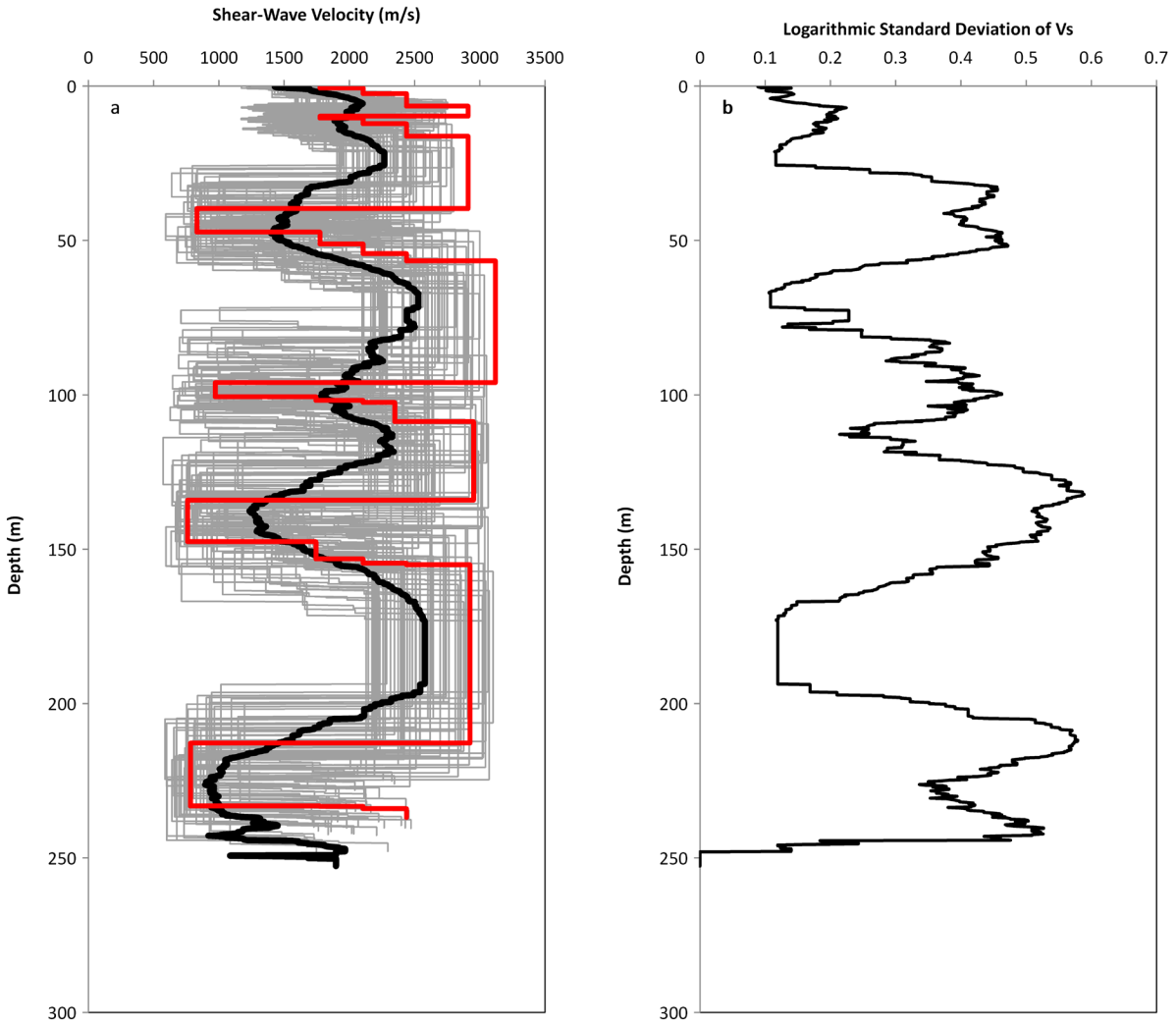

Figure 9.142. Synthetic V_S profiles for Site C, Profile 1 and summary statistics. Left: gray, synthetic profiles; black, logarithmic-mean V_S; red, base-case profile. Right: logarithmic standard deviation of V_S.

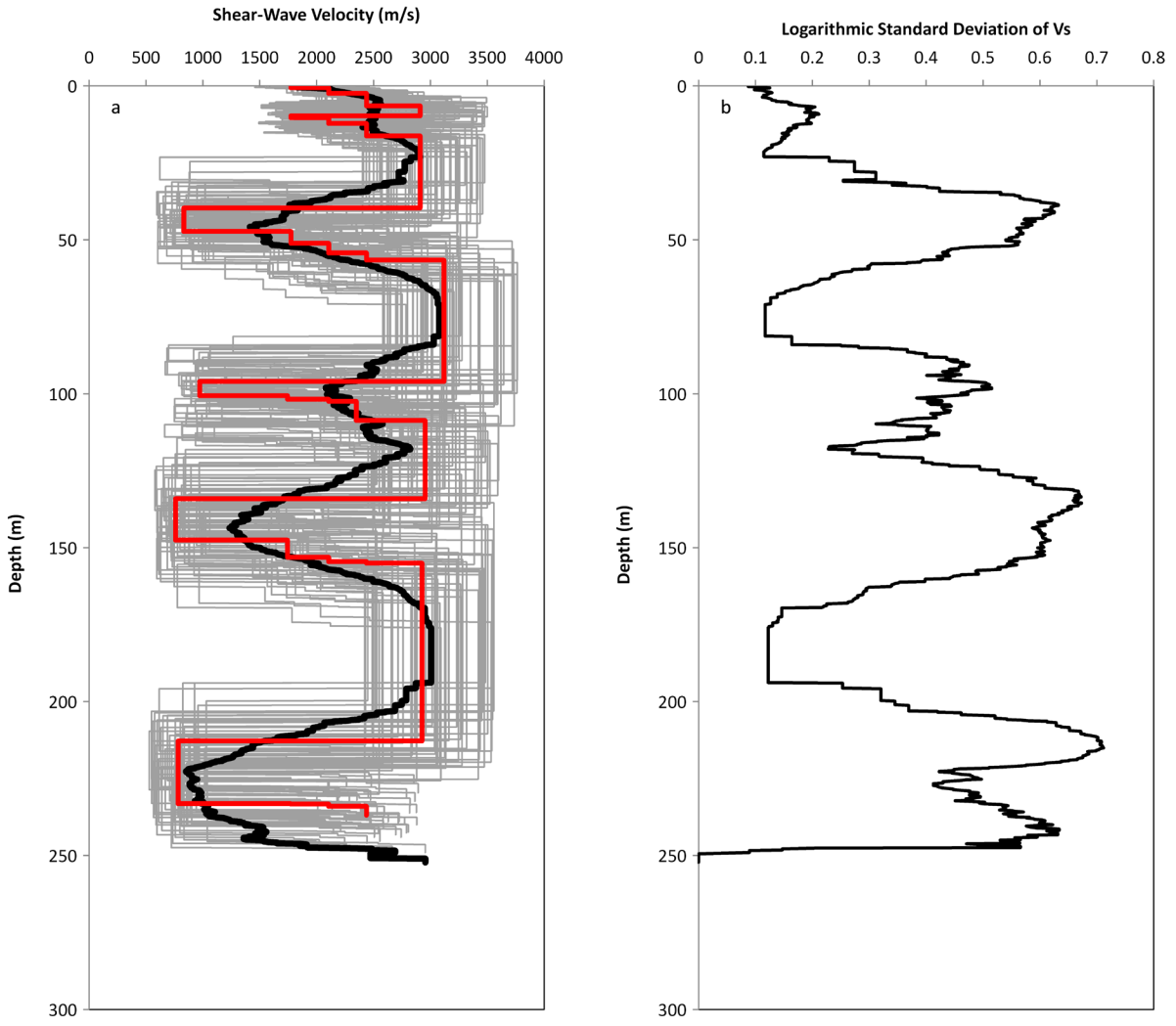

Figure 9.143. Synthetic V_S profiles for Site C, Profile 2 and summary statistics. Left: gray, synthetic profiles; black, logarithmic-mean V_S; red, base-case profile. Right: logarithmic standard deviation of V_S.

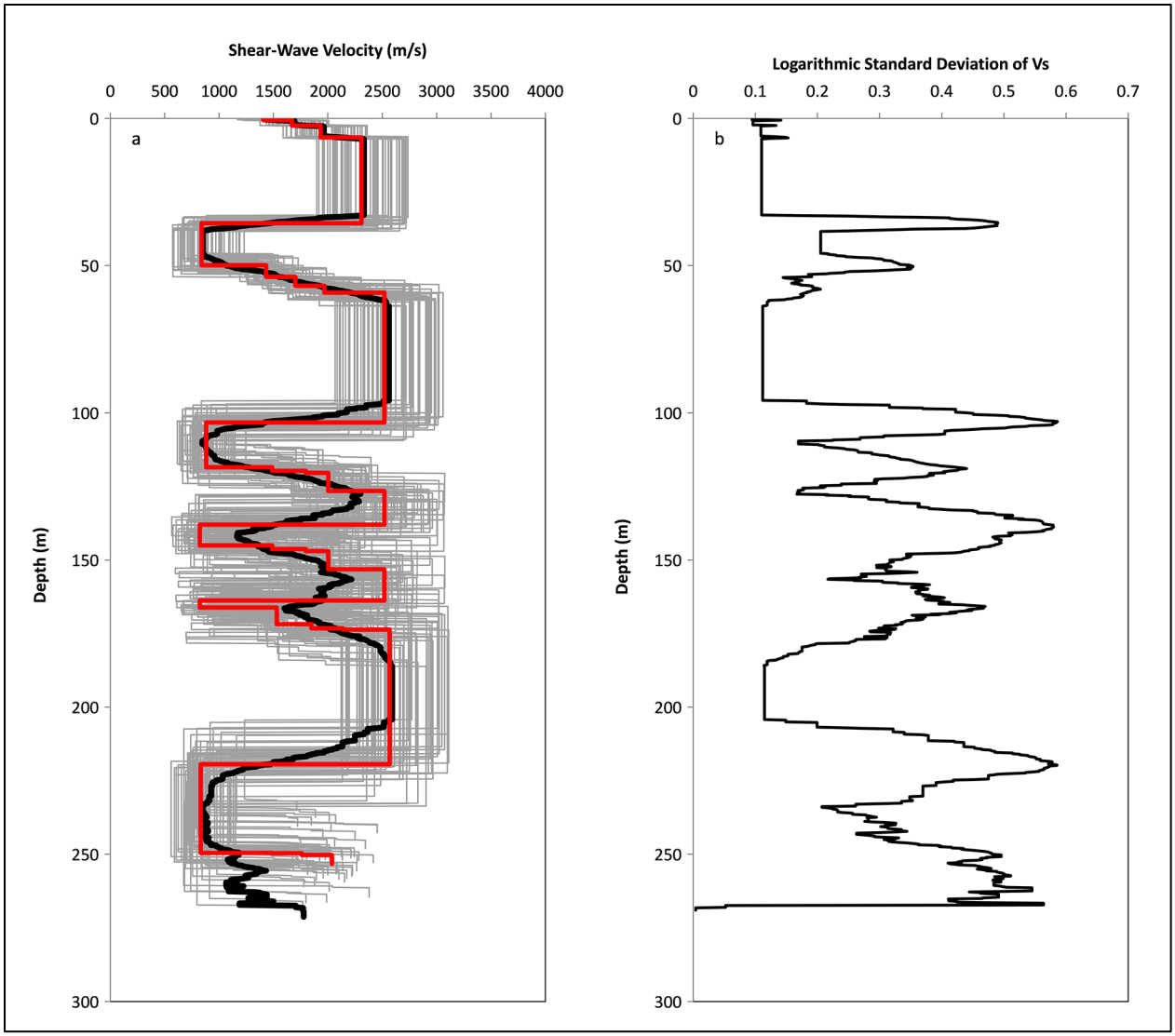

Figure 9.144. Synthetic V_S profiles for Site D, Profile 1 and summary statistics. Left: gray, synthetic profiles; black, logarithmic-mean V_S; red, base-case profile. Right: logarithmic standard deviation of V_S.

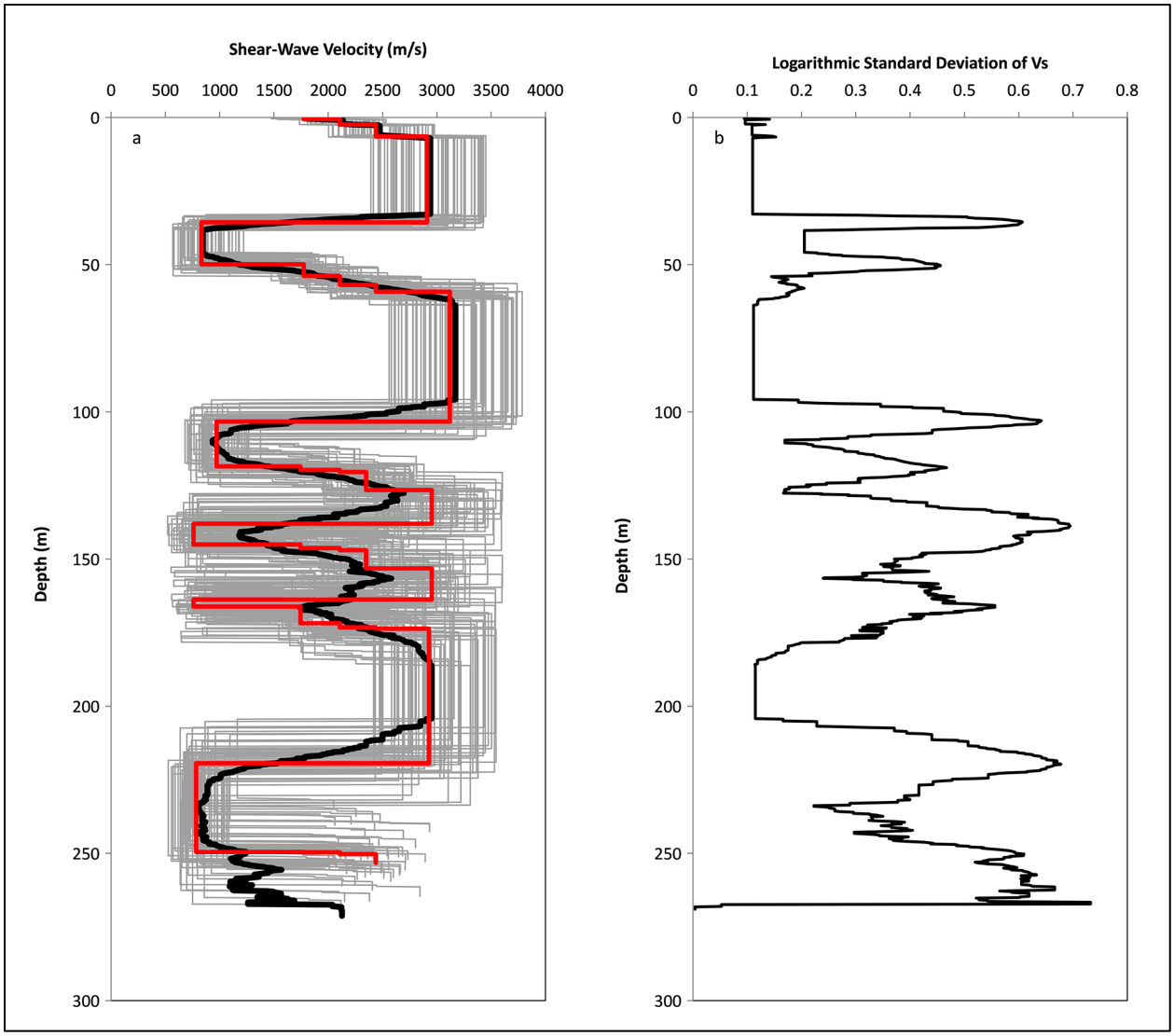

Figure 9.145. Synthetic V_S profiles for Site D, Profile 2 and summary statistics. Left: gray, synthetic profiles; black, logarithmic-mean V_S; red, base-case profile. Right: logarithmic standard deviation of V_S.

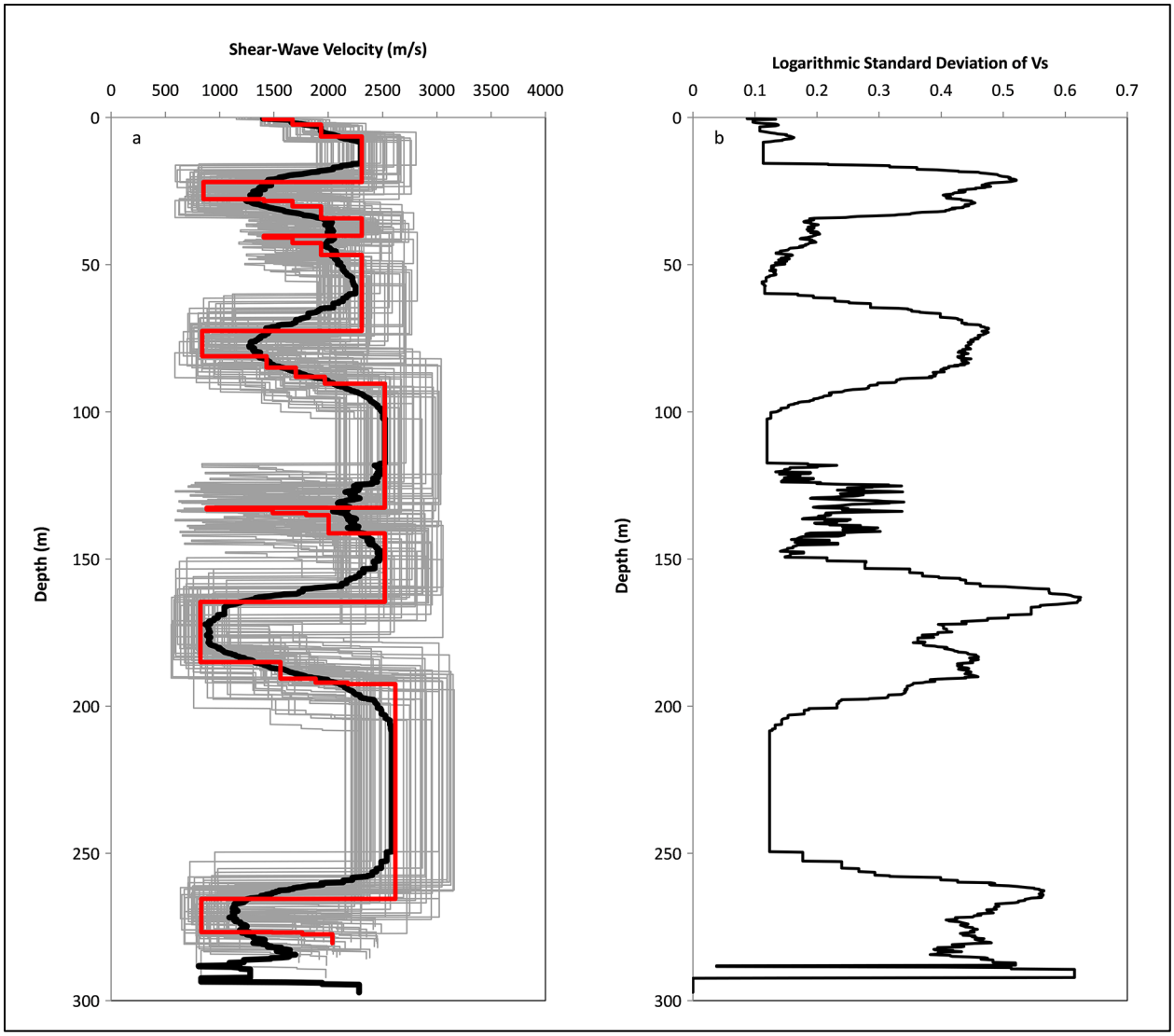

Figure 9.146. Synthetic V_S profiles for Site E, Profile 1 and summary statistics. Left: gray, synthetic profiles; black, logarithmic-mean V_S; red, base-case profile. Right: logarithmic standard deviation of V_S.

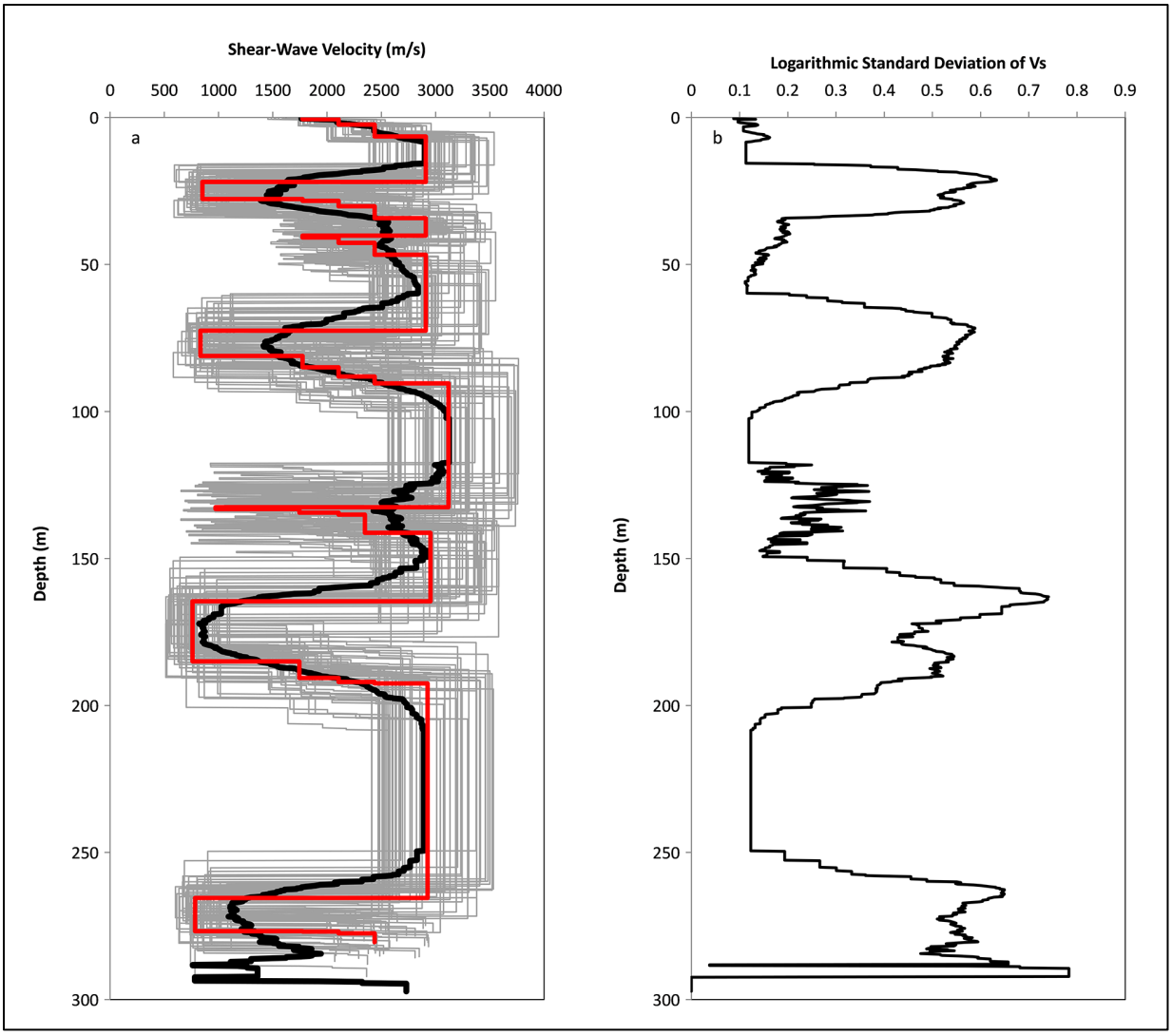

Figure 9.147. Synthetic V_S profiles for Site E, Profile 2 and summary statistics. Left: gray, synthetic profiles; black, logarithmic-mean V_S; red, base-case profile. Right: logarithmic standard deviation of V_S.

The selection of base-case G/G_{max} and damping models to use in the randomization of these properties is documented in Section 9.6.3. Basalts and flowtops are treated as behaving linearly. In other words, G/G_{max} is equal to 1.0, damping ratio is independent of strain, and damping ratios are inversely proportional to V_S (as documented in Section 7.3.5.4). Interbeds are treated as having strain-dependent G/G_{max} and damping, and the Darendeli (2001) model was selected to represent this behavior (except that the low-strain damping from Section 7.3.5.4 is used instead of the low-strain damping in the Darendeli model). Further details about the Darendeli (2001) model are given below.

In addition to strain, the Darendeli (2001) model requires the following input parameters :

- Plasticity Index (PI). Because the interbeds consist of granular materials, this project uses a value of 0.

- Effective confining pressure. This is an important parameter, given the range of depths spanned by the various SMB interbeds. Calculation of the confining pressure at the midpoint of an interbed requires the following inputs :
  - Total dry confining pressure at the top of the SMB stack. The values in Table 9.23 are calculated using the thickness of the suprabasalt units, as given in the Last (2014) plates, and the dry density of these units, as given in Table 6.7 of Rohay and Brouns (2007).
  - Confining pressure from SMB units above the interbed midpoint, using the thickness and density data from the SMB stack model described in Section 9.6.1.
  - The pressure of the water column above the interbed midpoint, taking into account the ground-water elevation given in Table 9.23.
- Other inputs, for which Darendeli (2001) provides recommended values for site response applications. These consist of the over-consolidation ratio or OCR (recommended value :1), the number of cycles N (recommended value = 10), and the frequency (recommended value = 1 Hz).

The equations for G/G_{max} and damping as a function of strain and of the other inputs listed above are given in Sections 9.2 and 9.3 of Darendeli (2001) and are not repeated here. As indicated earlier, the Darendeli (2001) equation for low-strain damping is not used, and project-specific values from Section 7.3.4 are used instead. The base-case degradation curves are calculated using the base-case V_S and thickness values, not the randomized values.

The randomization of the G/G_{max} and damping curves follows the recommendations of the EPRI SPID document (EPRI 2013b). The values of G/G_{max} and damping at a strain of $3x10^{-2}$ % (actually, this project does it at $3.16x10^{-2}$ %) are treated as lognormal, with logarithmic standard deviations of 0.15 and 0.3, respectively. For G/G_{max}, this variation must be tapered at low strains, so that all randomized curves converge (from below) to $G/G_{max} = 1$ at low strains (the symbol γ is used to represent percent strain in the description that follows). In this project, this is implemented using the approach described below.

First, transform the base-case $G/G_{max}(\gamma)$ (which varies from 0 to 1) to a quantity $f(\gamma)$ (which varies from 0 to infinity) by using the following equation :

$$f(\gamma) = \frac{G/G_{\max}(\gamma)}{1 - G/G_{\max}(\gamma)} \tag{9.43}$$

Second, randomize the base-case *f(γ)* by multiplying it by a lognormal random factor. To achieve a logarithmic standard deviation of 0.15 for G/G_{max} at $3.16x10^{-2}$ %, this lognormal factor in *f(γ)* space must have a logarithmic standard deviation equal to the quantity

$$0.15 \times \left. \frac{d\ln(f)}{d\ln(G/G\max)} \right|_{\gamma=3.16\times10^{-2}\%} = 0.15 \times \frac{1}{1 - G/G_{\max}(\gamma = 3.16\times10^{-2}\%)} \tag{9.44}$$

Finally, transform the randomized *f(γ)* back to $G/G_{max}(\gamma)$ space using the inverse relation of Equation 9.43, which is the relation

$$G / G_{\max}(\gamma) = \frac{f(\gamma)}{1 + f(\gamma)} \tag{9.46}$$

For the damping ratio, a lognormal factor, with a logarithmic standard deviation of 0.3 (which, as indicated earlier, is the value recommended by the EPRI SPID document; EPRI 2013b), is applied at all strains. This is done for the interbeds, as well as for the basalt flows and flowtops. In addition, the randomized damping ratio is capped at 15% of critical, in accordance with the EPRI SPID document (EPRI 2013b). For both G/G_{max} and damping, the underlying normal distributions are truncated at ±2 standard deviations, in the manner described earlier for V_S.

Figure 9.148 through Figure 9.159 show the randomized G/G_{max} and damping curves for the interbeds of the A1 profile, as well as their summary statistics. Similar figures were obtained for the other randomized profiles but are not shown for the sake of brevity. These figures show good agreement between the base-case curves and the logarithmic means of the 60 realizations, except where the truncation at 15% damping is imposed, thereby introducing the anticipated conservative bias. The logarithmic standard deviation of G/G_{max} is greater than 0.15 at high strains. This is a desirable deviation from EPRI (2013b), given that material behavior is highly uncertain at these high strains, and this deviation is roughly consistent with the variation of the uncertainty for sands at high strains in Figure 9 of Costantino (1996). Also, the logarithmic standard deviation of damping decreases at high strains, but this is the anticipated result of the conservative cap at 15% damping.

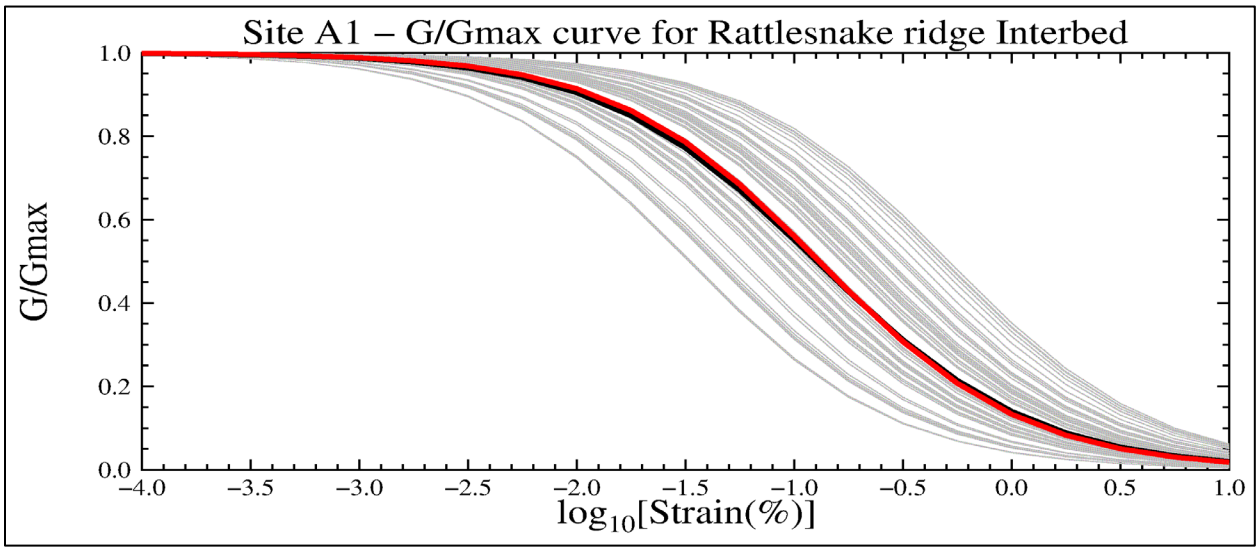

Figure 9.148. Synthetic G/G_{max} curves for Rattlesnake Ridge interbed at Site A1. Gray, synthetic profiles; black, logarithmic-mean; red, base-case curve.

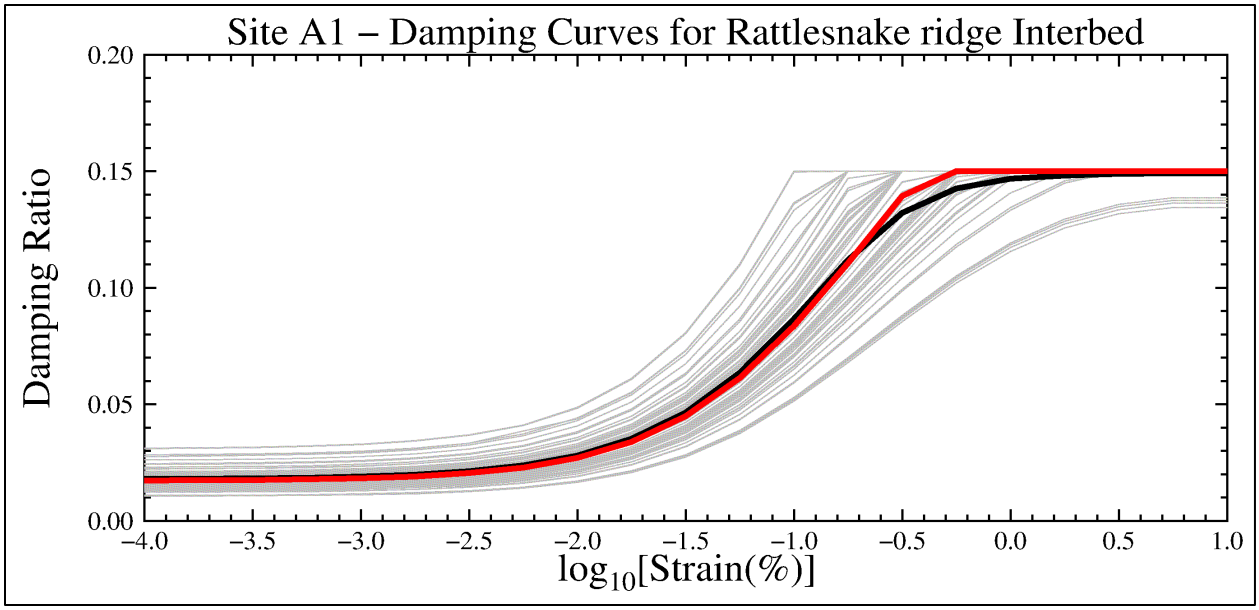

Figure 9.149. Synthetic damping curves for Rattlesnake Ridge interbed at Site A1. Gray, synthetic profiles; black, logarithmic-mean; red, base-case curve.

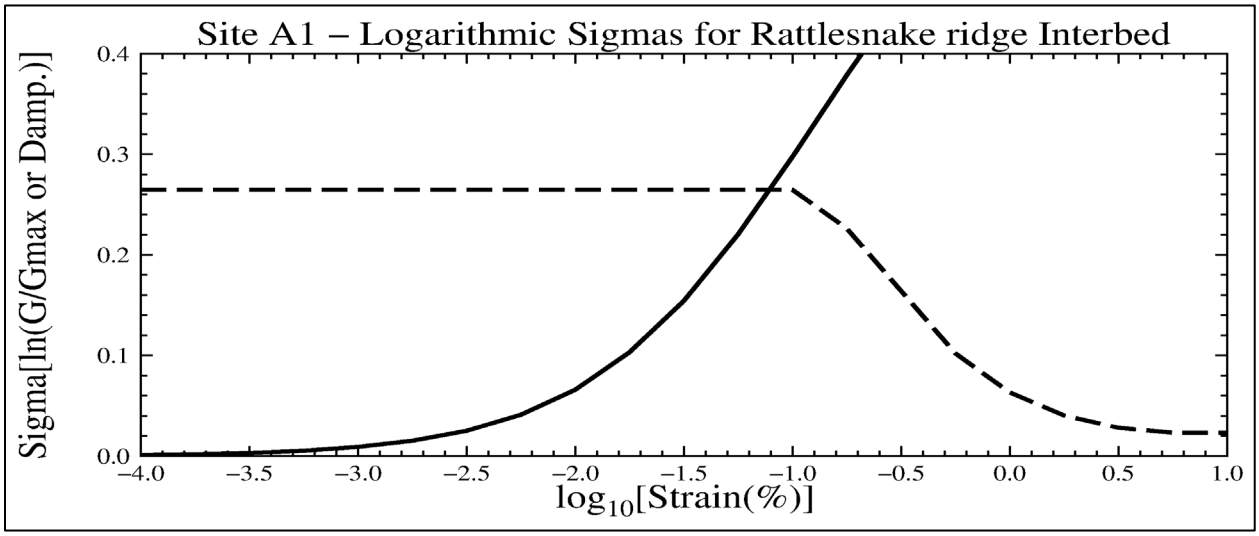

Figure 9.150. Logarithmic standard deviations of the synthetic G/G_{max} and damping curves for Rattlesnake Ridge interbed at Site A1. Solid, G/G_{max}; dashed, damping.

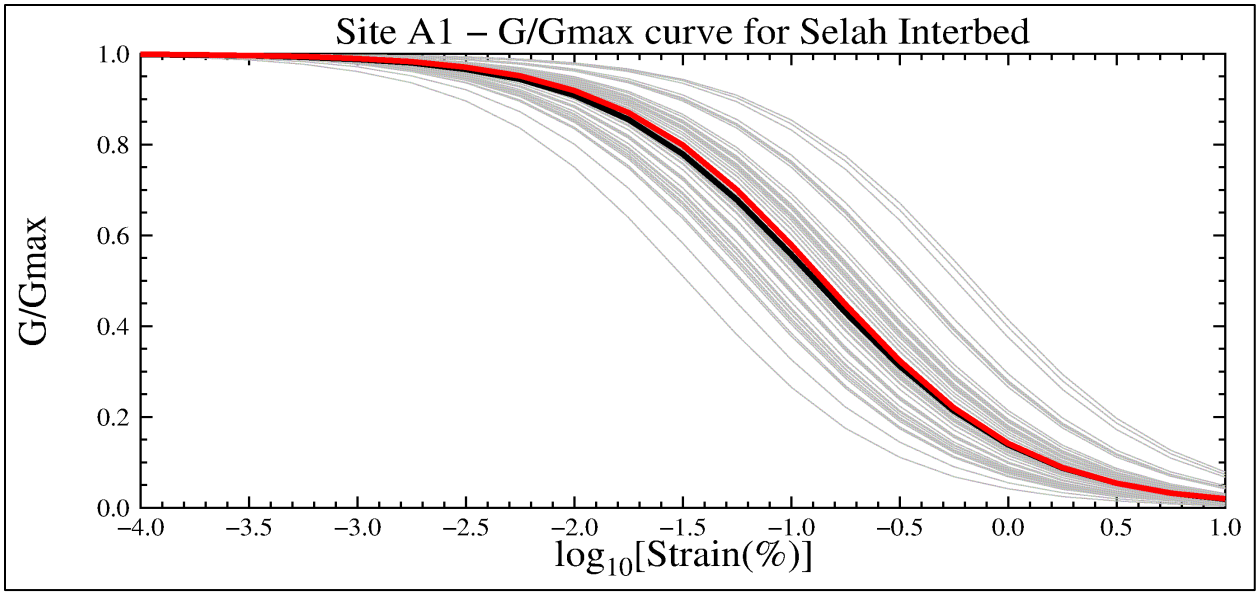

Figure 9.151. Synthetic G/G_{max} curves for Selah interbed at Site A1. Gray, synthetic profiles; black, logarithmic-mean; red, base-case curve.

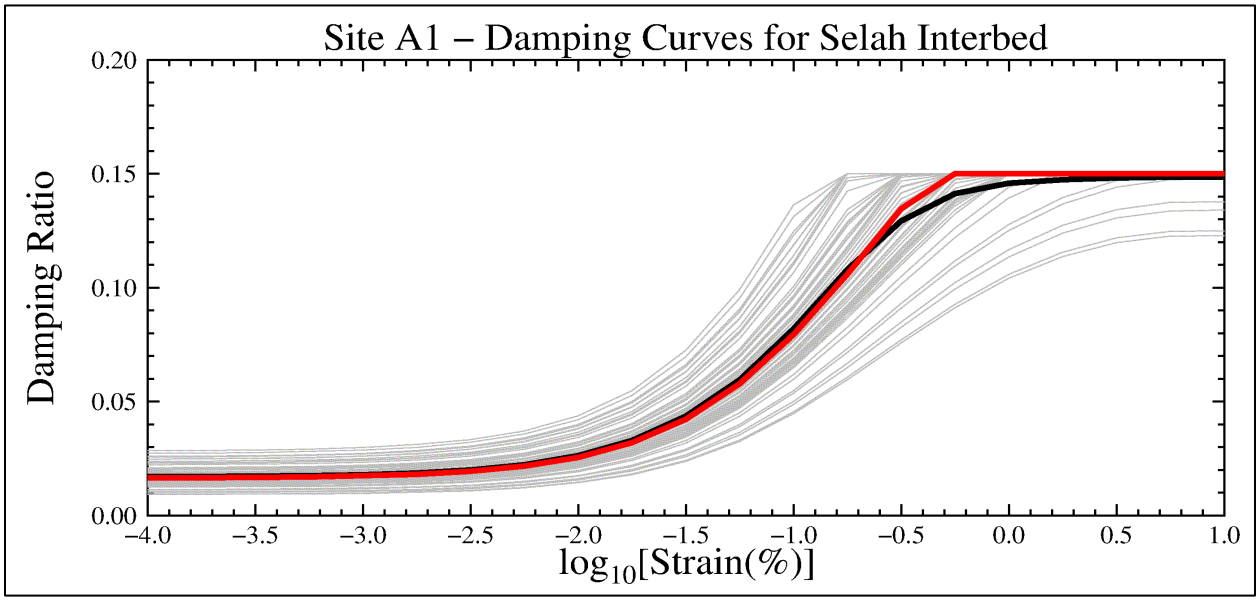

Figure 9.152. Synthetic damping curves for Selah interbed at Site A1. Gray, synthetic profiles; black, logarithmic-mean; red, base-case curve.

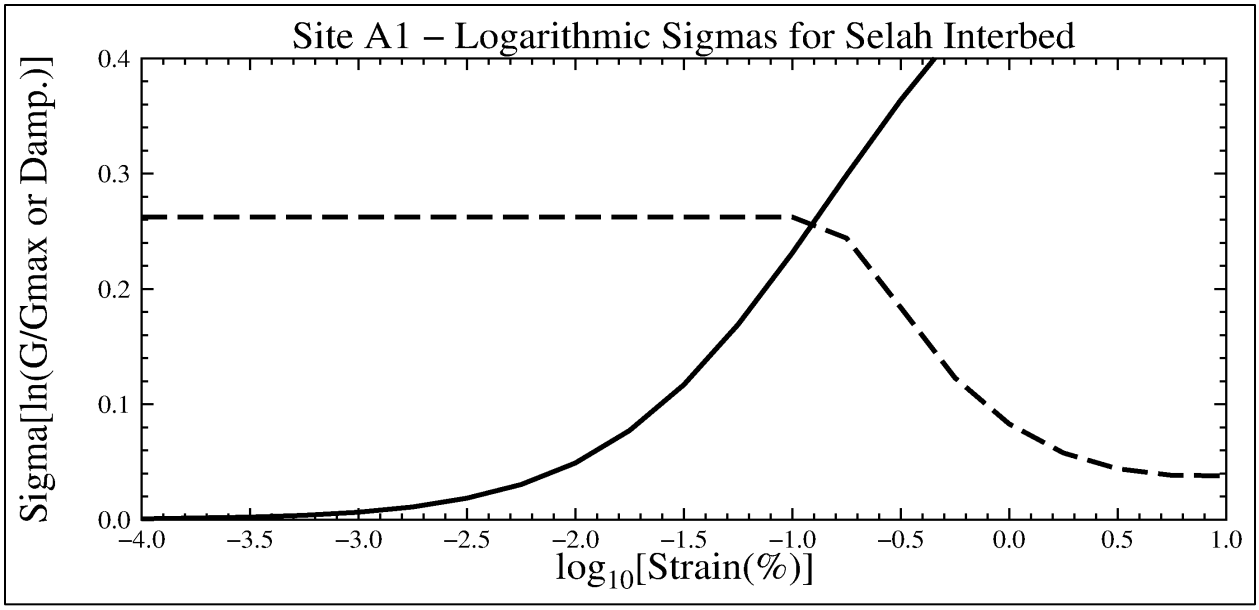

Figure 9.153. Logarithmic standard deviations of the synthetic G/G_{max} and damping curves for Selah interbed at Site A1. Solid, G/G_{max}; dashed, damping.

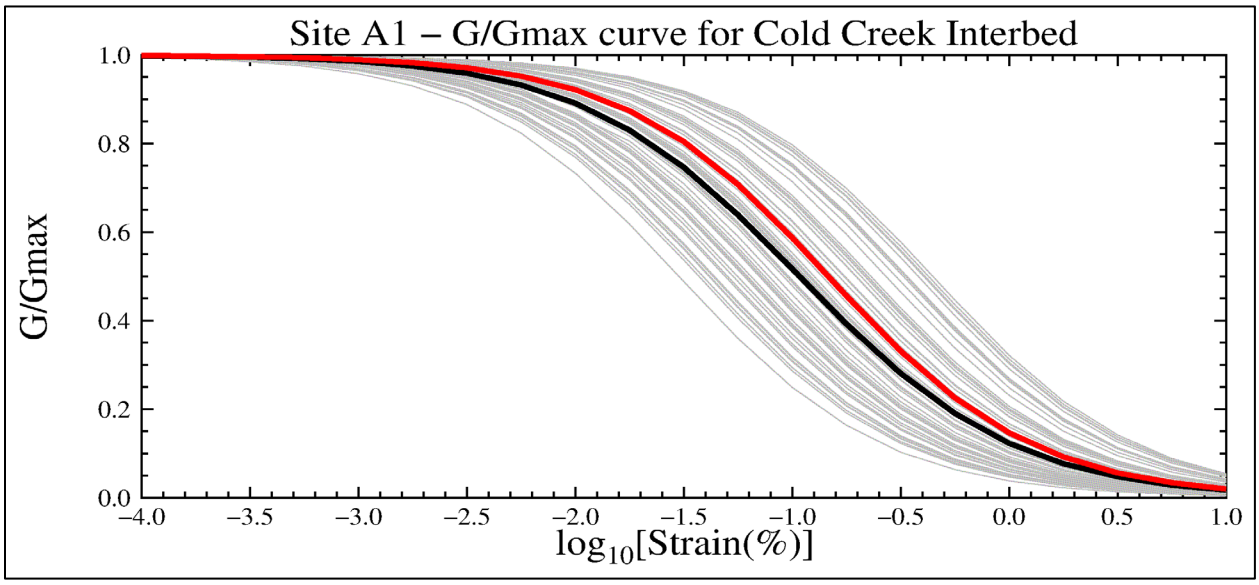

Figure 9.154. Synthetic G/G_{max} curves for Cold Creek interbed at Site A1. Gray, synthetic profiles; black, logarithmic-mean; red, base-case curve.

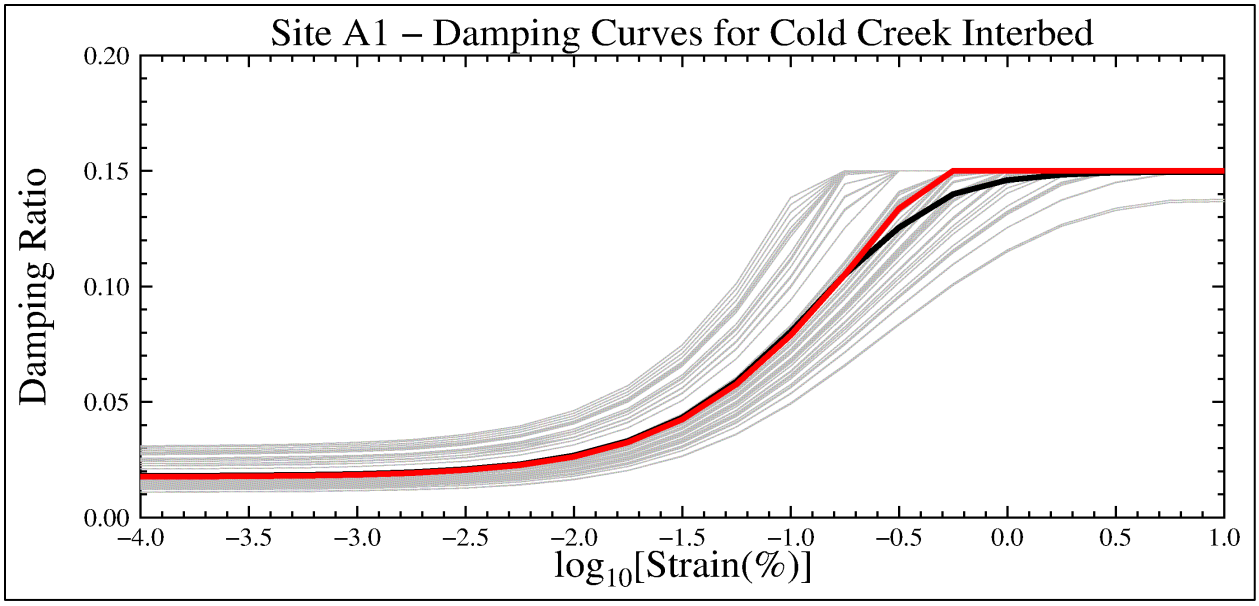

Figure 9.155. Synthetic damping curves for Cold Creek interbed at Site A1. Gray, synthetic profiles; black, logarithmic-mean; red, base-case curve.

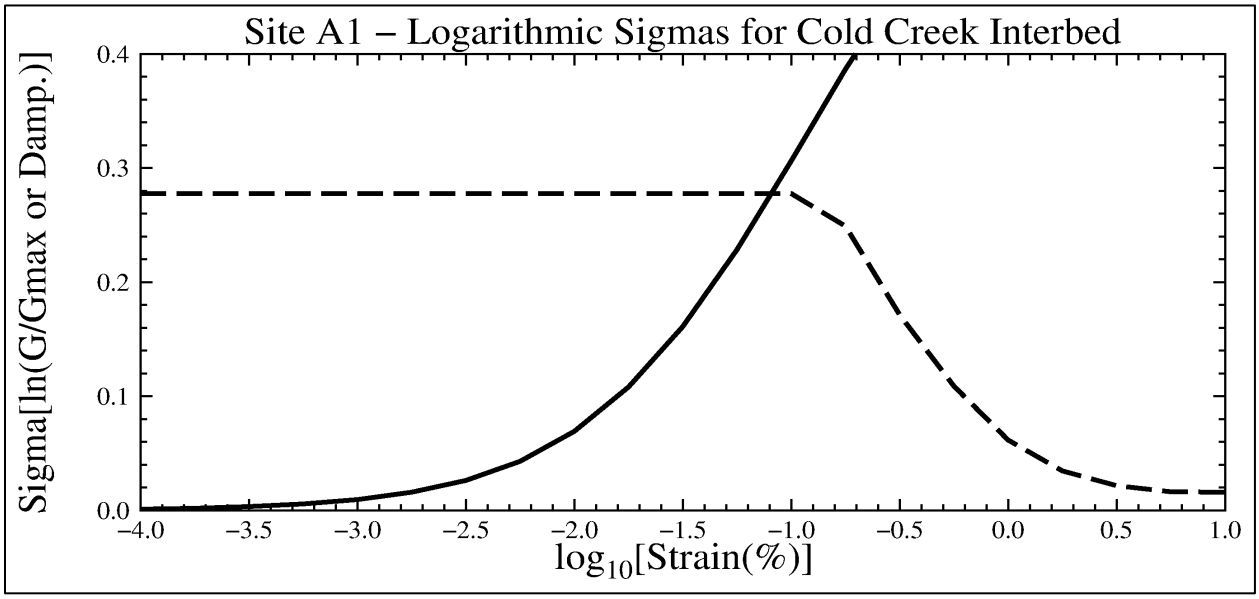

Figure 9.156. Logarithmic standard deviations of the synthetic G/G_{max} and damping curves for Cold Creek interbed at Site A1. Solid, G/G_{max}; dashed, damping.

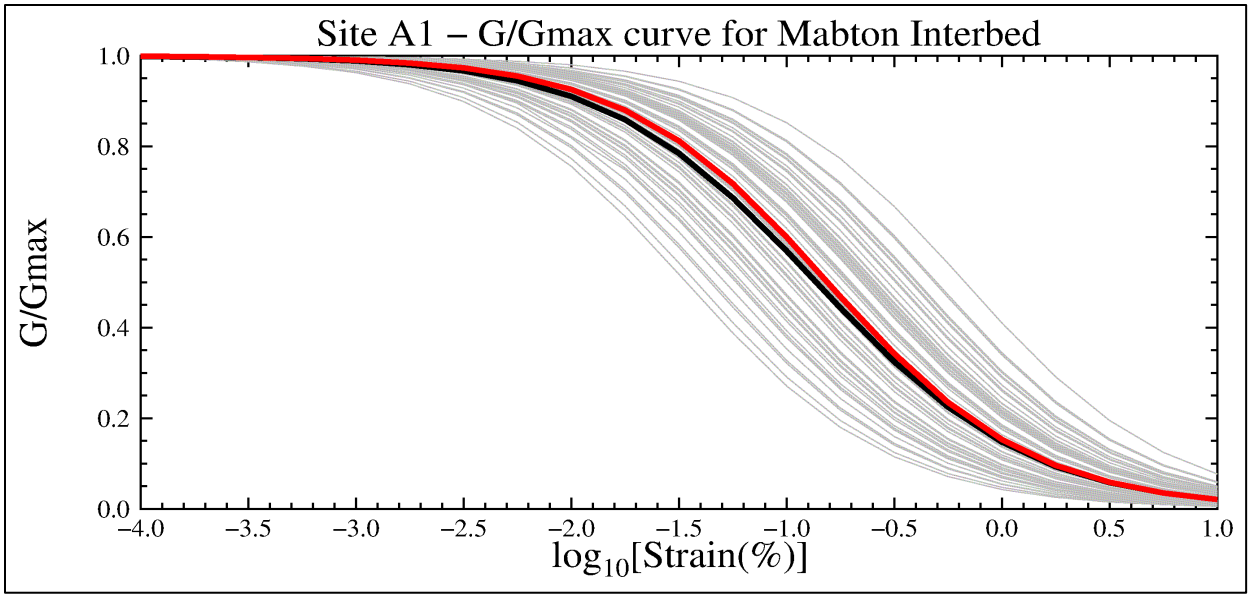

Figure 9.157. Synthetic G/G_{max} curves for Mabton interbed at Site A1. Gray, synthetic profiles; black, logarithmic-mean; red, base-case curve.

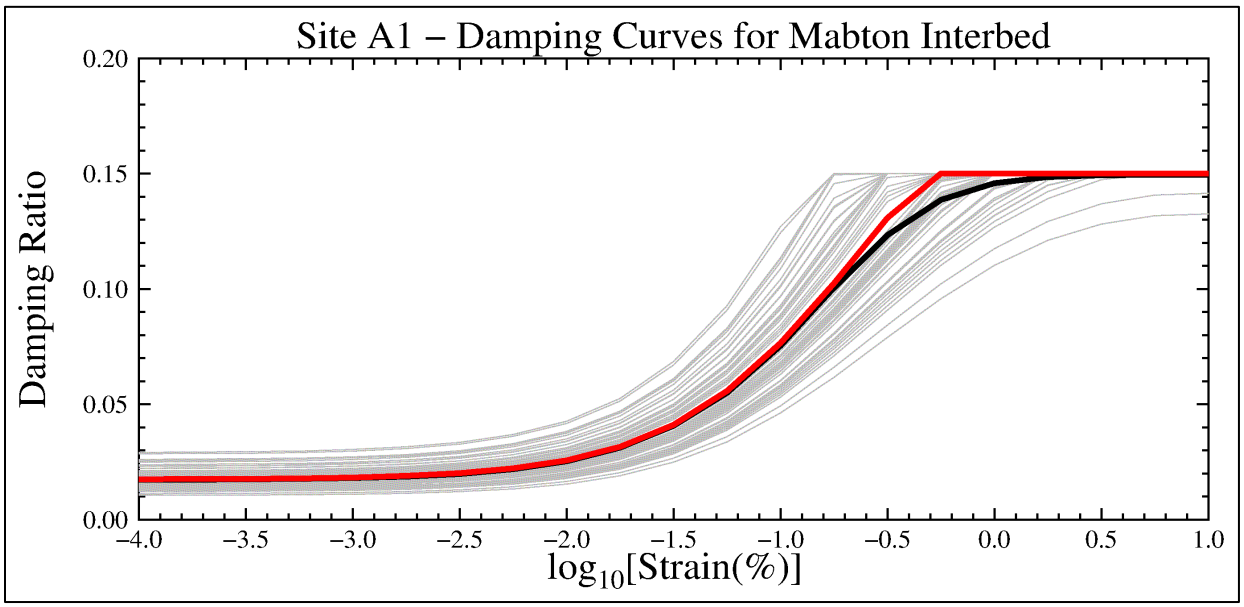

Figure 9.158. Synthetic damping curves for Mabton interbed at Site A1. Gray, synthetic profiles; black, logarithmic-mean; red, base-case curve.

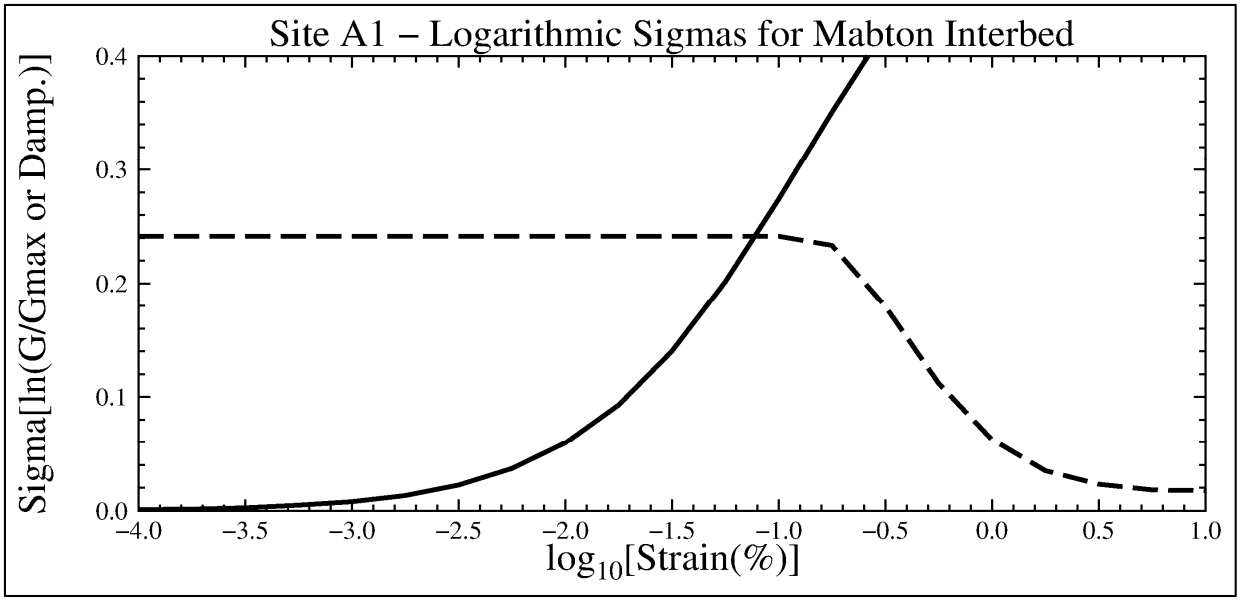

Figure 9.159. Logarithmic standard deviations of the synthetic G/G_{max} and damping curves for Mabton interbed at Site A1. Solid, G/G_{max}; dashed, damping.

9.6.5 Minimum Variability in Site Amplification Factors

As indicated in Section 9.5.1, one of the requirements for the use of single-station sigma is that uncertainty in the site term be properly accounted for as epistemic uncertainty. At intermediate and longer response periods, these conditions are not met for two reasons:

1. Conventional 1-dimensional site response analysis, even when using profile randomization, does not capture uncertainty in long-period seismic motions. The likely explanation for this is that the site response model does not extend to depths comparable to the wavelengths associated with these long response periods. Thus, the variability in response is limited to periods equal or shorter than the fundamental period of the site profile.

2. The possible presence of basin effects at intermediate periods at the five hazard calculation sites, as discussed in Section 7.6.3.

One could simply use the ergodic sigma for the baserock motions at these response periods and thereby conserve the total sigma. The GMC TI Team decided not to follow this course of action. From a philosophical perspective, it is not appropriate to assign this uncertainty to the baserock motion when in fact it arises from processes that occur above baserock. From a practical perspective, assigning this uncertainty to the baserock motions will result in baserock spectra with inflated amplitudes at long periods, which may unrealistically over-drive the entire site column, thereby resulting in overestimation of damping and underestimation of the surface motions.

Given that this uncertainty is not assigned to the baserock motion, one could introduce it into the site response calculations by inflating the uncertainty in one or more of the dynamic material properties of the site profile. The GMC TI Team decided not to follow this course of action either, again for philosophical and practical reasons. From a philosophical perspective, it is not appropriate to assign this additional uncertainty to a material property when it is caused by other processes. From a practical perspective, this

assignment may result in incorrect results, because the response is a nonlinear function of the uncertain material properties. Furthermore, the process of arbitrarily assigning these uncertainties to material properties is non-unique and will likely involve trial and error.

Therefore, the recommendation of the GMC TI Team is that any uncertainty in the surface motions that is not captured by the site response be introduced explicitly as an uncertainty in the surface-motion amplitude in the Approach 3 convolution (see Section 10.5), rather than introducing it as uncertainty in the baserock amplitude or in the material properties of the site column.

Section 9.5.6 develops the minimum value of the epistemic uncertainty in the site amplification factor and provides this minimum value (as a function of period) in Equation 9.29 and Figure 9.122. At each response period, the Approach 3 hazard convolution should use the greater of the uncertainty obtained in the site response calculations and the uncertainty derived in Section 9.5.6. This will ensure that the effect of the epistemic uncertainty in the surface motions is captured properly, without introducing any nonlinear artifacts that may bias the site spectrum.

The Approach 3 convolution operates with the baserock hazard curve for spectral acceleration at each frequency and the uncertainty in amplification factor (or the minimum uncertainty derived in Section 9.5.6, whichever is greater), to obtain the hazard curve for the spectral acceleration at the surface (although there are approximate implementations of Approach 3 that calculate the amplitude at the surface for a given mean exceedance probability, without explicitly calculating the surface hazard curve). The uncertainty in the amplification factor may depend on the rock spectral acceleration. For instance, the uncertainty in site response at high amplitudes may be greater than at low amplitudes because of increased sensitivity to uncertainty in the degradation curves. More details about the Approach 3 convolution are provided in McGuire et al. (2001) and in Appendix K.

9.7 Vertical-to-Horizontal Spectral Ratios

Vertical as well as horizontal response spectra are ultimately required at the surface locations where facilities on the Hanford Site are situated. Therefore, an element of the GMC model is a proposal for obtaining V/H ratios to be applied to the horizontal response spectra that will be obtained from convolution of the baserock hazard with the site amplification functions. This section begins with a brief explanation of why the approach of using V/H spectral ratios is adopted in place of direct calculation of the vertical component of motion. The issue of whether additional uncertainty should be captured in the construction of the vertical response spectra is also discussed. The preferred choice of the GMC TI Team from among the available models for V/H ratios reviewed in Section 7.7 is then selected, and some modifications to this model are proposed for application to the Hanford Site.

9.7.1 Justification for Choice of V/H Ratio Approach

There are essentially two ways to obtain vertical response spectra from PSHA, namely:

- Conduct a second PSHA using GMPEs for the vertical component of motion in exactly the same way as for the horizontal component of motion.
- Use V/H response spectral ratios to transform the horizontal spectra obtained from the PSHA into vertical response spectra.

The NRC's Regulatory Guide 1.208 (NRC 2007, Section 5.2) explicitly recommends the use of V/H ratios, in particular the V/H ratios for WUS and CEUS provided by McGuire et al. (2001), although this presumably applies to rock sites. There are several reasons why the first option listed above—direct calculation using GMPEs for vertical spectral ordinates—is not an attractive approach, particularly for the Hanford PSHA. Firstly, far fewer GMPEs are available for the vertical component of motion than for the horizontal component. This is probably the result of the fact that the earthquake-resistant design of structures has generally been focused primarily on the effects of lateral loads. The relative lack of GMPEs for vertical response spectral ordinates is reflected in the fact that none of the "backbone" models used in this study, for crustal or subduction earthquakes, currently has a companion model for vertical motions, although these will be forthcoming for the NGA-West2 crustal models (see Section 7.7.2). Secondly, even if abundant GMPEs for the vertical component were available, the execution of separate PSHA calculations for the vertical motions can lead to horizontal and vertical spectra that correspond to different earthquake scenarios (e.g., Gülerce and Abrahamson 2011). This is the result of different dependences on magnitude and distance, and leads to problems when developing acceleration time-histories for use in dynamic analyses.

An additional difficulty with using GMPEs for the vertical component arises from the application of NRC Approach 3 (McGuire et al. 2001) for including the influence of the uppermost layers of geo-materials at the site, which is being recommended for the Hanford Site. There is some evidence from borehole recordings for site amplification of the vertical component of motion (e.g., Elgamal and He 2004), which means that if the vertical motions were calculated for the deeper "bedrock" horizon, then the site response analyses would need to model the propagation to the target horizon of both the horizontal and vertical components. Approaches to site response analyses for vertical motion have been developed and applied in the past (e.g., EPRI 1993). In one approach the vertical component was assumed to be composed of vertically propagating P-waves. This approach has since been challenged by a study that asserts that the vertical component of motion is dominated by SV-waves (Beresnev et al. 2002), but the new approach for vertical site response analysis proposed therein have not been widely adopted. For the Hanford Site, as in most cases, the site response analyses (Section 10.5 and Appendix K) are to be based on vertically propagating SH waves only and hence only consider the horizontal component of motion.

9.7.2 Uncertainty in V/H Ratios

The V/H ratios that are to be used at the Hanford Site will be applied to horizontal spectra defined at the surface, which themselves will have been derived from PSHA using an extensive GMC logic tree as described in the preceding sections of this chapter. Each horizontal response spectrum will be transformed to a single vertical spectrum, so a unique value of the V/H ratio is required at each response period rather than a distribution of values. This could be the mean value from a logic tree, if it were considered necessary to capture uncertainty above the very considerable range of uncertainty already represented in the GMC logic tree. There are potentially two reasons for which it might be considered necessary to include additional uncertainty—or even conservatism—in the definition of the V/H ratios, these being if 1) the aleatory variability associated with predictions of vertical spectral ordinates is larger than that associated with predictions of the horizontal component, and (2) if there are reasons to believe that less is known about the vertical component of motion from future earthquakes than is the case for the horizontal motions.

To address the first of these questions, Figure 9.160 shows the ratios of the sigma values from GMPEs for vertical and horizontal components, for models that are well derived (in terms of data distribution and functional form). Although the sigma ratios fluctuate about the line representing equality, particularly at short and long periods, on average the ratio of sigma values is not very different from 1. The plot does not suggest that there is a large and systematic difference in the aleatory variability associated with the prediction of vertical and horizontal spectral ordinates. Even if one concludes that at short periods the vertical sigma is greater, the difference is not very large.

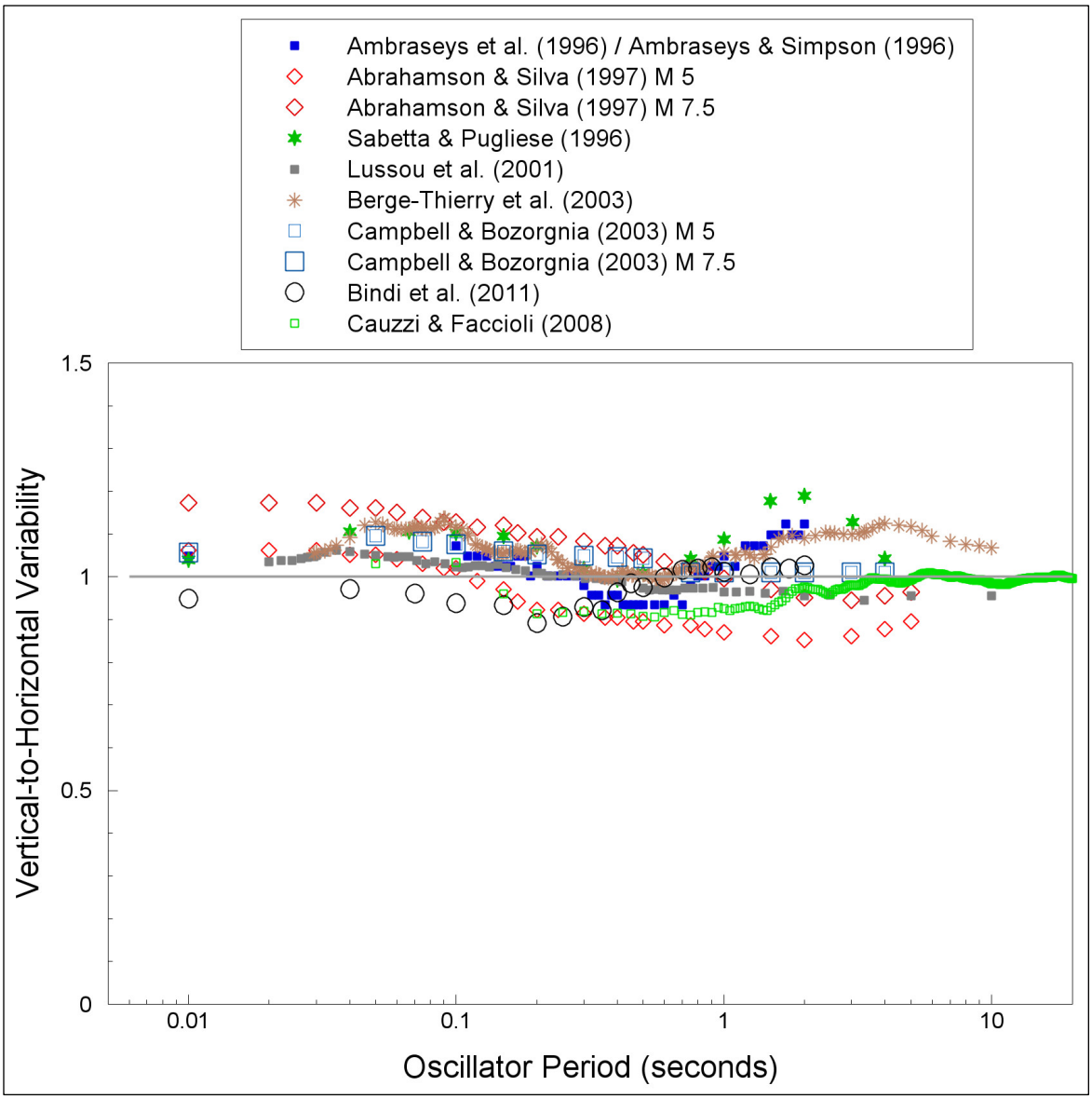

Figure 9.160. Ratios of sigma values from GMPEs for vertical and horizontal response spectral ordinates. Horizontal sigma values have been adjusted to the equivalent values for the geometric mean component, using the relationships of Beyer and Bommer (2006), for those GMPEs employing other definitions of the horizontal component

To address the second question of whether there is, in general, greater uncertainty associated with the prediction of vertical motions, it could be argued that this is the case simply because the vertical component of motion has received less attention. However, if equations such as that of Gülerce and Abrahamson (2011) are adopted, then it is reasonable to assume that sufficient care and attention have been given to the model development for no additional uncertainty to be considered in its application. The exception to this conclusion would be at longer (>3 sec) response periods because the model is simply extended to 10 sec rather than being constrained by the data.

The prediction of the vertical component of motion may also be more uncertain than the horizontal component because of issues related to accelerogram processing, especially because filter parameters may be selected from inspection of the horizontal components. This issue could give rise to greater uncertainty in the vertical motions, particularly at very short and very long periods. In the case of the Hanford PSHA project, the inclusion of a wide range of target kappa values and associated adjustments to the crustal GMPEs (Section 9.3) means that there is already a very large range of uncertainty captured in the short-period horizontal motions. As noted above, however, there are already reasons to consider additional uncertainty in the vertical components at longer periods.

9.7.3 Review of Available V/H Ratios

In Section 7.7, many available models for predicting V/H spectral ratios were reviewed and evaluated, and most of them were found wanting in several respects in terms of their applicability to the Hanford Site. None of the simplified approaches, which might be used in seismic design codes or as specified for nuclear applications by McGuire et al. (2001), were judged to be suitable for application to surface motions estimated at the five hazard calculation sites.

Among the many models predicting V/H ratios in terms of magnitude, distance, and other parameters, the model of Gülerce and Abrahamson (2011) was viewed as the clearly preferred model. Therefore, it was selected by the GMC TI Team, while noting that the predicted ratios are questionable for periods greater than about 3 sec. Moreover, the TI Team noted that Gregor et al. (2012) found this model worked well for the V/H ratios of motions from large subduction earthquakes at periods up to 1−2 sec but tended toward underestimation at longer periods. The analysis also suggested that the model under-predicts the ratios from such earthquakes for recordings obtained at greater distances, which is relevant to the location of the Hanford Site with respect to the Cascadia subduction zone. Therefore, although the Gülerce and Abrahamson (2011) model is the preferred choice of the GMC TI Team, it is recommended that it be applied with some modification at longer periods, as explained below.

9.7.4 Recommended V/H Model for the Hanford Site

The GMC TI Team recommends that vertical response spectra at surface locations at the Hanford Site be constructed by the application of V/H ratios to the horizontal response spectra. These ratios should be calculated using the median predictions from the model of Gülerce and Abrahamson (2011), for which a magnitude-distance pair is required from disaggregation. The model also requires V_{S30}, which should be obtained from the site characterization, and the style of faulting, which is likely to be reverse in all cases for the Hanford Site. The V/H ratios should be calculated using the model directly for periods of up to 2 sec. The model will not yield V/H ratios at all of the target periods at which the horizontal spectra will be defined up to this period, but it is recommended to simply interpolate either the V/H ratios or the

resulting vertical spectral ordinates, rather than interpolating the missing coefficients of the model. For periods beyond 2 sec, it is recommended to calculate the median V/H ratios using the modified values of the coefficient a_1 in Equation (1) of the paper by Gülerce and Abrahamson (2011); the modified values are listed in Table 9.24. These modified values of the coefficients have been determined so that the median predictions approximately match the trend in the residuals of the recordings from the Maule earthquake presented by Gregor et al. (2012) and shown in Figure 9.122. The original and modified V/H ratios for a soil site close to a large-magnitude reverse-faulting earthquake are compared in Figure 9.161.

Table 9.24. Proposed modifications to the long-period constant coefficients in Equation (1) of Gülerce and Abrahamson (2011) for the prediction of V/H response spectra ratios.

Period (sec)	Coefficient a_1	
	Original	Modified
2.0	-1.111	-1.111
3.0	-1.054	-0.862
4.0	-1.014	-0.686
5.0	-1.000	-0.549
7.5	-1.000	-0.300
10.0	-1.000	-0.300

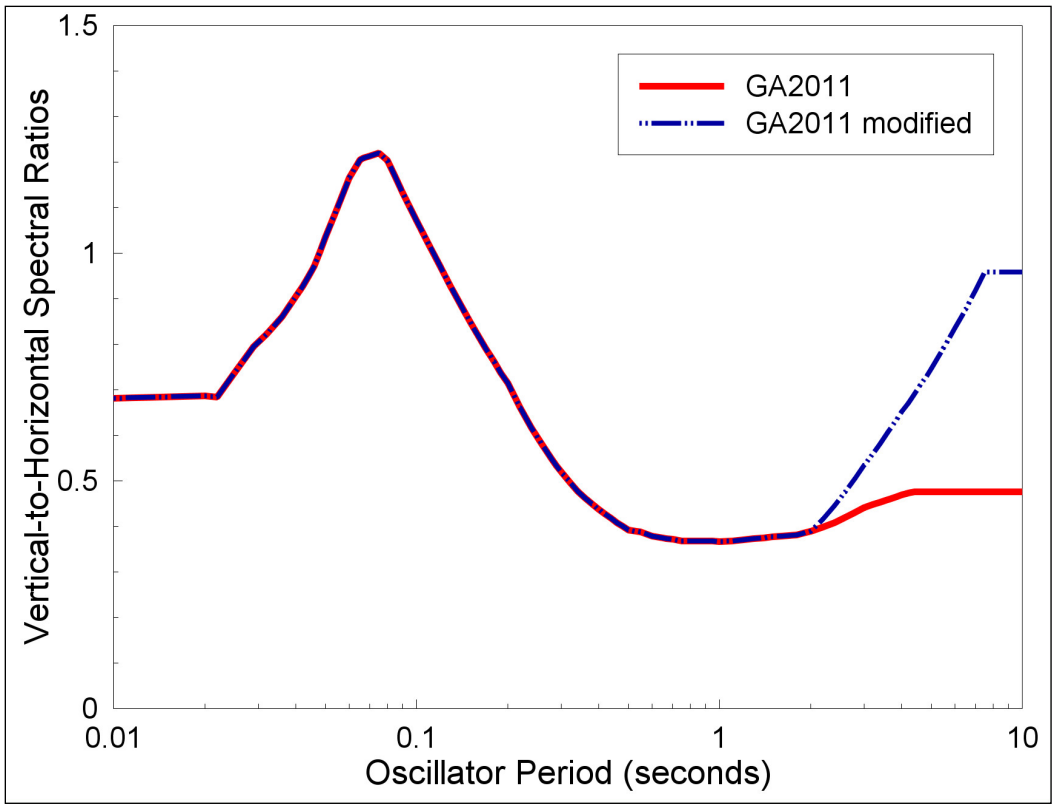

Figure 9.161. Comparison of V/H spectral ratios for a soil site (V_{S30} = 350 m/s) at 30 km from a magnitude 8 reverse-faulting earthquake as obtained from the original equation by Gülerce and Abrahamson (2011) and using the modified coefficients in Table 9.24.

The coefficients in Table 9.24 and the ratios shown in Figure 9.161 are all referenced to response spectral ordinates with 5% of critical damping. If vertical response spectra are required at other damping levels, it is not advisable to apply these factors to the horizontal spectra after scaling the latter to the target damping value. The reason for this is that scaling factors to adjust spectral ordinates for differences in damping ratios are a function of duration (e.g., Bommer and Mendis 2005), and vertical motions tend to have different durations than their horizontal counterparts. For generating vertical spectra at alternative damping levels, reference should be made to the work of Rezaeian et al. (2014).

The proposed approach for obtaining V/H ratios is only a suggestion; the GMC TI Team considers it to be within the remit of the sponsors, and the consultants, to choose alternative approaches, including a modification of what is suggested herein. At the time surface motions are estimated at any particular location on the site, any new models from which V/H ratios can be obtained should be considered, and if found to match the requirements for the Hanford Site, be adopted in place of the model proposed here. In particular, the vertical component models of the NGA-West2 GMPEs should be considered as suitable candidates, at least for response periods of up to 3 sec.

9.8. References

Abrahamson NA. 1998. Statistical properties of peak ground accelerations recorded by the SMART 1 array. *Bulletin of the Seismological Society of America* 78(1):26−41.

Abrahamson NA, GM Atkinson, D Boore, Y Bozorgnia, K Campbell, B Chiou, IM Idriss, W Silva, and R Youngs. 2008. Comparisons of the NGA Ground-Motion Relations. *Earthquake Spectra* 24**:**45−66.

Abrahamson NA and JJ Bommer. 2005. Probability and uncertainty in seismic hazard analysis. *Earthquake Spectra* 21(2):603−607.

Abrahamson NA, N Gregor, and K Addo. 2014a. BC Hydro ground motion prediction equations for subduction earthquakes. *Earthquake Spectra* (Submitted).

Abrahamson NA and WJ Silva. 1996. *Empirical Ground Motion Models*. Report prepared for Brookhaven National Laboratory, Upton, New York.

Abrahamson NA and WJ Silva. 1997. Empirical response spectral attenuation relations for shallow crustal earthquakes. *Seismological Research Letters* 68(1):94−127.

Abrahamson NA and WJ Silva. 2008. Summary of the Abrahamson & Silva NGA ground-motion relations. *Earthquake Spectra* 24(1):67−97.

Abrahamson NA, WJ Silva, and R Kamai. 2014b. Update of the AS08 Ground-Motion Prediction Equations Based on the NGA-West2 Data Set. *Earthquake Spectra* 30(3):1025-1055.

Abrahamson NA and PG Somerville. 1996. Effects of the hanging wall and footwall on the ground motions recorded during the Northridge earthquake. *Bulletin of the Seismological Society of America* 86:S93–S99.

Abrahamson NA and RR Youngs. 1992. A stable algorithm for regression analysis using the random effects model. *Bulletin of the Seismological Society of America* 82:505−510.

Akkar S and JJ Bommer. 2006. Influence of long-period filter cut-off on elastic spectral displacements. *Earthquake Engineering and Structural Dynamics* 35:1145−1165.

Akkar S, MA Sandıkkaya, and JJ Bommer. 2014a. Empirical ground-motion models for point- and extended-source crustal earthquake scenarios in Europe and the Middle East. *Bulletin of Earthquake Engineering* 12(1):359−387. DOI: 10.1007/s10518-013-9461-4.

Akkar S, MA Sandıkkaya, and JJ Bommer. 2014b. Erratum to: Empirical ground-motion models for point- and extended-source crustal earthquake scenarios in Europe and the Middle East. *Bulletin of Earthquake Engineering* 12(1):389−390. DOI: 10.1007/s10518-013-9506-8.

Al Atik L, NA Abrahamson, JJ Bommer, F Scherbaum, F Cotton, and N Kuehn. 2010. The variability of ground-motion prediction models and its components. *Seismological Research Letters* 81(5):794−801.

Al Atik L, A Kottke, N Abrahamson, and J Hollenback. 2013. Kappa (κ) Scaling of Ground-Motion Prediction Equations Using an Inverse Random Vibration Theory Approach. *Bulletin of the Seismological Society of America* 104(1):336−346.

Al Atik L and RR Youngs. 2014. Epistemic uncertainty for NGA-West2 models. *Earthquake Spectra* 30(3):1301-1318.

Ambraseys NN, KA Simpson, and JJ Bommer. 1996. The prediction of horizontal response spectra in Europe. *Earthquake Engineering & Structural Dynamics* 25:371−400.

Ambraseys NN and KA Simpson. 1996. The prediction of vertical response spectra in Europe. *Earthquake Engineering & Structural Dynamics* 25:401−412.

Anderson JG and JN Brune. 1999. Probabilistic seismic hazard assessment without the ergodic assumption. *Seismological Research Lett*ers 70:19−28

Anderson JG and SE Hough. 1984. A Model for the Shape of the Fourier Amplitude Spectrum of Acceleration at High Frequencies. *Bulletin of the Seismological Society of America* 74(5):1969–1993.

Ang AH-S and Tang WH. 2007. *Probability Concepts in Engineering: Emphasis on Applications to Civil and Environmental Engineering (v. 1)*. John Wiley and Sons.

Arango MC, FO Strasser, JJ Bommer, DA Hernández, and JM Cepeda. 2011. A strong-motion database from the Central American subduction zone. *Journal of Seismology* 15:261−294.

Arroyo D, D García, M Ordaz, MA Mora, and SK Singh. 2010. Strong ground-motion relations for Mexican interplate earthquakes. *Journal of Seismology* 14(4):769–785.

Atkinson GM. 2006. Single-station sigma. *Bulletin of the Seismological Society of America* 96:446−455.

Atkinson G and J Adams. 2013. Ground motion prediction equations for application to the 2015 national seismic hazard maps of Canada. *Canadian Journal of Civil Engineering* 40:988−998.

Atkinson GM, JJ Bommer, and NA Abrahamson. 2014. Alternative approaches to modeling epistemic uncertainty in ground motions in Probabilistic Seismic Hazard Analysis. Opinion Paper submitted to *Seismological Research Letters.*

Atkinson GM and DM Boore. 2003. Empirical ground-motion relations for subduction zone earthquakes and their application to Cascadia and other regions. *Bulletin of the Seismological Society of America* 93(4):1703–1729.

Atkinson GM and GM Boore. 2008. Erratum to: Empirical ground-motion relationships for subduction-zone earthquakes and their application to Cascadia and other regions. *Bulletin of the Seismological Society of America* 98:2567−2569.

Atkinson GM and R Casey. 2003. A Comparison of Ground Motions from the 2001 M 6.8 In-Slab Earthquakes in Cascadia and Japan. *Bulletin of the Seismological Society of America* 93(4):1823−1831.

Atkinson GM and M Macias. 2008. *Predicted Ground Motions for Great Interface Earthquakes in the Cascadia Subduction Zone*. Final Technical Report, USGS NEHRP Grant 07HQGR0041, U.S. Geological Survey. Available at: http://earthquake.usgs.gov/research/external/reports/07HQGR0041.pdf.

Atkinson GM and M Macias. 2009. Predicted ground motions for great interface earthquakes in the Cascadia subduction zone. *Bulletin of the Seismological Society of America* 99(3):1552–1578.

BC Hydro. 2012. *Probabilistic Seismic Hazard Assessment. Volume 3: Ground Motion Report*. Report No. E658 – Vol. 3, Vancouver, British Columbia.

Bechtel (Bechtel Power Corporation). 2013. *Assessment of Dynamic Geotechnical Data for the Columbia Generating Station Site*. Report prepared by Geotechnical & Hydraulic Engineering Services, Bechtel Power Corporation, Frederick, Maryland.

Beresnev IA, AM Nightengale, and WJ Silva. 2002. Properties of vertical ground motions. *Bulletin of the Seismological Society of America* 92(8):3152−3164.

Berge-Thierry C, F Cotton, O Scotti, D-A Griot-Pommera, and Y Fukushima. 2003. New empirical spectral attenuation laws for moderate European earthquakes. *Journal of Earthquake Engineering* 7(2):193−222.

Beyer K and JJ Bommer. 2006. Relationships between median values and aleatory variabilities for different definitions of the horizontal component of motion. *Bulletin of the Seismological Society of America* 94(4A):1512−1522.

Bindi D, M Massa, L Luzi, G Ameri, F Pacor, R Puglia, and P Augliera. 2014a. Pan-European ground-motion prediction equations for the average horizontal component of PGA, PGV, and 5%-damped PSA at spectral periods up to 3.0 s using the RESORCE dataset. *Bulletin of Earthquake Engineering* 12(1):391-430.

Bindi D, M Massa, L Luzi, G Ameri, F Pacor, R Puglia, and P Augliera. 2014b. Erratum to: Pan-European ground-motion prediction equations for the average horizontal component of PGA, PGV, and 5%-damped PSA at spectral periods up to 3.0 s using the RESORCE dataset. *Bulletin of Earthquake Engineering* 12(1):431−448.

Bindi D, F Pacor, L Luzi, R Puglia, M Massa, G Ameri, and R Paolucci. 2011. Ground motion prediction equations derived from the Italian strong motion database. *Bulletin of Earthquake Engineering* 9:1899−1920.

Bommer JJ. 2012. Challenges of building logic trees for probabilistic seismic hazard analysis. *Earthquake Spectra* 28(4):1723−1735.

Bommer JJ, KJ Coppersmith, RT Coppersmith, KL Hanson, A Mangongolo, J Neveling, EM Rathje, A Rodriguez-Marek, F Scherbaum, R Shelembe, PJ Stafford, and FO Strasser. 2014. A SSHAC Level 3 probabilistic seismic hazard analysis for a new-build nuclear site in South Africa. *Earthquake Spectra* DOI: 10.1193/060913EQS145M (In Press).

Bommer JJ, J Douglas, F Scherbaum, F Cotton, H Bungum, and D Fäh. 2010. On the selection of ground-motion prediction equations for seismic hazard analysis. *Seismological Research Letters* 81(5):783−793.

Bommer JJ and R Mendis. 2005. Scaling of displacement spectral ordinates with damping ratios. *Earthquake Engineering and Structural Dynamics* 34(2):145−165.

Boore DM. 2005. *SMSIM – FORTRAN Programs for Simulating Ground Motions from Earthquakes: Version 2.3 – A revision of OFR 96-80-A*. U.S. Geological Survey Open-File Report (A modified version of OFR 00--509, describing the program as of 15 August, 2005 [version 2.30]), Reston, West Virginia.

Boore DM. 2013. The Uses and Limitations of the Square-Root Impedance Method for Computing Site Amplification. *Bulletin of the Seismological Society of America* 103:2356−2368.

Boore DM and WB Joyner. 1997. Site Amplifications for Generic Rock Sites. *Bulletin of the Seismological Society of America* 87(2):327–341.

Boore DM, WB Joyner, and TE Fumal. 1997. Equations for estimating horizontal response spectra and peak acceleration from western North American earthquakes: A summary of recent work. *Seismological Research Letters* 68:128–153.

Boore DM, JP Stewart, E Seyhan, and GM Atkinson. 2014. NGA-West2 Equations for Predicting Response Spectral Accelerations for Shallow Crustal Earthquakes. *Earthquake Spectra* 30(3):1057-1085.

Campbell KW. 2003. Prediction of Strong Ground Motion Using the Hybrid Empirical Method and its Use in the Development of Ground-Motion (Attenuation) Relations in Eastern North America. *Bulletin of the Seismological Society of America* 93:1012–1033.

Campbell KW and Y Bozorgnia. 2003. Updated near-source ground motion (attenuation) relations for the horizontal and vertical components of peak ground acceleration and acceleration response spectra. *Bulletin of the Seismological Society of America* 93(1):314−331.

Campbell KW and Y Bozorgnia. 2008. NGA ground motion model for the geometric mean horizontal component of PGA, PGV, PGD and 5% damped linear elastic response spectra for periods ranging from 0.01 to 10 s. *Earthquake Spectra* 24(1):139−171.

Campbell KW and Y Bozorgnia. 2014. NGA-West2 Campbell-Bozorgnia Ground Motion Model for the Horizontal Components of PGA, PGV, and 5%-Damped Elastic Pseudo-Acceleration Response Spectra for Periods Ranging from 0.01 to 10 sec. *Earthquake Spectra* 30(3):1087-1115.

Cauzzi C and E Faccioli. 2008. Broadband (0.05 to 20 s) prediction of displacement response based on worldwide digital records. *Journal of Seismology* 12:453−475.

Chiou S-J, FI Makdisi, and RR Youngs. 2000. *Style-of-Faulting and Footwall/Hanging Wall Effects on Strong Ground Motion*. FY 1995 NEHRP Award Number 1434-95-G-2614, final report, Geomatrix, Oakland, California.

Chiou BS-J and RR Youngs. 2008. An NGA model for the average horizontal component of peak ground motion and response spectra. *Earthquake Spectra* 24(1):173−215.

Chiou BS-J and RR Youngs. 2014. Update of the Chiou and Youngs NGA Ground Motion Model for Average Horizontal Component of Peak Ground Motion and Response Spectra. *Earthquake Spectra* 30(3):1117-1153.

Cleveland WS. 1979. Robust locally weighted regression and smoothing scatterplots. *Journal of the American statistical association* 74(368):829−836.

Cleveland WS and Devlin SJ. 1988. Locally weighted regression: an approach to regression analysis by local fitting. *Journal of the American Statistical Association* 83(403):596−610.

Cools R and O Rabinowitz. 1993. Monomial cubature rules since "Shroud": a compilation. *Journal of Computational and Applied Mathematics* 48:309−326.

Costantino, C.J. 1996. Recommendations for uncertainty estimates in shear modulus reduction and hysteretic damping relationships. Published as Appendix D in WJ Silva, N Abrahamson, G Toro, and C Costantino. 1997. *Description and validation of the stochastic ground motion model.* Report Submitted to Brookhaven National Laboratory, Associated Universities, Inc. Upton, New York, Contract No. 770573.

Cotton F, F Scherbaum, JJ Bommer, and H Bungum. 2006. Criteria for selecting and adjusting ground motion models for specific target regions: Application to central Europe and rock sites. *Journal of Seismology* 10(2):137−156.

Crouse CB. 1991. Ground-motion attenuation equation for earthquake on Cascadia subduction-zone earthquake. *Earthquake Spectra* 7:210−236.

Crouse CB, KV Yogesh, and BA Schell. 1988. Ground motions from subduction zone earthquakes, *Bulletin of the Seismological Society of America* 78:1−25.

Darendeli MB. 2001. *Development of a New Family of Normalized Modulus Reduction and Material Damping Curves.* PhD Dissertation, University of Texas at Austin.

Dawood HM, A Rodriguez-Marek, J Bayless, C Goulet, and E Thompson. 2014. Processing the KiK-net strong ground motion database and compilation of metadata for GMPE development. *Earthquake Spectra* (Submitted).

Donahue J and N Abrahamson. 2014. Simulation-based hanging-wall effects. *Earthquake Spectra* 30(3):1269-1284.

Elgamal A and L He. 2004. Vertical earthquake ground motion records: an overview. *Journal of Earthquake Engineering* 8(5):663−697.

EPRI (Electric Power Research Institute). 1993. *Guidelines for Determining Design Basis Ground Motions*: *Method and Guidelines for Estimating Earthquake Ground Motions in Eastern North America*. Vol. 1-5, EPRI TR-102293, Palo Alto, California.

EPRI (Electric Power Research Institute). 2004. *CEUS Ground Motion Project Final Report*. EPRI TR-1009684, Palo Alto, California.

EPRI (Electric Power Research Institute). 2013a. *EPRI (2004, 2006) Ground-Motion Model Review Project*. EPRI TR-3002000717, Palo Alto, California.

EPRI (Electric Power Research Institute). 2013b. *Screening, Prioritization and Implementation Details (SPID) for the Resolution of Fukushima Near-Term Task Force Recommendation 2.1: Seismic.* Technical Report 1025287, Palo Alto, California.

García D, SK Singh, M Herráiz, M Ordaz, and JF Pacheco. 2005. Inslab earthquakes of central Mexico: Peak ground-motion parameters and response spectra. *Bulletin of the Seismological Society of America* 95(6): 2272–2282.

Ghofrani H, GM Atkinson, and K Goda. 2013. Implications of the 2011 M9.0 Tohoku Japan Earthquake for the Treatment of Site Effects in Large Earthquakes. *Bulletin of Earthquake Engineering* 11:171−203.

Gregor N. 2012. Subduction Zone GMPE Models for Application to Cascadia. Hanford PSHA Workshop 2 Presentation, December 8, 2012. In: PNNL (Pacific Northwest National Laboratory). 2013b. *Workshop Report Hanford Probabilistic Seismic Hazard Analysis Workshop 2: Review of Database and Discussion of Alternative Models*. PNNL-22254, Richland, Washington.

Gregor NJ, NA Abrahamson, KO Addo, and A Rodriguez-Marek. 2012. Vertical to horizontal (V/H) ratios for large megathrust subduction zone earthquakes. *Proceedings of 15th World Conference on Earthquake Engineering*. Available at: http://www.nicee.org/wcee/.

Gregor N, NA Abrahamson, GM Atkinson, DM Boore, Y Bozorgnia, KW Campbell, BS-J Chiou, IM Idriss, R Kamai, E Seyhan, W Silva, JP Stewart, and R Youngs. 2014. Comparison of NGA-West2 GMPEs. *Earthquake Spectra*. DOI: http://dx.doi.org/10.1193/070113EQS186M.

Gregor NJ, WJ Silva, IG Wong, and RR Youngs. 2002. Ground-motion attenuation relationships for Cascadia subduction zone megathrust earthquakes based on a stochastic finite-fault model. *Bulletin of the Seismological Society of America* 92(5):1923–1932.

Gregor N, W Silva, I Wong, and R Youngs. 2006. Updated Response Spectral Attenuation Relationship for Cascadia Subduction Zone Megathrust Earthquake. *Seismological Research Letters* 77(2):325−326.

Gülerce Z and NA Abrahamson. 2011. Site-specific design spectra for vertical ground motion. *Earthquake Spectra* 27(4):1023−1047.

Hastie T, R Tibshirani, J Friedman, T Hastie, J Friedman, and R Tibshirani. 2009. *The Elements of Statistical Learning* (Vol. 2, No. 1). Springer, New York.

Idriss IM. 2014. NGA-West2 Model for Estimating Average Horizontal Values of Pseudo-Absolute Spectral Accelerations Generated by Crustal Earthquakes. *Earthquake Spectra* (Submitted).

Idriss IM and HB Seed. 1968. An Analysis of Ground Motions during the 1957 San Francisco Earthquake. *Bulletin of the Seismological Society of America* 58(6):2013−2032.

Jayaram N and JW Baker. 2008. Statistical tests of the joint distribution of spectral acceleration values. *Bulletin of the Seismological Society of America* 98(5):2231−2243.

Jeon SY. 2008. *Dynamic and Cyclic Properties in Shear of Tuff Specimens from Yucca Mountain, Nevada*. PhD Dissertation, University of Texas at Austin.

Joyner WB and DM Boore. 1981. Peak acceleration and velocity from strong-motion records including records from the 1979 Imperial Valley, California, earthquake. *Bulletin of the Seismological Society of America* 71:2011−2038.

Kamai R, NA Abrahamson, and WJ Silva. 2013. *Nonlinear Horizontal Site Response for the NGA-West2 Project.* PEER Report 2013/12, Pacific Earthquake Engineering Research Center, University of California at Berkeley.

Keefer DI and SE Bodily. 1983. Three-point approximations for continuous random variables. *Management Science* 26(5):595−609.

Konno, K, and T Ohmachi. 1998. Ground-Motion Characteristics Estimated from Spectral Ratio between Horizontal and Vertical Components of Microtremor. *Bulletin of the Seismological Society of America* 88(1):228−241.

Kottke AR and EM Rathje. 2008. *STRATA*. Version alpha, Revision 381, University of Texas at Austin.

Last GV. 2014. *Stratigraphic Profiles for Selected Hanford Site Seismometer Stations and Other Locations*. PNNL-23126, Pacific Northwest National Laboratory, Richland Washington.

Lin P-S and C-T Lee. 2008. Ground-motion attenuation relationships for subduction-zone earthquakes in northeastern Taiwan. *Bulletin of the Seismological Society of America* 98(1):220–240.

Lussou P, P-Y Bard, F Cotton, and Y Fukushima. 2001. Seismic design regulation codes: contributions of K-Net data to site effect evaluations. *Journal of Earthquake Engineering* 5(1):13−33.

McCullagh P and FRS Nelder. 1989. Generalized Linear Models. *Monographs on Statistics and Applied Probability* 37.

McGuire RK, CA Cornell, and GR Toro. 2005. The case for the mean hazard curve. *Earthquake Spectra* 21(3):879−886.

McGuire RK, WJ Silva, and CJ Costantino. 2001. *Technical Basis for Revision of Regulatory Guidance on Design Ground Motions: Hazard- and Risk-Consistent Ground Motion Spectra Guidelines*. NUREG/CR-6728, U.S. Nuclear Regulatory Commission, Washington, D.C.

Menq F-Y. 2003. *Dynamic Properties of Sandy and Gravely Soils*. PhD Dissertation, University of Texas, Austin, May, 364 p.

Miller AC and TR Rice. 1983. Discrete approximations of probability distributions. *Management Science* 29:352−362.

Musson RMW. 2005. Against fractiles. *Earthquake Spectra* 21(3):887−891.

NRC (U.S. Nuclear Regulatory Commission). 2007. *A performance-based approach to define the site-specific earthquake ground motion*. Regulatory Guide 1.208, Washington, D.C.

NRC (Nuclear Regulatory Commission). 2012. Request for Information Pursuant to Title 10 of the Code of Federal Regulations 50.54(f) regarding Recommendation 2.1, 2.3, and 9.3, of the Near-Term Task Force Review of Insights from the Fukushima Dai-Ichi Accident. Washington, D.C. March 12, 2012.

Ordonez GA 2012. *SHAKE2000 – A computer program for the 1-D Analysis of Geotechnical Earthquake Engineering problems*. GeoMotions, LLC; Lacey, Washington.

Petersen MD, AD Frankel, SC Harmsen, CS Mueller, KM Haller, RL Wheeler, RL Wesson, Y Zeng, OS Boyd, DM Perkins, N Luco, EH Field, CJ Wills, and KS Rukstales. 2008. *Documentation for the 2008 Update of the United States National Seismic Hazard Maps*. USGS Open-File Report 2008-1128, U.S. Geological Survey, Reston, Virginia. Available at: http://pubs.er.usgs.gov/usgspubs/ofr/ofr081128.

Philips WS, KM Mayeda, and L Malagnini. 2014. How to invert multi-band, regional phase amplitudes for 2-D attenuation and source parameters: Tests using the USArray. *Pure and Applied Geophysics* 171(3-5):469−484. DOI: 10.1007/s00024-013-0646-1.

Poggi V, B Edwards, and D Fah. 2013. Reference S-Wave Velocity Profile and Attenuation Models for Ground-Motion Prediction Equations: Application to Japan. *Bulletin of the Seismological Society of America* 103(5):2645−2656.

Renault P, S Heuberger, and NA Abrahamson. 2010. PEGASOS Refinement Project: An improved PSHA for Swiss nuclear power plants. *Proceedings of the 14th European Conference of Earthquake Engineering,* Paper ID 991. Ohrid, Republic of Macedonia. Available at: http://toc.proceedings.com/11356webtoc.pdf.

Rezaeian S, Y Bozorgnia, IM Idriss, N Abrahamson, K Campbell, and W Silva. 2014. Damping scaling factors for vertical elastic response spectra for shallow crustal earthquakes in active tectonic regions. *Earthquake Spectra* 30(3):1335-1358.

Rodriguez-Marek A, F Cotton, NA Abrahamson, S Akkar, L Al Atik, B Edwards, GA Montalva, and HM Dawood. 2013. A model for single-station standard deviation using data from various tectonic regions. *Bulletin of the Seismological Society of America* 103:3149−3163.

Rodriguez-Marek A, GA Montalva, F Cotton, and F Bonilla. 2011. Analysis of Single-Station Standard Deviation Using the KiK-net Data. *Bulletin of the Seismological Society of America* 101:1242–1258.

Rodriguez-Marek A, EM Rathje, JJ Bommer, F Scherbaum, and PJ Stafford. 2014. Application of single-station sigma and site response characterization in a probabilistic seismic-hazard analysis for a new nuclear site. *Bulletin of the Seismological Society of America* 105(4):1601-1619.

Rohay AC and TM Brouns. 2007. *Site-Specific Velocity and Density Model for the Waste Treatment Plant, Hanford, Washington*. PNNL-16652, Pacific Northwest National Laboratory, Richland, Washington.

Rollins K, M Evans, N Diehl, and W Ill. 1998. Shear Modulus and Damping Relationships for Gravels. *Journal of Geotechnical and Geoenvironmental Engineering* 124(5):396-405.

Sabetta F and A Pugliese. 1996. Estimation of response spectra and simulation of nonstationary earthquake ground motions. *Bulletin of the Seismological Society of America* 86(2):337−352.

Schnabel PB. 1973. *Effects of Local Geology and Distance from Source on Earthquake Ground Motions.* PhD Thesis, University of California, Berkeley, California.

Schnabel P, HB Seed, and J Lysmer. 1972a. Modification of Seismograph records for effects of local soil conditions. *Bulletin of the Seismological Society of America* 62(6):1649−1664.

Schnabel PB, J Lysmer, and HB Seed. 1972b. SHAKE, a Computer Program for Earthquake Response. Earthquake Engineering Research Center Report EERC 72-12, University of California at Berkeley.

Seed HB and IM Idriss. 1970. *Soil Moduli and Damping Factors for Dynamic Response Analysis*. Report No. EERC 70-10, University of California, Berkeley.

Silva WJ, N Abrahamson, G Toro, and C Costantino. 1996. *Description and Validation of the Stochastic Model*. Report Submitted to Brookhaven National Laboratory, Associated Universities, Inc. Upton, New York, Contract No. 770573.

Somerville PG and NA Abrahamson. 1995. *Prediction of Ground Motions for Thrust Earthquakes*. Report to the California Strong Motion Instrumentation Program (CSMIP), California Division of Mines and Geology, Sacramento, California.

Somerville P, N Collins, R Graves, A Pitarka, W Silva, and Y Zeng. 2006. Simulation of ground motion scaling characteristics for the NGA-E project. *Proceedings of the 8th National Conference on Earthquake Engineering*, April 18-22, San Francisco, California, paper No. 1789.

Spudich P, JR Bayless, JW Baker, BS-J Chiou, B Rowshandel, S Shahi, and P Somerville. 2013. *Final report of the NGA-West2 directivity working group*. PEER Report 2013/09, Pacific Earthquake Engineering Research Center, University of California, Berkeley, California.

Sun JI, R Golesorkhi, and HB Seed. 1988. *Dynamic Moduli and Damping Ratios for Cohesive Soils*. Report No. UCB/EERC-88/15, University of California, Berkeley.

Toro GR. 1995. Probabilistic Models of Site Velocity Profiles for Generic and Site-Specific Ground Motion Amplification Studies. Published as Appendix C of WJ Silva, N Abrahamson, G Toro, and C Costantino. 1996. *Description and validation of the stochastic ground motion model.* Report Submitted to Brookhaven National Laboratory, Associated Universities, Inc. Upton, New York, Contract No. 770573.

Toro GR. 1997. *Probabilistic Models of Site Velocity Profiles at the Savannah River Site, Aiken, South Carolina.* Report by Risk Engineering, Inc. to Pacific Engineering and Analysis. Published as an appendix in RC Lee, ME Maryak, and MD McHood. 1997. SRS Seismic Response Analysis and Design Basis Guidelines. WSRC-TR-97-0085, Rev. 0, Westinghouse Savannah River Company, Aiken, South Carolina:

Toro GR. 2005. *Site-wide probabilistic model of shear-wave velocity profiles at the Savannah River Site, Aiken, South Carolina.* WSRC-OS-2006-00514, Revision 1, prepared by Risk Engineering for Bechtel Savannah River Company.

Toro GR, NA Abrahamson, and JF Schneider. 1997. Models of strong ground motions from earthquakes in Central and Eastern North America: Best estimates and uncertainties. *Seismological Research Letters* 68(1):41−57.

Walling M, W Silva, and N Abrahamson. 2008. Nonlinear site amplification factors for constraining the NGA models. *Earthquake Spectra* 24(1):243−255.

Watson-Lamprey JA. 2014. *Capturing Directivity Effects in the Mean and Aleatory Variability of the NGA-West 2 Ground Motion Prediction Equations*. PEER Report, Pacific Earthquake Engineering Center, Berkeley, California.

Wells DL and KJ Coppersmith. 1994. New empirical relationships among magnitude, rupture length, rupture width, rupture area, and surface displacement. *Bulletin of the Seismological Society of America* 84(4):974−1002.

Youngs, RR. 2007. *Updated Site Response Analyses for the Waste Treatment Plant, DOE Hanford Site, Washington.* PNNL-16653, Pacific Northwest National Laboratory, Richland, Washington.

Youngs R, B-SJ Chiou, W Silva, and J Humphrey. 1997. Strong ground motion attenuation relationships for subduction zone earthquakes. *Seismological Research Letters* 68:58–73.

Zhao JX. 2011. Magnitude scaling in ground-motion prediction equations for response spectra from large subduction interface earthquakes from Japan. *Proceedings of 4th IASPEI/IAEE Symposium on Effects of Surface Geology on Seismic Motion*, UC Santa Barbara, August 23-26, 11 pp.

Zhao JX and M Lu. 2011. Magnitude-scaling rate in ground-motion prediction equations for response spectra from large, shallow crustal earthquakes. *Bulletin of the Seismological Society of America* 101(6):2643−2661.

Zhao JX, J Zhang, A Asano, Y Ohno, T Oouchi, T Takahashi, H Ogawa, K Irikura, HK Thio, PG Somerville, Y Fukushima, and Y Fukushima. 2006. Attenuation relations of strong ground motion in Japan using site classification based on predominant period. *Bulletin of the Seismological Society of America* 96(3):898−913.